Transactions of the ASME

Journal of Fluids Engineering

Published Quarterly by The American Society of Mechanical Engineers

VOLUME 114 • NUMBER 3 • SEPTEMBER 1992

(Contents continued on page 361)

FLUIDS ENGINEERING DIVISION
Technical Editor
DEMETRI P. TELIONIS (1995)
Executive Secretary
PAT WHITE (1995)
Technical Editor's Office
SAAD A. RAGAB
Calendar Editor
M. F. ACKERSON

Associate Technical Editors
R. K. AGARWAL (1994)
O. BAYSAL (1995)
MICHAEL L. BILLET (1992)
DENNIS M. BUSHNELL (1993)
N. A. CUMPSTY (1995)
FRANKLIN T. DODGE (1992)
CHIH-MING HO (1993)
THOMAS T. HUANG (1993)
J. A. C. HUMPHREY (1994)
O. C. JONES (1995)
E. E. MICHAELIDES (1992)
R. L. PANTON (1995)
ANDREA PROSPERETTI (1993)
M. W. REEKS (1995)

BOARD ON COMMUNICATIONS
Chairman and Vice-President
R. D. ROCKE

Members-at-Large
T. BARLOW, W. BEGELL, T. F. CONRY,
T. DEAR, J. KITTO, R. MATES, W. MORGAN,
E. M. PATTON, S. PATULSKI, R. E. REDER,
A. VAN DER SLUYS, F. M. WHITE,

President, **J. A. FALCON**
Exec. Dir.
D. L. BELDEN
Treasurer,
ROBERT A. BENNETT

PUBLISHING STAFF
Mng. Dir., Publ.,
CHARLES W. BEARDSLEY
Managing Editor,
CORNELIA MONAHAN
Production Asstistant, **MARISOL ANDINO**

Transactions of the ASME, Journal of Fluids Engineering (ISSN 0098-2202) is published quarterly (Mar., June, Sept., Dec.) for $130.00 per year by The American Society of Mechanical Engineers, 345 East 47th Street, New York, NY 10017. Second class postage paid at New York, NY and additional mailing offices. POSTMASTER: Send address changes to Transactions of the ASME, Journal of Fluids Engineering, c/o THE AMERICAN SOCIETY OF MECHANICAL ENGINEERS, 22 Law Drive, Box 2300, Fairfield, NJ 07007-2300. **CHANGES OF ADDRESS** must be received at Society headquarters seven weeks before they are to be effective. Please send old label and new address. **PRICES:** To members, $40.00, annually: to nonmembers, $130.00. Single Issue, $45.00. Add $20.00 for postage to countries outside the United States and Canada. **STATEMENT** from By-Laws. The Society shall not be responsible for statements or opinions advanced in papers or . . . printed in its publications (B7.1, Par. 3).
COPYRIGHT © 1992 by The American Society of Mechanical Engineers. Authorization to photocopy material for internal or personal use under circumstances not falling within the fair use provisions of the Copyright Act is granted by ASME to libraries and other users registered with the Copyright Clearance Center (CCC) Transactional Reporting Service provided that the base fee of $3.00 per article plus $.30 per page is paid directly to CCC, 27 Congress St., Salem, MA 01970. Request for special permission or bulk copying should be addressed to Reprints/Permission Department.
INDEXED by Applied Mechanics Reviews and Engineering Information, Inc. Canadian Goods & Services Tax Registration #126148048

Downloaded 03 Jun 2010 to 171.66.16.159. Redistribution subject to ASME license or copyright; see http://www.asme.org/terms/Terms_Use.cfm

Contents (continued)

Technical Briefs

Announcements and Special Notices

Journal of Fluids Engineering

Technical Forum

Questions in Fluid Mechanics

By Lloyd M. Trefethen[1]

We engineers and scientists pool our visions and communicate our queries and answers. But in our written communications we are long on pronouncing answers and short on posing questions. The typical paper contains not a single question. It would be wise for us as a society to sharpen our focus on questions.

The Editorial Board of the *Journal of Fluids Engineering* has decided to proceed with a sequence of columns on unanswered questions. This is the first of that series.

An "unanswered question" in this context is clearly not the rhetorical or textbook question. Questions should point to an area of inquiry where people are unable to explain observations, are unable to decide whether something is possible, or are unable to agree on an explanation. Also important are questions of definition, where understanding is held back by inadequacies of vocabulary. These kinds of questions have been the subject of the question sessions that have been held within the Fluids Engineering and the Heat Transfer Divisions of ASME since 1986.

Below are examples of the questions that are being asked. Not all questions go so deeply as these into the roots of our traditional ways of thinking:

> How can the atmosphere of Venus at cloud-top level be rotating fifty times as fast as the planet?
>
> Are there compliant surfaces that reduce turbulent drag?
>
> How should turbulence be defined?
>
> What are the fluid motions at the edge of a liquid contact line advancing over a solid surface?
>
> At what smallness of scale, and for what reasons, does the Navier Stokes equation cease to describe fluid motions?

Although entirely focused on fluid mechanics, these five questions are all quite different. Each represents a separate, important area of inquiry. The first is very specific, and the last is very broad. They also go from planetary scale to the nanometer scale of muscle fibers. Three have been around for a long time, two are quite new. What they possess in common is that each focuses attention on an area where we need to know more.

Planetary atmospheres? Little was knowable a generation ago, but measurements now possible and being made are exposing much that we don't understand. There is no current understanding of how the atmosphere of Venus maintains its motion while in contact with the comparatively stationary planet. This is a specific question with, probably, an eventual straightforward answer.

Compliant surfaces? For forty years, in part a result of curiosity about dolphin swimming speeds, this question has been the subject of many studies. Surprisingly, the jury is still out. This is an engineering question, with no apparent problem in definition of terms.

How to define turbulence? Definition is important in this arena, and this question pops up often, in varying ways. Its importance is illustrated by the extent to which answers to questions about turbulence can depend on what the questioners assume turbulence to be. For example, there is probably little difficulty with the preceding question about compliant surfaces; there would be wide agreement on what was meant by "turbulent drag." But if one asks, "Is turbulent flow chaotic," definitions would have to be examined. "How can one distinguish between waves and turbulence in the atmosphere?" Where waves stop and turbulence starts requires agreement on definitions, not yet achieved. One even has to be careful using the word "vortex," unlike "vorticity" which is rigorously defined. The question, "Does energy cascade upwards as well as downwards in scale in some turbulent flows?" is controversial, the answer apparently depending on definitions. Turbulence is complex, and its words need to be strictly defined if answers are to be unambiguous.

The triple-line, or contact-line, problem goes back a century or more, and is one of the basic questions in one of the largest sets of questions people ask, questions about multi-phase flows. Understanding accumulates slowly but, since the motions are closely tied to the complexities of both the geometric and chemical natures of the surface, an answer (or perhaps one should say a description of motions) is still not available.

Finally, the question of scale is frequently asked as the technological interest in micron- and nanometer-sized flows explodes. As with the triple-line question above, physical-chemistry phenomena become increasingly important as scale contracts below the micron level where, for example, electrical forces often dominate. Clearly there is a smallness at which molecular events take over and the concept of a fluid disappears. Some find the Navier-Stokes Equations quantitatively useful in liquids at the 10 nanometer scale. There also are experiments, being carefully done because of the unusual nature of the results, showing unexplained deviations from Navier Stokes, even in 10 micron diameter channels. This question is one of many in micro fluid dynamics, a field that will generate questions for years to come.

Is it useful to pose questions such as these? In the opinion

---

[1] Mechanical Engineering Department, Tufts University, Medford MA 02155. Fellow ASME.

of the writer, the answer is a resounding "Yes." Questions are an economical way to identify the boundaries where understanding ends and new learning begins. They shake up our ways of thinking, occasionally so severely as to force us to change a cherished paradigm, thus propelling us forward in the process of illuminating natural phenomena hitherto opaque.

Future columns will go further than simply presenting a few questions as in this introduction. Each will be concerned with a single question, plus commentary (perhaps even agreement) by people close to the topic. Please suggest questions for such columns.

Questions are also solicited for the next Forum on Unanswered Questions in Fluid Mechanics, to be held at the ASME Winter Annual Meeting in 1993. Additionally, a more informal discussion of questions will occur in an electronic newsletter "Questions in Fluid Mechanics," initiated in June of 1992. This is available through Internet, on request from qbank@pearl.tufts.edu.

Appreciation is expressed to the following: Behrouz Abedian, George Batchelor, Dennis Bushnell, Carl Gibson, Peter Gierasch, Joseph A. C. Humphrey, John Lienhard IV, John Lumly, Ronald Panton, Peter Wayner, and Jay Zemel.

U.S. Technological Competitiveness: A Fluids Engineers' Viewpoint

Introduction: Are Fluids Engineers Contributing to the Gridlock Syndromes of the Economy?

By Jules L. Dussourd[2]

You are a valued engineering professional at peak performance; why is your employer offering you this early retirement package?

You are a young graduate, on your first industrial job and you are surprised at a culture, so different in its priorities, ethics and technologies, from what you were taught in school.

You are a high school junior interested in sciences, but you are concerned whether a career in engineering will provide the quality of life you expect? And in thirty years from now, will there indeed be enough demand to guarantee a lifelong living?

Much has been said in the news that these predicaments are some of the consequences of a state of gridlock hampering competitiveness in the manufacturing industries. This state of gridlock can be defined as one in which the expectations of some major sectors of a society are in such a conflict, that they dramatically impede movement. In such a climate, priorities cannot be sorted out, because of the polarization and inflexibility of this society's agendas. Such problems are perhaps especially acute in the U.S., but there is evidence that similar situations are developing in other industrialized countries.

It also has been said that a comparable, albeit on a smaller scale, state of gridlock can be detected in engineering practices including those of fluids engineers. The efficient exchange of technology between the basic and the applied is too often impeded by rigidly entrenched imperatives, well meant as they may be. The result is an ineffective transfer and assimilation of knowledge by those who need it, thereby throttling our engineering productivity. Technologies may well be generated, but they are not being used.

An outcome of such failings can be found in long lead times when bringing new products to the market. This in turn contributes to time and cost overruns and to a reluctance by industry to undertake new developments. In a similar fashion, persistent problems with the product's performance or with quality control tend to throw road-blocks against product sophistication, which now is perceived as incompatible with product cost and product reliability.

This sluggishness in technology assimilation has been identified in surveys by NSF, NASA, MAPI and many others as the result of problems with technology transfer between the sectors responsible for education, research and product development. The state of gridlock, at least in the U.S., has been traced to technical and cultural blocks all along the transfer chain from the basic to the applied.

What are these impediments to greater efficiency? What can be done to speed up the transfer and the assimilation of technical know-how? Are there certain inbred practices or sacred cows in need of reexamination?

Societies like the ASME occupy a unique vantage point, astraddle to the industry, academia and government sectors of technology. It is the most important responsibility of those Societies to keep alive and well the vital communication links between the sectors. They are in a unique position to facilitate the interchange of information, be it technical, educational or managerial, to help young people make career choices, to synergize the needs of the industrial community with the resources offered by schools or government agencies.

It is the purpose of this column and those to follow to examine these issues, with the objective of improving the effectiveness of fluids engineers as they contribute to the quality of life in the world and to our own competitiveness within it. Indeed, the problems of fluids engineers are no different from those of the other related disciplines, but for this Journal the focus will be on what is of significance to fluids engineers.

These columns will be prepared by the speakers of a well attended panel on the subject of U.S. Competitiveness, held at the ASME 1991 WAM in Atlanta under the auspices of the Fluids Engineering Division. Their comments will be supplemented and recapped in condensed form, with the expectation that a new awareness can be created on how we can more effectively and more successfully discharge our responsibilities as fluids engineers in the current global climate.

The next column will identify certain practices which are seen as obstacles, contributing to gridlock in the fluids engineering community; and in the following ones, the panelists' viewpoints will be stated with ideas on how these obstacles may be overcome.

---

[2] Jules L. Dussourd & Associates, Fluids Engineering Consultants, Princeton, NJ 08540.

of the writer, the answer is a resounding "Yes." Questions are an economical way to identify the boundaries where understanding ends and new learning begins. They shake up our ways of thinking, occasionally so severely as to force us to change a cherished paradigm, thus propelling us forward in the process of illuminating natural phenomena hitherto opaque.

Future columns will go further than simply presenting a few questions as in this introduction. Each will be concerned with a single question, plus commentary (perhaps even agreement) by people close to the topic. Please suggest questions for such columns.

Questions are also solicited for the next Forum on Unanswered Questions in Fluid Mechanics, to be held at the ASME Winter Annual Meeting in 1993. Additionally, a more informal discussion of questions will occur in an electronic newsletter "Questions in Fluid Mechanics," initiated in June of 1992. This is available through Internet, on request from qbank@pearl.tufts.edu.

Appreciation is expressed to the following: Behrouz Abedian, George Batchelor, Dennis Bushnell, Carl Gibson, Peter Gierasch, Joseph A. C. Humphrey, John Lienhard IV, John Lumly, Ronald Panton, Peter Wayner, and Jay Zemel.

U.S. Technological Competitiveness: A Fluids Engineers' Viewpoint

Introduction: Are Fluids Engineers Contributing to the Gridlock Syndromes of the Economy?

By Jules L. Dussourd[2]

You are a valued engineering professional at peak performance; why is your employer offering you this early retirement package?

You are a young graduate, on your first industrial job and you are surprised at a culture, so different in its priorities, ethics and technologies, from what you were taught in school.

You are a high school junior interested in sciences, but you are concerned whether a career in engineering will provide the quality of life you expect? And in thirty years from now, will there indeed be enough demand to guarantee a lifelong living?

Much has been said in the news that these predicaments are some of the consequences of a state of gridlock hampering competitiveness in the manufacturing industries. This state of gridlock can be defined as one in which the expectations of some major sectors of a society are in such a conflict, that they dramatically impede movement. In such a climate, priorities cannot be sorted out, because of the polarization and inflexibility of this society's agendas. Such problems are perhaps especially acute in the U.S., but there is evidence that similar situations are developing in other industrialized countries.

It also has been said that a comparable, albeit on a smaller scale, state of gridlock can be detected in engineering practices including those of fluids engineers. The efficient exchange of technology between the basic and the applied is too often impeded by rigidly entrenched imperatives, well meant as they may be. The result is an ineffective transfer and assimilation of knowledge by those who need it, thereby throttling our engineering productivity. Technologies may well be generated, but they are not being used.

An outcome of such failings can be found in long lead times when bringing new products to the market. This in turn contributes to time and cost overruns and to a reluctance by industry to undertake new developments. In a similar fashion, persistent problems with the product's performance or with quality control tend to throw road-blocks against product sophistication, which now is perceived as incompatible with product cost and product reliability.

This sluggishness in technology assimilation has been identified in surveys by NSF, NASA, MAPI and many others as the result of problems with technology transfer between the sectors responsible for education, research and product development. The state of gridlock, at least in the U.S., has been traced to technical and cultural blocks all along the transfer chain from the basic to the applied.

What are these impediments to greater efficiency? What can be done to speed up the transfer and the assimilation of technical know-how? Are there certain inbred practices or sacred cows in need of reexamination?

Societies like the ASME occupy a unique vantage point, astraddle to the industry, academia and government sectors of technology. It is the most important responsibility of those Societies to keep alive and well the vital communication links between the sectors. They are in a unique position to facilitate the interchange of information, be it technical, educational or managerial, to help young people make career choices, to synergize the needs of the industrial community with the resources offered by schools or government agencies.

It is the purpose of this column and those to follow to examine these issues, with the objective of improving the effectiveness of fluids engineers as they contribute to the quality of life in the world and to our own competitiveness within it. Indeed, the problems of fluids engineers are no different from those of the other related disciplines, but for this Journal the focus will be on what is of significance to fluids engineers.

These columns will be prepared by the speakers of a well attended panel on the subject of U.S. Competitiveness, held at the ASME 1991 WAM in Atlanta under the auspices of the Fluids Engineering Division. Their comments will be supplemented and recapped in condensed form, with the expectation that a new awareness can be created on how we can more effectively and more successfully discharge our responsibilities as fluids engineers in the current global climate.

The next column will identify certain practices which are seen as obstacles, contributing to gridlock in the fluids engineering community; and in the following ones, the panelists' viewpoints will be stated with ideas on how these obstacles may be overcome.

---

[2] Jules L. Dussourd & Associates, Fluids Engineering Consultants, Princeton, NJ 08540.

Brief Reviews of Some Time-Dependent Flows

T. Sarpkaya
Mechanical Engineering,
Naval Postgraduate School,
Monterey, CA 93943

Separated flows in general and time-dependent flows in particular provide fertile territory for fundamental research in fluid dynamics and account for much of the subject matter. Thus, it is thought appropriate to review some of these unsteady flows with special emphasis on hydrodynamic applications which are, admittedly, of special interest to this writer: unsteady separation; characteristics of impulsively and nonimpulsively-started flow about cylinders; excursion of separation points on circular cylinders in oscillating flow; separation and other flow phenomena governing the unsteady maneuvers of large submerged bodies, and, finally, the three-dimensional footprints of subsurface vortical structures rising toward the free surface. It is hoped that these concise reviews will enhance communication between various groups of researchers, draw attention to many exciting phenomena in naval hydrodynamics, and inspire new research topics.

Unsteady Separation

The requirement for separation point specification constitutes the weakest link in the analysis of many steady and unsteady flows about bluff bodies. Even in *steady* two-dimensional flow, separation points can only be predicted approximately and with difficulty for laminar flows and hardly at all for turbulent flows. In unsteady flow, the mobile separation points (when they are not fixed by sharp edges), may undergo large excursions. This experimental fact renders the treatment of boundary layers on bluff bodies subjected to periodic wake return extremely difficult, particularly when the state of the boundary layer changes during a given cycle. As noted by Simpson (1989), in his incisive review of turbulent boundary-layer separation, "Imposed and self-induced unsteadiness strongly influence detached flows. Detachment from sharply diverging walls leads to large transitory stall in diffusers and flapping shear layers around bluff bodies. Large-scale motions produced in such cases do not contribute much to turbulent shear stresses but change the mean flow and produce low-frequency pressure fluctuations. This behavior makes such flows difficult to calculate."

A definition of separation that is meaningful for all kinds of *unsteady flows* has not yet been established. It is now a well-known fact that the use of vanishing surface shear stress or flow reversal as the criterion for separation is unacceptable. In unsteady flow, the surface shear can change sign with flow reversal, but without breakaway. Conversely, the boundary layer concept may break down before any flow reversal is encountered (Sears and Telionis, 1975). If the vanishing of the wall shear is not the appropriate criterion for separation, then what is? The many criteria that have been proposed require the use of laminar boundary-layer equations (some at an infinite Reynolds number!) and a priori knowledge of certain flow features, such as the freestream velocity, which must be identified either experimentally or theoretically.[1] The outer flow is usually unknown and affected in an unknown manner by the boundary layer itself.

It is proposed in calculations of laminar boundary layers, using boundary-layer equations, that if at some location the calculated flow is found to be on the point of separation then the corresponding real boundary layer will actually separate at or near that location, even though the boundary-layer approximation may have failed there. The reasoning continues that if, at some lcoation in the course of the calculations, the results show appreciable instead of small changes in some, but not all, boundary-layer characteristics (e.g., the displacement thickness as shown in Fig. 1), there must also be appreciable changes in the same characteristics at that location in the corresponding real boundary layer. A failure of the boundary-layer approximation is not readily distinguishable from a limit point reached when the imposed pressure gradient is no longer adequate to describe the flow, in view of the well-known fact that the boundary-layer development is very dependent on the imposed pressure gradient. It seems that the boundary-layer assumption contains the very seeds of singularity which lead to the abrupt demise of the latter at a finite time. The singularity

---

Contributed by the Fluids Engineering Division for publication in the JOURNAL OF FLUIDS ENGINEERING. Manuscript received by the Fluids Engineering Division August 21, 1990. Associate Technical Editor: D. P. Telionis.

[1] The so-called MRS criterion (the proposition that the unsteady separation is the simultaneous vanishing of the shear and the velocity at a point within the boundary layer, and away from the solid surface, in a coordinate convected with the separation velocity) requires a prioi knowledge of the speed of separation (Moore, 1957; Rott, 1956; Sears, 1956). Telionis and Tsahalis (1974) adopted the appearance of the Goldstein singularity in the solutions of the boundary layer equations as the most general definition of separation. The relation of the occurrence of Goldstein singularity to the streakline separation is not yet clear.

structures (spontaneous separation of the viscous layer) seem to describe only the initial genesis of the separating shear layer, within an asymptotically short time, *without interactive effects*, i.e., within the limitations of the classical boundary-layer formulation (Van Dommelen and Cowley, 1990) (see also, Williams, 1977; McCroskey, 1982; Van Dommelen and Shen, 1983; Telionis and Mathioulakis, 1984; Geissler, 1985; Poling and Telionis, 1986).

Historically, it was the occurrence and perplexing consequences of separation that led Prandtl in 1904 to his boundary-layer or "transition layer" concept. It is rather ironic that even though the boundary-layer theory has revolutionized fluid dynamics, the phenomenon which gave impetus to its inception is associated with its failure. Attempts to interpret the failure of an approximate formulation as a precursor to an instability or to a new state of bifurcation are not uncommon in fluid mechanics. For example, the failure of the quasi-cylindrical approximation in swirling flows approaching a critical state is proposed to correspond to vortex breakdown (Hall, 1972) (see also Sarpkaya, 1971). On the other hand, the solutions to the full Navier-Stokes equations do not exhibit a singular behavior at separation. It seems that the breakdown of the boundary-layer assumption should not be viewed as a precursor or a predictor to viscous separation. In fact, it may not be too meaningful to ask "what is the proper criterion to define the onset of separation in terms of the boundary-layer concept?" This is because of the generally accepted fact that it is the breakdown of the boundary-layer assumption that is responsible for the emergence of a numerical singularity within a finite time at a point in space, even if the domain of integration is free from such singularities at earlier times (see, e.g., Telionis, 1979, 1981). Is there a direct relation between the loss of convergence of the numerical scheme and the onset of separation in the form of a spontaneous *breaking away of unsteady flow from the surface?* This can be ascertained only by showing the existence of the same spikes (Fig. 1) in the displacement thickness in the Navier-Stokes calculations as in the boundary-layer calculations. However, the N-S calculations do not exhibit such spikes. The existing results suggest that the occurrence of a saddle point, initiation of a local shear layer[2] (Ho, 1986), ejection of vorticity, abrupt thickening of the boundary layer, occurrence of large transverse velocity, separation of the streakline from the wall are indicative of physical mechanisms for unsteady flow separation. It is also known that unsteady separation can move either upstream or downstream in different flow configurations, the *flow reversal* occurring in the case of upstream moving separation, but not in the case of downstream moving separation.

Taneda (1977, 1980) has concluded on the basis of his extensive flow visualization experiments that (i) the shedding of fluid particles from the wall is the most meaningful definition of separation for most time-dependent flows, (ii) this definition coincides with the Prandtl criterion in the case of steady two-dimensional flow over a fixed wall, and (iii) flow separation can be detected only by observing the integrated streaksheet. Although the streamline pattern changes according to the reference frame, the streakline pattern is invariant. One must keep in mind the fact that it is not always easy to determine accurately the streakline separation point from flow visualization. Also, it is not yet clear how to predict the motion of the streakline separation from a point undergoing large excursions on a body immersed in a time-dependent flow. Thus, not only the genesis but also the tracking, at large times, of the unsteady separation remains unresolved, particularly for impulsively-started or harmonically oscillating turbulent flow about bluff bodies. Beyond the time of spontaneous separation, the evolution of the large-scale unsteady recirculating structures is not yet calculable, except at low Reynolds numbers through the use of space-discretization methods and at unknown but relatively large Reynolds numbers through the use of Lagrangian or mixed Lagrangian-Eulerian vortex-element methods (Sarpkaya, 1989). Separated unsteady flows at large Reynolds numbers are lesser developed but of greater practical importance relative to other classical component disciplines of fluid mechanics and it appears that they will have to be investigated both experimentally and numerically for a long time to come.

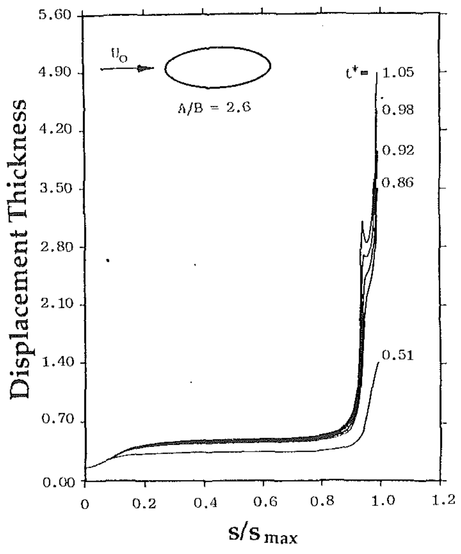

Fig. 1 Development of spikes in the displacement thickness of a Carafoli airfoil at times $t^* = 2\pi U_0 t/U_{max}$. *S* denotes the arc measured from the upstream stagnation point. The airfoil shown in figure is obtained by applying the conformal transformation: $z = \mathrm{Exp}(i\theta) + \mathrm{Exp}(-i\theta)/2.25$ to a unit circle. The body has a length-to-width ratio of 2.60 (for additional details, see Williams and Chen, 1990)

Impulsively/Nonimpulsively Started Flow

Among the numerous theoretical, numerical, and experimental investigations, impulsively-started steady flow about a circular cylinder has occupied a prominent place. The primary reasons for this are: It exhibits mobile separation points, it requires a relatively simple initial external flow, it is of intrinsic interest toward the understanding of the evolution of large-scale unsteady recirculating structures superimposed on a background of turbulence, it has practical importance in various aerodynamic applications (e.g., the impulsive flow analogy, flow about missiles, dynamic stall), it helps to understand the reasons and the consequences of the breakdown of the boundary-layer theory, and it provides the most fundamental case for the comparison and validation of various numerical methods and codes.

For a circular cylinder of radius R in a stream of velocity U_0, the classical potential flow is given by $U(x) = 2U_0\sin(x/R)$ where x denotes the arc measured from the upstream stagnation point. The earliest time at which the absolute value of dU/dx reaches its maximum is $t^* = U_0t/R = S/R = 0.351$ at $\theta = 180$ deg (the downstream stagnation point) (see, e.g., Schlichting, 1979, p. 418). The point of zero wall shear then moves toward the front stagnation point along the cylinder. The *instantaneous pattern* of streamlines shows a relatively thin layer of reverse flow embedded in the boundary layer. The reverse flow region is not a "closed bubble of fluid" in the boundary not exchanging fluid with its surroundings. At $t^* = 1.3$ to 1.4 (depending on the method of calculation) and

---

[2] According to Ho (1986), the local shear layer appears to be a generic flow module of the separated flows.

in the vicinity of $\theta = 115$ deg, the displacement thickness and the boundary layer begin to thicken locally and the viscous layer separates spontaneously. The point of separation rapidly moves to $\theta = 104.5$ deg, provided that the interaction between the outer flow and the separated region is ignored. In reality, the flow upstream of the separation point is strongly affected by the occurrence and motion of the separation point and by the circumstances leading to the formation, growth and motion of the wake. In any case, it is clear that *the definitions of unsteady separation on impulsively started cylinder depend on the imperfect nature of the boundary-layer equations, do not take into account the mutual interaction of the inner and outer flows, and do not enable one to make predictions on the evolution of the large-scale structures beyond the time of spontaneous separation*. Furthermore, the critical times and spontaneous behaviors noted above may depend not only on the shape of the body but also on the nonimpulsive nature of the flow since there can be no unique path to the time and space at which the boundary-layer equations will manifest a singularity.

Among the various numerical solutions of the evolution of large-scale structures in the wake of a circular cylinder, the works of Lecointe and Piquet (1984), Ta Phuoc Loc (1980), Ta Phuoc Loc and Bouard (1985), Chamberlain (1987), Rumsey (1988), Wang (1989), and Chang and Chern (1991a) are the more recent and relatively more accurate examples.

Thoman and Szewczyk (1969), among the first to calculate numerically the flow about a cylinder, found for $\mathrm{Re} = 4 \times 10^4$ that the drag coefficient C_d is very high at the impulsive start of flow, decays rapidly to a minimum that decreases with increasing Reynolds number, and then rises to a peak value of about 1.5 at $S/R \approx 4$ where S is the displacement of the ambient flow. The drag then decreases to its quasi-steady value at about $S/R \approx 9$ and remains nearly constant thereafter. This is rather remarkable in view of the fact that the steady-state value of the drag coefficient is reached even before a single vortex is shed! In Thoman and Szewczyk's (1969) calculations, the separation points reached their quasi-steady positions at about $S/R \approx 4$ for $\mathrm{Re} = 4 \times 10^4$. Likewise, the vorticity distribution about the cylinder showed only minor changes (near the base of the cylinder) for S/R larger than about 5.

Lecointe and Piquet (1984) used several compact schemes with the Navier-Stokes vorticity/stream function formulation to solve laminar flows around circular cylinders up to a Reynolds number of 9500. They studied both start-up and unsteady periodic phenomena. The predicted wake-region shape as a function of time showed good agreement with experimental flow visualizations. Ta Phuoc Loc (1980) solved the complete unsteady Navier-Stokes equations in vorticity/stream-function form, using a combination of second and fourth-order compact finite difference schemes. He obtained short-time *symmetric-wake* solutions at Reynolds numbers of 300, 550, and 1,000 and achieved good agreement with flow visualization results for both vortex size and center position. His calculations also showed clearly the small secondary vortices just behind the separation points. Ta Phuoc Loc and Bouard (1985) performed calculations at $\mathrm{Re} = 3{,}000$ and 9,500 using a fourth-order finite-difference technique for the Poisson equation for the stream function and a second-order technique for the vorticity-transport equation. They found good agreement between the numerical predictions and flow visualization. The calculations were confined, out of necessity, to relatively short times during which the wake became neither asymmetrical nor turbulent.

Chamberlain (1987) used a second-order fast Poisson solver based on FFT methods and found an accurate solution which agreed well with experiment and the previous computations. Rumsey (1988) used an upwind-biased implicit approximate factorization algorithm to calculate the impulsively started unsteady flow over a circular cylinder at a Reynolds number of 1200 and a Mach number of 0.3. Rumsey's results were in very good agreement with the previous calculations and showed, predictably enough, only a slight compressibility effect. Wang (1989) used the vorticity-stream function formulation and a third-order in time, second-order in space, three-level predictor-corrector finite-difference scheme to calculate a number of time-dependent flows about a circular cylinder. His impulsive flow calculations for Reynolds numbers up to 1000 agreed quite well with those obtained by others, both numerically and experimentally. Chang and Chern (1991a) devised a hybrid vortex algorithm and applied it to flow around an impulsively started circular cylinder. The numerical results (given only for $S/R < 6$) compared well with previous analytic, finite-difference and experimental results within the range of S/R values.

All numerical calculations using finite difference, finite element, or vortex-element methods (see e.g., Chang and Chern, 1991a, 1991b; Sarpkaya, 1989; Sarpkaya and Shoaff, 1979; Cheer, 1989; van der Vegt, 1988; Sarpkaya, 1975) have assumed an *impulsively*-started flow. This gives rise to the following questions: Is such a flow physically realizable? If not, for what values of the governing parameters a nonimpulsively-started flow may be regarded as an almost impulsively-started flow?

Several experimental investigations of impulsively-started flow around circular and rectangular cylinders have been carried out (Sarpkaya, 1966, 1978; Bouard and Coutanceau, 1980; Sarpkaya and Kline, 1982; Nagata et al., 1985; Sarpkaya and Ihrig, 1986). Bouard and Coutanceau (1980) investigated the shape and growth rate of the wake region behind the cylinder for Reynolds numbers between 40 and 10,000. Sarpkaya (1966, 1978) examined the evolution of the wake region and the development of the lift and drag forces with time for cylinders between Reynolds numbers of 15,000 and 120,000. Nagata et al. (1985) studied the start-up flow at Reynolds numbers between 250 and 1200, with the majority of the experiments performed at $\mathrm{Re} = 1200$. They gave detailed results for the time-evolution of the vortical region, boundary-layer parameters, and profile shapes at this Reynolds number. Sarpkaya and Kline (1982) examined the impulsively started flow about four types of bluff bodies. Sarpkaya and Ihrig (1986) performed experiments and vortex-element analysis of impulsively started flow about rectangular prisms and pointed out emphatically that one cannot generate a truly impulsive flow experimentally. In fact, experimental efforts to generate impulsive or uniformly accelerated flow at high Reynolds numbers may be hampered by the generation of compression and rarefaction waves and regions of intense cavitation (in liquids). Because of this reason at least one acceleration parameter such as $A_p = D(dU/dt)/V^2$ must be added to the list of the parameters governing the phenomenon for the simplest case of flow accelerating from rest (with $dU/dt =$ constant) and then reaching a constant velocity of V at the end of a prescribed acceleration period. In this case, the acceleration ramp levels off at $t_v = V/(dU/dt)$ or when $(S/R)_v = 1/A_p$. Thus, for $A_p = 1$, the acceleration period ends when the cylinder or the ambient flow has displaced one radius.

Figures 2(*a*) and 2(*b*) show representative drag and lift coefficients obtained by Sarpkaya (1978) for $A_p = 1$ (corresponding to a nearly impulsively started flow) at $\mathrm{Re} = 20{,}600 - 22{,}100$. A drag overshoot occurs at $S/R = 4$ in Fig. 2(*a*) where S is the actual displacement of the ambient flow. Depending on the unknown initial disturbances, the lift force exhibits wide variations from experiment to experiment as exemplified by Fig. 2(*b*). The period of vortex shedding decreases with increasing S/R. The Strouhal number increases from an initial value of about 0.17 to 0.205 within the range of S/R values shown in Fig. 2(*b*). The important facts to be noted in any run are that (i) at the time of drag overshoot, C_L is negligibly small (indicating that the vortex pair is still nearly symmetrical), (ii) the first reversal in the lift force occurs near $S/R = 12 - 14$,

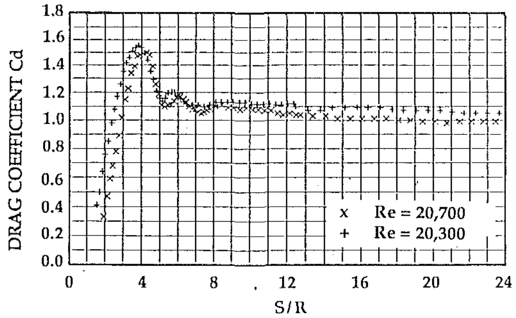

Fig. 2(a) Drag coefficient versus relative displacement (S/R) for A_p = 1 and Re ≈ 20,000. Note the drag overshoot at S/R ≈ 4.

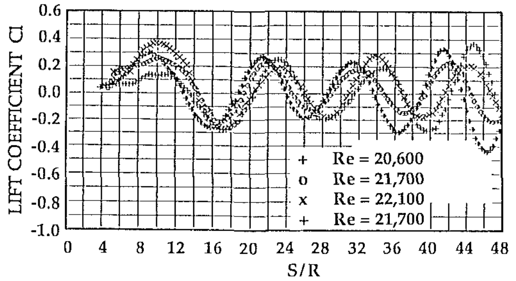

Fig. 2(b) Lift coefficient versus relative displacement (S/R) for A_p = 1 and Re = 20,600 − 22,100. Note the increase in vortex shedding frequency.

and (iii) in most cases, the period of lift oscillations decreases with increasing S/R.

The occurrence of a local maximum drag coefficient requires further discussion. During the initial and symmetric development of vortices (for S/R smaller than about 4), the vorticity rapidly accumulates in the wake. The symmetric vortices grow to sizes considerably larger than those which would be found in the later stages of the motion where the vortices shed alternatingly. However, the accumulation of vorticity and the reduction of the back pressure are not sufficient to explain the drag overshoot. The size of the wake region at S/R ≈ 4 is about one half of that at S/R ≈ 7 (see, e.g., Rumsey, 1988). Thus, simple vorticity accumulation is not sufficient for the C_d overshoot (note that for S/R larger than about 5, the vortex center does not change appreciably). The growth of the symmetric or nearly symmetric vortices (depending on the existing natural disturbances) is accompanied by other events. The so-called "α-phenomenon" (Bouard and Coutanceau, 1980) disappears between S/R ≈ 4.8 and 6.2, according to Rumsey's (1988) calculations at Re = 1200 (the range of S/R values, over which the said phenomenon disappears, depends on Re). The fact of the matter is that the pressure distribution in the vicinity of the secondary vortices changes accordingly. Finally, during the early stages of the motion the vorticity flux is expected to be considerably larger than the cross-wake transfer of oppositely-signed vorticity (in fact, this is one of the reasons for the rapid accumulation of vorticity). However, as the wake size grows and the vortices begin to exhibit asymmetry, as well as three-dimensionality, the cross-wake vorticity transfer is expected to increase significantly. It is surmised that it is the combination of the foregoing events that lead to the rapid rise and fall of the drag coefficient at or near S/R ≈ 4.5.

Figure 3(a) shows for A_p = 0.10 and 0.11, [corresponding to $(S/R)_v$ = 10 and 9.1, *the end of the acceleration period*], and for Re = 46,000 that C_d rises sharply to an initial value of $C_{din} = \pi A_p$ immediately after the start of motion and remains nearly constant for a distance of at least $\Delta(S/R) = 2$. For this flow, separation begins at the rear stagnation point after the flow has covered a distance of S/R = 0.52. The data shown in Fig. 3(a), and others (Sarpkaya, 1991), show that the effect of the symmetrically-growing small wake during a distance of about $\Delta(S/R)$ ≈ 1.5 on the total drag is negligible relative to that of the inertial force. As the flow continues to accelerate, C_d begins to rise almost linearly with S/R until the acceleration is removed or the boundary layer undergoes a transition. In Fig. 3(a), the acceleration is removed *rapidly* at S/R = 9.1 and 10, respectively, for the two cases shown. Clearly, C_d assumes its quasi-steady value almost immediately. The inflection in the rise of C_d, between S/R ≈ 5 and S/R ≈ 8, is due to the asymmetrical growth and shedding of the first vortex (see Fig. 3(b)). The secondary oscillations in C_d beyond S/R ≈ 8 are associated, as before, with the shedding of the additional vortices.

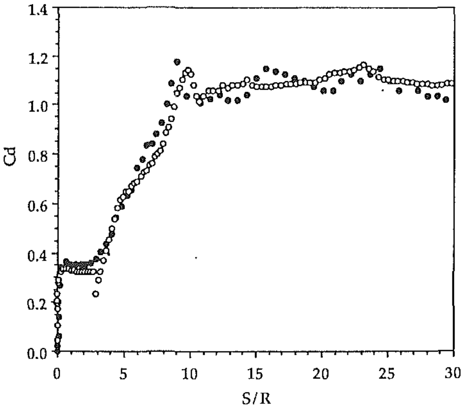

Fig. 3(a) Drag coefficient versus relative displacement for A_p = 0.10 (open circles) and for A_p = 0.11 (full circles). Note the significant difference between Figs. 2(a) and 3(a) showing the effect of initial acceleration.

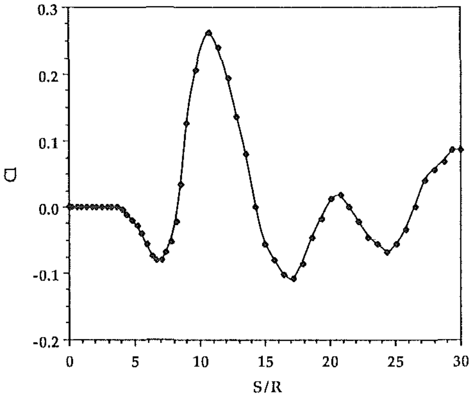

Fig. 3(b) Lift coefficient versus S/R for A_p = 0.11. Note that the shedding of the first vortex leads to a rather large lift force.

The behavior of the lift coefficient is also different from the previous case in several ways. The first vortex sheds at a smaller S/R value (at 7). The second vortex is often very large and sheds after a relative distance of $\Delta(S/R) = 4$ which corresponds to a Strouhal number of 0.25. However, the Strouhal number based on the first two minima is about 0.20. The data shown in Figs. 3(a) and 3(b) are typical of the data obtained with A_p values smaller than about 0.16.

In summary, (a) The relative distance S/R at which the local maximum drag coefficient occurs does not depend on the acceleration parameter A_p for A_p larger than about 0.27 (corresponding to an almost impulsively-started flow beyond the period of acceleration) and agrees reasonably well with the previous numerical predictions (Ta Phuoc Loc, 1980; Sarpkaya and Shoaff, 1979; Thoman and Szewczyk, 1969), based on impulsive start. (b) For accelerations which end near S/R ≈

5 (e.g., for $A_p = 0.2$), a smaller drag maximum occurs. (*c*) for A_p smaller than about 0.10 or 0.15, the drag coefficient remains nearly constant for S/R smaller than about 2 and the drag force is almost entirely due to the inertial effects [added mass plus the pressure gradient to accelerate the ambient flow, i.e., $C_i = F/(\pi\rho R^2 dU/dt) = 2$]. For $S/R > 2$, C_d rises almost linearly while exhibiting a small inflection due to the shedding of the very first vortex. The rise in C_d is halted either by the termination of the acceleration or by transition in the boundary layers (not discussed herein further). There is no drag overshoot and C_d reaches its quasi-steady value with usual lift-induced oscillations. (*d*) The inception and evolution of the lift force are sensitive to unknown and unknowable initial conditions. The lift force begins to develop for S/R larger than about 2, depending on A_p, initial disturbances and, probably, Re. (*e*) Impulsively started steady flow is a very special case of unsteady flows starting from rest and reaching a steady state over a time period. The existing numerical methods and codes should be applied to this type of unsteady flows. Such studies will help to resolve the consequences of a specific unsteady input of given type and duration (e.g., acceleration or deceleration or their combinations) on the subsequent stages of the motion of a viscous fluid. Furthermore, the simulations will provide an excellent opportunity to discover additional examples of the spontaneous breakdown of the boundary layer equations, many interesting and new vortex patterns, in addition to the well-known α and β phenomena (Bouard and Coutanceau, 1980), whose role on the understanding of time-dependent separation and resistance are worthy of study in their own right. It is also extremely desirable that the numerical calculations be carried out to S/R values considerably greater than 6 or so without imposing symmetry.

Separation on Cylinders in Oscillating Flow

Rapid acceleration or deceleration of flow from one steady state to another, *in times considerably smaller than the diffusion time*, results in a linear superposition of the initial fluid motion with the imposed irrotational motion. Subsequently, the two motions and their velocity fields interact nonlinearly and give rise to another state. In the case of flows subjected to varying accelerations and decelerations, with no steady-state to speak of, the motion of the separation points is indeed very complex. However, one can glean some useful information from two idealized states. If the flow is accelerated from a steady state, the existing boundary layer is washed downstream and a new boundary layer is created under the influence of the imposed flow. If the flow is decelerated, the existing boundary layer is washed upstream and the new boundary layer interacts with the existing wake returning to the body. In either case, one expects that some sort of a shear layer will develop between the existing boundary layer and the imposed flow.

The separated unsteady flow situations involving wake return, as in the case of a sinusoidally-oscillating flow about a cylinder, are an order of magnitude more complex and there are, at present, only a handful of applications of the finite-difference and vortex-element methods to their analysis (see, e.g., Baba and Miyata, 1987; Pattani and Olson, 1988; Mostafa, 1987; Murashige, et al., 1989; Wang, 1989; Justesen, 1991; Sarpkaya and Putzig, 1992a).

In steady flow, the position of the separation points is nearly stationary, except for small excursions about ±3 degrees (on a circular cylinder). Furthermore, the interference between the vortices and the body is confined mostly to the aft-body region. There is no obvious relation between the measured lift and drag coefficients and the excursion of the separation points. For example, while the separation angle remains nearly constant at about 80 degrees in the range of Reynolds numbers from about 2000 to 20,000, the drag coefficient increases from about 0.8 to 1.2 and the mean peak value of the lift coefficient varies anywhere from 0.0 to 0.6 (see, e.g., Sarpkaya and Isaacson, 1981).

For oscillating flows, the net effect of the shed vortices is twofold. First, their return to the body dramatically affects the boundary layer, outer flow, pressure distribution, and the generation and survival rate of the new vorticity. Second, they not only give rise to secondary separation points (during the early stages of the flow reversal) but also strongly affect the motion of the primary separation points. These effects are further compounded by the diffusion and decay of vortices and by the three-dimensional nature of the vortices (which give rise to cycle-to-cycle variations, numerous flow modes, etc.). However, it is clear from the previous discussion that the interaction of the imposed unsteadiness with the existing flow at a given instant depends on whether the velocity and acceleration are in the same or opposing direction (i.e., whether the acceleration is in the direction of the instantaneous velocity). The stronger and better correlated the returning vortices, the sharper and more pronounced the changes are in the pressure distribution on the body and in the integrated quantities such as lift, drag, and inertia coefficients.

In periodic flow, the mobile separation points (when they are not fixed by sharp edges), undergo large excursions (as much as 120 degrees during a given cycle of oscillation over a circular cylinder). This experimental fact renders the treatment of boundary layers on bluff bodies subjected to periodic wake return extremely difficult, particularly when the state of the boundary layer changes during a given cycle. As noted above, there are only a limited number of numerical predictions and the only recourse, at least at present, seems to be carefully conducted and fully documented laboratory experiments. In this effort, the flow visualization can serve as an excellent tool, not merely as an aid to understanding the physics of the flow but also as a means to acquire data.

Sarpkaya and Butterworth (1992b) performed a series of experiments in both a U-shaped oscillating-flow tunnel (Sarpkaya, 1976, 1977), with fixed smooth and rough circular cylinders, and in a small water basin with oscillating smooth cylinders of various sizes to cover a wide range of Reynolds numbers (Re = $U_m D/\nu$), Keulegan-Carpenter numbers ($K = U_m T/D$), and relative roughnesses (k/D). Here only the representative data obtained with a smooth cylinder at $K = 11.5$ are presented. Flow visualization was achieved either through the use of neutrally-buoyant beads or through the use of the electrolytic precipitation method. Illumination in a thin horizontal plane was accomplished by means of a quartz lamp housed inside the test cylinder. A motor-driven camera was attached to the cylinder and oscillated with it.

Figures 4–6 show typical photographs obtained with neutrally buoyant beads. The difficulty of determining the instantaneous position of the unsteady separation with great precision is obvious, even if it is taken to be the point at which the fluid particles shed from the wall (Taneda, 1977, 1980). The separation point excursions on cylinders mounted in the U-tunnel were determined with greater precision through the use of a "flow-direction-reversal probe" (also known as "differential-pressure probe" or "boundary-layer fence") which transversely projects only some thousandths of an inch into the boundary layer (Konstantinov and Dragnysh, 1955; Achenbach, 1971).

Even though every possible combination of the Keulegan-Carpenter number K, Reynolds number Re, and the relative roughness k/D represents an interesting state of oscillating flow about a circular cylinder, the approximate range of $8 < K < 13$ gives rise to a most interesting and precarious phenomenon known as the transverse vortex street. The case of $K = 11.5$ is chosen here to illustrate this intriguing phenomenon and the number of separation points which can occur simultaneously.

Figure 7 shows the excursion of the separation points over two cycles of flow oscillation (for easier comprehension) and

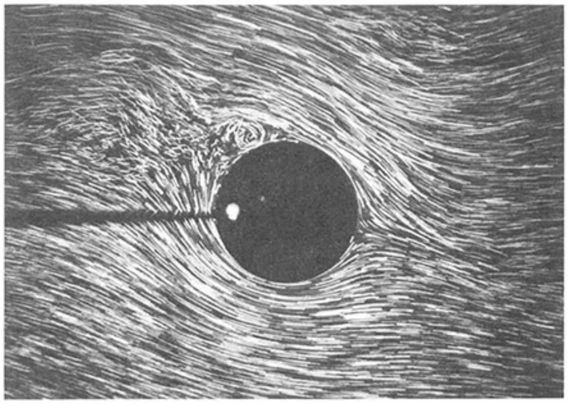

Fig. 4 Sinusoidally-oscillating flow about a circular cylinder, $K = 11.5$ and $t/T \approx 0$ (see also Figs. 7 and 8(*a*))

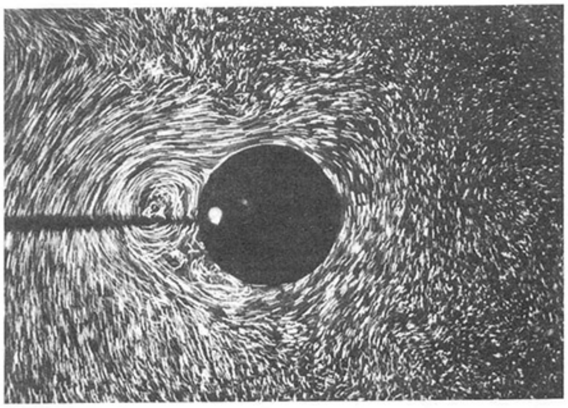

Fig. 5 Sinusoidally oscillating flow about a circular cylinder, $K = 11.5$ and $t/T \approx 0.25$ (see also Figs. 7 and 8(*c*))

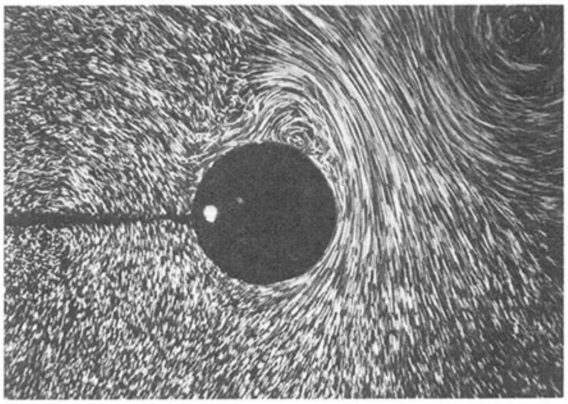

Fig. 6 Sinusoidally oscillating flow about a circular cylinder, $K = 11.5$ and $t/T \approx 0.65$ (see also Figs. 7 and 8(*f*))

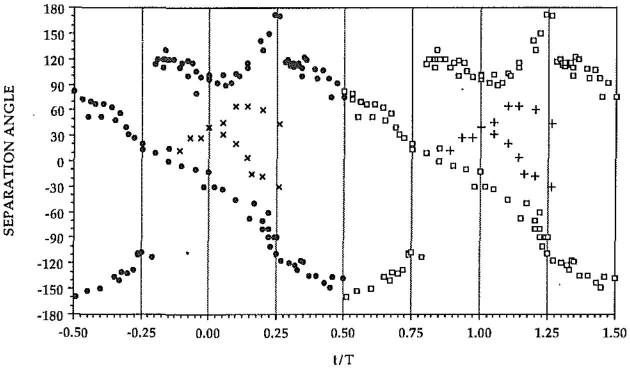

Fig. 7 Separation angle versus time for $K = 11.5$ and $Re = 37{,}000$ (symbols × and + denote secondary separations)

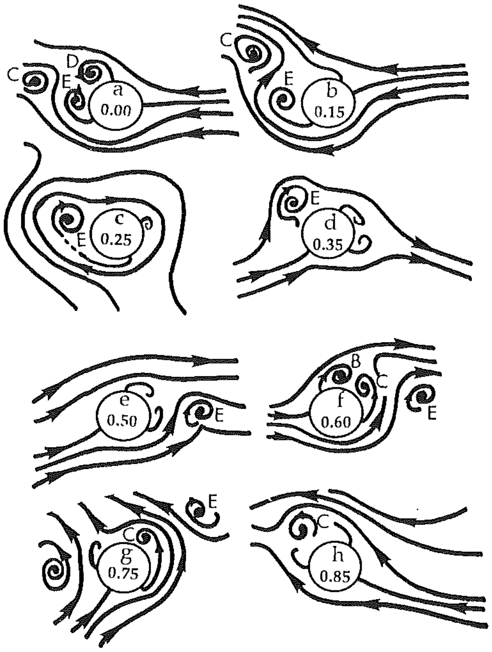

Fig. 8(*a*-*h*) Sketches of the evolution of the transverse vortex street for $K = 11.5$ and $Re = 37{,}000$

Figs. 8(*a*) through 8(*h*) show the evolution of the wake over a cycle for $K = 11.5$. In the interval $0 < t/T < 0.25$, the velocity of the ambient flow (directed to the left) decelerates from a maximum to zero as shown in Figs. 8(*a*)-8(*c*). This motion, plus the presence of vortex *C*, gives rise to the vortices *D* and *E*. The primary separation points are at about $\theta_s = -40$ and 110 degrees (measured from $x = -R$, $y = 0$). As the ambient flow comes to a full stop, vortex *D* is gradually annihilated partly due to the countersign vorticity it generates on the cylinder (also with some rebounding effect) and partly due to the overlapping of oppositely signed vorticity of vortices *D* and *E*. The vortex *E* grows and occupies a temporary position near $\theta = 60$ deg at $t/T = 0.25$ and the separation points move to about -110 and 130 degrees. As seen in Fig. 7, the primary separation points are not the only separation points on the cylinder. There are at least two more clearly identifiable separation points (secondary separations) on the cylinder in the wake region, situated between the primary separation points. In fact, there may be as many as four separation points on the cylinder at particular times in the cycle (e.g., at $t/T = 0.15$, or 1.15).

In the interval $0.25 < t/T < 0.50$, the flow accelerates to its maximum velocity (Fig. 8(*e*)). This causes the vortex *E* to move rapidly around and away from the cylinder. Furthermore, a new pair of counter-rotating vortices are generated (*B* and *C* in Fig. 8(*f*) where the separations are at approximately 60 and -140 degrees) partly in response to the acceleration of the cylinder and partly in response to the presence of vortex *E*. In the interval $0.50 < t/T < 0.75$, the cylinder decelerates to $U = 0$ (Figs. 8(*e*)-8(*g*)) and the vortex *B* gets annihilated for the very reasons leading to the annihilation of vortex *D* (Fig. 8(*a*)-8(*b*)). Subsequently, the cylinder reverses its direction and the vortex *C* in Fig. 8(*g*) plays the same role as the vortex *E* in Fig. 8(*d*). Then the cycle repeats itself, giving rise to a half transverse vortex street, in the $+y$ direction only, comprised of vortices like *C* and *E*. In the experiments it is possible to see as many as six such vortices at any one time.

The scatter in the data is not surprising in view of the methods available for the determination of the separation points and in view of the time-dependent nature of the phenomenon. In any case, it is clear that the numerical prediction of the excursion of multiple separation points in time-dependent flow and the development of methods to predict the instantaneous pressure distribution and the force acting on the body present extremely complex challenging problems.

As noted earlier, there exists only a handful of applications of the finite-difference and vortex-element methods to the analysis of sinusoidally oscillating flow about a smooth circular cylinder. A finite-difference analysis for a sinusoidally oscillating ambient flow about a circular cylinder at Keulegan-Carpenter numbers $K = 5$ (Re = 1000) and $K = 7$ (Re = 700) has been attempted by Baba and Miyata (1987), assuming a physically unrealistic symmetric wake in both simulations. Their results have shown that the calculations can be carried out only for short times (less than two cycles of flow oscillation) with a non-super computer. Murashige et al. (1989) have used a similar method to analyze three cases ($K = 5$, 7, and 10) at higher Reynolds numbers around 10^4. The flow was perturbed by artificial means to trigger asymmetry. At $K = 10$, a transverse vortex street appeared, in agreement with experimental observations. Wang (1989) used, as previously noted, the vorticity-stream function formulation to calculate a number of time-dependent flows about a circular cylinder. His predictions for an oscillating flow at relatively small K values were quite satisfactory. However, at $K = 10$, he was unable to obtain the transverse vortex street. Justesen (1991) used the stream-function/vorticity-formulation of the Navier-Stokes equations to analyze the flow around a circular cylinder in planar oscillating flow with K smaller than 26. Justesen introduced a straining parameter "a" in order to better resolve the large gradients near the cylinder surface. This is in addition to the logarithmic straining, commonly used as part of the transformations, for a better resolution of the gradients near the body. Evidently, Justesen's transformation for $a = 0$ defaults to the logarithmic straining. However, "a" becomes another disposable parameter, dependent on at least K and Re. Justesen had to choose judiciously the value of the straining parameter for each K in order to achieve drag and inertia coefficients in satisfactory agreement with those obtained experimentally.

Sarpkaya and Putzig (1992a) used the vorticity-stream function formulation of Wang (1989) to carry out numerical experiments on sinusoidally-oscillating flow (with zero mean) and on sinusoidally-pulsating flow (with non-zero mean, i.e., the in-line oscillations of a cylinder in uniform flow). The results (both numerical and experimental) have revealed, for the first time, the existence of a very interesting wake comprised of three rows of heterostrophic vortices (see Fig. 9) at certain Keulegan-Carpenter numbers and Reynolds numbers ($K \approx 4$, Re ≈ 800) and relative current velocities, ($V_r = V_c/U_m \approx 0.6 - 0.7$). For V_r larger than about one, the vortex wake returned to the asymmetric mode, as in a regular vortex street. The calculations of resistance in co-existing flows have shown that the inertia as well as the drag coefficients for $K = 4 - 6$ are in reasonable agreement with those obtained experimentally at corresponding V_r values.

Numerical experiments with non-sinusoidal but periodic oscillations have shown (for details, see Sarpkaya and Putzig, 1992a) that the three-row vortex wake does not occur and the wake is comprised of a series of relatively active and inactive vortical regions. The inactive regions result from the periods of rapid acceleration and the active regions from the time intervals during which the velocity is nearly steady. More significantly, however, the repetitive but non-sinusoidal nature of the flow causes dramatic changes in the in-line as well as the transverse force. Parts of the cycle become "inertia dominated" and parts of the cycle become "drag dominated." Had the flow been non-repetitive and non-sinusoidal (e.g., Gaussian), the drag and inertia dominated regions even at high K values would have randomly occurred throughout the history of the motion. It is because of this reason that it has not been easy to compare the ocean data with those obtained with planar sinusoidal oscillations under idealized conditions. The wake surrounding the body and the force-transfer coefficients exhibit surprising sensitivity in certain ranges of the governing parameters (K, Re, k/D, and V_r). For example, the drag coefficient at low K is very sensitive to the phase angle. The inertia coefficient is very sensitive to a number of parameters, in particular, the coherence of the flow along the cylinder, in the intermediate K range (where the transverse vortex street takes place). Such sensitivities are not uncommon in fluid mechanics. For example, free shear flows and low-Reynolds-number flows about cylinders are very sensitive to the spectral content of low level excitation. Small, periodic, free-stream-velocity perturbations can drastically alter the growth and mixing rate of a turbulent shear layer or wake embedded in a freestream. However, the spectral content of the ocean environment is expected to cover all possible mechanisms of excitation. Thus, small scale laboratory experiments, *particularly at very low Reynolds numbers*, may have very little or nothing to do with the sea truth, even though they may be of scientific interest in their own right.

Unsteady Motion of Large Submerged Bodies

Unsteady hydrodynamic phenomena are of far-reaching consequence in naval operations. They limit the speed, range, stability, and quiet operation of naval vessels, ordnance, and other underwater objects; the ability to detect or conceal acoustic signals while underway; and diverse ocean engineering operations on and under the sea. At the same time, they allow the possibility for detection and surveillance of others. It is the purpose of research in naval hydrodynamics to weaken continually the restrictions such phenomena impose on operations and at the same time to exploit the opportunities they offer. It has long been recognized that this requires a continual and sophisticated research effort at all levels, from basic to applied, because the motion of a submarine in the ocean environment involves some of the most complex fluid-structure interaction problems. For example, the steady and unsteady characteristics of ship and submarine wakes in the region of the stern, and especially with regard to the effect of the wake and rolled-up body vortices on propulsor unsteadiness, and the consequences for noise and hull vibrations are important

Fig. 9 Oscillatory plus mean flow about a circular cylinder and the evolution of three rows of heterostrophic vortices ($K = 4$, Re = 800, $V_c/U_m = 0.65$)

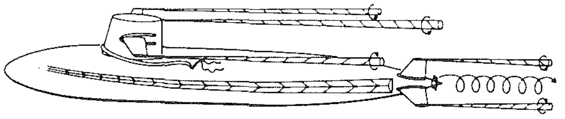

Fig. 10 Typical vortex structure about a submerged body (from Lugt, 1981)

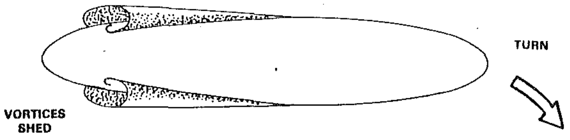

Fig. 11 Streamwise vortices generated by three-dimensional separation (from Chang and Purtell, 1986)

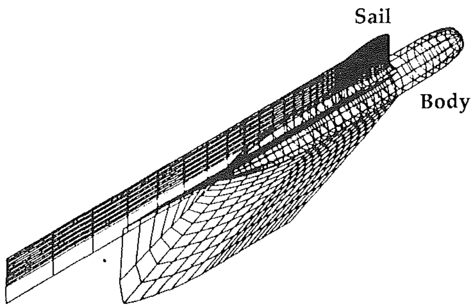

Fig. 12 Hull-sail configuration and vortex wakes (from Conway and Mackay, 1990)

problems of great concern. At present, too little is known in depth about the flow at the stern of ships and submarines (see, e.g., Fig. 10 and Lugt, 1981) and the footprints of their ensuing wakes in homogeneous and stratified media.

When an axisymmetric body moves at a sufficiently large angle of attack, the boundary layer vorticity may lift off the surface and sheets of vorticity are convected downstream while rolling up into streamwise vortices on the leeward side of the body (Fig. 11). This is quite similar to the vortex-sheet roll up over sharp-edged wings (e.g., a Delta-wing) with the added complexities that the separation lines for an axisymmetric body are not fixed or known a priori and that the *afterbody* (part of the body downstream of the separation lines), protruding into the wake as it does, plays a significantly different roll in the coiling of the vortices relative to that over a delta wing. This separation and roll-up phenomenon, known as the cross-plane separation, occurs on almost all maneuvering bodies at sufficiently large angles of attack. The roll-up of the vortices and their subsequent evolution are extremely important for the proper design of a submerged body (Sarpkaya and Kline, 1982) and more important for the determination of the interaction of the vortices with the stern and the propulsion system. It is this interaction that determines the maneuverability and control of a submerged body and the vibration and noise transmitted to the body by the propulsion system. When such a body is subjected to a turn of small radius, the local angle of attack varies significantly along the length of the body and will, in general, even reverse slightly near the bow.

The need for the solution and the complexity of hydrodynamic problems encountered in the design of submerged bodies have been recognized for over 50 years. However, their extreme complexity has prevented the development of reliable analytical tools. A satisfactory numerical model would enable one to calculate the complete topological structure of three-dimensional separated flows, i.e., the development of the turbulent boundary layer, separation lines, the evolution of the roll-up of vortex sheets and their subsequent trajectory. The problems noted above are sufficiently difficult even for a simple axisymmetric body moving at a constant angle of attack. Considerable work has been done on unsteady laminar boundary layer on impulsively-started prolate spheroids and in particular on the boundary layer along the symmetry plane (Wang, 1972).

There are a number of two and three-dimensional potential flow models (some of these are even called rational methods!). These methods suffer from the necessity to specify the separation lines (see, e.g., Thrasher, 1982; Chang and Purtell, 1986; Xu and Wang, 1988). Numerous approximations have been introduced to calculate the shed vorticity and none could be considered satisfactory or contributing to the understanding of the physics of the phenomenon. In relatively more sophisticated potential flow models, the external surface (a source distribution), the camber surfaces of lifting components (e.g., a bilinear doublet distribution) and the wake surfaces (spanwise linear doublet distribution) are replaced by a large number of panels. The cross-flow separation lines on the body are either specified arbitrarily (on the basis of past experience with bluff bodies) or approximately determined from flow visualization experiments, at a much smaller Reynolds number (see e.g., Fig. 12, reproduced from Conway and Mackay, 1990).

There are a number of Navier-Stokes computations of steady separated vortical flows past prolate spheroids at incidence (Newsome and Kandil, 1987; Shirayama and Kuwahara, 1987; Panaras and Steger, 1988; Wong et al., 1989). These use the unsteady incompressible thin-layer Navier-Stokes equations and the unsteady compressible thin-layer Navier-Stokes equations. In general, the two sets of the Navier-Stokes equations are solved using a pseudo-time stepping scheme on a curvilinear grid. The Baldwin and Lomax algebraic eddy viscosity model is used to model the turbulent flow. Even for steady ambient flow, the predictions are not quite satisfactory as far as the skin friction coefficient and the details of the primary and secondary vortices are concerned. Furthermore, one needs better transition and turbulence models than the over-simplified approach of switching on a turbulence model at a prescribed position (Wong et al., 1989). A schematic representation of the pattern of vorticity lines near a spheroid at incidence is shown in Figs. 13(*a–c*) and particle paths and surface streamlines on a longer spheroid at 30-degree incidence are shown in Fig. 13(*d*) (reproduced from Shirayama and Kuwahara, 1987).

The problems to be dealt with become even more difficult, both numerically and experimentally, when the body is subjected to a turn. Experiments on turning models are conducted through the use of a rotating arm. The motion of the body makes the measurement of detailed velocity and pressure distribution somewhat difficult. Clearly, a stationary model in a water or wind tunnel would be preferable, but the curving shear flow required for a turn would be nearly impossible to achieve (even though it has been tried). One approximate approach is the transformation of *the straight body in a curving flow to an appropriate curved body in a straight flow* (see Fig. 14). In two dimensions, this merely involves a logarithmic conformal transformation. In three-dimensional flow this approach has been further approximated so that the said transformation is applied to each plane of the body parallel to the plane of motion (Chang and Purtell, 1986).

As far as the numerical work is concerned, the existing methods require information on the location of separation lines either from boundary layer calculations or from approximate separation criteria [e.g., Stratford's (1959) turbulent separation criteria for 2-D flows], or experiments.

Chang and Purtell (1986) developed a numerical method for computing flow separation from a long three-dimensional body, based on the potential flow approach. By considering the similarities of the local separating cross-flow to a two-dimensional separation, they have derived a Kutta-like condition and incorporated it into the method of calculation of the separated

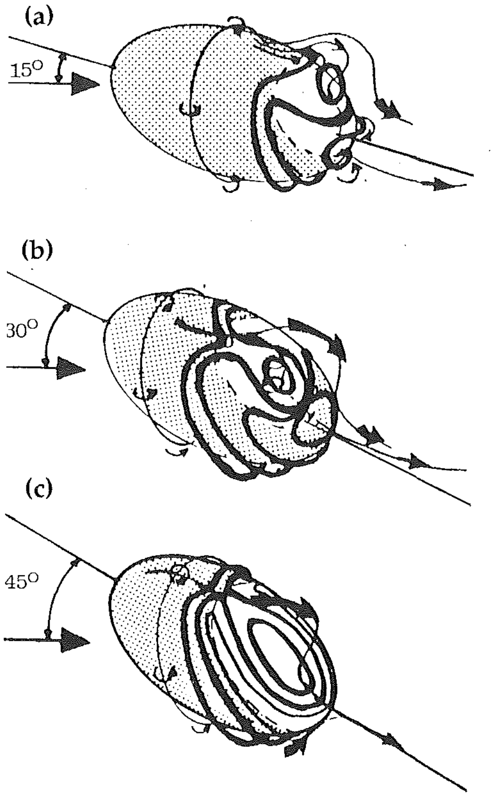

Fig. 13(*a–c*) Schematic representation of vorticity lines near a spheroid for various angles of incidence (from Shirayama and Kuwahara, 1987)

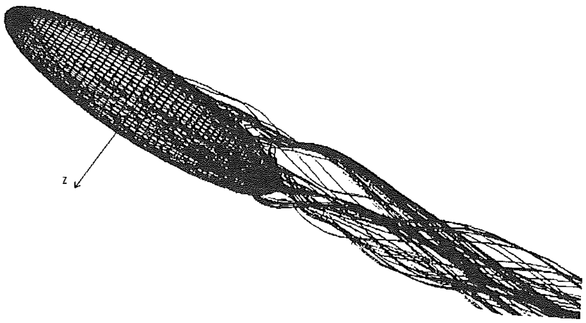

Fig. 13(*d*) Particle paths and surface streamlines for Re = 10,000 on a spheroid at 30 deg. incidence (from Shirayama and Kuwahara, 1987)

vortex sheet. A boundary layer model was used to predict the locations of the surface shear convergence lines. Computations were compared with experiments for an ogive-cylinder and prolate spheroid at angle of attack. As far as the turning body is concerned, they have developed a method to transform the body and the flow field into a curved body in a straight flow.

The submerged bodies encountered in the oceans are not simple axisymmetric bodies (autonomous underwater vehicles, submarines, offshore structures). For example, the asymmetry of a submarine (say because of sail), introduces reactions in the vertical plane in response to the imposed motion, such as a turn, in the horizontal plane. These reactions take the form of a downward force on the hull aft of the sail and, in consequence, give rise to a bow-up pitching moment. The analysis of such motions and the resulting non-axisymmetric flows offer many challenges which are not only timely from a practical point of view but also extremely important for increasing the physics content of our understanding of the hydrodynamic phenomena.

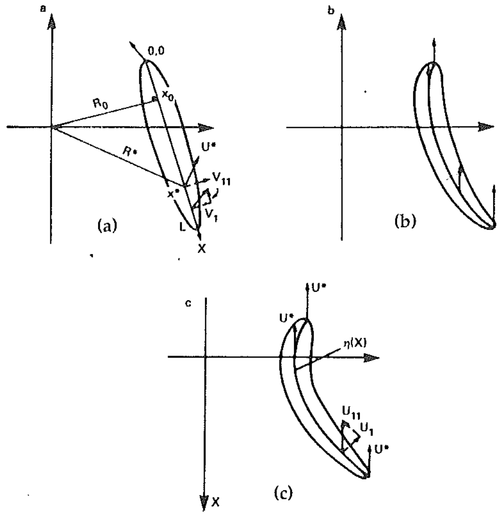

Fig. 14 Turning body dynamics: (*a*) Physical plane; (*b*) Curved body preserving angle of attack but with varying velocity magnitude; (*c*) Curved body preserving crossflow components and having constant forward velocity (from Chang and Purtell, 1986).

Vortex/Free-Surface Interactions

The motion of ships and submarines in homogeneous as well as stratified media gives rise to very complex turbulent wakes, Kelvin waves, internal waves, axial vortices (in the bow region), helical vortices (shed by the propeller), and a whole host of other phenomena such as bubble entrainment, surfactant transport and slicks, propeller cavitation, etc. These, in turn, may give rise to free surface signatures which can be detectable by both acoustic and non-acoustic means. This is the basis of current intense interest in the interaction as well as remote observation of internal waves, wakes, and vortices with the free surface.

Ship wakes produce a three-dimensional complex signature, comprised of a narrow dark band bordered by two bright lines in synthetic-aperture-radar (SAR) images (see, e.g., Lyden et al., 1988, and Figs. 15(*a*) and 15(*b*)). The dark band is the most prominent of all the signatures and is seen many kilometers downstream at all angles to the SAR azimuth direction even under severe weather conditions. It signifies the suppression of waves at the Bragg frequency as a consequence of various *short-wave-damping phenomena* such as turbulence, surface-active materials, and the redistribution of surface impurities to the surface by bubbles. The two bright lines, on the other hand, manifest themselves only in light winds and signify the occurrence of a range of waves which happen to be near the Bragg wavelength, possibly, as a consequence of the interaction between *quasi-two-dimensional and three-dimensional turbulent motions near the free surface and the restructuring and modulation of this interaction by wind*, unsteady Kelvin-wave-like disturbances, wave breaking, and momentum wake, just to name a few of the existing proposals. The central intent of this section is neither a discussion of the remote sensing of surface-ship wakes nor the establishment of cause-and-effect relationships for the observed events noted above, but, rather, to describe a number of kernel experiments, conducted during the past few years, which could eventually serve to elucidate the basic fluid mechanics phenomena relevant to the understanding of quasi-coherent, near-free-surface turbulence structures.

Turbulent flow near surfaces is not uncommon and there has been intense interest in understanding the behavior of vortices near a wall and the physics of the mechanisms sustaining the turbulent behavior (Robinson, 1991). Thus, it is not surprising that there should be turbulent flows at and near

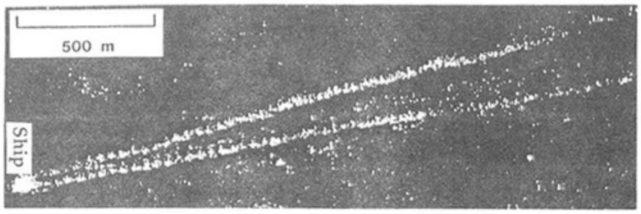

Fig. 15(*a*) The Synthetic Aperture Radar (SAR) image of a V-shaped narrow dark band bordered by two bright lines (from Lyden et al., 1988)

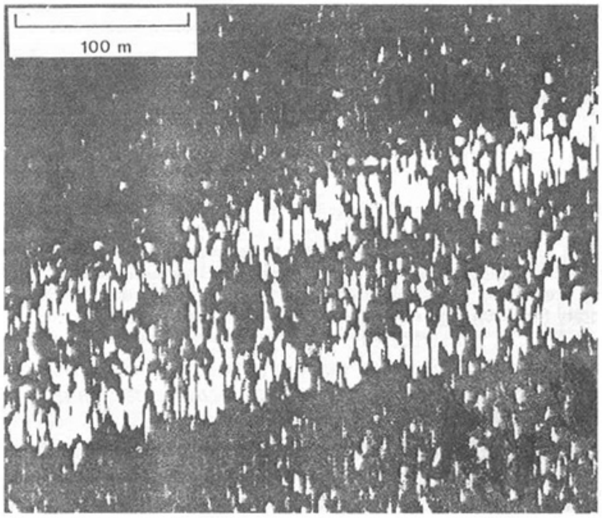

Fig. 15(*b*) The close-up view of a segment of the SAR image shown in Fig. 15(*a*)

deformable surfaces or fluid interfaces, in addition to various types of waves, due to complex ship wakes. What is rather surprising is that the resulting turbulent wake (in part, due to vortical motions) should give rise to coherent structures capable of absorbing the incident electromagnetic waves (negative spectral perturbation) for unexpectedly long times even under real ocean ambient conditions. This leads to two generic questions regarding the behavior of turbulence at the free surface: (1) How are the coherent structures created at the interface and what dynamical processes are responsible for their life cycle? (2) What characteristics of these structures (e.g., scale, shape, motion, mutual interaction) are responsible for the absorption of the incident electromagnetic waves?

Controlled laboratory experiments on free surface structures were first conducted by Sarpkaya in October 1983, as a continuation of his work on trailing vortices in homogeneous and density stratified media (Sarpkaya, 1983). These observations and measurements were reported by Sarpkaya and Henderson (Sarpkaya and Henderson, 1984, 1985) and by Sarpkaya (1985, 1986). They have shown that a pair of ascending vortices shed by a lifting surface (moving at a negative angle of attack) may interact with the free surface and give rise to scars and striations. The striations are essentially three-dimensional free-surface disturbances, normal to the direction of motion of the lifting surface (see Figs. 16–18). Sarpkaya and Suthon (1991) have shown that the scars are small free-surface depressions, comprised of many randomly distributed whirls (normal vorticity connecting with the free surface), and come into existence at the two ends of the striations and undergo mutual annihilation, dissipation, pairing, and merging. The striations come into existence as a subsurface instability, i.e., the free-surface proximity is not necessary but helps the striations to grow nonlinearly to larger amplitudes, depending on the prevailing free surface conditions (existing disturbances, contaminants, wind, current). In summary, an ascending laminar trailing vortex pair gives rise to two new components of vorticity: cross-axis vorticity in the striations and normal vorticity in the scars. The latter appears in part as distributed background vorticity and in (greater) part as randomly-distributed discrete structures (CW- and CCW-rotating whirls of various strengths), confined into a relatively narrow band.

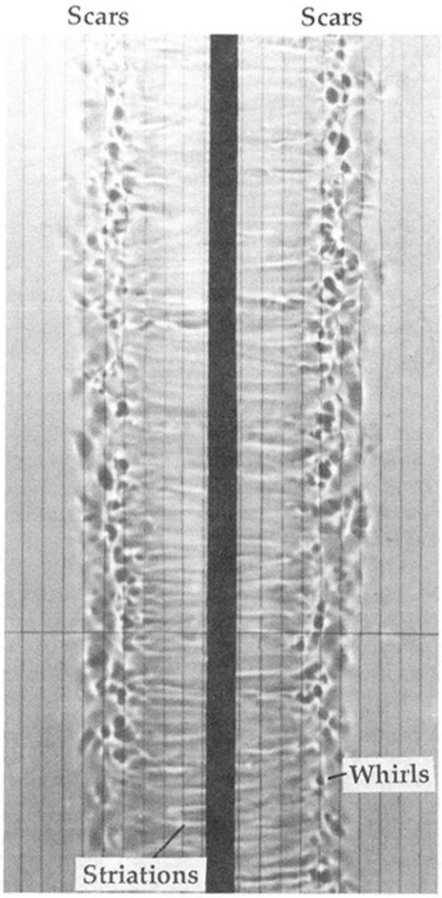

Fig. 16 A Shadograph picture showing the evolution of surface scars and striations above a trailing vortex couple. The black stripe is a narrow slit in a foam along the middle of the towing tank. The vortices (not seen in photograph) are generated by a delta wing.

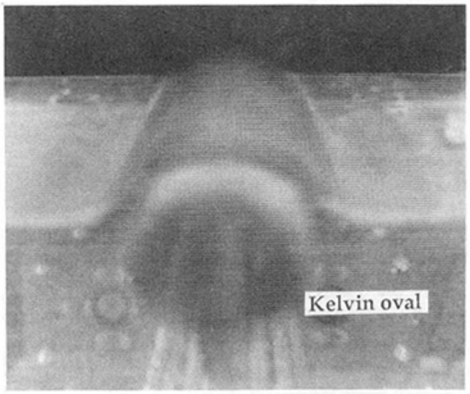

Fig. 17 The early stages of the formation of a dome-shaped surface deformation above a Kelvin oval. Note the absence of waves on either side of the dome.

When the vortices migrate large distances upward, they undergo various types of instabilities. Several theories have been proposed to explain the instabilities associated with the trailing vortices: Crow instability (Crow, 1970), Moore and Saffman (1973) instability, Batchelor's (1964) swirling flow instability, Singh and Uberoi's (1976) helical mode instability, and the free-stream turbulence proposals of Corsiglia et al. (1973), and Baker et al. (1974). Only the helical instabilities proposed by Singh and Uberoi (1976), and observed by Sarp-

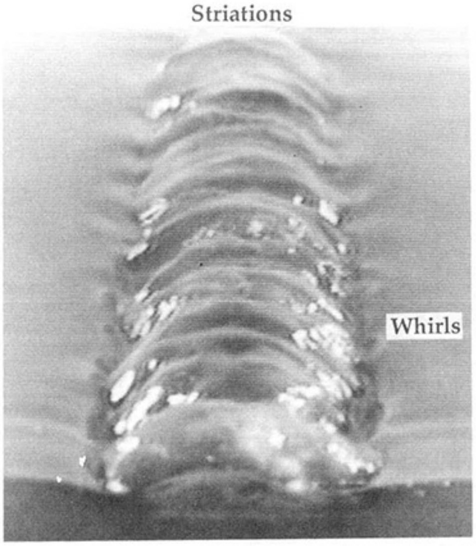

Fig. 18 The scar front during the later stages of motion. Whirl pairs are clearly visible. Note the absence of waves beyond the scars.

kaya (1985), appear to provide a satisfactory explanation. In fact, as shown by Sarpkaya (1992c), *tentacle-like sheets*, resulting from the helical instabilities, are thrown away from the outer edges of the core of a turbulent vortex. In other words, the vortex peels off randomly and sheds vorticity along its length. These vortex sheets interact with the free surface and either connect normally with the free surface (resulting in whirls) or stretch out parallel to the free surface and dissipate quickly.

Numerical simulations of the domed region (seen in Fig. 17), formed by the rise of a Kelvin oval, attracted considerable attention. Sarpkaya et al. (1988) modeled the vortex pair using *two point vortices (with small cores) and line vortices* to model the free surface without linearization. Subsequently, Marcus and Berger (1989), Telste (1989) and Ohring and Lugt (1991) used different two-dimensional models to investigate the interaction between a couple of heterostophic line vortices and a free, *initially* planar, surface. In these calculations, the critical time at which the numerical instability manifests itself does not correspond to the instability of the free surface or to its maximum position. The calculations of Ohring and Lugt are particularly noteworthy since they have presented results on the decay of the primary vortices and their paths, on the generation of surface vorticity and secondary vortices, on the development and final stages of the disturbed free surface, and on the influence of surface tension. They have also shown that, for an intermediate Froude number, the path of the primary vortex center portrays a complete loop (a special rebounding) due to the presence of secondary vortices. It must be emphasized, however, that *these calculations assume a two-dimensional flow*. In reality, the free surface quickly becomes three-dimensional (as manifested by the evolution of striations seen in Figs. 16 and 18).

Dommermuth and Yue (1991) solved the linearized Navier-Stokes equations in three dimensions with a free surface to study the interaction of vortex tubes and vortex rings with slip and no-slip rigid boundaries and a linearized free surface. Subsequently, Dommermuth (1992a) carried out numerical simulations of the interaction of laminar vortex tubes with *no-slip walls* to investigate the formation of U-shaped vortices without the complications of a free surface. They have concluded that two distinct types of vortices form: cam and snail vortices, as they preferred to call them. Cam vortices are formed as helical vorticity is stripped off of the primary vortex tubes. The *helical vortex sheets* are generated by the primary vortex tube due to the onset of a U-shaped instability previously identified by Sarpkaya (1985) and by Sarpkaya and Suthon (1991). Dommermuth (1992b) extended his numerical analysis to the interaction of a pair of vortex tubes with a free surface and confirmed Sarpkaya and Suthon's (1991) findings that the most interesting feature of the impingement of vortex tubes on a clean free surface is the reconnection of normal vorticity with the free surface, resulting *in strong whirls*. The *simulation* of more energetic transition (Dommermuth, 1992b) in vortices has tentatively shown that only the remnants of the primary vortex tube could be identified.

The interaction of jet flows with a free surface has attracted some attention (see, e.g., Ramberg et al., 1989; Madnia and Bernal, 1989; Anthony, 1990) for the expressed purpose of determining the topology and dynamics of the resulting turbulent structures. Although instructive in understanding the conversion of the azimuthal vorticity (vortex rings) into streamwise vorticity, the jet flow is neither as complicated as the ship wake nor representative of the turbulent phenomena that occur in the ocean environment partly because there is *no normal vorticity generation* in the nominal plane of the free surface. Furthermore, the interaction of the jet flow with the free surface leads to the generation of *gravity-capillary waves* propagating in a direction almost perpendicular to the jet axis.

Even though there is still some work to be done on the three-dimensional nature of the laminar vortex interaction, a number of kernel experiments, supported by analysis, is needed to elucidate the basic fluid mechanics of turbulent signatures. It is expected that the interaction of a single turbulent vortex (and its image) with the free surface will shed considerable light on the interaction betwen quasi-two-dimensional and three-dimensional turbulent motions. This is important not only near the free surface but also for the understanding of the processes of small-scale turbulence in the presence of highly stable stratification when *three-dimensional turbulence* shows a tendency to quasi-two-dimensional behavior due to the effect of buoyancy forces. Furthermore, the understanding of the properties of vortex-induced turbulence near the free surface will make it possible to explain the relationship between the *spatial and temporal scales of turbulence*, the evolution of

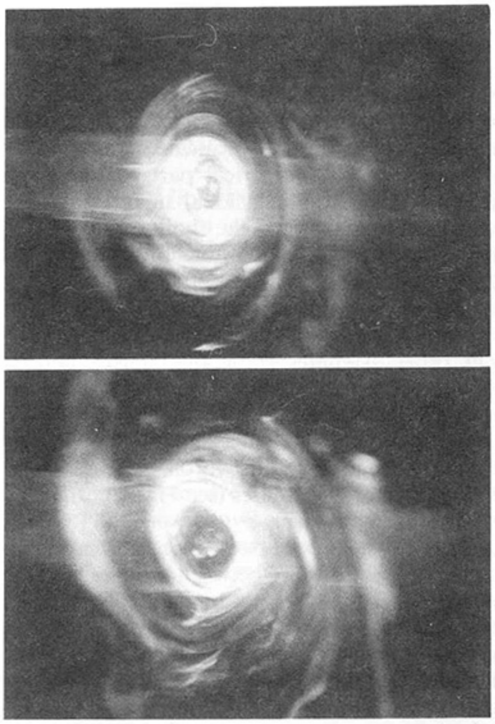

Fig. 19(*a–b*) Representative cross sections of a deeply submerged stationary vortex in a free-surface water tunnel. Note that the core of a turbulent vortex is not a benign, smooth, axisymmetric, solid body rotation. It has spins and splats.

Fig. 20(*a*) The connection of a vortex arm (or of a spin of vorticity) with the free surface.

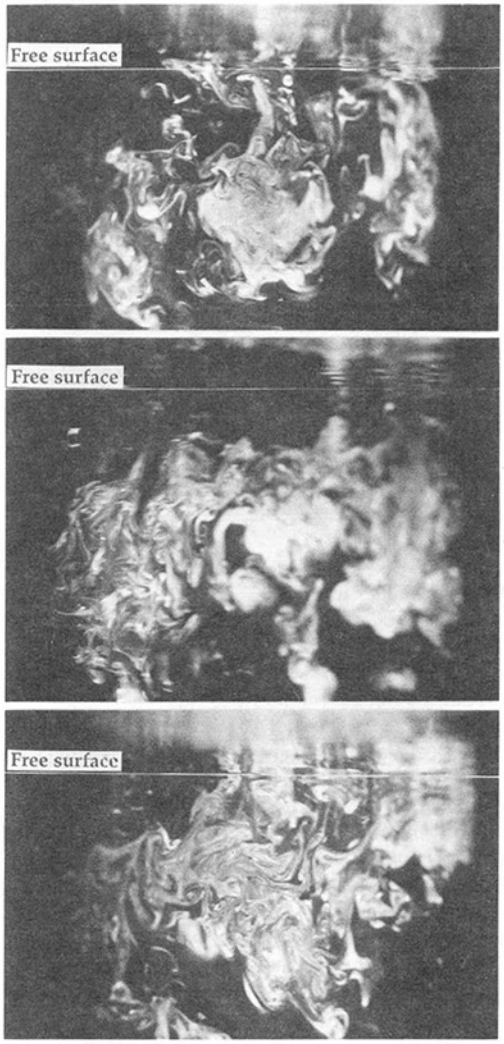

Fig. 20(*b–d*) The progression of the reconnection process of the normal vorticity and the evolution of whirls at the free surface as the vortex is brought closer to the free surface. Note that the core looses its identity and only the remnants of the original vortex can be seen. Figure 20(*a*) shows the growth of secondary vortex couples around the core.

surface inhomogeneities, and the characteristics of surface and sub-surface structures.

Sarpkaya (1992c and 1992d) carried out a series of exploratory measurements in a low turbulence water tunnel, with an open test section, through the use of several vertically mounted half Delta wings and rectangular foils. The interaction of the "single" vortex, emanating from the free end of the foil, with the free surface was investigated for representative distances between the vortex and the free surface. Velocity and turbulence measurements with an LDV and photographic observations with LIF (laser induced fluorescence) of the vortices and free surface were made. Certain unusual characteristics of the remnants of the turbulent vortex tube, reconnection of normal vorticity with the free surface and the stretching out and quick dissipation of turbulent patches in the tangential direction, and their role in the creation of a quasi-two-dimensional whirl field have been explored. The data for the fully submerged vortex were used to delineate the effects of the free-surface proximity. The numerical part of the investigation simulated the quasi-two-dimensional surface turbulence with vortex dynamics and explored the evolution of whirls, energy spectrum, and the fractal dimensions of the turbulence field.

Figures 19(*a*) and 19(*b*) show two deeply submerged vortex cores in a laser light sheet (*intersecting them at a 45-degree angle*, but photographed normal to the vortex axis). This and numerous other examples show that vortex cores are surrounded by helical patches that could have only come from the vortex sheet (dye was introduced into the vortex core). As the distance between the vortex and the free surface is decreased, the connection of the vortex patches with the free surface (and its image) increases (see Figs. 20(*a*) and 20(*b–d*)). These connections are not always between the free surface and the vortex sheets *still connected to the vortex core*. In fact, many of the connections are between the free surface and the run-away patches of vorticity with no visible connection to the core (presumably, thrown away from the core and leading to core oscillations to preserve angular momentum). The earliest connections with the free surface are due to independently "flying" patches (when the vortex core is not too close to the free surface).

Figures 20(*b–d*) show that the vortex core breaks up and spreads over a larger area as its proximity to the free surface increases. This is the mechanism whereby the three-dimensional turbulence below the free surface is transformed into a quasi-two-dimensional turbulence at the free surface. The viewing of the video tapes show that not all patches of vorticity are connected to the free surface. In fact some of these come close to the free surface rather quickly, stretch out in the horizontal plane (predominantly in the direction of largest strain), and then disappear just as fast. In other words, the generation and dissipation of horizontal vorticity is enhanced at the expense of the normal vorticity. The coherence of the vortex core is nearly lost and only the remnants of the original vortex may be seen. The numerical simulations of Dommermuth (1992a and 1992b) of the more energetic transition in vortices near the free surface have also shown that only the remnants of the primary vortex tube could be identified (see Figs. 21(*a–b*)). Some resemblance may be noted between Figs. 20(*c–d*) and 21(*a–b*) as far as the spreading and shredding of the vortex core is concerned. Clearly, the numerical model does not deal with finer structures of turbulence and with the whirls at the free surface.

Representative samples of the top view (taken with a laser light sheet, very near the free surface) of the surface structures are shown in Figs. 22(*a–d*) (the streaklines). The constellation of vortices seen in these figures emerged almost directly above, or slightly on the downwash side, of the trailing vortex. Two

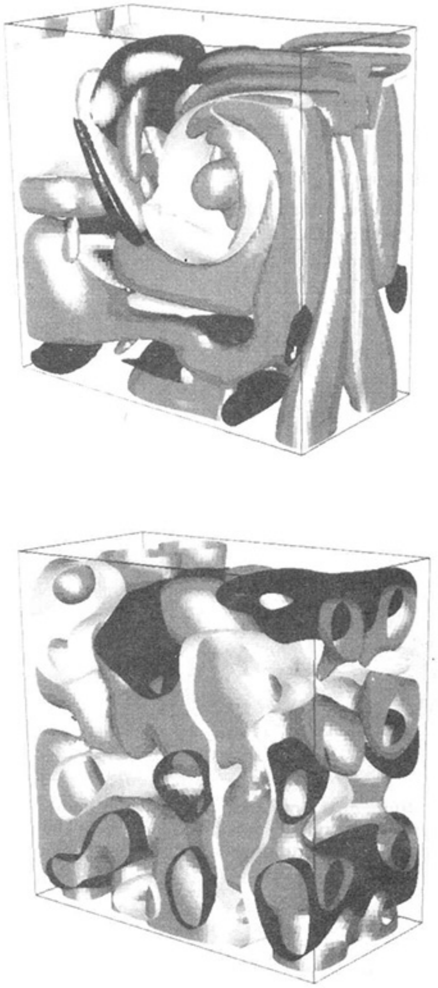

Fig. 21(*a–b*) Representative numerical simulations of the more energetic transition in vortices near the free surface (from Dommermuth, 1992a and 1992b).

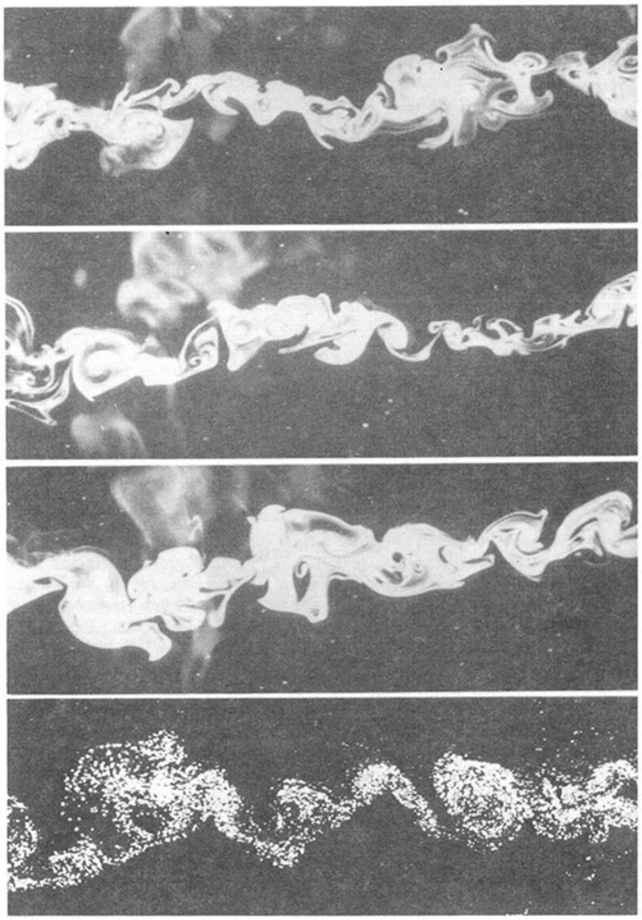

Fig. 22(*a–d*) Evolution of a scar above a single turbulent vortex. The top three frames are obtained with a laser-induced fluorescent dye. The last frame is obtained using laser light sheet and magnesium powder.

features of these whirls are particularly noteworthy. The first is the emergence of heterostophic vortices and the pairing of homostrophic vortices (pairing is best seen on the video films). The second salient feature of the whirls is their persistence. The whirls behave like as if they have become the "black holes" of vorticity in a sea of otherwise featureless structures of vorticity. The structures that are not part of a whirl dissipate quickly. It may thus be conjectured that the formation of whirls, as singularities of nearly concentrated vorticity, is a matter of survival of vorticity, either transported to the free surface or generated there. The tendency of the vortex couples of the same sign to transport energy from one area to another is severely limited partly by the swirling motion of the trailing vortex (directly below the scar), partly by the mutual interaction of the whirls, which keeps the scar intact, and partly by the uniform flow. Thus, the vortices created near the boundary of the scar cannot escape it but can unevenly modulate the edges of the scar.

The experiments have shown that the surface structures have the characteristic behavior of quasi-two-dimensional turbulence with energy cascading toward larger structures and stretched zones of weak vorticity dissipating slowly. The width of the wake above the trailing vortex increases slowly at the same rate at which the vortices grow in size through successive merging processes. Effective methods have been developed for structural and eddy center identification based on digital image analysis and shadowgraph technique. The size and angular velocities of the whirls were estimated from the video tapes in order to explore the statistics of the surface structures and to calculate the distribution of vorticity in the field of whirls. The instantaneous free-surface signatures are compared qualitatively with the predictions of a numerical model based on vortex dynamics in Figs. 23 and 24(*a–c*). Figure 23 may be compared with Fig. 16 and Figs. 24(*a–c*) may be compared with Figs. 22(*a–d*).

The facts emerging from these calculations are as follows: The whirls amalgamate up to a certain size as time increases (i.e., the amalgamation is self-limiting). It is remarkable that the band essentially retains its overall identity even though its width increases slightly due to the mutual interaction of the whirls. It is only rarely that one or two whirls leave the scar band due to mutual induction. The amalgamation process and, hence, the increase of the number of large structures slow down to stop as time increases and the whirl system would reach an equilibrium if there were no dissipation. The shift in the size distribution toward larger structures and the concentration of energy in these structures are an important ingredient of the scar formation and life-span. The increase of the number of large structures slows down and nearly stops after a critical time, when the whirl concentration has fallen below a critical value, and the population of whirls becomes dominated by viscous decay process. Apparently, the two-dimensional topological features (whirls) of concentrated vorticity on the free surface are inherent products of the quasi-two-dimensionalization of the three-dimensional turbulence, prevailing just below the free surface. The results have also shown that the global maximum of the energy spectrum is shifted toward smaller wave numbers (larger wave lengths), as expected on the basis of amalgamations.

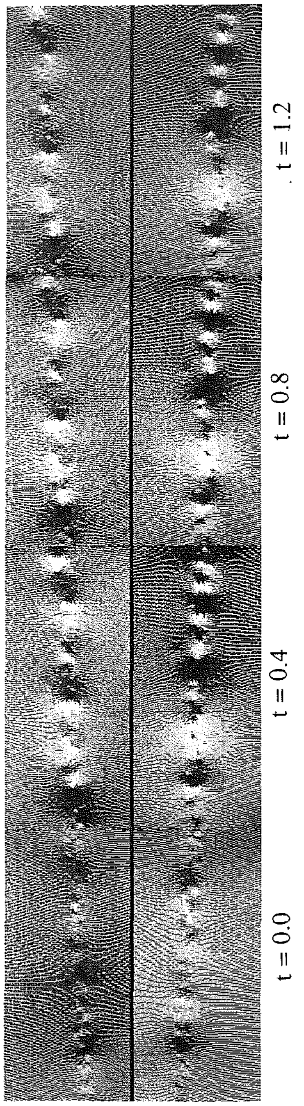

Fig. 23 Numerical simulation of the temporal growth of a segment of a V-shaped scar in a fixed frame of reference (total angle of divergence is about 4-deg). The numerical simulation is based on vortex dynamics (Sarpkaya, 1989; Sarpkaya and Suthon, 1991).

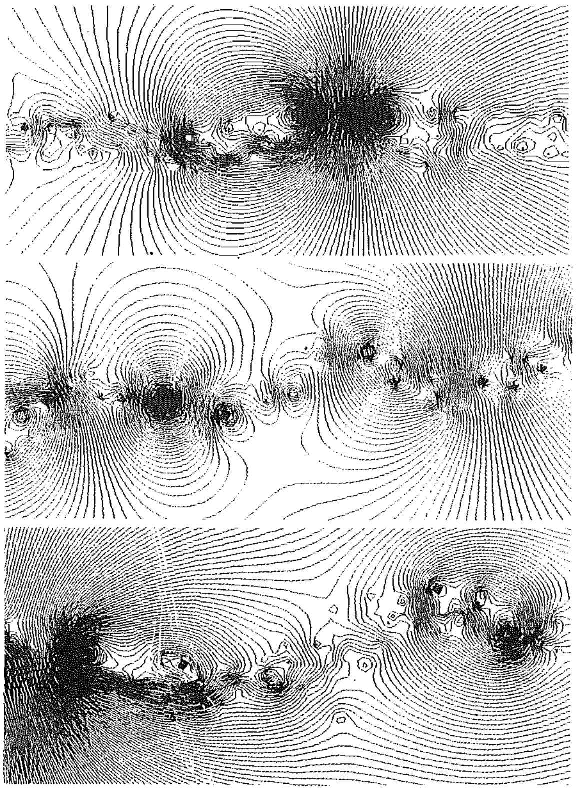

Fig. 24(*a–c*) Numerical simulation of the evolution of streamlines in a single scar above a turbulent vortex. The numerical simulation is based on vortex dynamics (for additional details, see Sarpkaya, 1989; Sarpkaya and Suthon, 1991).

In summary, the vortex sheets and turbulent patches (or finite regions of vorticity) interacting with the free surface give rise to whirls (reconnection of normal vorticity) or stretch out in the tangential direction and dissipate quickly. The closer the vortex to the free surface, the faster is its dissipation, as evidenced by the resulting scar at the free surface. The two fundamental modes of the vortex/free-surface interaction are suggestive of the "spin" and "splat" models of Bradshaw and Koh (1981), Hunt (1984), and Leighton et al. (1991). Their spin model (vortical structures originating in the buffer layer and attaching to the free surface) and the splat model (patches of vorticity or vortons impacting the free surface) in a turbulent open channel flow tend to support the observations made by Sarpkaya (1992c and 1992d) that the tentacles of vortex (helical sheets of vorticity) attach to the free surface and the patches of vorticity are thrown at the free surface. These similarities need to be explored further keeping in mind the fact that in the direct numerical simulations of Leighton et al. (1991) the nonlinear-time-dependent free surface conditions are linearized and the free surface is assumed to be nondeformable.

Evidently, the interaction of ship and submarine wakes with the free surface presents experimentally, theoretically, and numerically challenging problems in Naval hydrodynamics. However, their solution will go far beyond the naval applications and, in fact, will significantly increase our understanding of the physics of the inherently unstable air/liquid interface.

Conclusions

Unsteady separation; characteristics of impulsively and non-impulsively-started steady flow about cylinders; excursion of separation points on circular cylinders in sinusoidally oscillating flow; separation and other flow phenomena governing the unsteady maneuvers of large submerged bodies, and, finally, the three-dimensional footprints of subsurface vortical structures rising toward the free surface have been reviewed briefly. It appears that the prediction of the evolution of the wake, after the spontaneous separation of the viscous layer, is possible only for relatively small Reynolds numbers. For Reynolds numbers of any practical importance, the use of approximate turbulence models and experiments still appear to be the only recourse. As far as the unsteady maneuvers of large bodies are concerned, the subject is at best in the hands of panel methods and numerous approximations, requiring the specification of (mobile) separation points, among other things. It appears that in spite of the enormous progress made in experimentation and computational fluid dynamics, the question of where the separation lines are remains unresolved and challenging as ever. The vortex wakes at the free surface offer exceedingly complex three-dimensional problems for both clean and contaminated surfaces. In view of the foregoing, it seems appropriate to close this review with a thoughtful reminder by Sir Geoffrey Ingram Taylor (1974): "Though the fundamental laws of the mechanics of the simplest fluids, which possess Newtonian viscosity, are known and understood, to apply them to give a complete description of any industrially significant process is often far beyond our power."

Acknowledgments

The author's and his students' projects referred to herein were supported by the National Science Foundation, Chief of Naval Operations, Defense Advanced Research Projects Agency, and the Naval Postgraduate School. This support is gratefully acknowledged. The author wishes to thank the reviewers for their constructive comments. Professor D. P. Telionis made a number of valuable suggestions on earlier drafts of this paper. I wish to express my sincere appreciation to Dr. Edwin P. Rood (ONR) for his continued encouragement and support.

References

Achenbach, E., 1971, "Influence of Surface Roughness on the Cross-Flow Around a Circular Cylinder," *Journal of Fluid Mechanics*, Vol. 46, Part 2, pp. 321-335.

Anthony, D. G., 1990, "The Influence of a Free Surface on the Development of Turbulence in a Submerged Jet," Technical Report No. 90-2, The University of Michigan.

Baba, N., and Miyata, H., 1987, "Higher-Order Accurate Difference Solutions of Vortex Generation from a Circular Cylinder in an Oscillatory Flow," *Journal of Computational Physics*, Vol. 69, pp. 362-396.

Baker, G. R., Barker, S. J., Bofah, K. K., and Saffman, P. G., 1974, "Laser Anemometer Measurements of Trailing Vortices," *Journal of Fluid Mechanics*, Vol. 65, pp. 325-336.

Batchelor, G. K., 1964, "Axial Flow in Trailing Line Vortices," *Journal of Fluid Mechanics*, Vol. 20, pp. 645-658.

Bouard, R., and Coutanceau, M., 1980, "The Early Stage of Development of the Wake Behind an Impulsively Started Cylinder for $40 < Re < 10^4$," *Journal of Fluid Mechanics*, Vol. 101, Part 3, pp. 583-607.

Bradshaw, P., and Koh, Y. M., 1981, "A Note on Poisson's Equation for Pressure in a Turbulent Flow," *Physics of Fluids*, Vol. 24, pp. 777-779.

Chamberlain, R. R., 1987, "Unsteady Flow Phenomena in the Near Wake of a Circular Cylinder," AIAA Paper No. 87-0371.

Chang, C.-C., and Chern, R.-L., 1991a, "A Numerical Study of Flow Around an Impulsively Started Circular Cylinder by a Deterministic Vortex Method," *Journal of Fluid Mechanics*, Vol. 233, pp. 243-263.

Chang, C.-C., and Chern, R.-L., 1991b, "Vortex Shedding from an Impulsively Started Rotating and Translating Circular Cylinder," *Journal of Fluid Mechanics*, Vol. 233, pp. 265-298.

Chang, M.-S., and Purtell, L. P., 1986, "Three-Dimensional Flow Separation and the Effect of Appendages," *Proceedings of the 16th Symposium on Naval Hydrodynamics*, National Academy Press, pp. 352-370.

Cheer, A. Y., 1989, "Unsteady Separated Wake Behind an Impulsively Started Cylinder in Slightly Viscous Fluid," *Journal of Fluid Mechanics*, Vol. 201, pp. 485-505.

Conway, J., and Mackay, M., 1990, "Prediction of the Effects of Body Separation Vortices on Submarine Configurations Using the CANAERO Panel Method," AIAA-90-0302.

Corsiglia, V. R., Schwind, R. G., and Chigier, N. A., 1973, "Rapid Scanning, Three-Dimensional Hot-Wire Anemometer Surveys of Wing-Tip Vortices," *Journal of Aircraft*, Vol. 10, pp. 752-757.

Crow, S. C., 1970, "Stability Theory for a Pair of Trailing Vortices," *AIAA Journal*, Vol. 8, No. 12, pp. 2172-2179.

Dommermuth, D. G., 1992a, "The Formation of U-Shaped Vortices on Vortex Tubes Impinging on a Wall with Applications to Free Surfaces," *Physics of Fluids—A*, Vol. 4, No. 4, pp. 757-769.

Dommermuth, D. G., 1992b, "The Laminar Interactions of a Pair of Vortex Tubes with a Free Surface" (to appear in the *Journal of Fluid Mechanics*, 1992).

Dommermuth, D. G., and Yue, D. K., 1991, "A Numerical Study of Three-Dimensional Viscous Interaction of Vortices with a Free Surface," *Proceedings of the 18th Symposium on Naval Hydrodynamics*, National Academy Press, Washington, D.C, pp. 727-788.

Geissler, W., 1985, "Unsteady Laminar Boundary-Layer Separation on Oscillating Configurations," *AIAA Journal*, Vol. 23, No. 4, pp. 577-582.

Hall, M. G., 1972, "Vortex Breakdown," *Annual Reviews of Fluid Mechanics*, Vol. 4, pp. 195-218.

Hunt, J. C. R., 1984, "Turbulence Structure and Turbulent Diffusion Near Gas-Liquid Interfaces," *Gas Transfer at Water Surfaces*, D. Reidel Pub. Co.

Ho, C.-H., 1986, "An Alternative Look at the Unsteady Separation Phenomenon," *Recent Advances in Aerodynamics*, eds: A. Krothapalli and C. A. Smith), Springer-Verlag, N.Y., pp. 165-178.

Justesen, P., 1991, "A Numerical Study of Oscillating Flow Around a Circular Cylinder," *Journal of Fluid Mechanics*, Vol. 222, pp. 157-196.

Konstantinov, N. I., and Dragnysh, G. L., 1955, "The Measurement of Friction Stress on a Surface," D.S.I.R. RTS (1960).

Lecointe, Y., and Piquet, J., 1984, "On the Use of Several Compact Methods for the Study of Unsteady Incompressible Viscous Flow Round a Circular Cylinder," *Computers & Fluids*, Vol. 12, No. 4, pp. 255-280.

Leighton, R. I., Swean, T. F., Handler, R. A., and Swearingen, J. D., 1991, "Interaction of Vorticity with a Free Surface in Turbulent Open Channel Flow," AIAA-91-0236.

Lugt, H. J., 1981, "Numerical Modeling of Vortex Flows in Ship Hydrodynamics—A Review," *Proceedings of the Third International Conference on Numerical Ship Hydrodynamics*, Vol. 1, pp. V-1-1-V-1-20.

Lyden, J. D., Hammond, R. R., Lyzenga, D. R., and Shuchman, R. A., 1988, "Synthetic Aperture Radar Imaging of Surface Ship Wakes," *Journal of Geophysical Research*, Vol. 93 (C10), 12, 293-12, 303.

Madnia, K., and Bernal, L. P., 1989, "Interaction of a Turbulent Round Jet with the Free Surface," Technical Report No. 89-05, The University of Michigan.

Marcus, D. L., and Berger, S. A., 1989, "The Interaction Between a Counter-Rotating Vortex Pair in Vertical Ascent and a Free Surface," *Physics of Fluids*, A-1, Vol. 12, pp. 1988-2000.

McCroskey, W. J., 1982, "Unsteady Airfoils," *Annual Reviews of Fluid Mechanics*, Vol. 14, pp. 285-311.

Moore, F. K., 1957, "On the Separation of the Unsteady Laminar Boundary Layer," IUTAM-Symposium (Berlin). Boundary Layers, Freiburg, pp. 296-311.

Moore, D. W., and Saffman, P. G., 1973, "Axial Flow in Laminar Trailing Vortices," *Proc. Royal Society of London*, Vol. A 333, pp. 491-508.

Mostafa, S. I. M., 1987, "Numerical Simulation of Unsteady Separated Flows," Ph.D. thesis, Naval Postgraduate School, Monterey, CA.

Murashige, S., Kinoshita, T., and Hinatsu, M., 1989, "Direct Calculations of the Navier-Stokes Equations for Forces Acting on a Cylinder in Oscillatory Flow," *Proc. Eight International Conf. on Offshore Mechanics and Arctic Engineering*, The Hague, pp. 411-418.

Nagata, H., Funada, H., and Matsui, T., 1985, "Unsteady Flows in the Vortex Region Behind a Circular Cylinder Started Impulsively, 2nd Report, Velocity Fields and Circulations," *JSME*, Vol. 28, No. 245, pp. 2608-2616.

Newsome, R. W., and Kandil, O. A., 1987, "Vortical Flow Aerodynamics-Physical Aspects and Numerical Simulation," AIAA-87-0205.

Ohring, S., and Lugt, H. J., 1991, "Interaction of a Viscous Vortex Pair with a Free Surface," *Journal of Fluid Mechanics*, Vol. 227, pp. 47-70.

Panaras, A. G., and Steger, J. L., 1988, "A Thin-Layer Solution of the Flow About a Prolate Spheroid," *Zeitschrift fur Flugwissenschaften und Weltraumforschung*, Vol. 6, No. 3, pp. 173-180.

Pattani, P. G., and Olson, M. D., 1988, "Forces on Oscillating Bodies in Viscous Fluid," *International Journal for Numerical Methods in Fluids*, Vol. 8, pp. 519-536.

Poling, D. R., and Telionis, D. P., 1986, "The Response of Airfoils to Periodic Disturbances—The Unsteady Kutta Condition," *AIAA Journal*, Vol. 24, No. 2, pp. 193-199.

Ramberg, S. E., Swean, T. F., and Plesnia, M. W., 1989, "Turbulence Near a Free Surface in a Plane Jet," Naval Research Laboratory Memorandum Report 6367.

Robinson, S. K., 1991, "Coherent Motions in the Turbulent Boundary Layer," *Annual Review of Fluid Mechanics*, Vol. 23, pp. 601-639.

Rott, N., 1956, "Diffraction of a Weak Shock with Vortex Generation," *Journal of Fluid Mechanics*, Vol. 1, pp. 111-128.

Rumsey, C. L., 1988, "Details of the Computed Flow-field Over a Circular Cylinder at Reynolds Number 1200," ASME JOURNAL OF FLUIDS ENGINEERING, Vol. 110, pp. 446-452.

Sarpkaya, T., 1966, "Separated Flow About Lifting Bodies and Impulsive Flow About Cylinders," *AIAA Journal*, Vol. 3, No. 3, pp. 414-420.

Sarpkaya, T., 1971, "On Stationary and Traveling Vortex Breakdowns," *Journal of Fluid Mechanics*, Vol. 45, pp. 545-559.

Sarpkaya, T., 1975, "An Inviscid Model of Two-Dimensional Vortex Shedding for Transient and Asymptotically Steady Separated Flow Over an Inclined Flat Plate," *Journal of Fluid Mechanics*, Vol. 68, pp. 109-128.

Sarpkaya, T., 1976, "Vortex Shedding and Resistance in Harmonic Flow about Smooth and Rough Circular Cylinders at High Reynolds Numbers," Report No: NPS-59SL76021, Naval Postgraduate School, Monterey, CA.

Sarpkaya, T., 1977, "In-Line and Transverse Forces on Cylinders in Oscillatory Flow at High Reynolds Numbers," *Journal of Ship Research*, Vol. 21, No. 4, pp. 200-216.

Sarpkaya, T., 1978, "Impulsive Flow About a Circular Cylinder," Naval Postgraduate School Technical Report NO: NPS-69SL-78-008, Monterey, CA.

Sarpkaya, T., 1983, "Trailing Vortices in Homogeneous and Density Stratified Media," *Journal of Fluid Mechanics*, Vol. 136, pp. 85-109.

Sarpkaya, T., 1985, "Surface Signatures of Trailing Vortices and Large Scale Instabilities," *Proceedings of the Colloquium on Vortex Breakdown* (Sonderforschungsbereich 25), University of Aachen, pp. 145-187.

Sarpkaya, T., 1986, "Trailing-Vortex Wakes on the Free Surface," *Proceedings of the 16th Symposium on Naval Hydrodynamics*, National Academy Press, pp. 38-50.

Sarpkaya, T., 1989, "Computational Methods with Vortices—The 1988 Freeman Scholar Lecture," ASME JOURNAL OF FLUIDS ENGINEERING, Vol. 111, No. 1, March, pp. 5-52.

Sarpkaya, T., 1990, "Brief Reviews of Some Time-Dependent Flows," *Proceedings of the International Symposium on Nonsteaday Fluid Dynamics*, FED—Vol. 92, June 1990, pp. 3-14.

Sarpkaya, T., 1991, "Non-Impulsively Started Steady Flow about a Circular Cylinder," *AIAA Journal*, Vol. 29, No. 8, pp. 1283-1289.

Sarpkaya, T., 1992c, "Three-Dimensional Interactions of Vortices with a Free Surface," AIAA-92-0059.

Sarpkaya, T., 1992d, "Interactions of a Turbulent Vortex with a Free Surface," *Proc. of the Nineteenth Symposium on Naval Hydrodynamics*, 23-28 August 1992, Seoul, Korea (in print).

Sarpkaya, T., and Butterworth, W., 1992b, "Separation Points on a Cylinder in Oscillating Flow," ASME *Journal of Offshore Mechanics and Arctic Engineering*, Vol. 114, pp. 28-36.

Sarpkaya, T., Elnitsky, J., and Leeker, R. E., 1988, "Wake of a Vortex Pair on the Free Surface," *Proc. Seventeenth Symposium on Naval Hydrodynamics*, National Academy Press, Washington, D.C., pp. 53-60.

Sarpkaya, T., and Henderson, D. O., 1984, "Surface Disturbances due to Trailing Vortices," Naval Postgraduate School Technical Report No. NPS-69-84-004, Monterey, CA.

Sarpkaya, T., and Henderson, D. O., 1985, "Free Surface Scars and Striations Due to Trailing Vortices Generated by a Submerged Lifting Surface," AIAA 85-0445.

Sarpkaya, T., and Ihrig, C. J., 1986, "Impulsively Started Steady Flow About Rectangular Prisms: Experiments and Discrete Vortex Analysis," ASME Journal of Fluids Engineering, Vol. 108, pp. 47-54.

Sarpkaya, T., and Isaacson, M., 1981, *Mechanics of Wave Forces on Offshore Structures*, Van Nostrand Reinhold, New York, 690 pp.

Sarpkaya, T., and Kline, H. K., 1982, "Impulsively-Started Flow About Four Types of Bluff Body," ASME Journal of Fluids Engineering, Vol. 104, pp. 207-213.

Sarpkaya, T., and Putzig, C., 1992a, "Vortex Trajectories Around a Circular Cylinder in Oscillatory Plus Mean Flows," *Proceedings of the 11th International Conference on Offshore Mechanics and Arctic Engineering*, Vol. 1, Part A, pp. 69-77.

Sarpkaya, T., and Shoaff, R. L., 1979, "Inviscid Model of Two-Dimensional Vortex Shedding by a Circular Cylinder," *AIAA Journal*, Vol. 17, No. 11, pp. 1193-1200.

Sarpkaya, T., and Suthon, P. B. R., 1991, "Interaction of a Vortex Couple with a Free Surface," *Experiments in Fluids*, Vol. 11, pp. 205-217.

Schlichting, H., 1979, *Boundary-Layer Theory*, 7th ed. McGraw-Hill, New York.

Sears, W. R., 1956, "Some Recent Developments in Airfoil Theory," *Journal of Aerospace Sciences*, Vol. 23, pp. 490-499.

Sears, W. R., and Telionis, D. P., 1975, "Boundary Layer Separation in Unsteady Flow," *SIAM Journal of Applied Mathematics*, Vol. 28, No. 1, pp. 215-235.

Shirayama, S., and Kuwahara, K., 1987, "Patterns of Three-Dimensional Boundary Layer Separation," AIAA 87-0461.

Simpson, R. L., 1989, "Turbulent Boundary-Layer Separation," *Annual Reviews of Fluids Mechanics*, Vol. 21, pp. 205-234.

Singh, P. I., and Uberoi, M. S., 1976, "Experiments on Vortex Stability," *Physics of Fluids*, Vol. 19, pp. 1181-1188.

Stratford, B. S., 1959, "The Prediction of Separation of the Turbulent Boundary Layer," *Journal of Fluid Mechanics*, Vol. 5, pp. 1-16.

Ta Phuoc Loc, 1980, "Numerical Analysis of Unsteady Secondary Vortices Generated by an Impulsively Started Cylinder," *Journal of Fluid Mechanics*, Vol. 100, Part 1, pp. 111-128.

Ta Phuoc Loc and Bouard, R., 1985, "Numerical Solution of the Early Stage of the Unsteady Viscous Flow around a Circular Cylinder; a Comparison with Experimental Visualization and Measurements," *Journal of Fluid Mechanics*, Vol. 116, pp. 93-117.

Taneda, S., 1977, "Visual Study of Unsteady Separated Flows around Bodies," *Progress in Aerospace Sciences*, Vol. 17, pp. 287-348.

Taneda, S., 1980, "Definition of Separation," Reports of Research Institute for Applied Mechanics, Kyushu Univ., Vol. 28, No. 89, pp. 73-81.

Taylor, G. I. (Sir), 1974, "The Interaction Between Experiment and Theory in Fluid Mechanics," *Annual Reviews of Fluid Mechanics*, Vol. 6, pp. 1-16.

Telionis, D. P., 1979, "Review—Unsteady Boundary Layers, Separated and Attached," ASME Journal of Fluids Engineering, Vol. 101, pp. 29-43.

Telionis, D. P., 1981, *Unsteady Viscous Flows*, Springer-Verlag, N.Y.

Telionis, D. P., and Mathioulakis, D. S., 1984, "On the Shedding of Vorticity at Separation," *Unsteady Separated Flows*, Ed. M. W. Luttges, AFOSR, SRL, Univ. of Colorado, pp. 106-116.

Telionis, D. P., and Tsahalis, D. Th., 1974, "Response of Separation to Impulsive Changes of Outer Flow," *AIAA Journal*, Vol. 12, pp. 614-619.

Telste, J. G., 1989, "Potential Flow about Two Counter-Rotating Vortices Approaching a Free Surface," *Journal of Fluid Mechanics*, Vol. 201, pp. 259-278.

Thoman, D. C., and Szewczyk, A. A., 1969, "Time-Dependent Viscous Flow Over a Cylinder," *Physics of Fluids*, Vol. 12, Supplement II, pp. 76-86.

Thrasher, D. F., 1982, "Application of the Vortex-Lattice Concept to Flows with Smooth-Surface Separation," *Proc. ONR Symposium on Naval Hydrodynamics*, Ann Arbor, MI. (see also DTNSRDC-85/041, 1985).

Van der Vegt, J. J. W., 1988, "A Variationally Optimized Vortex Tracing Algorithm for 3-Dimensional Flows around Solid Bodies," Ph.D. thesis, Maritime Research Inst., Netherlands.

Van Dommelen, L. L., and Shen, S. F., 1983, "An Unsteady Interactive Separation Process," *AIAA Journal*, Vol. 21, No. 3, pp. 358-362.

Van Dommelen, L. L., and Cowley, S. J., 1990, "On the Lagrangian Description of Unsteady Boundary-Layer Separation. Part 1. General Theory," *Journal of Fluid Mechanics*, Vol. 210, pp 593-626.

Wang, K. C., 1972, "Separation Patterns on Boundary Layer Over an Inclined Body of Revolution," *AIAA Journal*, Vol. 10, pp. 1044-1050.

Wang, X., 1989, "A Numerical Study of Unsteady Flows Past a Circular Cylinder," Ph.D. thesis, Univ. of Houston, TX.

Williams, J. C., III, 1977, "Incompressible Boundary-Layer Separation," *Annual Reviews of Fluid Mechanics*, Vol. 9, pp. 113-144.

Williams, J. C., III, and Chen, C.-G., 1990, "Unsteady Separation on an Impulsively Set into Motion Carafoli Airfoil," *Proceedings of the International Symposium on Nonsteady Fluid Dynamics*, Eds: J. A. Miller and D. P. Telionis, FED—Vol. 92, June 1990, pp. 291-301.

Wong, T. C., Kandil, O. A., and Liu, C. H., 1989, "Navier-Stokes Computations of Separated Vortical Flows Past Prolate Spheroid at Incidence," AIAA 89-0553.

Xu, W. C., and Wang, K. C., 1988, "Unsteady Laminar Boundary Layer on Impulsively Started Prolate Spheroid," *Journal of Fluid Mechanics*, Vol. 195, pp. 413-435.

G. Vradis
Assistant Professor of
Mechanical Engineering.
Mem. ASME

V. Zalak[1]

J. Bentson
Associate Professor of
Aerospace Engineering.

Turbulent Fluid Mechanics Laboratory,
Polytechnic University,
Brooklyn, NY 11201

Simultaneous Variable Solutions of the Incompressible Steady Navier-Stokes Equations in General Curvilinear Coordinate Systems

A simultaneous variable solution technique for the incompressible, steady, two-dimensional Navier-Stokes equations in primitive formulation and general curvilinear orthogonal and nonorthogonal coordinate systems has been developed. The governing equations are discretized using finite difference approximations. The formulation is fully second order accurate and the well-known staggered grid of Welch and Harlow is used. The solution algorithm is based on an iterative marching technique in which the algebraic equations are linearized by evaluating the coefficients at the previous iteration level. The resulting system of linear equations is solved in a marching fashion by employing a block tridiagonal solution algorithm to obtain the solution along lines transverse to the main flow direction. The strong pressure-velocity coupling inherent in the present formulation results in high convergence rates. Flows in channels of different geometries have been computed and the results have been compared to available data in the literature. In all cases the method has demonstrated to be accurate, robust and computationally efficient.

Introduction

Over the last few years simultaneous variable solution methods for the incompressible steady Navier-Stokes equations have been receiving increasingly greater acceptance among fluid dynamicists over the traditional segregated methods. As demonstrated by the work of Bentson and Vradis (1987), Rubin and Reddy (1983), Zedan and Schneider (1985), and Vanka (1987), the inherently stronger pressure-velocity coupling in the simultaneous variable solution techniques results in higher convergence rates as compared to the standard segregated methods typified by the well-known SIMPLER algorithm of Patankar (1980). In addition, in contrast to the segregated methods which require the use of underrelaxation factors to promote and ensure convergence, the strongly implicit techniques need not make use of such factors. As a result such codes are more user-friendly and require minimal experience from the user.

Another group of solution techniques that has been developed lately is the one based on the approximate factorization scheme of Beam and Warming (1978) in conjunction with the artificial compressibility method of Chorin (1966). Such schemes, as described by Benocci and Ceresola (1985) and Chang et al. (1988), exhibit convergence rates which are dependent on the CFL condition. As a result the associated computation requirements might remain high.

Contrary to the segregated and approximate factorization schemes which have been employed in problems using generalized curvilinear coordinate systems, simultaneous variable solution techniques for the full Navier-Stokes equations in primitive variables have been developed and used only with Cartesian and cylindrical coordinate systems. While such coordinate systems provide the simplest possible form for the governing equations, they severely limit the number of problems to be solved with body fitted coordinates. For flow geometries involving irregularly shaped solid boundaries, the use of generalized orthogonal or nonorthogonal body-fitted coordinate systems is required.

Analytical and numerical methods for the generation of body fitted coordinate systems have been developed in recent years for the solution of flow problems in the presence of bodies of arbitrary shapes. This is due to the fact that such coordinate systems allow for the exact satisfaction of the boundary condition along the bodies' surfaces. The shortcoming of such an approach is that the grids are difficult to generate, particularly for complex body shapes and for multiple bodies. In addition, the appearance of the extra metric terms in the equations increases their complexity and computational time requirements.

The relative merits of nonorthogonal and orthogonal grids are well established and a wealth of information is available in the literature (see Thompson et al., 1985; Thompson, 1984; and Ghia and Ghia, 1983). While in general it is easier to

---

[1] Presently, Senior Engineer, Advanced Technology Division, Ebasco Services Inc., New York, NY 10048.

Contributed by the Fluids Engineering Division for publication in the JOURNAL OF FLUIDS ENGINEERING. Manuscript received by the Fluids Engineering Division March 4, 1991. Associate Technical Editor: C. J. Freitas.

generate nonorthogonal than orthogonal grids, the governing equations, written in such coordinate systems, are more involved because of the extra metric terms whose discretization often requires special attention due to the problems that they may create in terms of computational accuracy.

In the present work the simultaneous variable solution method developed by Bentson and Vradis (1987) is extended to general curvilinear orthogonal and nonorthogonal coordinate systems. A fundamental difference between the Cartesian-cylindrical formulation and the generalized one is that the mass conservation equation in the generalized orthogonal coordinate system is not satisfied to "machine accuracy" at any point of the calculation procedure, as was the case in the Cartesian and cylindrical systems. The effect of this on the convergence behavior of the algorithm is determined.

The Governing Equations

The Navier-Stokes equations for the case of two-dimensional, steady, laminar, incompressible flow take the following form if written in a general curvilinear nonorthogonal coordinate system (as given by Thompson et al., 1985):

$$y_\eta \frac{\partial u}{\partial \xi} - y_\xi \frac{\partial u}{\partial \eta} + x_\xi \frac{\partial v}{\partial \eta} - x_\eta \frac{\partial v}{\partial \xi} = 0 \qquad (1)$$

$$\begin{aligned} y_\eta u \frac{\partial u}{\partial \xi} - y_\xi u \frac{\partial u}{\partial \eta} + x_\xi v \frac{\partial u}{\partial \eta} - x_\eta v \frac{\partial u}{\partial \xi} &= y_\eta \frac{\partial p}{\partial \xi} - y_\xi \frac{\partial p}{\partial \eta} + \frac{1}{\mathrm{Re}\, J} \left[\alpha \frac{\partial^2 u}{\partial \xi^2} - 2\beta \frac{\partial^2 u}{\partial \xi \partial \eta} \right. \\ &\qquad \left. + \gamma \frac{\partial^2 u}{\partial \eta^2} + \sigma \frac{\partial u}{\partial \eta} + \tau \frac{\partial u}{\partial \xi} \right] \end{aligned} \qquad (2)$$

$$\begin{aligned} y_\eta u \frac{\partial v}{\partial \xi} - y_\xi u \frac{\partial v}{\partial \eta} + x_\xi v \frac{\partial v}{\partial \eta} - x_\eta v \frac{\partial v}{\partial \xi} &= x_\xi \frac{\partial p}{\partial \eta} - x_\eta \frac{\partial p}{\partial \xi} + \frac{1}{\mathrm{Re}\, J} \left[\alpha \frac{\partial^2 v}{\partial \xi^2} - 2\beta \frac{\partial^2 v}{\partial \xi \partial \eta} \right. \\ &\qquad \left. + \gamma \frac{\partial^2 v}{\partial \eta^2} + \sigma \frac{\partial v}{\partial \eta} + \tau \frac{\partial v}{\partial \xi} \right] \end{aligned} \qquad (3)$$

where:

$$x_\xi = \frac{\partial x}{\partial \xi}, \quad x_\eta = \frac{\partial x}{\partial \eta} \qquad (4a)$$

$$y_\xi = \frac{\partial y}{\partial \xi}, \quad y_\eta = \frac{\partial y}{\partial \eta} \qquad (4b)$$

$$J = x_\xi y_\eta - x_\eta y_\xi \qquad (4c)$$

$$\alpha = x_\eta^2 + y_\eta^2, \quad \beta = x_\xi x_\eta + y_\xi y_\eta, \quad \gamma = x_\xi^2 + y_\xi^2 \qquad (4d)$$

$$K_x = \alpha x_{\xi\xi} - 2\beta x_{\xi\eta} + \gamma x_{\eta\eta}, \quad K_y = \alpha y_{\xi\xi} - 2\beta y_{\xi\eta} + \gamma y_{\eta\eta}, \qquad (4e)$$

$$\sigma = [y_\xi K_x - x_\xi K_y]/J, \quad \tau = [x_\eta K_y - y_\eta K_x]/J \qquad (4f)$$

and u, v are the Cartesian coordinate velocity components.

The Numerical Approximation

Equations (1)-(3) form a system of second order partial differential equations which is elliptic in nature. They are discretized using finite difference approximations. The well-known staggered grid first proposed by Welch et al. (1966) has been used in the present analysis. The merits of this grid are well established (see Patankar, 1980) and they will not be repeated here. Centered, second order differences are used to approximate the first and second derivatives that appear due to the diffusion terms of the original P.D.Es. Second-order centered differences are used for the first-order derivatives in the convective terms in the direction transverse to the main flow direction. Second-order "upwinded" differences are used in the case of the first order derivatives appearing in the streamwise convective terms; thus resulting in a non-conservative difference scheme. The differencing of these derivatives depends on the sign of the velocity multiplying them. If that velocity is positive, a backward difference is employed, while if that velocity is negative, a forward difference is used. The algorithm is unconditionally stable and as a result it does not require the addition of artificial dissipative terms.

The metric terms appearing in the equations are evaluated using second-order accurate centered differences, with the exception of the points at the boundaries, where second-order accurate one-sided differences are used.

Based on the above discussion and using uniformly spaced grids in the transformed plane, the resulting discretized equations are:

$$\begin{aligned} & y_\eta \frac{u_{i,j} - u_{i,j-1}}{\Delta \xi} - y_\xi \frac{u_{i+1,j} + u_{i+1,j-1} - u_{i-1,j} - u_{i-1,j-1}}{4 \Delta \eta} \\ & + x_\xi \frac{v_{i+1,j} - v_{i,j}}{\Delta \eta} - x_\eta \frac{\hat{v}_{i+1,j+1} + \hat{v}_{i,j+1} - v_{i+1,j-1} - v_{i,j-1}}{4 \Delta \xi} = 0 \end{aligned} \qquad (5)$$

$$\begin{aligned} & (\hat{u} y_\eta - v_{av} x_\eta) \frac{1.5\, u_{i,j} - 2\, u_{i,j-1} + .5\, u_{i,j-2}}{\Delta \xi} \\ & \quad - (\hat{u} y_\xi - v_{av} x_\xi) \frac{u_{i+1,j} - u_{i-1,j}}{2 \Delta \eta} = - y_\eta \frac{\hat{p}_{i,j+1} - p_{i,j}}{\Delta \xi} \\ & \quad + y_\xi + \frac{\hat{p}_{i+1,j+1} + p_{i+1,j} - \hat{p}_{i-1,j+1} - p_{i-1,j}}{4 \Delta \eta} + \frac{1}{\mathrm{Re}\, J} \\ & \times \left[\alpha \frac{\hat{u}_{i,j+1} - 2\, u_{i,j} + u_{i,j-1}}{\Delta \xi^2} \right. \\ & \qquad - 2\beta \frac{\hat{u}_{i+1,j+1} - u_{i+1,j-1} - \hat{u}_{i-1,j+1} + u_{i-1,j-1}}{4 \Delta \xi\, \Delta \eta} \\ & + \gamma \frac{u_{i+1,j} - 2\, u_{i,j} + u_{i-1,j}}{\Delta \eta^2} + \sigma \frac{u_{i+1,j} - u_{i-1,j}}{2 \Delta \eta} \\ & \qquad \left. + \tau \frac{\hat{u}_{i,j+1} - u_{i,j-1}}{2 \Delta \xi} \right] \end{aligned} \qquad (6)$$

$$\begin{aligned} & (u_{av} y_\eta - \hat{v} x_\eta) \frac{1.5\, v_{i,j} - 2\, v_{i,j-1} + .5\, v_{i,j-2}}{\Delta \xi} \\ & \quad - (u_{av} y_\xi - \hat{v} x_\xi) \frac{v_{i+1,j} - v_{i-1,j}}{2 \Delta \eta} = - x_\xi \frac{p_{i,j} - p_{i-1,j}}{\Delta \eta} \\ & \quad + x_\eta \frac{\hat{p}_{i,j+1} + \hat{p}_{i-1,j+1} - p_{i,j-1} - p_{i-1,j-1}}{4 \Delta \xi} + \frac{1}{\mathrm{Re}\, J} \\ & \times \left[\alpha \frac{\hat{v}_{i,j+1} - 2\, v_{i,j} + v_{i,j-1}}{\Delta \xi^2} \right. \\ & \qquad - 2\beta \frac{\hat{v}_{i+1,j+1} - v_{i+1,j-1} - \hat{v}_{i-1,j+1} + v_{i-1,j-1}}{4 \Delta \xi\, \Delta \eta} \end{aligned}$$

Nomenclature

p = nondimensional pressure
Re = Reynolds number
u = "streamwise" velocity component in physical space
v = "transverse" velocity component in physical space
x = "streamwise" coordinate
y = "transverse" coordinate in physical space
η = coordinate in computational space
ξ = coordinate in computational space

$$+\gamma\frac{v_{i+1,j}-2v_{i,j}+v_{i-1,j}}{\Delta\eta^2}+\sigma\frac{v_{i+1,j}-v_{i-1,j}}{2\Delta\eta}+\tau\frac{\hat{v}_{i,j+1}-v_{i,j-1}}{2\Delta\xi}\Bigg] \tag{7}$$

where:

$$u_{av}=\frac{1}{4}\left(u_{i,j}+u_{i-1,j}+u_{i,j-1}+u_{i-1,j-1}\right) \tag{8a}$$

$$v_{av}=\frac{1}{4}\left(v_{i,j}+\hat{v}_{i,j+1}+v_{i+1,j}+\hat{v}_{i+1,j+1}\right) \tag{8b}$$

The resulting system of algebraic equations is nonlinear in nature due to the convective terms. The equations are linearized by "freezing" the coefficients of the convective terms to the previous iteration level (indicated by a hat in the above equations). As convergence is approached, these terms become asymptotically equal to the values of the nonlinear terms.

Such a procedure leads to a system of linear equations that is solved in a marching fashion, starting at the inlet section and moving toward the exit. Along each coordinate line perpendicular to the marching direction, the linear equations form a block tridiagonal coefficient matrix with 3×3 elements.

$$\begin{bmatrix} B_1C_1 & & & \\ A_2B_2C_2 & & & \\ \cdot\;\cdot\;\cdot & & & \\ & \cdot\;\cdot\;\cdot & & \\ & & \cdot B_{n-1}C_{n-1} & \\ & & A_n & B_n \end{bmatrix}\begin{bmatrix} W_1 \\ W_2 \\ \cdot \\ \cdot \\ W_{n-1} \\ W_n \end{bmatrix}=\begin{bmatrix} E_1 \\ E_2 \\ \cdot \\ \cdot \\ E_{n-1} \\ E_n \end{bmatrix} \tag{9}$$

The coefficient matrix is inverted through the use of an efficient algorithm due to Isaacson and Keller (1966).

The three difference equations at every grid point have the general form:

$$B_i W_{i-1}+A_i W_i+C_i W_{i+1}=E_i \tag{10}$$

where A_i, B_i and C_i are 3×3 matrices and W_i, E_i are 3×1 vectors, with:

$$W_i=[u_{i,j},\ v_{i,j},\ p_{i,j}]^T$$

After the last grid line at the downstream boundary has been reached, the residuals of all equations at every point of the computational domain are evaluated. If the maximum of these residuals is less than the prescribed acceptance value (usually of the order of 10^{-6}), then the solution has been obtained.

Boundary Conditions

Given the elliptic nature of the full Navier-Stokes equations, boundary conditions are to be prescribed at all the boundaries of the computational domain. The correct implementation of the appropriate boundary conditions is crucial in obtaining meaningful and accurate results. The application of the wrong boundary conditions in the case of incompressible flows results in erroneous solutions throughout the computational domain due to their elliptic nature.

At the inlet section a velocity profile is prescribed:

$$u=u(y),\quad v=v(y) \tag{11}$$

while zero gradient conditions for the velocities and uniformity of pressure are enforced at the exit section:

$$\frac{\partial u}{\partial x}=0,\quad \frac{\partial v}{\partial x}=0 \quad\text{and}\quad p=0 \tag{12}$$

This requires that the exit section is set downstream enough for fully developed flow conditions to exist. Violation of this condition leads to failure of the algorithm to converge with the residuals in the equations exhibiting an oscillatory behavior. Obviously, since the length of the developing flow region cannot be known a priori, some numerical experimentation is required in order to determine the proper location of this exit section.

The standard no-slip condition for viscous flows is imposed at solid impermeable boundaries, thus setting both components of the velocity equal to zero. The pressure boundary condition is obtained from the momentum equation perpendicular to the wall, resulting in the following expression:

$$u=0,\quad v=0 \quad\text{and}\quad \frac{\partial p}{\partial n}=\frac{1}{\text{Re}}\frac{\partial^2 U}{\partial n^2} \tag{13}$$

where n is the direction normal to the wall and U the velocity component parallel to the wall. In the case of staggered grids, as the one used in the present work, only one of the two velocity components is located on the physical boundaries of the calculation domain; in the problems discussed below, this will be the v component. As a result, a parabolic fit of the points next to the solid boundary is adopted to approximate the value of the velocity component which is located off the physical boundary, resulting in a second order accurate formulation of the boundary conditions along solid boundaries:

$$u_{i+1,j}=-2u_{i,j}+\frac{u_{i-1,j}}{3} \tag{13a}$$

The boundary value of the pressure along a solid wall is obtained through the solution of the momentum equations at the solid wall. In the case of a Cartesian grid this involves the solution of the momentum equation in the direction normal to the wall. In the case of general orthogonal or nonorthogonal coordinate systems, the equation for the pressure gradient normal to the wall is obtained through a linear combination of the momentum equations along the two coordinate directions so that the pressure gradient terms along the other direction are eliminated. This results in an equation giving the pressure derivative normal to the wall in the computational space as a function of the velocity field.

$$[x_\xi y_\eta - y_\xi x_\eta]p_\eta=\frac{1}{\text{Re}\,J}[x_\eta\gamma u_{\eta\eta}+x_\eta\sigma u_\eta+y_\eta\gamma v_{\eta\eta}+y_\eta\sigma v_\eta] \tag{13b}$$

This approach was shown by Benocci and Michelassi (1986) to be the more accurate way to implement the pressure boundary condition.

Along symmetry axes $\partial u/\partial y=0$, $\partial p/\partial y=0$ and $v=0$, where y is taken as the direction normal to the symmetry line.

Computational Results

Two test problems are used to study the accuracy and computational efficiency of the developed algorithm.

(i) Laminar Flow Through an Expanding Plane Channel. The two-dimensional channel proposed by Roache (1981) was used in the workshop of the IAHR Working Group on Refined Modeling of Flows to compare the performance of different finite-difference and finite-element based algorithms. Due to the availability of results from a different number of numerical formulations (Napolitano and Orlandi, 1985), the problem is selected here as a test problem for the newly developed method.

The geometry of the problem is given in Fig. 1. The geometry, as seen, depends on the Reynolds number (which is based on the upstream channel half-height and the bulk velocity of the flow). As the Reynolds number increases the channel becomes longer and the expansion smaller. Roache (1981) shows that for large Reynolds numbers the problem exhibits a quasi-self-similar solution.

The velocity profile specified at the channel's inlet, is the one that corresponds to the fully developed flow in a straight channel, i.e.,

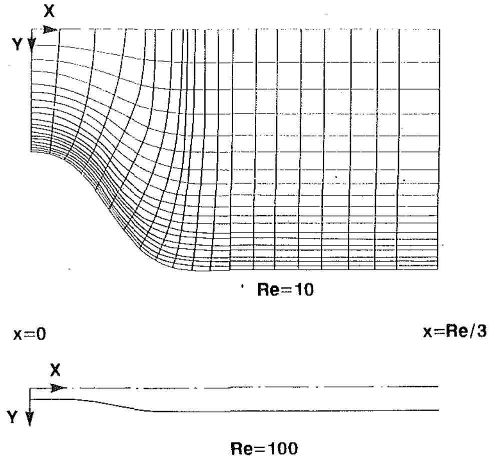

Y=1+1/2[tanh(2-30x/Re)-tanh2]

Fig. 1 Geometry of expanding channel and computational grid

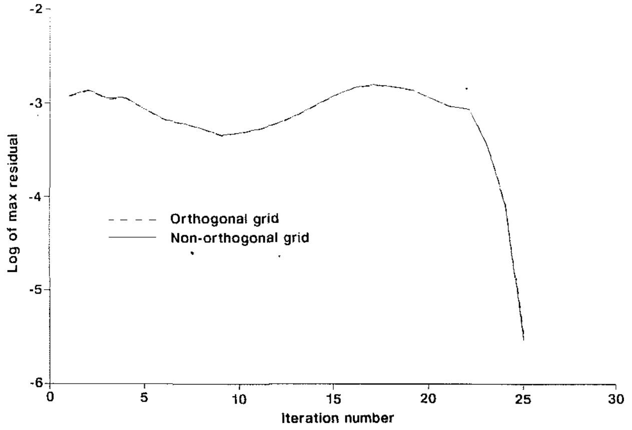

Fig. 3 Convergence history for Re = 100

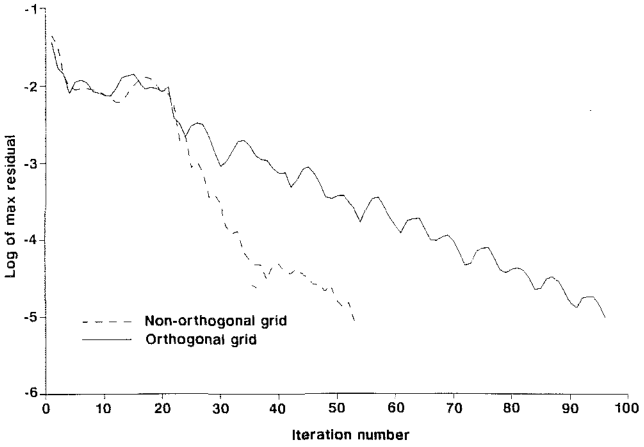

Fig. 2 Convergence history for Re = 10

$$u(y) = 1.5(1 - y^2), \quad v = 0 \tag{14}$$

The problem was solved using both orthogonal and nonorthogonal grids.

In the nonorthogonal case, the grid was generated algebraically using the following simple shear transformation:

$$\xi = x, \quad \eta = \frac{y}{y_w} \tag{15}$$

where y_w is the coordinate of the solid boundary. This simple transformation transforms the expanding channel wall to a flat plate.

The orthogonal grid was generated using the algebraic transformation given by Blottner and Ellis (1973), which maps the physical plane to a rectangle in the computational space (ξ, η). The $\eta = 0$ line coincides with the axis of symmetry of the channel while the $\eta = 1$ line coincides with the wall. All other η's are given by:

$$Y_i = \frac{\epsilon^N - \epsilon^{i-1}}{\epsilon^N - 1} Y_l(x) + \frac{\epsilon^{i-1} - 1}{\epsilon^N - 1} Y_u(x) \tag{16}$$

where ϵ is a parameter determining the clustering of the grid in the physical plane and $Y_l(x)$ and $Y_u(x)$ are the coordinates of the two boundaries.

The ξ = constant lines, orthogonal to the η = constant lines, are then obtained using a numerical integration of the following equation:

$$\left[\frac{\partial x}{\partial \eta}\right]_\xi = -\frac{\left[\dfrac{\partial y}{\partial x}\right]_\eta \left[\dfrac{\partial y}{\partial \eta}\right]_x}{1 + \left[\dfrac{\partial y}{\partial x}\right]_\eta^2} \tag{17}$$

with the calculation starting from prescribed points along the wall of the channel.

A 21 × 21 grid was employed in order to compare the results obtained using the current method to those presented in the workshop (Napolitano and Orlandi, 1985). Solutions were obtained for two Reynolds numbers, namely Re = 10 and Re = 100. The orthogonal grid used for the Re = 10 calculation is shown in Fig. 1.

Figures 2 and 3 show the convergence history for Re = 10 and Re = 100, respectively, both for the nonorthogonal and the orthogonal grids. As seen, in the case of Re = 10 there is a substantial difference in the convergence behavior of the orthogonal versus the nonorthogonal grid case, the orthogonal grid case converging slower, as has also been observed by other researchers using other solution techniques; this, despite the fact that in the nonorthogonal grid case the elliptic effects in the discretized equations are stronger than in the orthogonal grid case due to the appearance of extra metric terms that introduce additional downstream grid points into the finite difference equations. It can be concluded then that the determining factor is the fact that while in the nonorthogonal grid case the continuity equation is satisfied exactly at any iteration, in the orthogonal grid case it is not, due to the term multiplied by the x_η metrix. As a result, the residual in the mass conservation equation is different than "machine" zero. It is actually found to be the highest residual, thus determining the convergence rate. In addition, it is seen that the convergence rate increased in the higher Reynolds number case which is due to the change of the shape of the channel. As the Reynolds number increases, the expansion ratio decreases, the channel becoming smoother and the wall flatter, approaching asymptotically the case of a parallel plate channel. In this case, where all the metric terms are zero, the convergence rate is maximum. It should be emphasized here that no underrelaxation are artificial dissipation was needed in any case for convergence to be obtained.

Figures 4 and 5 show the vorticity distribution along the solid wall for Re = 10 and 100 respectively and for both the nonorthogonal and the orthogonal grids. In the higher Reynolds number case, the solutions are very close to each other in contrast to the lower Reynolds number case where there are substantial differences between the two solutions. This is attributed to the fact that as the Reynolds number increases the

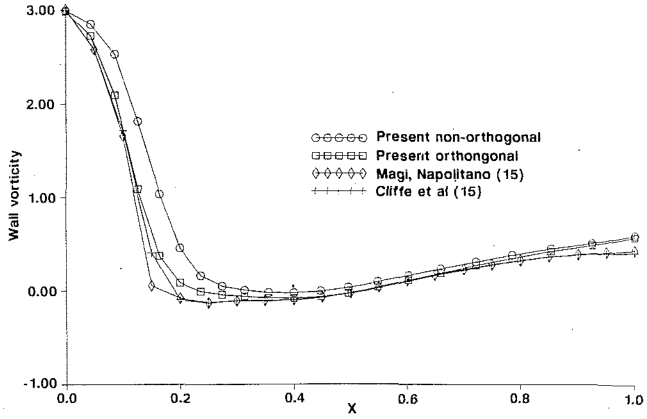

Fig. 4 Wall vorticity distribution for Re = 10

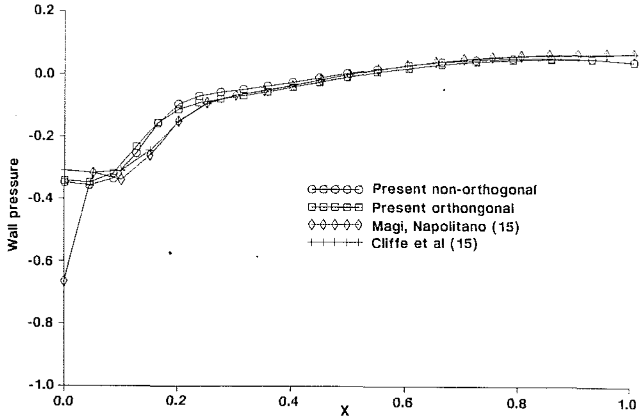

Fig. 6 Wall pressure distribution for Re = 10

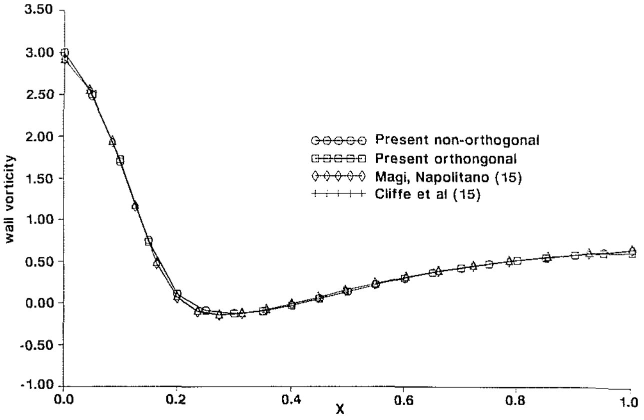

Fig. 5 Wall vorticity distribution for Re = 100

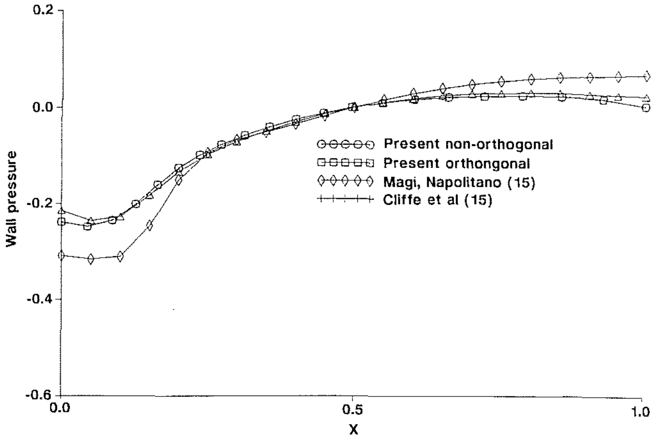

Fig. 7 Wall pressure distribution for Re = 100

nozzle expansion ratio decreases while at the same time the expansion is smoother. As a result, the nonorthogonal grid tends toward the orthogonal grid.

In the case of Re = 100 the agreement of the results obtained using the newly developed method with the results obtained by Cliffe et al. and Magi and Napolitano (see Napolitano and Orlandi, 1985) is very good. Cliffe et al.'s results are considered grid independent, the rest of the solutions always compared against theirs. In the Re = 10 case though, while the orthogonal solution is in good agreement with the rest, the nonorthogonal one deviates substantially. A more detailed study of the nonorthogonal solution demonstrated that this solution is very sensitive to the grid density and distribution. No particular effort was made in this analysis to find an "optimum" nonorthogonal grid that would produce results very close to the orthogonal case. In all cases studied though, it seems that the effect of the different nonorthogonal grids is limited to the area close to the inlet of the channel.

The pressure distribution along the solid wall is given in Figs. 6 and 7 for the Re = 10 and Re = 100 cases, respectively. Very close to the inlet, where the flow is assumed fully developed, there is a small drop in the pressure associated with the viscous effects. Once the channel starts expanding substantially the pressure starts rising as dictated by the inviscid effect. Close to the exit the pressure distribution is "flat" and beyond that, given that fully developed flow is established, it is expected to start dropping again. As seen, there is good agreement between the present results and those of Magi and Napolitano but poor agreement with those of Cliffe et al. It should be mentioned here that the pressure distribution obtained by Cliffe et al. close to the inlet in the Re = 10 case is substantially different than the ones obtained in the rest of the works presented in the workshop. It is felt that there is no physical justification for the sharp rise in pressure very close to the inlet.

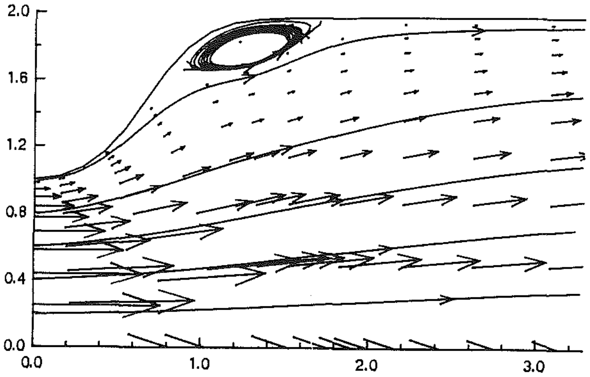

Fig. 8. Velocity vectors and streamlines for Re = 10

A comprehensive look into the flow field is given in Fig. 8 for the Re = 10 case. Velocity vectors and streamlines are overlaid to show the existence of the recirculating flow region as well as the extent of the redeveloping flow region.

(ii) Laminar Flow in a Channel With a Constriction. The second test problem is the laminar flow in a channel with a constriction. The constriction geometry is shown in Fig. 9(*a*) and is defined by a Gaussian distribution. The maximum of the distribution, appearing at $x = 2$, restricts the height of the

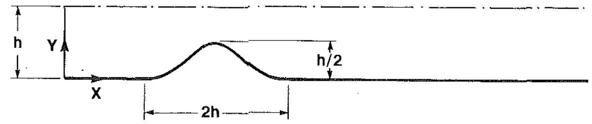

Fig. 9(*a*) Geometry of channel with symmetric bump

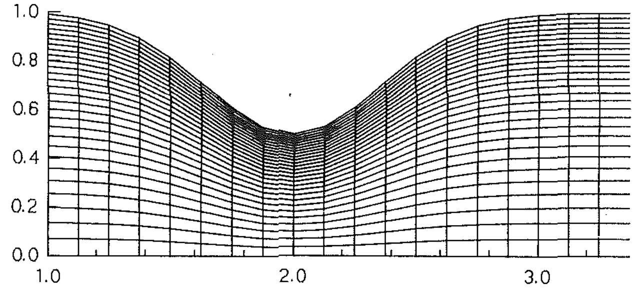

Fig. 9(*b*) Computational grid in the immediate region of the constriction

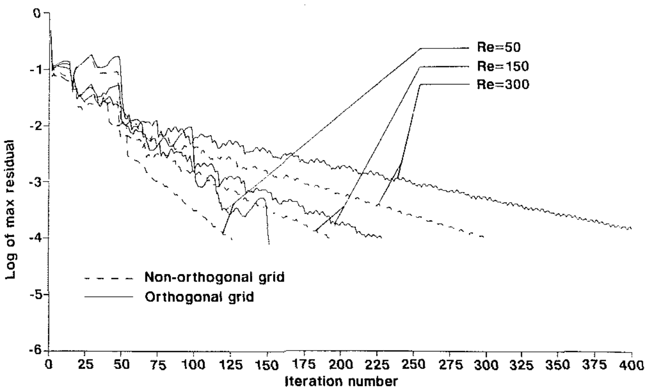

Fig. 10 Convergence history for Re = 50, 150, 300

channel to half of the original, while its width is twice the upstream channel height. The Reynolds number is defined using the bulk velocity at the inlet and half the channel height at the inlet.

All cases involved a 57×30 grid (57 grid points in the x direction). In the physical plane the grid was refined close to the wall in order to capture the wall boundary layer, as shown in Fig. 9(*b*) (only a detail is shown in the region of the contraction). The grid spacing distribution is the one described by Anderson et al. (1984) and is based on a sinh distribution that has been shown to introduce minimum errors in the calculation. In the streamwise direction the grid is refined in the region close to the constriction and becomes coarser away from it.

Figure 10 shows the convergence rate for three different Reynolds numbers, i.e., Re = 50, 150, and 300, and for both a nonorthogonal and an orthogonal grid. Again, no underrelaxation or artificial dissipation was needed for convergence to be otbained. For all Reynolds numbers, the nonorthogonal grid cases converge faster than the orthogonal ones. It is also seen that the convergence rate decreases as the Reynolds numbers increases.

The basic features of the flow field in the near region of the constriction are demonstrated in Fig. 11 for the Re = 50 case. The flow accelerates as the constriction is approached. Once the flow enters the expanding part of the channel, it separates under the influence of the adverse pressure gradient. Then it reattaches and redevelops in the downstream straight part until fully developed conditions are reached.

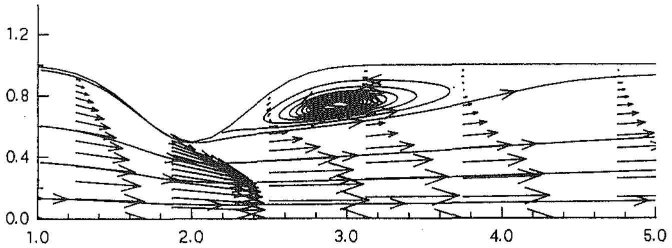

Fig. 11 Velocity vectors and streamlines for Re = 50

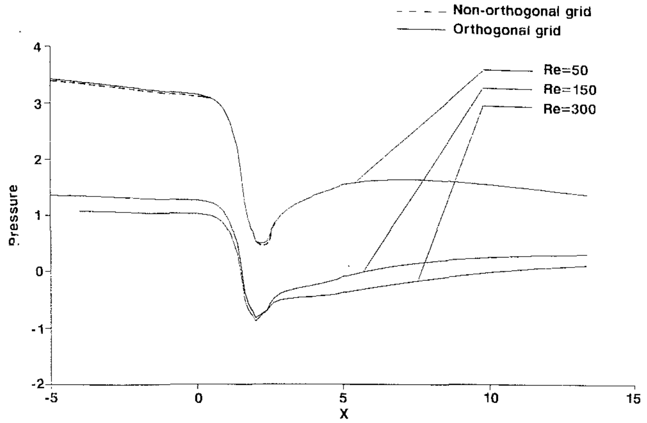

Fig. 12 Pressure distribution along wall for Re = 50, 150, 300

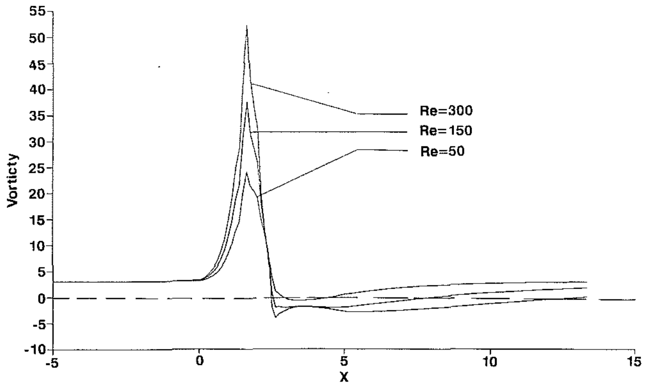

Fig. 13 Vorticity distribution along wall for Re = 50, 150, 300

Figure 12 shows the pressure distribution at the wall for the three different Reynolds numbers. In the initial straight section of the channel where the flow is fully developed, the pressure gradient is constant. As the channel converges, the pressure starts dropping rapidly reaching a minimum at the point of the minimum cross-sectional area. After that, as the flow expands, the pressure recovers and once the flow starts developing again the pressure gradient becomes negative reaching eventually the value corresponding to the fully developed flow. For the Re = 50 case, results are shown for both a nonorthogonal and an orthogonal grid. In this case an effort was made to obtain a nonorthogonal grid that gave results as accurate as an orthogonal one. As seen, the two solutions are very close to each other, the maximum difference being of the order of 3 percent.

The vorticity distribution along the wall is shown in Fig. 13. The vorticity remains constant in the straight section of the channel close to the inlet, increasing rapidly as the wall starts converging. It peaks at the point where the cross-sectional area becomes minimum ($x = 2$) and drops rapidly as the flow enters the diverging part of the channel. The vorticity becomes zero at the separation point and turns negative within the recirculation zone. It becomes zero again at the reattachment point and increases thereafter to its initial value (that at the inlet) as the flow develops in the straight portion of the channel after the constriction. As seen the length of the recirculating bubble (given by the length of the region of negative vorticity) increases with Reynolds number while the separation point moves upstream.

Discussion and Conclusions

A simultaneous variable solution technique for the two-dimensional incompressible steady Navier-Stokes equations in generalized orthogonal and nonorthogonal coordinate systems has been developed and tested. It is based on a second-order accurate finite-difference formulation of the governing equations. It employs a marching solution technique in which the linearized algebraic equations are solved for simultaneously along lines perpendicular to the marching direction.

It is well established that the traditional segregated methods require in many cases the use of underrelaxation parameters in order to secure convergence. The more modern methods based on the approximate factorization technique require the introduction of artificial dissipation terms for the same purpose. The present technique has not exhibited any convergence problems and has not required the use of any underrelaxation parameters or artificial dissipation terms, thus demonstrating its robustness.

In terms of computational efficiency no direct comparison of CPU times is given here, since, unfortunately, no such information is available in the literature for other codes. However, Benocci and Michelassi (1986) report, that using the approximate factorization technique for the solution of the first test problem in the present work, 300 to 400 iterations are required in order to reduce the residuals to a 10^{-4} level (using a 21×21 grid). As seen in Fig. 2 using the current method it takes about 70 iterations to reach the same residual level using an orthogonal grid and about 35 iterations using a nonorthogonal grid. In addition, one iteration in the present methods consists of sweeping the computational domain once in the marching direction while in the case of the approximate factorization technique it consists of two sweeps of the field, one in each of the coordinate directions. The computational effort required by each sweep is approximately the same in both methods given that it involves the inversion a block tridiagonal matrix along each coordinate line.

Therefore, based on the test cases presented in this work, it can be said that the above described method is a powerful technique for the solution of the incompressible two-dimensional steady Navier-Stokes equations in general curvilinear coordinate systems, being both computationally efficient and robust.

References

Anderson, D. A., Tannehill, J. C., and Pletcher, R. H., 1984, *Computational Fluid Mechanics and Heat Transfer*, McGraw-Hill.

Beam, R., and Warming, R., 1978, "An Implicit Factored Scheme for the Compressible Navier-Stokes Equations," *AIAA J.*, Vol. 16, No. 4, Apr., pp. 393–402.

Benocci, C., and Ceresola, N., 1985, "Solution of the Incompressible Navier-Stokes Equations with the Approximate Factorization Technique," Tech. Memo. 39, Von Karman Institute for Fluid Dynamics, Belgium.

Benocci, C., and Michelassi, V., 1986, "The Influence of the Wall Boundary Condition on a Solution of the Incompressible Navier-Stokes Equations," Tech. Memo. 42, Von Karman Institute for Fluid Dynamics, Belgium.

Bentson, J., and Vradis, G., 1987, "A Two-Stage Pressure Correction Technique for the Incompressibe Navier-Stokes Equations," AIAA-87-0545, paper presented at the AIAA 25th Aerospace Sciences Meeting, January 12–15, Reno, Nevada.

Blottner, P. R., and Ellis, M. A., 1973, "Finite Difference Solution of the Incompressible Boundary Layer Equations for a Blunt Body," *Computers and Fluids*, Vol. 1, pp. 133–158.

Chang, J. L. C., Kwak, D., Rogers, S. E., and Yang, R.-J., 1988, "Numerical Simulation Methods of Incompressible Flows and an Application to the Space Shuttle Main Engine," *Int. J. Num. Meth. Fluids*, Vol. 8, pp. 1241–1268.

Chorin, A. J., 1966, "A Numerical Method for Solving Incompressible Viscous Flow Problems," *J. Comput. Phys.*, Vol. 2, No. 1, pp. 12–26.

Ghia, K. N., and Ghia, U., 1983, *Advances in Grid Generation*, FED-Vol. 5, ASME.

Isaacson, E., and Keller, B. H., 1966, *Analysis of Numerical Methods*, Wiley, New York, pp. 58–61.

Napolitano, M., and Orlandi, P., 1985, "Laminar Flow in a Complex Geometry: A Comparison," *Int. J. Num. Meth. Fluids*, Vol. 5, pp. 667–683.

Patankar, S. V., 1980, *Numerical Heat Transfer and Fluid Flow*, Hemisphere, Washington, D.C.

Roache, P. J., 1981, "Scaling of High Reynolds Number Weakly Separated Channel Flows," *Proceedings of the Symposium on Numerical and Physical Aspects of Aerodynamic Flows*, California State University, Long Beach, CA, Jan. 19–21.

Rubin, S. G., and Reddy, D. R., 1983, "Analysis of Global Pressure Relaxation for Flows with Strong Interaction and Separation," *Computers and Fluids*, Vol. 11, No. 4, pp. 281–306.

Thompson, J. F., Warsi, Z. U. A., and Mastin, Wayne, 1985, *Numerical Grid Generation: Foundations and Applications*, North-Holland, pp. 124–128.

Thompson, J. F., 1984, "Grid Generation Techniques in Computational Fluid Dynamics," *AIAA J.*, Vol. 22, pp. 1505–1513.

Vanka, S. P., 1987, "Block-Implicit Computation of Viscous Internal Flows-Recent Results," AIAA-87-0058, paper presented at the AIAA 25th Aerospace Sciences Meeting, January 12–15, Reno, Nevada.

Welch, J. E., Harlow, F. H., Shannon, J. P., and Daly, B. J., 1966, "The MAC Method," Los Alamos Scientific Lab, Report LA-3425.

Zedan, M., and Schneider, G. E., 1985, "A Coupled Strongly Implicit Procedure for Velocity and Pressure Computation in Fluid Flow Problems," *Numerical Heat Transfer*, Vol. 8, pp. 537–557.

R. E. Spall
Department of Mechanical Engineering,
University of South Alabama,
Mobile, AL 36688

M. R. Malik
High Technology Corporation,
Hampton, VA 23666

The Linear Stability of a Flat Plate Boundary-Layer Approaching a Cylindrical Obstacle

The linear stability of the low-speed three-dimensional flow over a flat plate with an attached cylinder is studied. The region of interest is upstream of the initial separation point and includes the effects of both adverse and favorable pressure gradients, as well as crossflow. The resulting boundary-layer is subject to both the Tollmien-Schlichting (TS) and crossflow instabilities. Linear stability calculations, using N-factor correlations, indicate that the transition process would be dominated by TS instabilities, although for low frequencies crossflow-type disturbances are important.

Introduction

The majority of the flows occurring in nature are three-dimensional, and for applications such as laminar flow control and transition prediction, it is necessary to understand the stability mechanisms inherent in these boundary layers. In this paper we investigate the stability and transition of the low-speed three-dimensional boundary layer formed over a flat plate with an attached cylinder. This problem provides an ideal platform for studying the effects of crossflow and both favorable and adverse pressure gradients on boundary layer stability and transition.

In a low disturbance environment, the e^N method, first used by Smith and Gamberoni (1956), represents a viable method for estimating the location of the onset of transition. Correlations with experimental data over a wide range of flow conditions indicate that for Tollmien-Schlichting, Goertler and crossflow instabilities, the onset of transition correlates well with values of N ranging from 9 to 11 (see Malik, 1990). Here, N is computed as:

$$N = \ln(A/A_0) = \int_{s_0}^{s_t} \sigma(s)\,ds \tag{1}$$

where A_0 is the amplitude of the internalized disturbance at the location of the onset of instability and σ is the corresponding growth rate. The majority of N-factor calculations have been performed for two-dimensional or axisymmetric boundary layers, or for three-dimensional boundary layers formed over swept wings which were computed by employing the conical flow similarity transformation in the spanwise direction. Exceptions include the works of Cebeci and Chen (1989) and Spall and Malik (1990), in which the stability of a low-speed boundary layer formed over a prolate spheroid at incidence was investigated. In each of these works, excellent agreement was obtained with the experimentally determined transition location (Meier and Kreplin, 1980) using a value of $N = 10$.

The stability results presented herein have been computed using a modified version of the linear stability analysis code COSAL (Malik, 1982). The modifications are limited to additions necessary to integrate along a curve in a fully three-dimensional flow field, which requires interpolation of the mean flow variables. The boundary-layer solution was computed using a second-order accurate finite-difference procedure coded by Wie (1990). This procedure employs Matsuno's finite-difference method (Matsuno, 1981) and is well suited for three-dimensional boundary-layer calculations.

The three-dimensional boundary-layer considered in this paper is subject to both viscous (Tollmien-Schlichting) and inviscid Rayleigh waves. The latter instability may be present in both two and three-dimensional boundary layers provided the velocity profiles are inflected. The presence of an adverse pressure gradient, for example, will introduce the inflection point in the streamwise velocity profile, while the crossflow velocity profile in a three-dimensional boundary layer is always inflected. In this paper, we classify the instability (whether viscous or inviscid) associated with the streamwise velocity profile as TS, while that associated with the crossflow velocity profile is classified as crossflow instability.

Numerical Procedure

The three-dimensional boundary-layer equations for the compressible laminar flow in a Cartesian coordinate system may be written as:

continuity equation:

$$\frac{\partial}{\partial x}(\rho u) + \frac{\partial}{\partial y}(\rho v) + \frac{\partial}{\partial z}(\rho w) = 0 \tag{2}$$

x-momentum equation:

$$\rho\left(u\frac{\partial u}{\partial x} + v\frac{\partial u}{\partial y} + w\frac{\partial u}{\partial z}\right) = -\frac{\partial p}{\partial x} + \frac{\partial}{\partial z}\left(\mu\frac{\partial u}{\partial z}\right) \tag{3}$$

Contributed by the Fluids Engineering Division for publication in the JOURNAL OF FLUIDS ENGINEERING. Manuscript received by the Fluids Engineering Division February 20, 1991. Associate Technical Editor: C. S. Freitas.

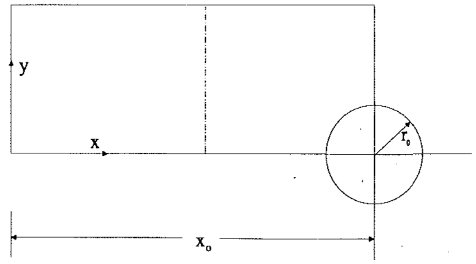

Fig. 1 Schematic of cylinder/flat plate configuration. Dash-dot line indicates end of computational region.

y-momentum equation:

$$\rho\left(u\frac{\partial v}{\partial x}+v\frac{\partial v}{\partial y}+w\frac{\partial v}{\partial z}\right)=-\frac{\partial p}{\partial y}+\frac{\partial}{\partial z}\left(\mu\frac{\partial v}{\partial z}\right) \tag{4}$$

energy equation:

$$\rho\left(u\frac{\partial H}{\partial x}+v\frac{\partial H}{\partial y}+w\frac{\partial H}{\partial z}\right)=\frac{\partial}{\partial z}\left\{\frac{\mu}{\Pr}\frac{\partial H}{\partial z}+\mu\left(1-\frac{1}{\Pr}\right)\frac{\partial}{\partial z}\left(\frac{V^2}{2}\right)\right\} \tag{5}$$

In the foregoing equations, (u, v, w) are the velocity components in the (x, y, z) directions (where z is normal to the surface), V is the total velocity given by $V = (u^2 + v^2)^{1/2}$, H is the total enthalpy, Pr is the constant Prandtl number (equal to 0.72), and μ is the dynamic viscosity. The perfect gas equations and Sutherland's law are used to close the equation set. As shown in Fig. 1, the geometry for the computations is a circular cylinder normal to the surface of a sharp leading edge flat plate.

The boundary layer was computed using analytic edge velocity boundary conditions (valid for an incompressible flow). The inviscid velocity components are given by (Sowerby, 1965):

$$u_e=U_\infty\left\{1+r_0^2\frac{y^2-(x-x_0)^2}{[(x-x_0)^2+y^2]^2}\right\} \tag{6}$$

$$v_e=-2U_\infty r_0^2\frac{y(x-x_0)}{[(x-x_0)^2+y^2]^2} \tag{7}$$

where r_0 is the cylinder radius, x_0 is the distance from the leading edge of the plate to the cylinder axis, and U_∞ is the uniform velocity at infinity in the x direction. We note that the freestream conditions employed (discussed in the results section) result in a Mach number of 0.11, which justifies the use of the incompressible inviscid solution.

A Levy-Lees type transformation is used in order to remove the singularity at $x = 0$. This transformation is of the form:

$$x=x,\ y=y,\ \zeta=\sqrt{\frac{\rho_e u_e}{\mu_e s}}\int_0^z\frac{\rho}{\rho_e}\,dz \tag{8}$$

Matsuno's finite-difference scheme is used to advance the solution in the streamwise direction (see Matsuno, 1981; Wie, 1990). The scheme is half-implicit in the ζ (transformed wall-normal coordinate) direction, explicit in the y direction, non-iterative and second-order accurate.

The stability results presented in this paper have been obtained using a modified version of the linear stability code COSAL. The modifications include provisions to accept fully three-dimensional boundary-layer profiles. In COSAL, a parallel flow approximation is employed, and the disturbed flow (say the u component) may be represented as:

$$u(x,y,z,t)=U(z)+\epsilon\hat{u}(z)e^{i(\alpha x+\beta y-\omega t)} \tag{9}$$

where α, β are the disturbance wave numbers in the x and y directions, respectively, and ω is the disturbance frequency. The compressible, linear (small ϵ) stability equations can be represented as:

$$\left(A\frac{d^2}{dz^2}+B\frac{d}{dz}+C\right)\overline{\Phi}=0 \tag{10}$$

where $\overline{\Phi}$ is a five element vector defined as $[\alpha\hat{u}+\beta\hat{v}, \hat{w}, \hat{p}, \hat{T}, \alpha\hat{v}-\beta\hat{u}]$ and the elements of the A, B, and C matrices are given in Malik and Orszag (1987) and in Malik (1989). This system is solved subject to the boundary conditions:

$$\Phi_1=\Phi_2=\Phi_4=\Phi_5=0 \text{ at } z=0. \tag{11a}$$

$$\Phi_1,\ \Phi_2,\ \Phi_4,\ \Phi_5\rightarrow 0 \text{ as } z\rightarrow\infty \tag{11b}$$

The above system provides, given the Reynolds number R, a complex dispersion relation of the form:

$$\omega=\omega(\alpha,\beta) \tag{12}$$

For temporal theory which is used in COSAL, α and β are real and ω is complex. The temporal theory results in a linear eigenvalue problem for ω, allowing a direct analysis using generalized eigenvalue techniques. The stability equations are discretized using a second-order accurate finite-difference formulation on a staggered grid, eliminating the need for pressure boundary conditions.

For the temporal problem the dispersion relation contains four arbitrary parameters, α, β, ω_r, and ω_i. The envelope method is used to prescribe the mode whose growth is integrated in the N-factor calculation. This requires the specification of the real frequency ω_r and the maximization of the growth rate ω_i with respect to wave numbers α and β. This procedure uniquely determines the wave numbers, and the wave orientation can then be defined as:

$$\psi=\tan^{-1}(\beta/\alpha) \tag{13}$$

A disturbance of fixed frequency ω_r, whose temporal growth rate is a maximum, satisfies the condition that the group velocity ratio $(\omega_\beta/\omega_\alpha)$ be real (Malik, 1990). The group velocity angle

$$\bar{\psi}=\tan^{-1}(\omega_\beta/\omega_\alpha) \tag{14}$$

provides the direction in which the integration of amplification rates is carried out for the N-factor procedure. To perform the integration, the temporal amplification rate ω_i needs to be converted to a spatial rate, which is accomplished using the group velocity transformation (Gaster, 1962). The disturbance amplitude at some downstream location is given as $A = A_0 e^N$, where A_0 is the amplitude of some disturbance at the critical point. The onset of transition is assumed to occur when N reaches some predetermined value, typically in the range of 9–11.

Results and Discussion

Results are presented for the stability of a low-speed boundary-layer formed over a flat plate with an attached cylinder. The geometry is schematically shown in Fig. 1. The cylinder radius, r_0, is given as 0.5 ft (0.1542 m). The distance from the leading edge of the flat plate to the axis of the cylinder is 7.5 r_0. Calculations were made with the free-stream axial velocity fixed at U_∞ = 125.4 ft/s (38.22 m/s), the free-stream temperature at T_∞ = 518 deg R (287.8° K) and the free-stream pressure at P_∞ = 2116 psf (101.3 kPa). These conditions result in a Reynolds number of 800,000/ft (2,624,670/m) and a free-stream Mach number of 0.11. The above geometry and flow conditions were chosen to provide a mean flow that exhibits a wide variety of stability behavior. In addition, the geometry provides for a short approach region (near the leading edge of the plate) in which the adverse pressure gradient and cross-flow Reynolds numbers are relatively small. Finally, we note that in the presentation that follows, distances have been made nondimensional with respect to the length scale L = 1.0 ft

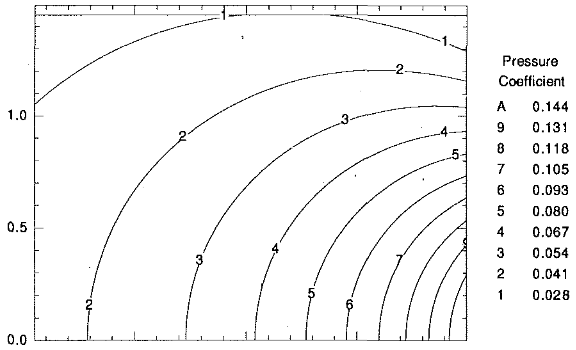

Fig. 2 Contours of constant pressure coefficient

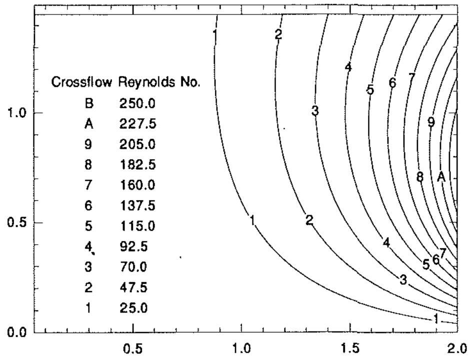

Fig. 3 Contours of constant crossflow Reynolds number

(0.3084 m), which, in the present case, is equal to the cylinder diameter.

The analytic inviscid velocity distribution (given by Eqs. (6), (7)) was used in the solution of the boundary-layer equations. The corresponding free-stream pressure distribution, which is imposed at the edge of the boundary layer, is shown in Fig. 2 for $0 \leq x \leq 2$. (We limit the domain to $0 \leq x \leq 2$ since the boundary layer separates at $x \approx 2.05, y = 0$. This limit is also indicated in Fig. 1 by the dashed vertical line.) The contours indicate that an adverse pressure gradient exists in the streamwise (x) direction along the $y = 0$ symmetry line. Off the line of symmetry, for $0 < y < 1.0$, the contours indicate, in addition to the adverse gradient in the streamwise direction, there exists a favorable pressure gradient in the transverse (y) direction. Beyond $y \approx 1.0$, the streamwise pressure gradient changes signs (from adverse to favorable for increasing (x)), although the transverse gradient remains favorable. This transverse pressure gradient provides for the three-dimensionality of the boundary-layer and is responsible for the development of cross-flow (i.e., a component of the velocity within the boundary layer that is perpendicular to the local inviscid flow direction). The adverse streamwise pressure gradient along the symmetry line results in velocity profiles containing points of inflection, while the favorable streamwise gradients at large transverse distances promote full, inflection-free velocity profiles. Thus, we can expect to find viscous Tollmien-Schlichting, and inviscid inflectional instabilities (both of the streamwise and crossflow velocity profiles) in the resultant boundary layer.

The boundary layer was computed using 101 equally spaced points in the wall normal direction ($\Delta\eta = 0.1$), and grid spacings of $\Delta x = 0.1r_0$ in the streamwise direction and $\Delta y = 0.1r_0$ in the transverse direction. To assess the sensitivity of the boundary layer to grid refinement, additional calculations were made by halving the grid size in the streamwise and transverse directions. Essentially no difference was found in the resulting velocity profiles or the location of separation. The boundary layer computed using grid spacing $\Delta x = \Delta y = 0.1r_0$ was used in the stability calculations that follow. We note that the cylinder/flat plate boundary layer has previously been computed by a number of investigators, including Dwyer (1968), Fillo and Burbank (1972), and Cebeci (1975).

The cross-flow Reynolds number is often used as a guide in estimating the location of transition due to crossflow instability. Poll (1984) provides a detailed discussion of this topic. For incompressible flows, crossflow Reynolds numbers on the order of 200 provide an approximate *upper limit* for the existence of laminar flow; that is, it is unlikely that laminar flow can be sustained in regions where the crossflow Reynolds exceeds ≈ 200. We present in Fig. 3 the computed cross-flow Reynolds number, $\mathrm{Re}_{cf} = U_n\delta_{0.1}/\nu$, corresponding to the previously described configuration, where U_n is the maximum velocity in the crossflow direction and $\delta_{0.1}$ is the distance from the wall at which the crossflow velocity decreases to $0.1\ U_n$. Figure 3 indicates that the maximum cross-flow Reynolds number is greater than 250, and thus, based on the above discussion we expect cross-flow-type disturbances to be important in the stability/transition analysis for this flow. Note that for $x < 1.0$, the crossflow Reynolds numbers are relatively small at all transverse locations. Of course, along the symmetry line the cross-flow Reynolds number is zero for all x. Figures 2 and 3 will be useful in the discussion and interpretation of the stability results that follow.

In the remainder of this section we present integrated amplification rates (N-factors) and stability characteristics in the form of contour plots. Recall (from the section on the numerical method) that we have chosen the envelope method to prescribe the mode whose growth is integrated in calculating the N-factor. This requires the specification of the real frequency, f; the growth rates are then maximized with respect to the disturbance wave numbers α and β. We present results for three frequencies, $f = 100$, 500 and 1000Hz.

Contours of constant N are shown in Figs. 4(*a*–*c*) for $f = 100$, 500, and 1000 Hz, respectively. We note that the onset of transition is usually assumed to occur (based on correlations with experimental data) when N reaches a value of 9 to 11. Thus, we see that for the frequencies shown, and within the computational domain, that N reaches 9 only for the frequency $f = 500$Hz. For this frequency, the maximum value of N occurs slightly off the symmetry line (at $y \approx 0.15$), and reaches a value of $N \approx 10$. We also note the absence of gradients in the transverse direction, especially for smaller values of x. At larger values of x, a gradient in the transverse direction forms, indicating a significant change in the boundary-layer stability characteristics with respect to a constant frequency disturbance. This will be discussed further when we present contours of the growth rates. Contours of constant N for the case $f = 100$ Hz reveal a maximum N of approximately 2.25. This occurs at $y \approx 0.75$, which also corresponds to the region in which the cross-flow Reynolds number is a maximum. The initial instabilities are also seen to occur downstream of those for the case $f = 500$ Hz. The final frequency examined, $f = 1000$ Hz, reaches a maximum value of $N \approx 7.0$ along the $y = 0$ symmetry line. In addition, the initial instabilities occur upstream of those for the case $f = 500$ Hz. We also note that the N-factor decreases beyond $x = 1.2$ for $y > 1.0$.

The above behavior in N-factor calculations will be further investigated in the remainder of the paper by examining contour plots of growth rates and disturbance wave angles and wavelengths. We will also look at the direction of disturbance propagation as determined by the group velocity vector. We also note that it is possible that some intermediate frequencies may result in values of $N = 10$ at some location for $x < 2.0$.

A contour plot of the growth rates for the disturbance frequency $f = 100$ Hz is shown in Fig. 5(*a*). Recall that the growth rates have been maximized with respect to the disturbance wave numbers α and β, and the corresponding contour plots of

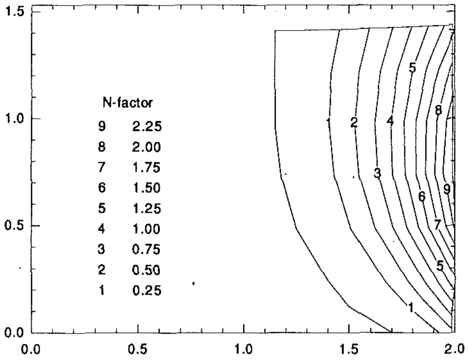

Fig. 4(*a*) *f* = 100 Hz

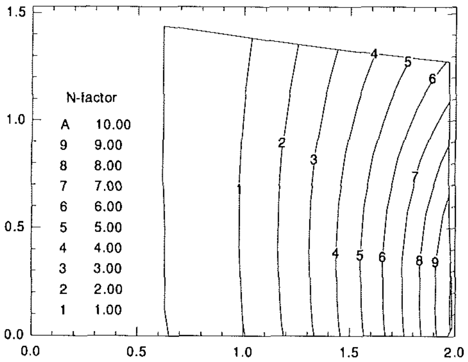

Fig. 4(*b*) *f* = 500 Hz

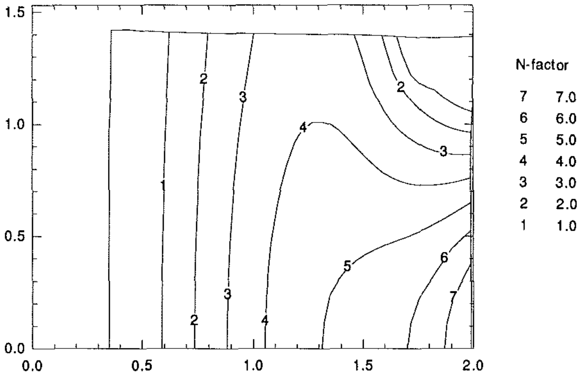

Fig. 4(*c*) *f* = 1000 Hz

Fig. 4 Contours of constant *N*-factor for various disturbance frequencies, *f*

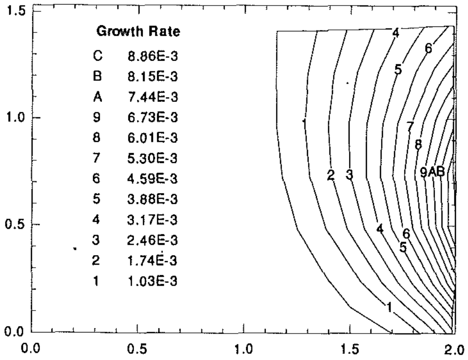

Fig. 5(*a*) Growth rate

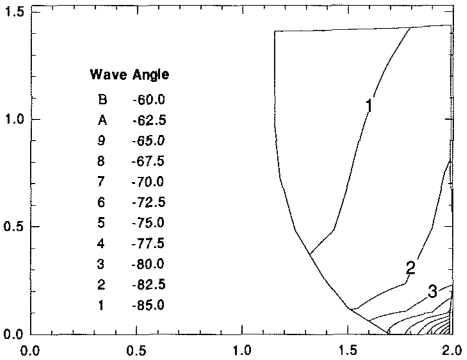

Fig. 5(*b*) Wave angle

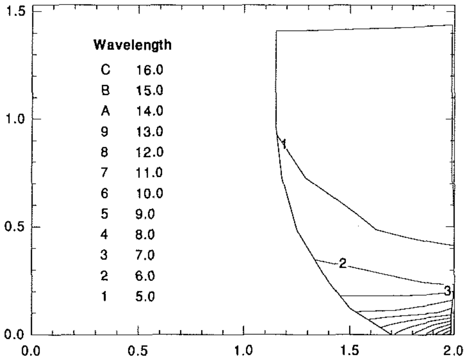

Fig. 5(*c*) Wavelength

Fig. 5 Disturbance characteristics for constant *f* = 100 Hz disturbance

constant wave angle and wavelength are shown in Figs. 5(*b*–*c*), respectively. From Fig. 5(*a*) we see that the initial instabilities take place well off the symmetry line ($y > 1.0$) for $x > 1.0$. Along the symmetry line, the flow is stable until $x \approx 1.7$. The maximum growth rates occur in the region near $y \approx 0.7$ and $x = 2.0$. By comparing with Fig. 3 we see that increasing growth rates correlate with levels of increased crossflow Reynolds number. This indicates that at this relatively low frequency the instability is of the crossflow type over most of the domain. Of course, as one approaches the symmetry line, where the crossflow Reynolds number is zero, this is not the case.

Further evidence that these are crossflow type instabilities can be inferred from the contours of constant wave angle and wavelength shown in Figs. 5(*b*–*c*), respectively. Typically, crossflow disturbances are characterized by wave angles oriented nearly perpendicular to the local inviscid streamlines of the flow. As shown in Fig. 5(*b*), the magnitudes of the most unstable wave angles are greater than 80 deg over most of the unstable region. Near and along the symmetry line, the magnitudes of these wave angles diminish to approximately 60 deg. Crossflow instabilities are also characterized as relatively short wavelength disturbances. We see from Fig. 5(*c*) that the ratio of $\lambda/\delta_{0.995}$ is less than 6.0 over most of the region. Again, as the symmetry line is approached the most unstable wavelength increases rapidly to values as high as 16.0. Thus, for $f = 100$ Hz, the boundary layer is most susceptible to crossflow-type instabilities except near the symmetry line where TS type instabilities may be present. This accounts for the fact that the *N*-factors are a maximum away from the symmetry line and correlate with the contours of crossflow Reynolds number.

The growth rates for the case $f = 500$ Hz are shown in Fig. 6(*a*). Here we see that the neutral curve is located upstream relative to the neutral curve for the disturbance $f = 100$ Hz.

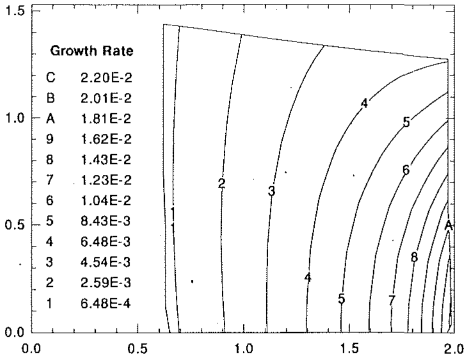

Fig. 6(*a*) Growth rate

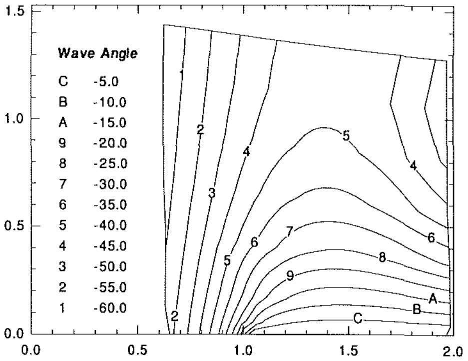

Fig. 6(*b*) Wave angle

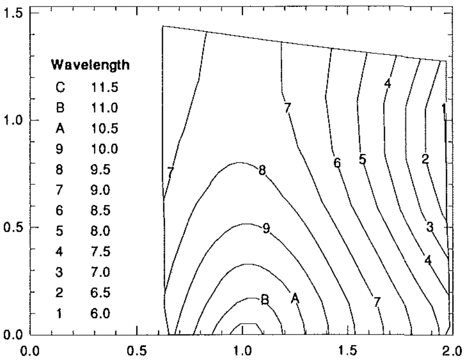

Fig. 6(*c*) Wavelength

Fig. 6 Disturbance characteristics for constant *f* = 500 Hz disturbance

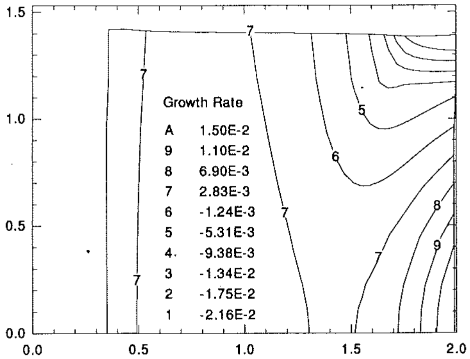

Fig. 7(*a*) Growth rate

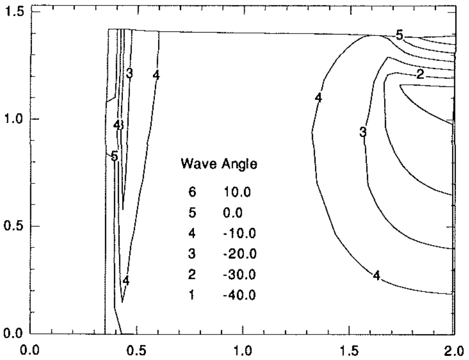

Fig. 7(*b*) Wave angle

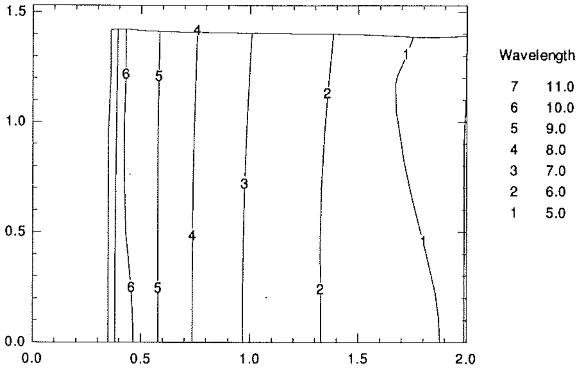

Fig. 7(*c*) Wavelength

Fig. 7 Disturbance characteristics for constant *f* = 1000 Hz disturbance

In addition, maximum amplification rates have increased, and now occur along and near the symmetry line. This indicates that the maximum growth rates are now of the TS type and are enhanced by the adverse pressure gradient, which is maximum along the symmetry line. As was apparent from the N-factor contours, the growth rates are nearly constant with respect to the transverse location for $x < 1.2$. Beyond this axial location, the growth rates diminish as a function of increasing transverse distance (for constant axial location). This is due to pressure gradient effects—as the transverse distance is increased, the adverse pressure gradient is lessened (see Fig. 2).

Additional information can be gained by examining the contours of constant wave angle and wavelength, which are shown in Figs. 6(*b–c*). Along the symmetry line, the magnitude of the most amplified wave angle rapidly decreases from $\psi \approx 55$ deg at the initial instability to $\psi \approx 0$ at $x = 1.1$. Beyond this location the most amplified wave angle remains near $\psi \approx 0$. For larger transverse distances we see that the magnitude of ψ is generally in the range of 20 deg $< \psi <$ 60 deg. As shown in Fig. 6(*c*), the longest wavelength disturbances correlate with the location along the symmetry line at which ψ approaches 0 deg. At this location, the ratio of $\lambda/\delta_{0.995}$ is approximately 11.5. As the disturbance moves downstream, the ratio decreases to approximately 8.0, consistent with the increasing thickness of the boundary layer. Away from the symmetry line we see that generally, $\lambda/\delta_{0.995} < 9.0$. Based on Figs. 6(*a–c*) it is apparent that the TS instability near the symmetry line is most amplified, and responsible for transition (based on $N = 10$). Off the symmetry line, the instability displays characteristics that are intermediate between TS and crossflow instabilities.

The growth rates for the disturbance $f = 1000$ Hz are shown

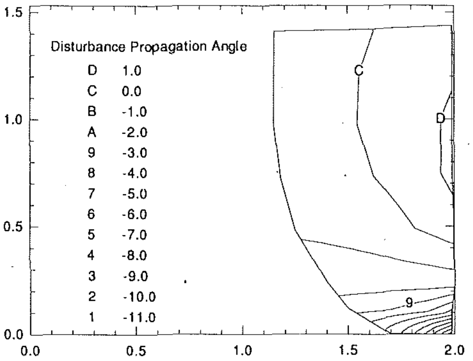

Fig. 8(*a*) f = 100 Hz

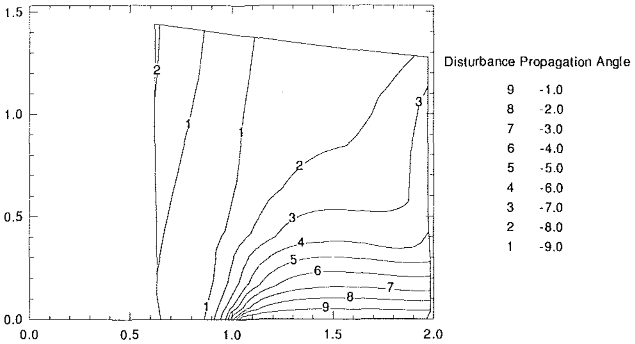

Fig. 8(*b*) f = 500 Hz

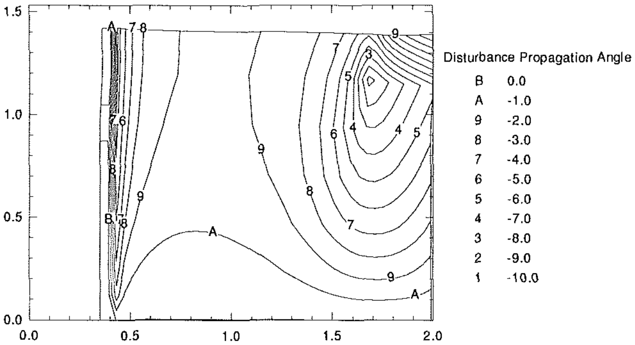

Fig. 8(*c*) f = 1000 Hz

Fig. 8 Disturbance propagation angle as determined by the group velocity vector for various disturbance frequencies

in Fig. 7(*a*). The corresponding wave angles and wavelengths are shown in Figs. 7(*b–c*), respectively. As was the case for f = 500 Hz the maximum growth rate at any axial location occurs along the symmetry line. We do note the occurrence of a local maximum at $x \approx 0.8$ and a local minimum at $x \approx 1.4$. This is undoubtedly due to pressure gradient effects. Beyond $x \approx 1.4$ the increasingly severe adverse pressure gradient begins to dominate the instability, halting the decline in growth rate (which would be expected to occur in the absence of a pressure gradient). At large transverse distances ($y > 1.0$), for $x > 1.4$, the boundary layer is stable to the 1000 Hz disturbance. This again can be attributed to the pressure gradient—Fig. 2 indicates the existence of a favorable pressure gradient in this region. At 1000 Hz, one would expect the most amplified disturbance to be of the TS type, and this is affirmed by the contours of constant wave angle and wavelength, shown in Figs. 7(*b–c*). Over most of the region the wave angle of the most unstable disturbance is small. Only in the region where the favorable pressure gradient exists, and the boundary layer is stable, are the wave angles relatively large. For all transverse locations, the most unstable wavelength is approximately 11.0 at the neutral curve, and decreases continuously to 5.0 at x = 2.0. This indicates that these disturbances are of the TS type over the entire region.

As discussed in the numerical procedure section, the growth rates are integrated along a path determined by the real part of the group velocity vector. Contours of the resulting disturbance propagation angle (measured with respect to the local inviscid flow direction) are shown in Figs. 8(*a–c*) for f = 100, 500 and 1000 Hz disturbances, respectively. These figures indicate that in regions where the growth rates are comparatively large, the disturbance propagation angle is nearly aligned with the free stream inviscid velocity vector. For instance, for the case f = 100 Hz away from the symmetry line where the crossflow is large (and thus the growth rates are relatively high) the propagation angle is within 2 deg of the inviscid velocity vector. For the cases f = 500 and 1000 Hz, the propagation angle is aligned in the streamwise direction along the downstream portion of the symmetry line (again, where the growth rates are high).

However, the computed propagation angle is large in the region where the growth rates are small. This is especially apparent along the symmetry line for the f = 100 Hz disturbance, which is highly oblique. Strictly speaking, the single normal mode analysis becomes particularly questionable along the line of symmetry for oblique disturbances. Perhaps, the harmonic point source analysis (Gaster, 1975; Balakumar and Malik, 1991) can be used to obtain more realistic information regarding wave propagation along the line of symmetry.

Conclusions

The results for the linear stability of a low-speed three-dimensional boundary-layer formed over a flat plate with an attached cylinder have been presented. The results indicate that transition, as predicted by the e^N method, first occurs along or near the y = 0 symmetry line and is due to Tollmien-Schlicting type disturbances. However, crossflow disturbances are most amplified at lower frequencies.

Acknowledgments

This work was funded by the Theoretical Flow Physics Branch, Fluid Mechanics Division, NASA Langley Research Center under contract NAS1-18240.

References

Balakumar, P., and Malik, M. R., 1990, "Waves Produced From a Harmonic Point Source in a Supersonic Boundary Layer," AIAA paper 91-1646.

Cebeci, T., 1975, "Calculation of Three-Dimensional Boundary Layers, II. Three-Dimensional Flows in Cartesian Coordinates," *AIAA J.*, Vol. 13, pp. 1056–1064.

Cebeci, T., and Chen, H. H., 1989, "Prediction of Transition on Airfoils with Separation Bubbles, Swept Wings and Bodies of Revolution at Incidence," *Symposium on Numerical and Physical Aspects of Aerodynamic Flows*, Long Beach, CA, Jan. 16–19.

Dwyer, H. A., 1968, "Solution of a Three-Dimensional Boundary-Layer Flow with Separation," *AIAA J.*, Vol. 6, pp. 1336–1342.

Fillo, J. A., and Burbank, R., 1972, "Calculation of Three-Dimensional Laminar Boundary-Layer Flows," *AIAA J.*, Vol. 10, pp. 353–355.

Gaster, M., 1962, "A Note on the Relation Between Temporally Increasing and Spatially Increasing Disturbances in Hydrodynamic Stability," *J. Fluid Mech.*, Vol. 14, pp. 222–224.

Gaster, M., 1975, "A Theoretical Model of a Wave Packet in the Boundary Layer on a Flat Plate," *Proc. R. Soc.*, Series A, Vol. 347, pp. 271–289.

Malik, M. R., and Orszag, S.A., 1987, "Linear Stability Analysis of Three-Dimensional Compressible Boundary Layers," *Journal of Scientific Computing*, Vol. 2, pp. 77–97.

Malik, M. R., 1989, "Numerical Methods for Hypersonic Boundary-Layer Stability," *J. Comp. Physi.*, Vol. 86, pp. 376–413.

Malik, M. R., 1982, "COSAL—A Black Box Compressible Stability Analysis Code for Transition Prediction in Three-Dimensional Boundary-Layers," NASA CR-165925.

Malik, M. R., 1990, "Stability Theory for Laminar Flow Control Design," *Progress in Astronautics and Aeronautics*, AIAA, Washington, D.C., Vol. 123.

Matsuno, K., 1981, "A Vector-Oriented Finite-Difference Scheme for Calculating Three-Dimensional Compressible Laminar and Turbulent Boundary Layers on Practical Wing Configurations," AIAA paper 81-1020.

Meier, H. U., and Kreplin, H., 1980, "Experimental Investigation of the Boundary-Layer Transition and Separation on a Body of Revolution," *Zeitschrift Fur Flugwissen und Weltraum-forschung*, Vol. 4, pp. 65–71.

Poll, D. I. A., 1984, "Transition Description and Prediction in Three-Dimensional Flows," AGARD Rept. No. 709, Special Course on Stability and Transition of Laminar Flow.

Smith, A. M. O., and Gamberoni, N., 1956, "Transition, Pressure Gradient, and Stability Theory," Douglas Aircraft Co., Report ES 26388.

Sowerby, L., 1965, "The Three-Dimensional Laminar Boundary-Layer on a Flat Plate," *J. Fluid Mech.*, Vol. 22, pp. 587–598.

Spall, R. E., and Malik, M. R., 1992, "The Linear Stability of Three-Dimensional Boundary-Layers Over Axisymmetric Bodies at Incidence," *AIAA J.*, Vol. 30, No. 4, pp. 905–913.

Wie, Y.-S., 1990, "Numerical Solution of the Boundary-Layer Equations for a General Aviation Fuselage," *AIAA J. Aircraft* (in press) also as AIAA paper 90-0305.

Boundary-Layer Transition in Accelerating Flows With Intense Freestream Turbulence: Part 1—Disturbances Upstream of Transition Onset

M. F. Blair
Senior Research Engineer,
United Technologies Research Center,
East Hartford, Conn. 06108
Mem. ASME

Hot-wire anemometry was employed to examine the laminar-to-turbulent transition of low-speed, two-dimensional boundary layers for two (moderate) levels of flow acceleration and various levels of grid-generated freestream turbulence. Flows with an adiabatic wall and with uniform-flux heat transfer were explored. All of the experimental test cases resulted in bypass-mode transitions, a conclusion based upon the observance of spots upstream of the theoretical minimum critical Reynolds number (three cases) or, for one case, upon the evidence that T-S mode amplification played no apparent role in the transition. Data obtained for the preonset stage indicate that the streamwise-component fluctuation-amplitude distributions, frequency distributions and outer-region waveforms of these bypass-mode transitions were similar to those reported in the literature for low-freestream-turbulence transitions. Within the zone upstream of the first appearance of turbulent spots: (1) The near-wall ($Y < \delta/2$) fluctuations were predominantly low-frequency (frequency approximately 1/5 of that of the most amplified T-S disturbances). (2) The maximum streamwise-component fluctuations occurred over the altitude band $0.3 < Y/\delta < 0.4$. (3) Very strong negative "spikes" in streamwise velocity were observed, just upstream of spot initiation, at boundary-layer altitudes near $Y/\delta = 0.6$.

Introduction

Until recently, nearly all in-depth investigations of incompressible boundary layer transition have been conducted in flows with weak freestream turbulence (see the reviews of Reshotko, 1976; Morkovin, 1977; and Arnal, 1984). The present study differs from this earlier work in that it examines transition in the presence of much higher levels of freestream turbulence. Such transition can have important engineering consequences, particularly in flows with negative streamwise pressure gradients where the acceleration stabilizes the boundary layer and extends the transitional zone. For example, the location and extent of transition on gas turbine airfoils strongly affects aerodynamic losses and heat load distributions.

Earlier studies of flows with negligible freestream turbulence have established that for such conditions, Tollmien-Schlichting (T-S) waves evolve from unstable-frequency disturbances downstream of a critical Reynolds number (Re_c). If these primary waves reach sufficient magnitude before crossing branch II of the neutral stability curve then a stage of nonlinear wave amplification ensues. The nonlinear stage is followed by strong transverse three-dimensional developments (Klebanoff et al., 1962). Comparisons between the characteristic behavior of such T-S mode transitions and the phenomena observed in the present study will be given in the body of the paper.

Second, it has been demonstrated in several studies involving weak but finite freestream turbulence that a natural broadband disturbance signature is generated within the boundary layer. Arnal et al. (1977), Kendall (1985), and Suder et al. (1988) have examined the weak-freestream-turbulence case and have independently shown that the fluctuation spectra were dominated by random, low-frequency, high-amplitude disturbances. Furthermore, Kendall (1985) has demonstrated that these low-frequency disturbances were narrow laterally (spanwise extent of a few boundary layer thicknesses). The amplitudes of these low-frequency disturbances were enormous compared to that of T-S waves; about an order of magnitude greater than that reached at the end of the linear amplification range for a conventional transition.

The present experiments were conducted with various combinations of streamwise acceleration and high levels of grid-generated freestream turbulence. The study focused on transitions in accelerating flows because of the potential utility of the results to turbomachinery design and because the phys-

---

Contributed by the Fluids Engineering Division for publication in the JOURNAL OF FLUIDS ENGINEERING. Manuscript received by the Fluids Engineering Division October 16, 1991. Associate Technical Editor: D. P. Telionis.

ical extension of the zone of transition made it feasible to obtain meaningful laboratory measurements. Particular emphasis was placed on examination of the spectral distribution of fluctuations near the onset of spot formation.

Experimental Arrangement

Wind Tunnel. The experiments were all conducted in the United Technologies Research Center Boundary Layer Wind Tunnel, a closed-loop driven by a centrifugal blower. A complete description of this facility including details of the boundary layer probe traverse system, the pressure data acquisition system and a series of facility qualification tests is given in Blair et al. (1981).

Test boundary layers developed along the flat, smooth upper wall of the test section, sketches of which are presented in Fig. 1. Two flat-wall test surfaces were employed in this study. One test surface consisted of a smooth aluminum plate with streamwise and spanwise rows of static pressure taps. A separate matrix of ports for mounting flush hot-film gages was also incorporated in this plate. The second boundary layer test surface was a uniform heat flux electrically heated plate instrumented for the measurement of local convective coefficients. Details concerning the geometry and instrumentation of the test-surface leading edge and the heated flat plate model are presented in Blair et al. (1981). In qualification tests performed with this heat transfer plate (Blair, 1983) streamwise heat transfer distributions were measured for both laminar and fully turbulent two-dimensional, zero-pressure-gradient flows. Measured distributions agreed within 2 percent of well-established boundary-layer heat transfer correlations for the respective flows.

Anemometry and Signal Processing. Measurements of the test section freestream turbulence characteristics were obtained using standard commercial single-element cylindrical hot-film and dual-element x film probes driven by linearized constant temperature anemometers. Mean flow and angular sensitivity calibration coefficients for the probes were obtained in a calibration jet. Distributions of the streamwise integral length scale were determined from autocorrelations generated with a Saicor Model SAI-42 Correlator and Probability Analyzer operated in the d-c coupled mode. Spectral density distributions were determined with an SD 340 MICRO FFT Analyzer.

A separate anemometry system, considerably different from the above, was employed to obtain the boundary layer turbulence data. In order to achieve adequate spatial and spectral resolution, platinum-plated-tungsten 2.5 μm dia. wires with 0.50 mm active length were installed in boundary-layer-type probes. The transverse separation between wires in the x arrays was 0.35 mm, a value chosen to produce a high correlation coefficient and minimal cross-talk between wires. Fulachier and Dumas (1976) employed a very similar sensor arrangement for boundary layer studies. Additional details of the probe design are given in Blair and Bennett (1987).

The hot-wire probes were driven with constant temperature anemometer units. Standard square-wave techniques were used to assure that the sensor anemometer frequency response exceeded 50 KHz. The anemometer outputs were passed through 5 KHz low-pass anti-aliasing filters to a four-channel, simultaneous sample-and-hold high-speed digitizer. A buck-and-gain (DC offset/AC amplifier) system was utilized to take advantage of the full 12-bit resolution of the digitizer. Signals were sampled for 5 seconds at 7813 samples/s/channel. The bandwidth of frequency resolution, then, was 1/5 to 3900 Hz. A minicomputer with 800 K Bytes available RAM was used to control the digitizer and temporarily store a stream of data. Longer term storage of the raw voltage-time records was achieved using 25 M Byte hard disks and digital tape. Reduction of the voltage-time records to velocity-time and velocity statistics was also accomplished using the minicomputer.

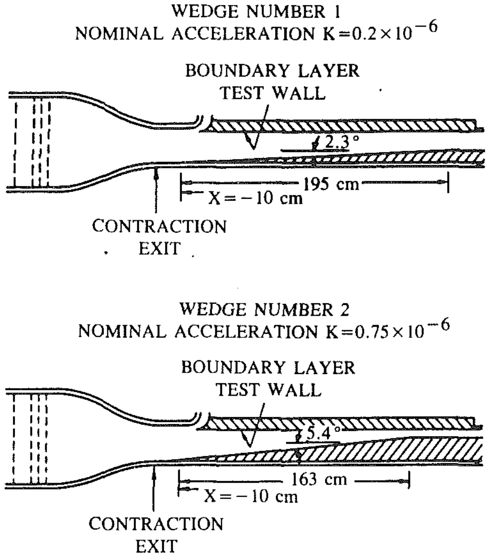

Fig. 1 Schematic of test configurations

The mean flow and angular sensitivity characteristics of the boundary layer probes were determined in a calibration jet. A least-squares technique was used to determine an optimum coefficient to fit the Champagne et al. (1967) angular law for each wire. Details of the data reduction procedures are given in Blair and Bennett (1987). For most of the wires the calibrations indicated an optimum coefficient within the range $0.10 < k < 0.15$. This range was slightly less than the value determined as typical ($K = 0.2$) for a $l/d = 200$ wire by Champagne et al. (1967).

Measurements of local wall shear were obtained on the flat aluminum plate model using TSI Model 1237W flush surface gages (sensor dimensions 0.12 × 1.0 mm). The voltage versus time-mean shear relationship of the gages was assumed to conform to the usual $\tau_\omega^{1/3} = AE^2 + B$ equation of Bellhouse and Schultz (1966). The gages were calibrated in situ in both zero pressure gradient and accelerating, artificially tripped turbulent boundary layer flows.

For the actual transitional test flows, signals from the surface hot-film gages and boundary-layer hot-wire probes were recorded simultaneously with the high-speed digitizer system.

Nomenclature

K = acceleration parameter
Re = Reynolds number
St = Stanton number
T = turbulence intensity
u', v', w' = fluctuating velocity components
U = mean streamwise velocity
$u'^2(f)$ = velocity fluctuations (squared) per Hertz
X = distance from leading edge
Y = distance from wall
δ = boundary layer thickness (U (long term average)/U_e = 0.99)
δ^* = displacement thickness
θ = momentum thickness
ν = kinematic viscosity

Subscripts

e = freestream

Table 1 The test matrix

Flow condition	K $x10^6$	Grid No.	T (at transition onset) %	Denoted
1	0.20	1	0.90	K.20G1
2	0.20	2	2.05	K.20G2
3	0.75	2	1.90	K.75G2
4	0.75	3	5.20	K.75G3

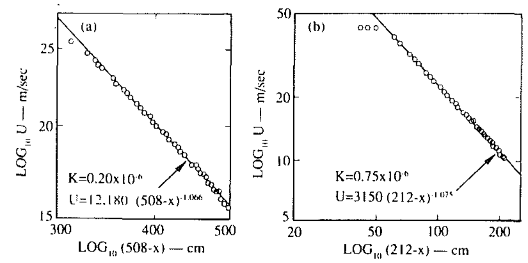

Fig. 2 Velocity distributions along test walls. (*a*) 2.3° wedge (wedge 1), (*b*) 5.4° wedge (wedge 2).

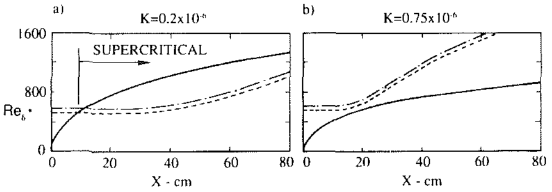

Fig. 3 Computation of the local and critical Reynolds number for the two velocity distributions. Predictions; ▬ local, —·— critical Re_δ^* (parallel theory), ∴.. critical Re_δ^* (nonparallel theory).

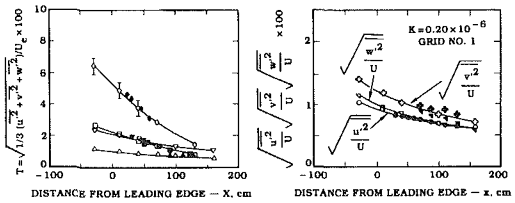

Fig. 4 Distributions of turbulence intensity in the test sections. (*a*) Total turbulence for the four test cases; △, K = 0.20 × 10^{-6}/grid 1, ▽, K = 0.20 × 10^{-6}/grid 2, □, K = 0.75 × 10^{-6}/grid 2, ◇, K = 0.75 × 10^{-6}/ grid 3. (*b*) Turbulence components for one test case; ○, u'/U, ▽, w'/U, ◇, v'/U. Both (*a*) and (*b*): open symbols x-hot films, solid symbols x-hot wires.

The surface hot film system bandwidth was limited by the sampling rate of the digitizer (7813 samples/s). At this sampling rate and for the typical incipient spot velocity (about 10 m/s) the minimum spot size detectable was approximately 2 mm or about $\delta/2$.

Test Conditions

Test Matrix. Boundary-layer transition was examined for four combinations of streamwise acceleration and freestream turbulence level. Two acceleration levels were employed. The acceleration parameter $K = \nu/U^2 \partial U/\partial x$ and a turbulence-generating-grid identification number associated with each flow are given in Table 1.

Velocity distributions computed from the test surface mid-span static pressure distributions measured for the two acceleration levels are presented in Fig. 2. The velocity distributions measured for the various turbulence grids agreed with the sample data of Fig. 2 within 1 percent and are omitted for clarity. Off-midspan static pressure data indicated that transverse gradients were negligible along the entire test surface for both wedge configurations. In addition, ink-streak surface flow visualization tests confirmed that the corner secondary flows were weak and that the flow along the test surface was two-dimensional over the central 75 cm of the tunnel span.

Instability Calculations. The boundary-layer code of Edwards et al. (1982) was employed to compute the integral thickness distributions of the developing laminar boundary layers for each of the two acceleration levels. (During the course of the program, it was confirmed that these predictions were in excellent agreement with integral thicknesses computed from mean velocity profile data.) Next, the stability charts of Wazzan et al. (1968) (linear theory/parallel flow) were employed, using interpolation, to predict the distributions of the minimum critical Reynolds number, Re_c, for both accelerations. Finally, the zero-pressure-gradient results of Gaster (1974) were used to estimate the impact of the boundary layer growth (nonparallel theory) on the respective critical Reynolds number distributions. Gaster's computations for zero-pressure-gradient flows indicate a reduction of approximately 100 in Re_c. Since boundary-layer growth effects would certainly be less important for accelerating flows, a reduction of 100 in Re_c was used as a conservative estimate of the maximum possible nonparallel effect for these present test conditions.

The results of these computations are presented in Fig. 3. Figure 3(*a*) reveals that for the $K = 0.2 \times 10^{-6}$ cases the test boundary layers were sub-critical for about the first 9 cm of development. For the remaining distance, the computations indicate that the boundary layers were supercritical for imposed disturbances within the range of unstable frequencies. For the $K = 0.75 \times 10^{-6}$ cases, Fig. 3(*b*), the computations indicated that the boundary layers were subcritical at all locations. These results show that for the lower acceleration level the test boundary layers were vulnerable to conventional (T-S) transition. For the higher acceleration level, however, only "bypass-mode" (Morkovin, 1977) transitions were feasible.

Freestream Turbulence Intensity. The wind tunnel residual turbulence intensity was approximately 0.20 percent at the contraction exit with a slight decrease along the test section. The higher freestream turbulence levels required for this study were generated using square-array biplane grids located at the entrance to the main tunnel contraction (contraction ratio 2.8:1—see Fig. 1). Three grids were employed, all having mesh/bar-width ratios of approximately 5 and about 63 percent open area. The data given by Baines and Peterson (1951) indicate that the turbulence generated by these grids should have been fully established at the test surface leading edge. The grids will be referred to as grids 1, 2, and 3 corresponding to mesh widths of 2.22, 6.51, and 17.8 cm, respectively.

The distributions of all three freestream components were documented for each combination of test-section insert and turbulence grid. Surveys of the streamwise distributions of the integral length scale and the spectral content of the streamwise component were also recorded.

The test section streamwise distributions of total turbulence intensity T, where

$$T = \sqrt{1/3(\overline{u'^2} + \overline{v'^2} + \overline{w'^2})}/Ue \qquad (1)$$

for the four grid/acceleration combinations are shown in Fig. 4(*a*). The plotted values represent the average of all samples taken at that streamwise location. Uncertainty bars indicate the range of measured data for cases where all values did not fall within the plotting symbol. It can be seen that streamwise decay was the strongest, by far, for grid 3 and that the grid 2 distributions were only slightly dependent on the acceleration level.

Two sets of data are included in Fig. 4(*a*). The freestream-survey data obtained with the linearized hot-film system are represented by the open symbols. The solid symbols indicate the turbulence levels measured with the analog/digital hot-wire system at the edge of the boundary layers. The agreement between these independent measurements is seen to be excellent.

A representative sample of the multicomponent turbulence intensity distributions, the data of case K.20G1, are shown in Fig. 4(*b*). These data indicate that the freestream turbulence was nearly isotropic. For all test cases, the relationship between the magnitudes of the three components was $v' > w' > u'$ with the differences decreasing along the test section. Again, good agreement resulted between the linearized hot-film and digitally sampled hot-wire data (frequency range 0.2 $H_z < f < 3.9$ KH_z).

The freestream turbulence intensity, length scale, and spectral distribution data for all acceleration/grid combinations are presented in Blair and Werle (1981).

Acoustic Disturbances. A number of axial and cross-duct acoustic disturbances were present in the test section during tunnel operation. These disturbances appear in the signals of the hot-wire and surface-hot-film sensors and must be differentiated from those effects associated with the boundary layer transition process. A description of the techniques used to identify the various acoustic signatures present in the test section is given in Blair (1991). In brief, acoustic signals (and their harmonics) which appear on the various spectral-distribution plots presented in this paper will be labeled as A (345 Hz), or B (1320 Hz).

Turbulent/Nonturbulent Decisions

During data acquisition, signals from the boundary layer hot-wire probes and surface hot-film gages were sampled continuously with the high speed A/D data system for blocks of five seconds duration. Data for each channel were compiled into continuous separate records stored on magnetic tape. Digital analysis techniques were subsequently employed to distinguish turbulent from nonturbulent sections of the records. A thorough description of the detector functions, smoothing periods and threshold values employed for the turbulent/nonturbulent decision making process is given in Blair (1991). Comparison of turbulent/nonturbulent decision-based statistics acquired with single-wire and x-wire probes ($(\partial u'/\partial t)^2$ and $(\partial u'v'/\partial t)^2$ detector functions, respectively) for the same conditions showed excellent agreement.

The performance of the turbulent/nonturbulent discrimination system was evaluated for sample records covering the entire range of freestream turbulence intensities, intermittencies and boundary layer altitudes tested. These evaluation tests indicated that the demarcation between the turbulent and nonturbulent zones was so sharp that the zonal discrimination was relatively insensitive to the threshold values employed.

Results and Discussion

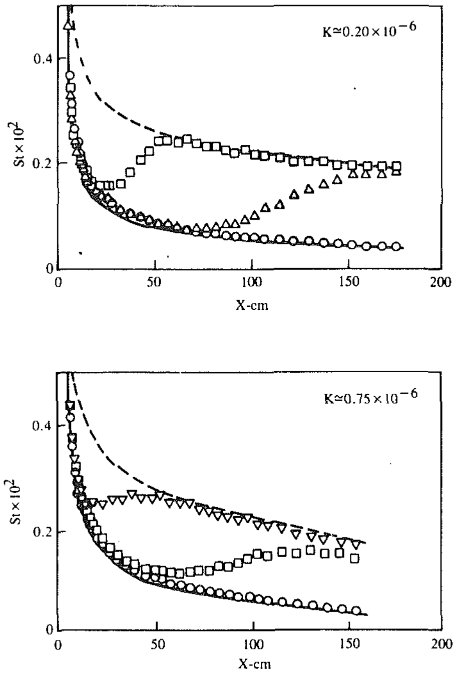

Fig. 5 Distributions of heat transfer along the test plate for various acceleration/freestream turbulence combinations. ○, no grid; △, grid 1; □, grid 2; ▽, grid 3; numerical boundary layer code predictions, —— laminar, . . . turbulent.

Heat Transfer. In order to introduce the general characteristics of the experimentally generated transitions, the first results presented will be the transitional heat transfer distributions (Figs. 5(*a*) and 5(*b*)). These particular data provide a clear indication of the location and extent of the transitions produced by the various acceleration/grid combinations. Each figure includes data obtained with specified turbulence grids installed and with only the tunnel residual turbulence ($T \sim 0.2$ percent). Laminar and fully turbulent heat transfer distributions predicted for these accelerations by the finite-difference boundary layer analysis of Edwards et al. (1982) are also presented. The data for the residual turbulence cases were in excellent agreement with their respective laminar predictions indicating a complete absence of transition for both accelerations. It is interesting to note that transition was not detected for the no-grid case for $K = 0.2 \times 10^{-6}$ even though the results of Fig 3(*a*) indicate that the boundary layer was supercritical downstream of $X = 9$ cm. No high-frequency-response (surface hot-film or boundary layer probe) data were obtained for the no-grid cases so it is not known if T-S waves or widely space spots, which would not influence the mean heat transfer, were present in the supercritical zone.

The heat transfer instrumentation pattern covered the central 60 percent of the uniform heat flux wall. Variations of the measured Stanton numbers across this central span generally did not exceed 3 percent of the local mean value for the laminar, transitional or fully turbulent regions. The single largest spanwise variations (±10 percent) in measured Stanton number were observed at a station about one-third through transition.

The results for the various grid/acceleration combinations demonstrate the expected interplay of the effects of freestream turbulence and acceleration on transition. For both acceleration levels, increases in the freestream turbulence intensity produced earlier transition onset and reduced transition length. The capacity of increased acceleration to delay and extend a transition for nearly the same freestream turbulence intensity can be seen by comparing the K.20G2 and K.75G2 cases. For both acceleration levels the post-transitional heat transfer distributions agreed very well with the fully turbulent boundary-layer predictions.

Particular attention should be given to the K.20G1 heat transfer results since this will be the "sample case" for which boundary layer turbulence data will be presented. Note that for this case there were extended regions of both laminar and transitional heat transfer. The minimum Stanton number is seen to be located at about $x = 65$ cm.

Disturbances Upstream of Transition. The development of

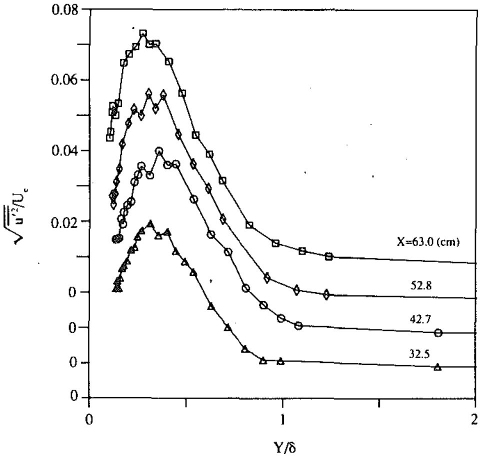

Fig. 6 u' **amplitude distributions in the boundary layer for four pretransitional streamwise stations for** $K = 0.20 \times 10^{-6}$ **and grid 1**

disturbances upstream of boundary-layer transition was studied using single-element hot-wire probes and surface thin-film gages. The hot-wire profile and wall-shear data were obtained simultaneously at the same streamwise locations but at spanwise locations offset 1.2 cm. Statistics of the velocity and wall-shear fluctuations were computed for each 5 second-length record. Spectral distributions of the velocity and shear-stress records were computed with an FFT routine contained in a commercial signal processing package.

Most of these pretransitional disturbance measurements were obtained for the K.20G1 case as this provided an extended region of pretransitional flow. Data were obtained at four stations (x = 32.5, 42.7, 52.8, and 63.0 cm) all of which were upstream of the location where the minimum Stanton number was observed (see Fig. 5(*a*)). As can be determined from an examination of Fig. 3(*a*) linear instability theory predicts the boundary layer to be supercritical at all these stations.

The streamwise development of the u' amplitude distribution within the boundary layer for the K.20G1 case is shown in Fig. 6. The streamwise evolution of both the shape and magnitude of these pretransitional amplitude-altitude distributions was consistent with results obtained in numerous independent studies of zero-pressure-gradient, low-freestream-turbulence flows. See, for example, the results of Arnal et al. (1977), Wang et al. (1985), Kendall (1985), and Suder et al. (1988). Figure 6 reveals that for all stations a rounded amplitude maximum was observed at about $\delta/3$. The magnitude of this amplitude maximum increased progressively with increasing x until reaching $u'/U_e = 0.072$ at $x = 63$ cm.

Power spectral distributions for both the boundary layer and freestream u' fluctuations are presented in Fig. 7. The boundary layer spectral distributions were obtained for the same four stations of Fig. 6 at a fixed altitude of $Y/\delta = 0.25$. The narrow spikes labeled A or as multiples of A correspond to acoustic waves from the tunnel blower and are not related to the boundary-layer transition process (see Blair, 1991). The power spectra, ϕ_u, of Fig. 7 are defined as:

$$\phi_u = u'^2(f)/\overline{u'^2}(\mathrm{s})$$

As would be expected far downstream of a biplane grid, the freestream spectral distribution of Fig. 7 was in excellent agreement with the von Karman one-dimensional spectrum for isotropic turbulence (comparison not shown). In contrast to the freestream distribution, the power in the boundary layer spectra was highly concentrated in the low ($\lesssim$100 Hz) frequency range. For example, for the spectrum at x = 32.5 cm there was more than a 6 decade rolloff over the measured bandwidth. These low-frequency, high-amplitude fluctuations dominated the disturbance spectra for the lower half of the boundary layer at all four streamwise stations. This result is consistent with the previously discussed (low freestream turbulence) results of Arnal et al. (1977), Kendall (1985), and Suder et al. (1988). For the altitude range $\delta/2 < Y < \delta$, (not shown) the relative contributions of the higher-frequency fluctuations increased progressively with Y. Near δ the boundary layer spectra asymptotically approached the freestream spectrum.

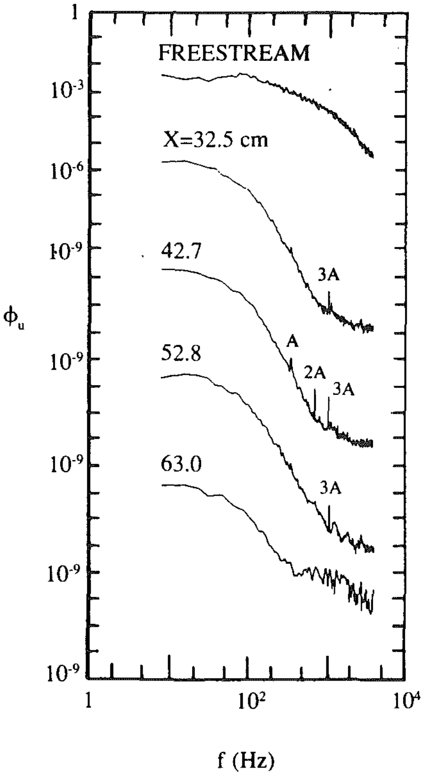

Fig. 7 Spectral distributions of u' **for a fixed altitude in the boundary layer (**Y/δ **= 0.25) with increasing** X**, each successive curve shifted by** 10^{-4}

Unstable frequencies for this boundary layer, computed using the previously described parallel and nonparallel linear theories, extended from 160 to 620 Hz. The spectra of Fig. 7 reveal no evidence of preferential amplification of disturbances within this bandwidth. In fact, there was no evidence in any of the data obtained for this test case that T-S waves played a role in the transition. For this reason, despite the fact that the boundary layer was theoretically supercritical, this test case qualifies as a bypass mode transition.

The contribution from higher-frequency events increased progressively with increasing distance along the test surface. For example, a comparison of the spectra for the x = 32.5 and x = 63 cm (Fig. 7) stations reveals that the power at 2000 Hz increased by a factor of about 1000. The shift, with increasing x, of power density toward higher frequencies is shown for three boundary layer altitudes (Y/δ = 0.25, 0.40 and 0.52) in Fig. 8. Figure 8(*a*) shows the progressive rise of the ratio of ϕ_u at 500 Hz to ϕ_u at 10 Hz while Fig. 8(*b*) gives similar results for ϕ_u at 2000 Hz. The relative power shift is most extreme at the lower altitudes but was still distinctly present at Y/δ = 0.52. The power ratios for the freestream (the von Karman spectrum) are included for reference.

Representative, sample time displays (500 ms duration) of the hot-wire probe signal at various boundary layer altitudes are presented for the four streamwise stations in Figs. 9(*a*-*d*). Included in each of these figures is a time display of the wall-shear signal obtained simultaneously with the respective min-

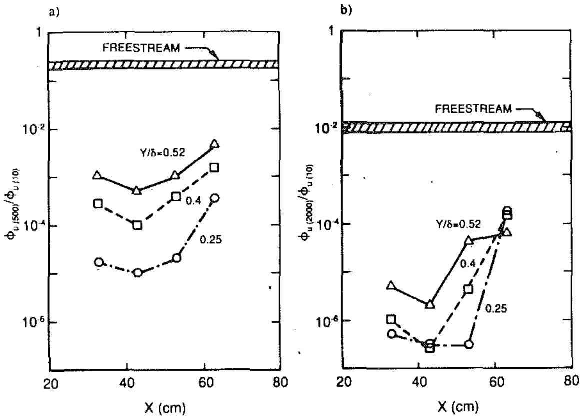

Fig. 8 Ratios of high-frequency/low-frequency power spectral density at fixed boundary-layer altitudes and increasing X

imum-altitude velocity display. For example, for Fig. 9(*a*) the wall-shear and $Y/\delta = 0.14$ displays show simultaneously recorded signals. The remaining three velocity displays were recorded independently of both the wall-shear and of each other. All five displays have a common time scale but the velocity amplitude scales were adjusted for purposes of clarity.

The time displays for the $x = 32.5$ cm station (Fig. 9(*a*)) demonstrate the magnitude of the previously discussed random, low-frequency fluctuations in the low-altitude portion of the boundary layer. They also show no evidence of the passage of turbulent spots at any altitude. In support of this, the turbulent/nonturbulent discrimination system indicated that no turbulent patches were detected, at any altitude, for the $x = 32.5$ cm station.

The only notable event shown in Fig. 9(*a*) was the strong negative spike at $Y/\delta = 0.54$. Similar, randomly spaced single spikes were observed over the altitude range $0.5 < Y/\delta < 0.8$ at this station.

A somewhat similar "negative-spike" stage has been reported by Klebanoff et al. (1962) and Kovasnay et al. (1962) for flows with negligible freestream turbulence and artificially induced T-S waves. Flow three dimensionalities which developed downstream of T-S amplification were characterized by strong transverse variations in the streamwise fluctuations (peaks and valleys) and by the simultaneous emergence of a regular pattern of large-scale vortex loops. The vortex loops intensified with distance but propagated more slowly than did the surrounding (outer region) boundary layer fluid. The flow of boundary-layer fluid over the vortex loops produced a sequence of high shear layers (Kovasnay et al. (1962)) which manifested themselves as a series of negative spikes in the outer region streamwise velocity record. The duration of the negative spikes indicated that the length scale of the vortex loops was about 1/10 of the T-S wavelength or about the local boundary layer thickness, δ. This stage was followed by the generation of hairpin eddies ("multiple spikes") and then by breakdown.

The negative spikes observed in the present study reflect the passage of much larger-scale structures than reported in these earlier works. An examination of Fig. 9(*a*) reveals that the duration of the negative spike of $Y/\delta = 0.54$ was approximately 10 ms. This would indicate that the scale of the associated structure was about 50δ or about 5 times larger than a T-S wavelength. A typical period of the random, low frequency fluctuations ($Y/\delta = 0.14$) was longer still, about twice as long as the spike duration.

Arnal et al. (1977) also observed negative spikes in the early stages of a transition induced by a weak-but-finite freestream turbulence ($u'/U = 0.25$ percent). As with the present case, their transition was dominated by naturally-induced, random,

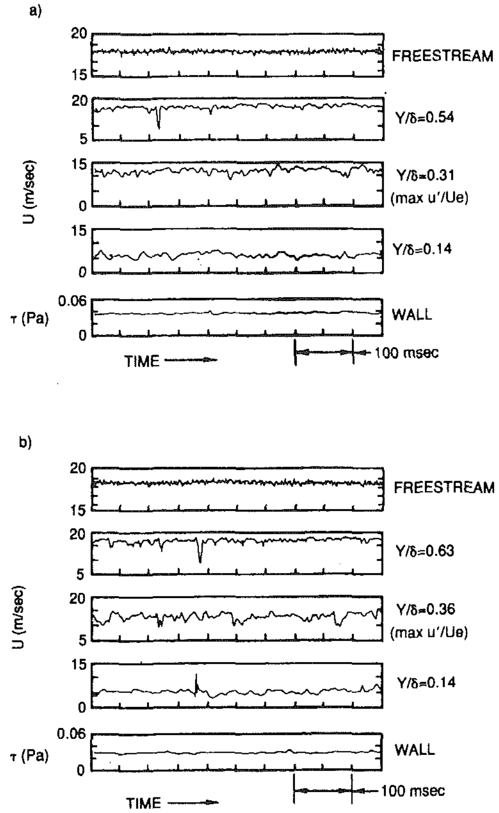

Fig. 9 Time displays of u and τ at various streamwise stations for $K = 0.20 \times 10^{-6}$ (*a*) $X = 32.5$ cm, $Re_\theta = 360$, $T_e = 0.90$ percent; (*b*) $X = 43.7$ cm, $Re_\theta = 410$, $T_e = 0.85$ percent—only τ and minimum Y/δ are simultaneous

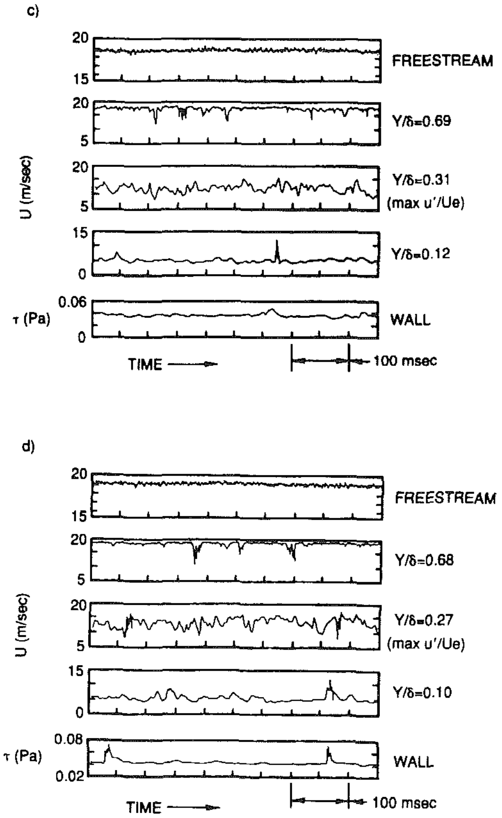

Fig. 9 Time displays of u and τ at various streamwise stations for $K = 0.20 \times 10^{-6}$ (*c*) $X = 52.8$ cm, $Re_\theta = 450$, $T_e = 0.82$ percent; (*d*) $X = 63.0$ cm, $Re_\theta = 480$, $T_e = 0.80$ percent—only τ and minimum Y/δ are simultaneous

low-frequency fluctuations. Weak T-S waves were detected but were not considered to be important to the transition. The scale of the negative spikes observed by Arnal et al. (1977) was very similar to that of the present study. Spike duration was about 1/4 of the period of their random fluctuations and corresponded to a length scale of about 40 local boundary layer thicknesses (δ).

The similarities linking the spikes observed by Arnal et al. (1977) and those for the present tests suggest that similar structures may have induced breakdown for both of these freestream-turbulence-driven transitions. However, the phenomenon which produced the spikes for these freestream-turbulence-driven transitions was clearly not the δ-scale vortex loops involved in the T-S dominated cases. Additional studies, perhaps employing flow-field visualization or arrays of hot wires, are required to determine the nature of the structures producing these large-scale negative spikes.

The first turbulent spots, widely separated in time and of extremely short duration, were observed at $x = 43.7$ cm. The turbulent/nonturbulent discriminator system indicated that spots were present only for $Y/\delta < 0.25$ and that the intermittency level over this altitude range was approximately 0.1 percent (the accuracy of this value was clearly compromised by the small number of spots occurring over the relatively short 5 s sample period). The velocity display at $Y/\delta = 0.14$ of Fig. 9(*b*) shows a typical example of these early spots. This particular spot was the only one observed at this altitude during the entire 5 s sampling period. The spanwise narrowness of this event is revealed by the fact that the simultaneous record for the wall-shear gage (offset spanwise by 1.2 cm) showed no evidence of the passage of this spot. It should be pointed out that even though no wall-shear-record spots were observed over this 500 ms period others were detected over the 5 s sample.

The velocity displays at $Y/\delta = 0.36$ and 0.63 show samples of the arrival of both single and multiple negative spikes. At this streamwise station spikes were observed over the altitude range $0.35 < Y/\delta < 0.9$. The events observed at this station, both multiple spikes and turbulent spots, are consistent with the so-called "breakdown" stage of transition.

An interesting comparison can be made between the u' amplitude distributions measured for this study (see Fig. 6) and the u' amplitude distributions recorded in the peak-valley stage of the artificial, T-S mode transition of Klebanoff et al. (1962). A plot (not shown) of the spanwise average of the peak-valley u' distributions at their "breakdown" has an amplitude distribution (shape and magnitude) that is very similar to the present u' distribution at $x = 42.7$ cm. The similarity between these u' distributions is striking given the disparity between a T-S mode and a high-freestream-turbulence driven natural transition.

Additional details of the transition process can be seen in the time displays of Fig. 9(*c*) ($x = 52.8$ cm). The sample turbulent spot shown at $Y/\delta = 0.12$ is of very short duration and appears, as with the spot at the previous station, to be narrow in the spanwise direction (there was some hint of the spot passage on the wall-shear gage). The signal at $Y/\delta = 0.31$ was dominated by low frequency fluctuations while at $Y/\delta = 0.69$ both single and multiple spikes were in abundance. At this station the distinction between spots and multiple spikes, both of which contain strong high-frequency fluctuations, started to blur. An examination of all the time displays indicated that clearly recognizable spots (positive spikes with high-frequency fluctuations) were present for $Y/\delta < 0.25$. Clearly recognizable single or double negative spikes were observed from $0.35 < Y/\delta < 1$. The turbulent/nonturbulent discriminator system indicated that the intermittency level was approximately constant at 0.3 percent.

The final set of pretransitional time displays is presented in Fig. 9(*d*) where high-frequency events were observed across the entire boundary layer. For example, the spectral distribution for $Y/\delta = 0.25$ for this station (Fig. 7) reflects the growing contributions of these widely separated but high-frequency events. The wall-shear and minimum-altitude velocity records show that one spot passed over the wall gage while missing the hot-wire probe (transverse separation of 1.2 cm) while another spot was sufficiently wide to encounter both. Simultaneous detection was still rare at this station; the sample shown in Fig. 9(*d*) was the only one observed for any of the records for the four stations of Fig. 9. If spots generated at $X = 43.7$ cm had grown with a spreading angle of 9 deg (typical zero pressure-gradient value) they would have been about 6 cm wide (approximately 5 times the probe/wall-gage separation) at $X = 63$ cm. The fact that simultaneous probe/wall-gage detection was rare at $X = 63$ cm indicates that the spreading angle for these early spots was significantly reduced by the presence of the favorable pressure gradient.

There were no events that could be clearly identified as single or double spikes at any altitude for this station. At $Y/\delta = 0.27$ the time display shows both negative and positive high-frequency excursions from the low-frequency disturbances. At $Y/\delta = 0.68$ only negative excursions were detected. Although near-wall positive excursions could be safely identified as spots, outer-region negative excursions with strong high frequency fluctuations could have been either hairpin eddies or spots, born at upstream stations, that had grown to reach that altitude. The turbulent/nonturbulent discriminator, unable to differentiate between these possibilities, indicated that the intermittency level was a near constant 1.5 percent from the wall to $Y/\delta = 0.7$.

In review, at the most upstream station single spikes appeared in the outer region of the boundary layer; no turbulent spots were observed at any altitude. At the following two stations spots could be identified for all $Y/\delta < 0.25$ while single or double negative spikes appeared from $0.35 < Y/\delta < 0.9$. The altitude ranges of spots and spikes became unclear at the last pretransitional station. Arnal et al. (1977) reported very similar results for their zero-pressure-gradient, weak-freestream-turbulence natural transition.

Note that by the $x = 63.0$ cm station the intermittency had grown to about 1.5 percent yet the Stanton number was still decreasing. The combination of low intermittency and the apparent narrow transverse spot dimensions probably accounts for the fact that the time-mean heat transfer was unaffected at this streamwise location. This result is consistent with the results of Dhawan and Narasimha (1958) and those of Feiereisen and Acharya (1986) who observed low values (~1 percent) of intermittency well upstream of minimum skin-friction stations.

Examination of Turbulent Spot Spectral Distributions. To further examine the character of these very early spots, the short-lived turbulent portions of the velocity and wall-shear records were extracted and analyzed in detail. These very short records, to be presented in Figs. 10 through 12, each consist

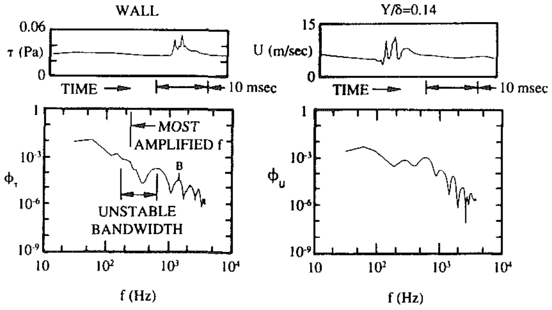

Fig. 10 Spectral distribution of τ' and u' for spots (nonsimultaneous) detected at $X = 42.7$ cm

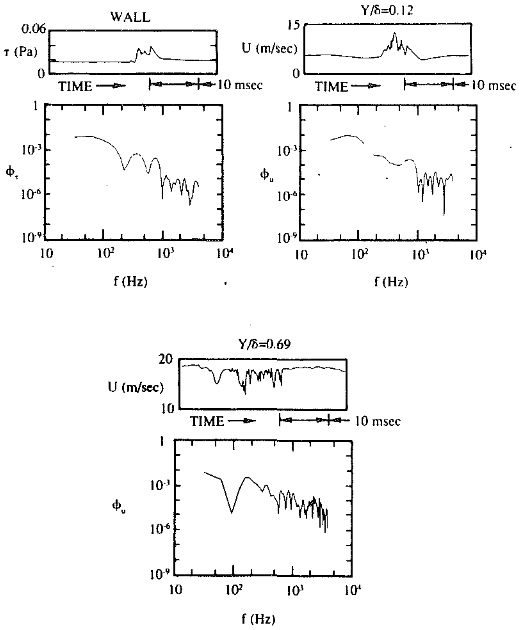

Fig. 11 Spectral distributions of τ' and u' for spots (nonsimultaneous) detected at X = 52.8 cm

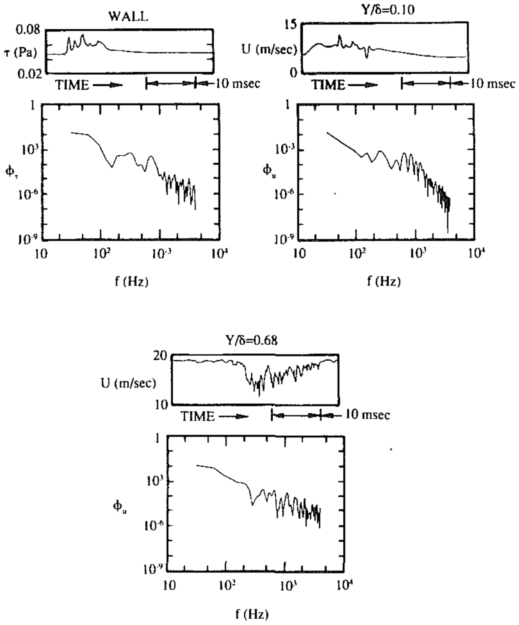

Fig. 12 Spectral distributions of τ' and u' for spots detected at X = 63.0 cm. Only the records shown for the wall (τ) and for Y/δ = 0.10 were simultaneous.

of 256 samples (FFT resolution: 128 spectral lines, frequency range 30–3900 Hz).

The single turbulent spot which appeared at $Y/\delta = 0.14$ in Fig. 9(*b*) is displayed in expanded form in the top right-hand side of Fig. 10. While the spot waveform consists of velocity fluctuations of considerably higher frequency than the background profile fluctuations, it displays no strong high-frequency (> KHz) activity. The spectral distribution of this short sample, presented directly beneath the time display, reveals the strong profile fluctuations (~50 Hz) and, at higher frequencies, the Fourier components of the spot fluctuations. The primary frequency of spot fluctuations is seen to be approximately 600 Hz ($F = 2\pi f\nu/Ue^2 = 1.5 \times 10^{-4}$).

The left-hand portion of Fig. 10 shows the waveform and spectral distribution of a sample spot detected by the wall gage at this station. Note that this wall-gage-spot did not appear in the sample shear display of Fig. 9(*b*) and was not the same event as the previously discussed velocity-profile spot. The characteristics of the waveform and spectral distribution plots for the wall-gage spot are, however, remarkably similar to those observed (at a different time) at $Y/\delta = 0.14$. Note the acoustic spike (*B*) at 1320 Hz. It is thought that the coincidence of this spike and the first harmonic of the spot fluctuations was fortuitous.

Also shown on the spectral plot are the cumulative-total band of unstable frequencies encountered by the boundary layer since crossing the upstream branch of the linear-theory neutral stability curve and the most-amplified frequency at this streamwise station. The primary frequency (and all the higher harmonic components) of the spot fluctuations fall to the right of the predicted unstable bandwidth. The observed primary frequency was about a factor of two higher than the most-unstable.

The results shown in Fig. 10 indicate that these very early spots were of extremely short duration and consisted of structures with streamwise scale approximately that of the overall boundary layer thickness. The primary frequency of the fluctuations in these spots was greater than any predicted for T-S mode instability. No high-frequency fluctuations indicating the existence of small-scale turbulent eddies were observed for any of these early spots.

Samples of spots observed at the next station downstream (x = 52.8 cm) are presented in Fig. 11. The wall-gage spot of Fig. 11 does not appear in the long-time-display of Fig. 9(*c*) but the spot at $Y/\delta = 0.12$ can be seen at about 320 ms, the event at $Y/\delta = 0.69$ at about 150 ms. At this station the spots detected at both the wall gage and at $Y/\delta = 0.12$ exhibit slightly more high-frequency activity than was observed at the previous station. These spots, however, were still dominated by relatively large scale phenomena.

The event observed at $Y/\delta = 0.69$ at this axial station contained a great deal of high-frequency activity, enough so that it cannot be categorized as a "multiple-negative-spike." Note, however, that the high-frequency activity was immediately preceded by a weak single negative spike. One possibility is that this record displays the passage of the remnants of a large-scale structure followed by an array of shed hairpin eddies. Another possibility, remote considering the altitude, is that the passage of a spot extending all the way to the wall was observed.

The radical difference in character between the events observed near the wall and the event observed at $Y/\delta = 0.69$ would seem to indicate that these are different phenomena. These data indicate that spots appeared either near or at the wall at the same axial station where the outer-region, large-scale structures were degenerating to turbulence.

The final spot-detail displays, recorded at x = 63.0 cm, are given in Fig. 12. All the events shown in Fig. 12 also appear in Fig. 9(*d*). The wall-gage and $Y/\delta = 0.10$ displays are for the spot which arrived simultaneously at those stations at 420 ms. The event at $Y/\delta = 0.68$ arrived 180 ms into the sample. Note the similarity between the three events displayed at this altitude in the sample of Fig. 9(*d*).

Even at this station, more than 20 cm downstream of where the first spots were observed, the wall-gage and $Y/\delta = 0.10$ displays indicate that there was not a great deal of high-frequency activity in this near-wall spot. Note that the spectral distribution plots for both the wall-gage and hot-wire records indicate spot power maxima at about 350 and 700 Hz.

At this station the outer-region event was almost exclusively high-frequency activity. As with the previous station, the outer-region events appear to be well ahead of the near-wall spots on their respective paths to becoming turbulent patches.

It is interesting that the present pretransitional disturbance measurements have some similarities with the "incipient-spot-formation" observations of Amini and Lespinard (1982) and Chambers and Thomas (1983). These previous studies demonstrated that the formation of artificial bypass-mode spots was preceded by extremely narrow (spanwise), disturbances. The hot-wire data of Amini and Lespinard (1982) indicated, as for the present study, that near-wall activity for these incipient spots was predominantly at relatively low frequencies.

Since these velocity profile data are single-point measurements, it is not possible to definitively establish the relationship between the outer-region and near-wall disturbances. However, for the three upstream stations (x = 32.5, 43.7 and 52.8 cm) no events (spots or spikes) were observed over an altitude range between the near-wall and outer regions. This result suggests that at this very early stage of incipient spot formation the outer and near-wall activities were interacting, but separate, phenomena.

One possibility is that at the "single or double spike" stage the outer-region large-scale structures induce wave packets/incipient spots at the wall similar to the bypass-mode spots observed by Amini and Lespinard (1982) and Chambers and Thomas (1983). The significant differences in frequency content for the near-wall and outer-region events at x = 52.8 and 63.0 cm further suggests that these phenomena follow separate paths until they either merge or interact to eventually create spots.

All the individual near-wall events, detected by either the wall gage or the hot wire probe, were isolated and examined for spectral content. This examination indicated that the primary frequency of these incipient spots was somewhat random but typically about two or three times the local, most-amplified, T-S frequency. No frequency-location dependence was observed and, significantly, the spots' primary frequency appeared to be entirely independent of the various acoustic disturbances (see Blair, 1991). In particular, the range of observed primary frequencies was well below that of the various strong resonant cross-duct acoustic waves.

Finally, these present results are in qualitative agreement with the trends predicted by the theoretical nonlinear disturbance model of Smith (1988). This analysis suggests that large-amplitude disturbances will produce breakdowns in the near-wall viscous sublayer with frequencies higher than the first-unstable mode predicted by classic weak-disturbance theory.

Conclusions

All four of the experimental test cases of this program resulted in bypass-mode transitions based upon the following two criteria: (1) Transition onset occurred upstream of the minimum critical Reynolds number for cases K.75G2, K.75G3 and K.20G2 or (2) T-S mode amplification played no detectable role in producing transition for case K.20G1.

The first clearly recognizable turbulent spots were observed, at low boundary-layer altitudes, at the same streamwise station where the first (outer-region) multiple-negative-spikes appeared. The primary frequency of these very early spots was about 2 to 3 times the most-amplified T-S frequency. One possibility is that at the "single or double-spike" stage outer-region large-scale structures induce wave packets/incipient spots at the wall similar to the bypass-mode spots observed by Amini and Lespinard (1987) and Chambers and Thomas (1983). A comprehensive flow visualization study of a high-freestream-turbulence bypass-mode transition might prove to be helpful in understanding these effects.

Early spots were apparently very narrow in the spanwise direction. Even 20 cm downstream of the station where spots first appeared, almost no spots were simultaneously observed by a boundary-layer hot-wire probe and a wall thin-film gage offset spanwise by 1.2 cm (3 δ at that station).

Acknowledgments

The author wishes to acknowledge the extensive contributions of Dr. Robert P. Dring to this study. Drs. M. V. Morkovin and R. Narasimha were kind to review this work and offer several important comments.

Research sponsored by the Air Force Office of Scientific Research (AFSC) under Contracts F49620-78-C-0064 and F49620-84-C-0050. The United States Government is authorized to reproduce and distribute reprints for governmental purposes notwithstanding any copyright notation hereon. The contract monitors for this research were Dr. James D. Wilson, Major Michael S. Francis and Dr. James McMichael.

References

Amini, J., and Lespinard, G., 1982, "Experimental Study of an 'Incipient Spot' in a Transitional Boundary Layer," *Physics of Fluids*, Vol. 25, No. 10, p. 1743.

Arnal, D., Juillen, J. C., and Michel, R., 1977, "Analyse Experimentale et Calcul de L'apparition et du Developpement de la Transition de la Couche Limite," AGARD-CP-224, 13-1. (English translation 1978 Experimental Analysis and Computation of the Onset and Development of the Boundary Layer Transition. NASA TM-75325.)

Arnal, D., 1984, "Description and Prediction of Transition in Two-Dimensional Incompressible Flow," AGARD-R-709, 2-1.

Baines, W. D., and Peterson, E. G., 1951, "An Investigation of Flow Through Screens," *Trans. ASME*, Vol. 73, p. 467.

Bellhouse, B. J., and Schultz, D. L., 1966, "Determination of Mean and Dynamic Skin Friction, Separation, and Transition in Low-Speed Flow With a Thin-Film Heated Element," *Journal of Fluid Mechanics*, Vol. 24, p. 379.

Blair, M. F., and Werle, M. J., 1981, "Combined Influence of Free-Stream Turbulence and Favorable Pressure Gradients on Boundary Layer Transition and Heat Transfer," United Technologies Research Center Report R81-914388-17.

Blair, M. F., Bailey, D. A., and Schlinker, R. H., 1981, "Development of a Large-Scale Wind Tunnel for the Simulation of Turbomachinery Airfoil Boundary Layers," ASME *Journal of Engineering for Power*, Vol. 103, p. 678.

Blair, M. F., 1983, "Influence of Free-Stream Turbulence on Turbulent Boundary Layer Heat Transfer and Mean Profile Development," ASME *Journal of Heat Transfer*, Vol. 105, p. 33.

Blair, M. F., and Bennett, J. C., 1987, "Hot-Wire Measurements of Velocity and Temperature Fluctuations in a Heated Turbulent Boundary Layer," *J. Physics E.*, Vol. 20, p. 209.

Blair, M. F., 1991, "Boundary Layer Transition in Accelerating Flows with Intense Freestream Turbulence," UTRC Report UTRC91-1.

Chambers, F. W., and Thomas, A. S. W., 1983, "Turbulent Spots, Wave Packets, and Growth," *Physics of Fluids*, Vol. 26, No. 5, p. 1160.

Champagne, F. H., Sleicher, C. A., and Wehrmann, O. H., 1967, "Turbulence Measurements With Inclined Hot Wires," *Journal of Fluid Mechanics*, Vol. 28, p. 153.

Dhawan, S., and Narasimha, R., 1958, "Some Properties of Boundary Layer Flow During Transition From Laminar to Turbulent Motion," *Journal of Fluid Mechanics*, Vol. 3, pp. 418–436.

Edwards, D. E., Carter, J. E., and Werle, M. J., 1982, "Analysis of Boundary Layer Equations Including a New Composite Coordinate Transformation," United Technologies Research Center Report No. UTRC81-30.

Feiereisen, W. J., and Acharya, M., 1986, "Modeling of Transition and Surface Effects in Boundary-Layer Flow," *AIAA J.* Vol. 24, p. 1642.

Fulachier, L., and Dumas, R., 1976, "Spectral Analogy Between Temperature and Velocity Fluctuations in a Turbulent Boundary Layer," *Journal of Fluid Mechanics*, Vol. 77, p. 257.

Gaster, M., 1974, "On the Effects of Boundary-Layer Growth on Flow Stability," *Journal of Fluid Mechanics* Vol. 66, p. 465.

Kendall, J. M., 1985, "Experimental Study of Disturbances Produced in a Pre-Transitional Laminar Boundary Layer by Weak Free-Stream Turbulence," AIAA-85-1695.

Klebanoff, P. S., Tidstrom, K. D., and Sargent, L. M., 1962, "The Three-Dimensional Nature of Boundary-Layer Instability," *Journal of Fluid Mechanics* Vol. 12, p. 1.

Kovasznay, L. S. G., Komoda, H., and Vasudeva, B. R., 1962, "Detailed Flow Field in Transition," *Proc. Heat Transfer & Fluid Mech. Inst.*, Vol. 1.

Morkovin, M. V., 1977, "Instability, Transition to Turbulence and Predictability," AGARD-AG-236, 1.

Reshotko, E., 1976, "Boundary-Layer Stability and Transition," *Ann. Rev. Fluid Mech.*, Vol. 8, p. 311.

Smith, F. T., 1988, "Interactions in Boundary-Layer Transition," ICTAM Conf., to be published by Springer-Verlag.

Suder, K. L., O'Brien, J. E., and Reshotko, E., 1988, "Experimental Study of Bypass Transition in a Boundary Layer," NASA TM-100913.

Wang, T., Simon, T. W., and Buddhavarapu, J., 1985, "Heat Transfer and Fluid Mechanics Measurements in Transitional Boundary Layer Flows," ASME *Journal of Engineering for Gas Turbines and Power*, Vol. 107, p. 1007.

Wazzan, A. R., Okamura, T. T., and Smith, A. M. O., 1968, "Spatial and Temporal Stability Charts for the Falkner-Skan Boundary-Layer Profiles," McDonnell Douglas Report No. DAC-67086.

Boundary-Layer Transition in Accelerating Flows With Intense Freestream Turbulence: Part 2—The Zone of Intermittent Turbulence

M. F. Blair
Senior Research Engineer,
United Technologies Research Center,
East Hartford, Conn. 06108
Mem. ASME

Hot-wire anemometry was employed to examine the laminar-to-turbulent transition of low-speed, two-dimensional boundary layers for two (moderate) levels of flow acceleration and various levels of grid-generated freestream turbulence. Flows with an adiabatic wall and with uniform-flux heat transfer were explored. Conditional discrimination techniques were employed to examine the zones of flow within the transitional region. This analysis demonstrated that as much as one-half of the streamwise-component unsteadiness, and much of the apparent anisotropy, observed near the wall was produced, not by turbulence, but by the steps in velocity between the turbulent and inter-turbulent zones of flow. Within the turbulent zones u'/v' ratios were about equal to those expected for equilibrium boundary-layer turbulence. Near transition onset, however, the turbulence kinetic energy within the turbulent zones exceeded fully turbulent boundary-layer levels. Turbulent-zone power-spectral-density measurements indicate that the ratio of dissipation to production increased through transition. This suggests that the generation of the full equilibrium turbulent boundary-layer energy cascade required some time (distance) and may explain the very high TKE levels near onset.

1 Introduction

Until recently, nearly all in-depth investigations of incompressible boundary-layer transition have been conducted in flows with weak freestream turbulence (see the reviews of Reshotko, 1976; Morkovin, 1977; and Arnal, 1984). The present study differs from this earlier work in that it examines transition in the presence of much higher levels of freestream turbulence. Such transition can have important engineering consequences, particularly in flows with negative streamwise pressure gradients where the acceleration stabilizes the boundary layer and extends the transitional zone. For example, the location and extent of transition on gas turbine airfoils strongly affects aerodynamic losses and heat load distributions.

Numerous earlier investigations have been conducted to study the zone, following breakdown, over which turbulent spots grow to fill the boundary layer, the zone of turbulent intermittency. The upstream edge of this region corresponds to the location where turbulent spots are first detected, its downstream boundary to the location where the boundary layer asymptotically approaches equilibrium, fully turbulent characteristics. Schubauer and Klebanoff (1956), Arnal et al. (1978), Wang et al. (1985), Acharya (1985), and Suder et al. (1988) have all documented the streamwise development of boundary-layer Reynolds stress distributions through the intermittent zone. These studies all indicate that in the early stages of spot growth (low intermittency) the streamwise fluctuations reach extremely high levels near the wall. Peak values about two times the level expected for an equilibrium fully turbulent boundary layer were observed.

In addition, Narasimha et al. (1984), Narasimha (1984), and Acharya (1985) have measured the streamwise distributions of boundary layer intermittency for a wide variety of flows subjected to streamwise pressure gradients. Their results show that strong gradients near the location of transition onset (i.e., spot formation) produce intermittency distributions skewed in relation to classic "universal" zero-pressure-gradient correlations.

The present experiments were conducted with various combinations of streamwise acceleration and high levels of grid-generated freestream turbulence. The study focused on transitions in accelerating flows because of the potential utility of the results to turbomachinery design and because the physical extension of the zone of transition made it feasible to obtain meaningful laboratory measurements. Within the intermittent region, turbulent-spot-triggered conditional processing techniques were employed to study the zonal and ensemble-averaged properties of the transitional boundary layers.

Contributed by the Fluids Engineering Division for publication in the JOURNAL OF FLUIDS ENGINEERING. Manuscript received by the Fluids Engineering Division October 16, 1991. Associated Technical Editor: D. P. Telionis.

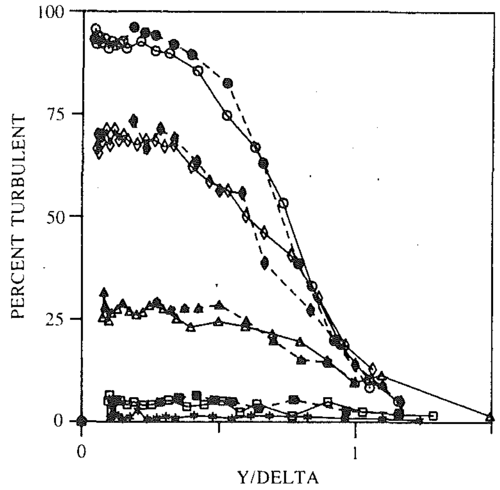

Fig. 1 Intermittency distributions across the boundary layer through transition, $K = 0.20 \times 10^{-6}$, grid 1. ∗, $X = 63.0$ cm; □, $X = 73.2$ cm; △, $X = 93.5$ cm; ◇, $X = 113.8$ cm; ○, $X = 134.1$ cm. Open symbols $(\partial u'/\partial t)^2$ criterion, solid symbols $(\partial u'v'/\partial t)^2$ criterion.

A description of the experimental equipment and techniques employed in this study can be found in Part 1 of this paper.

Results and Discussion

The streamwise development of the profiles of all three components of the fluctuating boundary-layer velocity were examined downstream of transition onset. Profile data were obtained with single-wire, horizontal-x wire and vertical-x wire probes; shear-stress data with wall thin-film gages. Tabulated profile data for all four test cases are given by Blair and Anderson (1987). In order to focus on the same sample test case for which pretransitional results were discussed (Part 1), the intermittent-zone data for the K.20G1 case will be presented here.

Intermittency Distributions. The streamwise development of the boundary layer intermittency profiles for the sample case is presented in Fig. 1. Intermittency distributions determined from the single-wire $(\partial u'/\partial t)^2$ and vertical-x $(\partial u'v'/\partial t)^2$ wire records are seen to be in good agreement for all stations and altitudes. Longer sample periods would probably have produced further reductions in profile scatter.

For all stations, a region of near-constant intermittency extended from the wall to an altitude of about $Y/\delta = 0.3$; the level of near-wall intermittency increasing with streamwise distance. The boundary-layer thickness (δ) is defined as the altitude where the long-term mean velocity equals 0.99 Ue. The finite values of γ for $Y > \delta$ reflect the random passage of maximum-altitude-positions on turbulent patches.

The form of the distributions of Fig. 1 are in excellent agreement with similar data obtained for non-bypass transitions by Arnal (1984) and Acharya (1985). This suggests that the character of turbulent patches in the intermittently-turbulent zone is independent of the route to spot initiation, i.e., bypass or non-bypass.

The random passage of spots such as proposed by Schubauer and Klebanoff (1956) would be expected to produce intermittency profiles similar to those of Fig. 1. The region of constant γ at the lower altitudes of each profile indicates that the height of all spots was $\geq 0.3\ \delta$. The decrease of intermittency at higher altitudes would be expected for the peaked-top Schubauer and Klebanoff (1956) spot shape, the decrease being made even greater by the fact that a fixed probe sees random transverse positions in passing spots. The possibility also exists that a distribution of spot altitudes passes a given streamwise location.

In contrast to the recently reported results of Sohn et al. (1989), there was no evidence of a near-wall minimum in intermittency for the present sample test case. For two other higher turbulence cases (K.20G2 and K.75G3), however, the intermittency distributions for the upstream portion of the transition zone did reveal a near-wall minimum, peaking at about $\delta/3$. The near-wall minimum does not seem to be a universal effect, its appearance may depend upon the particular environment in which a transition occurs.

Narasimha et al. (1985) has demonstrated that, for zero-pressure-gradient transitions, the streamwise distribution of the function $F(\gamma) = [-\ln(1-\gamma)]^{1/2}$ (γ = near-wall intermittency) increases linearly with x. He also showed that intermittency distributions for transitions in accelerating flows displayed two regions of distinctly differing slopes when plotted in these same coordinates (Narasimha, 1984 and Narasimha et al., 1984). The demarcation line separating the two regions was referred to as the "subtransition."

Streamwise intermittency distributions were determined for all four of the present test cases using profile distribution results such as those shown in Fig. 1. The maximum value determined for each profile was taken as the local streamwise intermittency level. The distributions for three of the four test cases, as can be seen in Fig. 2, showed distinct changes in slope, or "subtransitions." No slope-break was observed for case K.75G3, probably a result of the extremely high freestream turbulence of that test.

The present intermittency distributions are plotted in the zero-pressure-gradient "universal" coordinates of Narasimha (1985) in Fig. 3. The dimensionless distance through transition, ξ, was computed (open symbols) with X_t taken as the x intercept

Nomenclature

c_f = skin friction coefficient
K = acceleration parameter
H = shape factor, δ^*/θ
q^2 = turbulence kinetic energy
Re = Reynolds number
Re_θ = Reynolds number based on momentum thickness
St = Stanton number
t = time from beginning of turbulent period
T = turbulence intensity
u, v, w = instantaneous value of velocity components
u', v', w' = fluctuating velocity components
U = mean streamwise velocity
U^+ = dimensionless velocity, u/U_τ
U_τ = friction velocity
$\langle U \rangle$ = ensemble averaged velocity
$u'^2(f)$ = velocity fluctuations (squared) per Hertz
X = distance from leading edge
Y = distance from wall
Y^+ = dimensionless distance, YU_τ/ν
γ = intermittency
δ = boundary layer thickness
$\bar{\delta}$ = long-term average boundary layer thickness
$\Delta\tau$ = time interval from beginning to end of a turbulent period
θ = momentum thickness
ν = kinematic viscosity

Subscripts

e = freestream

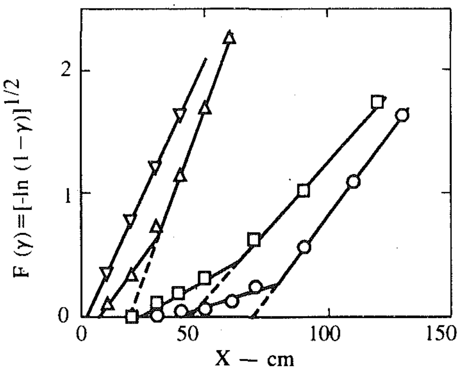

Fig. 2 Near-wall intermittency distributions for the four test cases. ○, K.20G1; □, K.75G2; △, K.20G2; ▽, K.75G3.

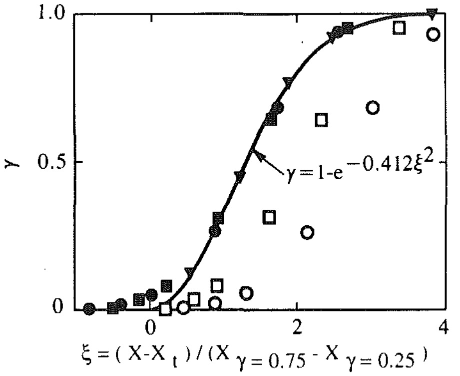

Fig. 3 Intermittency distributions in the coordinates ($\partial P/\partial X=0$) of Narasimha. ○, K.20G1; □, K.75G2; ▽, K.75G3.

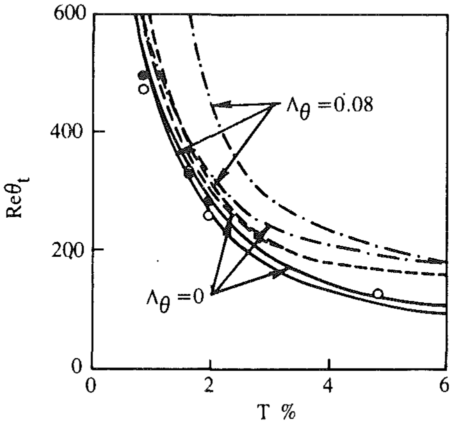

Fig. 4 Transition onset as a function of free stream turbulence and acceleration. ———, Van Driest and Blumer; - - -, Abu-Ghannam and Shaw; — · —, Dunham; ○, present heat transfer data; ●, present extrapolated intermittency distributions.

of the solid lines on the plots of Fig. 2 and also (solid symbols) with X_t determined by extrapolating the intermittency data for $x>$ "subtransition" to $F(\gamma)=0$. This latter definition, of course, forces agreement with the "universal" coordinates beyond the "subtransition" location. The extrapolation procedure failed for the K.20G2 case because the subtransition occurred beyond $\gamma=0.25$.

Figures 2 and 3 demonstrate the capacity (even in the presence of enhanced freestream turbulence) of acceleration to substantially inhibit the development of intermittency until some critical stage (the "subtransition") is reached. Following the "subtransition," intermittency distributions in accelerating flows appear to follow the same universal scaling law observed for zero-pressure-gradient flows.

The present results are supportive of the transition model of Narasimha (1985), i.e., linear spot growth from a narrow band of concentrated breakdown. The present results, in the coordinates of Fig. 2, reflect the existence of two distinct regions of linear intermittency (spot) growth. Experiments by Narasimha et al. (1984) and by Sankaran and Antonia (1988) may also explain the reduced slope of intermittency-growth prior to the "subtransition." These earlier studies of artificially-generated spots have demonstrated that spot lateral growth rates are significantly reduced in accelerating flows.

Mayle (1991) has recently published a comprehensive examination of bypass-mode transition. He concluded that the "subtransition" phenomenon observed in favorable pressure gradient flows should be interpreted as an indication of an extended spot production zone. He demonstrated (see Mayle (1991), Appendix B) that intermittency distributions obtained for accelerating flows, including those of the present study, can be well represented using a Gaussian spot production function.

Transition-Onset Correlations. A number of widely employed correlation-based techniques exist for the prediction of the onset of transition in accelerating, highly turbulent flows. Transition onset, for these predictions, refers to the location where the mean boundary-layer profile shape factor or the local skin friction coefficient first began to deviate from laminar behavior. Van Driest and Blumer (1963) developed a transition-onset criterion which employed empirically determined constants. Dunham (1972) and Abu-Ghannam and Shaw (1980) produced correlations from experimental data. Note that transition onset does not correspond to the location where spots first occur since, as previously discussed, symptoms of mean boundary layer changes appear at $\gamma \cong 1$ to 2 percent.

Predictions from the above three correlations are given in Fig. 4. The various predictions of transition-onset Re_θ are plotted against T for constant-velocity flow and for $\Lambda_\theta=(\theta^2/\nu)\,\partial U/\partial x = K\mathrm{Re}_\theta^2=0.08$. Each pair of curves, then, spans the range of accelerations studied in this program. All three correlations reflect similar dependence on turbulence and acceleration. However, at relatively low freestream turbulence levels, the correlation of Dunham (1972) predicts much stronger dependence on acceleration than do the other schemes.

For the present heat transfer results, onset was identified as the location where heat transfer first exceeded the predicted laminar value. For the very mild levels of heat transfer employed for these tests, it is expected that the effects of wall heating on the transition process were negligible (see Sohn and Reshotko, 1991). Agreement between the present heat transfer results (open symbols—Fig. 4) and the predictions of van Driest and Blumer (1963) is seen to be very good. It was observed that for all four of the present test cases the streamwise locations corresponding to $\gamma=0.05$ (or $F(\gamma)=0.26$) were in excellent agreement with the transition onset locations determined from the respective heat transfer data. This results should be interpreted with caution as the short sample periods prohibited accurate determination of the intermittency and because of the imprecision in determining the location of onset from the heat transfer data.

Finally, onset locations (solid symbols—Fig. 4) were determined from the x-intercepts of the post-subtransition intermittency distributions of Fig. 2. These results were in fair agreement with the heat transfer data and in excellent agreement with the predictions of van Driest and Blumer (1963).

Note that at high turbulence levels the predictions of van Driest and Blumer (1963) and the present data both indicate that onset will occur at $\mathrm{Re}_\theta<154$, the linear stability limit for weakly-disturbed, zero-pressure-gradient flow. This result is not, in itself, surprising, given that the disturbances are highly nonlinear. However, as discussed by Morkovin (1984), it may be important to consider the experimental arrangements in which such low-Re_θ, high-turbulence onset data have been acquired. High turbulence levels are nearly always associated with large turbulence scales, low Reynolds numbers with small distances from a boundary-layer origin. The interaction of a test-surface or airfoil leading edge with the turbulence field may produce instantaneous, local separations—another path to transition. In the present K.75G3 test case, the distance from the leading edge to onset was less than three turbulence integral length scales. In short, significant experimental-arrangement dependence should be expected for transitions in very high freestream turbulence.

Zonal Analysis. Continuous velocity-time records for all three components of boundary-layer velocity were generated with the previously described hot-wire data acquisition system. The conditional processing system, in turn, permitted the identification of the turbulent and inter-turbulent periods (zones) of flow. The turbulent and interturbulent blocks were then assembled into continuous, segregated records for further

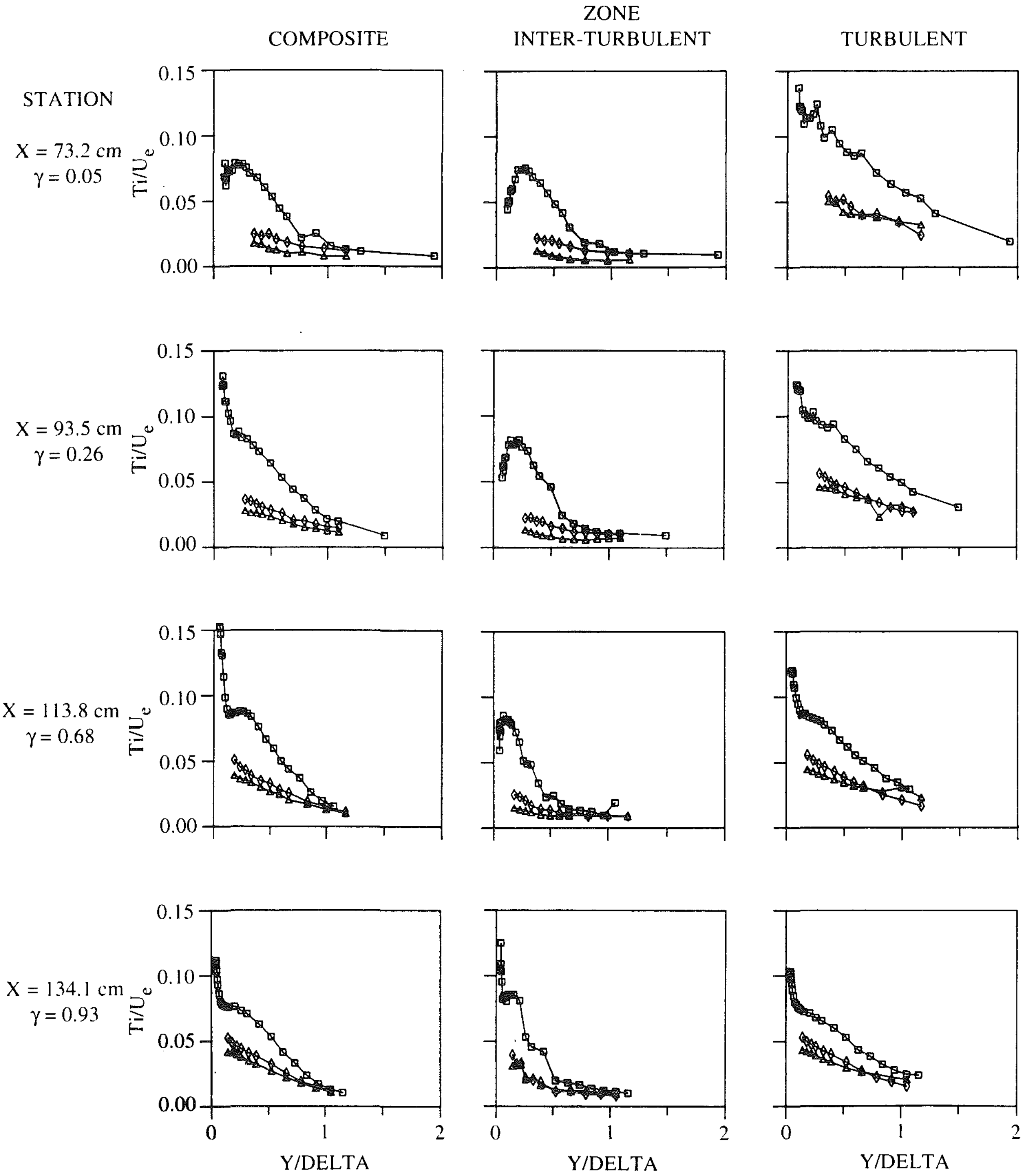

Fig. 5 Zonal distributions of the components of turbulence across the boundary layers for four streamwise locations, $K = 0.20 \times 10^{-6}$, grid 1. □, $\sqrt{\overline{u'^2}}/U_e$; △, $\sqrt{\overline{v'^2}}/U_e$; ◇, $\sqrt{\overline{w'^2}}/U_e$, ····Klebanoff.

processing. Simultaneity of multicomponent velocity records within individual data blocks was preserved.

The streamwise, normal, and transverse instantaneous velocity components are denoted as u_i, v_i, and w_i with $i=t$ for turbulent and $i=l$ for interturbulent zonal data. Moments of the fluctuating quantities were computed about the respective zonal means. For example, the turbulent-zone RMS of the fluctuations of the streamwise component are given by:

$$\sqrt{\overline{u_t'^2}}=\sqrt{\overline{(U-\overline{U}_t)^2}} \tag{1}$$

where $\overline{U}_t$ signifies the means of all the turbulent-zone streamwise instantaneous velocities.

In a similar manner the turbulent-zone Reynolds shear stress is given by:

$$\overline{u'v'}=\overline{(U-\overline{U}_t)(V-\overline{V}_t)} \tag{2}$$

Long-term composite averages were also computed without regard for zonal differentiation, i.e., from the continuous, original records. In reality, these long-term averages consist of a composite of intermittency-weighted turbulent-zone and

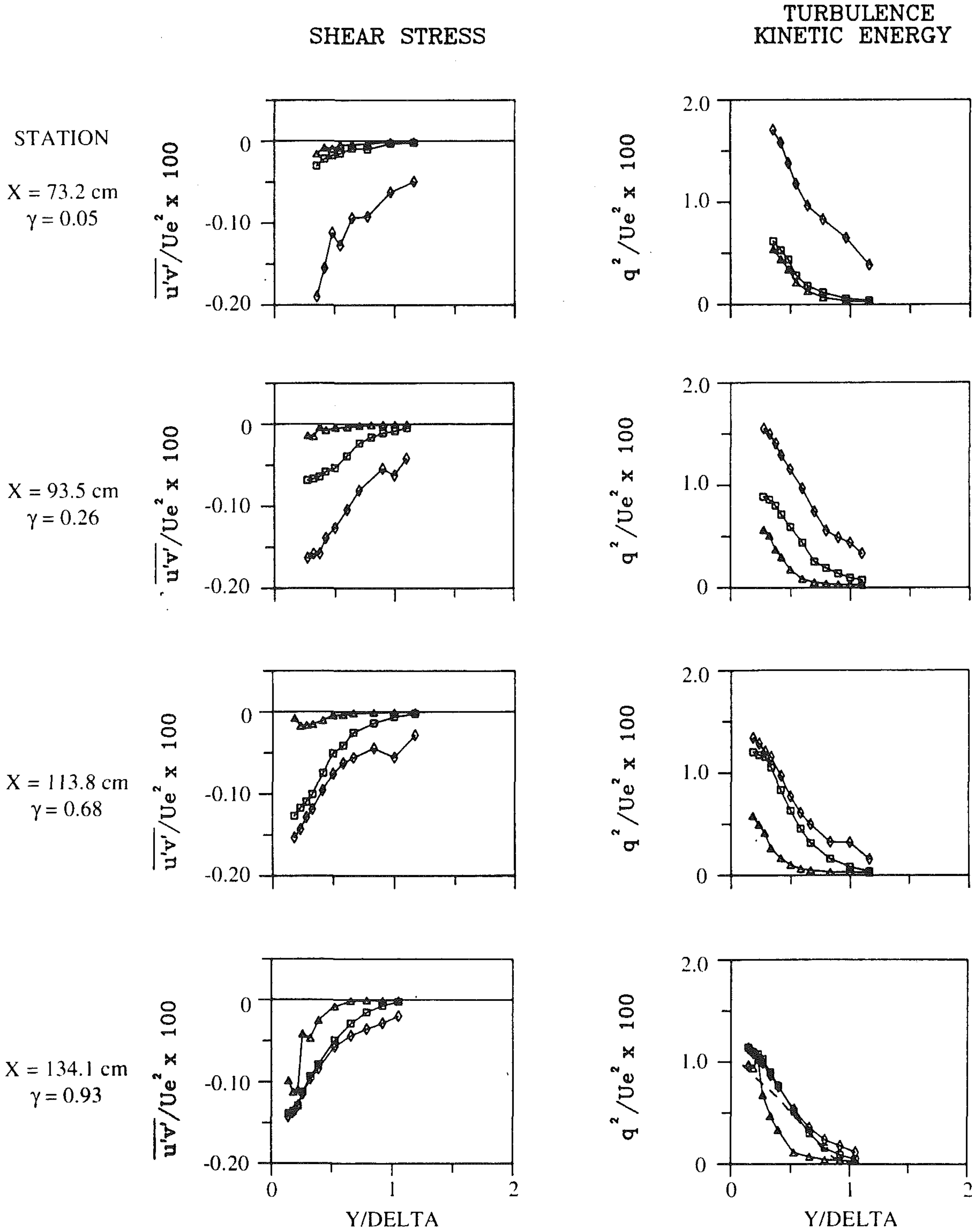

Fig. 6 Zonal distributions of the Reynolds shear stress and turbulence kinetic energy across the boundary layer for four streamwise locations, $K=0.20\times10^{-6}$, grid 1. □, composite average; ◇, turbulent-zone average; △, interturbulent-zone average; - - - -Klebanoff.

inter-turbulent-zone contributions and fluctuations arising from the steps between zonal-mean velocities. For example, the composite second moment of the fluctuations of the streamwise component is given by:

$$\overline{u_c'^2}=\gamma\overline{u_t'^2}+(1-\gamma)\overline{u_l'^2}+\gamma(1-\gamma)(\overline{U}_t-\overline{U}_l)^2 \qquad (3)$$

Checks of the present results verified that the composite statistics computed directly from the continuous records were in excellent agreement with values computed from assembly functions such as Eq. (3).

The last term of Eq. (3) gives the zonal-mean-step contribution to the long-term average. As will be shown below, this low-frequency effect is an important contributor to the overall fluctuations in the near-wall region.

Distributions of the three-components of turbulence intensity (T_i) within the sample-test-case transitional boundary layer are presented in Fig. 5. Profiles of both the composite turbulence and individual zonal contributions are given for four streamwise locations. The three-component profile plots of Fig. 5 are, in essence, a more comprehensive extension of the single-component profile plots presented for the four upstream (pretransitional) stations (Fig. 6, Part 1).

The near-wall intermittency for the most-downstream, pretransitional, single-component turbulence profile (see Fig. 6, Part 1) was approximately 1 percent (Fig. 1). Distinct changes in the form of the turbulence intensity profile developed between this station and the first three-component profile station ($x=73.2$ cm, Fig. 5) where γ had increased to 5 percent. Comparison of the composite streamwise-component turbulence profile obtained at $x=73.2$ cm with the $\sqrt{\overline{u'^2}}/Ue$ profile of $x=63$ cm reveals that the peak intensity occurred closer to the wall and spanned a wider range of altitudes for the downstream location. The peak intensity remained essentially constant at 7 percent between the two stations.

The composite, streamwise-component turbulence profiles changed dramatically with increased distance through transition. For the two mid-transition stations (at 93.5 cm and 113.8 cm) the maximum streamwise intensities moved to very near the wall where values exceeded the respective turbulent-zone intensities. These local composite maximums were extremely large, exceeding equilibrium turbulent boundary layer levels by about 50 percent. Much of this unsteadiness near the wall results from large velocity steps between zones at that altitude (the third term in Eq. (3)). At $x=113.8$ cm, for example, the peak streamwise, composite intensity was 15.5 percent. Decomposition of the recorded measurement into its zonal contributions revealed that 51 percent of the perceived turbulence was produced by the last term in Eq. (3). The turbulent-zone and laminar-zone contributions were 41 and 8 percent, respectively. At the same streamwise location, the local minimum in the composite turbulence intensity at $Y/\delta=0.13$ corresponds to the crossover altitude of the zonal-mean velocity profiles where the last term of Eq. (3) vanished.

The streamwise-component turbulence profiles for the interturbulent and turbulent zones appear to form two distinctly different families, each evolving (streamwise) consistently within that zone. The interturbulent profiles continued to mimic the form observed at the upstream, preonset locations with a relatively broad peak in turbulence occurring well away from the wall ($Y/\delta\approx 0.3$). The peak is seen to move closer to the wall at successive stations. (The form of the last interturbulent profile, $x=134.1$, was anamolous, probably a result of the extremely short interturbulent zonal samples at that station.) The turbulent-zone profiles assumed an equilibrium-turbulent-like form from the first station, $\gamma=5$ percent, onward. A narrow peak in turbulence was observed very close to the wall and its intensity dropped with increasing altitude. The magnitude of the streamwise-component turbulent-zone intensity decreased with distance through the intermittent zone.

The composite and inter-turbulent profiles for the three upstream stations, $X=73.2$, 93.5, and 113.8 cm, indicate a higher degree of anisotropy than is observed in turbulent boundary layers. For example, for the interturbulent-zone profiles at $x=93.5$ cm, $\sqrt{\overline{u'^2}}/\sqrt{\overline{v'^2}}>7$ at the lowest altitude for which v' was measured. This result suggests that the velocity fluctuations in the flow between turbulent bursts were primarily large-scale profile perturbations. The turbulent-zone profiles at these stations, however, indicate that even though the magnitudes of the intensities were higher, the $\sqrt{\overline{u'^2}}/\sqrt{\overline{v'^2}}$ ratios were about equal to those expected for equilibrium boundary-layer turbulence.

A comparison of the distributions of the turbulence components obtained by Klebanoff (1955) in a fully turbulent boundary layer with the present data is given in Fig. 5 for the turbulent-zone profiles at $x=134.1$ cm. Agreement for all components is seen to be excellent except near $Y/\delta=1$. The disagreement at the boundary layer edge resulted from the difference between the freestream turbulence of the present test and the extremely low freestream turbulence of Klebanoff (1955).

In general, the composite profiles of Fig. 5 show the development of the turbulence structure through transition. Near onset, $\gamma=0.05$, the velocity fluctuations were highly anisotropic and extremely intense; near the end of transition, $\gamma=0.93$, a structure much like equilibrium boundary-layer turbulence had developed.

The development of the Reynolds shear stresses and turbulence kinetic energy (TKE) through transition is shown in Fig. 6 for the same four locations as in Fig. 5. Profiles of both the composite and individual zonal averages of the quantities are given.

As would be expected, the interturbulent zone shear stresses were near zero for the upstream three locations. Clearly, the interturbulent component velocity fluctuations were weakly correlated. The finite interturbulent shear stresses shown at $x=134.1$ cm almost certainly reflect the imprecision of the detector scheme in this high intermittency, $\gamma=0.93$, circumstance (start-stop uncertainties become large compared to inter-burst length). Note that unlike the direct-stresses the turbulent-zone shear stresses always exceeded the composite values.

It was observed that the turbulent-zone mean velocity profiles conformed very well to the standard logarithmic law-of-the-wall, even for very low values of intermittency. Turbulent-zone wall shear stress values were extracted from the velocity profiles using a least-squares velocity-data fitting routine. For all streamwise locations the turbulent-zone Reynolds stresses measured nearest the wall were only about 70 percent of the wall shear computed from the turbulent-zone mean profiles. This result was reasonable in that the normal gradient of shear stress is extremely large for accelerating flows (Jones and Launder, 1972).

Turbulence kinetic energy distributions were computed from the three-component zonal contributions to the turbulence profiles. The turbulent-zone TKE is seen to reflect the trends observed in the component distribution plots of Fig. 5, i.e., a very high level at the furthest upstream station with a progressive decrease with increased distance through transition. At the last station, the measured distribution was in very good agreement with the equilibrium turbulent boundary-layer results of Klebanoff (1955).

Spectral distributions of the zonal and composite (continuous sample) fluctuating records are presented in Fig. 7 for the four streamwise stations in Figs. 5 and 6, all for the same boundary-layer altitude ($Y/\delta=0.1$). The zonal power spectra, ϕ_{u_i}, of Fig. 7 are defined as $\phi_{u_i}=u_i^2(f)/\overline{u_i'^2}$ (s), where $i=t$ (turbulent), l (interturbulent), or c (composite). A degree of imprecision was associated with this procedure in that the

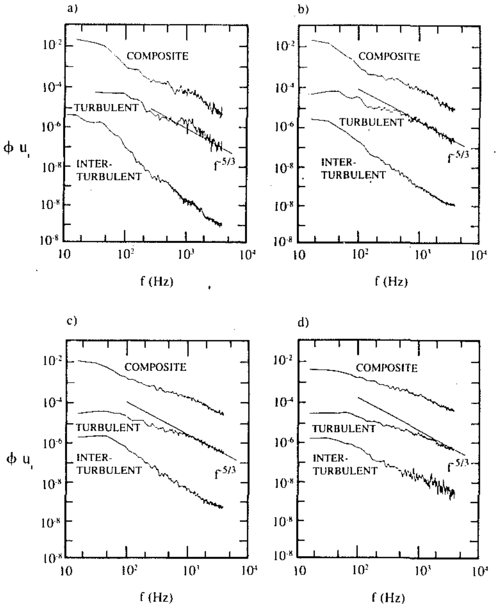

Fig. 7 Zonal streamwise component power spectra for $Y/\delta = 0.10$ for $K = 0.20 \times 10^{-6}$ and grid no. 1. (*a*) $X = 73.2$ cm, $\gamma = 0.05$; (*b*) $X = 93.5$ cm, $\gamma = 0.26$; (*c*) $X = 113.8$ cm, $\gamma = 0.68$; (*d*) $X = 134.1$ cm, $\gamma = 0.93$; each successive curve shifted by 10^{-2}.

velocity steps at the junctions of the "blocks" must produce some artificial (non-physical) higher-order Fourier terms (an artificial indication of high-frequency content in the computed spectra). The fact that the interturbulent spectrum for $X = 73.2$ cm (Fig. 7(*a*)) contained such steps but only indicated an extremely small high-frequency contribution was taken as evidence that this junction-step effect was very small.

The turbulent zone spectra show a progressive increase, with increasing x, in relative contribution from higher-frequency fluctuations. This effect can be observed by comparing the measured spectral distributions to the inertial subrange rolloff distributions ($f^{-5/3}$ slope) included in each figure. The $f^{-5/3}$ sloped lines were constructed to pass through the measured turbulent-zone spectra at $f = 3900$ Hz ($f = 3900$ Hz corresponds to a dimensionless wavenumber, $2\pi f\delta/U \approx 14$). As can be seen from an examination of Figs. 7(*a-d*), the rolloff of the measured spectra for the range $1000 < f < 3900$ decreases progressively with increasing x. For the furthest downstream station, Fig. 17(*d*), the spectral distribution is seen to become tangent to the $f^{-5/3}$ inertial subrange slope at about 2000 Hz. This value ($f = 2000$ Hz, $2\pi f\delta/U \approx 7$) for the beginning of the inertial subrange is in good agreement with the low-altitude spectra ($Y/\delta = 0.05$ and 0.20) measured by Klebanoff (1955) for equilibrium turbulent boundary layers. This result indicates that the ratio of production to dissipation was relatively higher for the early-transitional turbulent patches and may explain the high turbulent-zone TKE distributions at those locations. Although production was immediately present at transition onset, the generation of the full energy cascade evidently required more time (distance) to develop.

Momentum and displacement integral thicknesses were computed for each of the composite and zonal mean velocity profiles. The streamwise development of the shape factor, momentum thickness, and Re_θ through the sample-test-case transition are given in Fig. 8. As the interturbulent zone profiles maintained a laminar-like shape ($H \approx 2.5$) through transition, zonal skin friction values could be determined from the near-wall normal velocity derivative. The turbulent-zone mean profiles, as discussed previously, conformed to the log-wall shape permitting extraction of turbulent-zone skin friction values. The composite skin friction coefficients were computed by weighting the turbulent and interturbulent contributions according to the local near-wall intermittency.

$$C_{f_{\text{comp.}}} = \gamma C_{f_t} + (1-\gamma) C_f \tag{4}$$

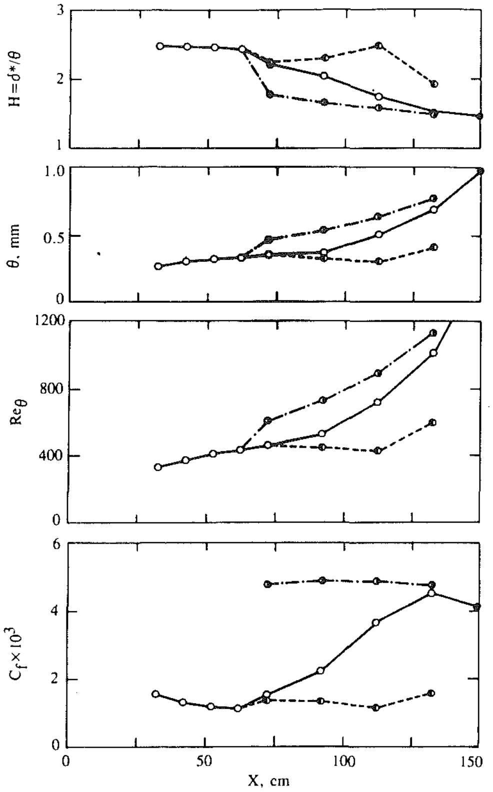

Fig. 8 Development of the mean velocity profile through transition for $K = 0.2 \times 10^{-6}$ and grid no. 1, —○—○— , composite; -·◐-·-◐- , turbulent; --◐--◐- , interturbulent

The various plots of Fig. 8 display the independent characteristics of the zones of transitional flow. Within each zone the shape factors, growth rates, and friction coefficients followed distinctly different paths, from the onset to the end of transition.

As part of this program (Blair, 1982), boundary layer profile data were obtained with miniature pitot probes. The solid symbols of Fig. 8 ($x = 150$ cm) represent the post-transitional measurements of those tests. These data are included here as an indication of the consistency between the hot-wire and pitot-probe results.

Ensemble-Averaged Burst Profiles. The variations of the mean and fluctuating velocity profiles through the turbulent patches were examined using ensemble averaging techniques. This analysis focused on a single profile location ($x = 113.8$ cm, $\gamma = 0.68$) selected from the sample test case ($K = 0.20 \times 10^{-6}$, Grid 1, Te = 0.74 percent).

A probe at a fixed location in a transitional boundary layer detects a wide range of turbulent patch durations. These varying durations correspond to the passage of turbulent patches of different size or to random transverse locations of the patches relative to the probe (the edge of a large patch clipping the probe may appear as a short duration patch).

In an attempt to determine a systematic means of grouping similar patches for ensemble-averaging, the statistics of the patch-duration distribution within the sample profile were examined. Probability density plots of patch duration are given for six boundary-layer altitude bands across the sample profile in Figs. 9(*a-f*). Data are included for both single-element $(\partial u'/\partial t)^2$ and x-wire $(\partial u'v'/\partial t)^2$ probes. Curve fits with unit total area are given for each figure.

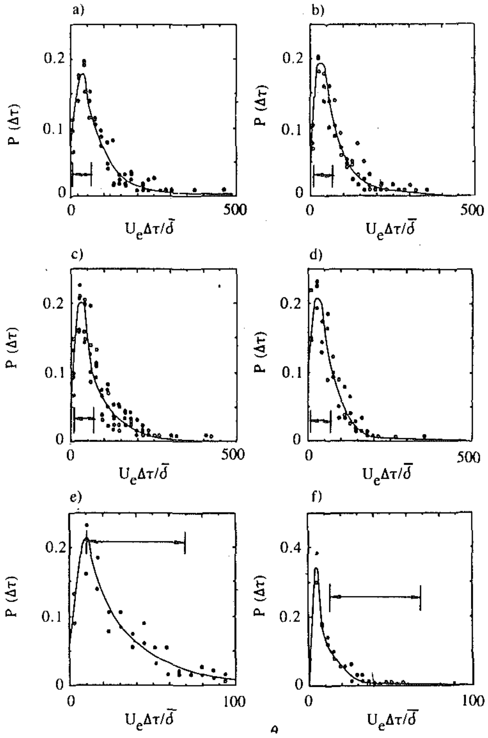

Fig. 9 Probability density of patch duration at various distances from the wall for $K = 0.2 \times 10^{-6}$, grid no. 1, $X = 113.8$ cm, (*a*) $0.053 < Y/\bar{\delta} < 0.060$, (*b*) $0.10 < Y/\bar{\delta} < 0.13$, (*c*) $0.20 < Y/\bar{\delta} < 0.28$, (*d*) $0.40 < Y/\bar{\delta} < 0.47$, (*e*) $Y/\bar{\delta} = 0.66$, (*f*) $0.97 < Y/\bar{\delta} < 1.0$: all cases open symbols $(\partial u/\partial t)^2$ criterion, solid symbols $(\partial u'v'/\partial t)^2$ criterion.

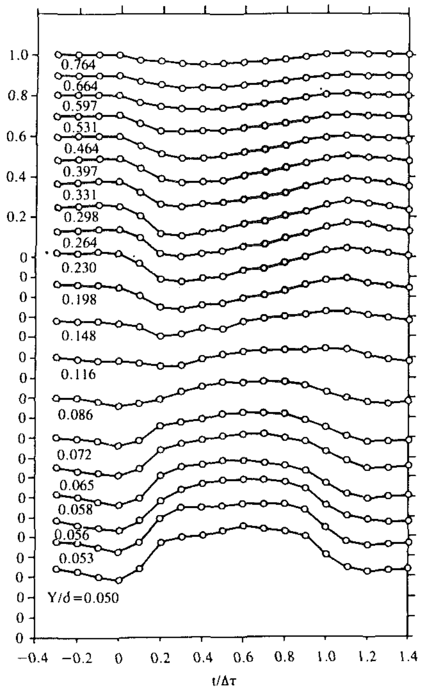

Fig. 10 Ensemble averaged velocity variations through the turbulent zone at various distances from the wall $X = 113.8$ cm, $K = 0.2 \times 10^{-6}$, $T_E = 0.74$ percent, $\gamma_{(\text{near-wall})} = 0.68$

The probability density functions were single-peaked at all boundary-layer altitudes. Since no evidence of multi-modal distributions emerged, it was concluded that ensemble averages (ignoring 3-D effects) could be constructed from those patches of near peak-probability duration. At each altitude, patches with durations between 30 and 200 samples were sorted out for ensemble processing. The range of selected patch durations is marked by arrows for each of Fig. 9. For each of the five lower altitudes this duration range included from 53 to 68 percent of all patches detected. This meant that about 50 to 100 patches were included in each ensemble. Although the "selection window" failed to include the most-probable patches at $Y/\delta = 1$ (Fig. 9(*f*)) it was used unchanged for purposes of consistency.

Comparison of Figs. 9(*a*) through 9(*f*) reveals that observations of patches of relatively long duration decreased and that the patch-duration distribution narrowed with increasing altitude. Note the change in abcissa scale for Fig. 9(*e*) and the change in both scales for Fig. 9(*f*). Agreement between the single-wire and *x*-wire results is seen to be excellent, further confirming the consistency of the two patch-detection functions.

Additional studies could be conducted to determine the dependence of patch characteristics on patch duration. For the present study, only patches that fell within the above "window" were examined.

For these ensemble computations the start of a turbulent patch, as determined by either the $(\partial u'/\partial t)^2$ or $(\partial u'v'/\partial t)^2$ detector function, is defined as $t = 0$; its duration as $\Delta\tau$. The ensemble-averaged mean velocity at any $t/\Delta\tau$ is defined, in the usual manner, as the average, over all patches within the ensemble, of the velocities at that $t/\Delta\tau$.

A meaningful definition of ensemble-averaged fluctuating quantities is considerably less obvious. Here, ensemble-averaged stresses were approximated by computing mean fluctuations about the respective zonal mean velocities. For example, the ensemble-averages of the streamwise component of fluctuating velocity and the Reynolds shear stress are given by:

$$\langle u'\rangle \equiv \langle\sqrt{\overline{u'^2}}\rangle = \langle\sqrt{\overline{(U-\bar{U}_t)^2}}\rangle \tag{5}$$

$$\langle\overline{u'v'}\rangle = \langle\overline{(U-\bar{U}_t)(V-\bar{V}_t)}\rangle \tag{6}$$

where $\bar{U}_t$ and $\bar{V}_t$ are the streamwise and normal turbulent-zone mean velocities at that boundary-layer altitude.

For each detected turbulent patch, the velocity/time record for each velocity component was arbitrarily broken into ten equal intervals with average mean and fluctuating velocities computed for each interval. For each patch, interval-averaged velocities were computed for the ten intervals within the patch and for five intervals before and after the patch. Ensemble-averaged mean and fluctuating velocity distributions through patches were then constructed from all the patches detected at a fixed streamwise location and boundary-layer altitude.

Ensemble-averaged streamwise mean velocity variations through a patch are given for 20 boundary-layer altitudes in Fig. 10. The ensemble-averaged velocities, $\langle U\rangle$, normalized by the freestream mean velocity, *Ue*, are plotted as a function of $t/\Delta\tau$. The "start" time of the detector function corresponds to $t/\Delta\tau = 0$ and the end to 1.0.

These ensemble-averaged plots are based on locally determined timing of the turbulent patches; the beginning and end of patches was determined at each individual altitude. This approach does not consider the shape of the leading and trailing edge faces of the turbulent patches in that all the $t = 0$ and $t/\Delta\tau = 1.0$ arrivals were plotted as if they were simultaneous.

The most distinct feature of Fig. 10 is the sharp increase in velocity near the wall at patch arrival. Also, patch arrival produced significant decrease in velocity in the outer region of the boundary layer.

The upstream ($t < 0$) and downstream ($t/\Delta\tau > 1$) velocities associated with each altitude were not constant, a consequence of the high intermittency ($\gamma = 0.68$). At this late stage of transition the interturbulent intervals were small compared to $\Delta\tau$. By including samples $\pm\Delta\tau/2$ upstream and downstream of the

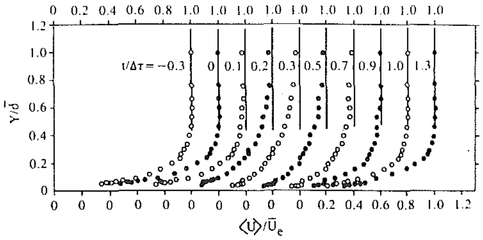

Fig. 11 Ensemble averaged velocity profiles through the turbulent zone (from Fig. 10) $X = 113.8$ cm, $K = 0.2 \times 10^{-6}$, $T_E = 0.74$ percent, $\gamma_{(\text{near-wall})} = 0.68$

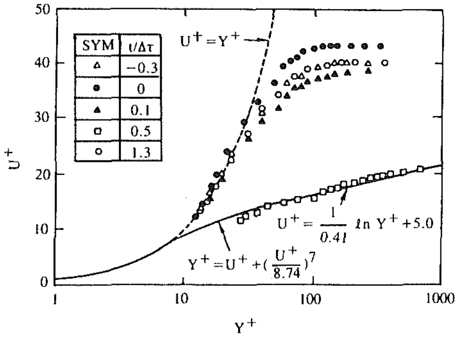

Fig. 12 Ensemble averaged velocity profiles through the turbulent zone in turbulent boundary layer coordinates $X = 113.8$ cm, $K = 0.2 \times 10^{-6}$, $T_E = 0.74$ percent, $\gamma_{(\text{near-wall})} = 0.68$

edges of the patches, random samples from neighboring patches have been included into the interturbulent ensembles.

The velocity histories of Fig. 10 were cross-plotted to create "instantaneous" ensemble-averaged profiles for Fig. 11. The ensemble-averaged velocity ratios are plotted against $Y/\bar{\delta}$ where $\bar{\delta}$ is the long-term average of the boundary layer thickness. The relative time ($t/\Delta\tau$) for each profile is given near the boundary layer edge. Note the large change in boundary layer thickness and change in profile shape as the turbulent patch passes by, from 40 percent of $\bar{\delta}$ at $t/\Delta\tau = -.03$ to >120 percent of $\bar{\delta}$ at $t/\Delta\tau = 0.3$.

Selected profiles from Fig. 11 are presented in Fig. 12 in the universal turbulent profile coordinates. The upstream and downstream profiles ($t/\Delta\tau = -0.3$ and 1.3) are seen to be in excellent agreement with each other and to exhibit a standard laminar shape. At $t = 0$, U^+ exceeds Y^+ for a few of the near-wall points, ($U^+ < 30$) suggesting a possible brief period of adverse pressure gradient. By $t/\Delta\tau = 0.1$, the profile had assumed a transitional shape and by the midpoint ($t/\Delta\tau = 0.5$) it conformed very well to the fully-turbulent law-of-the-wall. These "instantaneous" mean profile results support the concept that separate laminar and turbulent patches exist within the transitional zone.

The variations, with patch passage, of momentum thickness, shape factor, δ, and skin friction coefficient were determined from the "instantaneous" profiles. Skin friction values were computed from the near-wall velocity gradient for the interturbulent profiles, least-squares fits to the law-of-the-wall for the turbulent profiles and by a simple numerical average of the two for intermediate profiles.

These results, presented in Fig. 13, reveal the extreme difference between the interturbulent flow and that in the turbulent patches. The overall (δ) and momentum (θ) boundary layer thicknesses were, respectively, 200 and 100 percent larger in the turbulent patches than in the surrounding interturbulent flow. The shape factor is seen to drop from about 2.3 to about 1.6 and then return to its upstream value. At patch midpoint, the skin friction is nearly 5 times greater than the value computed for the interturbulent profiles. Note that these ensemble-averaged profile results are in very good agreement with the respective zonal-averages marked (IT, C, and T) on the plots of Fig. 13.

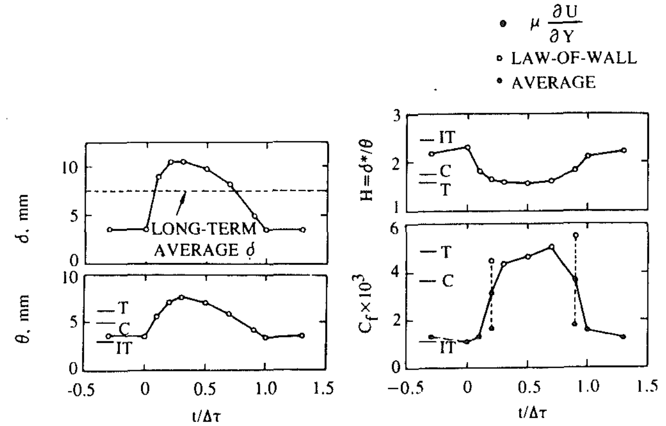

Fig. 13 Profile and skin-friction variations through the turbulent zone computed from the ensemble averaged velocity profiles $X = 113.8$ cm, $K = 0.2 \times 10^{-6}$, $T_E = 0.74$ percent, $\gamma_{(\text{near-wall})} = 0.68$

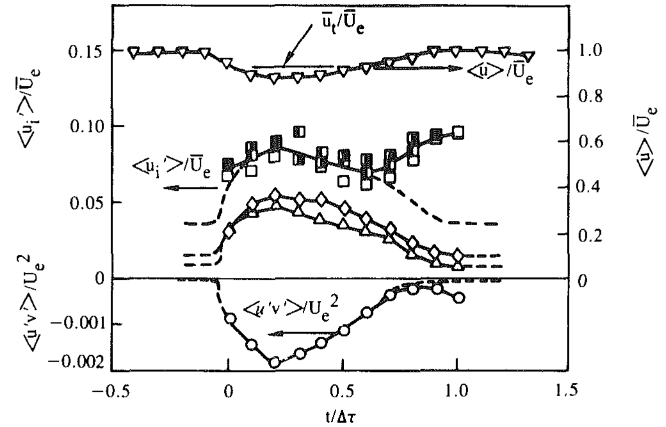

Fig. 14 Ensemble averages of velocity and Reynolds stresses through the turbulent zone for $Y/\bar{\delta} = 0.42$, $X = 113.8$ cm, $\gamma = 0.68$, $K = 0.20 \times 10^{-6}$ and grid no. 1. ▽, $\langle u \rangle/\bar{U}_e$; □, $\langle u' \rangle/\bar{U}_e$ (open squares-single wire data; ◧, vx wire data; ◨, hx wire data); △, $\langle v' \rangle/\bar{U}_e$; ◇, $\langle w' \rangle/\bar{U}_e$; ○, $\langle u'v' \rangle/U_e^2$; - - extrapolations to interturbulent zonal values.

The variation of the turbulent stresses with the passage of a patch is shown in Fig. 14. Sample distributions of ensemble-averages of the all three direct as well as the shear stresses are given for a boundary-layer altitude of $Y/\bar{\delta} = 0.42$. For the streamwise-component direct stresses, results are presented for single-wire, vertical x-wire, and horizontal x-wire measurements. Agreement between the three sets is seen to be very good.

The ensemble-averaged fluctuating quantities presented here were computed using the relatively simple method of averaging fluctuations about zonal means (e.g., Eq. (5)). This method, which is much easier to implement than the usual approach of computing interval-averaged fluctuations about ensemble-averaged means e.g., Antonia et al. (1981), generates only an approximation of the true ensemble stresses. This approximation produces significant differences only for streamwise fluctuations as the normal and transverse fluctuations are large relative to their respective mean excursions.

The ensemble-averaged mean-streamwise velocity plot included in Fig. 14 provides an indication of the magnitude of the approximation inherent in these present ensemble stress computations. A correct interval-mean streamwise direct stress was computed only when the zonal-mean velocity (U_t) happened to exactly equal the ensemble-mean velocity. In the case of the sample profile of Fig. 14, the streamwise zonal and ensemble-averaged means were in close agreement from $0.1 < t/\Delta\tau < 0.7$ so, within this interval, errors in the computed stresses were relatively small. However, near the beginning and end of patches, a significant error associated with computing moments about the zonal mean resulted in artificially high ensemble-averaged stresses. Fairings estimating the actual variation of the stress distributions near the edges of the patches are included in Fig. 14.

Bearing the above in mind, the data of Fig. 14 indicate that peak values of all stresses occurred at about $t/\Delta\tau = 0.25$ followed by a slow decline to the interturbulent levels. The peak shear stress level was approximately 100 percent higher than the turbulent-zone mean value.

Finally, the present ensemble-averaged Reynolds stress distribution results appear to be in excellent agreement with similar measurements obtained in the plane of symmetry of artificially-generated spots (Antonia et al., 1981). At similar boundary layer altitudes, both the magnitude and shape of the patch-induced streamwise-direct, normal-direct and turbulent-shear stress excursions agreed for these two experiments.

Transitional Boundary-Layer Heat Transport. Boundary-layer mean velocity (pitot probe) and mean temperature (thermocouple probe) profile data were obtained as part of the transitional heat transfer tests of this study. A thorough discussion of the techniques used to obtain and analyze these data is given by Blair (1982).

A sample set of these heat-transfer profile data, obtained for flow condition K.20G2 ($K = 0.20 \times 10^6$, Te $\cong 2$ percent) is presented in Blair (1982) in the form of velocity or temperature ratio versus $Y/\delta_{.995}$ and in the universal turbulent coordinates U^+ or T^+ versus Y^+. Comparison of the transitional profiles reveals that the streamwise evolution of the temperature distributions lagged behind that of the velocity distributions.

Transition lengths inferred from the surface heat transfer data of the various test cases (see Fig. 5, Part 1) were as much as one-third longer than lengths determined from shape-factor criterion (recall that the transition origins inferred from these two techniques were in good agreement). All of the above results indicate that the development of turbulent momentum transport in accelerating transitional flows leads the development of turbulent heat transport.

These results revealed that Reynolds' analogy is weaker in accelerating transitional than in zero-pressure-gradient, fully-turbulent flows. An equivalent interpretation is that the effective turbulent Prandtl number is higher for accelerating transitional than in zero-pressure-gradient, fully-turbulent flows. Wang et al. (1985) have observed similar behavior in zero-pressure-gradient transitions, suggesting that weak thermal transport may be common to all transitional flows. An important consequence of this effect is that a transition prediction scheme evaluated solely with velocity-profile dependent effects will predict higher than correct transitional heat transfer rates.

Conclusions

Intermittency profiles generated with conditional discrimination techniques suggest that the turbulent patches observed in these bypass transitions were consistent with passage of spots such as proposed by Schubauer and Klebanoff (1956). The present streamwise-intermittency-distribution results demonstrate the capacity of acceleration to substantially inhibit spot development until some critical stage, the "subtransition" of Narasimha (1984), is reached. Following the "subtransition," intermittency distributions in accelerating flows appear to follow the same scaling laws observed in zero-pressure-gradient flows.

Transition onsets for the various test cases were determined from the surface heat transfer, the intermittency distributions and from the boundary-layer mean velocity profile data. With appropriate definitions, the results from the three techniques were consistent and in very good agreement with predictions from the Van Driest and Blumer (1963) accelerating-flow transition model.

The turbulence kinetic energy (TKE) and Reynolds shear stress profiles developed along distinctly different paths for the turbulent and interturbulent zones. The profiles associated with the interturbulent zone preserved the characteristics of a highly disturbed laminar boundary layer all the way through transition. The turbulent-zone profiles, conversely, immediately assumed the general shapes expected for turbulent boundary layers. Direct stress magnitudes were very large near onset but dropped progressively to equilibrium turbulent levels near the completion of transition.

Turbulent-zone power-spectral-density measurements indicate that the ratio of dissipation to production increased through transition. This suggests that the generation of the full energy cascade required some time (distance) and may explain the very high TKE levels near onset.

Ensemble-averaging techniques were employed to examine the distribution of the mean velocity and the turbulent stresses within the turbulent bursts. The results of this analysis indicated that the "instantaneous" mean profiles at midburst conformed very well to the turbulent log-wall law. Interturbulent profiles corresponded to laminar boundary-layer form. These mean profile results support the use of intermittency-weighted, laminar-and-turbulent patch models of transitional boundary layers.

The turbulent-stress distributions extracted through ensemble averaging indicate that the maximum direct stresses occurred at about one-quarter-way through the total burst duration. Peak Reynolds shear stresses were nearly double the turbulent-zone mean value.

Acknowledgments

The author wishes to acknowledge the extensive contributions of Dr. Robert P. Dring to this study. Drs. M. V. Morkovin and R. Narasimha were kind to review this work and offer several important comments.

Research sponsored by the Air Force Office of Scientific Research (AFSC) under Contracts F49620-78-C-0064 and F49620-84-C-0050. The United States Government is authorized to reproduce and distribute reprints for governmental purposes notwithstanding any copyright notation hereon. The contract monitors for this research were Dr. James D. Wilson, Major Michael S. Francis and Dr. James McMichael.

References

Abu-Ghannam, B. J., and Shaw, R., 1980, "Natural Transition of Boundary Layers—The Effects of Turbulence, Pressure Gradient, and Flow History," *J. Mech. Eng. Sci.*, Vol. 22, p. 213.

Acharya, M., 1985, "Pressure-Gradient and Free-Stream Turbulence Effects on Boundary Layer Transition," Brown Boveri Report KLR 85-127 C.

Antonia, R. A., Chambers, A. J., Sokolov, M., and Van Atta, C. W., 1981, "Simultaneous Temperature and Velocity Measurements in the Plane of Symmetry of a Transitional Turbulent Spot," *Journal of Fluid Mechanics*, Vol. 108, p. 317.

Calcul de L'apparition et du Developpement de la Transition de la Couche Limite," AGARD-CP-224, 13-1. (English translation 1978 Experimental Analysis and Computation of the Onset and Development of the Boundary Layer Transition. NASA TM-75325).

Arnal, D., 1984, "Description and Prediction of Transition in Two-Dimensional, Incompressible Flow," AGARD-R-709, 2-1.

Blair, M. F., 1982, "*Influence of Free-Stream Turbulence on Boundary Layer*

Transition in Favorable Pressure Gradients," ASME *Journal of Engineering for Power*, Vol. 104, p. 743.

Blair, M. F., and Anderson, O. L., 1987, "Study of the Structure of Turbulence in Accelerating Transitional Boundary Layers," United Technologies Research Center Report R87-956900-1.

vanDriest, E. R., and Blumer, C. B., 1963, "Boundary Layer Transition: Freestream Turbulence and Pressure Gradient Effects," *AIAA J.*, Vol. 1, p. 1303.

Dunham, J., 1972, "Predictions of Boundary Layer Transition in Turbomachinery Blades," AGARD-AG-164, p. 55.

Jones, W. P., and Launder, B. E., 1972, "Some Properties of Sink-Flow Turbulent Boundary Layers," *J. Fluid Mech.*, Vol. 56, p. 337.

Klebanoff, P. S., 1955, "Characteristics of Turbulence in a Boundary Layer With Zero Pressure Gradient," NACA Rep. 1247.

Mayle, R. E., 1991, "The Role of Laminar-Turbulent Transition in Gas Turbine Engines," ASME *Journal of Turbomachinery*, Vol. 113, p. 509.

Morkovin, M. V., 1977, "Instability, Transition to Turbulence and Predictability," AGARD-AG-236, p. 1.

Morkovin, M. V., 1984, "Bypass Transition to Turbulence and Research Desiderata," NASA CP-2386, p. 161.

Narasimha, R., Subramanian, C., and Badri Narayanan, M. A., 1984, "Turbulent Spot Growth in Favorable Pressure Gradients," *AIAA J.*, Vol. 22, p. 837.

Narasimha, R., Devasia, K. J., Gururani, G., and Badri Narayanan, M. A., 1984, "Transitional Intermittency in Boundary Layers Subjected to Pressure Gradient," *Exper. in Fluids*, Vol. 2, p. 171.

Narasimha, R., 1984, "Subtransitions in the Transition Zone," *IUTAM Symposium*, Novosibirsk, USSR, p. 141.

Narasimha, R., 1985, "The Laminar-Turbulent Transition Zone in the Boundary Layer," *Prog. Aero. Sci.*, Vol. 22, p. 29.

Reshotko, E., 1976, "Boundary-Layer Stability and Transition," *Ann. Rev. Fluid Mech.*, Vol. 8, p. 311.

Sankaran, R., and Antonia, R. A., 1988, "Influence of a Favorable Pressure Gradient on the Growth of a Turbulent Spot," *AIAA Journal*, Vol. 26, No. 7, p. 885.

Schubauer, G. B., and Klebanoff, P. S., 1956, "Contributions on the Mechanics of Boundary-Layer Transition," NACA TR 1289.

Sohn, K. H., O'Brien, J. E., and Roshotko, E., 1989, "Some Characteristics of Bypass Transition in a Heated Boundary Layer," *7th Symposium on Turbulent Shear Flows*, Stanford, Calif., pp. 2.4.1–2.4.6.

Sohn, K. H., and Roshotko, E., 1991, "Experimental Study of Boundary Layer Transition with Elevated Freestream Turbulence on a Heated Flat Plate," NASA CR 187068.

Suder, K. L., O'Brien, J. E., and Reshotko, E., 1988, "Experimental Study of Bypass Transition in a Boundary Layer," NASA TM-100913.

Wang, T., Simon, T. W., and Buddhavarapu, J., 1985, "Heat Transfer and Fluid Mechanics Measurements in Transitional Boundary Layer Flows," ASME *Journal of Engineering for Gas Turbines and Power*, Vol. 107, p. 1007.

A Three-Layer Model for Separated Turbulent Flows

U. C. Goldberg
Member Technical Staff,
Rockwell International Science Center,
Thousand Oaks, CA 91360

A model for turbulent backflows is presented and evaluated. The model is based on experimental observations, in particular, the wake-like behavior of the turbulence and the diffusion/dissipation energy balance observed in detached flow regions. These lead to an ODE for the eddy viscosity, based on a reduced form of the turbulence kinetic energy equation. This ODE is solvable analytically. The model is applied as a module within a "host" eddy viscosity model (such as a $k-\epsilon$ model) using a three-layer framework wherein the host model predicts the eddy viscosity distribution in the inner and outer layers, while the backflow model provides the eddy viscosity field in the middle layer. Predictions of several flow cases, using this approach, are shown.

Introduction

Turbulent backflow regions exhibit a strong wake-like behavior down to the immediate vicinity of solid surfaces. This behavior precludes the use of the Law-of-the-Wall as a tool for analyzing such flow regions and necessitates development of specialized models for the treatment of these flows.

Such a model was developed by Goldberg (Goldberg and Chakravarthy, 1990) and used successfully to predict a large class of flows involving detached flow regions. It was an algebraic model applied as a module within a "host" model (such as a $k-\epsilon$ model) to determine the eddy viscosity field inside backflow regions.

Experiments in turbulent recirculation zones by Simpson (1981) and Delery (1983) indicate that there is a wide class of such flows in which the backflow region is characterized by negligible turbulence production. In such cases the balance of turbulence energy is between diffusion of energy from the outer (large-scale turbulence) flow into the reversed flow region and its dissipation within that region. Further experimental evidence by Devenport and Sutton (1991) indicates that separated flows obey the linear law $u^+ = y^+$ within a thin layer adjacent to the wall, typically in the range $0 \leq y^+ \leq 3$. These observations form the basis for a three-layer turbulence model wherein the eddy viscosity field is determined by a low Reynolds number $k-L$ or $k-\epsilon$ host model in the wall-layer and beyond the backflow edge, while a dedicated backflow model sets the eddy viscosity field in the middle-layer between the outer edge of the wall-layer and the backflow edge.

The latter model, featuring the analytical solution of an ordinary differential equation (ODE) in the normal-to-wall direction, is introduced and tested. Like the previous model (Goldberg and Chakravarthy, 1990), it is used as a module within a host model to determine the eddy viscosity within backflow regions; unlike the previous model, it needs the host model to supply the local maximum value of the turbulence kinetic energy.

Middle-Layer Model Formulation

The standard turbulence kinetic energy equation (with gradient diffusion model) is given by

$$\frac{\partial}{\partial t}(\rho k) + \frac{\partial}{\partial x_i}(\rho U_i k) = \frac{\partial}{\partial x_i}\left[(\mu + \mu_t/\sigma_k)\frac{\partial k}{\partial x_i}\right] - \rho\overline{u_i' u_j'}\frac{\partial U_i}{\partial x_j} - C_k\frac{(\rho k)^2}{\mu_t} \quad (1)$$

where k is the turbulence kinetic energy, ρ is density, U_i and u_i' are the cartesian mean and fluctuating velocity components, respectively, μ and μ_t are the laminar and eddy viscosities, respectively, x_i are the cartesian coordinates, and t is time. The modeling constants are $\sigma_k \cong 1.0$, $C_k \cong 0.08$.

This equation will be simplified based on the following experimental observations of turbulent backflows (Simpson, 1981; Delery, 1983): the kinetic energy of turbulent, k, scales as the Reynolds shear stress $-u'v'$ and generally behaves in a way representable by a sine function between the wall and the freestream with its local maximum reached approximately at the location where $-u'v'$ reaches its own local maximum value (see Fig. 1*a*). The latter usually coincides with the local maximum of the mean steamwise velocity's normal gradient. Thus the turbulence kinetic energy distribution may be modeled in the form

$$\frac{\rho k}{(\rho k)_{\max}} = \frac{\cos\beta - \cos[\beta(1 + y/y_0)]}{1 + \cos\beta} \quad (2a)$$

$$\beta = \frac{\pi}{1 + y_{u_s}/y_0}, \quad 2(b)$$

y_{u_s} is the distance from the wall to the location of $u_s = [-(\overline{u'v'})_{\max}]^{1/2}$, and $k_{\max}$ is the turbulence kinetic energy at that location, supplied by the host model, since y_{u_s} is outside the backflow region.

y_0 is the local wall-layer edge, which, according to Devenport and Sutton (1991), is located at

$$y_0^+ \equiv y_0(\rho_w|\tau_w|)^{1/2}/\mu_w \cong 3, \quad (3)$$

Contributed by the Fluids Engineering Division for publication in the JOURNAL OF FLUIDS ENGINEERING. Manuscript received by the Fluids Engineering Division April 2, 1991. Associate Technical Editor: R. K. Agarwal.

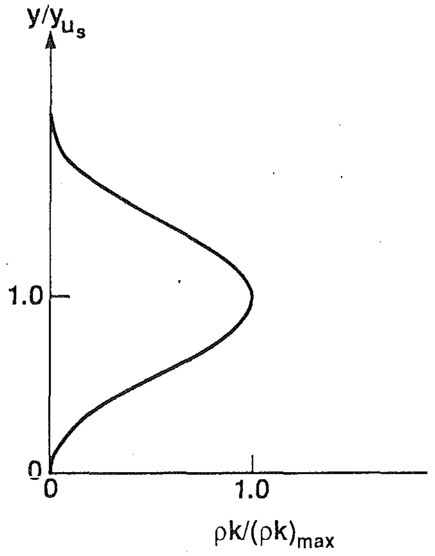

A

Fig. 1(*a*)

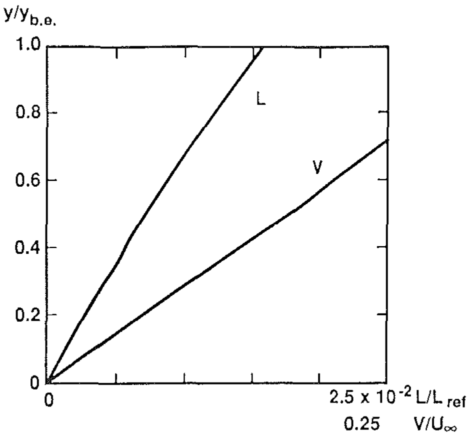

B

Fig. 1(*b*)

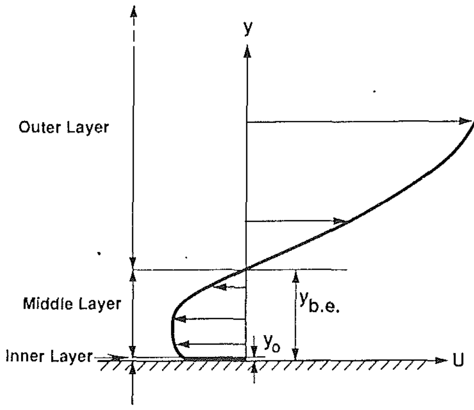

C

Fig. 1(*c*)

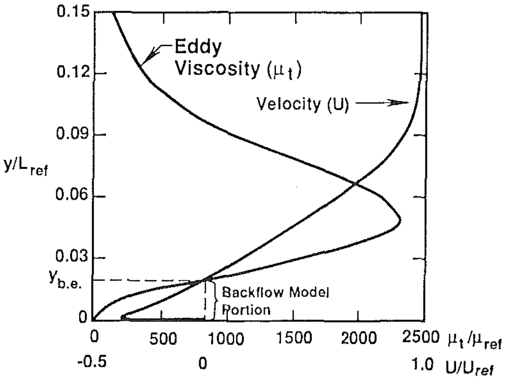

D

Fig. 1(*d*)

where τ is the laminar shear stress and w denotes evaluation at walls.

For the purpose of modeling the turbulence within backflow regions, k is treated as a function of the normal distance, y, given by Eq. (2), with streamwise variations in k effected implicitly through the corresponding variations in $(\rho k)_{\max}$ and y_{u_s}. Using this concept in Eq. (1) and retaining only the diffusion and dissipation terms, results in the equation

$$\frac{d}{dy}\left[(\mu+\mu_t/\sigma_k)\frac{dk}{dy}\right]-C_k\frac{(\rho k)^2}{\mu_t}=0. \tag{4}$$

Since this equation is to be applied for $y > y_0$, the effect of molecular diffusion is assumed negligible compared to turbulent diffusion, further reducing Eq. (4) to read

$$\frac{d}{dy}\left(\mu_t\frac{dk}{dy}\right)-\sigma_k C_k\frac{(\rho k)^2}{\mu_t}=0 \tag{5}$$

or, equivalently,

$$\frac{d\phi}{dy}=\left[\sigma_k C_k(\rho k)^2\frac{dk}{dy}\right]\frac{1}{\phi} \tag{6a}$$

where

$$\phi\equiv\mu_t\frac{dk}{dy}. \tag{6b}$$

Using the model Eq. (2) for k and dk/dy, the solution to Eq. (6) is given by

$$\boxed{\mu_t=\frac{\rho y_0}{\beta\sin\varphi}\left\{\frac{2}{3}\sigma_k C_k\frac{(\rho k)_{\max}}{1+\cos\beta}\left[\frac{(\cos\beta-\cos\varphi)^3}{\rho}-\frac{(\cos\beta-\cos 2\beta)^3}{\rho_0}\right]+\left(\frac{\beta\sin 2\beta}{\rho_0 y_0}\mu_{t_0}\right)^2\right\}^{1/2}} \tag{7a}$$

where

$$\varphi(y)=\frac{y_0+y}{y_0+y_{u_s}}\pi \tag{7b}$$

and the boundary condition $\mu_t = \mu_{t_0}$ at $y=y_0$ is applied. Here μ_{t_0} is the value of eddy viscosity at the local wall-layer edge, supplied by the host model.

It is noted that, while

$$\frac{dk}{dy}=\frac{\beta\sin\varphi(y)}{1+\cos\beta}\frac{(\rho k)_{\max}}{\rho y_0}-k\frac{\partial\ln\rho}{\partial y},$$

the term involving the density gradient has been neglected in the solution of Eq. (6). This simplification is not expected to significantly change the quality of the predicted eddy viscosity field in near-wall reversed flow regions for a wide range of practical flow situations.

The eddy viscosity formula, Eq. (7), is applied between the wall-layer edge and the local backflow edge ($y_0 < y < y_{b.e.}$). Accordingly, the velocity scale in the middle layer is

$$V=k^{1/2}=\left(\frac{\cos\beta-\cos\varphi}{1+\cos\beta}\frac{\rho_{\max}}{\rho}k_{\max}\right)^{1/2} \tag{8}$$

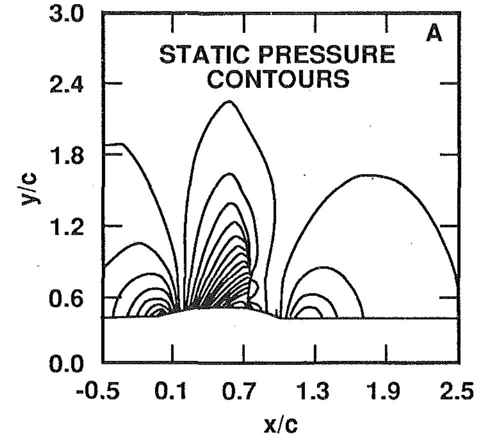

Fig. 2(*a*)

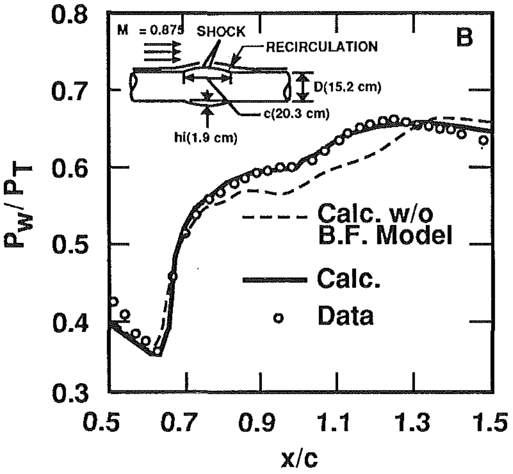

Fig. 2(*b*)

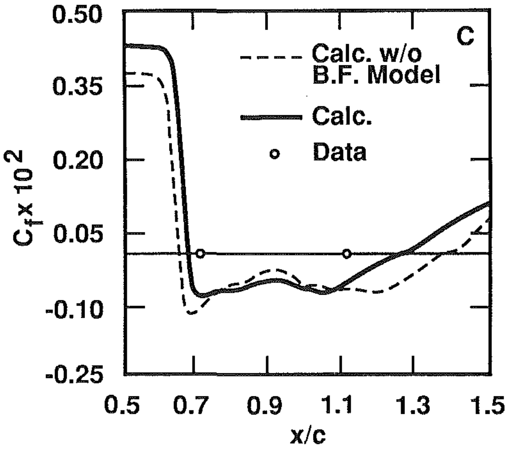

Fig. 2(*c*)

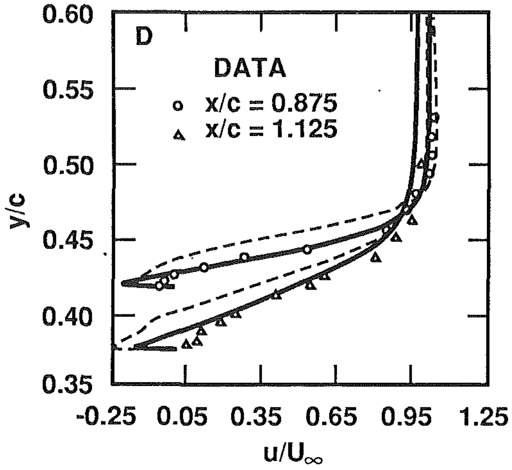

Fig. 2(*d*)

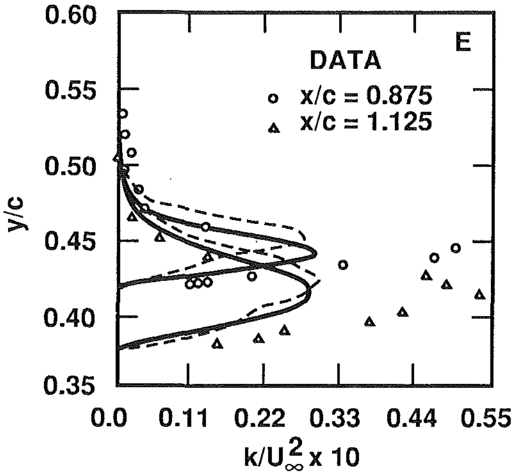

Fig. 2(*e*)

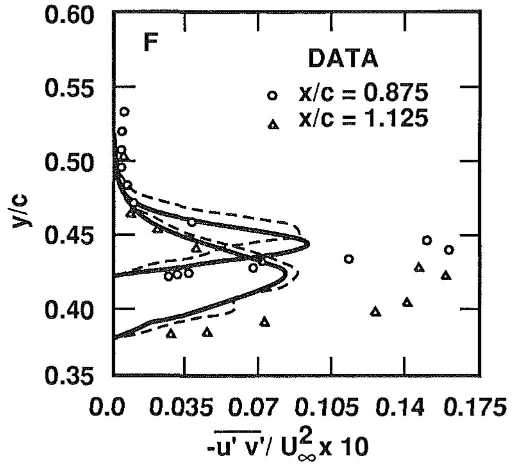

Fig. 2(*f*)

and the length scale results implicitly from the μ_t distribution

$$L = \frac{\mu_t}{C_k \rho \sqrt{k}}. \tag{9}$$

Figure 1(*b*) shows typical length-and velocity-scale profiles within a backflow region.

It is noted that the above model is valid for both two-and three-dimensional flows. It is further observed that there are no case-dependent "constants" in the entire model formulation.

Inner and Outer-Layer Modeling

The backflow model was included as a module in the $k-L$ and $k-\epsilon$ turbulence models available in the USA Reynolds-averaged Navier- Stokes flow solver, which is a highly (up to 3rd order) accurate solver, based on a TVD formulation for the convection terms, within a finite volume framework (Chakravarthy et al., 1988). These serve as host models, supplying the eddy viscosity field in the wall-layer ($y<y_0$) and in the outer-layer ($y>y_{b.e.}$). In general, any model which solves the turbulence kinetic energy equation may serve as a host model.

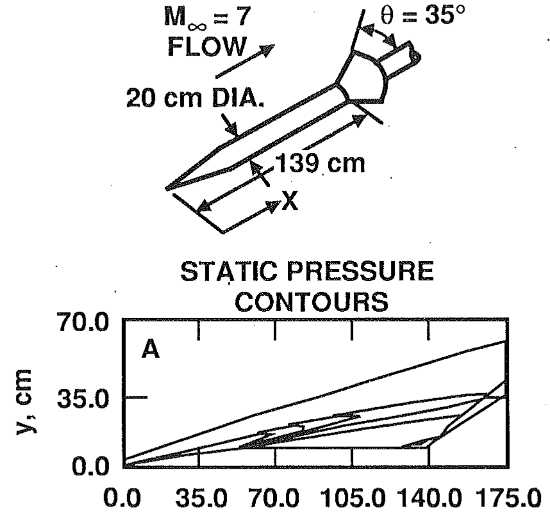

Fig. 3(*a*)

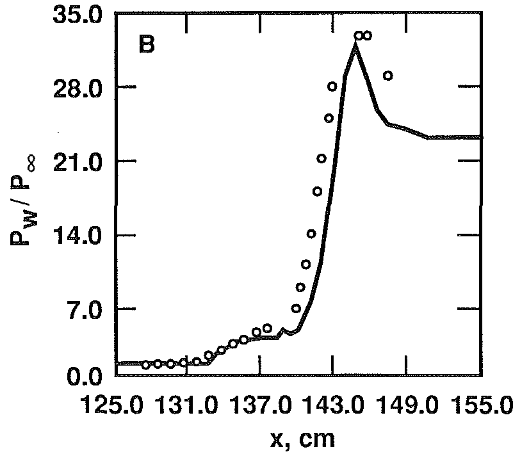

Fig. 3(*b*)

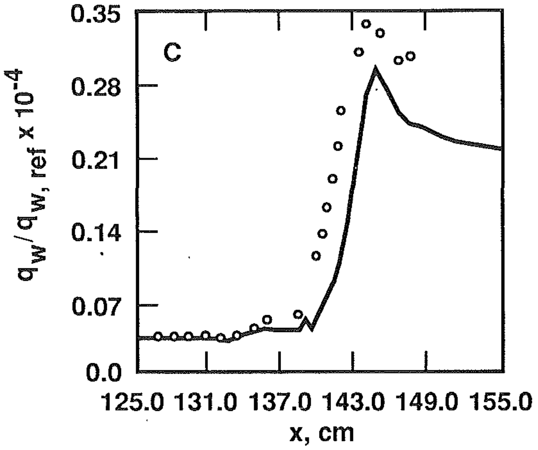

Fig. 3(*c*)

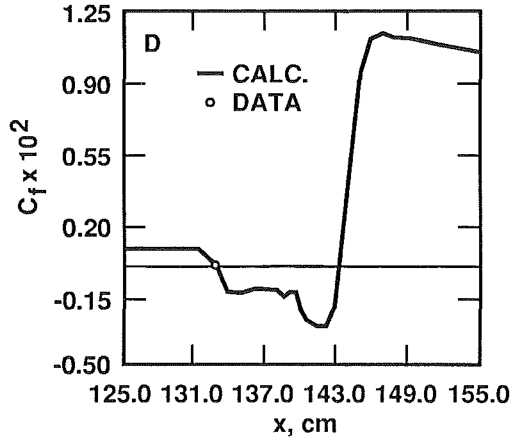

Fig. 3(*d*)

Figure 1(*c*) indicates the location of the three layers used in the present composite turbulence model. Figure 1(*d*) shows a typical eddy viscosity profile calculated with this model. The corresponding velocity profile is also shown on the same plot.

Model Evaluation

Several flow cases were computed, using the three-layer model, and the results agreed fairly well with experimental data. Two of these cases are presented here:

Case 1. This case is the transonic flow over an axisymmetric bump of Bachalo and Johnson (1979). Figure 2 presents comparisons between predictions and data for surface pressure, skin friction, axial velocity profiles at two streamwise locations within the reversed flow region, and the corresponding Reynolds shear stress and turbulence kinetic energy profiles. Two sets of predictions, one with the backflow model on, the other with the model off, are shown. Pressure contours are also included to show the shock location. The host turbulence model was the 1-equation $k-L$ model (Goldberg and Chakravarthy, 1990). A 101×50 grid size was used, with at least three cells inside the viscous sublayer ($y^+ \leq 11$).

Case 2. This case is the hypersonic axisymmetric flow over an ogive-cone- cylinder-35° flare configuration of Kussoy and Horstman (1989). Figure 3 shows predictions and data comparisons for surface pressure, skin friction, and surface heat transfer. The pressure contour plot is included to show shock structure and extent of upstream influence. Here, too, the $k-L$ turbulence model served as the host model. A 125×50 grid size was employed, with at least three cells within the viscous sublayer.

Summary

A model for turbulent backflows was introduced and tested. The model was based on experimental observations, in particular, the wave-like behavior of the turbulence and the type of energy balance observed in detached flow regions. These led to an ODE for the eddy viscosity, resulting from a reduced form of the kinetic energy equation. This ODE was solvable analytically. The model was applied as a module within a "host" eddy viscosity model (such as a $k-\epsilon$ model) using a three-layer framework wherein the host model supplied the eddy viscosity distribution in the inner (wall) layer and in the outer (wake) layer, while the backflow model predicted the eddy viscosity field in the middle (backflow) layer. This approach is readily applicable to three-dimensional flows.

Calculation of several flow cases involving reversed-flow regions, using this approach, were encouraging. Since the model is firmly based on observed physics, as discussed above, and since it contains no "tuning" constants, in contrast with currently available approaches, further evaluation of this model is in order before its success and shortcomings, relative to other existing models, may be properly assessed.

References

Bachalo, W. D., and Johnson, D. A., 1979, "An Investigation of Transonic

Turbulent Boundary Layer Separation Generated on an Axisymmetric Flow Model," AIAA Paper 79-1479.

Chakravarthy, S. R., Szema, K.-Y., and Haney, J. W., 1988, "Unified 'Nose-to-Tail' Computational Method of Hypersonic Vehicle Applications," AIAA Paper 88-2564.

Delery, J. M., 1983, "Experimental Investigation of Turbulence Properties in Transonic Shock/Boundary-Layer Interactions," *AIAA Journal*, Vol. 21, pp. 180–185.

Devenport, W. J., and Sutton, E. P., 1991, "Near-Wall Behavior of Separated and Reattaching Flows," *AIAA Journal*, Vol. 29, pp. 25–31.

Goldberg, U. C., and Chakravarthy, S. R., 1990, "Separated Flow Predictions Using a Hybrid $k-L$/Backflow Model," *AIAA Journal*, Vol. 28, pp. 1005–1009.

Kussoy, M. I., and Horstman, C. C., 1989, "Documentation of Two- and Three-Dimensional Hypersonic Shock Wave/Turbulent Boundary Layer Interaction Flows," NASA TM 101075.

Simpson, R. L., 1981, "A Review of Some Phenomena in Turbulent Flow Separation," ASME JOURNAL OF FLUIDS ENGINEERING, Vol. 103, pp. 520–533.

W. L. Keith
Mem. ASME

D. A. Hurdis
Mem. ASME

B. M. Abraham
Mem. ASME

Submarine Sonar Department,
Naval Underseas Warfare Center
Detachment,
New London, Conn.

A Comparison of Turbulent Boundary Layer Wall-Pressure Spectra

Turbulent boundary layer wall-pressure spectra from various experimental investigations and a recent numerical simulation are presented. The spectra are compared in nondimensional form with three commonly used scaling laws. Attenuations resulting from inadequate sensor spatial resolution are shown to be of primary importance at the higher frequencies. The dependence of the scaling laws on momentum thickness Reynolds number is discussed. The ratio of the outer to the inner boundary layer length scale is shown to provide insight into the observed trends in the spectra.

Introduction

Over the past thirty years, many measurements of the autospectra of wall-pressure fluctuations beneath turbulent boundary layers have been reported. These have been aimed both at gaining knowledge of the physics of turbulent boundary layers, and at solving practical engineering problems such as reducing the flow-induced noise within an aircraft that results from boundary layer excitation of the aircraft skin. Spectral data are nondimensionalized with appropriate scales for mass, length and time. The effectiveness of any particular scaling law is determined by the extent to which the data collapse to a single curve.

Farabee (1986) considered the general form of the spectral solution to the Poisson equation, which governs the wall-pressure fluctuations. He concluded that spectral contributions at high frequencies result from turbulent velocity fluctuations in the wall region of the boundary layer. Contributions at low frequencies were found to result from turbulent velocity fluctuations across the entire boundary layer. Separate nondimensional parameters are therefore required for scaling the low and high frequency portions of the spectra. This paper contains a comparison of three different scaling laws commonly used for wall-pressure spectra. The effectiveness of each one is assessed by comparing the spectral data from a number of experimental investigations and also from a recent computational effort.

Comparisons of Spectral Data

An ideal flow facility for the measurement of wall-pressure fluctuations would have negligible free stream turbulence intensity and no acoustic background noise. The pressure sensors should be sufficiently small to resolve turbulent scales of the order of ten viscous lengths and should be calibrated to establish their wavenumber-frequency response. In addition, the boundary layer parameters τ, δ, δ^*, and θ should be measurable to a high degree of accuracy. Uncertainties in these quantities constitute sources of error in the nondimensional spectral levels. The errors at higher frequencies due to the finite sensor size will be discussed here in detail. At low frequencies, where the effects of sensor size are negligible, the uncertainty in the spectral levels depends on the signal processing as well as the facility characteristics mentioned above. The majority of the investigations compared here did not include a statement as to the uncertainty in the spectral levels. Therefore it is not possible to establish precise uncertainties and associated confidence levels for many of the investigations due to lack of information. Based upon personal communications with particular authors as well as information in the respective articles, the uncertainty in the published nondimensional spectral levels was within ± 1 dB for all cases. In the comparisons presented here, all ambiguities with regard to single or double-sided spectra, or from factors of 2π have been taken into account. For data sets in which required scaling parameters were not given, values were estimated from Coles' (1953) results for ideal flat plate boundary layers.

Bull and Thomas (1976) concluded that the use of pinhole sensors in air led to errors in the measured spectra. However, Farabee (1986), Farabee and Casarella (1991), and Gedney and Leehey (1989) have concluded that pinhole sensors are effective for wall-pressure measurements. We have therefore included in this comparison the data of Farabee (1986) which were obtained with pinhole sensors. Present sensor technology requires the use of pinhole sensors in air in order to resolve the smallest turbulent scales. Also, none of the data compared here were obtained using noise cancellation techniques.

For the purpose of comparing frequency spectra from these various data sets, the following three scaling laws for the spectra will be considered:

---

[1] In technical literature on acoustics, pressure is generally expressed in units of micropascals. For consistency with previously published data, we have chosen to use British units throughout this paper. However, all spectra are presented in dimensionless form.

Contributed by the Fluids Engineering Division and presented at the Winter Annual Meeting, Symposium on Flow Noise Modeling, Measurement, and Control, Atlanta, Ga., December 1-6, 1991, of THE AMERICAN SOCIETY OF MECHANICAL ENGINEERS. Manuscript received by the Fluids Engineering Division August 16, 1991. Associate Technical Editor: J. C. Humphrey.

(*i*) *Outer Variables.* The frequency is scaled as $\omega\delta^*/U_o$ and the spectrum is scaled as $\Phi(\omega)/(\rho^2\delta^* U_o^3)$.

(*ii*) *Mixed Inner and Outer.* The frequency is scaled with outer variables as $\omega\delta^*/U_o$ and the spectrum is scaled with inner and outer variables as $\Phi(\omega)U_o/(\tau^2\delta^*)$.

(*iii*) *Inner Variables.* The frequency is scaled as $\omega\nu/u_\tau^2$ and the spectrum is scaled as $\Phi(\omega)u_\tau^2/(\tau^2\nu)$.

The outer variable scaling given above appeared in the early literature, and has also been used in recent investigations. We note that the choice of δ^* as the outer length scale is subject to discussion. Although the displacement thickness is an integral length scale for the boundary layer, it is not a direct measure of the outer length scale of the boundary layer. A more direct measure of the outer length scale is δ. Since the relationship between δ and δ^* varies with Reynolds number, the two quantities are not equivalent as length scales. Here, we use δ^* largely for consistency, since many of the investigators also chose δ^*. Other outer variable scalings may well prove to be more appropriate in the future. Similarly, although the inner scaling and mixed scaling given above have also been used by many investigators, they should not be viewed as definitive. We note that Farabee and Casarella (1991) have recently scaled frequency as $\omega\delta/u_\tau$ and the spectrum as $\Phi(\omega)u_\tau/\tau^2\delta$.

In comparing these three scalings, the following approach is taken:

(i) The data from the various investigations will first be presented with the outer variable scaling. The general trends in the data sets with this scaling including the attenuations resulting from inadequate spatial resolution will be discussed.

(ii) The relationship between the outer variable and mixed variable scaling is presented. The effectiveness of each of these scalings for collapsing the data at the lower frequencies is discussed.

(iii) The relationship between the outer variable and inner variable scaling is presented. The effectiveness of the inner variable scaling for collapsing the data at the higher frequencies is discussed.

(iv) Data from the internal and external flows are compared to determine any apparent trends.

(a) Outer Scaling and the Effect of Sensor Spatial Resolution. Following Willmarth and Roos (1965) the measured wavenumber-frequency spectrum, $\Phi_m(k_1,k_2,\omega)$, is related to the true wavenumber-frequency spectrum, $\Phi_t(k_1,k_2,\omega)$, through the expression

$$\Phi_m(k_1,k_2,\omega)=\Phi_t(k_1,k_2,\omega)s(k_1,k_2,\omega) \qquad (1)$$

where $s(k_1,k_2,\omega)$ is the wavenumber-frequency response of the pressure sensor. Using the relationship

$$\Phi(\omega)=\int_{-\infty}^{\infty}\int_{-\infty}^{\infty}\Phi(k_1,k_2,\omega)dk_1dk_2, \qquad (2)$$

Equation (1) may be expressed in the form

$$\Phi_m(\omega)=\int_{-\infty}^{\infty}\int_{-\infty}^{\infty}\Phi_t(k_1,k_2,\omega)s(k_1,k_2,\omega)dk_1dk_2. \qquad (3)$$

It is apparent from Eq. (3) that knowledge of the wavenumber-frequency characteristics of both the true turbulent wall-pressure field and of the pressure sensor are required to determine the effects of the sensor spatial resolution on the measured frequency spectrum, $\Phi_m(\omega)$. Direct measurements of the wavenumber-frequency spectrum $\Phi_m(k_1,k_2,\omega)$ require a large number of matched sensors as well as extensive signal processing capabilities. Very few direct measurements of $\Phi_m(k_1,k_2,\omega)$ have been reported to date. In general, models for the quantity $\Phi_t(k_1,k_2,\omega)$ are inexact due to the limitations in the measurement upon which they are based.

The Corcos (1963) model of the cross-spectrum was derived from the cross correlation measurements of Willmarth and Wooldridge (1962). With this model, Corcos showed that the ratio of the measured frequency spectrum to its true value, $\Phi_m(\omega)/\Phi_t(\omega)$, depends only upon the quantity $\omega r/U_c$, where r is the radius of the pressure sensor. In this formulation, Corcos assumed a uniform sensitivity distribution over the face of the circular pressure sensor, and also an instantaneous temporal response. With these assumptions, the wavenumber-frequency response of the sensor is given by Willmarth and Roos (1965) as

$$s(k_1,k_2,\omega)=[1/\pi^2]\cdot[J_1(kr)/(kr)]^2. \qquad (4)$$

Nomenclature

$d(=2r)$ = circular sensor diameter, (in)
d^+ = du_τ/ν
d^* = $(du_\tau/\nu)(u_\tau/U_o)=d^+(u_\tau/U_o)$
f = cyclic frequency, (Hz)
H = δ^*/θ = boundary layer shape factor
$J_1(kr)$ = Bessel function of the first kind, first order
k_1 = streamwise wavenumber of a convected turbulent wall-pressure disturbance, (rad/in)
k_2 = spanwise wavenumber of a convected turbulent wall-pressure disturbance, (rad/in)
k = $\sqrt{k_1^2+k_2^2}$, (rad/in)
k_c = ω/U_c = convective wavenumber, (rad/in)
$p(t)$ = fluctuating wall-pressure, (psi)^1
$p_{\rm rms}$ = $\{\int_0^\infty\Phi(\omega)d\omega\}^{1/2}$ = fluctuating wall-pressure root mean square, (psi)
R_* = δ^*u_τ/ν = ratio of the outer to the inner length scale
R_θ = $U_o\theta/\nu$ = momentum thickness Reynolds number
$s(k_1,k_2,\omega)$ = dimensionless wavenumber-frequency response of a pressure sensor
u_τ = $\sqrt{\tau/\rho}$ = friction velocity (shear velocity), (ft/s)
$U_c(\omega)$ = frequency dependent convection velocity of a turbulent wall-pressure disturbance, (ft/s)
U_o = free-stream (or centerline) velocity, (ft/s)
δ = boundary layer thickness, (in.)
δ^* = displacement thickness, (in.)
θ = momentum thickness, (in)
ν = kinematic viscosity of fluid, (ft^2/s)
ρ = fluid density, (lb$_m$/ft^3)
τ = mean wall-shear stress, (psi)
$\Phi(\omega)$ = single-sided autospectral density of the fluctuating wall-pressure, (psi)^2/(rad/s)
$\Phi(k_1,k_2,\omega)$ = wavenumber-frequency spectral density of the fluctuating wall-pressure, (psi)^2/(rad^3/(in$^2\cdot$s))
ω = $2\pi f$ = angular frequency, (rad/s)
ω_u = frequency cut-off for effects of sensor spatial resolution, (rad/s)

Subscripts

m = measured quantity
t = true quantity

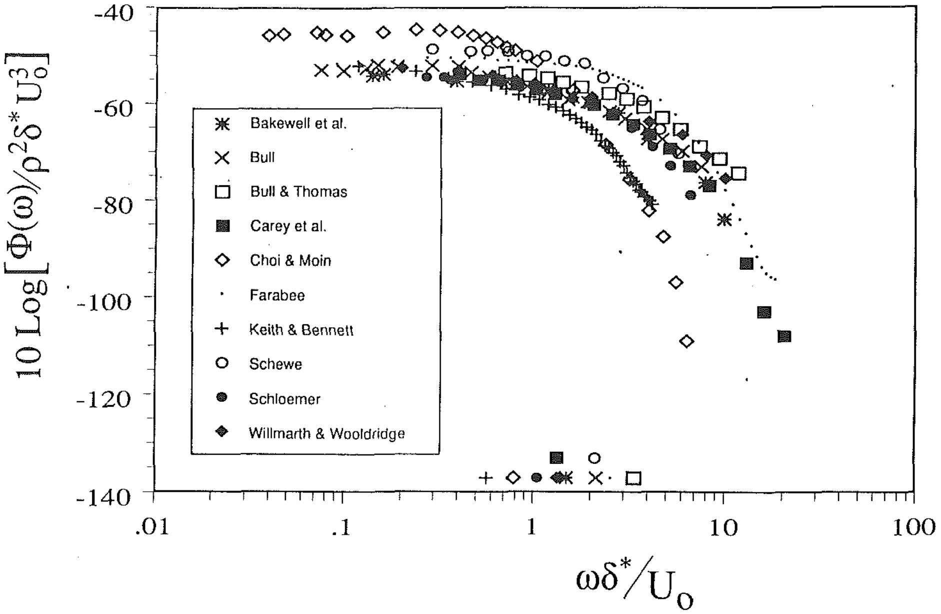

Fig. 1 Nondimensional wall pressure spectra scaled on outer variables

In general, the sensitivity distribution over the face of a sensor is not uniform and not readily measurable. Sensors are often calibrated in a known acoustic field, such that their response to only long wavelength pressure fluctuations is determined. The true sensor wavenumber-frequency response is therefore an additional unknown quantity. For these reasons, correction procedures of the type provided by Corcos are only approximate in nature. Hence, the true frequency spectrum $\Phi_t(\omega)$ cannot accurately be recovered from measurements that were influenced by the spatial resolution of the pressure sensor. Correction procedures do, however, allow an estimate of the spectral frequency range over which the sensor spatial resolution effects are important.

For each data set, the following method was used to determine the frequency range over which spatial resolution effects were negligible. Corrections to the measured spectra were determined using the Corcos method with no modifications. The frequency, ω_u, at which the ratio of the corrected to the measured spectrum was 1.26 (or 1 dB) was determined. The value 1 dB was chosen arbitrarily. The spectral levels at frequencies higher than ω_u were then assumed to have been attenuated by the spatial resolution of the sensors. Figure 1 contains the wall-pressure spectral data from each data set, with the outer variable scaling. The value of $\omega_u\delta^*/U_o$ for each data set is noted by the respective symbol located immediately above the frequency axis. The Corcos correction was applied to the Choi and Moin (1990) data, assuming a sensor diameter equal to the streamwise numerical grid length. For $\omega\delta^*/U_o > 3.3$, the spectral levels from all of the data sets were influenced by the resolution of the respective sensors.

From the Corcos correction method discussed above, the spectral attenuation due to spatial resolution depends only upon the quantity $\omega r/U_c$ or equivalently $k_c r$, where k_c is the convective wavenumber. The quantity $k_c r$ may be expressed as

$$k_c r = (\omega\delta^*/U_o)(U_o/U_c)(d/2\delta^*) \qquad (5)$$

For a fixed value of $\omega\delta^*/U_o$, the quantity $(U_o/U_c)(d/2\delta^*)$ will determine the attenuation. For $\omega\delta^*/U_o > 1$, the quantity U_c/U_o has typically been reported to approach a constant value of approximately 0.6. The variation in this value among data sets is generally within 10 percent. Variations in U_c/U_o within 10 percent lead to variations in the spectral attenuations to within 0.5 dB. The quantity d/δ^* varied from 0.13 to 0.89 for the data sets compared here. The effect of variations in U_c/U_o among data sets is therefore small compared to the effect of variations in the quantity d/δ^*. For frequencies $\omega\delta^*/U_o$ where attenuations due to spatial resolution are significant, a trend of decreasing spectral levels with increasing d/δ^* should occur. The scaling of $\Phi(\omega)$ will also clearly affect the spectral levels. Depending upon the particular frequency, the inner scaling may be more appropriate than the outer. Rather than attempting to identify a priori particular frequency ranges, we assume the outer scaling is to some extent valid over the entire frequency range and look for the above trend.

For the case of the inner scaling, the quantity $k_c r$ may be expressed as

$$k_c r = (\omega\nu/u_\tau^2)(u_\tau/U_o)(U_o/U_c)(d/2)(u_\tau/\nu) \qquad (6)$$

The above arguments for the effect of convection velocity also apply here. The quantity $d^+ = du_\tau/\nu$ is currently used by investigators as the metric for sensor spatial resolution. However, the quantity u_τ/U_o also appears. For the data sets considered here, u_τ/U_o varies from 0.05 at the lowest R_θ to 0.03 at the highest. For the inner scaling, this variation must also be considered in addition to the quantity du_τ/ν. The quantity $d^* = (du_\tau/\nu)(u_\tau/U_o)$ therefore is the parameter that determines the spatial resolution for the case of the inner scaling.

In Eq. (6) we have introduced the quantity U_o in order to consider the quantities u_τ/U_o and U_o/U_c. We note that U_o does not appear explicitly in the inner variable scaling. An equivalent form of Eq. (6) may be considered, in which the quantity $(u_\tau/U_o)(U_o/U_c)$ is replaced with the quantity u_τ/U_c. This formulation does not involve U_o explicitly, and may therefore be more consistent with respect to the inner variable scaling. However, the former formulation is believed to be more easily interpreted, as the quantity u_τ/U_c is somewhat obscure. Both formulations are equivalent with regard to determining the effects of sensor spatial resolution.

Table 1 contains the quantities d/δ^*, du_τ/ν, and d^* for each data set. In addition, Table 1 shows that the ratio R_* of the outer length scale to the inner varies significantly among the data sets. Sensor size in relationship to both scales should therefore be considered. For example, we note the comparatively low value of R_* for the numerical data of Choi and Moin (1990).

For the case of the outer scaling, the dominant trend in Fig.

Table 1 Investigations of turbulent boundary layer wall-pressure fluctuations

Investigation	Test Section	Fluid	U_o (ft/s)	δ (in)	δ^* (in)	Θ (in)	ν/u_τ (in)	R_θ	R_*	d (in)	d/δ^*	$d^+ = du_\tau/\nu$	$d^* = d^+u_\tau/U_o$
Bakewell et al. (1962)	Fully Developed Pipe Flow	Air	178	1.75	0.22	0.175	3.5×10^{-4}	1.5×10^{4}	630	0.07	0.32	202	6.9
Bull (1967)	Wind Tunnel	Air	329	1.188	0.149	0.107	1.67×10^{-4}	1.95×10^{4}	890	0.029	0.195	173	5.69
Bull & Thomas (1976)	Wind Tunnel	Air	78.7	1.80	0.224	0.18	6.87×10^{-4}	7×10^{3}	330	0.0295	0.13	44	1.58
Carey et al. (1967)	Fully Developed Pipe Flow	Water	55.7	1.75	0.22	0.175	7.65×10^{-5}	7.5×10^{4}	2860	0.07	0.32	915	27.7
Choi & Moin (1990)	Fully Developed Channel Flow	arbitrary	$3200\ \nu/\delta$	arbitrary	0.141δ	0.087δ	$5.56\times10^{-3}\delta$	2.85×10^{2}	25.4	$\Delta x_1 = 0.098\delta$	$\Delta x_1/\delta^* = 0.696$	$\Delta x_1^+ = 17.6$	0.99
	[Numerical]	Air	6.0	1.0	0.141	0.087	5.56×10^{-3}	2.85×10^{2}	25.4	$\Delta x_1 = 0.098$	$\Delta x_1/\delta^* = 0.696$	$\Delta x_1^+ = 17.6$	0.99
Farabee (1986)	Wind Tunnel	Air	50.8	1.097	0.177	0.128	9.47×10^{-4}	3.4×10^{3}	188	$1/32$	0.177	33	1.33
Keith & Bennett (1991)	Developing Channel Flow	Water	20	0.74	0.09	0.08	1.9×10^{-4}	1.34×10^{4}	480	0.08	0.89	430	14.
Schewe (1983)	Wind Tunnel	Air	20.7	1.18	0.181	0.130	2.13×10^{-3}	1.4×10^{3}	86	0.0394	0.22	19	0.84
Schloemer (1967)	Wind Tunnel	Air	79	1.1	0.158	0.118	6.77×10^{-4}	4.5×10^{3}	235	0.06	0.38	89	3.4
Willmarth & Wooldridge (1962)	Wind Tunnel	Air	156	4.488	0.456	0.408	4.25×10^{-4}	2.9×10^{4}	1070	0.163	0.36	383	12.7

1 over the frequency range $\omega\delta^*/U_o > 3.3$ is that of decreasing spectral level with increasing d/δ^*. As an exception to that trend, the levels of Farabee (1986) for d/δ^* of 0.18 lie above those of Bull and Thomas (1976) for d/δ^* of 0.13. The data of Bull and Thomas were obtained with piezoelectric sensors. The levels of Bakewell et al. (1962), Carey et al. (1967), and Schloemer (1967), all of which have comparable values of d/δ^*, are grouped together, with Schloemer's data showing a slightly more rapid roll-off, consistent with his slightly greater value of d/δ^*. The levels of Willmarth and Wooldridge (1962) for d/δ^* of 0.36 lie above the other data sets with comparable d/δ^* values. The trend of decreasing spectral level with increasing d/δ^* is, therefore, not monotonic with respect to all of the data sets.

From the Corcos correction method, a value for $k_c r$ of 0.34 corresponds to an attenuation of 1 dB. For the outer frequency scaling, from Eq. (5) we have $\omega_u\delta^*/U_o = 0.34(U_c/U_o)(2/(d/\delta^*))$. The trend of decreasing $\omega_u\delta^*/U_o$ with increasing d/δ^* should therefore exist for the various data sets. From Table 1, the ordering of the data sets with increasing d/δ^* is Bull and Thomas (1976), Farabee (1986), Bull (1967), Schewe (1983), Bakewell et al. (1962), Carey et al. (1967), Willmarth and Wooldridge (1962), Schloemer (1967), Choi and Moin (1990), and Keith and Bennett (1991). From Fig. 1, the decreasing ordering of $\omega_u\delta^*/U_o$ agrees with the above ordering of increasing d/δ^*. A minor exception is that $\omega_u\delta^*/U_o$ for Bakewell et al. is slightly higher than $\omega_u\delta^*/U_o$ for Carey et al., although they have identical values of d/δ^*. For the inner frequency scaling, from Eq. (6) we have $\omega_u\nu/u_\tau^2 = 0.34(U_c/U_o)(2/d^*)$. The trend of decreasing $\omega_u\nu/u_\tau^2$ with increasing d^* should exist. The ordering of the data sets with increasing d^* is Schewe (1983), Choi and Moin (1990), Farabee (1986), Bull and Thomas (1976), Schloemer (1967), Bull (1967), Bakewell et al. (1962), Willmarth and Wooldridge (1962), Keith and Bennett (1991) and Carey et al. (1967). From Fig. 6, the decreasing ordering of $\omega_u\nu/u_\tau^2$ agrees with the above, with the exception that $\omega_u\nu/u_\tau^2$ for Keith and Bennett is slightly greater than that for Willmarth and Wooldridge.

Figure 2 contains the data from Fig. 1 corrected using the Corcos method. Comparison of the corrected and uncorrected data shows the significant attenuations which exist for data sets corresponding to larger values of d/δ^*. Although the scatter between the data sets is reduced when corrections are applied, comparison of the corrected spectra to determine the effectiveness of the outer, mixed, or inner scaling is not valid due to the uncertainties in the correction method previously discussed.

As previously noted, the sensor spatial resolution depends upon the quantity $k_c r$. Clearly the sensor spatial resolution does not depend explicitly upon R_θ. However, for a particular investigation in which R_θ is varied, the sensor spatial resolution which exists at a particular nondimensional frequency will vary with R_θ. We now discuss how R_θ may be varied, and how the sensor spatial resolution is affected by this.

For an ideal external boundary layer experiment with constant fluid density and viscosity and fixed transition location, R_θ may be increased at a particular measurement location by increasing U_o (with δ, δ^*, θ, and ν/u_τ decreasing slightly). Alternatively, R_θ may be increased by holding U_o constant and moving the measurement location downstream such that δ, δ^*, θ, and ν/u_τ increase. For a particular frequency scaled on outer variables, $\omega\delta^*/U_o$, the effects of sensor spatial resolution on

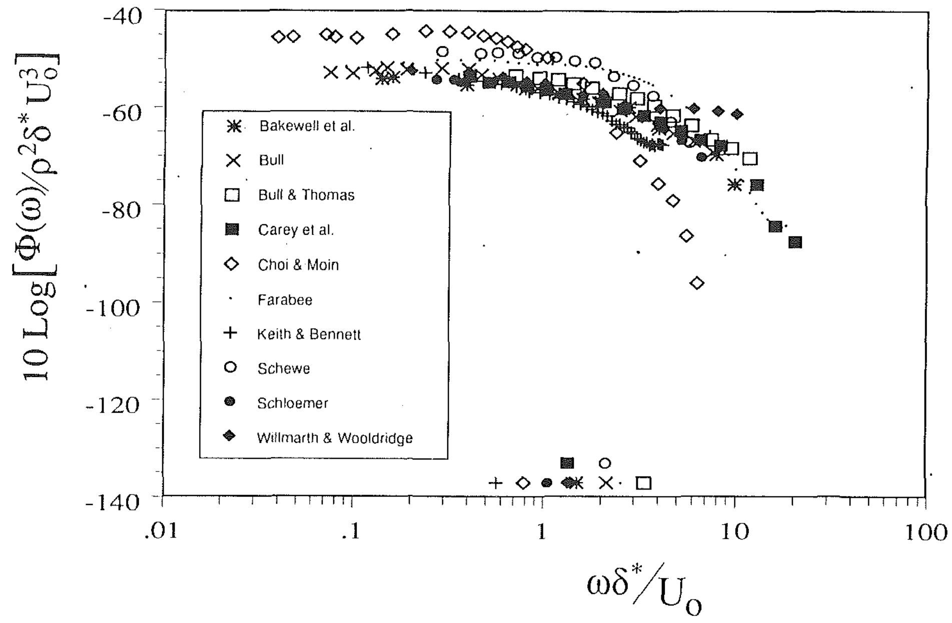

Fig. 2 Nondimensional wall pressure spectra scaled on outer variables, corrected for spatial resolution errors

the measured spectra vary with R_θ as follows. For a fixed value of $\omega\delta^*/U_o$, the attenuation due to the sensor spatial resolution will increase if R_θ is increased by increasing U_o and holding the measurement location fixed. This results from the increase in d/δ^* due to the decrease in δ^*. For a fixed value of $\omega\delta^*/U_o$, the attenuation due to the sensor spatial resolution will decrease if R_θ is increased by holding U_o constant and moving the measurement location downstream. This results from the decrease in d/δ^* due to the increase in δ^*.

Bull (1967) varied R_θ by using different measurement locations (with U_o held constant) and also by varying U_o at a particular measurement location. The trends noted above are supported by his spectra scaled on outer variables. For $\omega\delta^*/U_o > 2$, where spatial resolution effects are significant, his nondimensional spectra displayed lower levels as U_o was increased at a fixed measurement location. The levels increased as the measurement location was moved downstream with U_o held constant. The data of Keith and Bennett (1991), which were taken at a fixed measurement location, showed similar trends.

Bull's results also allow evaluation of the effectiveness of the outer variable scaling. Bull presented his spectra with corrections for spatial resolution applied. Bull's corrected spectra measured at various U_o and different streamwise locations all collapsed well with the outer variable scaling. The variations in the uncorrected spectral levels (scaled on outer variables) are therefore primarily due to spatial resolution effects. In view of this, the approach taken here involving the use of the outer variable scaling to determine the effects of sensor spatial resolution is reasonable.

The dependence of sensor spatial resolution on R_θ for the inner scaling is based on $d^* = (du_\tau/\nu)(u_\tau/U_o)$. The length scale $\nu U_o/u_\tau^2$ varies with both U_o and streamwise measurement location in the same manner as δ^*. Increasing R_θ by increasing U_o at the same measurement location results in an increase in d^* due to the increase in u_τ. This decreases sensor spatial resolution. Increasing R_θ by moving the measurement location downstream and holding U_o constant decreases u_τ so that d^* is smaller, leading to better sensor resolution.

For these reasons, no conclusion can be reached with regard to the effect of R_θ on the measured spectra at higher frequencies when spatial resolution effects are significant. For both inner and outer scaling, increasing R_θ can either increase or reduce resolution depending on whether U_o is increased or the measurement location is changed. Due to the implicit dependence of the sensor spatial resolution on R_θ, conclusions as to the effects of R_θ on the true spectra are limited to the lower frequencies.

(b) Comparison of the Mixed Scaling With the Outer Scaling, and R_θ Effects. Figure 3 contains the spectral data from each data set with the mixed inner and outer variable scaling. As the mixed frequency scaling is the same as the outer frequency scaling, the ratio d/δ^* for each data set is again required to establish the effect of sensor resolution on the measured spectra. The ordering of the spectral levels with increasing d/δ^* is not the same as for the case of the outer scaling, due to the effects of the mixed scaling itself on $\Phi(\omega)$. Figure 4 contains the data from Fig. 3 corrected using the Corcos (1963) method. We note that the scatter among the various data sets at higher frequencies in Fig. 4 is comparable to that in Fig. 2 for the corrected spectra scaled on outer variables.

The outer scaling of the spectrum, $\Phi(\omega)$ is related to the mixed scaling by the relationship

$$\{\Phi(\omega)/(\rho^2\delta^* U_o^3)\}\cdot\{1/(u_\tau/U_o)^4\} = \Phi(\omega)U_o/(\tau^2\delta^*). \quad (7)$$

From Coles' (1953) results for an ideal flat plate boundary layer, the quantity u_τ/U_o decreases with increasing R_θ. The mixed variable scaling may be interpreted as imposing this particular Reynolds number effect on the outer scaling. Equation (7) may, therefore, be viewed as a mapping from the outer scaling to the mixed scaling. The quantity $\Phi(\omega)/(\rho^2\delta^* U_o^3)$ is mapped upward by an amount $1/(u_\tau/U_o)^4$. Due to the variation in u_τ/U_o with R_θ, the spectra measured at lower values of R_θ are mapped upward by a smaller amount than those for higher R_θ. In order for the mixed scaling to collapse the spectra more effectively than the outer scaling, the spectra scaled on outer variables should therefore display the trend of decreasing spectral levels with increasing R_θ values.

Figure 5 contains the quantity $10\,\mathrm{Log}\{1/(u_\tau/U_o)^4\}$ graphed as a function of R_θ. The results of Coles are shown as a solid line and a point is shown for each data set. The effect of the mixed scaling with respect to the outer scaling may be determined for any particular data set from Fig. 5. As an example, we compare the data set of Bull (1967) with that of Choi and Moin (1990). From Fig. 1, for $\omega\delta^*/U_o < 1$, the spectral levels of Bull are approximately -52 dB, while those of Choi and Moin are approximately -45 dB. From Fig. 5, the 10 Log

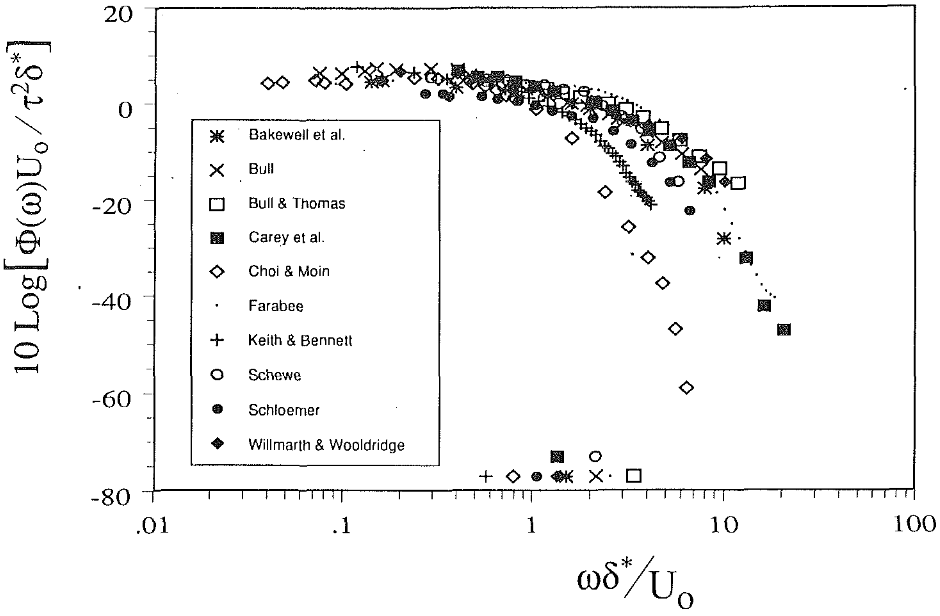

Fig. 3 Nondimensional wall pressure spectra scaled on mixed variables

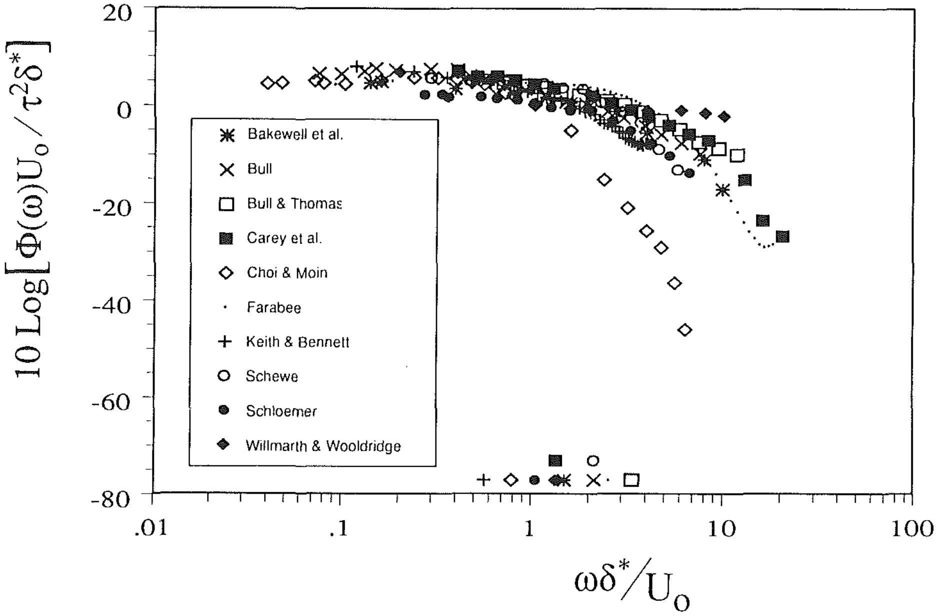

Fig. 4 Nondimensional wall pressure spectra scaled on mixed variables, corrected for spatial resolution errors

$\{1/(u_\tau/U_o)^4\}$ factor for Bull ($R_\theta = 19{,}500$) is +59 dB while that for Choi and Moin ($R_\theta = 285$) is +50 dB. Hence, with the mixed scaling, the spectral levels for Bull are +7 dB, while the levels for Choi and Moin are +5 dB. Thus, by imposing a Reynolds number effect on the outer scaling, spectra from two data sets that have widely different values of R_θ collapse together at low frequencies. These results can be verified in Fig. 3.

For the following comparisons, we again consider the nondimensional frequency range $\omega\delta^*/U_o < 1$, where spatial resolution effects are not significant. The results in Fig. 1 for the outer variable scaling show that the trend of decreasing spectral levels with increasing R_θ is supported by the data of Choi and Moin, Schewe (1983), and Farabee (1986). No clear trend is displayed by the remaining data sets which have R_θ values of 4500 or greater. For these higher R_θ cases, the outer scaling results in a slightly better collapse of the data sets than the mixed. Moreover, the data of Carey et al. (1967) and Bakewell et al. (1962) collapse extremely well with the outer scaling, but are spread somewhat with the mixed. The R_θ value of Carey et al. was 5 times greater than that of Bakewell et al. Both investigations were for fully developed pipe flow.

Bradshaw (1971) states that Reynolds number effects are negligible for R_θ greater than approximately 5000. This value represents a very approximate lower bound on R_θ for an equilibrium turbulent boundary layer. It is possible that the higher spectral levels of Choi and Moin and Schewe with lower R_θ values (significantly below 5000) reflect a Reynolds number effect. It should be noted that the spectral data (in dimensional form) presented by Schewe, measured with different sized sensors (with all other boundary layer parameters fixed) displayed measurable scatter at low frequencies where the effects of sensor size should be negligible. The reason for this is not clear. Also, we note that the spectral levels of Schloemer (1967)

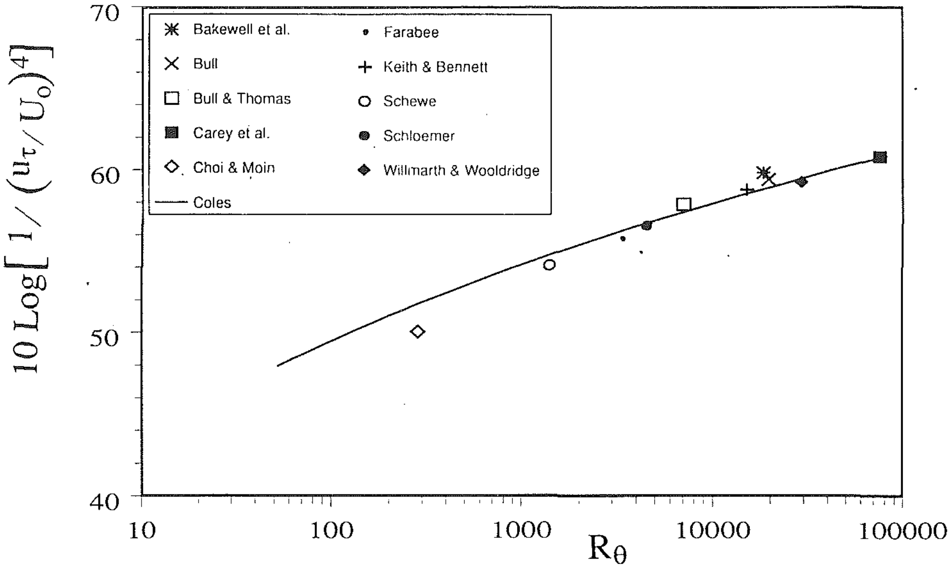

Fig. 5 Scale factor relating the mixed scaling to the outer scaling

are significantly lower than those of Farabee (1986), although the R_θ values for the two data sets are comparable.

The effectiveness of the mixed as compared to the outer scaling may be investigated by varying R_θ in a particular investigation. Farabee (1986) found that the mixed scaling more effectively collapsed the low frequency spectral levels measured at R_θ values of 6000 and 3400. Keith and Bennett (1991) found the opposite trend at low frequencies for R_θ values of 13,400 and 8200. For their case the outer scaling collapsed the data more effectively than the mixed. The higher free stream turbulence intensity in the water tunnel used by Keith and Bennett may possibly have masked the R_θ effect measured by Farabee. The spectral data of Willmarth and Wooldridge (1962) measured in a wind tunnel at R_θ values of 38,000 and 29,000 collapsed extremely well when scaled on outer variables. The data of Bull (1967) also collapsed well with the outer variable scaling, as previously noted.

In summary, these results show that for data sets having R_θ values lower than 4500, Reynolds number dependence can be taken into account by use of the mixed scaling (through u_τ/U_o in Fig. 5). We note that the very high spectral levels from Choi and Moin's (1990) numerical computations, as shown in Fig. 1, cannot be readily accounted for without an argument for Reynolds number dependence. Additional experimental data at R_θ values less than 1000 are required in order for firm conclusions to be drawn regarding R_θ effects at low R_θ.

The effectiveness of outer versus mixed scaling must be regarded as inconclusive for data sets having R_θ values higher than 4500. Particular data sets obtained at higher R_θ values collapse less well with the mixed than with the outer scaling. The contributions from large scale vorticity or other boundary layer irregularities in experimental facilities may mask the effectiveness of the mixed scaling. Studies conducted in one experimental facility at various R_θ values, such as that of Farabee (1986), are more accurate for establishing the effectiveness of the mixed scaling.

(c) Comparison of the Inner Scaling With the Outer Scaling. The characteristic length scale associated with the inner or wall region of the turbulent boundary layer is defined as ν/u_τ. The characteristic inner time scale is defined as ν/u_τ^2. In comparison to the outer length and time scales, δ^* and δ^*/U_o, the inner scales depend explicitly on the kinematic viscosity of the fluid. The inner frequency scaling is related to the outer frequency scaling through the relationship

$$\{\omega\delta^*/U_o\}\cdot\{1/R_*\}\cdot\{1/(u_\tau/U_o)\} = \omega\nu/u_\tau^2 \qquad (8)$$

The inner scaling for $\Phi(\omega)$ is related to the outer through the expression

$$\{\Phi(\omega)/(\rho^2\delta^* U_o^3)\}\cdot\{R_*\}\cdot\{1/(u_\tau/U_o)^3\} = \Phi(\omega)u_\tau^2/(\tau^2\nu) \qquad (9)$$

Here, both the frequency and spectral scaling are influenced by the parameters u_τ/U_o and $R_* = \delta^* u_\tau/\nu$. The quantity R_* is related to R_θ through the expression

$$R_* = H\cdot(u_\tau/U_o)\cdot R_\theta \qquad (10)$$

where $H = \delta^*/\theta$ is the shape factor. The inner scaling therefore imposes a Reynolds number effect on both the frequency and the spectral levels, with respect to the outer scaling.

The inner scaling does not collapse the spectral levels well at lower frequencies, as shown in Fig. 6. Farabee and Casarella (1991) concluded that the inner variable scaling was effective for their data for $\omega\nu/u_\tau^2 \geq 0.3$. Over this frequency range, the data sets of Carey et al. (1967), Keith and Bennett (1991), Bakewell et al. (1962), Bull (1967), Schloemer (1967), and Willmarth and Wooldridge (1962) were all influenced by the spatial resolution of the respective sensors. The data of Bull and of Bakewell et al., having values of d^* of 6 and 7, respectively, agree well for $\omega\nu/u_\tau^2 > 0.05$.

Over the frequency range $0.1 \leq \omega\nu/u_\tau^2 \leq 0.3$, the data of Choi and Moin (1990), Schewe (1983), Farabee (1986), and also Bull and Thomas (1976) were not influenced by spatial resolution effects. The data of Schewe and that of Bull and Thomas collapse well in this frequency range. The levels of Farabee are slightly higher, and those of Choi and Moin are lower. For $\omega\nu/u_\tau^2 > 0.6$, these data sets were all influenced by the spatial resolution of the sensors. A reasonable collapse of the four data sets occurs over this high frequency range. The expected ordering of these spectral levels from highest to lowest, due to spatial resolution effects, is Schewe ($d^* = 0.8$), Choi and Moin ($d^* = 1.0$), Farabee ($d^* = 1.3$), and Bull and Thomas ($d^* = 1.7$). With the exception that the spectral levels of Choi and Moin fall just below those of Farabee, the data support that trend. The discrepancy in ordering may be due to the uncertainty associated with estimating the effective sensor size for Choi and Moin's numerical data set.

The conclusion of Farabee and Casarella as to the frequency range over which inner variables collapse the spectral data is supported by the comparisons presented here. Again, the spatial responses of the sensors lead to complications. Future

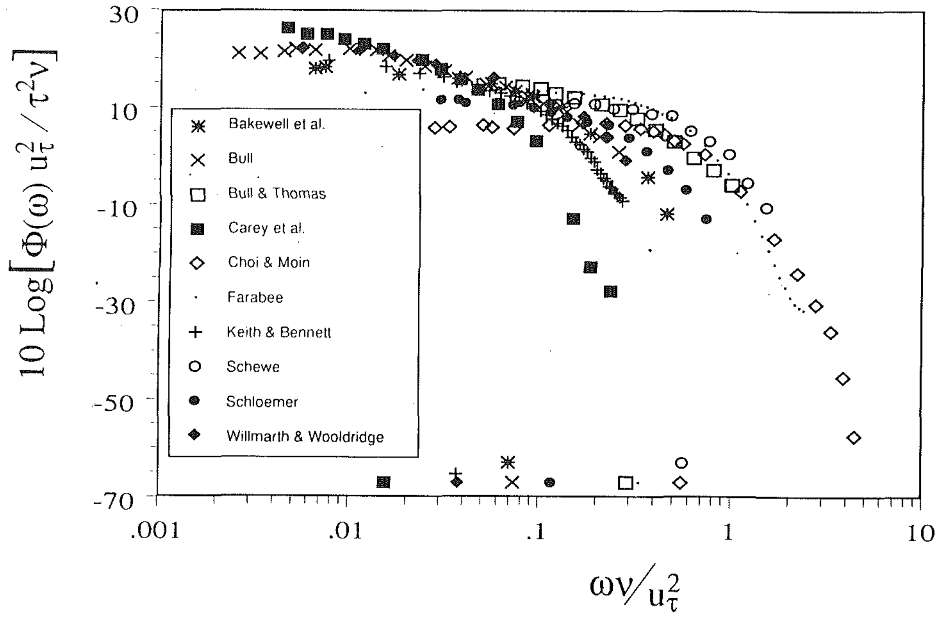

Fig. 6 Nondimensional wall pressure spectra scaled on inner variables

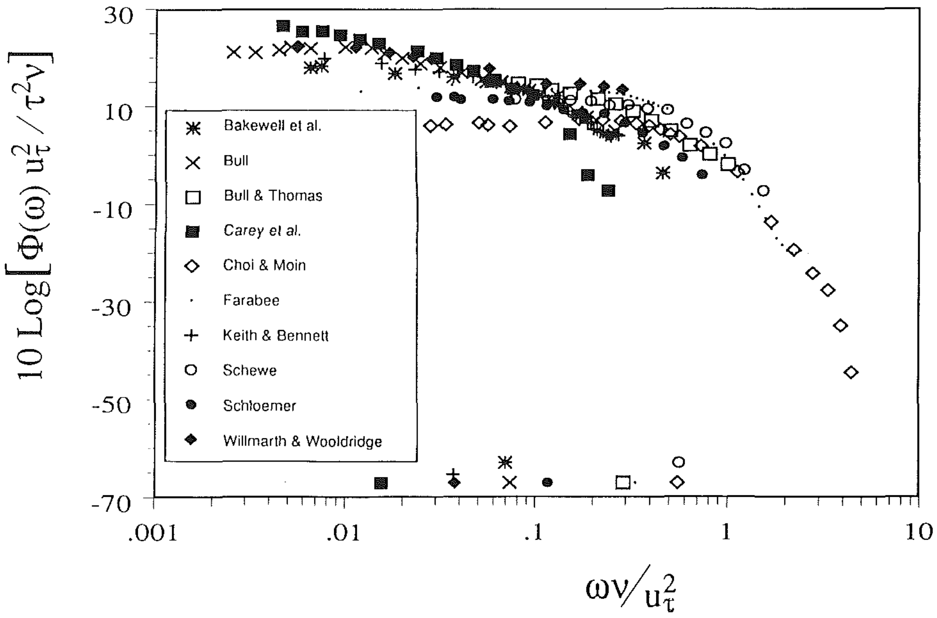

Fig. 7 Nondimensional wall pressure spectra scaled on inner variables, corrected for spatial resolution errors

measurements made with smaller sensors would provide additional insight. We note that for R_θ values greater than 5000, sufficiently small pressure sensors become very difficult to obtain or fabricate.

Figure 7 contains the data from Fig. 6 corrected using the Corcos (1963) method. At the higher frequencies, the scatter in the corrected data is comparable to that for the corrected spectra with the mixed scaling and outer scaling.

(d) Comparison of Internal and External Flows. Farabee and Casarella (1991) noted that for external boundary layers, contributions to the pressure spectra may result from velocity fluctuations associated with the interaction of the free stream with the outer region of the turbulent boundary layer. They found the velocity fluctuations measured in the intermittent region (at a distance from the wall of approximately 2δ) were correlated with the wall-pressure fluctuations. Panton et al. (1980) found a similar correlation at a distance from the wall of 2.6δ for the case of turbulent boundary layer flow over a glider airplane. In that case, the freestream turbulence was negligible. Such large scale contributions with lower convective wavenumbers affect the low frequency portion of the spectrum. These particular contributions do not exist in fully developed pipe or channel internal flows, due to the absence of a free stream.

For internal flows, contributions to measured spectra may, in principle, result from velocity fluctuations in the boundary layers on adjacent (or opposite) walls, due to their proximity to the measurement location. The dominant contributions from the adjacent boundary layers would likely be from the large scale turbulence with low convective wavenumbers. These contributions would, therefore, appear in the low frequency portion of the spectra. In addition, when large scale vorticity is generated in contraction nozzles, it convects downstream into flow test sections, and contributes to the wall-pressure spectrum at low frequencies. The spatial scale of such vorticity varies between internal and external flows, due to the differences in cross sectional geometry. Such contributions are inherent to specific flow facility test sections, and in general are not well characterized by boundary layer parameters. Detailed surveys of the mean and fluctuating velocities are required to characterize these sources. Measurements of the correlation between the wall-pressure and velocity fluctuations are further required to relate the two quantities. In many cases, velocity surveys are limited due to mechanical constraints.

For the outer scaling of Fig. 1, we consider the frequency range $\omega\delta^*/U_o < 1$ over which the spectral levels of the following data sets were not influenced by spatial resolution effects. The internal pipe flows of Carey et al. (1967) in water, and Bakewell et al. (1962) in air have spectral levels that agree very well. The agreement at the higher frequencies reflects the identical d/δ^* values for the two data sets. We note that both investigations were conducted in 3.5 in. I.D. pipes, and that R_θ for Carey et al. was approximately five times greater than that of Bakewell et al. Fluctuating velocity measurements were not reported for either investigation. The spectral levels for the external flows of Bull (1967), and Farabee (1986) are higher than those of Carey et al. and Bakewell et al. The spectral levels for the external flow of Schloemer (1967) agree well with Carey et al. and Bakewell et al.

The spectral levels for the fully developed channel flow of Choi and Moin (1990) with the outer scaling applied, were significantly higher than those for the pipe flow and external flow data sets. The R_* value of 25.4 for the data set of Choi and Moin was significantly lower than the other data sets. A larger percentage of their boundary layer was occupied by the inner region. Their half channel height δ corresponded to 180 viscous lengths. For the pipe flows of Bakewell et al. and Carey et al., the pipe radius values corresponded to 5000 and 23,000 viscous lengths, respectively. One might therefore expect the spectra of Choi and Moin to be dominated by contributions from the inner region. As previously noted, contributions to

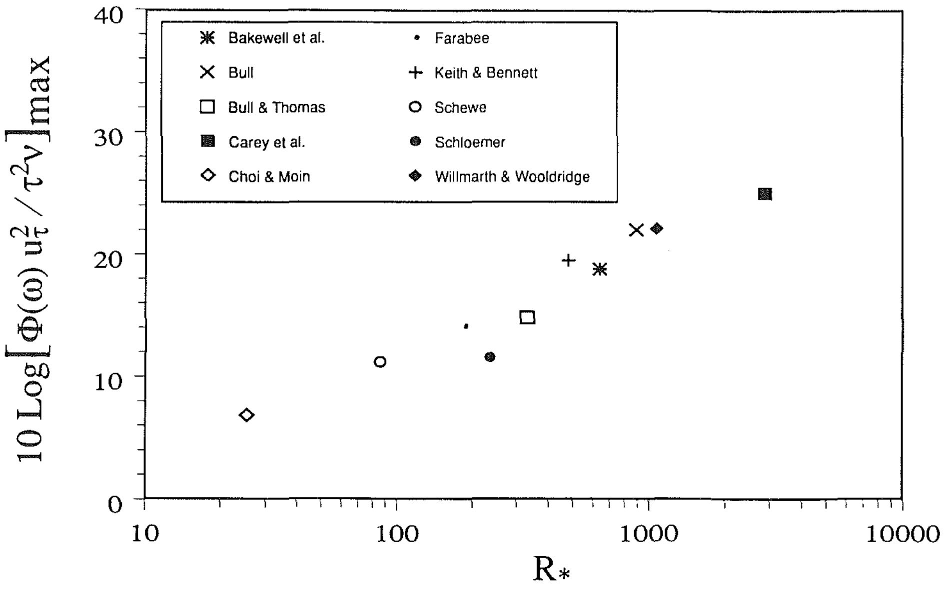

Fig. 8 Maximum spectral levels scaled on inner variables as a function of R_*

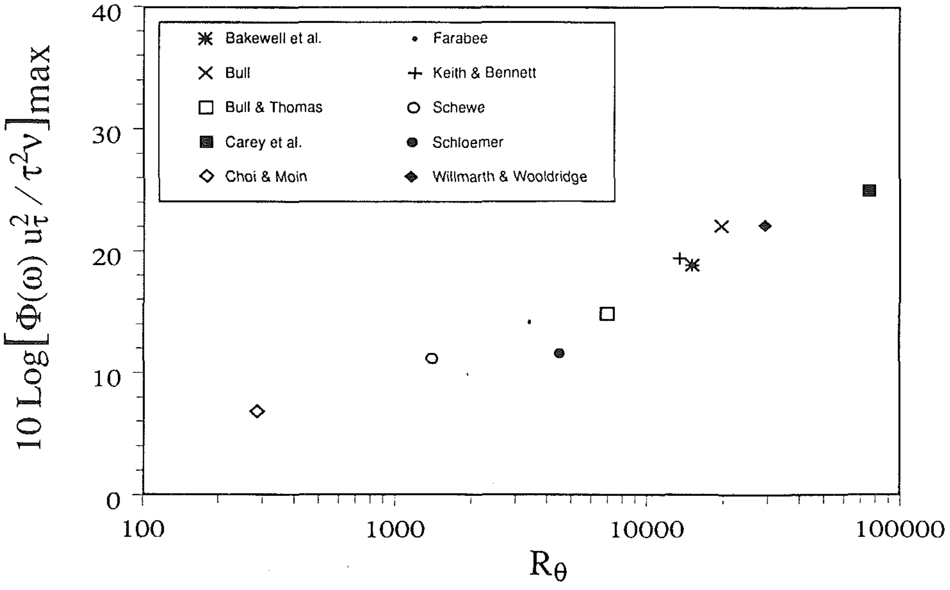

Fig. 9 Maximum spectral levels scaled on inner variables as a function of R_θ

the spectra from both the inner and outer regions of the turbulent boundary layer exist at low frequencies. The fact that the spectra do not collapse well at low frequencies with the inner variable scaling suggests that for the experimental data sets, contributions from the outer region are comparable to or greater than contributions from the inner region.

Figure 8 contains the maximum spectral level from each data set, scaled with inner variables, as a function of R_*. The trend of increasing maximum spectral level with increasing R_* is supported by all of the data sets. As the length scale of the outer region relative to the inner region increases, the maximum spectral level increases. The low spectral levels at low frequencies for Choi and Moin's numerical simulation may possibly be attributed to the small spatial extent of the outer region and the associated contributions to the spectra. The relationship between R_* and R_θ was given by Eq. (10). Figure 9 contains the data of Fig. 8 with R_* replaced by R_θ. A similar trend exists. While this trend may be interpreted as a Reynolds number effect, the dependence upon R_* is believed to provide more physical insight than the dependence upon R_θ. If one assumes δ rather than δ^* is the appropriate outer length scale, a value for R_* may be defined with δ^* replaced by δ.

Over the low frequency range, there is no consistent trend supported by all of the data sets. Based upon the excellent agreement between the two pipe flow data sets with significantly different R_θ values, an argument may be made for the validity of the outer scaling for pipe flows. The pipe flow data sets exhibit lower spectral levels than most of the external flows. Contributions resulting from the proximity of the neighboring boundary layers therefore appear to be small.

The measurements of Keith and Bennett (1991) were made in a developing channel flow of water, with $R_\theta = 13{,}400$. The channel height at the measurement location was 6δ, and the width was 16δ. The free stream turbulence intensity was 1 percent. The pressure spectra might, therefore, be expected to display some characteristics of both internal and external flows due to the existence of a free stream and also the proximity of the boundary layers on the adjacent walls. Over the frequency range $0.1 < \omega\delta^*/U_o < 0.3$, the spectral levels of Keith and Bennett decrease from the levels of the external flows to the levels of the internal pipe flows.

Conclusions

The effect of sensor spatial resolution is of primary importance. When resolution effects are accounted for, variations among data sets are significantly reduced at higher frequencies. The correction procedure proposed by Corcos is effective for predicting trends in the spectra. At lower frequencies, the outer scaling results in a reasonable collapse of the data from all data sets for which $R_\theta \geq 4500$. The mixed scaling was shown to impose a Reynolds number effect on the outer scaling. The data sets having R_θ values lower than 4500 collapse significantly better with the other investigations under this scaling. Additional spectral data, experimentally obtained at R_θ values less than 1000, are needed. Particular data sets obtained at higher R_θ values collapse less well with the mixed than with the outer scaling. The inner scaling is effective at the higher frequencies, and not at the lower, consistent with the conclusions of Farabee and Casarella (1991). The effect of sensor spatial resolution limited the number of data sets which could be compared with the inner scaling. Additional measurements with very small sensors at moderate to high R_θ values are needed.

The investigator interested in comparing measured or computed wall pressure spectral data with other investigations must consider the respective sensor sizes, the momentum thickness Reynolds numbers, and the nondimensional frequency ranges, prior to determining the appropriate scaling to use. For hydrodynamic investigations at moderate to high momentum thickness Reynolds numbers, inadequate spatial resolution will always be a problem. Due to attenuations resulting from sensor spatial resolution, it was not possible to determine precise nondimensional frequency ranges over which the various scalings were effective. Additional experimental and computational spectral data are required to determine these and other details of interest. For tabulated data from all of the investigations compared here, the reader is referred to Keith, et al. (1991), an expanded version of this paper.

Acknowledgments

The authors are grateful to Prof. R. Lueptow of Northwestern University, Dr. T. Farabee of the David Taylor Research Center (DTRC), and Dr. W. Strawderman of the Naval Underwater Systems Center (NUSC) for many constructive suggestions. Funding for this work was provided by the Naval Underwater Systems Center IR/IED Program.

References

Bakewell, H. P. Jr., Carey, G. F., Libuha, J. J., Schloemer, H. H., and Von Winkle, W. A., 1962, *Wall Pressure Correlations in Turbulent Pipe Flow*, USL Rpt. No. 559, 1-052-00-00, Naval Underwater Systems Center, New London, CT.

Bradshaw, P., 1971, *An Introduction to Turbulence and Its Measurement*, Pergamon Press, New York.

Bull, M. K., 1967, "Wall-Pressure Fluctuations Associated with Subsonic Turbulent Boundary Layer Flow," *Journal of Fluid Mechanics.*, Vol. 28, No. 4, pp. 719–754.

Bull, M. K., and Thomas, S. W., 1976, "High Frequency Wall Pressure Fluctuations in Turbulent Boundary Layers," *Physics of Fluids*, Vol. 19, No. 4, pp. 597–599.

Carey, G. F., Chlupsa, J. E., and Schloemer, H. H., 1967, "Acoustic Turbulent Water-Flow Tunnel," *J. Acoust. Soc. Amer.*, Vol. 41, No. 2, pp. 373–379.

Choi, H., and Moin, P., 1990, "On the Space-Time Characteristics of Wall-Pressure Fluctuations," *Physics of Fluids A*, Vol. 2, No. 8, pp. 1450–1460.

Coles, D., 1953, *Measurements in the Boundary Layer on a Smooth Flat Plate in Supersonic Flow, Pt. 1, The Problem of the Turbulent Boundary Layer*, Report No. 20–69, Jet Propulsion Laboratory, California Institute of Technology, Pasadena, CA.

Corcos, G. M., 1963, "Resolution of Pressure in Turbulence," *J. Acoust. Soc. Amer.*, Vol. 35, No. 2, pp. 192–199.

Farabee, T. M., 1986, *An Experimental Investigation of Wall Pressure Fluctuations Beneath Non-equilibrium Turbulent Flows*, DTNSRDC Technical Report No. 86/047, Bethesda, MD, May.

Farabee, T. M., and Casarella, M. J., 1991, "Spectral Features of Wall Pressure Fluctuations Beneath Turbulent Boundary Layers," *Physics of Fluids A*, Vol. 3, No. 10, pp. 2410–2419.

Gedney, C. J., and Leehey, P., 1989, "Wall Pressure Fluctuations During Transition on a Flat Plate," *ASME Procs., Symposium on Flow Induced Noise Due to Laminar-Turbulent Transition Process*, NCA Vol. 5.

Keith, W. L., and Bennett, J. C., 1991, "Low Frequency Measurements of the Wall Shear Stress and Wall Pressure in a Turbulent Boundary Layer," *J. A.I.A.A.*, Vol. 29, No. 4, pp. 526–530.

Keith, W. L., Hurdis, D. A., and Abraham, B. M., 1991, "A Comparison of Turbulent Boundary Layer Wall-Pressure Spectra," *Proceedings of the Symposium on Flow Noise Modeling, Measurement, and Control*, ASME NCA-Vol. 11/FED-Vol. 130, Dec. 1–6.

Panton, R. L., Goldman, A. L., Lowery, R. L., and Reischman, M. M., 1980, "Low Frequency Pressure Fluctuations in Axisymmetric Turbulent Boundary Layers," *Journal of Fluid Mechanics.*, Vol. 97, pp. 299–319.

Schewe, G. S., 1983, "On the Structure and Resolution of Wall-Pressure Fluctuations Associated with Turbulent Boundary Layer Flow," *Journal of Fluid Mechanics*, Vol. 134, pp. 311–328.

Schloemer, H. H., 1967, "Effects of Pressure Gradients on Turbulent-Boundary-Layer Wall-Pressure Fluctuations," *J. Acoust. Soc. Amer.*, Vol. 42, No. 1, pp. 93–113.

Willmarth, W. W., and Roos, F. W., 1965, "Resolution and Structure of the Wall Pressure Field Beneath a Turbulent Boundary Layer," *Journal of Fluid Mechanics.*, Vol. 22, No. 1, pp. 81–94.

Willmarth, W. W., and Wooldridge, C. E., 1962, "Measurements of the Fluctuating Pressure at the Wall Beneath a Thick Turbulent Boundary Layer," *Journal of Fluid Mechanics*, Vol. 14, No. 2, pp. 187–210.

Willmarth, W. W., 1965, "Corrigendum: Measurements of the Fluctuating Pressure at the Wall Beneath a Thick Turbulent Boundary Layer," *Journal of Fluid Mechanics*, Vol. 21, No. 1, pp. 107–109.

D. P. Telionis
Professor.
Mem. ASME

M. Gundappa[1]
Research Scientist.

T. E. Diller
Professor.

Virginia Polytechnic Institute
and State University,
Blacksburg, VA 24061

On the Organization of Flow and Heat Transfer in the Near Wake of a Circular Cylinder in Steady and Pulsed Flow

Skin friction, pressure, and heat transfer gages are employed to monitor the flow and heat transfer field along the periphery of a circular cylinder in steady and pulsed flow at Reynolds numbers, Re=23,000 to 50,000. Averaged distributions, RMS, and power spectra of all measurements are displayed. Special attention is directed at the organization of the near wake, as detected by the three types of surface gages. The response of the wake to pulsing of the oncoming stream is also examined. It is found that when the wake is locked on the driving frequency, the basic character of the flow is not changed, but the organized motion stands out more clearly. Moreover, the signals become cleaner and background noise in the spectra is reduced. Skin friction and heat transfer gages are shown to respond to local variations of the corresponding quantities, whereas pressure gages respond to global characteristics of the flow.

1 Introduction

The flow over a circular cylinder has been extensively studied in fluid mechanics. Its geometric simplicity allows convenient machining of laboratory models and the development of simple analytical or numerical solutions, while exhibiting a rich collection of fluid mechanics phenomena. Moreover, this configuration has many applications in industrial processes. A large number of contributions have been devoted to this problem. Cantwell and Coles (1983) compiled the most complete table on relevant contributions. They list 73 papers along with the corresponding information on blockage, aspect ratio, turbulence level, Reynolds number range, and others. Several review articles have also appeared in the last couple of decades (Mair and Maull, 1971; Berger and Wille, 1972; Parkinson, 1974; Sarpkaya, 1979; Bearman and Graham, 1980; and Bearman, 1984). The majority of the investigations were concerned with global features of the flow, such as base pressure, vortex shedding frequency, or forces exerted on the cylinder.

Experimental studies of flows over circular cylinders often concentrate on certain regions of the flow, or special values of the Reynolds number, or address a specific physical phenomenon. A great effort has been directed at understanding the flow features in the critical Reynolds number regime. The reader can trace most of the references on this topic in the recent contribution of Horvath et al. (1986). The spread of the experimental data on this regime can be traced back to the influence of transition on separation (Schewe, 1986). The attached boundary layers leading to separation have also been well documented. For a recent contribution and a list of other references the reader is referred to Varty and Currie (1984).

The wake region has been especially challenging, because it involves a seemingly chaotic motion, which, however, displays some elements of organization. In most of the studies in this area the far wake of the cylinder is examined. For recent contributions see Gerrard (1977), Cantwell and Coles (1983), Wei and Smith (1986), Kurosaka et al. (1987), and Ongoren and Rockwell (1988). In the last two papers the authors examine the region downstream of separation and address questions like three-dimensionality and stability of free shear layers.

Heat transfer over a circular has been studied for many decades. In many of the studies only the average overall heat transfer between the fluid and cylinder was reported (Morgan, 1975). Numerous authors presented data on the local distribution of time-averaged heat transfer around cylinders (Schmidt and Wenner, 1943; Kestin and Wook, 1971; Kraabel et al., 1982; Achenbach, 1975; Zukauskas, 1985). Very little information is available, however, on the effect of vortex shedding on the local, time-resolved heat transfer on a cylinder (Boulos and Pei, 1974; Campbell and Diller, 1989).

A region which has so far been overlooked is the immediate neighborhood of the wake. Little is known about local, time-resolved wall quantities like skin friction or heat transfer on the aft half of the cylinder. Achenbach (1968) reported on mean skin friction values and later Barbi et al. (1986) presented qualitative unsteady skin friction measurements. No data are

---

[1] Present Address: Radian Corporation, Research Triangle Park, N.C. 27709.

Contributed by the Fluids Engineering Division for publication in the JOURNAL OF FLUIDS. Manuscript received by the Fluids Engineering Division October 5, 1990. Associate Technical Editor: F. M. White.

available on time-resolved heat transfer measurements. This paper presents results of skin friction, pressure, and heat transfer time-resolved measurements in the wake region of circular cylinders. This information sheds some light on the organization of the near wake, which together with the properties of the flow disclosed earlier will provide an integral picture of this complex phenomenon. Moreover, the present contribution expands upon the relationship between skin friction and heat transfer. A direct link between the two quantities is well established for attached boundary-layer flow. Now, evidence is offered on the nature of the relation between the two quantities in regions of separated flow.

The organization in the wake of bluff bodies can be controlled by discrete oscillations, as for example vibrations of the body itself or oscillations of the stream. The organization of the wake then can lock on the driving frequency, its harmonics, or subharmonics. A review of contributions to the lock-on effects due to body motion normal to the flow is given in Ericsson (1980). Lock-on is also possible if the cylinder vibrates in the direction of the stream (Tanida et al., 1973; Armstrong et al., 1987; Griffin and Hall, 1990), or if the stream oscillates over a fixed cylinder (Barbi et al., 1986). In the majority of these contributions only global characteristics are reported, such as the range of amplitudes and frequencies for which lock-on is possible, or amplitudes of the unsteady forces thus generated. What appears to be missing from the literature are data on the local fluid mechanics and heat transfer properties. The present paper attempts to fill this void with local, time-resolved data over a circular cylinder immersed in pulsating streams.

The purpose of this investigation is to provide information on the organization of the activity in the immediate vicinity of the wall, on the wake side of the body. The flow in this region is very difficult to predict numerically, because it involves many length scales, orders of magnitude apart from each other. Turbulence in this region cannot be modeled by the traditional methods. Moreover, the flow there combines random characteristics with some form of organization. The experimental results presented here could serve as a test case for numerical calculations of flow characteristics like skin friction and heat transfer on the wall of the cylinder.

2 Facilities and Instrumentation

Tests were conducted in a wind tunnel especially designed for this project. This facility is a blower-type tunnel with a contraction ratio of 6:1. The test section is 124 cm long and has a cross section of 74.1×52.9 cm. The settling chamber contains an aluminum honeycomb, flow straightener, and six screens. The tunnel can provide up to 33 m/s of steady flow, which is uniform across the test section to within 1.2 percent, if the tunnel wall boundary layers are excluded.

Six rotating vanes mounted on parallel shafts immediately upstream of the settling chamber were used to pulse the flow at frequencies up to 23 Hz. The vanes directed alternately part of the flow either into the settling chamber or out of the tunnel through two openings located above and below the vanes. The pulsation waveforms were nearly sinusoidal, with at least 93 percent of the pulsation energy at the fundamental frequency. The wave amplitudes, ϵ were 4 to 30 percent of the mean flow velocity, U_∞. The oncoming stream was thus approximately given by

$$U = U_\infty (1 + \epsilon \sin 2\pi f_D t)$$

where f_D is the driving frequency.

The free-stream turbulence was less than 0.5 percent (VandenBerghe, 1985) and was not influenced by flow pulsation. Description of the facility capabilities, calibration data, and the ranges of the parameters that can be achieved are provided in earlier publications (Andraka and Diller, 1985; VandenBerghe, 1985).

Two cylinders each 8.9 cm in diameter were employed in the measurements. The first was instrumented with skin friction and pressure transducers. The second was equipped with heat transfer gages. Hot-wire and hot-film probes were used to monitor the flow field around the model. Pressure transducers and sensitive microphones (B and K) were employed to record the mean and fluctuating pressure, respectively, and skin-friction gages (DISA and TSI) were used to measure instantaneous values of shear stresses on the wall. Time-resolved heat flux was measured with a specially designed thin-film gage system. The cylinders were rotated by a stepping motor to allow proper orientation of the sensors and measurements at different azimuthal positions.

The skin friction gage was calibrated on the model on which it was mounted. This was achieved by taking data at $\theta = 10$ and 30 deg on a cylinder positioned in the stream for a range of velocities. Here θ was measured from the mean front stagnation point. The reduced readings were then contrasted against earlier experimental data (Achenbach, 1968), as well as our own numerical calculations. A fourth degree polynomial was passed through the experimental points. This calibration curve was then employed to convert the voltage output to reduced skin friction values. This type of skin friction measurement is certainly not without problems, however. No calibration of the unsteady component was possible. Moreover, such sensors cannot detect the direction of skin friction and indicate larger deviations around a point of zero skin friction, especially if the latter is oscillating. We estimated that errors in the skin friction measurements could be as large as 10 to 15 percent. Nevertheless, some useful information can be obtained, especially if coupled with readings of other instruments. It is interesting to note that these measurements are repeatable and therefore their precision limit is very low, as noted in the figure caption. More details as well as an overview of similar methods can be found in Diller and Telionis (1988). The deviations from the true value are mostly due to bias errors.

A third model, a thick-walled aluminum cylinder was used for time-resolved, local, heat transfer measurements. This model was cut lengthwise in half to facilitate assembly. Two separately powered silicon-rubber wire resistance heaters supplied heat to the inside surface of the cylinder. The power of each heater was controlled to create a nearly constant surface temperature over the entire cylinder. The heat flux gage was designed, constructed, and tested especially for this project. It consisted of a heated gold film which covers the entire surface of a 2.0 mm by 12.7 mm probe. The gage was installed in a slot machined on the cylinder, with the gage surface flush with the cylinder surface. A hot-wire anemometer (TSI Model IFA-100) was used to maintain the gage temperature constant at about a 30°C overheat above the free-stream air temperature. There were no adiabatic surfaces on the gage to disturb the thermal boundary layer. In addition, there was a small thermocouple imbedded in the substrate immediately below the film and a matching thermocouple imbedded in the surrounding cylinder surface. A millivolt controller (Eurotherm model 810) and a phase-angle-fired power supply (Eurotherm model 831) were used to control the resistance heating of the cylinder, based on the differential signal of these two thermocouples.

This system can control the temperature differential between the gage and surrounding cylinder to within 0.2°C. The use of two controllers insures both a static and dynamic match of the temperatures. The anemometer bridge has a very fast time response, maintaining the gage temperature nearly constant. The millivolt controller has a much slower time response, insuring that the cylinder temperature is matched with the gage temperature, even if the gage has a slow temperature drift with time. The measured frequency response of the gage to changes

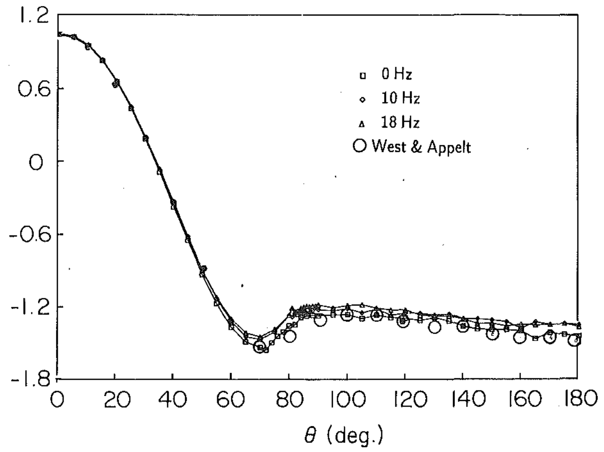

Fig. 1 Mean pressure coefficients for steady and pulsating stream. Here $\theta = 0$ is at the mean location of stagnation; Re = 50,000. Precision limit: ±0.06, Uncertainty estimate: ±0.025

in the surface heat flux was better than 60 Hz (Campbell et al., 1987).

3 Averaged Distributions

Averaged pressure distributions for cylinders immersed in steady flows have appeared in literature for many decades. Considerable deviations exist between such data obtained in different facilities. It is now well documented that these deviations are due to different levels of free-stream turbulence, possible discrete-frequency tunnel disturbances, tunnel blockage, and model aspect ratio. A good set of references on this topic can be found in West and Apelt (1982) and Higuchi et al. (1989). Flow separation is very sensitive to tunnel turbulence levels for flows near the critical regime. In the present case we ran tests at three Reynolds numbers, Re = 23,000, 33,000, and Re = 50,000. These values are about two decades away from critical values. Indeed it was found that separation locations correspond to laminar flow.

Blockage effects are inescapable and in the present case the blockage ratio at 17 percent was not negligible. However, it is believed that today's experiments should aim at identifying fluid mechanics phenomena and providing data for comparison with numerical results. Indeed, the test section configuration, namely a rectangular enclosure can be modeled numerically easily and accurately. No effort was therefore made to correct these data for blockage.

Averaged pressure distributions are presented in Fig. 1, in which some data of West and Apelt (1982) for an aspect ratio of 15.2 are also presented. The experimental values of West and Apelt were obtained at the same interval spacings, namely $\Delta\theta = 10$ deg and practically coincide with our data. It would thus be impossible to clutter symbols representing their data in our figure in this range. Instead, we calculated the percent deviation and found that for $\theta \leq 50$ deg this deviation is less than 0.5 percent and for 60 deg $\leq \theta \leq$ 80 deg the deviation is less than 2 percent.

Of greater interest here is comparison of such distributions with data obtained in pulsating flow. We present in Fig. 1 the distribution of averaged static pressure over the cylinder, for steady as well as oscillating streams for a Reynolds number of about 50,000. Pulsation frequencies here are less than the natural frequency of shedding.

Pressure distributions follow the classical pattern, with rather little influence of pulsation. Apparently, increase of the frequency results in a slight upstream shift of the point of separation, while the base pressure increases. Surprisingly, this is exactly opposite the trends obtained earlier by the present group (Borell et al., 1984). However, the data of Borell et al. were obtained with driving frequencies higher than the natural shedding frequency. The experimental uncertainty of the pressure measurements was estimated to be about 0.025 for mean values and 0.006 for fluctuating values.

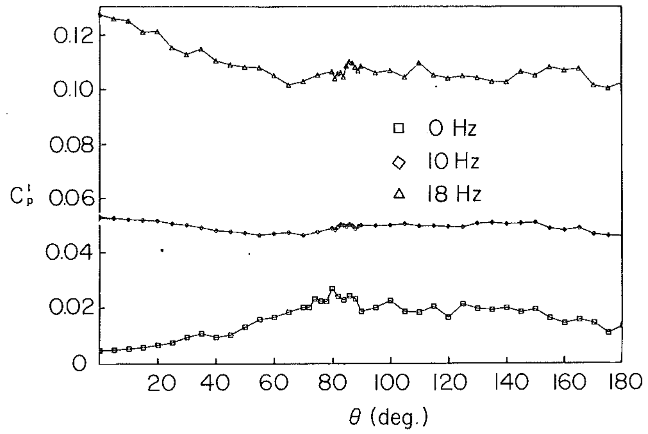

Fig. 2 The RMS of the pressure coefficients for static and pulsating streams; Re = 50,000. Precision limit: ±0.001; Uncertainty estimate: ±0.006.

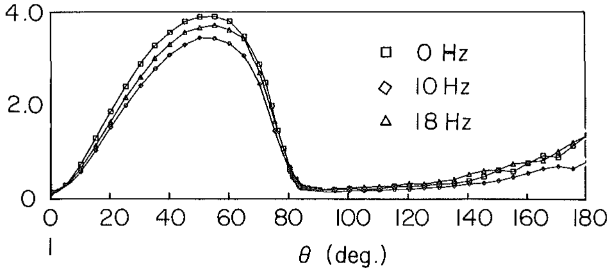

Fig. 3 Mean skin friction coefficients for steady and pulsating streams; Re = 50,000. Precision limit: ±0.1; Uncertainty estimate: ±0.6.

Figure 2 presents the RMS fluctuations of pressure and the trends this time are in agreement with the data of Borell et al. (1984). The overall level increases and tends to become spatially uniform as the frequency of imposed fluctuation increases.

Turning now to the averaged skin friction distribution (Fig. 3) we observe a well-known behavior in the attached region (Achenbach, 1968). The skin friction starts from zero at the stagnation point, peaks at about 50 deg and drops from then on. Pulsing the flow results in lower values of the skin friction but the trend is not monotonic. Moreover, such measurements are probably meaningless in the separated region. This is because a hot film is not sensitive to reversing flow and therefore the signal is rectified. For example, signals which are purely oscillatory and therefore must have a zero mean, will appear through this process as having a nonzero mean. This is the case at $\theta = 180$ deg where the oscillation must be symmetric.

Moreover, experimental and numerical studies indicate that skin friction is negative from the point of separation and on. With rectified signals, it is thus not possible to identify in Fig. 3 the actual point where the curves cross the axis, i.e., the point of zero wall shear. Figure 4 presents the RMS of the shear stress signal. The interpretation of such data is subject to the limitations discussed above. However, some interesting facts emerge. Wall shear amplitudes are the order of 10 to 15 percent of corresponding mean quantities in the attached flow region for steady flow. There is a considerable increase if the flow is pulsed, again at frequencies below the shedding frequency. The maximum amplitudes are found a little upstream of separation with magnitudes of the order of 25 percent of the maximum mean. Of greater interest is the fact that in the separated region which was thought for some time to be

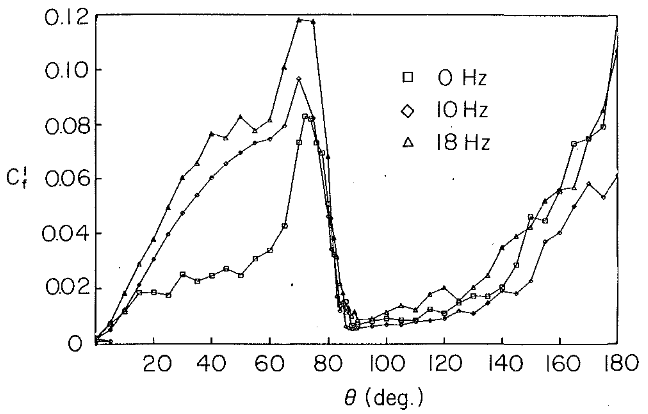

Fig. 4 The RMS of skin friction coefficients for steady and pulsating streams; Re = 50,000. Precision limit: ±0.002; Uncertainty estimate: ±0.004.

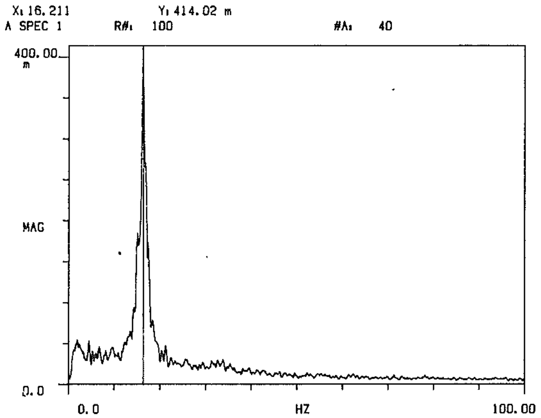

Fig. 5 A typical velocity spectrum in arbitrary units, obtained by a hot wire located two diameters downstream of the center and 1 diameter away from the axis of symmetry; Re = 36,000, St = 0.2. Uncertainty estimate in frequency 0.1 Hz.

"dead," skin friction amplitudes increase, reaching near $\theta = 180$ deg, values as high as the amplitudes in the attached flow region. Both Figs. 3 and 4 indicate a sharp decrease towards the value of zero near $\theta = 82$ deg. In fact, it appears that data for both undisturbed and pulsed flow collapse in this region.

The error involved in the skin friction measurement estimated by comparison with other experimental results and theoretical calculations was about 10 percent and perhaps 15 percent in regions of very small values. It is noted that such measurements could be quite misleading because they are perfectly repeatable. It therefore appears that the bulk of the experimental uncertainty is due to bias errors.

4 Spectral Data for Steady Streams

Let us consider now the organization of the flow in the near-wake region. A lot has been published in the literature about the structure of the flow further downstream, in the region where large-scale vortices are organized. Here we concentrate our attention on the wall surface in the separated region. Figure 5 displays the autospectrum of the velocity obtained by hot-wire anemometry in the wake. A spike due to vortex shedding at a frequency $f_s = 16.21$ Hz is present. This corresponds to a Strouhal number of about 0.2, as expected.

Spectra of skin friction records for the above conditions at azimuthal positions from $\theta = 90$ to $\theta = 180$ deg are displayed in Fig. 6. At $\theta = 90$ deg a clear spike at the shedding frequency is present. The position of mean separation is approximately at $\theta = 82$ deg as indicated from mean pressure and skin friction plots. However, in response to the shedding process, the point of separation performs excursions about this location, as detected by the fact that the signal appears to be organized even at $\theta = 90$ deg. Moreover, since skin friction attains periodically negative values, our sensor rectifies this portion of the signal. As a result, a weak second harmonic appears in the spectrum for $\theta = 90$ deg. Based on such data (not all shown here) we estimated that the point of zero skin friction oscillates between 78 ± 2 deg and 91 ± 1 deg. These data should be contrasted against the values 82 and 94 deg measured by Higuchi et al. (1989) at $\mathrm{Re} = 1.02 \times 10^5$ and an aspect ratio $\mathrm{AR} = 8$ and the values 75 and 88 reported by Dwyer and McCroskey (1983). There is reasonable agreement in the amplitude but considerable deviation in the mean.

Single-time records of the wall hot film and a hot wire positioned above the wake are shown in Fig. 7. For the azimuthal position, $\theta = 90$ deg, the behavior of the two signals corroborates the discussion above. Moreover, it is interesting to note that there is no phase difference in the signals.

As we move to $\theta = 100$ and 110 deg (Fig. 6) we lose completely any organization on the wall. This must therefore represent a truly dead-air region. The boundaries of this region must be fluctuating, but apparently the positions $\theta = 100$ and 110 deg remain always inside, as shown schematically in Fig. 8. The averaged and RMS values of skin friction (Figs. 3 and 4) indicate similarly very low overall mean and fluctuating values in this domain.

A single spike appears in the skin friction spectra at $\theta = 120$ deg (Fig. 6) but again, it seems to submerge at $\theta = 140$ deg. Finally, the wall flow develops a very powerful pattern at $\theta = 150$ deg which is reinforced at $\theta = 160$ deg. At this position, the actual skin friction must be passing through a zero, because the second harmonic appears again. Further down, at $\theta = 170$ deg, the second harmonic picks up amplitude at the expense of the first harmonic but at $\theta = 180$ deg both diminish in strength. These data indicate that for this range of Reynolds numbers, the large-scale vortical structures which develop behind the cylinder, periodically return to the aft of the cylinder and wash over its surface. A region spanning about 80 deg around the position $\theta = 180$ deg is periodically immersed in either of the two vortices, but the largest effect is observed between $\theta = 120$ and 150 deg, where the direction of the organized flow is consistently pointing upstream and the organization is very strong.

In the spectra of Fig. 6 a very low frequency spike is also present. It is believed that this is due to a low-frequency modulation of the shedding process. This has been observed by many investigators as well as the present group. It is believed that this effect does not interfere with the phenomena under investigation.

In the actual time records for the same locations (not shown here), one observes that in the back of the cylinder the wall activities are at an 180 deg phase difference with respect to the outer flow. This is because the actual skin friction is most of the time negative in this region and its absolute increase appears rectified in Fig. 6.

Subsequently, we obtained skin friction and heat transfer data with identical conditions and experimental rigs. The two identical cylinders were used with the appropriate orientation for time-resolved skin friction and heat transfer measurements. Figure 9 displays these results together with velocity spectra obtained at the same azimuthal position but away from the wall. The skin friction and heat transfer spectra show the same characteristic organization, in agreement with the data of Fig. 6. This evidence indicates that the amplitudes of the unsteady

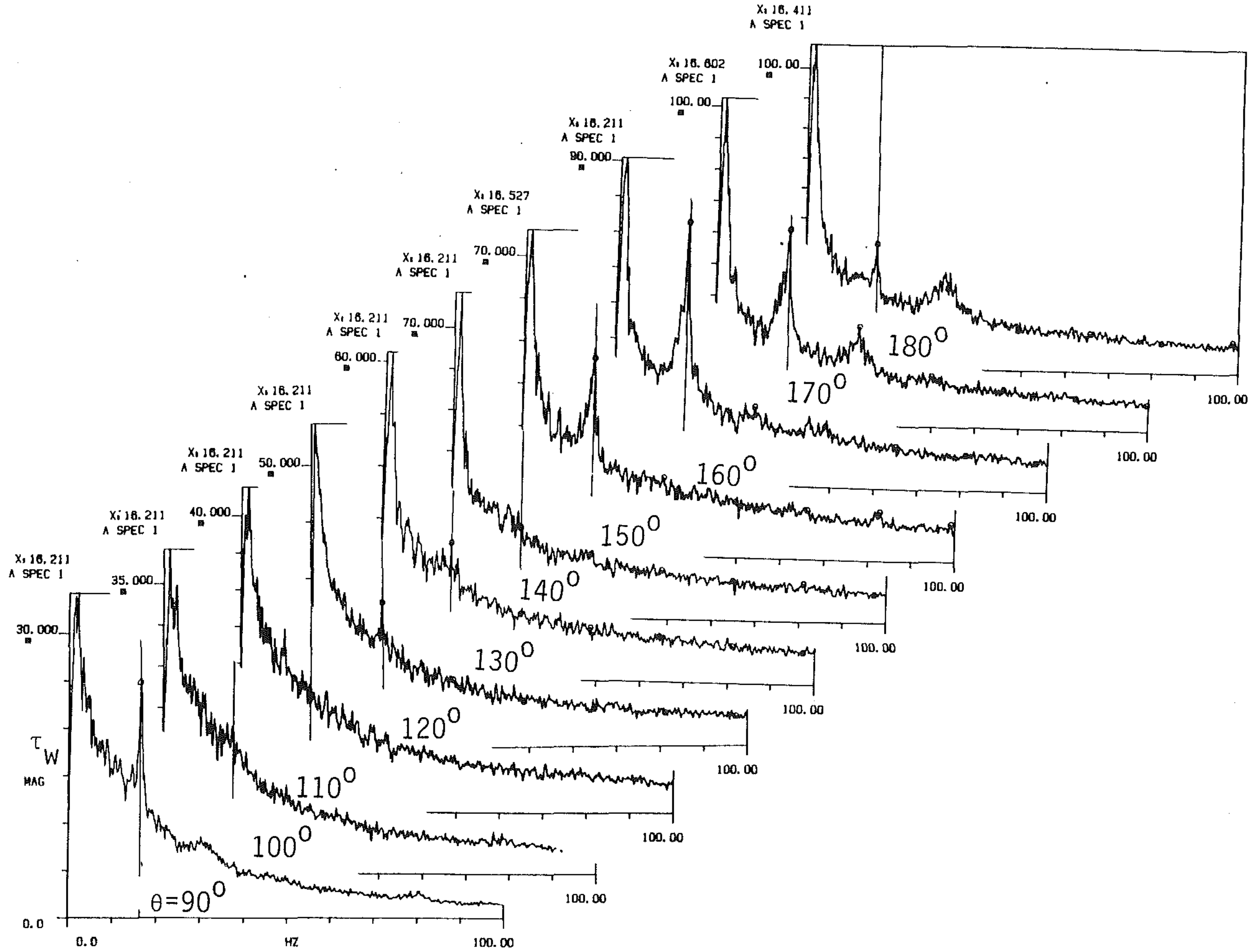

Fig. 6 Skin friction spectra at different azimuthal locations for Re = 36,000. The signal was not calibrated. Uncertainty estimate in frequency, 0.1 Hz.

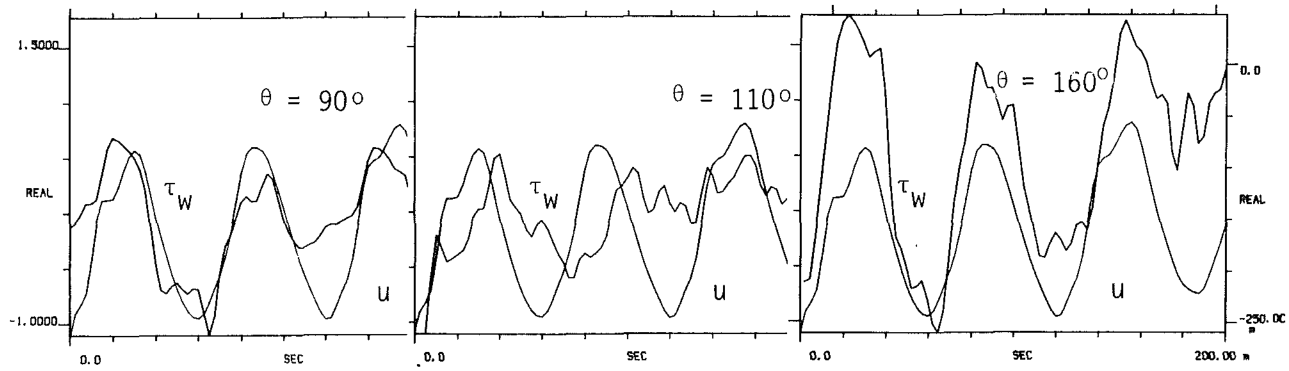

Fig. 7 Comparison of voltage waveforms of skin friction, τ_w and velocity u. In all three graphs, the velocity output was obtained above $\theta = 90$ deg and at distance of R/10, from the wall, for the condition of Fig. 6. Uncertainty estimate in frequency, 0.1 Hz.

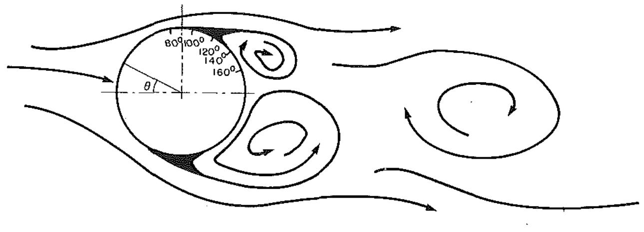

Fig. 8 Schematic sketch of the separated region. The dead-air region is shaded black.

part of heat transfer and skin friction have very similar behavior, even in regions of recirculating flow.

The data presented correspond to a rather high blockage ratio, as discussed earlier. There was no attempt to correct for blockage. However, it appears that the effect of blockage on the Strouhal number is negligible. West and Appelt (1982) measured at a Reynolds number of 50,000, Strouhal numbers ranging from 0.194 to 0.205 for blockage ratios of 2 to 15. More interesting is the fact that the aspect ratio has an even less significant effect on shedding characteristics. West and

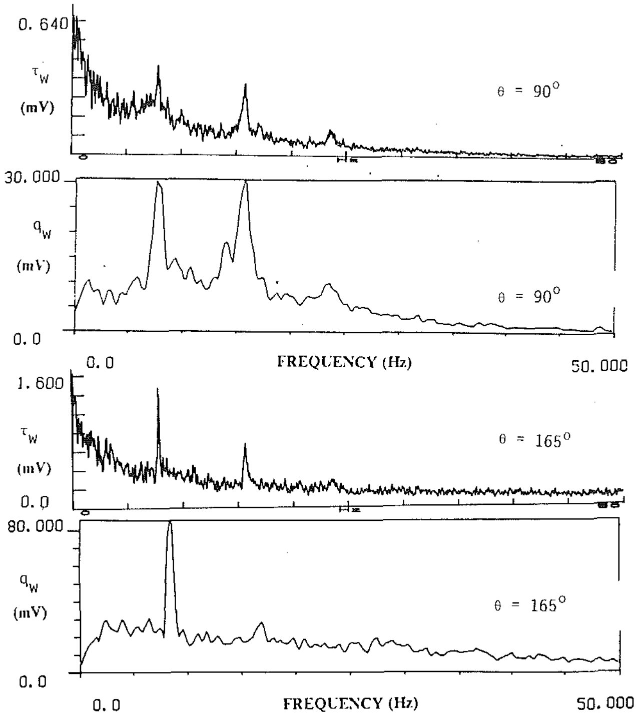

Fig. 9 Skin friction and heat transfer spectra; for Re = 33,000. The signals were not calibrated for magnitude. Uncertainty estimate in frequency, 0.1 Hz.

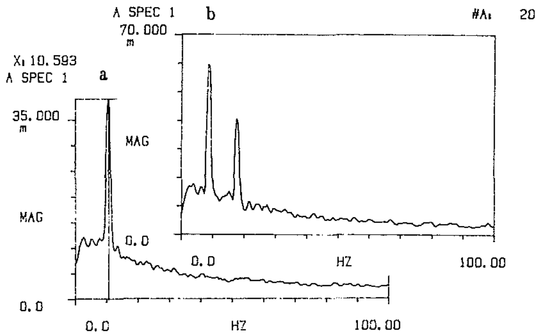

Fig. 10 Velocity spectra for steady flow and flow driven at $f_D = 18$ Hz; Re = 23,000. (*a*) Steady flow, (*b*) pulsed at 18 Hz. Uncertainty estimate in frequency, 0.5 Hz.

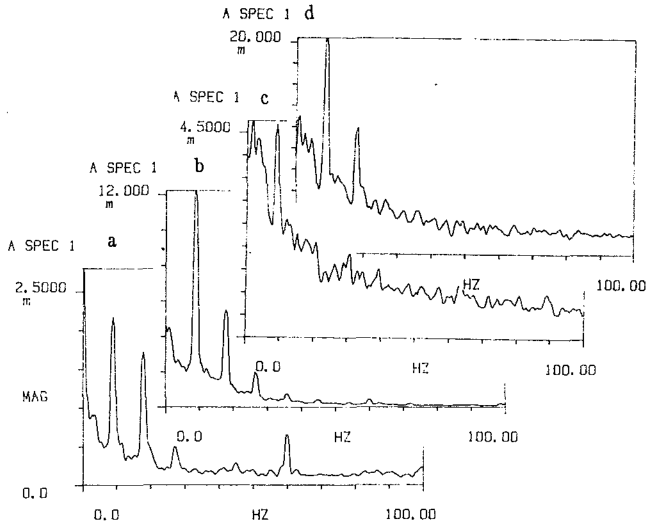

Fig. 11 Skin friction spectra for flow driven at $f_D = 9$ Hz; Re = 23,000. (*a*) $\theta = 0$ deg; (*b*) $\theta = 84$ deg; (*c*) $\theta = 140$ deg; (*d*) $\theta = 180$ deg. Uncertainty estimate in frequency, 0.5 Hz.

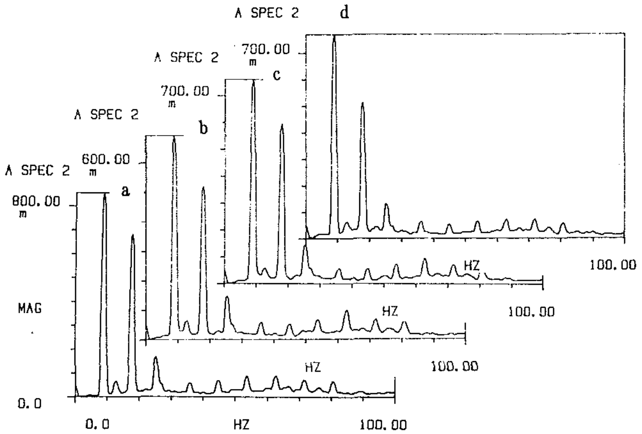

Fig. 12 Pressure spectra for flow driven at $f_D = 9$ Hz; Re = 23,000. (*a*) $\theta = 0$ deg; (*b*) $\theta = 84$ deg; (*c*) $\theta = 140$ deg; (*d*) $\theta = 180$ deg. Uncertainty estimate in frequency, 0.5 Hz.

Appelt (1982) found that for relatively high aspect ratios, the Strouhal number varies from 0.203 to 0.205 in a Reynolds number span of $10{,}000 < \mathrm{Re} < 160{,}000$.

5 Spectral Data for Pulsating Streams

Tests were conducted with pulsating flow at frequencies near the natural shedding frequency and its harmonic. The first group of measurements were conducted at a Reynolds number of about 33,000. At the conditions of the tests, the natural shedding frequency was $f_S = 14.08$ Hz. The flow was pulsed at $f_D = 14.1$ Hz. Skin friction and pressure data are included in Telionis et al. (1990). At the stagnation point, both skin friction and pressure pick up the harmonic of the natural. Driving the flow has a very small influence on the skin friction. However, the magnitude of the pressure organization increases. This trend pertains all around the periphery of the model. Apparently, pulsation at the natural frequency affects mostly the far field which is then detected by surface pressures.

Another set of tests were then conducted at a Reynolds number of Re = 23,000, at which we measured a natural shedding frequency of $f_S = 10.5$ Hz. This time the flow was driven at $f_D = 9$ Hz and 18 Hz. In both cases, the flow was locked on the driving frequency. However, the influence of lock-on was most pronounced when the flow locked at the first harmonic of the driving frequency. In Fig. 10, we display spectra of velocity measurements, obtained by hot wires in the wake of the cylinder, for steady and pulsed flow. Natural shedding is organized at approximately 10.5 Hz. When the flow is driven at $f_D = 18$ Hz, two spikes appear in the spectra of the velocity, one at $f_D/2$ and the other at f_D.

Driven at $f_D = 9$ Hz, the flow locks on the driving frequency. For this case we present skin friction and pressure data at selected azimuthal locations in Figs. 11 and 12, respectively. A complete set of data is included in Telionis et al. (1990). In all locations, the pressure spectra display two dominant spikes, one at the driving frequency and another at its harmonic. The amplitude of the pressure fluctuation is rather insensitive to the azimuthal location. Skin friction spectra on the other hand vary considerably along the periphery of the model. The skin friction spectrum at $\theta = 0$ is most useful in interpretating the

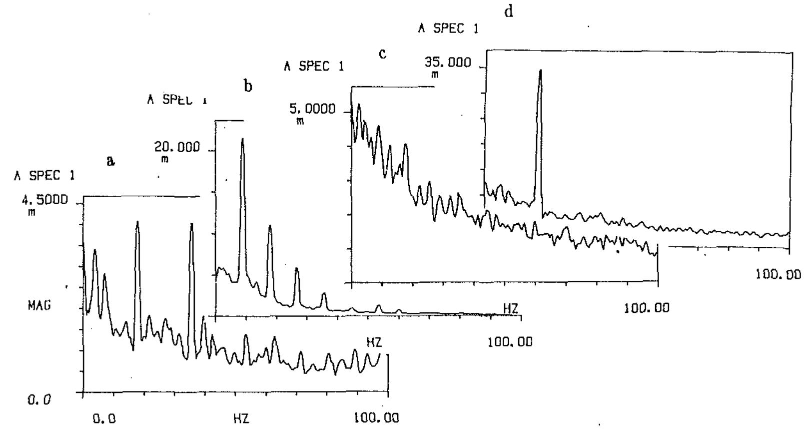

Fig. 13 Skin friction spectra for flow driven at $f_D = 18$ Hz; Re = 23,000. (*a*) $\theta = 0$ deg; (*b*) $\theta = 84$ deg; (*c*) $\theta = 140$ deg; (*d*) $\theta = 180$ deg. Uncertainty estimate in frequency, 0.5 Hz.

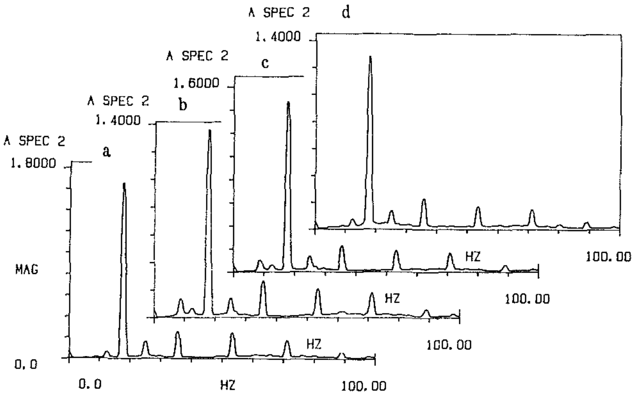

Fig. 14 Pressure spectra for flow driven at $f_D = 18$ Hz; Re = 23,000. (*a*) $\theta = 0$ deg; (*b*) $\theta = 84$ deg; (*c*) $\theta = 140$ deg; (*d*) $\theta = 180$ deg. Uncertainty estimate in frequency, 0.5 Hz.

data. This is because the excursions of the point of stagnation respond directly to the global periodic motion over the body. In other words, the point of stagnation executes a periodic motion with the frequency of the vortex shedding. The skin friction gage now detects only magnitude variations and therefore its spectrum at stagnation always displays both the shedding frequency and its harmonic.

Data for a driving frequency of $f_D = 18$ Hz are displayed in Figs. 13 and 14, for skin friction and pressure, respectively. Shedding is now locked at the driving frequency which is very near to the harmonic of the natural frequency of vortex shedding. This is evident from the skin friction spectra at $\theta = 0$, where the two spikes are at 18 and 36 Hz. Pressure spectra indicate everywhere a dominant frequency equal to the driving frequency. These data are a little inconclusive at $\theta = 180$ deg, because the skin friction seems to lack the harmonic of the shedding. This evidence indicates the possibility of a vortex shedding pattern whereby one vortex is shed with each period of the oncoming pulsed stream. This phenomenon was observed visually by Barbi et al. (1986). It is also interesting to note that in the wake region, $\theta = 140$ deg, skin frequency spectra are buried in turbulence noise, and yet, at the same location, the pressure gage can clearly pick up the shedding frequency.

Conclusions

This investigation was concentrated on wall properties of the wake side of a circular cylinder in subcritical flow. It was found that the behavior of unsteady heat transfer is similar to the behavior of unsteady skin friction. Both display pockets of high level of organization. The region immediately downstream of laminar separation extending up to $\theta = 110$ deg is practically dead. No activity can be detected there. Further downstream, some organized activity is displayed. The region between approximately $\theta = 140$ and 160 deg contains well-organized, periodically upstream-moving flow. This activity is reduced somewhat in magnitude as the position $\theta = 180$ deg is approached.

Pulsing the flow results in lock-on, if the pulsation frequency is not far from the natural frequency of shedding, or its first harmonic. The effects of pulsation are more pronounced if the flow is pulsed at twice the natural frequency. This investigation also indicated that the basic character of the flow is not altered when the motion is locked on an external periodic disturbance. The random characteristics are in fact a little reduced and the motion becomes better organized. It therefore appears that locked motions offer a cleaner case for the study of the events that lead to vortex shedding. It was also found that pressure fluctuations respond to global characteristics of the flow and are therefore sensitive to large-scale disturbances occurring far from the location of measurement. On the other hand, skin friction and heat flux are very sensitive to local variations of the flow.

These data provide for the first time detailed time-resolved information in the near wake of a bluff body. The flow in this region has defied up to now numerical modeling of the turbulence. It is believed that the present data will improve by a small increment our understanding of the behavior of the flow in this region and will provide information that will help numerical analysts in modeling such flows.

Acknowledgment

The support of the Department of Energy, grant No. DE-A505-82ER12022 is gratefully acknowledged. This is a project in the program of Dr. Oscar P. Manley, Division of Engineering, Mathematical and Geosciences of the Office of Basic Energy Sciences.

References

Achenbach, E., 1968, "Distribution of Local Pressure and Skin Friction Around a Circular Cylinder in Cross-flow up to Re = 5×10^6," *Journal of Fluid Mechanics*, Vol. 34, pp. 625-639.

Achenbach, E., 1975, "Total and Local Heat Transfer from a Smooth Circular Cylinder in Cross-flow at High Reynolds Number," *Int. J. Heat Mass Transfer*, Vol. 18, pp. 1387-1396.

Andraka, C. E., and Diller, T. E., 1985, "Heat Transfer Distribution Around a Cylinder in Pulsating Crossflow," ASME *Journal of Engineering for Gas Turbine and Power*, Vol. 107, pp. 976-982.

Armstrong, B. J., Barnes, F. H., and Grant, I., 1986, "The Effect of a Perturbation on the Flow over a Cylinder," *Physics of Fluids*, Vol. 29, pp. 2095-2102.

Barbi, C., Favier, D. P., Maresca, C. A., and Telionis, D. P., 1986, "Vortex Shedding and Lock-on of a Circular Cylinder in Oscillatory Flow," *Journal of Fluid Mechanics*, Vol. 170, pp. 527-544.

Bearman, P. W., 1984, "Vortex Shedding from Oscillatory Bluff Bodies," *Annual Review of Fluid Mechanics*, Vol. 16, pp. 195-222.

Bearman, P. W., 1980, "Vortex Shedding from Bluff Bodies in Oscillatory Flow: A Report on Euromech 119," *Journal of Fluid Mechanics*, Vol. 99, pp. 225-245.

Bearman, P. W., 1969, "On Vortex Shedding from a Circular Cylinder in the Critical Reynolds Number Regime," *Journal of Fluid Mechanics*, Vol. 327, pp. 577-585.

Berger, E., and Wille, R., 1972, "Periodic Flow Phenomena," *Annual Review of Fluid Mechanics*, Vol. 24, pp. 313-340.

Borell, G. P., Kim, B. K., Ekham, W., Diller, T. E., and Telionis, D. P., 1984, "Pressure and Heat Transfer Measurements Around a Cylinder in Pulsating Crossflow," *Unsteady Turbulent Boundary Layers and Friction*, eds., D. C. Wiggert and C. S. Martin.

Borell, G. P., and Diller, T. E., 1987, "A Convection Calibration Method for Local Heat Flux Gages," ASME *Journal of Heat Transfer*, Vol. 109, pp. 83-89.

Boulos, M. I., and Pei, D. C. T., 1974, "Dynamics of Heat Transfer from Cylinder in a Turbulent Air Stream," *International Journal of Heat & Mass Transfer*, Vol. 17, pp. 767-783.

Campbell, D. S., Gundappa, M., and Diller, T. E., 1989, "Design and Calibration of a Local Heat-Flux Measurement System for Unsteady Flows," ASME *Journal of Heat Transfer*, Vol. 111, pp. 552-557.

Campbell, D. S., and Diller, T. E., 1985, "Design and Calibration of a Local Heat-Flux Measurement System for Unsteady Flows," *Fundamentals of Forced and Mixed Convection*, eds., F. A. Kulacki and R. D. Boyd, ASME, pp. 73-80.

Cantwell, B., and Coles, D., 1983, "An Experimental Study of Entrainment and Transport in the Turbulent Near Wake of a Circular Cylinder," *Journal of Fluid Mechanics*, Vol. 136, pp. 935-944.

Diller, T. E., and Telionis, D. P., 1989, "Time-resolved Heat Transfer and Skin Friction Flow," Chapter 8 in *Advances in Fluid Mechanics Measurements, Lecture Notes in Engineering*, eds., M. Gad-el-Hak, Springer-Verlag, Berlin, pp. 323-355.

Dwyer, H. A., and McCroskey, W. J., 1973, "Oscillating Flow over a Cylinder at Large Reynolds Number," *Journal of Fluid Mechanics*, Vol. 61, pp. 753-767.

Ericcson, L. E., 1980, "Karman Vortex Shedding and the Effect of Body Motion," *AIAA Journal*, Vol. 18, pp. 935-944.

Gerrard, J. H., 1978, "The Wakes of Cylindrical Bluff Bodies at Low Reynolds Numbers," *Philosophical Transactions, Royal Society of London*, Series A, Vol. 288, pp. 351-382.

Griffin, O. M., and Hall, M. S., 1990, "Vortex Shedding and Lock-on in Bluff-Body Wakes," *Nonsteady Viscous Flows*, eds., J. S. Miller and D. P. Telionis.

Higuchi, H., Kim, H. J., and Farell, C., 1989, "On Flow Separation and Reattachment Around a Circular Cylinder at Critical Reynolds Numbers," *Journal of Fluid Mechanics*, Vol. 200, pp. 149-171.

Horvath, T. J., Jones, G. S., and Stainback, P. C., 1986, "Coherent Shedding from a Circular Cylinder at Critical, Supercritical and Transcritical Reynolds Numbers," SAE Technical Paper Series No. 861768.

Kestin, J., and Wood, R., 1971, "The Influence of Turbulence on Mass Transfer from Cylinders," ASME *Journal of Heat Transfer*, Vol. 93, pp. 321-327.

Kraabel, J. S., McKillop, A. A., and Baughn, J. W., 1982, "Heat Transfer to Air from a Yawed Cylinder," *International Journal of Heat & Mass Transfer*, Vol. 25, pp. 409-418.

Kurosaka, M., Gertz, J. B., Graham, J. E., Goodman, J. R., Sundaram, P., Riner, W. C., Kuroda, H., and Hankey, W. L., 1987, "Energy Separation in a Vortex Street," *Journal of Fluid Mechanics*, Vol. 178, pp. 1-29.

Mair, E. S., and Maull, D. J., 1971, "Bluff Bodies in Vortex Shedding—A Report on Euromech 17," *Journal of Fluid Mechanics*, Vol. 45, pp. 209-224.

Morgan, Vincent, T., 1975, "The Overall Convective Heat Transfer from Smooth Circular Cylinders," *Advances in Heat Transfer*, Vol. 11, pp. 199-264.

Ongoren, A., and Rockwell, D., 1988, "Flow Structure from an Oscillating Cylinder—Part I. Mechanisms of Phase Shift and Recovery in the Near Wake," *Journal of Fluid Mechanics*, Vol. 191, pp. 197-223.

Parkinson, G. V., 1974, "Mathematical Models of Flow-Induced Vibrations," *Flow-Induced Structural Vibrations*, ed., E. Naudascher, Spring, pp. 81-97.

Sarpkaya, T., 1979, "Vortex-Induced Oscillations: A Selective Review," ASME *Journal of Applied Mechanics*, Vol. 46, pp. 241-258.

Schewe, G., 1986, "Sensitivity of Transition Phenomena to Small Perturbations in Flow Round a Circular Cylinder," *Journal of Fluid Mechanics*, Vol. 172, pp. 33-46.

Schmidt, E., and Wenner, K., 1943, "Heat Transfer Over the Circumference of a Heated Cylinder in Transverse Flow," NASA TM-1050.

Tanida, Y., Okajima, A., and Watanabe, Y., 1973, *Journal of Fluid Mechanics*, Vol. 61, pp. 769-784.

Tavakoli, A., Kim, B. K., Borell, G. J., Diller, T. E., and Telionis, D. P., 1983, "Design and Evaluation of a Pulsating Flow Wind Tunnel," VPI & SU Engineering Report No. VPI-E-83-41.

Telionis, D. P., Gundappa, M., and Diller, T. E., 1990, "Velocity and Heat Transfer Fields in the Near Wake of a Circular Cylinder in Steady and Pulsed Flow," VPI & SU Engineering Report in press.

VandenBerghe, T. M., 1985, "Heat Transfer from In-Line and Perpendicular Arrangements of Cylinders in Steady and Pulsating Crossflow," M.S. thesis, VPI & SU.

Varty, R. L., and Currie, I. G., 1984, "Measurements Near a Laminar Separation Point," *Journal of Fluid Mechanics*, Vol. 138, pp. 1-19.

Wei, T., and Smith, C. R., 1986, "Secondary Vortices in the Wake of Circular Cylinders," *Journal of Fluid Mechanics*, Vol. 169, pp. 513-533.

West, G. S., and Appelt, C. J., 1982, "The Effects of Tunnel Blockage and Aspect Ratio on the Mean Flow Past a Circular Cylinder with Reynolds Numbers between 10^4 and 10^5," *Journal of Fluid Mechanics*, Vol. 114, pp. 361-377.

Zukauskas, A., 1985, *Heat Transfer of a Cylinder in Crossflow*, Hemisphere, Washington, D. C.

Three-Dimensional Flow Patterns in Two-Dimensional Wakes

G. S. Triantafyllou
The Benjamin Levich Institute and
Department of Mechanical Engineering,
The City College of New York,
New York, N.Y. 10031

The development of three-dimensional patterns in the wake of two-dimensional objects is examined from the point of view of hydrodynamic stability. It is first shown that for parallel shear flows, which are homogeneous along their span, the time-asymptotic state of the instability is always two-dimensional. Subsequently, the effect of flow inhomogeneities in the spanwise direction is examined. Slow modulations of the time-average flow in the spanwise direction, and localized regions of strongly inhomogeneous flow are separately considered. It is shown that the instability modes of an average flow with a slow modulation along the span have a spanwise wavelength equal to twice that of the average flow. Moreover, for the same average flow two instability modes are possible, identical in every respect except from their spanwise structure. Localized inhomogeneities on the other hand can generate through linear resonances inclined vortex filaments in the homogeneous part of the fluid. The theory provides an explanation for the vortex patterns observed in recent flow visualization experiments, and a theoretical justification of the cosine law for the frequency of inclined vortex shedding (Williamson, 1988).

1 Introduction

The appearance of three-dimensional patterns in nominally two-dimensional wakes is an issue of great importance for the problem of transition to turbulence. The onset of three-dimensionality always precedes transition, and plays a very important role in the subsequent development of turbulence. A recent comprehensive review of the relevant experimental findings can be found in Coutanceau and Defaye, (1991). It appears therefore, that a theory of transition should start with the appearance of three-dimensionality. For engineering purposes, such a study is also of interest because of the prospect of controlling transition, which has attracted renewed interest in recent years. The study of three-dimensional instability patterns is also related to the issue of the "correlation length" in the turbulent wake behind a very long cylinder (see the review articles by Sarpkaya, 1979, and Bearman, 1984, for a discussion of correlation lengths).

The average flow behind a bluff object has been shown to be absolutely unstable to two-dimensional perturbations (see Bers, 1983, for a rigorous discussion of absolute and convective instabilities). Various aspects of the instability of the average flow have been treated by Koch (1985), Triantafyllou et al. (1986), Monkewitz and Nguyen (1987), Triantafyllou et al. (1987), Chomaz et al. (1988), Unal and Rockwell (1988), Karniadakis and Triantafyllou (1989), Hanneman and Oertel (1989), Yang and Zebib (1989), Griffin (1989), Strykowski and Sreenivasan (1990). The common base in all studies is that, by linearizing the two-dimensional Navier-Stokes (or Euler) equations around the time-average flow, and assuming that the latter is nearly parallel, a dispersion relation is obtained for two-dimensional disturbances, which we denote by by $D(\omega, k) = 0$, where ω is the frequency and k the wavenumber. The dispersion relation has the form of an eigenvalue problem for the Orr-Sommerfeld (or Rayleigh) equation, subject to boundary conditions at the flow boundaries in the transverse direction.

The criterion for absolute instability in homogeneous media (Bers, 1983) can then be applied, by determining the "pinching" double roots of the dispersion relation ω_0, k_0. If the imaginary part (growth rate) of ω_0 is positive, randomly excited disturbances are amplified in time at every location and the instability is absolute. The real part of ω_0 gives the natural frequency of the flow. As comparison with experiments and numerical simulations show, the real part of ω_0 predicts well the Strouhal frequency of vortex streets, and the real part of k_0 the spacing of vortex streets. Thus linear theory gives the general "shape" of the oscillatory part of the flow, i.e., its frequency and wavelength, whereas the amplitude of oscillation is determined by non-linear effects. One should keep in mind, however, that the resulting unsteady patterns strongly influence the time-average flow (Hanneman and Oertel, 1989; Karniadakis and Triantafyllou, 1989). It is therefore necessary to think of the process as an interaction of the instability wave with the time-average flow, rather than as an instability around some fixed initial state (Triantafyllou and Karniadakis, 1990).

In the present paper, this approach is extended to three-dimensional disturbances around two-dimensional time-average flows, in order to investigate the spontaneous appearance of three-dimensionality in wakes. Subsequently the effect of inhomogeneities of the time-average flow along the span is investigated. Inhomogeneities can result from local geometrical

---

Contributed by the Fluids Engineering Division for publication in the JOURNAL OF FLUIDS ENGINEERING. Manuscript received by the Fluids Engineering Division March 14, 1990. Associate Technical Editor: D. P. Telionis.

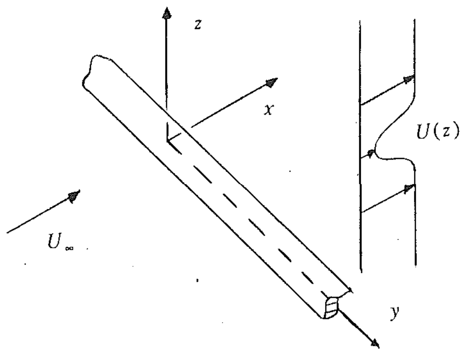

Fig. 1 Definition sketch

imperfections, or from secondary instabilities of saturated two-dimensional waves. A preliminary discussion of these issues can be found in Triantafyllou, 1990.

2 Three-Dimensional Instabilities in Shear Flow Homogeneous Along the Span

In linear theory the distinction between absolute and convective instabilities for parallel shear flows is made by determining the long-time behavior of the response of the flow to a two-dimensional impulsive excitation (Green's function). In reality however, even if the average flow is perfectly two-dimensional, perturbations will always be three-dimensional. How this affects the long-time response of the flow, i.e., whether a three-dimensional unsteady pattern will develop as $t\rightarrow\infty$, has not been investigated so far. In order to answer this question, we have to consider the response of a parallel shear flow to a three-dimensional pulse.

We consider a parallel shear flow with velocity profile $U(z)$ in a direction parallel to the x-axis of the coordinate system, and homogeneous in the x and y directions (see definition sketch in Fig. 1). Perturbations around this flow can thus be decomposed into harmonic components in the x, y directions through a double Fourier transformation, and have an eigenfunction type of dependence in the direction of the shear z. Consequently, the response to a three-dimensional impulsive excitation applied at time $t = 0$ can be expressed by a triple inverse Fourier-Laplace integral, as follows:

$$G=\frac{1}{(2\pi)^3}\int_L d\omega\int_{F_x} dk_x\int_{F_y} dk_y\,\frac{\exp(i(k_xx+k_yy-\omega t))}{D(\omega,k_x,k_y)} \qquad (1)$$

where ω is the frequency, k_x and k_y the wavenumbers in the x and y directions respectively, and $D(\omega,k_x,k_y)=0$ is the dispersion relation of the medium. Finally, L, F_x, F_y are integration contours in the complex ω, k_x, k_y planes respectively, chosen such that causality is satisfied. The long time behavior of (1) is determined by the "pinchpoint" double roots of the disperison relation, defined from the simultaneous solution of the following equations (Bers, 1983):

$$D(\omega,k_x,k_y)=\frac{\partial D}{\partial k_x}(\omega,k_x,k_y)=\frac{\partial D}{\partial k_y}(\omega,k_x,k_y)=0 \qquad (2)$$

plus the requirement that the double root of the dispersion relation, specified by the simultaneous solution of Eqs. (2), be of the "pinch-point" type. Verification of this requirement can be summarized as follows (Bers, 1983): We start by choosing both contours F_x, F_y to coincide with the real axis in their respective planes, and the contour L to be above the highest branch of ω (k_x,k_y), in order to satisfy the requirement of causality that the Green's function is equal to zero for negative times. Then the reverse mapping of the L contour into the complex k_x plane through the dispersion relation, with k_y kept real, must have two branches, one on each side of the real k_x axis (points 1 in Fig. 2(c)). If we deform the contour L to a new position, $\bar{L}$, passing through the point ω_0 in the complex ω plane specified by the solution of (2), while keeping k_y real, one of the two aforementioned branches must partly cross the real axis in the complex k_x plane (points 2 in Fig. 2(c)). If we now vary k_y from its real value to the value specified by the simultaneous solution of (2), the two branches in the k_x plane should meet ("pinch") each other at the point in the complex k_x plane specified by (2) (point 3 in Fig. 2(c). The same procedure should be repeated afterwards by interchanging the roles of the k_x,k_y planes.

By solving the dispersion relation with respect to the frequency, $\omega = \omega(k_x,k_y)$, Eq. (2) can be written as:

$$\frac{\partial\omega}{\partial k_x}=\frac{\partial\omega}{\partial k_y}=0 \qquad (3)$$

plus the pinching requirement. Equations (3) are more convenient for the question that is addressed in this section.

In parallel shear flows, we find by linearizing the Navier-Stokes equations. around the basic flow, that the dispersion relation for three-dimensional disturbances consists of the following equation for the perturbation velocity w in the z-direction (Drazin and Reid, 1981):

$$(Uk_x-\omega)\left(\frac{d^2}{dz^2}-(k_x^2+k_y^2)\right)w-k_x\frac{d^2U}{dz^2}w-\frac{1}{iR}\left(\frac{d^2}{dz^2}-(k_x^2+k_y^2)\right)^2w=0 \qquad (4)$$

subject to the boundary conditions at the flow boundaries in the z direction. The two-dimensional dispersion relation for the same Reynolds number is obtained by setting $k_y = 0$ into (4).

We first show that the pinch-point determined from the two-dimensional dispersion relation is also a pinch-point for the three dimensional one with $k_y = 0$. This follows directly from the symmetry of the dispersion relation with respect to k_y: From (4), if $D(\omega,k_x,k_y;R)=0$, then also $D(\omega,k_x,-k_y;R)=0$. This implies that for any pair (ω,k_x) that satisfy the two-dimensional dispersion relation, we have:

$$\frac{\partial D}{\partial k_y}(\omega,k_x,0;R)=0 \qquad (5)$$

Thus, owing to (5), any double-root of the two-dimensional dispersion relation $D(\omega,k_x,0;R)=\partial D(\omega,k_x,0;R)/\partial k_x=0$, is also a double root of the three-dimensional dispersion relation. Moreover, verification of the pinching requirement is trivial here: The fact that the double root has $k_y = 0$ eliminates the need for the last step in the procedure, because points 2 in Fig. 2(c) coincide. This implies that once the pinching condition has been verified for the two-dimensional problem (this accounts for the first two steps in the previously discussed procedure), it is valid for the three-dimensional problem too.

The question now arises as to whether any pinch-points of the three-dimensional dispersion relation with nonzero k_y exist. This can be investigated using the Squire transformation (Squire, 1933), which transforms the three-dimensional dispersion relation (4) into a two-dimensional at an "equivalent" Reynolds number, R', defined by:

$$K=(k_x^2+k_y^2)^{1/2}$$

$$\omega=\Omega\frac{k_x}{K} \qquad (6)$$

$$R'=R\frac{k_x}{K}$$

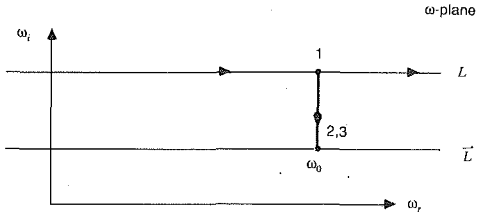

Fig. 2(*a*)

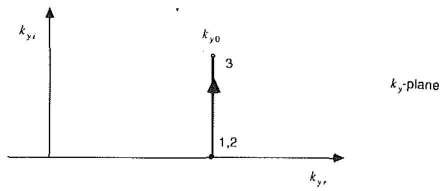

Fig. 2(*b*)

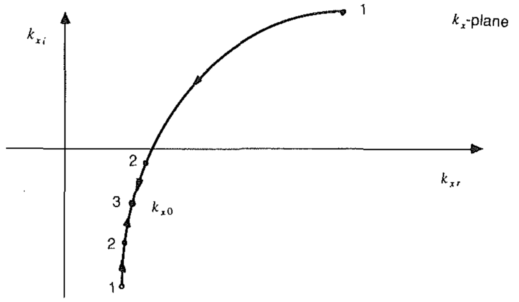

Fig. 2(*c*)

Figs. 2(*a*, 2*b*, 2*c*) Verification of the pinching requirement for three-dimensional perturbations. Fig. (2*a*): ω-plane; Figs. 2(*b*), 2(*c*); k_y, k_x planes.

The transformed quantities Ω, K, R' are related through the two-dimensional dispersion relation $\Delta(\Omega,K,R')=0$, which is the Orr-Sommerfeld equation:

$$(UK-\Omega)\left(\frac{d^2}{dz^2}-K^2\right)w-K\frac{d^2U}{dz^2}w-\frac{1}{iR'}\left(\frac{d^2}{dz^2}-K^2\right)^2w=0 \tag{7}$$

subject to the boundary conditions at the flow boundaries in the z direction. By solving the transformed eigenvalue problem, we can write $\Omega=\Omega(K,R')$.

We can now express the conditions in (3) in terms of the Squire transformed quantities using chain-differentiation. We obtain after some rather straightforward manipulations:

$$\frac{\partial\omega}{\partial k_x}=\frac{\Omega}{K}\frac{k_y^2}{K^2}+\frac{\partial\Omega}{\partial K}\frac{k_x^2}{K^2}+\frac{\partial\Omega}{\partial R'}\frac{R'}{K}\frac{k_y^2}{K^2}=0 \tag{8}$$

$$\frac{\partial\omega}{\partial k_y}=-\Omega\frac{k_xk_y}{K^3}+\frac{\partial\Omega}{\partial K}\frac{k_xk_y}{K^2}-\frac{\partial\Omega}{\partial R'}R'\frac{k_xk_y}{K^3}=0 \tag{9}$$

We solve (9) with respect to $\partial\Omega/\partial R'$, and substitute into (8). This gives:

$$\frac{\partial\Omega}{\partial K}=0 \tag{10}$$

$$\frac{\partial\Omega}{\partial R'}=-\frac{\Omega}{R'} \tag{11}$$

Equations (10) and (11) are the Squire-transformed conditions for the existence of a double root of the dispersion relation (4) with nonzero k_y. In general all three Ω,K,R' which satisfy the two conditions will be complex. Whether such a solution exists depends therefore on the dispersion relation of the specific flow under consideration. We also note that, if a double root (ω_0,k_{x0},k_{y0}) exists, then, from the symmetry of the Orr-Sommerfeld equation with respect to k_y, $(\omega_0,k_{x0},-k_{y0})$ is also a double root. Consequently, if k_{y0} is real, the resulting instability pattern will have the form of a standing wave in the y-direction.

At high Reynolds numbers, the solutions of the Orr-Sommerfeld equation for shear flows with inflection points, such as wakes, shear layers, and jets, tend to those of the Rayleigh equation. As three-dimensional flow patterns are observed in wakes for Reynolds numbers higher than, about, 200 (Williamson, 1989) we can safely assume that the dispersion relation will be defined in this range by the Rayleigh equation. In this case, it is straightforward to show that the pinch-point with $k_y = 0$ is the only one. For inviscid flows, Eqs. (10) and (11) take a very simple form, which can be obtained either directly by applying Squire's transformation on the three-dimensional Rayleigh equation, or by simply setting $\partial\Omega/\partial R' = 0$ in Eq. (11). Either way we have:

$$\frac{\partial\Omega}{\partial K}=\Omega=0 \tag{12}$$

which is a degenerate case because it also implies that $\omega = 0$. Consequently no double root of the dispersion relation with nonzero spanwise wavenumber exists, and the long-time behavior of three-dimensional perturbations will invariably be two-dimensional, as determined from a two-dimensional instability analysis. We can conclude therefore that three-dimensionality in wakes does not appear spontaneously as a result of a three-dimensional absolute instability of the two-dimensional flow. In fact the only way that three-dimensional instability modes can appear in such flows is if the average-flow itself becomes three-dimensional.

3 Flow With a Slow Modulation Along the Span

One of the main mechanisms through which two-dimensional flows become three-dimensional is the so-called secondary instability. The secondary instability acts on two-dimensional waves of finite amplitude, and leads to the formation of three-dimensional patterns (Pierrehumbert and Widnall, 1982; Orszag and Patera, 1983). We note that, once such three-dimensional patterns have been generated, they will create a spanwise modulated average flow (Karniadakis and Triantafyllou, 1990). Consistent with the approach we follow in this paper, we consider that the unsteady flow can be understood as the absolute instability mode of this final time-average flow, which is modulated along the span. We will discuss some basic properties of the flow which follow from this approach.

For any shear flow $U(y,z)$, the instability modes have the form of waves in the streamwise direction, and eigenfunction-type of dependence in the other two directions. Substitution of these modes into the linearized equations of motion gives an eigenvalue problem for ω, once k is specified, and vice-versa; this defines the dispersion relation. For an inviscid fluid, the eigenvalue problem consists of the following second-order partial differential equation for the perturbation pressure (Drazin and Howard, 1966):

$$(kU-\omega)\left(\frac{\partial^2p}{\partial z^2}+\frac{\partial^2p}{\partial y^2}-k^2p\right)-2k\left(\frac{\partial U}{\partial z}\frac{\partial p}{\partial z}+\frac{\partial U}{\partial y}\frac{\partial p}{\partial y}\right)=0 \tag{13}$$

subject to appropriate boundary conditions at the ends of the domain. For the problem that we are considering, the boundary conditions are: (i) periodicity condition along the span, and (ii) for $|z|\rightarrow\infty, p(y,z)\rightarrow 0$.

For a general velocity profile $U(y,z)$ solution of this eigenvalue problem can only be accomplished numerically. If we

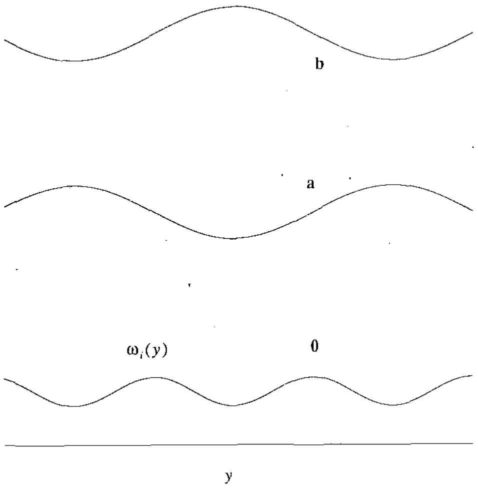

Fig. 3 **Schematic representation of the instability modes of a spanwise modulated flow. Curve 0 represents the local growth-rate of two-dimensional perturbation, $\omega_i(y)$, which follows the spanwise modulation of the time-average flow. Curves (*a*) and (*b*) represent the spanwise modulation of the two instability modes, which have a spanwise wavelength twice that of the time-average flow. Mode b can be produced by shifting Mode a by half its wavelength, and vice-versa.**

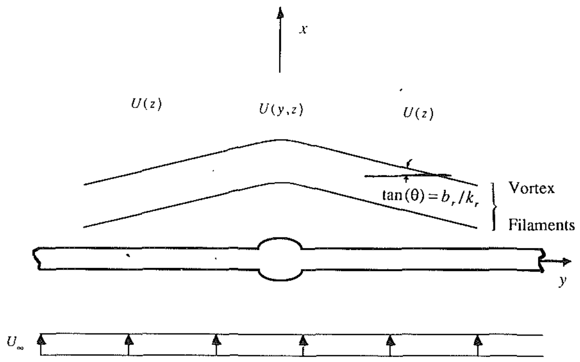

Fig. 4 **Guided waves in a flow with localized geometrical imperfection. The average flow depends on *y* and *z* behind the geometrical imperfection, and only on *z* far from the imperfection. The vortex filaments are curved in the inhomogeneous flow region, and inclined straight lines in the homogeneous flow region; their inclination asymptotically approaches the value b_r/k_r**

consider that the average flow $U(y,z)$ has a weak slow modulation along the span, which is a reasonable assumption for wakes (see Karniadakis and Triantafyllou, 1990), we will show that the eigenvalue problem can be reduced to one requiring the solution of the classical Rayleigh equation only. More specifically, the assumption of weak slow variation along the span implies that the term $\partial U/\partial y$ in the left side of (13) is two orders of magnitude smaller than the other terms. Consequently we can neglect this term, and (13) is reduced to the classical Rayleigh equation, with the important difference that U is also a function of y:

$$(kU-\omega)\left(\frac{\partial^2 p}{\partial z^2}+\frac{\partial^2 p}{\partial y^2}-k^2 p\right)-2k\,\frac{\partial U}{\partial z}\,\frac{\partial p}{\partial z}=0 \tag{14}$$

plus the same boundary conditions as the ones imposed to Eq. (13).

Because of the assumption of slow variations along the span, we can employ the usual WKB formalism (see Nayfeh, 1973), and write the following approximation for the pressure eigenfunction:

$$p\sim\exp(i\textstyle\int b(y)dy)\,Y(z,y) \tag{15}$$

where $b(y)$ is the "local" spanwise wavenumber, and $Y(z,y)$ the corresponding local eigenfunction; both b, Y are slowly varying functions of y.

We substitute Eq. (15) into Eq. (14) and we obtain to leading order:

$$(kU-\omega)\left(\frac{\partial^2 Y}{\partial z^2}-(k^2+b^2)Y\right)-2k\,\frac{\partial U}{\partial z}\,\frac{\partial Y}{\partial z}=0 \tag{16}$$

Equation (16) thus implies that at each y the pressure eigenfunction is to leading order the same as the eigenfunction of a fictitious shear flow $U(y,z)$ with y fixed. For inviscid flows two-dimensional perturbations are always the most unstable (Squire, 1933). Thus the only way that Eq. (16) can be satisfied for all y as follows: The eigenvalue ω should be equal to the two-dimensional eigenvalue ($b=0$), of $U(y,z)$ at its least unstable location; then at all other locations, $b(y)$ can be chosen through Squire's transformation such that Eq. (16) is satisfied. Clearly $|b(y)|$ will obtain its maximum value at the locations where the flow is most unstable, will be zero at the locations where the flow is least unstable, and will have intermediate values at all other locations. It is then a simple geometrical exercise (see Fig. 3) to verify that the instability mode will have a spanwise wavelength twice that of the time-average flow. In Fig. 3 curve (0) represents the spanwise variation of the growth-rate of two-dimensional perturbations, $\omega_i(y)$, which follows the modulation of the average flow. Curve (*a*) represents the spanwise variation of the instability mode, which has been drawn such that its tangent at each y has a slope proportional to $b(y)$. (Numerical verification of Fig. 3 can be found in Karniadakis and Triantafyllou (1990)). We note that, for the same average flow (0) in Fig. 3, there is a second acceptable instability mode, represented by curve (*b*), the tangent of which at each y has a slope proportional to $-b(y)$. In fact mode (*b*) is mode (*a*) shifted by half its wavelength, and vice-versa. We can conclude therefore that, unlike a spanwise homogeneous flow where the instability mode is unique, a spanwise modulated flow has two possible instability modes, which are identical in every respect, except from their spanwise structure.

4 Flow With a Localized Strong Inhomogeneity

In physical experiments inhomogeneities along the span are unavoidable, caused by imperfections in the geometry of the object and by end effects. Such inhomogeneities create regions of rapid variation of the average flow with y, where slowly varying approximation of the previous section is inappropriate. We will show that localized regions of inhomogeneous flow can influence the flow all along the span of a long structure, by acting as boundary conditions for the instability waves in the y-direction. We can call such waves "guided," since their spanwise structure is determined by boundary conditions along the span.

We consider a time-average flow with an inhomogeneity in the y direction localized around $y=0$, i.e., the flow becomes independent of y for $|y|\rightarrow\infty$. Such a flow develops for example behind a two-dimensional structure with a hump (Fig. 4). Assuming again that the average flow is inviscid and almost parallel, the dispersion relation consists of Eq. (13) of the previous section, subject to the following boundary conditions: (i) $z\rightarrow\infty$, $p\rightarrow 0$ for all y, and (ii) for $|y|\rightarrow\infty$, the time average flow becomes independent of the coordinate y. Consequently, for large y, we can set:

$$p(y\rightarrow\pm\infty,z)=f(z)\exp(\pm iby) \tag{17}$$

By substituting (17) into (13) we find that b is related to k, and ω through the dispersion relation for three-dimensional disturbances of the parallel flow $U(z)$, and that $f(z)$ is the corresponding pressure eigenfunction:

$$(kU-\omega)\left(\frac{d^2f}{dz^2}-(k^2+b^2)f\right)-2k\frac{dU}{dz}\frac{df}{dz}=0 \qquad (18)$$

plus the condition that $f(|z|\rightarrow\infty)\rightarrow 0$.

Equations (13) and (17) define the dispersion relation for the instability waves in the inhomogeneity region, which has to be solved numerically. This is an enormous task, further complicated by the boundary condition (18), which renders the dispersion relation transcendental with respect to both ω and k. Thus the numerical solution has to be carried out in an iterative manner (see Triantafyllou, 1990, for more details). We note that the instability mode is strongly three-dimensional in the region of inhomogeneous flow, and has the form of a wave with inclined crests in the region of homogeneous flow, with an inclination slope equal to the ratio of the real part of b over the real part of k_0 (Fig. 4).

Now assuming that the localized instability mode has be determined, we address the question of whether this localized mode can extend into the homogeneous region of the fluid too, thus causing three-dimensionality throughout the span. In order for that to happen, the localized mode has to resonate with some inclined absolute instability mode in the homogeneous region having the same streamwise wavenumber k and a spanwise wavenumber equal to b. Within linear theory, this resonance condition means that the double root of the dispersion relation in the strongly inhomogeneous region is also a double root of the dispersion relation (18) of the far field, for that specific value of the spanwise wavenumber b:

$$D(\omega_0,k_0,b)=\frac{\partial D}{\partial k_x}(\omega_0,k_0,b)=0 \qquad (19)$$

where ω_0,k_0 are the frequency and wavenumber of the pinch-point double root of the dispersion relation in the localized region. If Eq. (19) is satisfied, the instability waves which develop in the inhomogeneity region extend throughout the homogeneous region of the wake too. It not, we can anticipate that instability waves will independently develop in the homogeneous region. Because of the non-linear coupling of two modes with incommensurate frequencies, the resulting flow state will not be periodic.

End effects act in much the same way as discussed above, by creating regions of strongly inhomogeneous flow near the ends. (Viscous terms may have to be included too in the region, but that does not change the essence of the previous discussion.) It is therefore appropriate at this point to discuss the relation between the theory presented here, and the semi-empirical "cosine law" proposed by Williamson (1988), who justified it using an intuitive linear stability argument.

If θ denotes the angle of inclined shedding with respect to the mean flow, Williamson (1988) proposed that the frequency of the inclined vortex shedding St_θ is related to the frequency of two-dimensional vortex-shedding St by the following simple equation:

$$\mathrm{St}_\theta=\mathrm{St}\cos(\theta) \qquad (20)$$

Equation (20) can be justified according to the theory presented here, if it is possible to Squire-transform the inclined wave defined by Eq. (19) into the two-dimensional wave defined by the pinch-point of the dispersion relation in infinite fluid. Then (20) follows directly from the second of (6) (albeit heuristically, because the frequencies and wavenumbers are in general complex).

It is straightforward to show however that this is not the case. Since (ω_0,k_0,b) satisfies Eq. (19), then from Eq. (8) with $\partial\Omega/\partial R'=0$, we have that it will be Squire-transformed into a two-dimensional wave (Ω,K) which satisfies:

$$\frac{d\Omega}{dK}=-\frac{\Omega}{K}\left(\frac{b}{k_0}\right)^2 \qquad (21)$$

i.e., it is different from the wave corresponding to the two-dimensional pinch-point $d\Omega/dK=0$. We do note, however, that if the slope of the inclined filaments tan (θ) is small, the absolute value ratio b/k_0 will also be small, and the right-hand side of (21) will be approximately zero. In this case the cosine law can be justified approximately, with an error proportional to $(\tan(\theta))^2$. In Williamson's (1989) systematic tabulations this angle is indeed small, not exceeding a maximum value of 18.80 degrees. This suggests that the right-hand side of (21) will also be small, and might explain the good fitting of the experimental data by the cosine law (Williamson, 1989). Strictly speaking, however, the validity of the cosine law can only be justified in an approximate sense. A recent study of the two-dimensional Ginzburg-Landau equation (Albarede and Monkewitz, 1991) also concluded that the cosine law is only approximately valid.

5 Conclusions

It has been shown that three-dimensional instability modes can only develop when the time-average flow has inhomogeneities along the span. We can distinguish two types of such inhomogeneities:

(i) Localized regions of strong inhomogeneity, which can create coherent three-dimensional patterns throughout the wake through linear resonance.

(ii) Slow modulations of the average flow throughout the span which result from a secondary instability of the two-dimensional vortex street. Slowly modulated average flows have instability modes with a spanwise wavelength equal to twice that of the average flow. Two instability modes with different spanwise structure are possible for the same average flow.

Spanwise modulations develop even behind bodies of infinite span at high Reynolds numbers (over 200). Guided waves on the other hand seem more important at lower Reynolds numbers, and offer the possibility of controlling the flow in the wake of objects with finite span through appropriate design of the end conditions. Examples of such designs include the use of end-plates (Gerich and Eckelmann, 1982; Ramberg, 1983; and Williamson, 1989) or the application of constant pressure boundary conditions (Hammache and Gharib, 1989); two-dimensional shedding can thus be achieved, but not beyond the Reynolds number at which the secondary instability is triggered.

Acknowledgments

This work was supported by the Office of Naval Research, under contracts N00014-91-J-1287, and N00014-91-J-1373.

References

Albarede, P., and Monkewitz, P. A., 1991, "A Model for the Formation of Oblique Shedding Patterns and Chevrons in Cylinder Wakes," submitted to *Phys. Fluids A*.

Bearman, P. W., 1984, "Vortex-Shedding from Oscillating Bluff Objects," *Ann. Rev. Fluid Mech.*, Vol. 16, pp. 195–222.

Bers, A., 1983, "Space-Time Evolution of Plasma Instabilities: Absolute and Convective," *Handbook of Plasma Physics*, M.N. Rosenbluth and R. Z. Sagdeev, gen. eds., Vol. 1, Ch 3.2, North Holland.

Coutanceau, M., and Defaye, J. R., 1991, "Circular Cylinder Wake Configurations: A Flow Visualization Survey," *Appl. Mech. Rev.*, Vol. 44, No. 6, pp. 255–305.

Chomaz, J. M., Huerre, P., and Redekopp, L. G., 1988, "Bifurcations to Local and Global Modes in Spatially Developing Flows," *Phys. Rev. Letters*, Vol. 60, No. 1, pp. 25–28.

Drazin, P. G., and Howard, L. N., 1966, "Hydrodynamic Stability of Parallel Flow of Inviscid Fluid," *Advances in Applied Mechanics*, Vol. 7, pp. 1–89.

Drazin, P. G., and Reid, W. H., 1981, *Hydrodynamic Stability*, Cambridge University Press.

Gerich, D., and Eckelmann, H., 1982, "Influence of End Plates and Free Ends on the Shedding Frequency of Circular Cylinders," *Journal of Fluid Mechanics*, Vol. 122, pp. 109–121.

Griffin, O. M., 1989, "Flow Similitude and Vortex Lock-On in Bluff Body Near Wakes," *Phys. Fluids A*, Vol. 1, pp. 697–703.

Hammache, M., and Gharib, M., 1989, "A Novel Method to Promote Parallel

Vortex Shedding in the Wake of Circular Cylinders," *Phys. Fluids A*, Vol. 1, pp. 1611-1614.

Hanneman, K., and Oertel, H., 1989, "Numerical Simulation of the Absolutely and Convectively Unstable Wake," *Journal of Fluid Mechanics*, Vol. 199, pp. 55-89.

Karniadakis, G. E., and Triantafyllou, G. S., 1989, "Frequency Selection and Asymptotic States in Laminar Wakes," *Journal of Fluid Mechanics*, Vol. 199, pp. 441-469.

Karniadakis, G. E., and Triantafyllou, G. S., 1990, "Direct Numerical Simulation of the Three-Dimensional Vortex Street," 28th Aerospace Sciences Meeting, Reno, Nevada, AIAA Paper 90-0113.

Koch, W., 1985, "Local Instability Characteristics and Frequency Determination of Self-Excited Wake Flows," *J. Sound Vibr.*, Vol. 99, pp. 53-83.

Monkewitz, P. A., and Nguyen, L. N., 1987, "Absolute Instability in the Wake of Two-Dimensional Bluff Objects," *J. Fluids Struct.*, Vol. 1, pp. 165-184.

Nayfeh, A. H., 1973, *Perturbation Methods*, Wiley, New York.

Orszag, S. A., and Patera, A. T., 1983, "Secondary Instabilities of Wall-Bounded Shear Flows, " *Journal of Fluid Mechanics*, Vol. 128, pp. 347-385.

Pierrehumbert, R. T., and Widnall, S. E., 1982, "The Two- and Three-Dimensional Instabilities of a Spatially Periodic Shear Layer," *Journal of Fluid Mechanics*, Vol. 114, pp. 59-82.

Ramberg, S. E., 1983, "The Effects of Yaw and Finite Length Upon the Vortex Wakes of Stationary and Vibrating Cylinders," *Journal of Fluid Mechanics*, Vol. 128, pp. 81-107.

Sarpkaya, T., 1979, "Vortex-Induced Vibrations: A Selective Review," ASME *Journal of Applied Mechanics*, Vol. 46, pp. 241-258.

Squire, H. B., 1933, "On the Stability for Three-Dimensional Disturbances of Viscous Fluid Flow Between Parallel Walls," *Proc. Roy. Soc. London*, Series A, Vol. 142, pp. 621-626.

Strykowski, P. J., and Sreenivasan, K. R., 1990, "On the Formation and Suppression of Vortex Shedding at Low Reynolds Numbers," *Journal of Fluid Mechanics*, Vol. 218, pp. 71-107.

Triantafyllou, G. S., 1990, "Three-Dimensional Flow Patterns in Two-Dimensional Wakes," *Proceedings, International Symposium on Unsteady Fluid Mechanics*, Toronto, Ontario, AMD-Vol. 92, pp. 395-402.

Triantafyllou, G. S., and Karniadakis, G. E., 1990, "Computational Reducibility of Unsteady Viscous FLows," *Phys. Fluids A*, Vol. 2, No. 5, pp. 653-656.

Triantafyllou, G. S., Kupfer, K., and Bers, A., 1987, "Absolute Instabilities and Self-Sustained Oscillations in the Wake of Circular Cylinders," *Phys. Rev. Letters*, Vol. 59, No. 17, pp. 1914-1917.

Triantafyllou, G. S., Triantafyllou, M. S., and Chryssostomidis, C., 1986, "On the Formation of Vortex Streets Behind Stationary Cylinders," *Journal of Fluid Mechanics*, Vol. 170, pp. 461-477.

Unal, M., and Rockwell, D., 1988, "On Vortex Formation From Cylinders, Part I: The Initial Instability," *Journal of Fluid Mechanics*, Vol. 190, pp. 419-512.

Williamson, C. K. H., 1988, "Defining a Universal and Continuous Strouhal-Reynolds Number Relationship for the Laminar Shedding of a Circular Cylinder," *Phys. Fluids*, Vol. 31, pp. 2742-2745.

Williamson, C. K. H., 1989, "Oblique and Parallel Modes of Vortex Shedding in the Wake of a Circular Cylinder at Low Reynolds Number," *Journal of Fluid Mechanics*, Vol. 206, pp. 579-628.

Yang, X., and Zebib, A., 1989, "Absolute and Convective Instability of a Cylinder Wake," *Phys. Fluids A*, Vol. 1, pp. 689-696.

G. J. Morris

J. T. Jurewicz

G. M. Palmer

Mechanical and Aerospace Engineering,
West Virginia University,
Morgantown, WV 26506-6101

Gas-Solid Flow in a Fluidically Oscillating Jet

The motion of air and solid particles is examined in a fluidically oscillating slot jet using time-averaged and cycle-resolved laser Doppler anemometry measurements. These measurements reveal the time dependent relative velocity magnitudes between the phases as well as the detailed nature of the flulidcally oscillating slot jet. Temporal phase differences between the gas and solid phases ranged up to 40 degrees for jet oscillation frequencies up to 50 Hz. The results indicate that the fluidic nozzle is an effective particle spreading device and the fuel injector attributes are inherently present such as enhanced mixing and low velocity regions for flame anchoring.

Introduction

For many years researchers have studied the mixing characteristics of jets and have attempted to fully understand as well as to enhance the mixing process of the primary flow with the surrounding media. The large majority of these studies have historically involved steady jet phenomena, while it has been shown that unsteady jets yield more intimate mixing and entrainment with the surrounding media. The objective of the research reported within this paper was to experimentallly investigate the characteristics of a two-phase (gas-solid), oscillating slot jet. The application which inspired this research is the proposed use of a two-phase, oscillating jet as a fuel injector for a pulverized fuel combustor system.

The available literature on jets can be classified as those concerning steady, single-phase, and two-phase flows and those concerning unsteady, single-phase flows. Few reports related to the motion of solid particles in an unsteady jet flow exist. There are volumes of reports on research concerning steady single-phase work, so they will not be discussed here. Additionally, further discussions within this paper will be limited to experimental determinations of the behavior of self-excited, unsteady jet flows.

Unsteady Single-Phase Flow. Hill and Green (1977) pioneered a device called a whistler nozzle which is basically a convergent nozzle followed by straight section followed by a step expansion to a second straight section. The second straight section was open to the atmosphere. This geometry created a standing acoustic wave within the nozzle which resulted in increased turbulent mixing due to acoustically stimulated vortex shedding. The centerline velocity of this single phase jet decayed more rapidly in the whistling mode than in the non-whistling mode and was accompanied by a flattening of the axial velocity profile.

Crow and Champagne (1971) examined a single phase jet excited by acoustical disturbances emitted from a loud speaker upstream of the jet exit. Their results were similar to those of Hill and Green (1977). It is noted, however, that the axial velocity decay for Hill and Green's whistler nozzle was more pronounced than Crow and Champagne's loudspeaker excited jet for similar flow conditions.

Viets et al. (1975) investigated the flow characteristics of a fluidically controlled, oscillating slot jet which injected water into stagnant air. In this design, the two-dimensional jet was caused to laterally oscillate by capturing a small portion of the fluid jet and injecting it normal to the flow at the nozzle diffuser entrance. Each side of the nozzle was equipped with a scoop connected to a channel leading to an injection port at the diffuser entrance. The injected flow, periodically captured by the scoops, caused the jet to oscillate from side to side within the diffuser at a frequency proportional to the volume of the channel connecting the scoop to the injection ports. Viets found that the spread rate of the oscillating jet was signficantly increased when compared to a similar non-oscillating jet. From high speed photographs, it was shown that an intimate mixing process occurs between the primary and entrained fluids. Captured pockets of the entrained fluids within the primary jet tend to increase the mixing interface between the two fluids.

Another study by Viets (1975) involved an experimental parametric examination of various physical configurations of the fluidic nozzles. This study considered air being injected into a body of stagnant air. It was concluded that contracting sections at the nozzle exit destroyed the nozzle oscillation characteristics. It was also concluded that the oscillating jet half-width spread rate exceeded the non-oscillating spread rate by more than a factor of three, thus indicating enhanced interaction of the unsteady primary flow with the surrounding quiescent fluid.

Piatt and Viets (1979) examined the flow characteristics of a fluidically oscillating air jet exiting into a coflowing air stream. With all other parameters constant, flow visualization showed that the spread rate of the jet increased with decreasing velocity of the secondary flow. From the time-average velocities determined by hot wire anemometry, Piatt and Viets discovered that the velocity profile of the jet was dependent upon the axial location. Very near the nozzle exit, the average velocity profile was represented by one narrow peak symmetric about the jet centerline. At intermediate axial locations, the average

---

Contributed by the Fluids Engineering Division for publishing in the JOURNAL OF FLUIDS ENGINEERING. Manuscript received of the Fluids Engineering Division May 25, 1990. Associate Technical Editor: E. E. Michaelides.

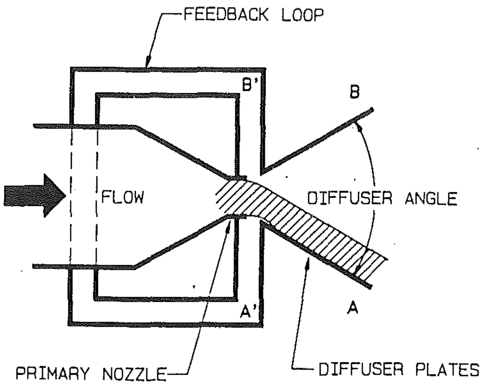

Fig. 1 A simple fluidic nozzle schematic

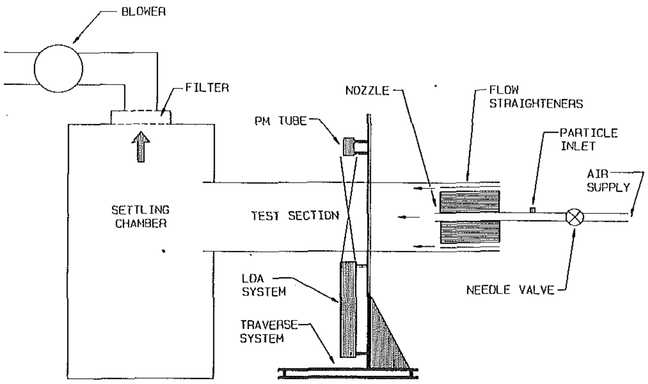

Fig. 2 Nozzle test facility

velocity profile showed two peaks—one on either side of the jet centerline which was itself a local axial velocity minimum. This phenomemon was attributed to the oscillating nature of the jet. At large axial distances from the exit, the average velocity profiles returned to a single broad peak centered about the centerline of the flow field. The axial velocity decay rates normalized with respect to the centerline velocity were high compared to steady jet results, especially at lower oscillation frequencies of the jet.

Platzer et al. (1978) investigated the entrainment characteristics of various forms of unsteady subsonic jets including jets with time varying jet deflection such as a fluidically oscillating jet and pulsating jets with time-varying mass flow. Both unsteady forms of the jets exhibited enhanced entrainment of the surrounding media with respect to their steady jet counterparts. A fluidically oscillating jet had enhanced entrainment of over fifty percent compared to a similar steady jet.

Bremhorst and Watson (1981) studied a steady annular jet with a periodically pulsed core flow. It was determined that the jet centerline velocity decayed slower than for a comparable steady jet but that the entrainment was enhanced for the pulsed core jet.

Kato and Groenewegen (1987) examined mixing in unsteady turbulent jets using visible pH indicators to quantify the mixing process compared to steady jets. Compared to steady jets, the unsteady jets were approximately 50 percent wider indicating that the unsteady effects had modified the mixing process.

Fluidic Nozzle. A simple fluidic nozzle is depicted in Fig. 1. The fluid flows through a contraction, past two ports, into an expansion section. The output lines from the ports are attached to each other. Due to the proximity of the walls, the jet is bistable and must attach to one of the diffuser walls. If the jet attaches to the lower wall, *A*, then due to the large amount of entrainment into the jet, the pressure at the control port *B*' is relatively high compared to the pressure at port *A*'. Since the ports are acoustically connected, a compression wave travels from port *B*' to *A*' tending to raise the pressure there, and if the nozzle is properly tuned, the jet will be pushed away from diffuser wall *A* and traverse to diffuser wall *B* due its bistable nature and the Coanda effect of the walls. In a well designed nozzle, this pattern is regularly repeated yielding a jet oscillation frequency that is dependent upon the length of the feedback loop and the volume flow rate through the nozzle. Frequencies of greater than 100 Hertz are possible.

The fluidic nozzle used in this study had a throat spacing of 2.54 mm and a throat height of 25.4 mm. The jet Reynold's number was 4900 based on the throat hydraulic diameter.

Experimental Apparatus

Test Facilities. A sketch of the nozzle test facility is shown in Fig. 2. This facility was a transparent walled, enclosed channel through which ambient air was drawn in as thin air curtains along the top and bottom surfaces to maintain clean window surfaces for the laser Doppler anemometry (LDA) apparatus. The nozzle air issued into this environment between the air curtains. The seed particles for the LDA and the larger glass microspheres were injected approximately 0.5 meter from the nozzle entrance. The LDA system was mounted vertically and was operated in the forward scatter node to maximize the signal quality resulting from the 15 mW He-Ne laser used. A single channel LDA system was used complete with an acousto-optic cell to detect flow reversals and to resolve areas with low magnitude velocities. The optics were rotated to attain both axial and transverse jet velocities. The entire LDA system was mounted on a two-degree of freedom traversing table that was stepper driven and microcomputer controlled.

Titanium dioxide particles (2.0μm diameter) were used to seed the air flow to characterize the gaseous phase velocity field. Glass microspheres in batches of 21μm and 54μm diameter were chosen to serve as the solid phase which could be considered to be representative of solid fuel particles such as pulverized coal. All types of particles were metered into the primary nozzle inlet with fluidized bed particle feeders in separate batches.

Cycle-Resolved and Ensemble Averaged Data Acquisition. For periodic flows, times-averaged velocity measurements do not represent the detailed flow field phenomena. Cycle-resolved or conditioned sampled data acquistion techniques must be employed to fully characterize the time dependent nature of the flow. As with any conditioned sampled measurement, a reference must be identified with which all other measurements must be synchronized. For the fluidic nozzle device, a sensitive pressure transducer was installed into the feedback loop to monitor the jet oscillation frequency and to serve as the reference for the cycle-resolved data acquisition. It was determined that the output signal from the pressure transducer exactly indicated the position of the jet with respect

Nomenclature

D = nozzle throat spacing
U = axial velocity
U_o = nozzle throat velocity (61 m/s)
V = transverse velocity
X = axial coordinate in flow field
Y = transverse coordinate in flow field

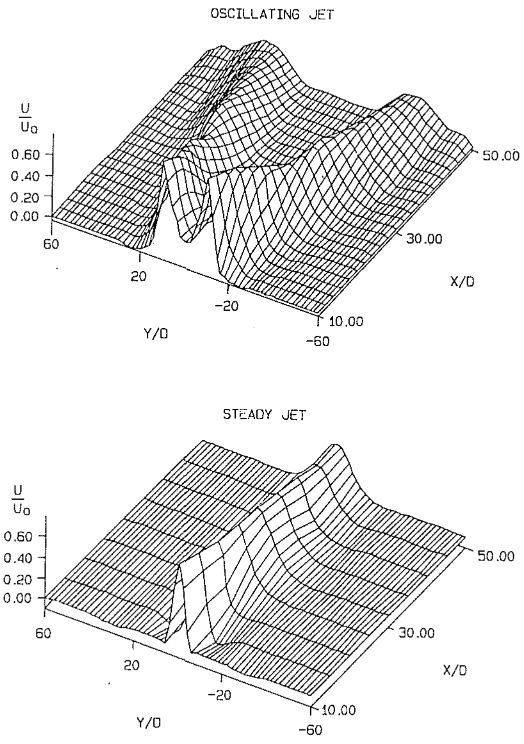

Fig. 3 Flow field comparison of the oscillating air jet with the steady air jet for equal volume flow rates. The oscillating jet was operating at 50 Hz with a 75 deg diffuser angle.

to the diffuser walls and the nearby feedback pressure ports. This was accomplished by positioning a hot wire anemometer probe at exit end of one of the diffuser walls and connecting both the anemometer output and the pressure transducer output to a dual trace oscilloscope. The signals exactly correlated indicating that the pressure transducer could be used to synchronize the data acquisition in absence the hot wire probe which would not be able to survive the gas-solid flow environment.

The cycle-resolved data were acquired for one complete jet oscillation cycle at a time using the pressure transducer signal to trigger the LDA counter processor to accept data during the oscillation period. The velocity realizations were then sorted into discreet, equal interval time bins with respect to their time of occurrence form the start of the oscillation period. The data acquisition procedure continued until each of the fifty time bins were sufficiently populated to yield statistically meaningful, ensemble averages that would be representative of the velocity for each time interval or bin.

Results and Discussion

Both time-average and cycle-resolved axial and transverse velocity measurements of each phase were acquired. The time-average velocity profiles are useful to compare with the velocity profiles from an identical geometry steady jet as far as centerline velocity decay and jet spreading are concerned. Comparisons of the cycle resolved velocity profiles of each phase indicate the relative velocity magnitudes between the phases and also indicate how well the particles are dispersed. For each figure shown, the 95 percent confidence interval based the students' T-distribution is smaller than the size of the plotted symbols unless otherwise shown by a bar symbol displaying the largest 95 percent confidence interval. The cycle-resolved data have the greater uncertainty since the ensemble averages of each discreet time interval of the period of oscillation consisted of fewer data realizations compared to the time-average measurements.

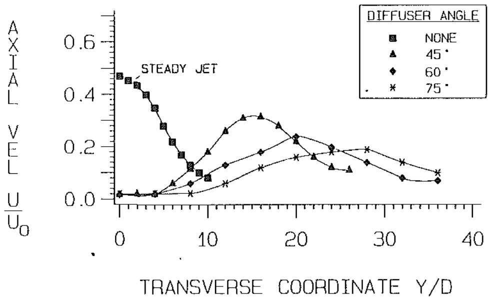

Fig. 4 Effect of diffuser angle on the 50 Hz oscillating air jet width compared to the steady jet at 40 throat widths downstream

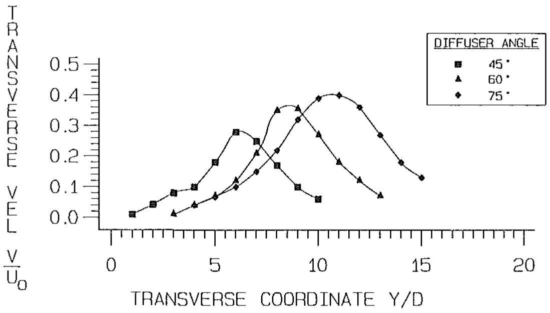

Fig. 5 Effect of diffuser angle on the 50 Hz oscillating air jet transverse velocity component at 10 throat widths downstream

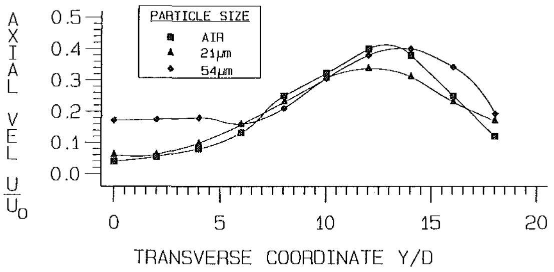

Fig. 6 Effect of particle size on the 50 Hz oscillating jet axial velocity component at 30 throat widths downstream

Time-Average Velocity Results. Figure 3 shows a comparison of the axial velocity fields created by a steady slot jet and an oscillating slot jet for air flow. Both velocity fields are normalized by the steady jet exit plane velocity, U_o (61 m/s). The axial coordinate, X, and the transverse coordinate, Y, centered at the axis of symmetry are both normalized by the nozzle throat width, D (2.54mm). Figure 3 dramatically displays the enhanced transverse spreading of the oscillating jet compared to the steady jet. Also, the rate of centerline axial velocity decay was greatly increased in the oscillating case as evidenced by comparing the centerline axial velocity of the steady jet with the symmetric double peak, time-average velocity profile of the oscillating jet. Both of these phenomena indicate that the unsteady jet interacted more with the stagnant surrounding air than did the steady jet counterpart for equal volume flows through the nozzles.

Figure 4 shows more detailed comparisons of the steady air jet behavior compared to that of the oscillating air jet for a fixed axial location and jet oscillation frequency (50 Hz) with the nozzle exit diffuser angle varied as a parameter. In Figs. 4-7, only one-half of the flow field is represented due to symmetry about the jet centerline. Figure 4 illustrates the axial velocity profile comparison, while Fig. 5 illustrates the behavior of the oscillating air jet transverse velocity field. No steady jet results are shown in Fig. 5 due to the extremely low magnitudes that result in the transverse direction for a steady

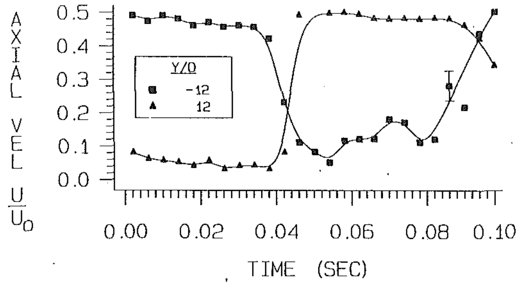

Fig. 7 Time dependent axial velocity character of the oscillating air jet at 30 throat widths downstream with a 45 deg diffuser angle and a 10 Hz frequency

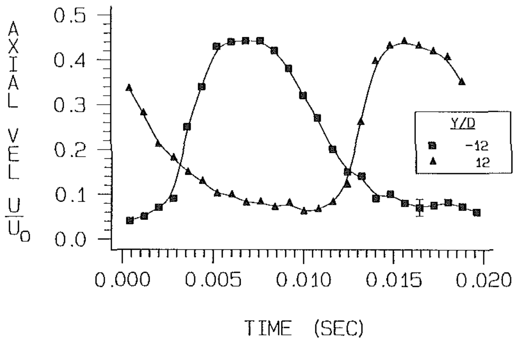

Fig. 8 Time dependent axial velocity character of the oscillating air jet at 30 throat widths downstream with a 45 deg diffuser angle and a 50 Hz frequency

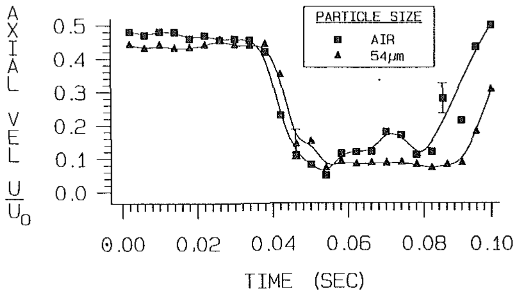

Fig. 9 Time dependent axial velocity character of the oscillating two-phase jet at 30 throat widths downstream and 12 throat widths left of centerline with a 45 deg diffuser angle and a 10 Hz frequency

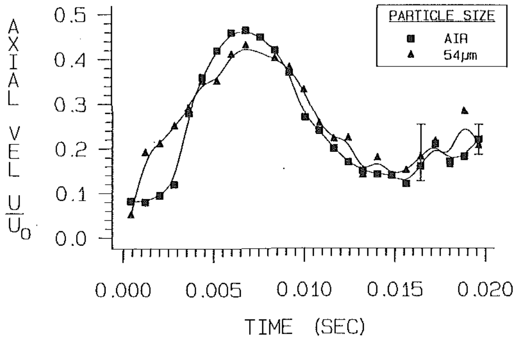

Fig. 10 Time dependent axial velocity character of the oscillating two-phase jet at 30 throat widths downstream and 16 throat widths left of centerline with a 60 deg diffuser angle and a 50 Hz frequency

slot jet. As the nozzle diffuser angle was increased from 45 to 75 deg, the transverse location of the maximum velocity for both the axial and transverse velocity components also increased in proportion indicating that the jet remained attached to the diffuser walls for up to the maximum tested angle of 75 total included angle. Subsequent work has shown that the fluid can attach to the diffuser walls even at angles of 120 deg. Opposite trends in the relative maxima of the axial and transverse velocities occur as the diffuser angle was increased. The axial velocity maximum decreased with increasing diffuser angle as it entrained more surrounding fluid, while the transverse velocity maximum increased with increasing diffuser angle owing to the effect that a larger component of transverse velocity was generated as the jet was increasingly deflected laterally.

The normalized axial velocity profiles for the air and two different particle sizes are shown in Fig. 6 at 30 nozzle throat widths downstream of the oscillating jet exit plane. Near the centerline of the jet, the 21 μm diameter particles closely followed the air flow behavior although some amount of velocity overshoot was present. In this same region, however, the 54 μm particles have approximately a fourfold increase in axial velocity compared to the air. Because of their inertia, the larger particles had a longer stopping distance which caused them to overshot the rapidly decaying axial air velocity near the centerline region. It is also illustrated in Fig.6 that the larger particles seemed to disperse to larger transverse locations while maintaining increased axial velocity magnitudes when compared with the air flow behavior. Particle concentration measurements at these locations would facilitate more definite conclusions with respect to actual particle dispersion characteristics of the fluidically oscillation jet.

Cycle-Resolved Velocity Results. The results for the cycle-resolved air velocity measurements in the axial direction for selected locations are shown in Figs. 7 and 8 for jet oscillation frequencies of 10 Hz and 50 Hz, respectively. Like the time averaged velocity results, these cycle-resolved velocities have been normalized by the nozzle throat velocity, U_o (61 m/s). Each of the figures displays two curves with each curve representing the cycle-resolved axial velocity profile at symmetric transverse locations with respect to the flow field centerline. These transverse locations were selected for presentation since the locations correspond to the local, time-averaged axial velocity maxima. The results reveal that the time dependent, axial velocities at these symmetric transverse locations were 180 deg out of phase with each other. Also illustrated by Figs. 7 and 8 is the difference in behavior of the oscillating nature of the jet. Figure 7 shows that for the 10 Hz jet the axial velocity as a function of time closely resembled a square wave form while Fig. 8 shows that the 50 Hz axial velocity as a function of time more closely resembled a sinusoidal wave form. A comparison of these wave form types indicates that the jet resided near the centerline region of the flow field for a proportionately larger fraction of the oscillation period for the 50 Hz jet than it did for the 10 Hz jet. This conclusion is supported by the fact that for the time-averaged, axial velocity measurements, the centerline velocities magnitudes were higher for the 50 Hz jet than for the 10 Hz jet with all other nozzle parameters such as diffuser angle and volume flow rate being equal. Additionally, Figs. 7 and 8 give further credence to the method employed for the cycle-resolved data acquisition since the temporal relationship results between the velocity profiles at locations equidistant from the flow field centerline are intuitive.

Comparisons of time dependent particle and air axial velocities for single LDA measuring volume locations and two jet oscillation frequencies are shown in Figs. 9 and 10. These figures are representative of the cycle-resolved velocity measurements performed in this study. It is observed that the 54 μm particle motion is very similar to the air motion for the frequencies tested. Consistent phase and velocity amplitude lags were not observed. In fact, the phases frequently switched their relative positions with respect to temporal phase. For the 10 Hz jet,the particle motion, in general, did not significantly differ for the air motion. The general behavior of the particles in the 50 Hz jet was to lead and then lag the air velocity waveform around its peak region. The local phase differences between the air and particles were as high as 40 degrees.

Conclusions

The time-average velocity measurements indicate that the oscillating jet interacts with the surrounding media significantly better than a similar steady slot jet. The oscillating jet, while its detailed nature is partially governed by the oscillation frequency, resides near the diffuser walls for a longer fraction of its period than near the centerline which yields a very low centerline velocity with rapidly decaying axial velocity peaks on either side of the centerline. The analysis of the dependent nature of the flow field supports the time-average velocity field results based on the locations of high and low velocity magnitudes regions. The nozzle exit diffuser angle dictates the overall spreading of the jet for angles at least up to 75 degrees. The solid particles are very well dispersed by the device with no moving parts and significant temporal phase lags and relative velocities between the phases are apparent all of which suggest that the resulting flow field would be conducive to environments requiring enhanced transport phenomena such as a combustion field with a particulate or droplet fuel form.

Acknowledgments

The authors gratefully acknowledge United Technologies, Inc., Power Systems Division and the West Virginia University Energy and Water Research Center for supporting this research.

References

Bremhorst, K., and Watson, R. D., 1981 "Velocity Field and Entrainment of a Pulsed Core Jet," ASME JOURNAL OF FLUIDS ENGINEERING, Vol. 103, pp. 605–608.

Crow, S. C., and Champagne, F., 1971, "Orderly Structure in Jet Turbulence," *Journal of Fluid Mechanics*, Vol. 48, Part 3, pp. 547–591.

Hill, W. G., and Greene, P., 1977, "Increased Turbulent Jet Mixing Rates Obtained by Self-Excited Acoustic Oscillation," JOURNAL OF FLUIDS ENGINEERING, Vol. 99, pp. 520–525.

Kato, S. M., and Groenewegen, B. C., 1987, "Turbulent Mixing in Nonsteady Jets," *AIAA Journal*, Vol, 25, No. 1.

Piatt, M., and Viets, H., 1979, "Conditioned Sampling in an Unsteady Jet," AIAA Aircraft Systems and Technology Meeting, Aug. 20–25, New York, NY.

Platzer, M. F., Simmons, J. M., and Bremhorst, K., 1978, "Entrainment Characteristics of Unsteady Subsonic Jets," *AIAA Journal*, Vol. 16, No. 3, pp. 282–284.

Viets, H., Balster, D., and Toms, H., 1975 "Time Dependent Fuel Injectors," AIAA/SAE 11th Propulsion Conference, Anaheim, CA, pp. 1–8.

Viets, H., 1975, "Flip-Flop Jet Nozzle, *AIAA Journal*, Vol. 13, No. 10, pp. 1375–1379.

Sen Nieh
Associate Professor.

Jian Zhang
Graduate Research Assistant.

Department of Mechanical Engineering,
The Catholic University of America,
Washington, D.C. 20064

Simulation of the Strongly Swirling Aerodynamic Field in a Vortex Combustor

This paper presents the simulation of the strongly swirling aerodynamic field in a coal-fired vortex combustor (VC) recently developed for commercial heating applications. A new version of algebraic Reynolds stress model was employed for the closure of non-isotropic turbulence. The calculated results of the 25 cm I.D. bench-scale and the 61 cm I.D. full-scale VC cold test models showed the pertinent aerodynamic features of the VC in terms of strongly swirling, developing, recirculating, and non-isotropic turbulent flow. The dynamic similarity was generally maintained for VCs of different scales.

1 Introduction

Coal-fired VCs featured with a progressive air injection, sizable exhaust center tube, and strongly swirling, nonslagging, and low temperature combustion environment were recently developed for commercial space/water heating applications. High combustion efficiencies (≥97 percent), large firing intensities (1 ~ 5 MW/m^3), broad fuel flexibility, and low emissions were demonstrated during the 250-hour systematic tests firing dry pulverized coals and their slurries. Good operational performance, such as large turndown ratio (≥3:1), no need of air preheating, and easy control of particle behavior and combustion temperature were also noted (Nieh and Fu, 1990a; 1990b; Nieh, 1991). The outstanding technical performance of the VCs is largely attributed to its strongly swirling flow created by the multiple air injection and the pertinent combustor configuration of coaxial circular tubes. These make the VCs different from the conventional coal-fired cyclone combustors and swirl burners.

As schematically shown in Fig. 1, secondary air is tangentially injected into the annular chamber of the VC through the nozzles arranged at various strategic levels to form a strong swirl. Coal-based fuels in either dry powdered form or slurry form are injected (or atomized) with primary air at the bottom. Combustion takes place primarily in the annular space. Hot flue gas spirally ascends to the top, and finally exits through the center tube. It was found in a series of cold/hot model tests that the strongly swirling flow intensifies the combustion and provides an effective control of the motion of fuel particles. Experimental evidence also indicated that the swirling flow gives a vigorous gas turbulence, large gas-particle slip motion, long particle residence time, and intensified mixing and heat/mass transfer (Nieh and Fu, 1990a; 1990b; Nieh, 1990; 1991).

Because of the pronounced effects of the swirling flow on combustor performance, it is desirable to know the detailed aerodynamic structure and the distinct flow characteristics of the VC. However, since the VC is a new combustion device, no study pertaining to its flow properties has ever been made. Parallel efforts on numerical simulation and cold flow measurements of the VC were thus pursued (Nieh, 1990). This paper presents the numerical results of the isothermal gas flow in a 25 cm I.D. bench-scale and a 61 cm I.D. full-scale VC cold test models, along with the measured results for comparison. This investigation should provide a better understanding of mean flow, turbulence, and scaling features of the VC and help the design of the combustor. Since the gas turbulence in a strongly swirling flow exhibits a nonisotropic nature, a new version algebraic Reynolds stress model (ASM) developed earlier (Zhang et al., 1992) was employed in the present calculation.

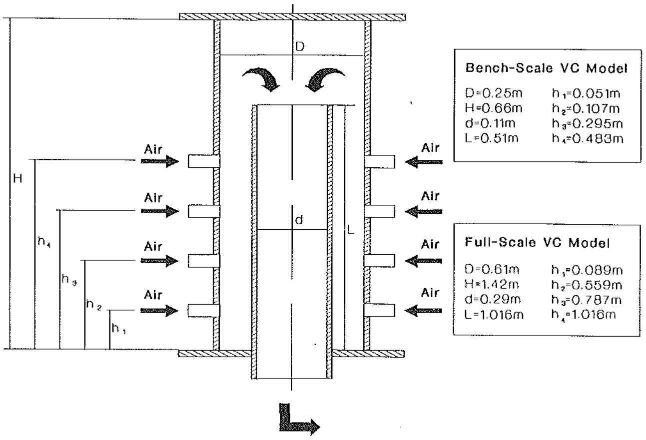

Fig. 1 Configuration of bench·scale and full·scale isothermal gas flow test models of the VC

Contributed by the Fluids Engineering Division for publication in the JOURNAL OF FLUIDS ENGINEERING. Manuscript received by the Fluids Engineering Division August 6, 1991. Associate Technical Editor: C. J. Freitas.

2 Governing Equations and Solution Procedure

Governing Equations. The analysis of the strongly swirling gas flow in the VC is primarily based on the time-averaged Navier-Stokes equations. The governing equation set includes six conservation partial differential equations: continuity, tangential, axial, and radial-momentum, turbulent kinetic energy (TKE), and TKE dissipation rate. Since our cold flow measurements revealed that the strongly swirling gas flow in the VC is generally axisymmetric (three-dimensional flow was only found locally in the close proximity of air injection ports (Nieh, 1990)), the governing equations are formulated in a two-dimensional axisymmetric cylindrical coordinate. The resultant equations can be expressed in a generalized form:

$$\frac{\partial}{\partial x}(\rho u \phi)+\frac{\partial}{r \partial r}(r \rho v \phi)=\frac{\partial}{\partial x}\left(\Gamma_{\phi x} \frac{\partial \phi}{\partial x}\right)+\frac{\partial}{r \partial r}\left(r \Gamma_{\phi r} \frac{\partial \phi}{\partial r}\right)+S_\phi \quad (1)$$

where ϕ stands for the generalized variables ($\phi = 1$, u, v, w, k, and ϵ, respectively, for each of the six governing equations); $\Gamma_{\phi x}$ and $\Gamma_{\phi r}$ being turbulent transport coefficients in x and r-direction; and S_ϕ being the source terms. The detailed expressions of these governing equations are given in Eqs. (2)–(7) in Table 1.

New Version ASM. It was found by some researchers that the k-ϵ model and the original ASM based on Rodi's approximation (Rodi, 1976) were not generally suitable for simulating strongly swirling flows in cylindrical coordinates (Sloan et al., 1986; Fu et al., 1988). The differential Reynolds stress transport equation model (DSM) can account for more physical processes but, in the meantime, it requires much extra computational effort to solve the six Reynolds stress transport equations simultaneously (Jones and Pascau, 1989). A new version ASM integrating the advantages of both original ASM and DSM was developed (Zhou et al., 1990; Zhang et al., 1992). It was obtained by reducing the DSM written in axisymmetric cylindrical coordinates into algebraic expressions, during which the swirl-related nongradient convection terms and the source terms were retained; while the diffusion terms and the gradient convection terms were treated in accordance with Rodi's approximation. Based on the observed flow features of $w \gg u$, $w \gg v$, and $\partial/\partial r \gg \partial/\partial x$ in most regions of the VC (Nieh, 1990), the resultant new version ASM was further simplified to an explicit form for easy solution. Table 2 gives this simplified form in 12 algebraic expressions (Eqs. (8)–(19)), which were used in the present calculations. The values of the six model constants used in Eqs. (2)–(19) are specified in Table 3. It is noted that the magnitudes of the model constant β in the new version ASM are chosen to be 0.8 and 0.6 for simulating the bench-scale cold flow model and the full-scale cold flow model, respectively.

Numerical Solution Procedure. The calculations in this paper were performed on the Catholic University's VAX 8650s computer using the flow subprogram of the CCVC (Coal Combustion in Vortex Chamber) computer program. The CCVC program was specifically developed for simulating the strongly swirling gas-particle flow and combustion (Nieh, 1990; Nieh and Zhang, 1991; Zhang et al., 1991). The hybrid scheme for the discretization of convection and diffusion terms, the SIMPLER strategy for pressure/velocity decoupling, and the under-relaxation TDMA line-by-line sweeping technique (Patankar, 1980) were utilized in the calculation. To ensure the stability and satisfactory convergence of the iterative processes, optimal under-relaxation factors for three velocity components ranging from 0.1 to 0.2 and TDMA sweeping direction were carefully selected. A nonuniform staggered grid system was used for the solution domain of a half vertical plane passing through the chamber axis. u and v velocities were stored at the midway between the grid nodes, and Reynolds stress components were stored in the regular grid nodes. To examine the error by numerical diffusion, two grid systems of 40 × 22 (880) nodes and 52 × 25 (1300) nodes in axial and radial-direction were employed in the calculation. Figure 2 shows the comparison of the gas tangential velocity profiles in the bench-scale model. Due to the large pressure gradient (or source term) in the vortex core region and the relatively strong turbulent diffusion in other regions of the combustor, the error by numerical diffusion was found small and relatively insignificant. The results for the two grid systems are quite close. Although higher order discretization schemes, such as QUICK (Leonard, 1979), may be used to improve the accuracy of the calculation, the present numerical scheme and the grid system were acceptable to predict the flow characteristics of the vortex combustor.

3 Calculation Examples: Cold Flow in the Vortex Chambers

Systematic measurements of the isothermal gas flow were conducted in the bench-scale and full-scale VC test models (Nieh, 1990). The strongly swirling aerodynamic flow fields in both models were simulated in this paper. Figure 1 shows schematically the configuration of the test chambers. They are made of coaxial Plexiglas tubes. The bench-scale model has a height of 66 cm and an inside diameter of 25 cm. The center tube of 11 cm diameter has an adjustable height ranging from 28 to 51 cm. Three sets of secondary air nozzles (four each) are provided at the 5 cm, 30 cm, and 48 cm levels measured from the bottom. Two primary air nozzles are set at the 11 cm level. The full-scale model has a height of 142 cm and an inside diameter of 61 cm. A center tube of 29 cm diameter is also made adjustable in its height and normally set at 71–102 cm in the tests. Four nozzles, at the 9 cm level from the bottom,

Nomenclature

D = inner diameter of VC chamber
d = inner diameter of center tube
H = height of VC chamber
h_1, h_2, h_3, h_4 = heights of nozzle set
k = turbulent kinetic energy (TKE)
L = height of center tube
p = static pressure
R = inner radius of VC chamber
r = radial coordinate from axis of VC chamber
u, v, w = axial, radial, and tangential components of mean velocity
u', v', w' = axial, radial, and tangential components of turbulent fluctuating velocity
x = axial coordinate from inner bottom of VC chamber
ϵ = TKE dissipation rate
μ = dynamic viscosity
ν = kinematic viscosity
ρ = density

Subscripts and Superscripts

e = effective
t = turbulent
x, r, θ = axial, radial, azimuthal coordinates
$\overline{}$ = time-averaged quantities

Table 1 Governing equations for gas flow using the new version ASM

Equation	ϕ	$\Gamma_{\phi x}$	$\Gamma_{\phi r}$	$S\phi$	Eq. No.
Continuity	1	0	0	0	(2)
x-Momentum	u	μ_e	$\mu_{e,xr}$	$\frac{\partial}{\partial x}\left(\mu_e \frac{\partial u}{\partial x}\right)+\frac{\partial}{r\partial r}\left(r\mu_{e,xr} \frac{\partial v}{\partial x}\right)$ $-\frac{\partial}{\partial x}(\rho\overline{u'u'})-2\frac{\partial}{\partial x}\left(\mu_t^{*} \frac{\partial u}{\partial x}\right)$ $-\frac{\partial p}{\partial x}$	(3)
r-Momentum	v	$\mu_{e,xr}$	μ_e	$\frac{\partial}{\partial x}\left(\mu_{e,xr} \frac{\partial u}{\partial r}\right)+\frac{\partial}{r\partial r}\left(r\mu_e \frac{\partial v}{\partial r}\right)$ $-\frac{\partial}{r\partial r}(r\rho\overline{v'v'})-2\frac{\partial}{r\partial r}\left(r\mu_t \frac{\partial v}{\partial r}\right)$ $-\frac{2\mu v}{r^2}+\frac{\rho w^2}{r}+\frac{\rho\overline{w'w'}}{r}-\frac{\partial p}{\partial r}$	(4)
θ-Momentum	w	$\mu_{e,\theta x}$	$\mu_{e,\gamma\theta}$	$-\frac{\rho v w}{r}-\frac{w}{r^2}\frac{\partial}{\partial r}(r\mu_{e,r\theta})$ $-\frac{\partial}{\partial x}\left((\overline{w'u'}+\mu_{t,\theta x}^{**}\frac{\partial w}{\partial x}\right)$	(5)
Turbulent Kinetic Energy	k	$\frac{\mu_e}{\sigma_k}$	$\frac{\mu_e}{\sigma_k}$	$G_k^{***}-\rho\epsilon$	(6)
TKE Dissipation Rate	ϵ	$\frac{\mu_e}{\sigma_\epsilon}$	$\frac{\mu_e}{\sigma_\epsilon}$	$\frac{\epsilon}{k}(C_{\epsilon_1}G_k-C_{\epsilon_2}\rho\epsilon)$	(7)

$$^{*}\mu_t = \frac{2}{3}\rho\lambda\frac{k^2}{\epsilon}$$

$$^{**}\mu_{t,\theta x} = \rho\lambda\frac{k}{\epsilon}\overline{u'^2}$$

$$^{***}G_k = -\rho\frac{\partial u}{\partial r}\overline{u'v'} - \rho r\frac{\partial}{\partial r}\left(\frac{w}{r}\right)\overline{v'w'}$$

$$\mu_{e,(ij)} = \mu_{t,(ij)} + \mu$$

are used for primary air injection. Three sets of nozzles (four each) are provided at the 56 cm, 79 cm, and 102 cm levels for secondary air injection. The two test chambers were designed to have geometric similarity in their major dimensions. However, protruded nozzles are used in the bench-scale model; while peripheral nozzles are used in the full-scale model. The major instrument used in the tests was a United Sensor DA&DAT 5-point directional (3-D) probe with four inclined manometers. Three velocity components (u, v, and w) and the static pressure (p) were measured with this probe. The errors of measurement are within 5 percent for p and w and 10 percent for u and v. The air flow rate through each set of nozzles were individually controlled and measured by SEE-FLO van type flowmeters in the bench-scale test model and by Kruz digital velocimeters in the full-scale test model (Nieh, 1990). The errors of air flow rate measurements are within 5 percent. Table 4 lists the calculation conditions for the two cases which were arranged the same as the test conditions in the bench-scale and full-scale models.

4 Results of Aerodynamic Characteristics

Figures 3 and 4 show the calculated distributions of mean flow properties including gas tangential (w), axial (u), and radial (v) velocities, static pressure (p), and streamlines in the bench-scale and the full-scale models, respectively. The open circles are the measured data points under the same conditions. Figures 5 to 6 show the calculated distributions of turbulent properties in the two models, including TKE and Reynolds stresses at two heights of the chamber.

Tangential, Axial, and Radial Velocities. As seen in Figs. 3 and 4, the calculated gas tangential and axial velocities are in generally good agreement with the measured data. Qualitative agreement in radial velocity is also achieved. It is noted that different scales for u, v, and w are used for clear presentation. The gas flow in the annular space (designated as Zone I) exhibits different features as that in the top cylindrical space (designated as Zone II). The tangential velocity are generally an order of magnitude larger than the axial and radial velocities in Zone I and in most regions of Zone II, indicating that the strong swirl dominates the flow in the VC. The weakly swirling flow can only be found in the vortex core region of Zone II where three velocity components are of the same order of magnitude. It is worth noting that due to the presence of the center tube this weakly swirling zone is blocked and effectively avoided in Zone I, giving a strong centrifugal force field and relatively uniform swirling velocity profiles for the entire Zone I. This is deemed one of the pertinent features of the VC gas flow, distinctly different from that of conventional cyclone combustors and swirl burners. The strong swirl in Zone I is attributed to the confinement of circular vertical walls on both sides of the annular space. In Zone II, the tangential velocity exhibits Rankine type of vortex flow, which has a

Table 2 Simplified form of the new version ASM for the VC flow

$$\overline{u'v'} = -\nu_{t,xr}\,\frac{\partial u}{\partial r} \tag{8}$$

$$\overline{v'w'} = -\nu_{t,r\theta}\, r\,\frac{\partial}{\partial r}\left(\frac{w}{r}\right) \tag{9}$$

$$\overline{u'w'} = -\lambda\,\frac{k}{\epsilon}\,\overline{u'^2}\,\frac{\partial w}{\partial x} - \lambda\,\frac{k}{\epsilon}\left[\left(\frac{\partial w}{\partial r} + \beta\,\frac{w}{r}\right)\overline{u'v'} + \frac{\partial u}{\partial r}\,\overline{v'w'}\right] \tag{10}$$

$$\overline{u'^2} = \frac{2}{3}\,k + \frac{2}{3}\,\lambda\,\frac{k}{\epsilon}\left[-2\,\frac{\partial u}{\partial r}\,\overline{u'v'} + r\,\frac{\partial}{\partial r}\left(\frac{w}{r}\right)\overline{v'w'}\right] \tag{11}$$

$$\overline{v'^2} = \frac{2}{3}\,k + \frac{2}{3}\,\lambda\,\frac{k}{\epsilon}\left\{\frac{\partial u}{\partial r}\,\overline{u'v'} + \left[\frac{\partial w}{\partial r} + (2+3\beta)\,\frac{w}{r}\right]\overline{v'w'}\right\} \tag{12}$$

$$\overline{w'^2} = \frac{2}{3}\,k + \frac{2}{3}\,\lambda\,\frac{k}{\epsilon}\left\{\frac{\partial u}{\partial r}\,\overline{u'v'} - \left[2\,\frac{\partial w}{\partial r} + (1+3\beta)\,\frac{w}{r}\right]\overline{v'w'}\right\} \tag{13}$$

$$\nu_{t,xr} = \frac{b_1 - a_1 b_2 r\,\frac{\partial}{\partial r}\left(\frac{w}{r}\right)}{1 - a_1 a_2\,\frac{\partial u}{\partial r}\, r\,\frac{\partial}{\partial r}\left(\frac{w}{r}\right)} \tag{14}$$

$$\nu_{t,r\theta} = \frac{b_2 - a_2 b_1\,\frac{\partial u}{\partial r}}{1 - a_1 a_2\,\frac{\partial u}{\partial r}\, r\,\frac{\partial}{\partial r}\left(\frac{w}{r}\right)} \tag{15}$$

$$a_1 = \frac{\left(\lambda\,\frac{k}{\epsilon}\right)^2\left[\left(\frac{7}{3} + 3\beta\right)\frac{w}{r} + \frac{2\partial w}{3\partial r}\right]}{1 + \left(\lambda\,\frac{k}{\epsilon}\right)^2\left[\frac{2}{3}\left(\frac{\partial u}{\partial r}\right)^2 + (1+\beta)\,\frac{w\partial w}{r\partial r} + (1+\beta)\beta\left(\frac{w}{r}\right)^2\right]} \tag{16}$$

$$a_2 = \frac{\frac{2}{3}\left(\lambda\,\frac{k}{\epsilon}\right)^2\frac{\partial u}{\partial r}}{1 + \frac{2}{3}\left(\lambda\,\frac{k}{\epsilon}\right)^2\left[\left(\frac{\partial w}{\partial r}\right)^2 + (4+6\beta)\,\frac{w\partial w}{r\partial r} + (1+6\beta+6\beta^2)\left(\frac{w}{r}\right)^2\right]} \tag{17}$$

$$b_1 = \frac{\frac{2}{3}\,\lambda\,\frac{k^2}{\epsilon}}{1 + \left(\lambda\,\frac{k}{\epsilon}\right)^2\left[\frac{2}{3}\left(\frac{\partial u}{\partial r}\right)^2 + (1+\beta)\,\frac{w\partial w}{r\partial r} + (1+\beta)\beta\left(\frac{w}{r}\right)^2\right]} \tag{18}$$

$$b_2 = \frac{\frac{2}{3}\,\lambda\,\frac{k^2}{\epsilon}}{1 + \frac{2}{3}\left(\lambda\,\frac{k}{\epsilon}\right)^2\left[\left(\frac{\partial w}{\partial r}\right)^2 + (4+6\beta)\,\frac{w\partial w}{r\partial r} + (1+6\beta+6\beta^2)\left(\frac{w}{r}\right)^2\right]} \tag{19}$$

Table 3 Turbulence model constants used in governing equations and ASM

β	λ	σ_k	σ_ϵ	C_{ϵ_1}	C_2
0.6–0.8	0.135	0.9	1.22	1.44	1.92

forced vortex in the core region and a free vortex in the outer region. The tangential velocity increases linearly with the radius in the forced vortex and decreases inversely with the radius in the free vortex. The interface of the combined vortexes gives the highest swirling velocity (peak of the profile). The gas axial and radial velocities are generally small in magnitudes, but they go through a rapid and frequent change in the chamber.

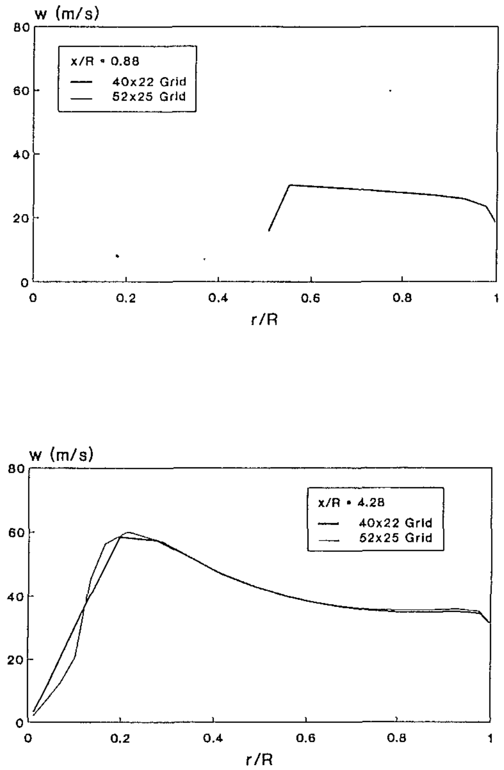

Fig. 2 Effect of grid refinement on gas tangential velocity

Table 4 Test and calculation conditions for the bench-scale and full-scale VC models

Parameter	Magnitude
1. Bench-scale VC model	
Air flow rate distribution, m^3/hr	226/0/226/226
Inlet air tangential velocity, m/s	24.6/0/24.6/24.6
Inlet averaged tangential velocity, m/s	24.6
Air temperature, K	300
2. Full-scale VC model	
Air flow rate distribution, m^3/hr	678/681/680/0
Inlet air tangential velocity, m/s	25/25.1/25.1/0
Inlet averaged tangential velocity, m/s	25.1
Air temperature, K	300

Local flow recirculations occur alternatively in both Zones I and II. The repeated acceleration and deceleration of the flow in axial and radial directions are caused by the multistage injection of air and the 180 deg turn of main flow at the center tube inlet. These results confirm that the gas flow in the VC is largely in the "developing" mode. This is advantageous for gas-gas and gas-particle mixing and heat/mass transfer, and should be regarded as another pertinent feature of the VC gas flow.

Static Pressure. As shown in Figs. 3(*b*) and 4(*b*), the calculated distributions of gas static pressure are in good agreement with the bench-scale model measurements and in qualitatively agreement with the full-scale model measurements. The pressure profiles in Zone I is relatively uniform, which is primarily due to the blockage of the weakly swirling zone by the center tube. The pressure in Zone II exhibits a typical profile of cyclonic flows. It drops rapidly in the core region, indicating a large radial pressure gradient and energy dissipation there. The contour plot of the static pressure for both models are shown in Figs. 3(*c*) and 4(*c*). The straight vertical lines illustrate the pressure stratification in this strong centrifugal force field, which was verified in the cold flow measurements (Nieh, 1990). The calculated net pressure drop

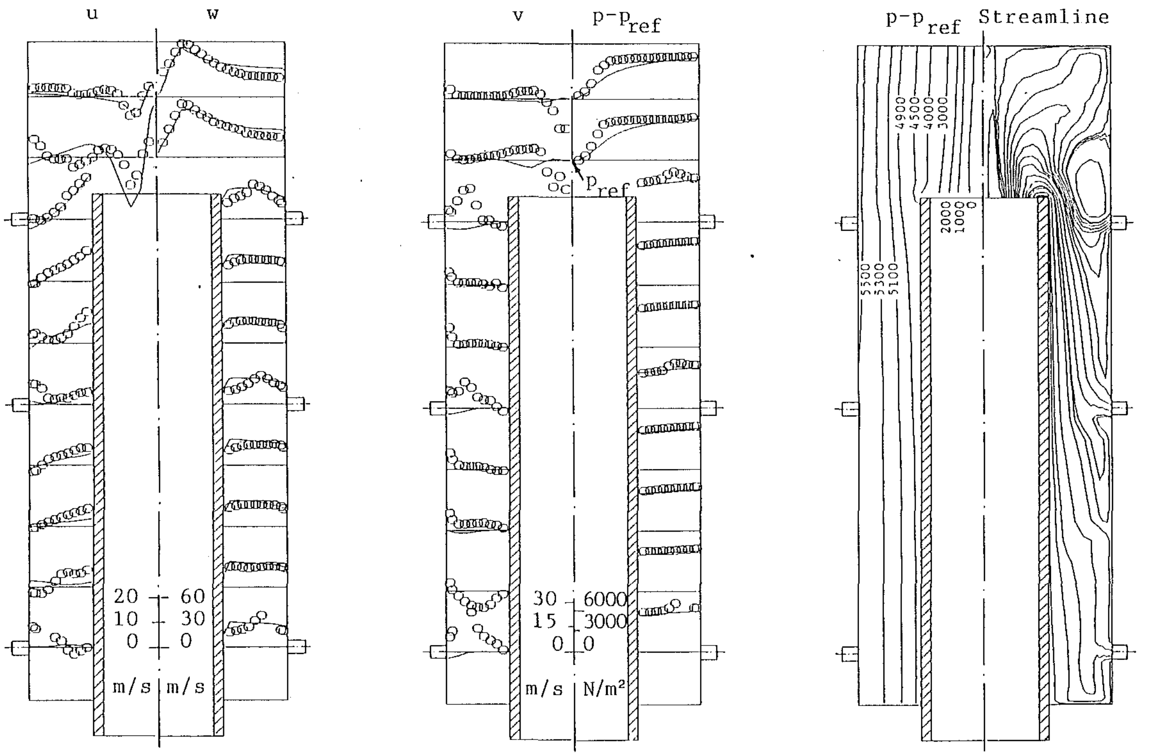

(a) Axial and Tangential Velocities (b) Radial Velocity and Static Pressure (c) Contour Plot of Static Pressure and Streamline

Fig. 3 Gas velocities, static pressure, and streamline in the beach-scale VC model

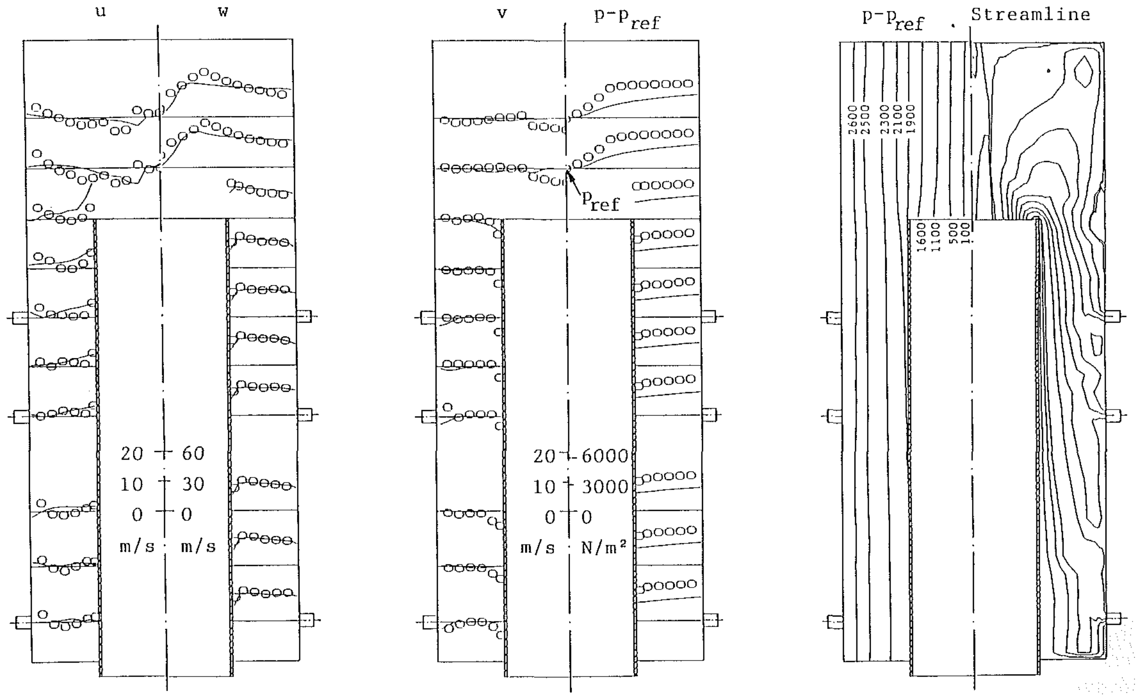

(a) Axial and Tangential Velocities (b) Radial Velocity and Static Pressure (c) Contour Plot of Static Pressure and Streamline

Fig. 4 Gas velocities, static pressure, and streamline in the full-scale VC model

through the bench-scale model is 6.3×10^3 N/m^2, which agrees with the measured data of 6.6×10^3 N/m^2. The pressure drop is 2.7×10^3 N/m^2 for the full-scale model, which is close to the measured value of 4.1×10^3 N/m^2.

Streamlines. The streamlines in Figs. 3(*c*) and 4(*c*) show the main flow patterns in the bench-scale and full-scale VC models. They were qualitatively verified by the cold flow measurements and observations (Nieh, 1990). The main flow is

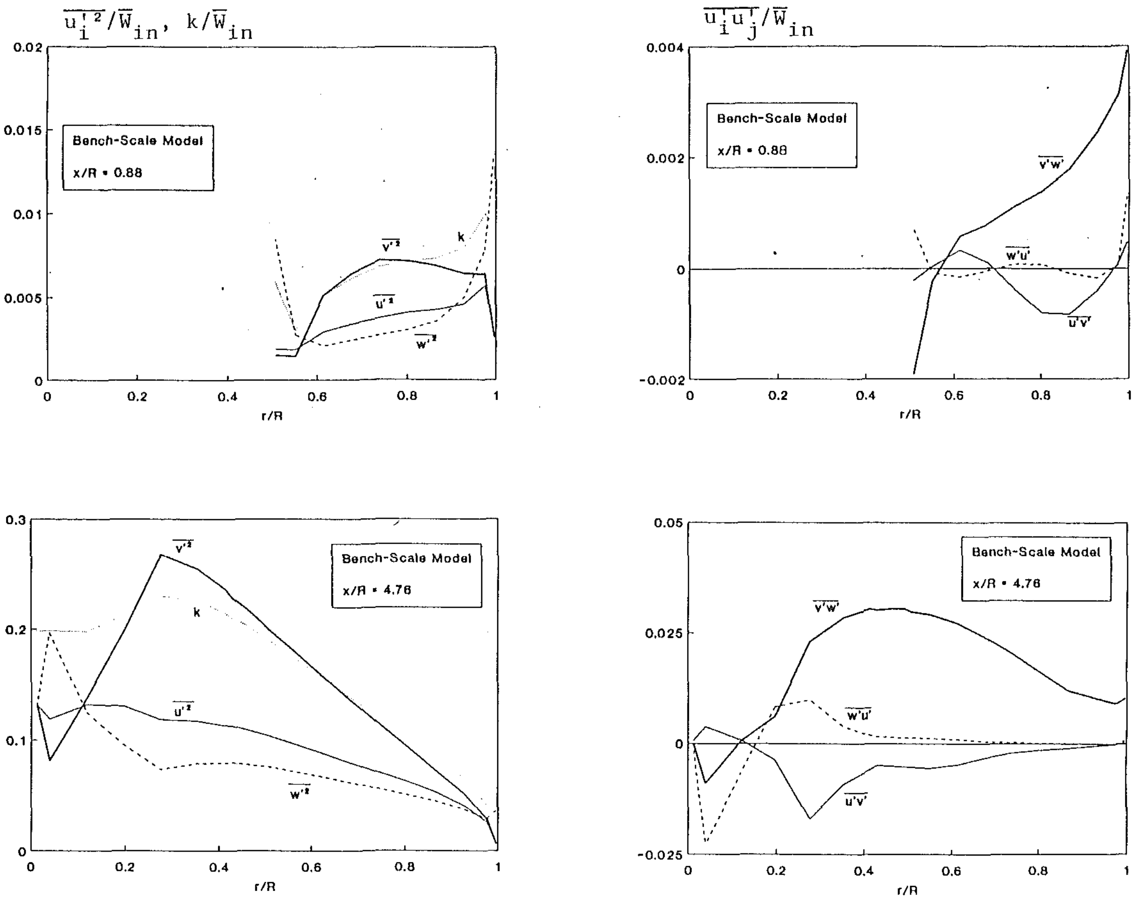

(a) Normal Reynolds Stresses and Turbulent Kinetic Energy

(b) Shear Reynolds Stresses

Fig. 5 Reynolds stresses and turbulent kinemaic energy in the bench-scale VC model

established by the primary/secondary air injection through multiple nozzles. It spirally ascends through the annular space, and turns 180 deg into the center tube. Along with the movement of the main flow, a number of recirculation zones are found in the vicinity of injecting nozzles, at the chamber bottom, at the top entrance of the center tube, and in the vortex core region of Zone II. The recirculating flows in the VC are primarily due to the arrangement of multiple air injection and the coaxial center tube of the combustor. Axial/radial recirculations associated with the strong swirl are beneficial to fuel ignition, flame stabilization, heat/mass transfer, and char burnout. The recirculating flow is therefore considered as one of the pertinent features of the VC gas flows.

Turbulence Characteristics. Figures 5 and 6 show the calculated TKE (k), normal Reynolds stresses ($\overline{u'^2}$, $\overline{v'^2}$, and $\overline{w'^2}$, and shear Reynolds stresses ($\overline{u'v'}$, $\overline{v'w'}$, and $\overline{w'u'}$) at two different heights of the bench-scale and full-scale VC models. The data shown in the figures were normalized by the averaged inlet tangential velocity for each case. Since the magnitudes of Reynolds stresses change greatly along the combustor height, different scales were used in drawing figures of the same quantity. For the normal Reynolds stresses in Zone I, it is seen that the peaks of both profiles of $\overline{u'^2}$ and $\overline{v'^2}$ occur near the center of the annular space, while the peak of $\overline{w'^2}$ occurs on the side walls. The shear stresses near the chamber wall are generally higher than those near the center tube wall. In Zone II, a clear peak of the $\overline{v'^2}$ profile can be found in the region of $0.2 \leq r/R \leq 0.5$, which is also found true for the $\overline{v'w'}$ profile. Comparing the relative magnitudes of Reynolds stresses, it is seen that $\overline{v'^2}$ is the largest followed by $\overline{u'^2}$ and $\overline{w'^2}$ in most regions of Zones I and II, while in the vicinity of the walls and the chamber axis $\overline{w'^2}$ is the largest. This reveals the nonisotropic turbulence nature of the strongly swirling flow. Furthermore, the absolute magnitudes of shear stress $\overline{v'w'}$ is found generally larger than both $\overline{u'v'}$ and $\overline{w'u'}$; and $\overline{u'v'}$ is generally larger than $\overline{w'u'}$ in Zones I and II. These are desirable from combustion viewpoint because the weak convection of main flow in radial direction is now supplemented by a relatively strong turbulent diffusion. As seen in Figs. 5 and 6, TKE and the absolute values of Reynolds stresses are found to increase along the flow direction. For example, the dimensionless turbulence intensity ($[2/3k]^{1/2}/W_{in}$) increases approximately from 5 percent at $x/R = 0.88$ (bottom of Zone I) to 30 percent at $x/R = 4.76$ (Zone II) in the bench-scale model, and from 5 percent at $x/R = 1$ (bottom) to 20 percent at $x/R = 4$ (Zone II) in the full-scale model. This indicates that the gas turbulence is enhanced by the progressive air injection, which is another pertinent feature of the VC gas flow.

Scaling Property. The two cases being studied share the geometric similarity in their major dimensions, as can be seen in Table 5. The dynamic similarity between the bench-scale and full-scale models is of great interest to the scale up (or down) of the VC design. It is seen from Figs. 3 and 4 that the profiles of the tangential velocity and the static pressure for both models are quite similar, which lends support to the dynamic similarity of the gas flow between the two models. The similarity of the axial and radial velocities is, however, not as clear as the tangential velocity. This may be caused by

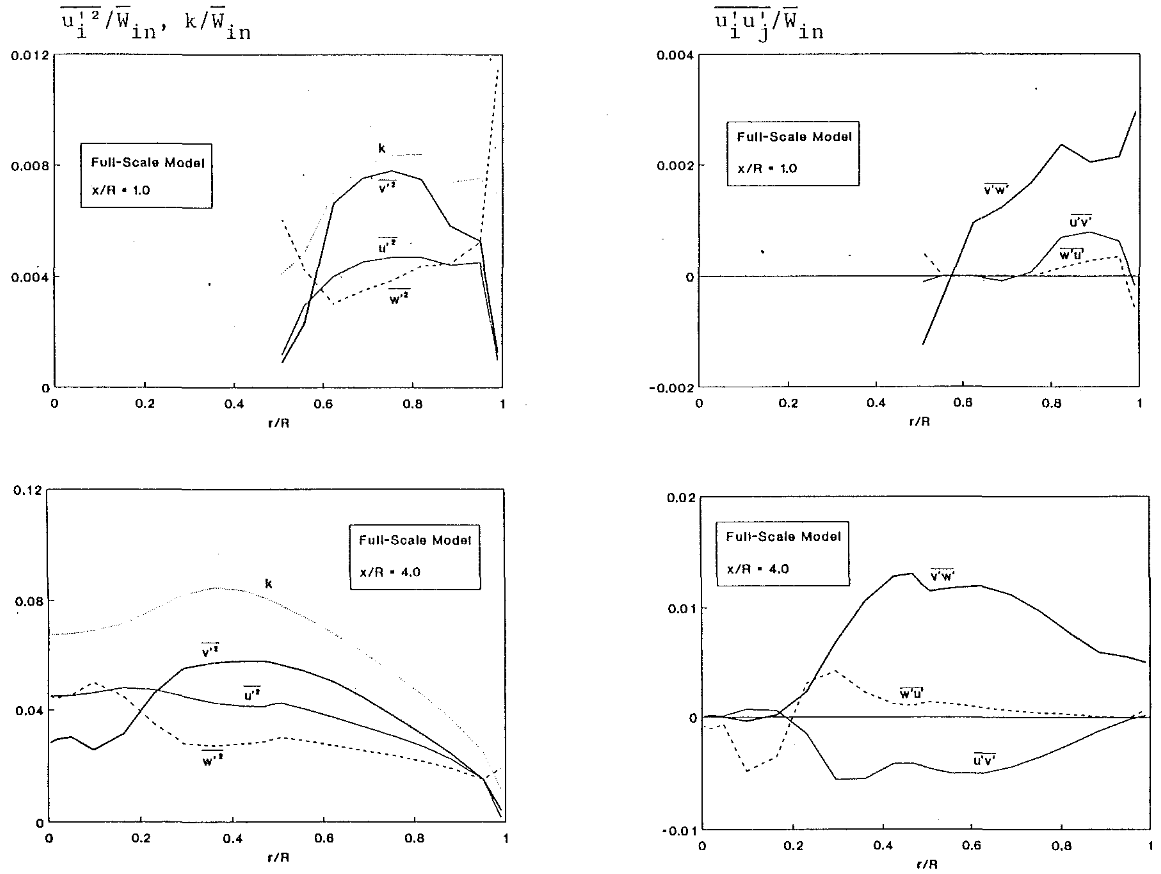

(a) Normal Reynolds Stresses and Turbulent Kinetic Energy

(b) Shear Reynolds Stresses

Fig. 6 Reynolds stresses and turbulent kinetic energy in the full-scale VC model

Table 5 Comparison of major dimensions for the bench-scale and full-scale VC models

VC Model	H/D	D/d	h_1/H	h_2/H	h_3/H	h_4/H	L/H
Bench-scale	2.6	2.3	0.08	0.16	0.45	0.73	0.77
Full-scale	2.3	2.1	0.06	0.39	0.55	0.72	0.72

the multiple air injection and the "developing" nature of the VC gas flow. The similar main flow patterns and local recirculating flows as seen in the streamline plots in Figs. 3(*c*) and 4(*c*) also shed light to the dynamic similarity of the two models. If the turbulent quantities in Figs. 5 and 6 are examined further, they can also be found quite close between the two models. In general, the dynamic similarity exists in geometrically-similar VC test models of diameter ratio of 1:2.4 and volume ratio of 1:12.4. This finding should help in scaling up (or down) a successful VC design. The overall similarity of swirling flow and combustion in the coal-fired VC is an on-going study at the Catholic University. More evidence on the scaling characteristics of particle flows, heat transfer, and combustion among VCs of different thermal inputs will be reported at later dates.

5 Conclusion

The strongly swirling isothermal gas flows in a 25-cm I.D. bench-scale VC test model and a 61-cm I.D. full-scale VC test model were simulated by using a new version ASM. The calculated results are found in generally good agreement with the measured data. The basic flow characteristics of the VC are summarized below:

The gas flow in the VC is characterized as a strongly swirling, developing, recirculating, and nonisotropic turbulent flow. The tangential velocity dominates the flow. Local recirculating flows are found near the injecting nozzles, at the chamber bottom, at the top entrance of the center tube, and in the vortex core region of Zone II.

The gas flow shows different features in the annular space (Zone I) and in the top cylindrical space (Zone II). The tangential velocity exhibits a relatively uniform profile in Zone I and Rankine type of vortex in Zone II. The static pressure also shows a relatively uniform profile in Zone I and cyclonic type profile in Zone II. The magnitudes of turbulent intensities in Zone II are generally several times larger than those in Zone I.

The dynamic similarity in terms of gas velocity, pressure, flow pattern, and turbulent quantities is found generally true for geometrically-similar VC models of scaling ratio of 1:2.4.

Acknowledgment

This study was funded primarily by the Pittsburgh Energy Technology Center, U.S. Department of Energy under Contract No.: DE-AC22-87PC79661. Mr. Anthony Mayne was the technical project officer. The test data used in this paper were taken from the cold flow measurements conducted by C. S. Zhao and A. Q. Zhu. The authors are grateful to the above supports and help.

References

Fu, S., Huang, P. G., Launder, B. E., and Leschziner, M. A., 1988, "A Comparison of Algebraic and Differential Second-Moment Closures for Axisymmetric Turbulent Shear Flows With and Without Swirl," ASME JOURNAL OF FLUIDS ENGINEERING, Vol. 110, pp. 216–221.

Jones, W. P., and Pascau, A., 1989, "Calculation of Confined Swirling Flows with a Second Momentum Closure," ASME JOURNAL OF FLUIDS ENGINEERING, Vol. 111, pp. 248–255.

Leonard, B. P., 1979, "A Stable and Accurate Convective Modelling Procedure Based on Quadratic Upstream Interpolation," *Computer Methods in Applied Mechanics and Engineering*, Vol. 19, pp. 409–425.

Nieh, S., 1990, "Development of a Vortex Combustor (VC) for Space/Water Heating Applications (Cold Flow Modeling)," final report to PETC, U.S. DOE under Contract No.: DE-AC22-87PC79661.

Nieh, S., and Fu, T. T., 1990a, "Development of a Vortex Combustor for Commercial Space/Water Heating Applications," *Proc. 6th Annual Coal Preparation, Utilization, and Environmental Control Contractors Conference*, PETC, DOE, Pittsburgh, PA, pp. 135–142.

Nieh, S., and Fu, T. T., 1990b, "A Non-Slagging Vortex Combustor Firing Coal-Water Fuel for Commercial Heating Applications," *Proc. 7th International Coal Conference*, Pittsburgh, PA, pp. 223–232.

Nieh, S., 1991, "An Innovative Vortex Combustor Firing Dry Pulverized Coals and Their Slurries," *Proc. 2nd International Symposium on Coal Combustion*, Beijing, China, pp. 726–733.

Nieh, S., and Zhang, J., 1991, "Numerical Simulation of a Vortex Combustor Firing Dry Ultrafine Coal at 0.6 MW Thermal Input," *Combust. Sci. Tech.*, Vol. 77, pp. 59–71.

Patankar, S. V., 1980, *Numerical Heat Transfer and Fluid Flow*, Hemisphere Publishing Co., New York.

Rodi, W. A., 1976, "New Algebraic Relation for Calculating the Reynolds Stresses," *Z. Angew. Math. Mech.* (*ZAMM*), Vol. 56, pp. 219–221.

Sloan, D. G., Smith, P. J., and Smoot, L. D., 1986, "Modeling of Swirl in Turbulent Flow System," *Prog. Energy Combust. Sci.*, Vol. 12, pp. 163–250.

Zhang, J., Hu, Z., and Nieh, S., 1991, "Simulation of Flow and Combustion Processes in a 44 kW Coal-Fired Vortex Combustor," *Proc. 2nd International Symposium on Coal Combustion*, Beijing, China, pp. 303–309.

Zhang, J., Nieh, S., and Zhou, L., 1992, "A New Version of Algebraic Stress Model for Simulating Strongly Swirling Turbulent Flows," to be published in *Numerical Heat Transfer*.

Zhou, L., Nieh, S., and Yang, G., 1990, "Modeling of Vortexing Gas-Particle Flows, Combustion, and Flow Field Predictions," *Chinese J. Engineering Thermophysics*, Vol. 2, pp. 131–141.

Novel Optical Fiber Installation by Use of Spiral Airflow

K. Horii
Mem. ASME

Y. Matsumae

Shirayuri Women's College,
Tokyo, Japan

K. Ohsumi
Toa Kikai Kogyo Co., Ltd.,
Yamaguchi, Japan

X. M. Cheng

S. Kage

B. Hashimoto

Waseda University,
Tokyo, Japan

A high performance apparatus for installing optical fiber has been developed. With this apparatus, a 2 mm-diameter optical fiber was blown through a 6 mm-diameter rolled tube over a distance of 1200 meters, which is longer than the 700 meters achieved by the best conventional techniques. The heart of the apparatus is a novel nozzle with an annular slit and a conical cylinder to create a spiral airflow. In the spiral flow, the back flow of air is prevented due to the Coanda effect and the fiber scraping along the tube wall is minimized, owing to the ordered flow structure, leading to effective fiber installation. To obtain a spiral flow, pressurized air is forced into the buffer area of a nozzle and then through the angled annular slit into the tube entrance. Due to the Coanda effect of the annular jet from the slit attaching to the nozzle walls and the conical cylinder, the downstream flow in the tube develops a highly stable spiral structure with a steep axial velocity distribution that is more ordered than typical turbulent tube flows at the same mass-flow rate.

1 Introduction

Installation of optical fibers through a long thin tube is a challenge in the telecommunication industry. One of the conventional techniques is the "pig" method. In this method, a solid pig is attached to the fiber, which is then forced through the tube by back pressure. This method is effective for short and straight tubes. However, it is ineffective for tubes with bends or variable tube cross section.

Many techniques including the pig method have been employed to install an optical fiber through a 6 mm-diameter rolled tube over distances of 1000 meters, but none is found to be completely satisfactory. This newly developed system using a spiral flow has proven to be completely successful.

2 Experimental Program

The objectives of the experiment are to elucidate the mechanisms of effective fiber installation by studying the influence of characteristics of fluid flow on fiber motion and to measure the installation length of an optical fiber with both the traditional system and the new system. The heart of the new system is its fluid dynamic control using a new spiral device which prevents back flow of air and avoids fiber scraping of the walls. On the other hand, the traditional system depends on mechanical control using a hypodermic needle and a pair of wheels. The main differences in system features are outlined in Table 1.

2.1 Traditional System. The traditional equipment required to install fiber packages by compressed air is shown in Fig. 1 (Hornung et al., 1986). A pressurized metal block houses a pair of electrically driven rubber tire wheels, which draw the fiber package in through an air sealing hypodermic needle. Compressed air is let into the block and carries the fiber package into a preinstalled tube.

2.2 New System. The new system consists of two Coanda

Table 1 The main differences in system

	traditional system	new system
installation force	turbulence pipe flow	ordered pipe flow with spiral sturucture
flow direction	flow with a back flow	smooth flow into downstream
sealing method against back flow	mechanical sealing with hypodermic needle	fluid dynamic sealing due to the Coanda effect
minimization of fiber scraping	mechanical holding with a pair of wheels	ordered flow with a spiral structure
role of wheels	inportant role to overcome pressure drop and friction due to hypodermic needle to provide the force to draw the fiber off its drum	auxiliary to align the entering fiber

---

Contributed by the Fluids Engineering Division for publication in the JOURNAL OF FLUIDS ENGINEERING. Manuscript received by the Fluids Engineering Division June 24, 1991. Associate Technical Editor: F. M. White.

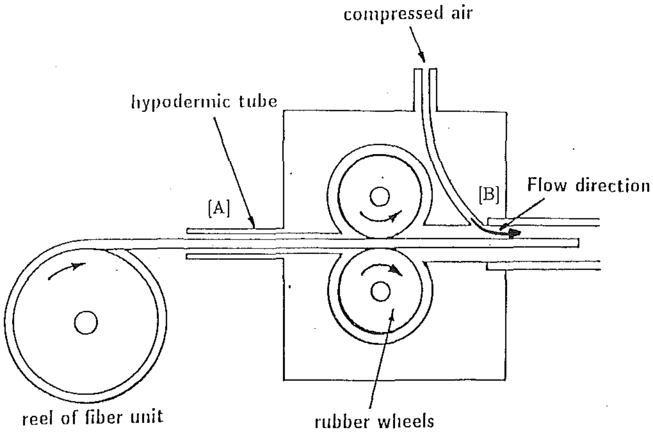

Fig. 1 Traditional system

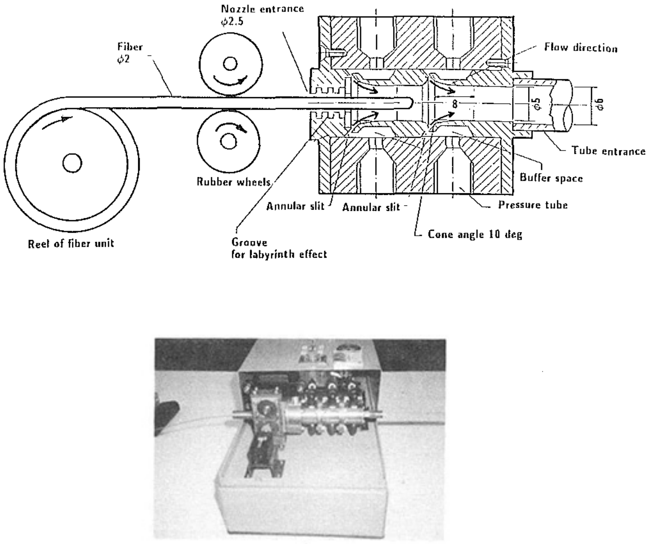

Fig. 2 New system

spiral devices connected in series (Horii, 1988). The geometry and dimensions of the spiral device are shown in Fig. 2. The device consists of a nozzle with an annular slit connected to conical cylinder, which is attached to the entrance of a preinstalled tube.

Pressurized air is forced through the sides of the device into the buffer area and then through the angled annular slit into the tube entrance. This annular flow creates a fiber-port suction which brings in additional air flow through the nozzle entrance.

In installing an optical fiber through a tube over distances of many meters using the conventional device, the pressurized air tends to back flow out of the nozzle entrance. However, in the spiral device, due to the Coanda effect resulting in the annular jets attaching to the nozzle walls and the labyrinth effect of the complex flow pathway, the air is kept from flowing out of the nozzle entrance and the downstream flow with a spiral structure is developed. This spiral flow is much more ordered than typical turbulent tube flow at the same mass-flow rate (Horii, 1990; Horii, 1991). This ordered spiral flow orients the fiber axially and positions the fibers at the center of the tube, and carries them a long distances without fiber scraping and back flow of air.

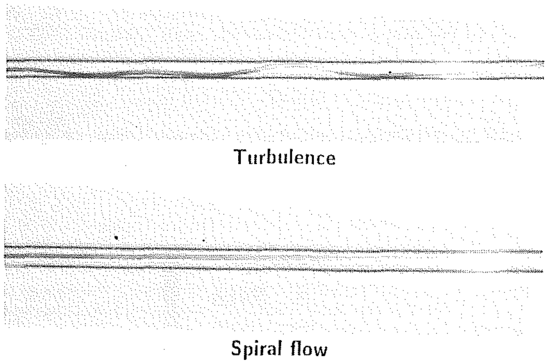

Fig. 3 Fiber motion in both flows

2.3 Visualization of Fiber Motion in Both Flows. Visual inspection showed that the spiral flow pattern persists for about 50m from the tube inlet and the flow was then gradually converted to ordinary turbulent flow. To study the influence of flow characteristics on fiber motion, both the turbulence and the spiral flow were tested at a mean air velocity of 15 m/s. As shown in Fig. 3, the spiral-flow device orients and positions the fiber near the axis, greatly reducing its friction against the walls. However, in the turbulent tube flow, the fiber undergoes irregular transverse vibrations, forming a wave which scrapes against the tube walls and fails to blow through.

2.4 Experimental Procedure and Fiber Installation Results. Experiments with long 6 mm-diameter tubes, which were coiled and varied to 500 meters and 1000 meters in length, were performed to test passage of an optical fiber 2 mm in diameter weighing 2.0 g/m. Airflow was generated by using both the spiral device and a simple constant-diameter turbulent-flow entrance device. The device pressure was raised to 500 kPa-gage at the inlet of the tube to develop an average pipe flow velocity of 47 m/s and 30 m/s, corresponding to a tube-length of 500 m and 1000 m at the exit of the tube, respectively. In the first experiment, the fibers were installed through 500 meters of polyethylene tube coiled with a radius of 100 cm. With normal turbulent flow, the fibers could not be installed in a shorter time than the fastest time which was

Nomenclature

B = constant
C_d = drag coefficient
F_d = drag on the arbitrary part of the fiber, N
F_{dH}, F_{dL} = sum of the drags, N
$H(r_H,\theta_H,z_H)$ = cylindrical coordinate
K = constant
l = length of fiber from M to H, L, m
lm = length of fiber, m
$L(r_L,\theta_L,z_L)$ = cylindrical coordinate
M = moment of the centroid, Nm
M_H = sum of the moments of upper half of the fiber, Nm
M_L = sum of the moments of lower half of the fiber, Nm
s = subtle square, m^2
S = swirl number
v = mean velocity, m/s
$v_{z_{\max}}$ = maximum axial velocity, m/s
$v_{\theta_{\max}}$ = maximum azimuthal velocity, m/s
v_H = axial velocity at the upper half of the fiber, m/s
v_L = axial velocity at the lower half of the fiber, m/s
w = diameter in project of the fiber, m
β = angle between the fiber and the y-axis on the x-y plane, deg
ρ = density, $kg \cdot s^2/m^4$

13 s under the best conditions. In contrast, using the spiral-flow device, the fiber was installed through the tube in only 8 minutes under the best condition and 10 minutes on the average of 20 measurements for a mean installation speed of 0.83 m/s.

In the second experiment, 1000 meters of 6 mm-diameter polyethylene tubes made by connecting two 500 meters tube coiled into a radius of 100 cm in series were used. The normal turbulent flow could not install the fibers because the fibers scraped, meandered, and stuck to the tube wall in a short distance from the entrance.. However, the spiral nozzle sucked in fibers and installed them through the 1000 meters of the tube in 50 minutes on the average of 20 measurements, for mean installation speed of 0.17 m/s.

3 Discussion

From fluid dynamics viewpoint, this high performance installation system must control two factors to increase the efficiency of the drag force acting on the fibers; namely, fluid velocity distribution and instability to reduce fiber scraping, and back flow of air.

3.1 Effect of Spiral Flow on Reducing Fiber Scraping. To minimize fiber scraping, the traditional system employs a mechanical method using rubber wheels, which are housed in the compressed area. The wheels must be positioned between the hypodermic tube [*A*] and the compressed air entrance [*B*] in Fig. 1, to minimize the fiber vibration caused by flow instability. In the spiral flow system, the flow is oriented axially and positioned at the center of the tube section, resulting in less contact with the inner wall and scraping (Fig. 3).

3.2 Annular Jet Due to the Coanda Effect and Back Flow Control. In the traditional system, the back flow of air has to be controlled by using an air sealing hypodermic needle set in *A* (Fig. 1), because the fluid tends to flow back in the *A* direction due to the friction of the long tube. This sealing method causes a pressure drop and friction in the hypodermic needle, resulting in a complex sealing system and loss in fiber installation efficiency.

In the new system, the Coanda effect, created by the special nozzle with an annular jet attached to the nozzle walls, generates a smooth spiral flow downstream with little back flow. The labyrinth effect due to the complex pathway of the inlet air through the device further prevents any back flow. Thus, through the Coanda and labyrinth effects, the spiral device becomes a simple yet effective back flow controlling system.

3.3 Application to Optical Fiber Installation. The efficiency of optical fiber installation is determined by the drag force and the friction force. The drag force arises from the friction between the fluid and the fiber, and is the motive force to blow the fiber through the tube. The friction between the tube wall and the fiber impairs the installation of fiber. Thus, the net force for fiber installation equals the drag force minus the friction. For successful fiber installation, this net force must be positive and is the larger the better.

The relative importance of these two opposite force depends on the location of the tube. In the first part of the tube, the flow velocity is low, therefore the drag force is small. As a result, for the efficient installation, it is critical to reduce the friction to obtain a positive and large net force. This is accomplished by the use of the spiral flow.

In the latter part of the tube, the static pressure decreases and the fluid flow velocity increases, leading to an increased drag force. This increased drag force can overcome the friction between fiber and tube wall caused by the turbulent flow. Therefore, the breakdown of spiral flow does not significantly impair the efficiency of optical fiber installation.

There is no significant twisting of the optical fiber in the spiral flow. The transmission characteristics of the fiber is the same as that installed by the conventional method. Significant twisting of the optical fiber would have resulted in transmission degradation.

The twisting of optical fiber is determined by the intensity of the swirling flow and the stiffness of optical fiber. The intensity of swirling flow can be quantified by use of swirl numbers,

$$S=2\left(\frac{v_{\theta_{\max}}}{v_{z_{\max}}}\right)\Bigg|\left[4-\left(\frac{v_{\theta_{\max}}}{v_{z_{\max}}}\right)^2\right]$$

For the spiral flow, the swirl number is 0.3 which is too low to twist the optical fiber because the optical fiber is rather stiff.

4 Theoretical Analysis

The fiber installation efficiency is mainly determined by the friction between the tube wall and fiber due to fiber scraping. This friction is particularly important at the first part of the tube where the drag force is small. To discuss the fiber scraping at the first part of tube, the moment acting on the fiber due to the velocity profile has been analyzed, because the scraping is caused by the moment of rotations.

4.1 Moment Acting on Fiber. The theoretical analysis focuses on flow from the nozzle outlet. A single phase flow is used in order to simplify this analysis.

An arbitrary part of the fiber shall be $2lm$ in length. The following assumptions were made:

(1) Only the force due to the axial velocity is considered; the others are ignored.

(2) Since the fiber is homogeneous, the geometric central point corresponds to the centroid.

(3) Since the fiber width is sufficiently narrow compared to the nozzle diameter, v_z, the velocity in the axial section is uniform.

(4) ρ = const

Various drag values from the axial velocity profile were applied to the fiber in the spiral flow, as shown in Fig. 4; then the drag of the subtle square $ds = wdl$ was calculated. The moment M is obtained as follows:

$$dF_d=\frac{1}{2}C_d\rho v^2ds=\frac{1}{2}C_d\rho wv^2dl$$

$$dM=ldF_d=\frac{1}{2}C_d\rho wv^2ldl \tag{1}$$

where ρ is density and v is mean velocity. Since $v = v(r, z)$ and this flow is axisymmetric and constant in time, the effect of (t, θ) is ignored.

The mean axial velocity of the spiral flow is replaced by $v = Kz + Br^2$. The sum of the drags, F_{dH}, is given as

$$\sum F_{dH}=\frac{1}{2}C_dw\rho\cos\beta\int_0^{lm}v_H^2dl \tag{2}$$

where v_H is the axial velocity at the upper half of the fiber measured from the centroid and is obtained by

$$v_H=Kz_H+Br_H^2$$

M_H, the sum of the moments of the upper half of the fiber, is given by

$$M_H=\frac{1}{2}C_dw\rho\cos\beta\int_0^{lm}v_H^2ldl$$

Similarly, for the lower part of the fiber from the fiber centroid, F_{dL}, v_L, and M_L are given by the following equations:

$$\sum F_{dL}=w\rho\cos\beta\int_0^{lm}v_L^2dl \tag{3}$$

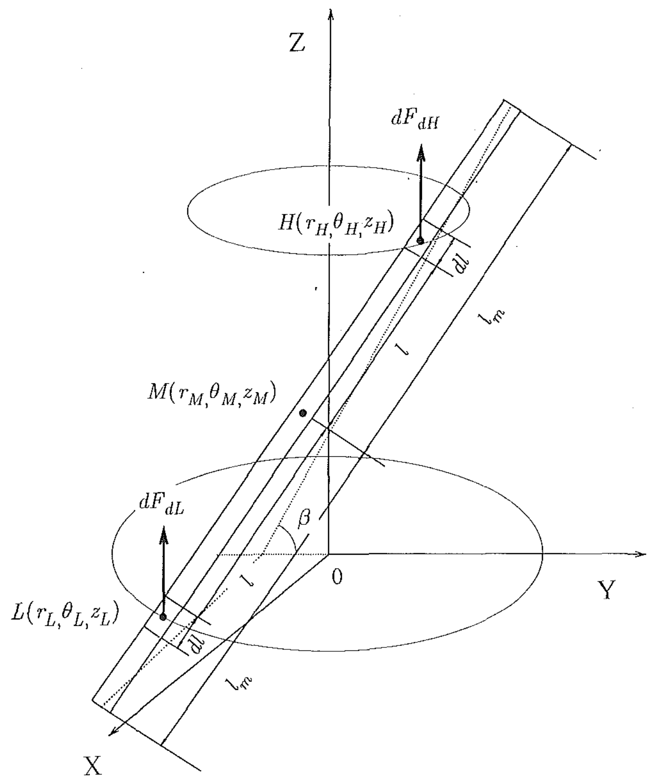

Fig. 4 Force on fiber in coordinate system

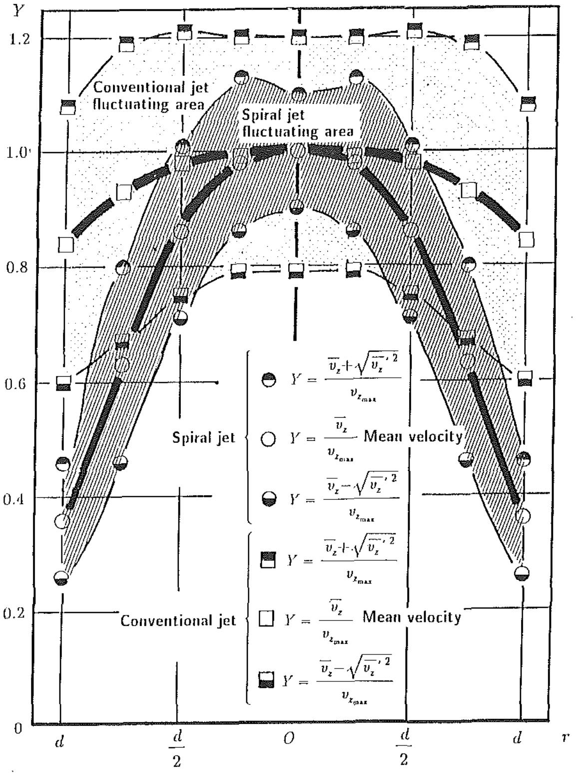

Fig. 5 Velocity profile of both jets

$$v_L = Kz_L + Br_L^2$$

$$\sum M_L = \frac{1}{2} C_d w\rho\cos\beta \int_0^{lm} v_L^2 l\,dl$$

The sum of the moments of the centroid P is obtained by

$$\sum M = \frac{1}{2} C_d w\rho\cos\beta \int_0^{lm} l(v_H^2 - v_L^2)\,dl$$

The condition for the fiber to stabilize in the flow is $\Sigma M = 0$. Figure 5 shows the axial velocity profile in both flows. It can be seen that the possibility of taking $v_H^2 - v_L^2$ to 0 on the fiber in the spiral flow is low, because the velocity profile in spiral flow is steeper than that in turbulence, resulting in the decrease of the fiber scraping in the first part of the tube.

5 Conclusion

A new system using spiral flow for fiber installation has been developed. A device with an annular slit and conical cylinder creates a spiral air flow that helps blow a 2mm-diameter optical fiber through a 6mm-diameter rolled tube over distances of 1200 meters.

The mechanism and operation of the new equipment is simplified due to fluid dynamic control. The new system does not require a pair of wheels to draw the fiber package off its drum and minimize the scraping of fiber, because an ordered spiral-flow plays in place of wheels. Furthermore, removing the air sealing hypodermic needle, because of the annular jet attached to the nozzle walls due to the Coanda effect, prevents a back flow.

This high performance, simplified system for fiber installations is achieved by the ordered structure of spiral-flow and the Coanda effect.

Acknowledgments

The authors are pleased to acknowledge the valuable help given by Prof. Frank M. White (University of Rhode Island) and Prof. Yasuhiko Aihara (University of Tokyo).

References

1 Horri, K., 1988, U.S. Pat. No. 4,721,126, U.K. Pat. No.2, 180,957.

2 Horii, K., 1990, "Using Spiral Flow for Optical Cord Passing," *Mechanical Engineering*, ASME, Vol. 112, No. 8, pp. 68–69.

3 Horii, K., Matsumae, Y., Cheng, X. M., Takei, M., Yasukawa, E., and Hashimoto, B., 1991, "Focusing Phenomenon and Stability of Spiral-Flow Jet," *Transactions of the Japan Society for Aeronautical and Space Science*, Vol. 33, No. 102, pp. 141–153.

4 Hornung, S., Cassidy, S. A., Yennadhiou, P., and Reeve, H. M., 1986, "The Blown Fiber Cable," *IEEE Journal of Sel Areas Communications*, Vol. 4, No. 5, pp. 679–685.

Study of Branched Turboprop Inlet Ducts Using a Multiple Block Grid Calculation Procedure

A. K. Tolpadi

M. E. Braaten

Fluid Mechanics Program,
General Electric Research
& Development Center,
Schenectady, NY 12301

An important requirement in the design of an inlet duct of a turboprop engine is the ability to provide foreign object damage protection. A possible method for providing this protection is to include a bypass branch duct as an integral part of the main inlet duct. This arrangement would divert ingested debris away from the engine through the bypass. However, such an arrangement could raise the possibility of separated flow in the inlet, which in turn can increase pressure losses if not properly accounted for during the design. A fully elliptic three-dimensional body-fitted computational fluid dynamics (CFD) code based on pressure correction techniques has been developed that has the capability of performing multiple block grid calculations compatible with present day turboshaft and turboprop branched inlet ducts. Calculations are iteratively performed between sets of overlapping grids with one grid representing the main duct and a second grid representing the branch duct. Both the grid generator and the flow solver have been suitably developed to achieve this capability. The code can handle multiple branches in the flow. Using the converged flow field from this code, another program was written to perform a particle trajectory analysis. Numerical solutions were obtained on a supercomputer for a typical branched duct for which experimental flow and pressure measurements were also made. The flow separation zones predicted by the calculations were found to be in good agreement with those observed in the experimental tests. The total pressure recovery factors measured in the experiments were also compared with those obtained numerically. Within the limits of the grid resolution and the turbulence model, the agreement was found to be fairly good. In order to simulate the path of debris entering the duct, the trajectories of spherical particles of different sizes introduced at the inlet were determined.

1 Introduction

Figure 1 shows a typical turboshaft and turboprop aircraft engine installation. Such an installation requires duct designs which should provide performance and durability commensurate with modern aircraft requirements. These requirements include FOD (foreign-object-damage) protection and low inlet total pressure loss.

FOD protection and low total pressure loss impose conflicting design constraints that must be carefully reconciled or balanced. Inlet ducts that include an integral bypass provide FOD protection by diverting ingested objects such as birds, stones, and other debris from the engine thus reducing maintenance actions. However, separated flow and recirculation caused by the bypass can increase total pressure losses.

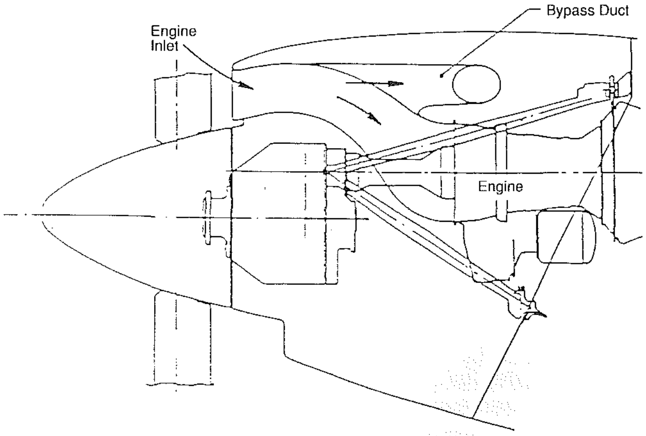

Fig. 1 Typical turboprop installation with bypass-protected inlet duct

The development of inlet ducts has typically relied upon two-dimensional (2-D) analysis followed by extensive model evaluation in a component test facility. This process is expensive in terms of both time and dollars. A viscous three-dimensional (3-D) fully elliptic body-fitted CFD code based on pressure correction techniques (Patankar, 1980) has been developed to improve the inlet design process. This code has the capability of performing multiple block grid calculations of

---

Contributed by the Fluids Engineering Division for publication in the JOURNAL OF FLUIDS ENGINEERING. Manuscript received by the Fluids Engineering Division April 29, 1991. Associate Technical Editor: R. K. Agarwal.

the kind required in branched inlet ducts. This multiple grid capability was developed by modifying an existing code for a single grid. The single grid code developed earlier has been the subject of several papers (Braaten and Shyy, 1986) and (Shyy et al., 1985).

The block grid capability employs a point matched multiple overlapping domain decomposition technique (Karki and Patankar, 1986) whereby the main duct constitutes one domain and the branch duct forms the second domain. Grids are generated in each domain with a set of computational cells that overlap. Numerical calculations are performed in each domain with information being passed from one domain to the other through the overlap region. This methodology will be described in more detail in the next section. Dimitriadis and Leschziner (1985a) have proposed a numerical technique based on a zonal finite volume approach to compute the flow in duct junctions. Dimitriadis et al. (1985b) used this technique to obtain the fluid dynamic characteristics of a special type of junction termed "pulse converter." Experimentally, the pressure and velocity fields were measured which compared very well with the numerical simulation indicating that the coupled solution procedure performed satisfactorily.

The purpose of this paper is to describe the analysis of a typical turboprop branched inlet duct that was performed using the code. Experimental data for this duct were obtained in a test facility. To validate the CFD code, numerical solutions were obtained under identical inlet conditions. The agreement was found to be quite good and it demonstrated that the flow field in such complex inlet ducts can be computed efficiently.

A program was written that calculates the 3-D trajectories of particles (debris) that enter the main duct. A Lagrangian approach was used whereby a set of ordinary differential equations for a particle was solved numerically in the presence of the calculated fluid velocity field and with an assumed drag coefficient correlation for the particle (Gosman and Ioanides, 1983). The incoming debris was assumed to be spherical in shape and having different diameters.

2 Methodology

Governing Equations. The governing equations are the full compressible Navier-Stokes equations representing the conservation of mass and momentum in the three coordinate directions. Turbulence is modeled using the standard k-ϵ model (Launder and Spalding, 1974) along with the wall function treatment for near-wall regions. The flow in the inlet duct of an aircraft engine is essentially isothermal (with adiabatic walls) and therefore the total temperature is assumed to be constant. The density of the air is updated in the calculations and is computed as a function of the pressure and temperature using the ideal gas law. The flow is entirely subsonic in the duct. The fully elliptic form of the 3-D conservation equations may be written in general for a conserved variable ϕ in Cartesian coordinates as

$$\frac{\partial}{\partial x}(\rho u\phi)+\frac{\partial}{\partial y}(\rho v\phi)+\frac{\partial}{\partial y}(\rho w\phi)=\frac{\partial}{\partial x}\left(\Gamma\frac{\partial\phi}{\partial x}\right)+\frac{\partial}{\partial y}\left(\Gamma\frac{\partial\phi}{\partial y}\right)+\frac{\partial}{\partial z}\left(\Gamma\frac{\partial\phi}{\partial z}\right)+R(x,y,z) \quad (1)$$

where ρ is the fluid density, Γ is the effective diffusion coefficient, u, v and w are the three Cartesian velocity components, and R is the source term which depends on the equation being considered. The number of equations solved were six in number with the dependent variable ϕ representing each of u, v, w, pressure correction (corresponding to the continuity equation), turbulent kinetic energy k and turbulent dissipation ϵ. When new independent variables ξ, η, and γ are introduced, Eq. (1) changes according to the general transformation $\xi=\xi(x, y, z)$, $\eta=\eta(x, y, z)$, $\gamma=\gamma(x, y, z)$. The result of this coordinate transformation is to transform the arbitrarily shaped physical domain into a rectangular parallelopiped.

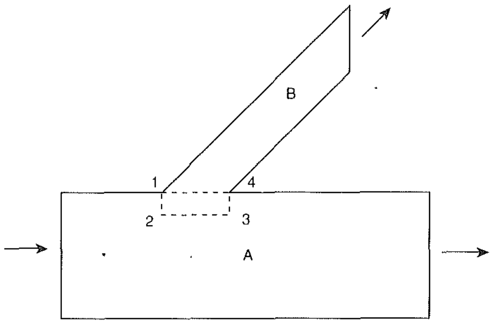

Fig. 2 Domain decomposition procedure

Equation (1) can be rewritten in (ξ, η, γ) coordinates as follows:

$$\frac{\partial}{\partial\xi}(\rho U\phi)+\frac{\partial}{\partial\eta}(\rho V\phi)+\frac{\partial}{\partial\gamma}(\rho W\phi)=\frac{\partial}{\partial\xi}\left[\frac{\Gamma}{J}(q_{11}\phi_\xi+q_{12}\phi_\eta+q_{13}\phi_\gamma)\right]+\frac{\partial}{\partial\eta}\left[\frac{\Gamma}{J}(q_{21}\phi_\xi+q_{22}\phi_\eta+q_{23}\phi_\gamma)\right]+\frac{\partial}{\partial\gamma}\left[\frac{\Gamma}{J}(q_{31}\phi_\xi+q_{32}\phi_\eta+q_{33}\phi_\gamma)\right]+S(\xi,\eta,\gamma)\cdot J \quad (2)$$

where U, V, and W are the contravariant velocity components, the q_{ij}'s are the various metric terms arising from the coordinate transformation, and S (ξ, η, γ) is the source term of the governing equation in (ξ, η, γ) coordinates. The formulas for these quantities are given in (Shyy and Braaten, 1986).

A staggered grid system as described in (Patankar, 1980) is used for the calculation. The scalar variables (p, ρ, k, ϵ, etc.) are located at the center of the control volumes, while the velocity components are located on the control volume faces. Finite difference approximations to the conservation laws are obtained by taking the integral of Eq. (2) over the control volume and discretizing it, as done in Cartesian coordinates. These equations are solved by a SIMPLE-like algorithm (Patankar, 1980) extended to the curvilinear coordinate system. This formulation is applicable for subsonic compressible flows. The detailed implementation of the numerical algorithm is given in (Shyy et al., 1985) and (Braaten and Shyy, 1986).

Domain Decomposition. The idea of domain decomposition will be illustrated in a 2-D situation with reference to Fig. 2. The extension of this idea to a 3-D situation is obvious. Two domains, A and B, are shown. The dotted region 1-2-3-4 indicates the overlap region and consists of one row of cells within domain A. Domain B is bounded by the lines 1-2, 2-3 and 3-4 below. The line 1-4 forms part of the upper boundary of domain A. The grid for the lower two planes of domain B are extracted directly by using portions of the grid along the upper two planes of domain A. This ensures that the grid point locations in the interface region are perfectly identical in the two domains. Calculations are initiated by solving the governing equations in domain A. Any reasonable profile can be initially assumed along line 1-4. Next, a solution is obtained in domain B by using as a boundary condition values of variables along lines 1-2, 2-3 and 3-4 that are obtained from the interior of A. Domain A is next revisited by using as a boundary condition the values of the variables along line 1-4 that are obtained from the interior solution of domain B. Next, the calculations are repeated in domain B. This cyclical procedure is continued until the values of the variables in the overlapping region obtained from the two domains agree within a certain tolerance.

Particle Trajectory Analysis. Many computational formulations for the trajectory of particles in a flow field use the Eulerian conservation equations to represent the fluid motion and the Lagrangian equations to represent the motion of the particles once the flow field is computed. The commonly adopted equation of motion of a spherical particle is given by the following equation, where the dynamic mechanism of the motion is based on the concept of relaxation time (Gosman and Ioanides, 1983).

$$\frac{dV_p}{dt}=\frac{V_c-V_p}{\tau_d} \qquad (3)$$

where

V_p = velocity vector of particle
V_c = velocity vector of fluid
τ_d = dynamic relaxation time of particle

The dynamic relaxation time of particle, τ_d, is defined as

$$\tau_d=\frac{4}{3}\left(\frac{\rho_p D^2}{\mu_c}\right)\left(\frac{1}{C_D\mathrm{Re}}\right) \qquad (4)$$

where

D = particle diameter
ρ_p = particle density
ρ_c = density of fluid
C_D = viscous drag coefficient
μ_c = viscosity of the fluid

The particle Reynolds number is defined as

$$\mathrm{Re}=\frac{\rho_c|V_c-V_p|D}{\mu_c} \qquad (5)$$

The position vector of the particle is given by

$$\frac{dX_p}{dt}=V_p \qquad (6)$$

Integration of Eq. (3) gives the velocity of the particle and a further integration of Eq. (6) gives the position of the particle. The integrations are performed numerically using a Runge-Kutta scheme. An important quantity here is the drag coefficient C_D. There are several expressions available in the literature, each of which has an experimental basis. In this study, C_D is taken from Wallis (1969):

$$\begin{aligned} C_D&=\frac{24}{\mathrm{Re}}\left(1+0.15\mathrm{Re}^{0.687}\right),\ \mathrm{Re}\le 10^3 \\ C_D&=0.44,\ \mathrm{Re}>10^3 \end{aligned} \qquad (7)$$

3 Results

Grid Generation. Generation of a suitable body-fitted grid for the branched inlet duct is very challenging. The problem is complicated by the following factors: (1) The cross-section of the main duct changes shape significantly from the inlet to the exit (engine face), (2) the branch duct that comes off the main duct must be properly meshed, and (3) there is a torque shaft present near the end of the main duct that starts at the engine face and leaves through the lower surface inside the duct (Fig. 1).

A generalized grid generation program was developed for the purpose of creating 3-D grids for such branched ducts having obstacles embedded within the domain. The approach adopted was to generate a series of 2-D grids, one for each cross-section and then stack all these grids together to form the 3-D grid. Each cross-section is bounded by a closed curve on which four fictitious corner points were specified, thus identifying a top, bottom, left, and right boundary on the curve. This "fictitious corner point approach" (Knight, 1982) maps the physical domain into a simply connected rectangular domain in the transformed space in which the governing equations are solved. A 2-D body-fitted mesh was then generated for each cross-section using an elliptic equation technique (Thompson et al., 1985). The code has the capability of meshing a grid around an obstacle that may be present in each cross-section.

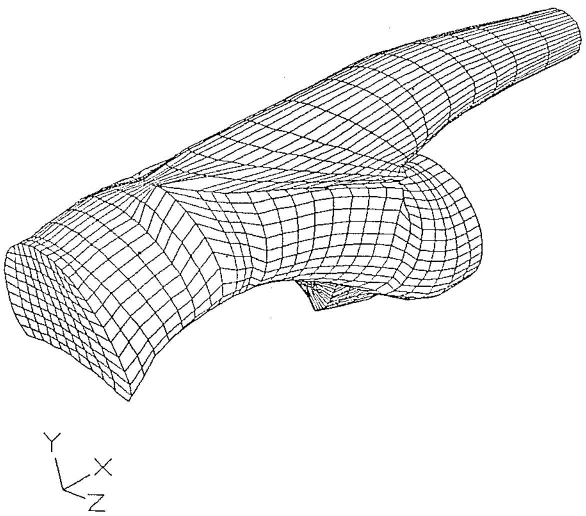

Fig. 3 Grid model of the inlet duct with the branch and torque shaft

The grid for the branch is next generated by specifying the grid point location on the surface of the main duct where the branch originates. The procedure for generating the 3-D branch duct grid by specifying a series of 2-D cross-sections is the same as that used for the main duct but with one difference. The coordinates for the first two planes are extracted from the main duct, i.e., the first plane comes from one row of cells inside a portion of the top surface of the main duct and the second plane comes from the top surface itself. This is in keeping with the multiple block grid calculation method outlined earlier. Figure 3 shows the completed 3-D grid. The branch may be seen coming off the top of the main duct and a portion of the torque shaft coming off the bottom surface of the main duct is visible. This torque shaft goes all the way to the engine face where it comes out along the center. This procedure is an extension of the procedure reported in (Miller et al., 1991) for a single duct with no internal objects.

Generation of the grid in cross-sections containing the torque shaft was performed using two approaches. In the first approach, henceforth referred to as Method 1, the torque shaft is treated as an obstacle in the cross-section, and the grid is meshed around it. Fig. 4(*a*) shows the grids in a typical cross section. This is the most obvious grid one would generate for this application. The "corner point" locations are ABCD and are maintained to be in the same location in each cross section. A projected view of the grid in the vertical midplane is shown in Fig. 4(*b*). The grid is fairly orthogonal in each cross section. As seen in Fig. 4(*b*), within the computational domain, the torque shaft starts from the lower boundary and leaves the exit boundary along the center. It is treated by using a stair-stepping procedure in the transformed space. The grid, together with the shaft, is then mapped back into the physical space. The surface of the shaft in reality is stepped but the grid is so fine that the stepping is gradual and is not visible in Fig. 4(*b*). This grid had 56 × 31 × 31 points in the main duct and 23 × 29 × 31 points in the branch duct, for a total of

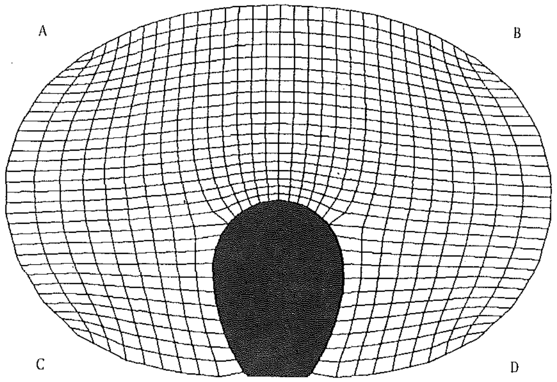

Fig. 4(*a*) Grid in a typical cross section through the torque (Method 1)

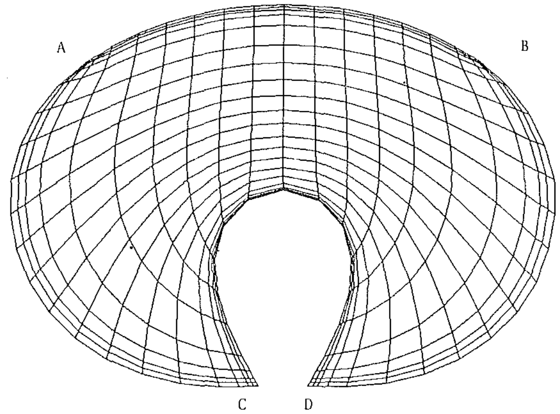

Fig. 5 Grid in a typical cross section through the torque shaft (Method 2)

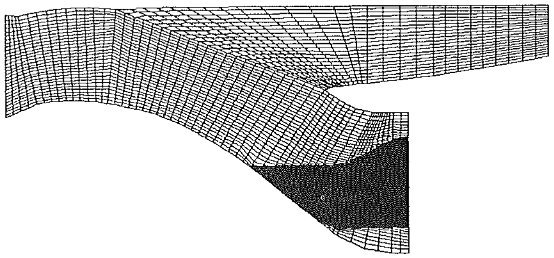

Fig. 4(*b*) Projected view of the grid in a vertical midplane (Method 1)

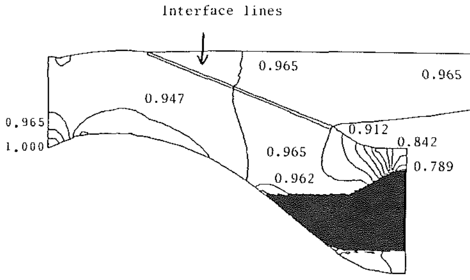

Contour interval = 0.018

Fig. 6 Contours of nondimensional pressure (p/p_{inlet}) in the vertical midplane (Method 1)

74,493 points. Some numerical experiments were performed to study the effect of grid size on the solution but will be described in a later section.

In the second approach which will be referred to as Method 2, the torque shaft is not treated as an obstacle but rather as a part of the lower boundary as shown in Fig. 5. The corner point locations are shown as ABCD. In this method, the corner point locations are successively moved with care from the earlier cross-sections and through the torque shaft in such a way as to properly accommodate the shaft. This grid conforms better to the shape of the torque shaft and has points more closely packed near the walls, which gave a better solution as will be seen later. It also does not have any wasted cells in the shaft (unlike Method 1); however, it is significantly more nonorthogonal. This grid has 31 × 21 ×21 points in the main duct and 9 × 18 × 21 points in the branch, for a total of 17,073 points. The approximate value of the nondimensional distance $y+$ at the near wall point is 1000 and was regarded as being sufficient for the turbulence model.

Numerical Solutions. Numerical solutions were obtained using grids created both by Method 1 and Method 2 and will now be presented. To debug the code, solutions were initially obtained on a coarse grid. Subsequently all of the fine grid solutions (on the grids described in the previous section) were obtained on a Cray Y-MP. The number of grid points used in Method 1 was close to the highest that was affordable within the limits of the computing resources. A converged solution with the grid of Method 1 required 2.5 hours of Cray time. With the grid of Method 2, the time required was about 50 minutes. With the Method 2 grid, the code was run for 95 overall cycles. In each cycle, 20 iterations were performed in the main duct and 10 iterations in the branch duct. The total pressure recovery factor was calculated for the main duct at the end of each cycle. Calculations were stopped when the change in this parameter was 0.040 percent per cycle. The residues in the continuity equation were also observed to have decreased by about three orders of magnitude at this stage.

The Mach number of the air entering at the inlet was 0.22 and was not found to change much until the torque shaft was reached. The flow was found to accelerate significantly around the torque shaft to a peak Mach number of 0.54 at the duct exit. The majority of the pressure drop was found to occur in the region around the shaft. Experimental test data was also obtained under the same conditions. These measurements indicated that 14.3 percent of the incoming flow escaped through the branch while the rest passed into the engine face. These data were used as the outlet boundary condition for both branches in the numerical calculations. Initially, solutions were obtained using Method 1. However, the total pressure recovery factor obtained with this grid was found to be below the measurements. This is the motivation for attemping to create a mesh using Method 2. Recognizing the fact that the wall boundary layer near the exit of the duct is very thin, it was felt that the grid needed to be greatly refined near the walls to enable a better prediction of the recovery. The grid generated using Method 2 has points clustered close to all walls and conforms better to the shape of the torque shaft. Wall functions were used near the wall in the turbulence model, which obviates the need for having extremely fine grids adjacent to the wall. With this grid, the computed pressure recovery factor greatly improved. However, to prevent the solution from diverging with this mesh, the under-relaxation factors for all the equations had to be decreased. This is because of the nonorthogonality of this mesh and the fact that a large number of cells around the shaft are significantly skewed. As a result, this solution required far more iterations to converge which is consistent with the findings reported in (Braaten and Shyy, 1986) where it was observed that mesh skewness is crucial in determining the convergence rate. Thus, in order to obtain a more accurate prediction of the pressure field and the wall shear stresses, a second type of grid had to be regenerated even though the solution with this grid was found to converge with difficulty.

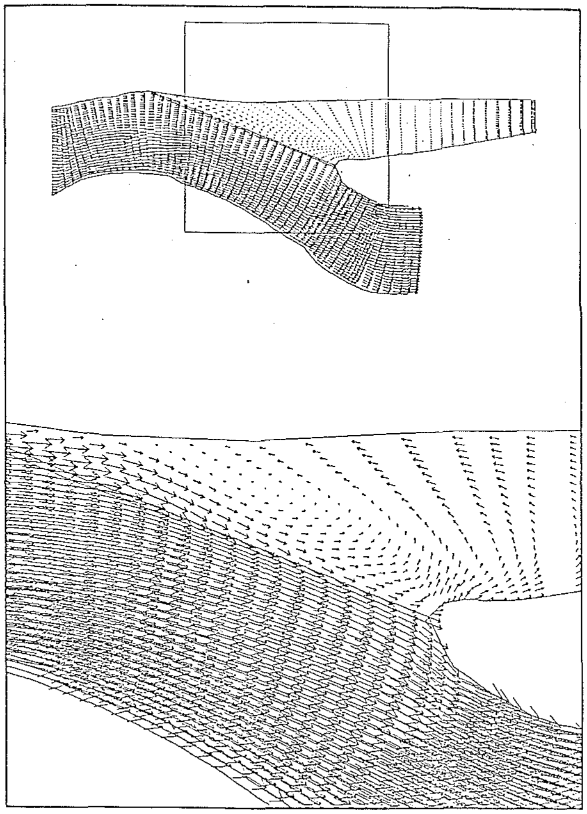

Fig. 7 Projected view of the velocity vectors in a vertical plane through the fluid near the front wall of the duct

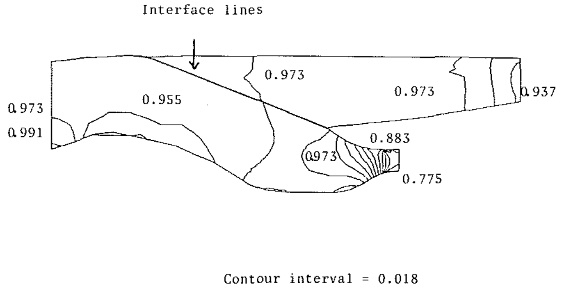

Fig. 8 Contours of nondimensional pressure (p/p_{inlet}) in the vertical midplane (Method 2)

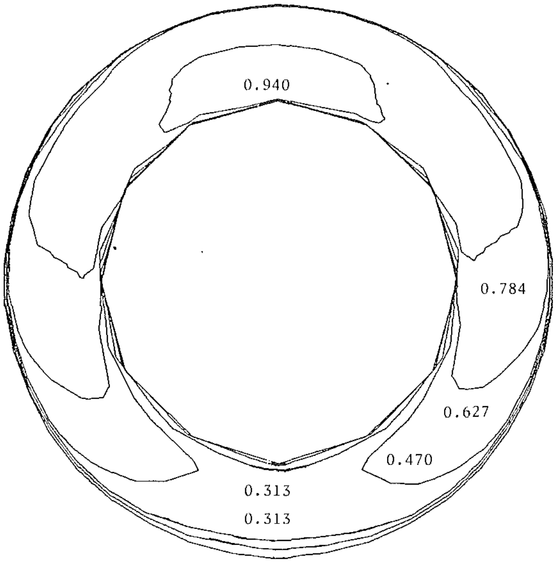

Fig. 9 Contours of nondimensional axial velocity ($u/u_{\max}$) at the engine face

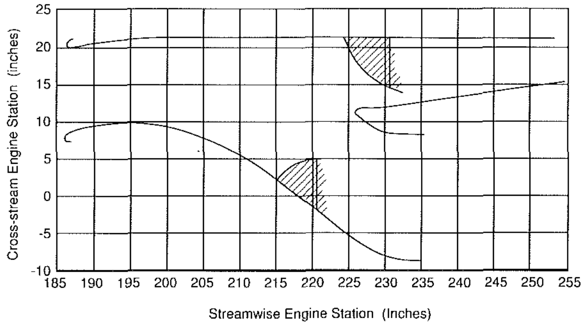

Fig. 10 Experimentally observed regions of separated flow

Figure 6 shows the pressure distribution in a vertical midplane through the duct obtained using Method 1. The continuity of contours across the interface indicates that a coupled solution has been obtained. From the contour lines, it is evident that the pressure is fairly uniform within most of the main duct and the branch, but it falls rapidly in the last part of the main duct around the torque shaft where the flow accelerates. Figure 7 shows the projected velocity vectors in a vertical plane close to the front wall. The flow may be seen to practically conform to the shape of the main duct and it accelerates near the torque shaft. There is a marked zone of separation in the upper part of the branch duct. This part of the duct has been magnified in order to see the velocity vectors more closely. Similar velocity vector plots in other planes in the depth direction indicated that the flow also separates near the lower wall of the main duct close to the exit.

Figure 8 shows the pressure contours in a vertical midplane obtained using the grid from Method 2. Again, the continuous pressure distribution across the interface shows that a coupled converged solution has been obtained. These contours also indicate that the pressure falls rapidly near the exit of the duct.

It is important for designers to know the distribution of streamwise velocity at the engine face. A more uniform velocity distribution ensures a more uniform flow through the engine. It is of interest to determine whether the branch which draws some of the incoming air has any effect on the velocity field at the exit. Figure 9 shows the contours of axial velocity at the engine face. The velocity distribution is more uniform with a very thin boundary layer in the upper half. The boundary layer is thicker, and the velocity field is lower below the torque shaft.

Comparison With Experiments. The experimental tests were conducted on a full-scale fiberglass model of the geometry. This work was performed by personnel at GE Aircraft Engines in a suction facility with ambient inlet conditions. Airflow was measured by orifices in the facility piping. Measurements also included engine inlet pressure recovery, engine inlet distortion, and bypass flow pressure recovery. Both the main and bypass duct walls were instrumented with static pressure taps. Small plexiglass windows were built into the model in the regions of the engine inlet and bypass juncture for flow visualization tests. An oil-chalk mixture was used as the medium for observing the possibility of separation.

Figure 10 shows the experimentally observed zones of flow separation which must be compared with Fig. 7 on which the numerically observed zone is marked. The agreement may be observed to be qualitatively good. The flow separates in the

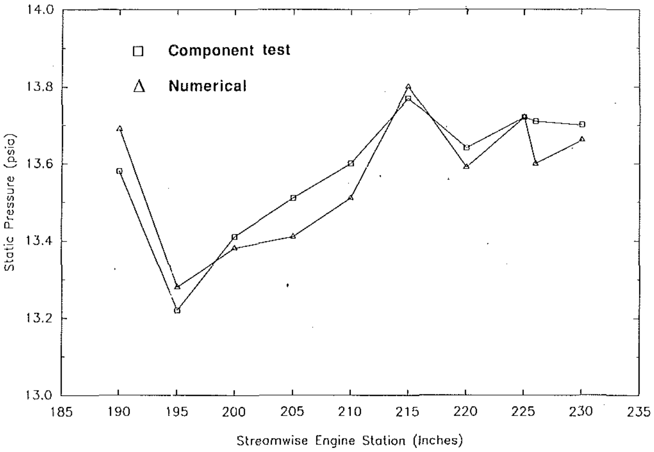

Fig. 11 Lower wall static pressure distribution

Table 1 Recovery factors: measured and calculated

	P_{texit}/P_∞
Component test	0.9949
Calculated (grid 1)	0.9735
Calculated (grid 2)	0.9893

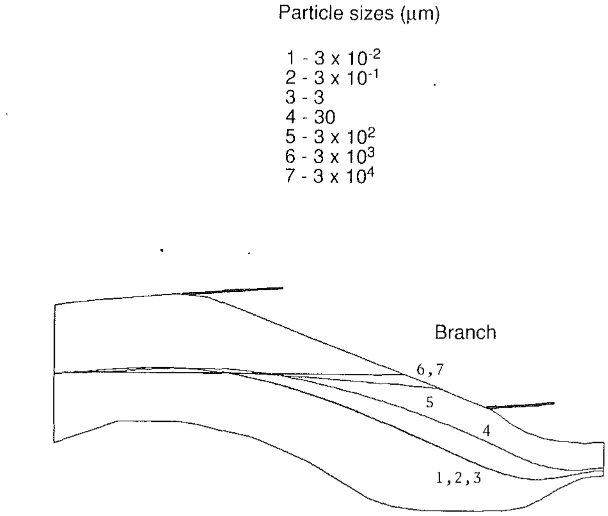

Fig. 12 Trajectories of particles of different sizes that start at the center of the inlet (2-D projection)

top of the branch just past the interface region, and reattaches further downstream. Although not seen in Fig. 7, in other sectional views just behind the shaft, the flow was also observed to separate in the lower part of the main duct near the exit.

Figure 11 compares the static pressure distribution along the lower wall. The squares indicate the component test, and the triangles indicate the numerically computed values. The agreement may be seen to be quite good.

The purpose of having a bypass duct is to divert debris that enters the inlet away from the engine. But, at the same time, it is important to ensure that there is little or no compromise on duct performance. Table 1 shows the values of the total pressure recovery factor (ratio of mass averaged total pressure at the duct exit to that at the inlet) as measured and those obtained from the numerical solutions. The recovery calculated using Method 2 is seen to be better than that obtained using Method 1 despite the fact that the grid used in Method 2 has less than a quarter of the total number of grid points. As mentioned earlier, Method 2 uses a more efficient grid and is finer near the walls than Method 1, which results in a better prediction of the recovery. It is interesting to observe that in spite of the presence of the shaft in the duct and its odd shape, the duct is extremely efficient in terms of recovery performance and is a fact that has been predicted by the numerical computations.

It is appropriate to make a comment at this stage about the effect of grid size on the solution. Initially, a coarse grid having a total of 6720 points was generated using Method 1. The computed total pressure recovery factor with this grid was 0.9550. Subsequently, the finer grid mentioned earlier and having 74,493 points was generated. Table 1 indicates the recovery factor with this grid to be 0.9735. The trend with grid refinement was definitely seen to be in the direction of improved recovery. Since the grid using Method 2 with a total of 17,073 points gave a recovery factor of 0.9893 that is very close to the measurements, it was felt that further refinement of this grid was not required.

The size of the debris and its entry location at the inlet determine whether or not they will make their way into the engine itself. Figure 12 shows the trajectories of particles of seven different sizes entering approximately at the center of the inlet. The particles are assumed to be spherical in shape in this analysis. For the purpose of this trajectory analysis, the debris was considered to be a bird and therefore having the same density as that of water. The gaseous phase is, of course, air. The full three-dimensional trajectories of the particles are actually obtained. However, Fig. 12 shows a 2-D projection of these trajectories. In this case, particles of size smaller than 30 microns essentially follow the fluid streamline and pass through the engine face. However, particles that are larger have trajectories that remain almost unaffected by the flow field and enter the branch duct. Most debris such as birds and stones are likely to fall in the latter category.

4 Conclusions

It has been demonstrated that the flow field in complex nonaxisymmetric branched turboprop inlet ducts of the type analyzed in this paper can be calculated successfully using the multiple block grid viscous flow analysis code developed. A body-fitted grid for this complex geometry was generated and a coupled block grid solution of the flow was obtained. The predicted flow solutions compared very well to the test data. The total pressure recovery factor, which is a quantity of interest to designers of such ducts, has been calculated to agree well with the measurements within the limits of the grid resolution. It was shown that with a refined grid, the calculated value was in closer agreement with the measurement. The computed flow field indicated areas of flow separation that agreed with the observations. The code provided the distribution of the flow at the engine face, something that is of great value to designers. The trajectory analysis provided information concerning the path of various debris entering the duct.

5 Acknowledgments

The authors of this paper would like to thank General Electric for permission to publish the results presented in this paper. Also, the authors would like to thank Tom Scott and his group at GE Aircraft Engines, Lynn, MA, for sponsoring work on the branched inlet duct program and for providing the experimental data.

References

Braaten, M. E., and Shyy, W., 1986, "A Study of Recirculating Flow Computation Using Body-Fitted Coordinates: Consistency Aspects and Mesh Skewness," *Numer. Heat Trans.*, Vol. 9, pp. 559–574.

Dimitriadis, C., and Leschziner, M., 1985a, "Computation of Three-Dimensional Duct Junction Flow by a Zonal Approach," Presented at 4th Int. Conference on Numerical Methods in Laminar and Turbulent Flow, Swansea.

Dimitriadis, C., Leschziner, M., Winterbone, D., Alexander, G., and Sierens, R., 1985b, "Computation of Three-Dimensional Flow in Manifold-Type Junctions," Presented at ASME Winter Annual Meeting, Miami, *ASME Fluids Engineering Division Publication*, Vol. 28, pp. 57-62.

Gosman, A. D., and Ioanides, E., 1983, "Aspects of Computer Simulation of Liquid-Fueled Combustors," *J. Energy*, Vol. 7, pp. 482-490.

Karki, K. C., and Patankar, S. V., 1986, "Use of Subdomains for Flow Computations in Complex Geometries," Presented at ASME Winter Annual Meeting, Anaheim, *Numerical Methods in Heat Transfer*, pp. 7-12.

Knight, D. D., 1982, "Application of Curvlinear Coordinate Generation Techniques to the Computation of Internal Flows," *Numerical Grid Generation*, Thompson, J. F., ed., Elsevier Science Publishing Co., pp. 357-379.

Launder, B. E., and Spalding, D. B., 1974, "The Numerical Calculation of Turbulent Flows," *Comput. Meths. Appl. Mech. Eng.*, Vol. 3, pp. 269-289.

Miller, D. P., Braaten, M. E., and Kornowski, M., 1991, "Numerical Prediction of the Flow Distribution in an Aircraft Engine Blower Inlet Duct," submitted to *AIAA J. of Propulsion & Power*.

Patankar, S. V., 1980, *Numerical Heat Transfer and Fluid Flow*, McGraw-Hill, New York.

Shyy, W., and Braaten, M. E., 1986, "Three-Dimensional Analysis of the Flow in a Curved Hydraulic Turbine Draft Tube," *Int. J. Num. Meths. Fluids*, Vol. 6, pp. 861-882.

Shyy, W., Tong, S. S., and Correa, S. M., 1985, "Numerical Recirculating Flow Calculations Using a Body-fitted Coordinate System," *Numer. Heat Trans.*, Vol. 8, pp. 99-113.

Thompson, J. F., Warsi, W. U. A., and Mastin, C. W., 1985, *Numerical Grid Generation*, North Holland, Amsterdam, Netherlands.

Wallis, G. B., 1969, *One Dimensional and Two Phase Flow*, McGraw-Hill, New York.

V. K. Gahlot
Civil Engineering Department,
M. A. College of Technology,
Bhopal-462007, India

V. Seshadri

R. C. Malhotra

Department of Applied Mechanics,
Indian Institute of Technology,
New Delhi-110 016, India

Effect of Density, Size Distribution, and Concentration of Solid on the Characteristics of Centrifugal Pumps

Experimental data on the performance of the centrifugal pumps pumping mixtures of solids and water have been presented. The solids used were coal of density 1480 kg/m^3 and zinc tailings of density 2850 kg/m^3. Maximum size of particles was approximately 3 mm. Tests have been conducted with a rubber lined impeller pump and a metal impeller pump. Effects of solid properties (viz: density, size, and size distribution as well as concentration of solids) on the performance of the pumps have been studied. The measured performance of pumps is compared with the predictions based on the correlations available in literature and a modified empirical relationship has been proposed for the prediction of the pump performance with slurries.

Introduction

Centrifugal pumps, because of their inherent advantages of high and consistent flow rate, low cost, and ease of maintenance and better operational stability are being increasingly used for pumping slurries in the pipeline transportation systems. In short distance, in plant, slurry pipe lines where the head requirements are normally low, centrifugal pumps are best suited. The selection of pumps for any pipeline transportation system depends mainly on the past experience and/or based on the performance of the pump with clear water. Many researchers have shown that the performance of centrifugal pumps with slurries will be different from that with clear water. The performance of the pump will improve or deteriorate depending upon whether the slurry behaves as Newtonian fluid or Bingham fluid. The general conclusions drawn by most investigators are that the head developed and efficiency of the pump decrease whereas the input power increases when mixtures of solid (heavier than water) and water being pumped. The variables which affect the pump performance are the concentration of solids in the mixture, the physical properties of solid like its density, shape, size and size distribution of particles, size of pumps, and the flow inside the pump. Several investigators have attempted to correlate their experimental data of pump tests to some of these variables and have presented correlations for estimating the pump performance with slurries from its performance with water.

Fairbank (1942) has given a theoretical method of computing the head developed by slurry pumps. The velocities of water and solid particles at the exit of the impeller are first computed and are then used to calculate the head developed for slurry. Vocadlo et al. (1974), in their theoretical analysis have assumed that the head loss due to solid particles is mainly due to interaction among the solid particles and between solid and liquid as well as due to the energy spent in maintaining the solids in suspension. Burgess and Riezes (1976), Cave (1976), Sellgren (1979), and McElvain (1974) have also presented correlations for calculating the head reduction factor. It is generally accepted that the efficiency reduction of the pump is in the same ratio as the head reduction. Comparison of these relationships with the experimental results made by (Holzenberger, 1980, and Mez, 1984) have shown that the correlations are much in error and are far from satisfactory for different types of slurries.

In the present paper, the effect of slurry properties on the hydraulic characteristics of centrifugal pumps has been discussed. Two different types of pumps namely a rubber lined and a metal impeller pump were used in the investigation. These pumps were tested with slurries of two different materials namely zinc tailings and coal. Measurements have been made over a wide range of solid concentrations. The head, discharge, and input power to the pump have been measured at varying conditions of operation and the head reduction factors are calculated. A correlation for predicting head reduction factor is proposed, which accounts for specific gravity, concentration, and size distribution of particles.

Experimental Setup

The schematic diagram of the experimental setup used is shown in Fig. 1. The test rig consists of a 50 mm diameter open circuit pipe test loop. The slurry was prepared in a hopper shaped mixing tank by mixing the required quantities of water and solids. The slurry preparation tank is provided with a stirrer so that mixture could be kept well mixed with the solids in suspension. The flow rate could be varied over a wide range by suitably operating the plug valve provided near the delivery end of the pump. The slurry flowing out of the delivery line

---

Contributed by the Fluids Engineering Division for publication in the JOURNAL OF FLUIDS ENGINEERING. Manuscript received by the Fluids Engineering Division March 1991. Associate Technical Editor: W. Tabakoff.

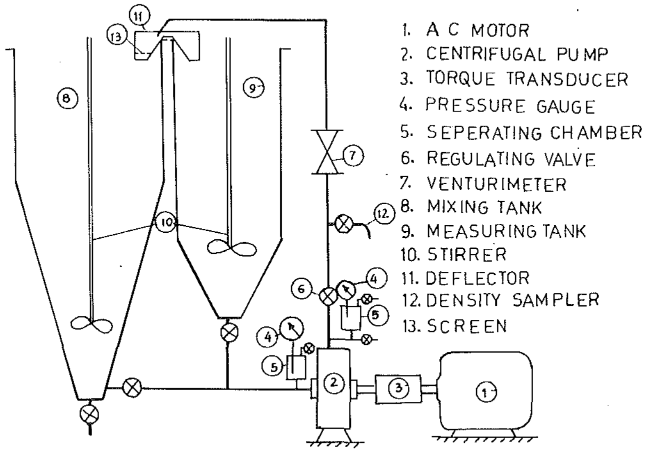

Fig. 1 Schematic diagram of experimental setup

can be either made to flow back into the mixing tank or to a measuring tank by means of a quick action diverter mechanism. A stirrer is also provided in the measuring tank to facilitate proper mixing of solids and preventing them from settling down. The flow rate could be ascertained by measuring the rise in the level of slurry in the measuring tank to an accuracy of ± 1 mm over a known interval of time. The return line from the measuring tank enables the emptying of the tank after flow measurements. A precalibrated venturimeter is also provided in the delivery line for quick and continuous monitoring of the flow rate. The suction and delivery heads are measured using Bourdon tube type pressure gauges within an accuracy of ± 0.025 kg/cm^2. The calibration of these gauges was periodically checked using a dead-weight tester. Separation chambers using clear water as the separating liquid are used to connect the pressure gauges to the pipe line in order to prevent chocking of gauges. The position of the gauges was as per the relevant I. S. Code (1977). A sampling tube with a valve is provided in the delivery pipe which facilitated the collection of slurry sample flowing through the pipe for determination of various slurry properties.

The pump is directly coupled to a 22 kw, 415V, 40A, a-c motor. A torque transducer (model: TT2-4-cc, M/s Experimental & Electronic Ltd., U. K.) is connected between the shafts of the motor and the pump. It measures the pump speed, torque transmitted to the pump shaft, and the input power to the pump within an accuracy of ± 0.2 KW. The input voltage to the motor is controlled by a three-phase voltage regulator. The input power to the pump is also determined by measuring the input power to the motor, by two wattmeter method within an error limit of 25-watts, and using its efficiency characteristics. Pump speed is also measured using an optical type digital electronic tachometer. The supply voltage, current, and line frequency were measured by voltmeter, ameter, and frequency meter, respectively. The calibration of the meters was checked before and after each set of runs.

Types of Pumps

Two types of pumps namely (i) rubber lined semiopen impeller pump (VAC-SEAL M/s International Combustion Ltd.) and (ii) Ni-hard casing closed impeller metal pump (WILFLEY, M/s Hindustan Dorr-Oliver Ltd.) were used in the investigation. The specifications of the two pumps are given in Table 1.

Properties of the Solid Materials

The following two materials were used in the investigations:

(*i*) Coal sample obtained from a steel plant
(*ii*) Tailing materials from a zinc plant

Table 1 Specification of the pumps used in the investigation

Specification	Rubber lined Vacseal pump	Ni-hard casing metal pump
Suction flange size (mm)	65	100
Delivery flange size (mm)	50	50
Impeller diameter (mm)	280	270
Type of Impeller	Semi-open	Closed
Num. of blades	3	5
Specific speed (metric)	66	89
Rated speed (rpm)	1400	1450
Design Head (m)	20.0	16.0
Design Discharge (l/s)	14.0	12.5

Table 2 Properties of the materials used

Property	Zinc Tailings	Coal
Specific gravity (S)	2.85	1.48
Max. particle size (mm)	1.0	3.0
Particles weighted mean diameter (d_w) (mm)	0.1704	0.90
Max. static settled concentration by weight	72.6%	60%

The various physical properties of the two materials used are given in Table 2.

Test Procedure and Measurements

After the completion of the pump test with clear water, precalculated amount of solid material for a solids concentration was slowly added to water in the mixing tank with the stirrer in operation. The slurry was kept in circulation for approximately 15 minutes for thorough mixing before starting any measurements and then the concentration of solids in the slurry was checked. The input voltage to motor was adjusted to the rated voltage and the delivery valve is adjusted to the required position. Input voltage, current, and power to motor were measured. The pump speed, torque, and power to pump were noted from the Torque Transducer. Suction and delivery gauge and venturimeter readings were taken. Volumetric measurements of flow rate were made by diverting the flow into the measuring tank by quick action divertor for a known length of time and measuring the raise in the height. The temperature and density of the slurry were obtained from a slurry sample collected from sampling tube. Four samples were taken during each measurement. The average of these is taken as the concentration of solids. The absolute errors in the individual measurements of concentration were less than ± 2 percent. The efflux sample was dried in an oven and was analyzed for determination of the specific gravity and particle size distribution of solids as per the standard procedure. The measurements were repeated for various settings of the delivery valve to cover the entire range of operation of the pump. The range of concentration of solids tested is 0-57 percent by weight. Measurements of pump characteristics with clear water were performed both before and immediately after the set of measurements with a slurry of any given material.

Test Results

As the rotational speed of the pump varied between 1440 to 1500 rpm during the various test runs, the test data of head, discharge, and input power were transferred to a single speed of 1450 rpm using the affinity laws for the pumps. Stepnoff (1965) and Cave (1976) have confirmed that the affinity laws of pumps for water are also valid for slurry pumps. Head, efficiency, and input power to pump were plotted against discharge both for water and slurries of different concentrations. It was observed that the head and efficiency of the pump decreased while the input power to pump increased with increase in concentration of solids. The variation of the average values of the head ratio (H_R) and efficiency ratio (η_R) at

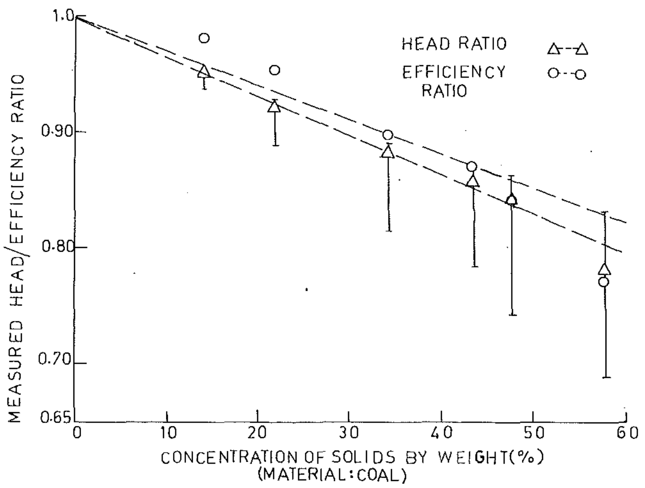

Fig. 2 Variation of head and efficiency ratios with concentration

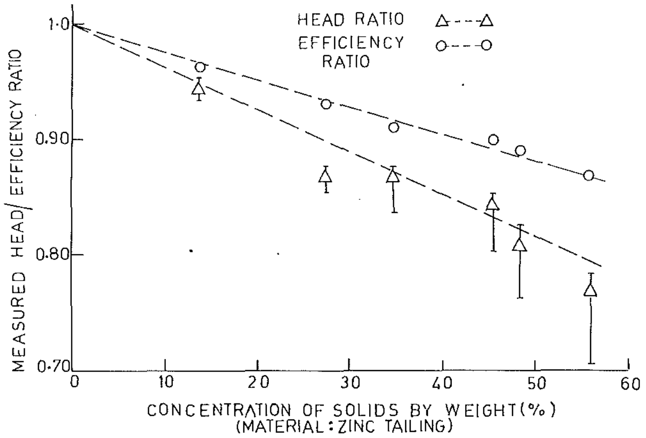

Fig. 3 Variation of head and efficiency ratios with concentration

different concentration of solids shows that both H_R and η_R vary linearly with concentration of solids up to a value of 25 percent by volume. At higher concentrations, head ratio dropped more rapidly than predicted by linear relationship. The phenomenon is illustrated in Fig. 2 and Fig. 3. The vertical bands shown in these figures represent the range in the measured value of H_R at various discharges for a particular concentration. The data points represent the mean of such values. Stepnoff (1965) and Vocadlo et al. (1974) have concluded that as the ratio of BHP for slurry and water at the same flow rate varies as the density of slurry, the efficiency ratio of the pump should be equal to its head ratio. Sellgren (1979) have found that η_R is equivalent to H_R up to volumetric concentration of 20-25 percent. Figure 2 and Fig. 3, which show the variation of H_R and η_R with solid concentration for metal pump for the two materials tested show that η_R is higher than H_R by approximately 2 to 9 percent.

The head reduction factor (K) defined as $K=(1-H_R)$ was calculated from the measurements. Measured head reduction factor $(K)_m$ was compared with the predicted values. None of the correlations gave satisfactory agreement with the measured values for both materials and pumps. A typical comparison of the predicted head reduction factor with the measured head reduction factor is illustrated in Fig. 4. The predicted values are lower by 35 to 65 percent. The larger deviations in the predicted results for the coal slurry could be attributed to the following causes:

(*a*) The correlation used was based on test data for heavier solids.

(*b*) Improper accounting for the sp. gravity of solids and

(*c*) Use of d_{50} as the representative size for solids having a broader range of size distribution.

The test results were further analyzed to identify the effect of solids concentration, sp. gravity, size and size distribution of solids on the head reduction factor.

Effect of Concentration of Solids: From Fig. 2 and Fig. 3 it is clear that the head ratio varies approximately in a linear fashion with concentration of solids except at very high concentrations. Hence we can write

$$K \propto C_W \tag{1}$$

Effect of Specific Gravity of Solids. As the particle size distribution of the two materials tested differed considerably, no comparison of results could be made to find the effect of specific gravity on the head ratio. As the velocity of solid particles plays a major role in head reduction, the effect of sp. gravity could be better accounted either by the particle Reynolds number or by the terminal settling velocity of particles. Cave (1976) has concluded in his analysis of data that K varies as (S-1). This corresponds to Stokes flow where the terminal settling velocity also varies as (S-1) for particle Reynolds number less than 1. Vocadlo et al. (1974) have shown that the particle Reynolds numbers within the impeller for most of the slurry pumps lie in the transition regime ($1<\mathrm{Re}<1000$) where the terminal settling velocity varies as $(\mathrm{S}\text{-}1)^{0.72}$ according to Allen's law (Gahlot, 1987). Thus it is reasonable to conclude that K varies as $(\mathrm{S}\text{-}1)^{0.72}$ for the present slurries. This is supported by the results of Sellgren (1979) who has found that K varies as $(\mathrm{S}\text{-}1)^{0.7}$.

Effect of Particle Size Distribution. Effect of particle size is given in terms of the diameter of particles. For a narrow range particle size distribution, d_{50} (screen diameter through which 50 percent solids passed) may be chosen as the representative diameter of particles. However, for broad size distribution, weighted mean diameter of particles would be a better choice. A proportionate weightage is given to different sizes.

Effect of Particle Size. To determine the effect of particle size on head reduction factor, the head ratio for a slurry of 25 percent concentration by volume was obtained. If K' is the value of K at 25 percent concentration by volume, then the ratio of K' for two different solids can be written as

$$\frac{K_1'}{K_2'}=\frac{(S_1-1)^{0.72}}{(S_2-1)^{0.72}}$$

In order to eliminate the effect of sp. gravity, the measured values of K' are converted to an imaginary solids of sp. gravity 3. The modified head reduction factor $[K'(3)]$ is calculated as

$$\frac{K'}{K'(3)}=\frac{(S-1)^{0.72}}{(3-1)^{0.72}} \text{ or } K'(3)=\frac{(2)^{0.72}K'}{(S-1)^{0.72}} \tag{2}$$

These values of $K'(3)$ from the present investigation as well as for some other materials obtained from published literature are plotted as against weighted mean diameter (d_w) in Fig. 5.

A straight line could be fitted to these points. The equation of the line can be written as

$$K'(3)=0.092\ \log_e(50d_w)$$

Substituting for $K'(3)$ in Eq. (2) and solving for K' we get

$$K'=0.056(\mathrm{S}-1)^{0.72}\log_e(50d_w) \tag{3}$$

Combining Eq. (1) and Eq. (3), a general expression for effect of solids concentration, sp. gravity, size and size distribution can be written as

$$K=0.00056(\mathrm{S}-1)^{0.72}\left(1+\frac{3}{S}\right)C_w\log_e(50d_w) \tag{4}$$

The predicted head reduction factors obtained using above equation have been compared with measured values Fig. 6. It is seen that the data points are equally distributed on both

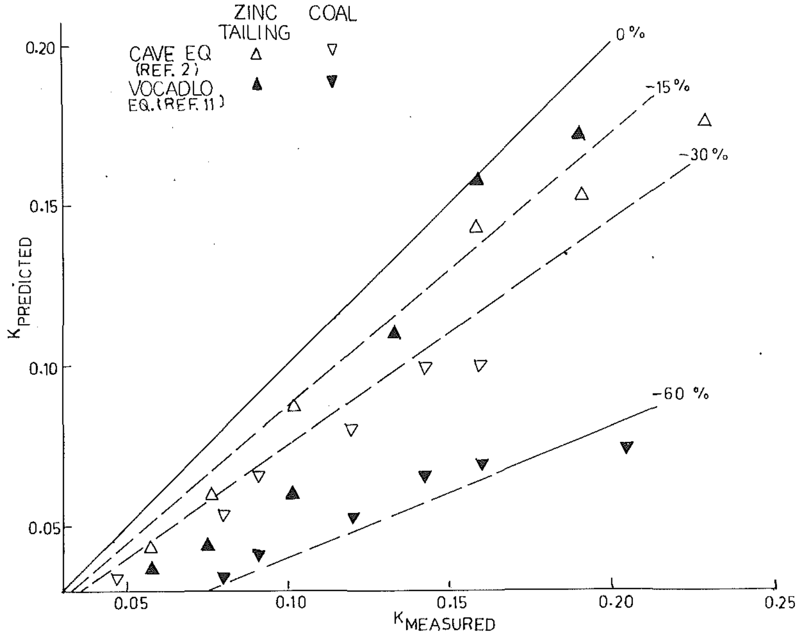

Fig. 4 Comparison between calculated and measured head reduction factor

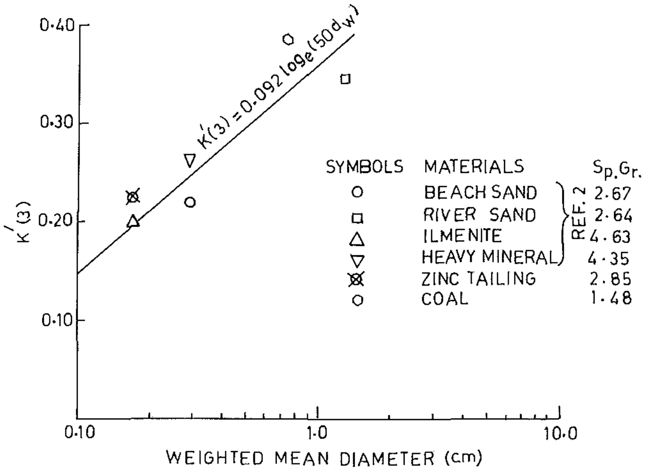

Fig. 5 Variation of k' with particle size

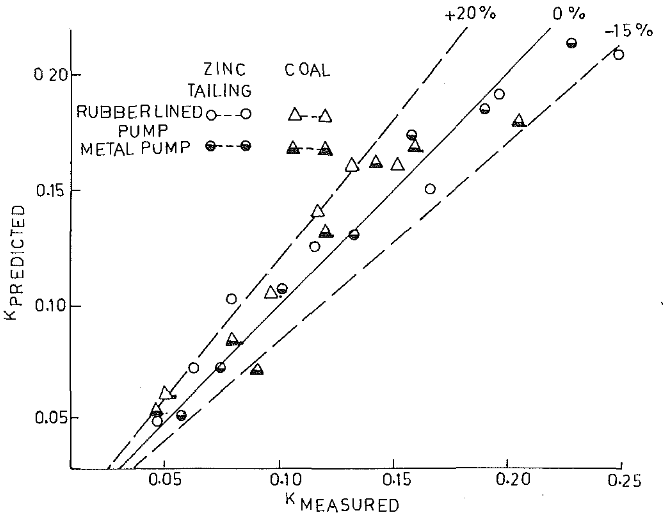

Fig. 6 Accuracy of proposed correlation for head reduction factor

sides of the ideal line and the deviations are in the range -15 to $+20$ percent. This is a significant improvement over the existing correlations.

Concluding Remarks

On the basis of the present investigation and the analysis of data available in literature, we can conclude that Eq. (4) can be used for prediction of the centrifugal pump performance while handling slurries. It is to be noted that this equation is similar in form to that proposed by Cave (1976). The difference is in the magnitude of the exponent of the term (S-1) which accounts for the effect of specific gravity of solid. Secondly, d_w has been used as representative particle size as compared to d_{50}. The modified equation has given more accurate predicting particularly for slurries with solids having a wide particle size distribution. However, more detailed experiments with different solid materials are in order before firm conclusions can be drawn. Wear characteristics of the pump have not been included in the present investigation.

References

Burgess, K. E., and Reizes, A., 1976, "The Effect of Sizing, Specific Gravity and Concentration on the Performance of Centrifugal Pumps," *Proc. Inst. Mech. Engr.* Vol. 190 36/76, p. 391.

Cave, I., 1976, "Effect of Suspended Solids on the Performance of Centrifugal Pumps," *Proc. Hydro Transport 4*, paper H3.

Fairbank, L. G., 1942, "Effect on the Characteristics of Centrifugal Pumps," *Trans. A.S.C.E.*, Vol. 68, p. 1563.

Gahlot, V. K., 1987, "Studies on the Effect of Particles Size Distribution and Material Properties on the Rheological Parameters of Slurries and the Performance of Slurry Pumps," Ph. D. thesis, I.I.T. New Delhi.

Holzenberger, K., 1980, "Working Behaviour of Centrifugal Pumps on Hydraulik Transport of Solids," Conf. Trans. Rohn 80, VDI Berichtre 371.

I. S. Code 5120, 1977, "Technical Requirement for Roto-Dynamic Special Purpose Pumps."

McElvain, R. E., 1974, "High Pressure Pumping," *Skilling Mining Review*, Vol. 63, No. 4.

Mez, W., 1984, "The Influence of Solid Concentration, Solid Density and Grain Size Distribution on the Working Behaviour of Centrifugal Pumps," *Proc. Hydro Transport 9*, Paper H1, BHRA Fluid Engineering.

Stepnoff, A. J., 1965, *Pumps and Blowers, Two Phase Flow*, John Wiley & Sons.

Sellgren, A., 1979, "Performance of Centrifugal Pumps When Pumping Ores and Industrial Minerals," *Proc. Hydro Transport 6*, Paper G-1, BHRA Fluid Engineering.

Vocadlo, J. J., Koo, J. K., and Prang, A. J., 1974, "Performance of Centrifugal Pumps in Slurry Services," *Proc. Hydro Transport 3*, paper J-2, BHRA Fluid Engineering.

Quantitative Visualization of the Flow Within the Volute of a Centrifugal Pump. Part A: Technique

R. Dong

S. Chu

J. Katz

Department of Mechanical Engineering,
The Johns Hopkins University,
Baltimore, MD 21218

This paper describes a series of quantitative flow visualization experiments within the volute of a centrifugal pump by implementing the "Particle Displacement Velocimetry" method (PDV or PIV). Part A focuses on the measurement procedures and includes an uncertainty analysis. This technique involves illuminating sections of a flow field with pulsed laser sheets while seeding the water with microscopic, neutrally buoyant particles containing imbedded fluorescent dye. By pulsing the laser more than once while recording a single photograph each particle leaves multiple traces on the same film. The analysis procedures consist of dividing the image to a large number of small sections (windows) and computing of the mean shift of all particles within each window. This shift is determined by computing the auto-correlation function of the image within the window. Digital image processing and specially written software are being utilized while analyzing the data. It is demonstrated that by controlling the magnification and particle concentration, the relative error can be maintained at about 1 percent. A sample analyzed image is presented. The rest of the data are included in Part B.

I Introduction

"Particle Displacement Velocimetry" (PDV or PIV) is a quantitative, two dimensional flow visualization technique that enables mapping of the instantaneous velocity distribution within sections of a flow field. Developmental stages of this method are summarized in several recent review papers (Adrian, 1986a, 1989, 1991 and Willert and Gharib, 1991). In principle PDV consists of illuminating a desired section of the flow field with a laser sheet while seeding the water with microscopic tracer particles. When the laser is pulsed more than once while recording a single photographic frame each particle leaves multiple traces on the same recording medium. Two distinct approaches have been utilized for determining the velocity distribution form the particle traces. The first method is based on matching between traces of the very same particle and measuring the distance between them (Shekarriz et al., 1991 and Gharib, M., Willert, 1989). The second method is based on dividing the image to small windows and finding the mean shift of all the particles within each window. Two different approaches have been developed for this purpose. The first method involves computation of the auto-correlation of the intensity distribution within the selected sample window (will be defined as "auto-correlation" method). This approach has been adopted to the present study, and will be discussed in detail later. The second method is usually referred to as "Particle Speckle Velocimetry" (Adrian, 1989). In the present paper we'll focus on the flow structure within the volute of a centrifugal pump. Since this is the first of a series of publications involving the implementing of PIV to the study of pump flows, the experimental setup, analysis procedures, accuracy, and the uncertainty receive substantial attention.

Optical Setup

A schematic illustration of the optical setup in the pump facility is presented in Fig. 1. The laser beam is expanded to a 1 mm thick light sheet by a combination of cylindrical and spherical lenses. This sheet illuminates any desired section of

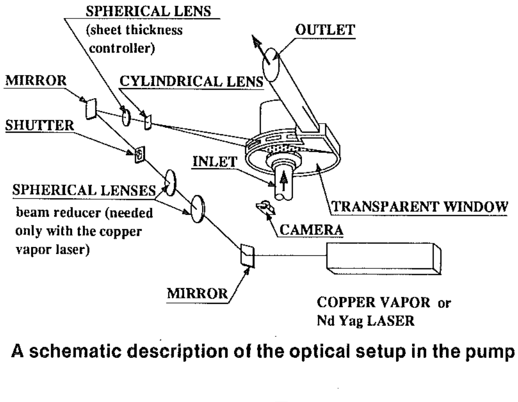

Fig. 1 A schematic description of the optical setup in the pump facility

---

Contributed by the Fluids Engineering Division for publication in the JOURNAL OF FLUIDS ENGINEERING. Manuscript received by the Fluids Engineering Division November 26, 1990. Associate Technical Editor: J. Tuzson.

the volute through the transparent perimeter. Illumination from the bottom in order to study normal places is also possible. The image is recorded by a camera located below the pump. Two types of laser have been used. The first is the continuously pulsed copper vapor laser (511 and 578 nm are the primary wavelengths), and the second is a frequency doubled Nd-Yag laser (532 nm). Most of the experiments were performed with a Nd-Yag laser. It can generate up to three pulses within less than 500 μsec, the minimum delay being 1 μsec. The intensity of each pulse can be modulated independently which enables identification of the order at which the laser is fired. Three laser pulses were used for recording a single image. The delay between them was kept at 160 μs.

Since the instantaneous flow field within the volute depends on the exact location of impeller blades, the timing of each laser pulse is synchronized with the impeller. A perforated plate and an encoder, consisting of a LED and a photo-diode, were installed on the pump shaft for this purpose. Its output was fed to the control system that provided signal to each of the components involved with the PDV system. An internal clock enabled precise (up to 1 μs) control of the delay between the encoder signal and the laser pulses.

Seed Particles

Since PDV consists of measuring the motion of microscopic particles within a flow field, these particles should follow the fluid without significant slip. Ideally this requirement means that the particles should be neutrally buoyant and as small as possible, preferably much less than the typical Kolmogorov scale. However, the smaller the particles are, the harder it is to detect them clearly. Based on discussions by Agui and Jimenez (1987) the slip velocity of a particle can be estimated as:

$$\left(\frac{\Delta u}{u}\right)^2 \approx \left(\frac{\Delta \rho}{\rho}\right)^2 \frac{d^2 f}{10\nu} \qquad (1)$$

where Δu and $\Delta\rho$ are the velocity and density differences, respectively; d is the particle diameter, ν is the viscosity, and f the typical eddy frequency. For a particle diameter of 30μ, frequency of 100 Hz (approximately the blade rate Frequency) and density difference in the order of 5 percent, the velocity difference is less than 0.5 percent. Adrian (1991) approximated the slip velocity of particles by equating their inertia to the drag force while neglecting the effects of pressure gradients and virtual mass. Conclusions from his analysis are not significantly different from results obtained by using Eq. (1).

Based on this analysis the diameter of a tracer particle should be kept below 30μ and its density should not differ by more than about 5 percent from water. Due to their size and the characteristic speed in the pump facility the intensity of light reflected from such particles is quite low and hard to record (see Adrian, 1991 for a complete analysis). Consequently, we developed procedures for manufacturing particles containing imbedded fluorescent dyes that respond efficiently to green lasers. The specific gravity of these particles varies between about 0.95 to 1.05. We have recently filed for a patent on the production techniques as well as the chemistry of these particles (more information will be provided when these procedures are completed). Because of their size these tracers are practically invisible in most of the flow field, but they can be easily detected within the light sheet (see Fig. 2). The entire pump facility was flooded with these particles in order to generate a uniform dense distribution. As will be discussed later their density affects the accuracy of the results.

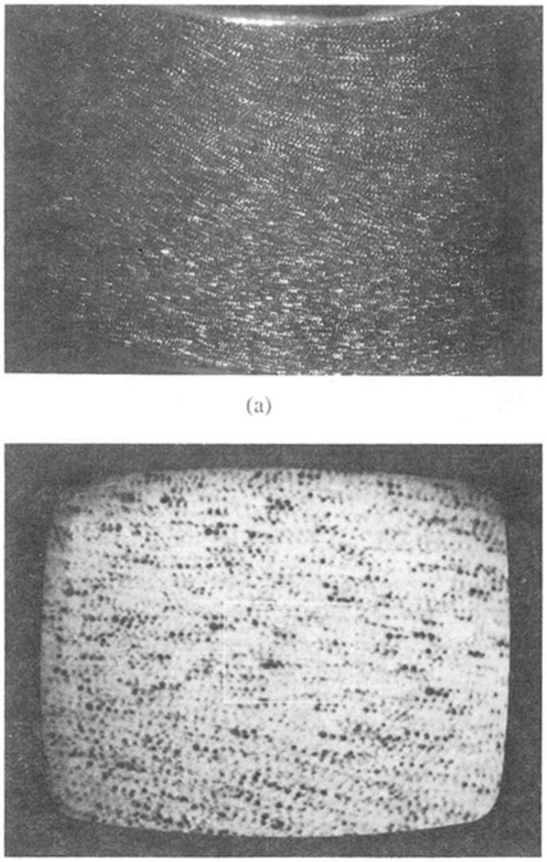
(a)

(b)

Fig. 2 (*a*) Original triple exposure image of particle traces; (*b*) a video frame of a magnified section

Analysis Procedures

The analysis procedure selected for the present study (auto-correlation methods) requires high resolution images and as a result the original photographs are always recorded on film. The negatives are illuminated from behind and examined by a video camera equipped with a microscopic objective. A sample triple exposure original image and a typical video frame are presented in Figs. 2(*a*) and (*b*), respectively. Typically the video camera covers an area of 5×5 mm, which means that a 35 mm negative is converted to 35 video frames (7 rows and 5 columns). Each frame is digitized to an 8 bit 512×512 pixels array, filtered and enhanced (if necessary). Consequently a single negative is converted to about 3500×2500 pixels. As will be discussed shortly, this resolution is required in order

Nomenclature

$D(m, n)$ = auto-correlation function
d = particle diameter
$F(i, j)$ = Gray level of a pixel
f = typical fluctuation frequency
u = velocity
u', v' = deviations from the mean velocity
$\bar{u}, \bar{v}$ = phase averaged velocity components
Δu = slip velocity of particles
U_T = impeller tip speed
$\Delta x, \Delta y$ = horizontal and vertical dimensions of a cell
ρ = liquid density
$\Delta\rho$ = density difference between particle and liquid
ν = liquid kinematic viscosity
$\xi(i, j)$ = vorticity

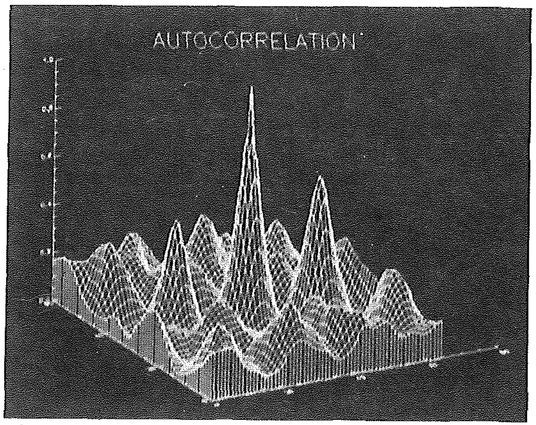

Fig. 3 Auto-correlation of the image enclosed within the window outlined in the middle of Fig. 2(*b*)

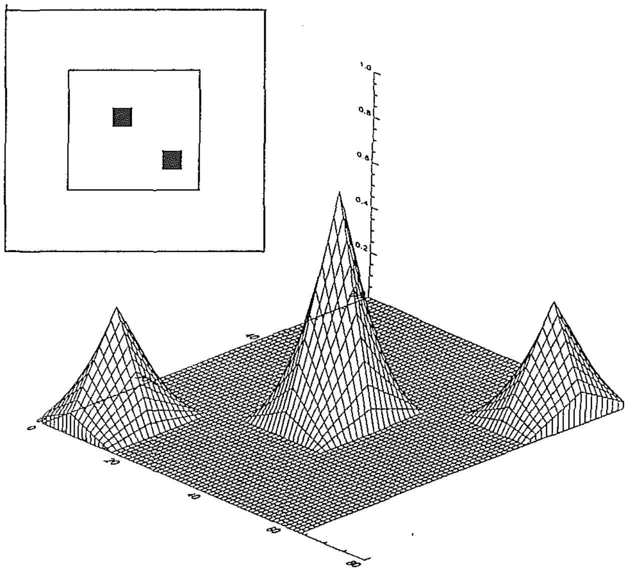

Fig. 4 A computer generated pair of squares simulating a displaced particle and its computed auto-correlation

to keep the error in velocity measurements at about 1 percent and still generate at least 1000 velocity vectors per image. This resolution is beyond the capability of any video camera (typical resolution of 500 × 500 lines), but is within the limits of a typical 35 mm film (100 lines/mm). In the present setup a PC contains the image digitizer and the controller for the motorized drive of the video camera. The digitized images are shipped from the PC to a SUN SPARC Station 1 which is used for most of the computations.

The auto-correlation method is particularly suitable but not limited to particle densities ranging between 1000 and up to about 10,000 per image. It consists of dividing the image to a large number of small sections, each with a typical size of 1 × 1 mm, (can be easily changed) and determining the average displacement of all particles within each section. This mean displacement is determined by computing the auto-correlation function of the intensity distribution, $D(m, n)$, defined as:

$$D(m,n)=\sum_{j}\sum_{k}F(j,k)F(j-m,\ k-n) \qquad (2)$$

where $F(j, k)$ is the "gray level" of a pixel located at (j, k). When the image is digitized to an eight bit array, the values of $F(j, k)$ vary between 0 (black) and 255 (white). Since we actually analyze a negative (not a necessity), the brighter the particle is, the darker is its gray level. The result of an auto-correlation analysis to the window marked in Fig. 2(*b*) is presented in Fig. 3. Three distinct peaks are clearly evident in this 3-D plot. The middle and largest peak corresponds to $m=n=0$. The other two are located symmetrically on both size of the center, and their location indicates both the mean distance between particle traces and the angular orientation of the velocity. In order to illustrate this point, let's look at the auto-correlation of a computer generated image of two squares shown in Fig. 4. The result is different than zero, either when $m=n=0$ providing the value of the intensity squared (multiplying two identical images), or when n and m are equal in magnitude to the horizontal and vertical distances between the two dots, respectively. For any other value of n and m, the product $F(j, k)F(j-m, k-n)$ is equal to zero, since at least one of the intensities is zero. The location of the peaks then indicates the distance between the two squares. If the sample area contains more than a single pair of squares (Fig. 5), there is some matching between traces of different particles, but distinct peaks still appear when several traces match at the same time. The same principle can be implemented while analyzing the motion of a multiple exposure image (Fig. 2). Note that m and n are integers and as a result only discrete values of $D(m, n)$ are computed. One can then interpolate between these values and obtain a better estimate for the location of the correlation maxima at sub-pixel levels. This procedure was used on the image presented in Fig. 2(*a*) and the results are presented in Fig. 6. Further information associated with this vector map will be provided following a discussion on the accuracy of these results.

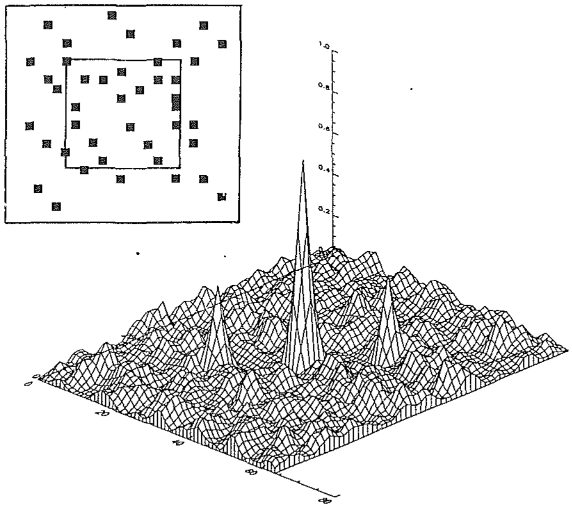

Fig. 5 Computer generated pairs of squares simulating double exposure particle traces and their computed auto-correlation

It is quite tempting to perform the analysis in the frequency domain by computing the Fourier transform of the original image either numerically (by using FFT) or optically (essentially the speckle velocimetry method). However, the process can be simplified in flow fields that do not involve substantial differences in the magnitude and direction of the velocity in neighboring windows (can be insured by appropriate selection of window sizes and spacing). Instead of repeating the entire analysis one can start by "guessing" the location of auto-correlation peaks by assuming that velocities in neighboring windows are identical. Then, the values of $D(m, n)$ are computed around that value only until a peak (maximum) is clearly identified. Some additional neighboring values are also computed to insure that it is the only peak and for better interpolation between discrete values. Our experience indicates that for most cases the peaks in neighboring windows are located within 5 pixels of each other. Thus, instead of computing

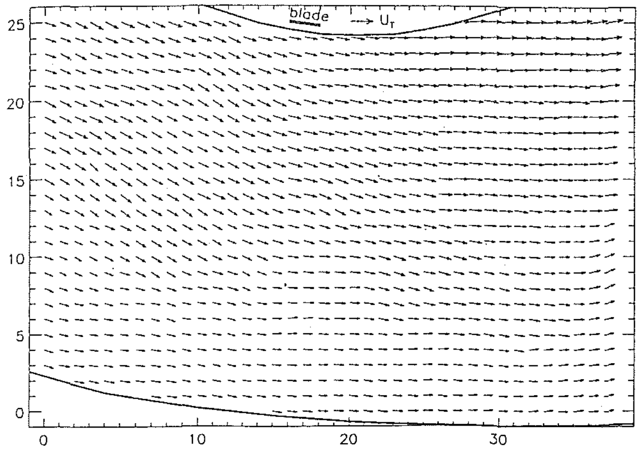

Fig. 6 Vector map of the velocity distribution computed from the image presented in Fig. 2(*a*)

64×64 values for $D(m,n)$, one has to compute only 10×10 values. The required computations are reduced by 97.6 percent. However, the results must be checked by performing a complete analysis every 10–20 windows to prevent from "locking" on a secondary peak.

In general, the auto-correlation method can compute the magnitude and angular orientation of the velocity vector but cannot identify the direction of flow without additional means. The difficulty can be overcome by image shifting (Adrian, 1989), recording images on different frames (Willert and Gharib, 1989) and when the particles reflect light, by modulation of the polarization of the illuminating laser (Adrian, 1989). The latter method is not suitable for fluorescent particles, and the former two are difficult to manage when the characteristic velocity is high. As a result we chose to identify the direction of flow by intensity modulation, namely by generating laser pulses with varying intensities. Automated techniques for detecting the weaker trace will be discussed in future papers. This process was unnecessary for the flow within the volute since it was unidirectional.

Uncertainty Analysis

Obvious potential problems, such as distortions introduced by the video camera and the lenses, should be minimized by using high quality optics and verified with photographs of reference grids. The later were used to confirm that image distortion did not seem to play any noticeable role in the quality of present data. Additional potential sources of error become significant when the number of traces per image is very small. For example, when a window contains a pair of traces of one particle and a single trace of a second. The auto-correlation then contains peaks associated with the appropriate velocity, but also peaks associated with the distance between the second particle and either trace of the first particle. These difficulties can be resolved, either by comparing the result to velocities computed in neighboring windows, or by increasing the size of the window.

In order to quantify the overall accuracy of the present procedure we performed a series of calibration experiments.They consisted of recording an image of a known uniform flow and analyzing the data following the very same procedures used during the present study. We chose the flow within the potential core of an axisymmetric jet. Sample results are summarized in Fig. 7. It displays the distribution of velocities (or averaged distance traveled by particles) computed in 169 different windows and that include a fluid supposedly moving at the same velocity. Since the turbulence level within the potential core is very low (it is injected from a 16:1 contoured nozzle equipped with a honeycomb and screens), namely less than 0.1 percent, then variations in the computed velocity are directly related to our analysis procedures. As is evident from Fig. 7(*a*), the mean distance between particles is 26.6 pixels, and the standard deviation is 0.22 pixels. For a confidence level of 95 percent the error should then be set at twice the standard deviation, namely at 0.44 pixels. Thus, the maximum expected error in these measurements is in the order of 1.6 percent. The mean number of particle pairs per window in this series of calibration measurements is 8.

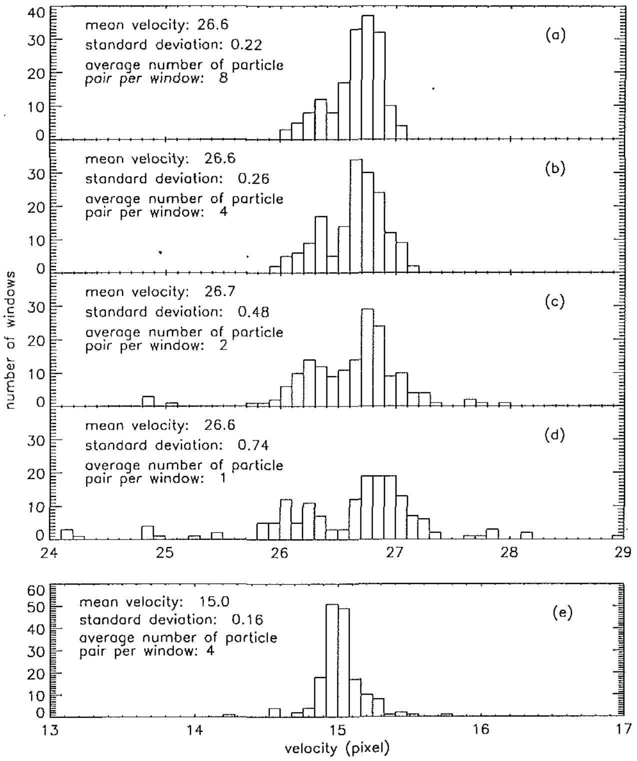

Fig. 7 Probability histogram of the velocity distribution of a uniform flow computed by using the auto-correlation method

If the magnification of the very same image is reduced such that the distance between traces is 15 pixels and the analysis is repeated, the absolute error (still defined as 2σ) actually drops slightly (Fig. 7(*e*)) to 0.32 pixels. However, the distribution already contains a few windows with a larger error. This trend is actually a warning that we are getting close to the resolution limit the image processing system (traces are too small). Consequently, in sections with still sufficiently large particle traces the reduction in magnification creates sharper images with a lower error. However, a few windows contain some digitized particle traces that are already too small to be resolved clearly. As we have found, reliable results require traces covering about 5 pixels.

In order to determine the effect of reducing the number of particles per image, the size of the window was reduced to include less particles without changing the magnification. Probability distributions obtained for the same data, but with window sizes reduced to include averages of 4, 2, and 1 particle pairs per window are presented in Figs. 7(*b–d*). The respective uncertainty levels (with 95 percent confidence) are 0.52 (2 percent), 0.9 (3 percent), and 1.5 pixels (5 percent). Thus, the accuracy depends strongly on the number of traces per window. This trend should be expected since the auto-correlation method computes the mean displacement of all the particles within each window. When the sample size is increased, the accuracy of the result improves.

There are ways to improve the accuracy of the computed

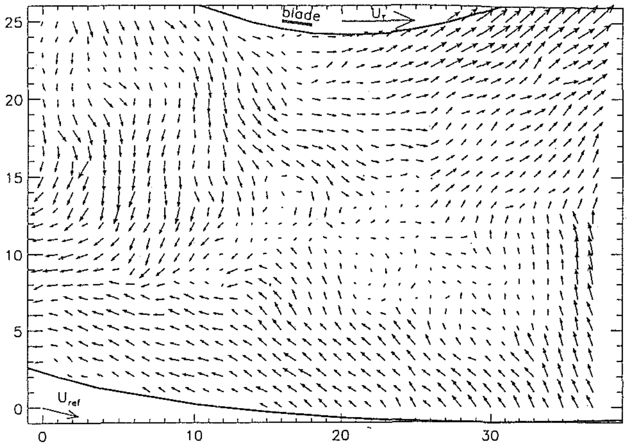

Fig. 8 The data presented in Figure 6 after subtracting the mean velocity from each vector

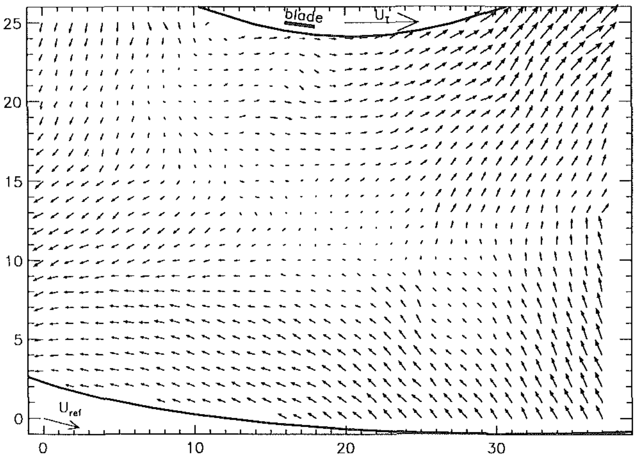

Fig. 9 A sample phase averaged velocity distribution at mid sections of the volute. Flow rate is 270 gpm. Data is presented as $u - U_{ref}$. Tip speed and U_{ref} are also shown.

velocity even when the number of particles per window is low and it is impractical to increase the window size. Since the intensity distribution within each particle is not uniform (it is typically gaussian), one can interpolate between discrete pixels values and determine the particle center and its displacement at sub-pixel levels. Sridhar et al. (1991) calibrated this procedure for an image consisting of a single particle pair. They showed that for trace diameters of 15, 20 and 25 pixels, the relative errors (difference between exact value and computed result) were 4, 0.85, and 0.35 percent, respectively. Note that such a high accuracy involves a substantial payoff in computation time. Since the typical particle size during the present analysis is 5 pixels, these results indicate that for substantial improvements in accuracy, the digitized array must be 25 times larger. Thus, heavier seeding is a simpler and more efficient method for maintaining high accuracy.

In general the window size is limited only by the film quality (100-300 line pairs per mm for a 35 mm film) and the density of particles. The objective zoom lens on the scanning video camera can handle magnifications exceeding the film resolution. For 100, 200, and 300 lines/mm films, and images digitized to maintain the same resolution (1 pixel = 1 film line), a 64 × 64 pixels window corresponds to 0.64 × 0.64, 0.32 × 0.32 and 0.21 × 0.21 mm on the negative, respectively. However, as the window size is reduced it becomes harder to maintain the required particle density.

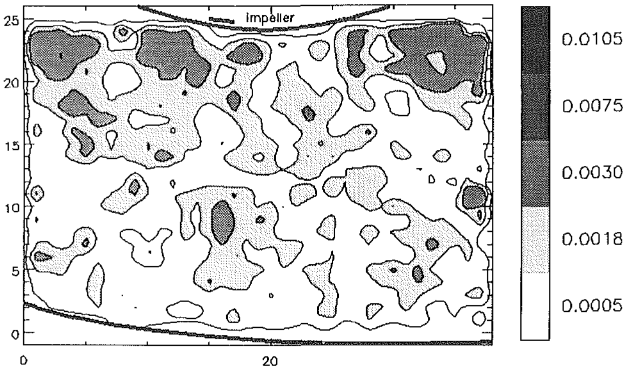

Fig. 10 Mean deviations of the instantaneous data from the phase averaged results as defined in Eq. (3)

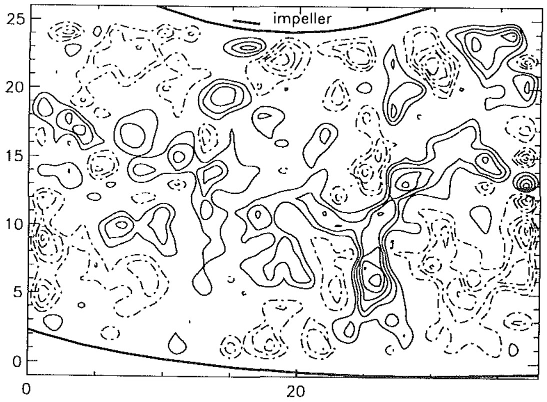

Fig. 11 The vorticity distribution computed from the vector map presented in Fig. 9 (data scaled with the angular velocity of the impeller). Incremental increase between lines is 0.2. Solid lines — negative vorticity; dashed lines — positive vorticity.

Sample Results

The characteristic window size selected for the present study included at least 8 particles per image, but was small enough to insure that flow structures were not averaged out (autocorrelation peaks were large and distinct). In some cases the windows actually overlapped in order to increase the window size without reducing the number of computed velocity vectors. A typical window size covered an area ranging between 1 × 1 mm to 2.5 × 2.5 mm in the original flow field, or up to 1 × 1 mm on the negative. After being digitized it occupied at most 128 × 128 pixels (typically 64 × 64). Note that windows located close to an edge of a negative are prone to difficulties since some values of n and m extend to regions for which $F(i-m, j-n)$ is not defined. It is usually quite easy to detect such "mishap" by comparing computed velocities to results obtained in neighboring windows. In such cases the window size was changed to provide reliable data.

Numerous images such as Fig. 2 were recorded and analyzed during the course of the present study. Most of the results are summarized and analysed in the second part of this paper. Since the flow in the volute is unidirectional, it is easier to identify interesting trends by computing the mean velocity and subtracting it from each vector as shown in Fig. 8. One can also record several images at the exact same blade orientation (more details will be provided in Part B) and compute the phase average velocity distribution for that specific flow condition (Fig. 9). Then, the extent of "random" turbulent fluctuations can be determined by computing the mean deviation of instantaneous data from the phase averaged results. These deviations, namely the values of $[u'^2 + v'^2]/U_T^2$, were computed by using Eq. (3)

$$[\overline{u'^2}+\overline{v'^2}]/U_T^2=\frac{1}{n}\left[\sum_{i=1}^{n}(u_i-\overline{u})^2+\sum_{i=1}^{n}(v_i-\overline{v})^2\right]/U_T^2 \qquad (3)$$

U_T is the impeller tip speed and u and v are the horizontal and vertical velocity components (" - " indicates phase averaged property, and " ' " a deviation). A contour plot of the deviation for the data presented in Fig. 9 is presented in Fig. 10. This expression can be interpreted also as a "turbulent kinetic energy" of the phase averaged velocity distribution. A vorticity distribution computed from the same vector map is presented in Fig. 11. The equation used for evaluating the vorticity is:

$$\xi(i,j)=\frac{1}{2}\left\{\frac{[v(i+1,j)-v(i-1,j)}{\Delta x}-\frac{[u(i,j+1)-u(i,j-1)]}{\Delta y}\right\} \qquad (4)$$

where i and j are the horizontal and vertical indices and Δx and Δy are the horizontal and vertical dimensions of a cell, respectively. As is evident form this sample, the flow within the volute is nonuniform and dominated by large vortex structures. Deviations from the phase averaged results also vary substantially and in the present example are higher near the impeller. The characteristics of the flow within the volute, and its dependence on flow rate, orientation of impeller blades, location within the volute etc. are presented in part B of this paper.

Summary and Conclusions

This paper introduces the technique and procedures presently being used for quantitative visualization of the flow within the volute of a centrifugal pump. It involves recording of multiple exposure images of a flow field illuminated by a laser sheet and seeded with microscopic neutrally buoyant particles. The analysis consists of dividing the image to a large number of small windows and determining the mean shift of all the particles within each window. The mean shift is determined by computing the autocorrelation function of the intensity distribution. The recording and analysis procedures are calibrated by recording the image of particle traces within a uniform flow. It is demonstrated that if the particle density and magnification are chosen such that each window contains at least 8 pairs of particles, the uncertainty can be kept at about 1 percent. Methods of increasing the speed and efficiency of the analysis are also discussed. The paper concludes by presenting a sample vector map of the velocity distribution within the volute of a pump. A contour plot of the vorticity distribution computed from the same data is also included.

Acknowledgment

This project has been sponsored by the Office of Naval Research under contract number N00014-89-J-1672. We are particularly grateful to Jim Fein for his continued support.

References

Adrian, R. J., 1991, "Particle Imaging Techniques for Experimental Fluid Mechanics," *Annual Review of Fluid Mechanics*, Vol. 23, pp. 261–304.

Adrian, R. J., 1989, "Application of Particle Image Velocimetry," *Flow Visualization - 1989*, Presented at the Winter Annual Meeting of the ASME, San Francisco, CA, December 10–15, Ed., Khalighi, Braun, and Freitas, pp. 23–28.

Adrian, R. J., 1986, "Multi-Point Optical Measurement of Simultaneous Vectors in Unsteady Flow - A Review," *Int. J. Heat and Fluid Flow*, Vol. 7, No. 2, pp. 127–145.

Agui, J. C., and Jimenez, J., 1987, "On The Performance of Particle Tracking," *Journal of Fluid Mechanics*, Vol. 185, pp. 447–468.

Gharib, M., Willert, 1989, "Particle Tracing: Revisited," *Advances in Fluid Mechanics Measurements*, ed., M. Gad-el-Hak, Springer-Verlag, 1989, pp. 109–199.

Shekarriz, A., Fu, T. C., Katz, J., Liu, H. L., and Huang, T. T., 1991, "Quantitative Visualization of Junction and Tip Vortices Using Particle Displacement Velocimetry," AIAA paper 91-0269.

Sridhar, G., Katz, J., 1991, "Implementation of Particle Image Velocimetry to Multi-Phase Flows," ASME Cavitation and Multi-Phase Flow Forum - 1991, Presented at the Spring Annual Meeting, Portland, Oregon.

Willert, C. E. and Gharib, M., 1991, "Digital Particle Image Velocimetry," *Experiments in Fluids*, Vol. 10, pp. 181–193.

Quantitative Visualization of the Flow Within the Volute of a Centrifugal Pump. Part B: Results and Analysis

R. Dong

S. Chu

J. Katz

Department of Mechanical Engineering,
The Johns Hopkins University,
Baltimore, MD 21218

PDV is used for measuring the velocity within the volute of a centrifugal pump at different impeller blade orientations, on and off design conditions. It is demonstrated that the flow is "pulsating" and depends on the location of the blade relative to the tongue. The leakage also depends on blade orientation and increases with decreasing flow rate. The velocity near the impeller is dominated by the jet/wake phenomenon. Differences in the outflux from the impeller, resulting from changes in flow rate, occur primarily near the exit. Away from the tongue the distributions of v_θ mostly agrees with the assumption that $v_\theta \propto 1/r$. Sites prone to high velocity fluctuations include the blade wake, interface between the jet and the wake and near the tongue. Angular momentum and kinetic energy fluxes, turbulent stresses and tubulence production are also computed. It is shown that at the same θ the momentum flux can increase near the impeller and decrease at the perimeter. Consequently, the mean flux cannot be used for estimating conditions near the impeller. Torques caused by $\tau_{r\theta}$ and $\tau_{\theta\theta}$ can be as high as 2 and 5 percent of the change in angular momentum flux, respectively.

Introduction

Most of the past research related to pump volutes involved static pressure measurements (Iversen et al., 1960, for example), and was associated with attempts to estimate asymmetric (radial) loading on the shaft. Experiments that did include velocity measurements showed that the flow was nonuniform, particularly off design conditions (Binder and Knapp, 1936; Acosta and Bowerman, 1957; Bowerman and Acosta, 1957; Hamkins and Flack, 1987; Miner et al., 1989). Most of the attention was given to the outflux from the impeller.

It was found that on top of circumferential variations, the radial velocity at the exit from the impeller was higher on the pressure side of the blade, consisting of what was typically referred to as a "jet" and a "wake" (Dean and Senoo, 1960 and Eckardt 1975, 1976). The effect of blade orientation on the velocity distribution away from the impeller received less attention. According to Miner et al. (1989), the location of the blade affects the flow only up to about $r/r_T = 1.2$.

While attempting to model the flow within the volute on design conditions, researchers typically assume that $v_\theta r$ is constant (Lorett and Gopalakrishnan, 1986), relying on conservation of angular momentum. Off design conditions, due to absence of data, the analysis either involves assumptions that v_θ is uniform and changes only with θ (Iversen et al., 1960), or is limited to mean properties. It is also assumed that $v_r < v_\theta$ and consequently, only $v_\theta^2/2$ is accounted for while using the Bernoulli equation. Turbulent dissipation is neglected, primarily due to lack of information, and the wall friction is accounted for by using empirical relations developed for pipe flows. As realized by Lorett and Gopalakrishnan (1986), a critical factor affecting the validity of any model is a realistic estimate of the leakage between the tongue and the impeller. The flow around the tongue is also known to be a primary site of unsteady loading and a source of noise (Yuasa and Hinata, 1979). Although it is known that the leakage decreases as the overall pump flow rate increases, and that an increase in the size of the gap decreases the efficiency, there is little quantitative information about the extent of this leakage. *Qualitative* flow visualization experiments reported by Brownwell et al. (1985) demonstrate that the entire flow structure, including the location of stagnation on the tongue, varies with flow rate and blade position. They even observe that flow separation occurs on the tongue above design conditions.

As noted before, lack of information is a primary cause for the simplified models of volute flows. The present paper provides some answers, such as circumferential, radial and axial variations in the velocity distribution, conservation of angular momentum on and off design conditions, the extent of a jet/wake phenomenon, the effect of blade orientation on the velocity and overall flux, the extent of leakage between the tongue and the impeller and the significance of turbulent stresses and dissipation on the energy and angular momentum of the fluid. These results can then be used for evaluating typically made

---

Contributed by the Fluids Engineering Division for publication in the JOURNAL OF FLUIDS ENGINEERING. Manuscript received by the Fluids Engineering Division November 26, 1990. Associate Technical Editor: J. Tuzson.

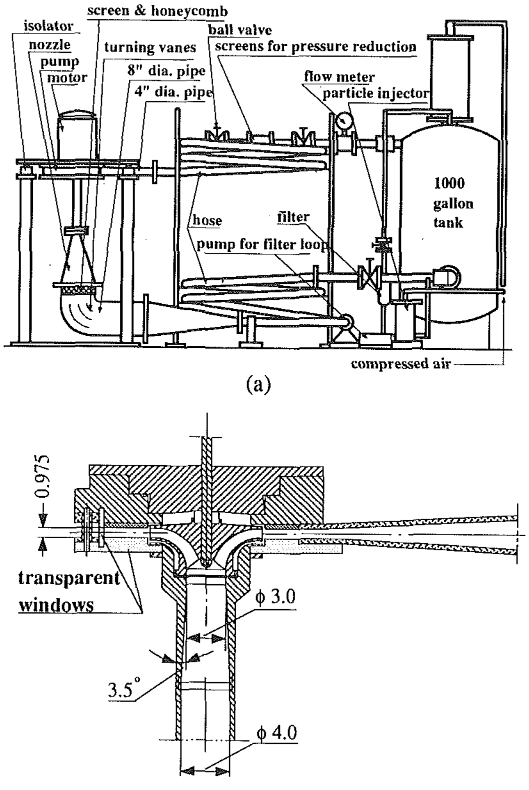

(a)

(b)

Fig. 1 Schematic descriptions of the: (*a*) pump loop; (*b*) impeller and modified volute

assumptions. In order to determine the flow structure, the experiments are performed by implementing PDV. The technique and analysis procedures are described in Part A of this paper.

Experimental Setup

The experiments were performed in a pump flow visualization facility illustrated schematically in Fig. 1. The settling chamber and turning vanes were installed to regulate the influx to the pump. The pump was also vibration isolated and flexible hoses were used for separating it from the rest of the facility. The test model was a vertical centrifugal pump operating at 890 rpm. The impeller was 9.95 in. in diameter, and had 7 blades, all of them with an exit angle of 15 deg. The original casing of this pump was replaced with a fiberglass frame and lucite windows, such that the entire perimeter and the bottom side of the casing became transparent. The configuration of the perimeter (in inches) was $r_v = r_T + t + 4(\theta/360 \text{ deg})$ where $\theta = 0$ deg was located 3 deg upstream of the tip of the tongue. The volute had constant thickness ($H = 0.975$ in.) which was equal to the thickness of the impeller. The 4 × 0.975 in. exit gradually expanded to a 4 in. pipe by using a fiberglass diffuser with maximum expansion angle of 7 deg. The design flux of this volute was 200 gpm, but the maximum efficiency occurred at a slightly lower flux. Performance curves of this pump are provided in Fig. 2.

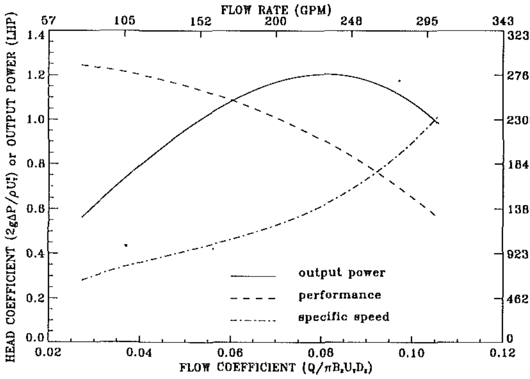

Fig. 2 Performance curves of the modified pump

As described in Part A of this paper the experiments consisted of illuminating sections of the flow field with a laser sheet while seeding the water with microscopic, fluorescent, neutrally buoyant particles. The laser sheet (triple pulse Nd-Yag laser) could illuminate any desired section of the volute either through the transparent perimeter or from the bottom. The intensity of each pulse was modulated independently which enabled identification of the order at which the laser was fired. The delays between pulses were kept at 160 μs, and their timing was synchronized with the impeller. The images were recorded on a 35 mm film and analyzed following the procedure described in Part A.

Results

Effect of Impeller Blade Orientation. In order to separate between periodic and random phenomena within the volute, we selected five different impeller blade orientations, and analyzed at least eight images at each angle. The exact orientations are sketched in Fig. 3(*a*). Each set of eight vector maps was then averaged in order to estimate the "mean" (phase averaged) velocity distribution at a specific angle. Sample vector maps are presented in Fig. 4, and additional results can be found in Part A, Chu et al. (1991) and Dong et al. (1991). Note that a typical reference velocity, U_{ref}, is subtracted from each vector for the purpose of clarifying the flow characteristics. Selected velocity distributions at 270 gpm (above design conditions) are also replotted in Figs. 5–6 in order to highlight blade effects. In agreement with Miner et al. (1989), the blade orientation affects the distributions of v_θ mostly near the impeller. However, when the blade lines up with the tip of the tongue (when blade 1 is at $\theta \cong 10$ deg) v_θ is consistently higher throughout the volute. Away from the impeller v_θ decreases

Nomenclature

e, e' = mean and turbulent kinetic energy
E_0 = $\rho U_T^3 r_T^2$
$h, 1$ = coordinates used in the axial planes
H = thickness of impeller and volute
I = angular momentum flux
I_0 = $\rho U_T^2 r_T^3$
K.E = kinetic energy flux
Q = flow rate
r, θ = radial and lateral coordinates
r_T = radius of the impeller
$r_v(\theta)$ = external radius of the volute
t = space between impeller and tongue-0.34 in.
T = torque
Π = turbulent energy production
u_0 = velocity normal to axis in planes S1–S3
U_{ref} = reference velocity
U_T = impeller tip speed
v_r, v_θ, w = radial, circumferential and axial velocities, respectively
$\tau_{\theta\theta}, \tau_{r\theta}, \tau_{z\theta}$ = Reynolds stresses

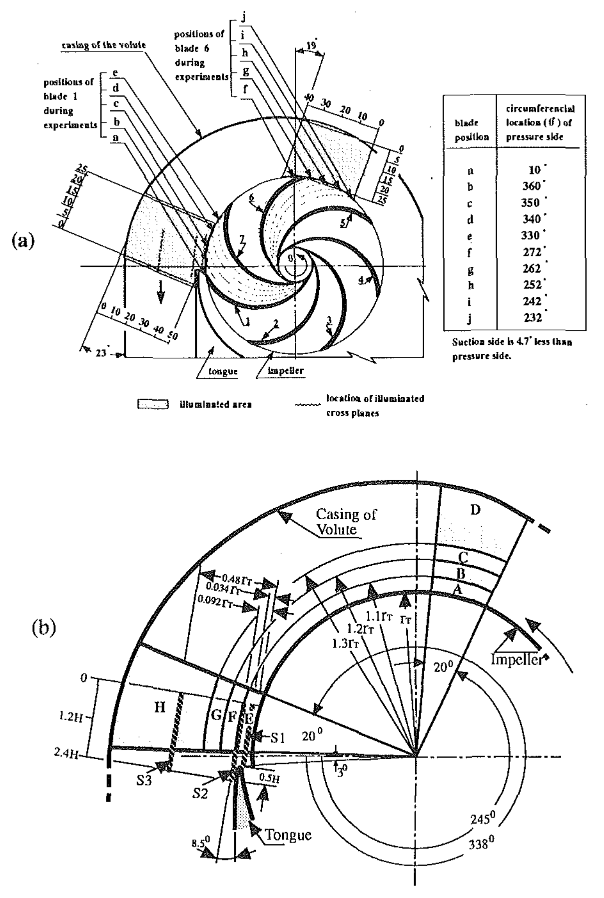

blade position	circumferencial location (θ) of pressure side
a	10°
b	360°
c	350°
d	340°
e	330°
f	272°
g	262°
h	252°
i	242°
j	232°

Suction side is 4.7° less than pressure side.

Fig. 3 Location of: (*a*) blades and sample sections during the experiments; (*b*) axial sheets and control sections used during the analysis

with increasing r. This trend changes only in the immediate vicinity of the tongue (θ = 345–355 deg and $r/r_T < 1.2$) due to the stagnation point on the tongue, and the relatively low leakage at this flow rate (see Fig. 4).

Irrespective of blade orientation, the outflux from the impeller (v_r at $r/r_T = 1.0$) at mid sections (θ = 245–265 deg in Fig. 6) increases with θ from a typical value of 0.09 to about 0.12. This trend is a result of circumferential pressure gradients (see Table 2). Specific values depend on the orientation of impeller blade. Consistent with the "jet/wake" phenomenon, the outflux peaks in the pressure side of the blade and is minimal in the suction side. For example, when blade 6 is at 252 deg v_r/U_T drops to 0.03 on the suction side and reaches 0.13 on the pressure side. With increasing distance from the impeller the impact of the nonuniform outflux weakens (in agreement with Miner et al., 1989), but remains evident even at r/r_T = 1.4. The same jet/wake structure appears also near the exit. In order to highlight this trend, the values of v_r and v_θ at r/r_T = 1.0 are replotted in Figs. 7(*a*) and (*b*), but this time the distributions are shifted such that the blade is located at a fixed position. The jet with $v_{r\max} = 0.18$ and $v_{\theta\min} = 0.39$, as well as the wake with $v_{r\min} = 0.03$ and $v_{\theta\max} = 0.71$ are clearly evident. Note the existence of separate maxima (not related to the jet/wake) in the distributions of v_r when blade 6 is at θ = 330 deg, 340 deg. They are caused by partial blockage to the space between blades that results in an increase in v_r in the unblocked portion. When the blade lines up with the tip of the tongue (10 deg) this peak disappears. At larger radii the flow is dominated by the presence of the tongue that causes an increase in v_r and a reduction in v_θ (see Fig. 4).

Effect of Flow Rate. Comparative velocity distributions

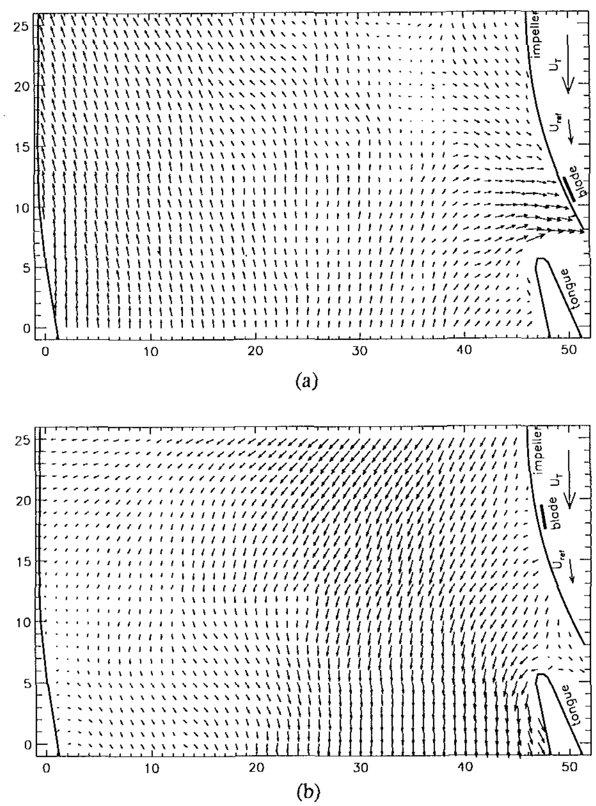

Fig. 4 Sample phase averaged velocity distributions near the exit. Data is presented as $u - U_{ref}$. Tip speed and U_{ref} are also shown on each map. Flow rates and blade orientations are: (*a*) 90 gpm and blade 1 at 360 deg; (*b*) 270 gpm and blade 1 at 350 deg

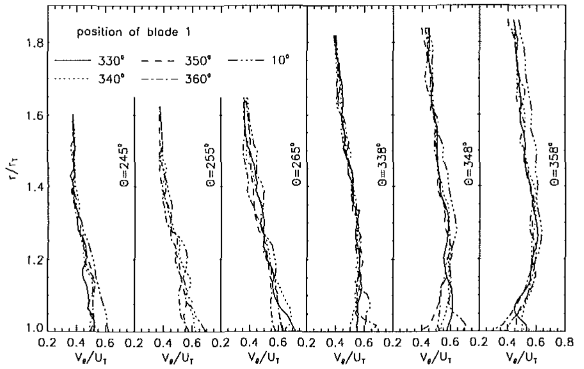

Fig. 5 Distributions of the circumferential velocity at different impeller blade orientations (270 gpm)

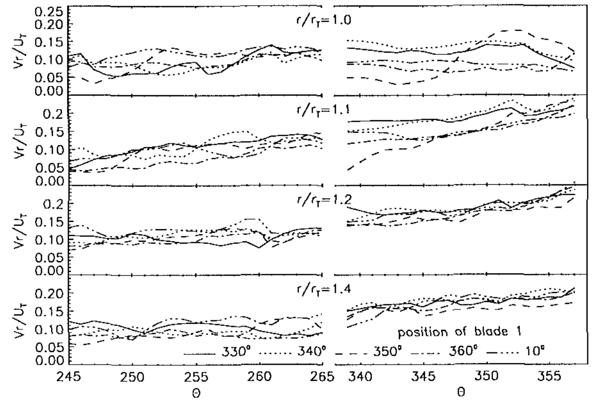

Fig. 6 Distributions of the radial velocity at different impeller blade orientations (270 gpm)

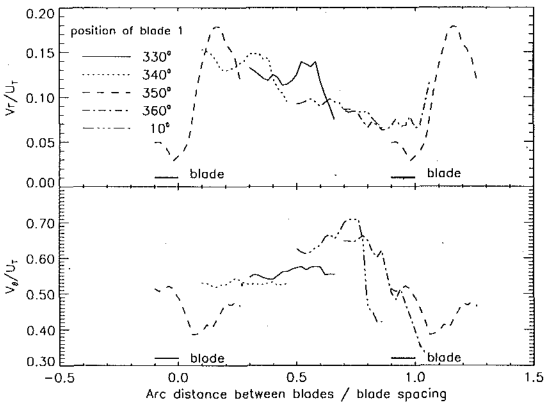

Fig. 7 V_r and V_θ near the exit at r/r_T = 1.0. Data are shifted in order to keep the blade at a fixed location.

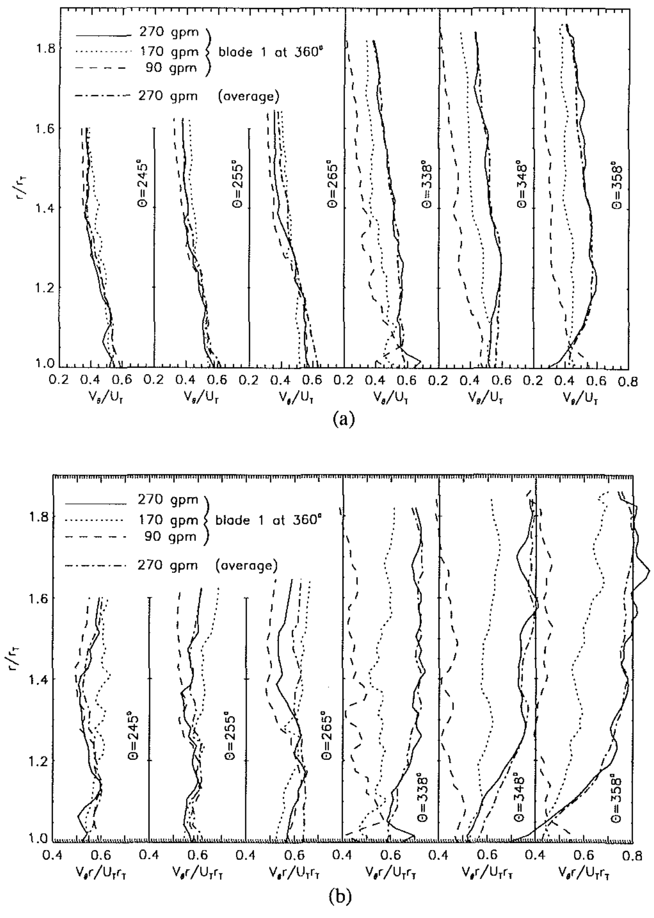

Fig. 8 Distributions of (*a*) v_θ; (*b*) $v_\theta r$ at different flow rates

representing the flow above (270 gpm), close to (170 gpm), and below design conditions (90 gpm) are presented in Figs. 8-9. Circumferential variations, namely an increase in v_θ with increasing θ above design conditions and a decrease below design conditions, agree with expectations (continuity). Since typical analysis of volute flows involves balance of angular momentum (Lorett and Gopalakrishnan, 1986), we present also sample distributions of $v_\theta \cdot r$ in Fig. 8(*b*). On design conditions $v_\theta \cdot r$ increases slightly with r (even away from the impeller), namely v_θ is more uniform than the typically assumed distribution ($v_\theta \propto 1/r$). Below design conditions $v_\theta \cdot r$ decreases, and above design conditions there are varying trends, particularly at mid sections (an increase, followed by a decrease around $r/r_T = 1.3$, and then an increase at the outer perimeter).

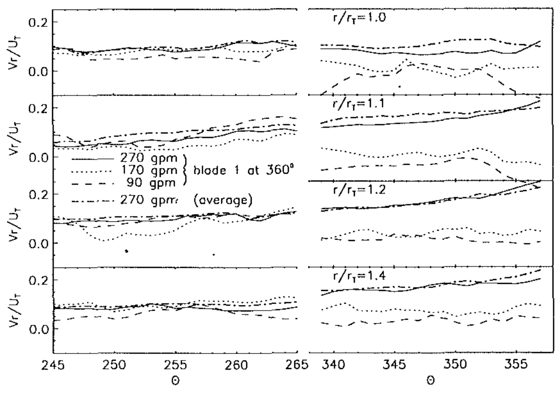

Fig. 9 Distributions of v_r at different flow rates

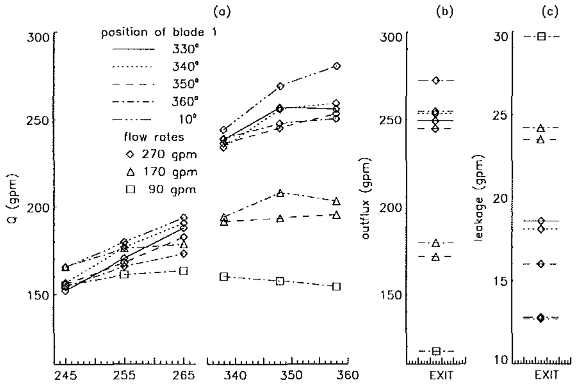

Fig. 10 Computed: (*a*) $Q(\theta)$; (*b*) outflux from the pump; (*c*) leakage

The overall mean distributions at 270 gpm is smoother than results for a single blade orientation. For all the cases presented an assumption that $v_\theta \cdot r$ is constant leads to an error in the order of 5-10 percent (compared to the mean value). This assumption is invalid in the vicinity of the tongue.

Unlike the computed trends of Lorett and Gopalakrishnan (1986), and in spite of differences in the static pressure (some experimental results in Table 2), there is little difference between the outflux from the impeller at 270 gpm and 170 gpm at mid sections (Fig. 9). Most of the differences occur near the exit, where close to design conditions the outflux drops to zero (also unlike typical assumptions of a constant outflux). At 90 gpm there is already backward flow into the impeller.

Overall Flux and Axial Distributions. The overall flux at any section, $Q(\theta)$, can be computed by integrating v_θ, $(\Sigma H v_\theta(r, \theta)\Delta r)$. The leakage and outflux from the pump are computed by integrating the velocity normal to a line, that touched the tip of the tongue. Changes in the location of stagnation point on the tongue, that agree with Brownwell et al. (1985) are accounted for while computing the leakage. According to the results (Fig. 10), the outflux from the impeller in the last quadrant of the volute ($270 < \theta < 360$) contributes about 30 percent of $Q(\theta)$ at 270 gpm and only less than 10 percent at 170 gpm. This trend agrees with the distributions of v_r. It is also evident that both $Q(\theta)$ and the outflux vary by as much as 10 percent, depending on the orientation of impeller blades. They both reach a maximum level when the blade lines up with the tip of the tongue (as noted also from the distribution of v_θ), minimizing, as a result, the blockage to the outflux from the impeller. As expected, the leakage decreases from 25 percent of the outflux at 90 gpm down to only 6.1 percent of the outflux at 270 gpm. The leakage also varies by as much as 50

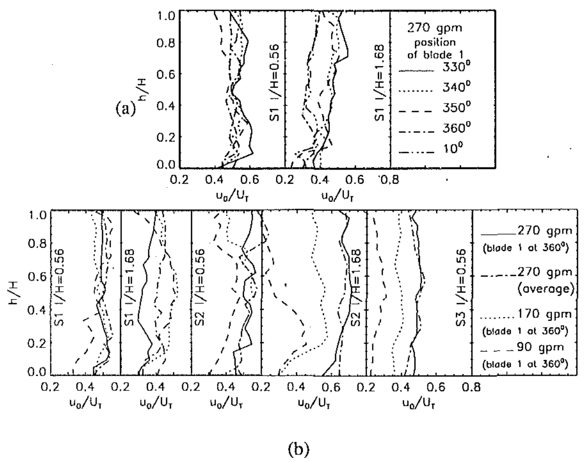

Fig. 11 Sample distributions of u_0 in the axial planes S1, S2, and S3 shown in Fig. 3(*a*). (*a*) Effect of blade orientation; (*b*) effect of location and flow rate.

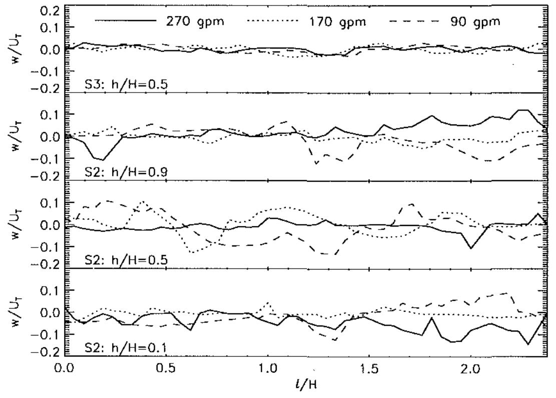

Fig. 12 Sample distributions of *w*, the axial velocity

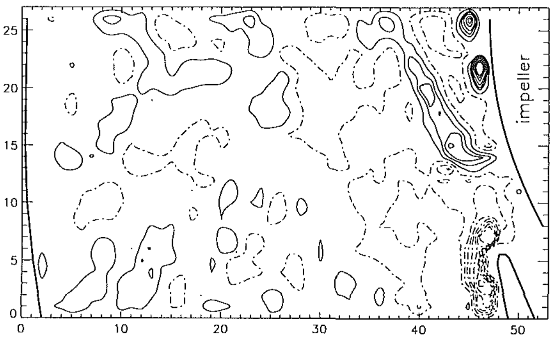

Fig. 13 Vorticity distribution scaled with the angular velocity (U_T/r_T) near the exit. Flux is 270 gpm and blade 1 is at 10 deg. Incremental increase between lines is 0.4. (Solid lines—negative vorticity; dashed lines—positive vorticity.)

percent (at least at 270 gpm), depending on the orientation of impeller blades. It is minimum when the blade is located near the tongue (360 deg and 10 deg), probably since the passage is more constricted at this orientation.

There is a discrepancy between the computed outflux and the reading of the flow meter. In order to identify reasons for this discrepancy, the assumption of a 2-D flow was evaluated by mapping the velocity in three axial planes, identified as S1, S2 and S3 in Fig. 3. From the samples presented in Figs. 11(*a*-*b*), particularly the distribution in section S3, one should expect an overestimate of $Q(\theta)$ at 90 gpm while using the velocity distribution at $h/H = 0.5$. Distributions near the impeller and the tongue are highly nonuniform, and blade effects discussed before are also evident. Sample distributions of w, the axial velocity, are presented in Fig. 12. Note that near the tongue (S2) the flow diverges from the center line (positive above the center and negative below) at 270 gpm, and converges at 90 gpm. Qualitative examination of several images at this region reveals that above design conditions the flow remains attached at the center plane (unlike Brownell et al., 1985), but two large counter rotating longitudinal vortex structures develop at the upper and lower corners of the tongue. Entrainment into this vortex is what causes flow divergence near the surface of the tongue. Below design conditions, the values of u_0 decrease in the upper and lower corners causing convergence of the flow toward the center plane.

Vorticity Distribution and Velocity Fluctuations. A sample contour plot of the vorticity distributions near the exit is presented in Fig. 13 (additional samples are presented in Part A of this paper, Chu et al., 1991 and Dong et al., 1991). Near the exit and at 270 gpm the vorticity map contains an extended train of vortex structures, all of them with negative vorticity, extending from the point on the impeller where v_θ is maximum. In the rest of the space near the impeller the vorticity is predominantly positive. The same phenomenon appears consistently at other blade orientations (see Chu et al., 1991). The source of this train is the high shear stress caused by the sudden increase in v_θ (Figs. 7(*b*)) in a region characterized by low v_θ (tongue effect). It causes rollup of vortex structures which are then convected into the volute. Their location can be predicted (analysis not shown here) by assuming convection at the local velocity. As the blade moves behind the tongue the vortex train detaches from the impeller and "climbs" around the tongue. However, its outer traces remain within the volute since the convection velocity decreases with r. This phenomenon occurs only when the local v_θ is low, and does not appear either at mid section or near the exit at lower flow rates (Chu et al., 1991). In fact, the only consistent trend for these conditions is an appearance of several positive vorticity peaks just ahead of the blade. High vorticity peaks, some with values as high as four times the impeller angular velocity, appear also near the tip of the tongue.

The distribution of velocity fluctuations within the volute can be estimated from the mean deviations of instantaneous data from the phase averaged velocity, as defined in Part A. At mid sections (Fig. 14(*a*)) there are two distinct peaks. The first is located at the interface between the "jet" and the "wake," and the second trails behind the blade. Close to design conditions the deviation peaks are smaller by 20 percent and more evenly distributed, and at 90 gpm the peaks are twice as high, particularly ahead of the jet. Thus, the jet/wake interface and the blade wake seem to be primary contributors to turbulence generation. Near the exit and at 270 gpm (Fig. 14*b*) the velocity distribution correlates well with blade orientation, and high fluctuations appear only near the tongue. At 170 gpm (Fig. 14*c*) there is little outflux from the impeller near the exit, and the blade acts as "turbulence generator." Consequently, the deviation peaks are concentrated near the blade. At 90 gpm the trends are similar but typical values are higher.

Analysis and Discussion

As noted in the introduction, most models of the flow within the volute are limited to mean properties and neglect the effect of mixing (turbulent losses) on the energy and angular momentum of the fluid. In order to evaluate these assumptions we use the present data to perform momentum and energy balances on several control volumes (A–H), defined in Fig. 3(*b*). Changes in the mean angular momentum flux, ΔI, are estimated by using Eq. (1).

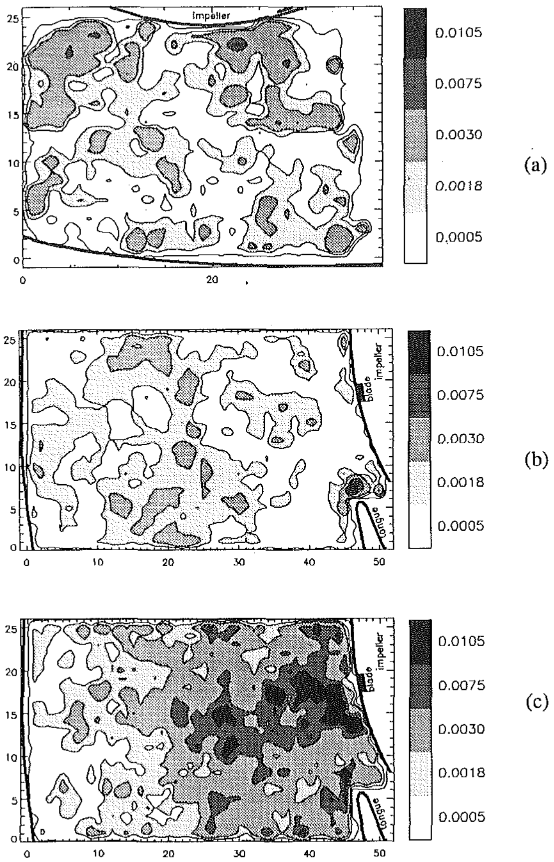

Fig. 14 Deviations of the instantaneous data from the phase averaged results $\{(1/n)\Sigma[(u - \bar{u})^2 + (v - \bar{v})^2]/U_T^2\}$ at: (*a*) mid section, 270 gpm and blade 6 at 272 deg; (*b*) exit, 270 gpm and blade 1 at 350 deg; (*c*) exit, 170 gpm and blade 1 at 350 deg

$$\Delta I/\rho H = \left(\sum_{i=1}^{n} v_\theta^2 r_i \Delta r\right)_{\theta_2} - \left(\sum_{i=1}^{n} v_\theta^2 r_i \Delta r\right)_{\theta_1} + \left(\sum_{i=1}^{n} v_\theta v_r r^2 \Delta\theta_i\right)_{r_2} - \left(\sum_{i=1}^{n} v_\theta v_r r^2 \Delta\theta_i\right)_{r_1} \quad (1)$$

The subscripts r and θ identify the variable kept constant on a specific surface, $r_2 > r_1$ and $\theta_2 > \theta_1$. Changes in kinetic energy flux, ΔK.E are estimated by replacing $v_\theta r$ with $e = 0.5(v_\theta^2 + v_r^2)$ in Eq. (1). For comparison, since most researchers neglect $v_r^2/2$, the flux of $v_\theta^2/2$ is also computed separately. We also estimate the torque, T, associated with Reynolds stresses by using Eq. (2) and *all the 40 data points* available for each location. Values of $\tau_{z\theta}$ are available only for limited locations (Sections S1, S2, S3). They are typically of the same order as $\tau_{r\theta}$.

$$(T/\rho)_{\tau\theta\theta} = \left(\sum_{r_1}^{r_2} - \overline{v_\theta'^2} H r \Delta r\right)_{\theta_2} - \left(\sum_{r_1}^{r_2} - \overline{v_\theta'^2} H r \Delta r\right)_{\theta_1}$$

$$(T/\rho)_{\tau r\theta} = \left(\sum_{\theta_1}^{\theta_2} - \overline{v_r' v_\theta'} H r^2 \Delta\theta\right)_{r_2} - \left(\sum_{\theta_1}^{\theta_2} - \overline{v_r' v_\theta'} H r^2 \Delta\theta\right)_{r_1} \quad (2)$$

Unlike these stresses, wall friction is included in existing volute flow models (Iversen et al., 1960). It can be estimated by assuming a friction factor of 0.025 (based on the roughness and Reynolds number). One can also use the present data for estimating the rate of turbulent kinetic energy production, Π, defined in Eq. (3).

$$\Pi/H\rho = \iint_{c.s} \frac{1}{2}\left(\frac{\partial v_i}{\partial x_j} + \frac{\partial v_j}{\partial x_i}\right)(\overline{v_i' v_j'})\,dxdy \quad (3)$$

This term represents the work performed by turbulent stresses, causing typically a reduction in the mean kinetic energy (Tennekes and Lumley, 1972). w' and $\tau_{\theta z}$ are not included in the computations of Π due to lack of data. However, since $w' < v_\theta'$, this assumption does not alter the results substantially. The analysis is performed by using a two-dimensional flow. As discussed before, this assumption is inaccurate, particularly near the tongue. Furthermore, since the characteristic window size is 2 mm (1 mm for vertical sheets) one can only resolve larger turbulent structures. Additional energy is associated with smaller eddies. Thus, the computed dissipation is only a lower bound. The results are presented in Table 1. For comparison purposes, the values of ΔI and ΔK.E. are *followed by the respective total fluxes* ($I_{\theta 2}$ and $(\text{K.E.})_{\theta 2}$) at the exit from each control volume. Thus, for example, at 270 gpm the overall ΔI in sections $A+B+C+D$ is 13 percent of the total angular momentum flux, whereas at 170 it drops to about 1.2 percent.

The results indicate that at mid-sections (A–D) the net torque caused by $\tau_{r\theta}$ is at most about 2 percent of ΔI and it is always positive (causes an increase in I). $T_{\tau\theta\theta}$ and the friction are negative and their values are at most 5 and 10 percent of ΔI, respectively. The magnitudes of $\tau_{\theta\theta}$ and wall shear stresses are actually comparable, and the torques are different primarily due to the different surface area. Near the exit the effect of turbulent stresses is negligible. Production of turbulent kinetic energy is about 1.1 percent of the overall kinetic energy flux

Table 1 Angular momentum flux, moments of shear stresses, mean and turbulent kinetic energy flux, and turbulence production on sample volumes identified in Fig. 3(*b*). $I_0 = \rho U_T^2 r_T^3$ and $E_0 = \rho U_T^3 r_T^2$

Flux (gpm)	Volume	A	B	C	D	A+B+C+D	E	F	G	H	E+F+G+H
270	$\Delta I/I_0 \times 10^5$	250	300	130	−180	500	150	230	200	20	600
	$I_{\theta 2}/I_0 \times 10^5$	740	780	660	1590	3770	350	680	830	4140	6000
	$T_{\tau r\theta}/I_0 \times 10^5$	3.1	1.8	0.1	4.5*	9.5**	6.4	4.5	0.1	0.4*	11.2**
	$T_{\tau\theta\theta}/I_0 \times 10^5$	−9.5	−0.3	−3.4	−10.9	−24.1	+2.1	+2.5	+2.5	−1.7	+5.4
	$T_{\text{friction}}/I_0 \times 10^5$	−6.6	−6.6	−6.6	−26.8†	−46.6†					
	$\Delta\text{K.E.}/E_0 \times 10^5$	51	74	6.0	−4.0	127	24	64	53	17	158
	$(\text{K.E.})_{\theta 2}/E_0 \times 10^5$	223	195	133	263	815	98	205	233	848	1385
	$(v_\theta^2/2)_{\theta 2}/E_0 \times 10^5$	212	191	129	244	777	88	179	213	817	1296
	$\Pi/E_0 \times 10^5$	1.8	1.0	1.2	5.3	9.3	0.0	0.0	0.0	3.4	3.4
170#	$\Delta I/I_0 \times 10^5$	−40	170	240	−330	40	−130	130	190	110	300
	$I_{\theta 2}/I_0 \times 10^5$	510	600	600	1750	3460	340	440	470	2440	3690
90#	$\Delta I/I_0 \times 10^5$	310	40	−110	−290	−50	−160	140	−40	−30	−90
	$I_{\theta 2}/I_0 \times 10^5$	570	720	560	1090	2940	430	350	260	1190	2230

*Moment of shear stress at $r/r_T = 1.3$.
**Moment of shear stress at the impeller.
†Including side wall.
#Values for blade 1 at 360 deg only.

Table 2 Measured $(p - p_{\text{atm}})/\rho U_T^2$ at selected points

location	$r = 1.07$	1.07	1.41	1.41	1.41	1.07	1.07	1.07
→	$\theta = 251.4°$	263.8°	253.6°	256.0°	258.3°	334.5°	347.6°	360°
270 gpm	0.287	0.260	0.353	0.357	0.360	0.237	0.230	0.277
170 gpm	0.435	0.441	0.495	0.504	0.508	0.458	0.460	0.493
90 gpm	0.532	0.545	0.584	0.591	0.598	0.589	0.589	0.578

at mid sections and it seems to be distributed quite uniformly. Although a small percentage, it represents a significant loss considering that section $A+B+C+D$ is only 1/18 of the volute, and that the present results are an underestimate. Table 1 also shows that by neglecting the radial velocity while computing the kinetic energy, the overall error is about 5 percent. However, the discrepancy is higher than 10 percent near the tongue.

As expected, above design flow rate the overall change in angular momentum flux is positive. However, the increase is not uniform. In fact, at mid sections ΔI is negative in the outer half of the volute (section D), and almost zero in most of the exit area (section H). The increase in angular momentum flux occurs only near the impeller. Similar conclusions can be drawn from the kinetic energy flux. Since the effects of turbulent stresses and friction are small, ΔI is dominated by circumferential pressure gradients ($\Delta I = -[\partial p/\partial\theta]\Delta\theta r \Delta r H$). Thus, at the same θ there are high *negative* pressure gradients near the impeller (evidenced also by 30 percent increase in v_r between $\theta = 245$ and 265 deg—see Fig. 6), and smaller *positive* gradients at the outer perimeter. The measured pressure distribution on the surface of the volute (selected values are presented in Table 2) confirms these conclusions. $(\Delta p/\Delta\theta)/\rho U_T^2$($\theta$ in radians) computed from ΔI in sections A is -0.34, and the measured is -0.12. In section D the computed and measured values are $+0.05$ and $+0.08$, respectively. The mean computed pressure gradient is -0.090, namely only 26 percent of the gradients near the impeller. Thus, the mean pressure distribution provides a poor estimate for conditions near the impeller, even at mid-sections of the volute.

The results provided for 90 and 170 gpm are computed from data at a single blade angle and ΔI is affected by the blade orientation. At 170 gpm, the overall ΔI at mid-sections is small, in agreement with being close to design conditions. However, the distribution is highly nonuniform. At 90 gpm the overall ΔI is negative, but it is actually positive near the impeller (probably blade effect, since the measured $\Delta p/\Delta\theta$ is positive). For both cases, the mean $\partial p/\partial\theta$ cannot represent conditions near the impeller. In the vicinity of the tongue (section E) ΔI is negative due to the adverse pressure gradients there. At 170 it becomes positive at larger r, whereas at 90 gpm it is positive only in section F due to local acceleration caused by leakage.

Conclusions

Although most of the presently observed blade effects occur at $r/r_T < 1.2$ (as reported by Miner et al., 1989), and consist of the "jet/wake" phenomenon, they are not limited to this region. In fact, the entire flux within the volute is pulsating, reaching a maximum when the blade lines up with the tip of the tongue. The leakage also depends on blade orientation, and amounts to a substantial portion of the total flux (6–25 percent), particularly below design conditions. Tongue induced blockage also causes an increase in v_r in the unobstructed part of the space between blades. Changes in the location of stagnation on the tongue agree with Brownwell et al. (1985). However, instead of flow separation above design conditions, the present observations show that two large counter rotating longitudinal vortices develop at the upper and lower corners of the tongue.

The radial distribution of v_θ in mid-sections of the volute deviates only by 5–10 percent from the traditional assumption that $v_\theta \propto 1/r$. Large changes occur near the tongue due to the stagnation point on its tip and due to leakage. The circumferential changes follow our expectations, namely v_θ increases with θ above design conditions and decreases below design conditions. Axial variations in v_θ are more likely to occur below design conditions, as well as near the impeller and the tongue at any flow rate.

The radial velocity at mid sections remains between 5–12 percent of the impeller tip speed and contains traces of the jet/wake phenomenon at any r. Differences in the outflux from the impeller, resulting from changes in pump flow rate, occur primarily near the exit. At mid sections the outflux (v_r at $r = r_T$) increases very little when the pump flow rate is increased beyond design conditions, in spite of substantial changes in local mean static pressure. Near the exit the outflux remains positive only above design conditions. It drops to nearly zero on design conditions, and becomes negative (local back-flow into the impeller) at about 50 percent of design flow rate. The axial velocity remains small in regions outside of the immediate vicinity of the impeller and the tongue.

It is shown that extended trains of vortex structures can be generated due to a mismatch between the instantaneous v_θ exiting from the impeller and the local velocity in the volute. The blade wake can only be identified in its immediate vicinity. Particularly high "random" velocity fluctuations (mean deviations of the instantaneous data from the phase averaged results) occur ahead of the "jet," near the tongue, and near the blade, especially when the outflux is low.

Although circumferential changes in overall angular momentum flux follow expected trends, the changes are nonuniform. At the same θ the momentum flux can increase near the impeller and decrease at the outer perimeter, both above and below design conditions. In general the mean properties at a certain θ (pressure gradients, momentum flux) cannot be used for estimating conditions near the exit from the impeller, even at mid-sections of the volute. It is also shown that turbulence production within the volute in a region consisting of 1/18 of the volute amounts to more than 1.1 percent of the total kinetic energy flux. The torque caused by $\tau_{\theta\theta}$ is comparable to the estimated surface friction. Combined, they can amount to more than 14 percent of the reduction in momentum flux. The effect of $\tau_{r\theta}$ is typically smaller and it causes an increase in momentum flux.

Acknowledgment

This project has been sponsored by the Office of Naval Research under contract number N00014-89-J-1672. We are particularly grateful to Jim Fein for his continued support.

References

Acosta, A. J., Bowerman, R. D., 1957, "An Experimental Study of Centrifugal Pump Impellers," *Trans. ASME*, Vol. 79, pp. 1821–1839.

Binder, R. C., Knapp, R. T., 1936, "Experimental Determination of the Flow Characteristics in the Volute of Centrifugal Pumps," *Trans. ASME*, Vol. 58, pp. 649–661.

Bowerman, R. D., and Acosta, A. J., 1957, "Effect of Volute on Performance of a Centrifugal Pump Impeller," *Trans. ASME*, Vol. 79, No. 5, pp. 1057–1069.

Brownell, R. B., Flack, R. D., Kostrzewsky, G. J., 1985, "Flow Visualization in the Tongue Region of a Centrifugal Pump," *J. of Thermal Engineering*, Vol. 4, No. 2, pp. 35–45.

Chu, S., Dong, R., and Katz, J., 1991, "The Flow Structure in the Cutoff Region of a Centrifugal Pump," Presented at the 4th International Conference on Laser Anemometry—Advances and Applications, August, Cleveland, Ohio.

Dean, R. C., and Senoo, Y., 1960, "Rotating Wake in Vaneless Diffusers," ASME *Journal of Basic Engineering*, Vol. 82, No. 3, pp. 563-574.

Dong, R., Chu, S., and Katz, J., 1991, "Quantitative Visualization of the Flow Within the Volute of a Centrifugal Pump," First ASME/JSME Joint Fluids Engineering Conference, June 23-26, Portland, Oregon.

Eckardt, D., 1975, "Instantaneous Measurements in the Jet/Wake Discharge Flow of a Centrifugal Compressor Impeller," ASME *Journal of Engineering for Power*, Vol. 97, No. 3, pp. 337-346.

Eckardt, D., 1976, "Detailed Flow Investigation Within a High Speed Centrifugal Impeller," ASME JOURNAL OF FLUIDS ENGINEERING, Vol. 98, pp. 390-402.

Hamkins, C. P., Flack, R. D., 1987, "Laser Velocimeter Measurements in Shrouded and Unshrouded Radial Flow Pump Impellers," ASME *Journal of Turbomachinery*, Vol. 109, pp. 70-76.

Iversen, H. W., Rolling, R. E., Carlson, J. J., 1960, "Volute Pressure Distribution, Radial Force on the Impeller, and Volute Mixing Losses, of a Radial Flow Centrifugal Pump," ASME *Journal of Engineering for Power*, pp. 136-144.

Lorett, J. A., Gopalakrishnan, S., 1986, "Interaction Between Impeller and Volute of Pumps at Off-Design Conditions," ASME JOURNAL OF FLUIDS ENGINEERING, Vol. 108, pp. 12-18.

Miner, S. M., Beaudoin, R. J., Flack, R. D., 1989, "Laser Velocimeter Measurements in a Centrifugal Flow Pump," ASME *Journal of Turbomachinery*, Vol. 111, pp. 205-212.

Tennekes, H., and Lumley, J. L., 1972, *A First Course in Turbulence*, The MIT Press.

Thomas, R. N., Kostrzewsky, G. J., and Flack, R. D., 1986, "Velocity Measurements in a Pump Volute With a Non-Rotating Impeller," *Int. J. Heat & Fluid Flow*, Vol. 7, No. 1, pp. 11-20.

Yuasa, T., and Hinata, T., 1979, "Fluctuating Flow Behind the Impeller of Centrifugal Pump," *Bulletin of JSME*, Vol. 22, No. 1974, pp. 1746-1753.

Numerical Study of the Effects of Longitudinal Acceleration on Solid Rocket Motor Internal Ballistics

J. J. Gottlieb
Institute for Aerospace Studies,
University of Toronto,
Ontario, Canada M3H 5T6

D. R. Greatrix
Surveillance Systems Division,
Bombardier Canadair,
Montreal, Quebec
Canada H3C 3G9

The internal ballistics of a solid-propellant rocket motor subjected to both constant and oscillatory longitudinal accelerations are studied. The one-dimensional time-dependent equations of motion governing the unsteady two-phase core flow in the accelerating motor chamber and nozzle are solved numerically by using the random-choice method, along with pressure-dependent and crossflow-dependent burning-rate equations for propellant combustion. A constant forward acceleration produces negligible effects, whereas longitudinal motor vibrations near the natural frequency of waves criss-crossing the length of the motor chamber can produce large but bounded oscillatory motor-chamber pressures.

1 Introduction

A solid-propellant rocket motor (SRM) is normally subjected to a considerable longitudinal forward acceleration during a free-flight launch, and the severity of this acceleration depends on the mass, thrust and aerodynamic design of the motor. The effects of this strong acceleration on the SRM's internal ballistics are known to be fairly weak on the basis of a quasi-steady flow analysis (Langhenry, 1986). However, during a static test firing the SRM may experience a severe longitudinal oscillatory acceleration from a nonrigid, vibrating test stand, and no information has been reported for this case. The analysis and numerical results presented herein are intended to help clarify the effects of such accelerations on the internal ballistics of SRMs.

Although constant and oscillatory accelerations have not been studied with nonstationary flow analyses, past unsteady flow analyses of axial combustion instability by Kooker and Zinn (1973), Levine and Baum (1983), and Baum and Levine (1986), for example, have produced fairly good numerical models for an SRM combustor. These models are beneficial in setting the groundwork for this study on axial acceleration effects on the internal ballistics of SRMs, even though these earlier models did not include acceleration terms in the equations.

2 Governing Equations and Solution Procedure

2.1 Core Flow Equations. In the case of SRMs with cylindrical grains (Fig. 1) having moderate to large length-to-diameter ratios ($L/D > 15$), the two-phase subsonic core flow along the propellant grain and the combined subsonic and supersonic two-phase flow in the convergent-divergent nozzle can be modelled adequately by employing one-dimensional unsteady flow equations and the concept of bulk-averaged flow properties for each phase. Before these equations are given, however, it should be noted that the use of an appropriate reference frame can simplify the expressions and solution procedure. The equations and solution have the simplest form when expressed in a reference frame attached to the accelerating rocket motor.

In this reference frame the mass, momentum and energy equations in weak conservation form for the compressible gas phase of the core flow may be expressed as

$$\frac{\partial}{\partial t}[\rho_g]+\frac{\partial}{\partial x}[\rho_g u_g]=-\frac{2\rho_g u_d}{D}\frac{dD}{dx}-[(1-\alpha_p)\rho_s-\rho_g]\frac{4r_b}{D}, \quad (1)$$

$$\frac{\partial}{\partial t}[\rho_g u_g]+\frac{\partial}{\partial x}[\rho_g u_g^2+p_g]=-\frac{2\rho_g u_g^2}{D}\frac{dD}{dx}-\rho_g u_g\frac{4r_b}{D}-\frac{\rho_g u_g^2}{2D}f_e-\frac{\sigma_p}{m_p}F-\rho_g\beta, \quad (2)$$

$$\frac{\partial}{\partial t}[e_g]+\frac{\partial}{\partial x}[u_g e_g+u_g p_g]=-\frac{2(u_g e_g+u_g p_g)}{D}\frac{dD}{dx}-e_g\frac{4r_b}{D}+(1-\alpha_p)\rho_s\left(C_{p_g}T_f+\frac{1}{2}v_w^2\right)\frac{4r_b}{D}-\frac{\sigma_p}{m_p}(u_p F+Q)+\frac{4h_c}{D}(T_w-T_g), \quad (3)$$

where D is the local diameter of the core flow at distance x

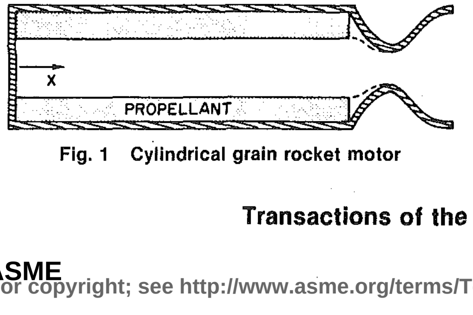

Fig. 1 Cylindrical grain rocket motor

Contributed by the Fluids Engineering Division for publication in the JOURNAL OF FLUIDS ENGINEERING. Manuscript received by the Fluids Engineering Division January 22, 1991. Associate Technical Editor: E. E. Michaelides.

measured from the head end of the motor, and ρ_g, p_g, T_g, $e_g = (\gamma_g - 1)^{-1}p_g + \frac{1}{2}\rho_g u_g^2$, C_{p_g} and u_g are the density, pressure, temperature, energy per unit volume, specific heat at constant pressure, and flow velocity for the gas phase. Also, m_p, σ_p, and α_p are the average mass of an incompressible particle, concentration of particles per unit volume and fraction of inert particulate mass in the propellant, ρ_s and r_b are the density and burning rate of the propellant material, T_f and T_w denote the flame and exposed metal wall temperatures, f_e is the effective friction factor between the core flow and propellant grain surface with or without transpiration or between the core flow and exposed metal surface, F and Q are the viscous drag force and rate of heat transfer from the core flow to a particle, v_w denotes the total velocity of propellant mass inflow above the flame ($\rho_s r_b/\rho_g$), β denotes the rocket-motor acceleration at time t, and $h_c = (k_g/D)\mathrm{Re}_D\mathrm{Pr}^{1/3}(f_e/8)$ is the local convective heat-transfer coefficient (where k_g, Re_D and Pr denote the gas thermal conductivity, Reynolds number and gas Prandtl number). Note that heat transfer between the core flow and propellant are included in the combustion model (next section), and that the last term in Eq. (3) accounts for heat transfer between the core flow and the metal wall, which occurs in nozzle cells and also cells afterwhich the propellant has burned completely and the metal wall is thereby exposed to the core flow. Similarly, friction occurs between the core flow and metal walls, and also between the core flow and propellant surface, corresponding to whether propellant exists or not.

The corresponding equations for the inert particulate phase can be expressed as

$$\frac{\partial}{\partial t}[\sigma_p] + \frac{\partial}{\partial x}[\sigma_p u_p] = -\frac{2\sigma_p u_p}{D}\frac{dD}{dx} + (\alpha_p\rho_s - \sigma_p)\frac{4r_b}{D}, \qquad (4)$$

$$\frac{\partial}{\partial t}[\sigma_p u_p] + \frac{\partial}{\partial x}[\sigma_p u_p^2] = -\frac{2\sigma_p u_p^2}{D}\frac{dD}{dx} - \sigma_p u_p\frac{4r_b}{D} + \frac{\sigma_p}{m_p}F - \sigma_p\beta, \qquad (5)$$

$$\frac{\partial}{\partial t}[e_p] + \frac{\partial}{\partial x}[u_p e_p] = -\frac{2u_p e_p}{D}\frac{dD}{dx} - e_p\frac{4r_b}{D} + \alpha_p\rho_s\left(C_pT_f + \frac{1}{2}v_w^2\right)\frac{4r_b}{D} + \frac{\sigma_p}{m_p}(u_pF + Q), \qquad (6)$$

where u_p, C_p, $e_p = \sigma_p C_p T_p + \frac{1}{2}\sigma_p u_p^2$ and T_p denote the velocity, specific heat, energy per unit volume and temperature of the inert particulate phase.

Although the gas and particulate phases are separate and move independently, the particulates are constrained in that they have a common set of bulk-averaged properties at each axial location (e.g., one velocity and one temperature). Hence, as inert particles enter the core flow from the propellant surface, at various cell locations along the propellant grain, they instantly acquire these local bulk-averaged properties. This is a fairly strong assumption on the mixing of the particles, valid only in the event of numerous particle-particle collisions for velocity equilibration and sustained surface contact for temperature equilibration.

Small effects of radiation, heat conduction in the axial direction, details of particle-particle collisions, and particulate volume have been neglected (Gottlieb and Coskunses, 1985). The meaning and importance of various terms on the right side of Eqs. (1) to (6) have been discussed elsewhere by Kuo and Summerfield (1984) and Greatrix et al. (1987).

The drag force from the viscous interaction between the gas and particulate phases, due to their different velocities, may be expressed as

$$F = \frac{\pi d_p^2}{8} C_d \rho_g (u_g - u_p)\,|u_g - u_p|, \qquad (7)$$

where d_p is the mean diameter of a particle. The drag coefficient C_d is specified primarily on the basis of existing experimental data for a single particle in a steady flow with low flow turbulence, and the effects on C_d of the relative Reynolds number, relative flow Mach number and temperature difference between the gas and particles are all included. The basic correlation for C_d versus Reynolds number was taken from a book (table 5.2 on page 112) by Clift et al. (1978), and the incorporation of the small effects of compressibility and temperature differences are detailed in the report by Gottlieb and Coskunses (1985).

Heat transfer from the core flow to the particles may be expressed in the form

$$Q = \pi d_p k_g \mathrm{Nu}(T_g - T_p), \qquad (8)$$

where the Nusselt number can be expressed in terms of the Prandtl and particle Reynolds numbers as $\mathrm{Nu} = 2 + 0.6\mathrm{Pr}^{1/3}\mathrm{Re}_d^{1/2}$. This relationship includes both conduction and convection (first and second terms on the right side), and it is also based primarily on experimental data for a single sphere in a steady flow (Clift et al. 1978; Gottlieb and Coskunses, 1985). To this day the effects of flow transients or flow unsteadiness, viscous drag from multiple interacting particles, and flow turbulence are insufficiently understood to be included in the correlations for both the drag coefficient and Nusselt number.

The previous equations can be solved if the burning rate r_b is specified (next section), when the perfect gas equation of state $p_g = \rho_g R_g T_g$ is included, and when two boundary conditions for the gas and particulate phases are introduced. At the head-end of the motor ($x = 0$), the velocities of both the gas and particulate phases are set to zero, in the frame of reference attached to the motor. At the other end, at the nozzle expansion exit where the two-phase outflow is supersonic, a simple non-reflecting or transmissive boundary condition is included for both the gas and particles, because waves do not enter from the atmosphere and travel upstream into the supersonic flow.

2.2 Burning Rate Equations. For solid composite propellants the pressure-dependent burning rate r_0 typically follows the empirical St. Robert relationship $r_0 = cp_g^n$ over most of the operating pressure range for rocket motors (Kuo and Summerfield, 1984). In addition to this pressure-dependent combustion, erosive burning due to the crossflow parallel to the propellant surface is appreciable for SRMs with a nozzle throat to grain port area ratios from one-quarter to unity. Although numerous models for erosive burning have been proposed, a recent one by Greatrix and Gottlieb (1987) is used in this study, and a summary of the relevant equations is presented next.

The total burning rate (r_b) for this phenomenological model of erosive burning is obtained by summing the pressure-dependent (r_0) and erosive burning (r_e) components and given by

$$r_b = r_0 + r_e = cp_g^n + \frac{h(T_f - T_s)}{\rho_s C_s (T_s - T_{s_i}) - \rho_s \Delta H_s}, \qquad (9)$$

for which

$$h = \frac{\rho_s r_b C_{p_g}}{\exp(\rho_s r_b C_{p_g}/h_c) - 1}, \qquad (10)$$

$$h_c = \frac{k_g}{D}\mathrm{Re}_D \mathrm{Pr}^{1/3}\frac{f}{8}, \qquad (11)$$

$$f^{-1/2} = -2\log_{10}\left[\frac{2.51}{f^{1/2}\mathrm{Re}_D} + \frac{\epsilon}{3.7D}\right], \qquad (12)$$

where T_{s_i} is the initial propellant temperature and the Reynolds number Re_D is defined by $\rho_g\,|u_g|\,D/\mu_g$. The core flow is assumed fully turbulent from vigorous transpiration (mass addition from

Table 1 Motor and propellant characteristics

	Motor 1	Motor 2
propellant grain length	83.5 cm	83.5 cm
outer grain diameter	6.35 cm	6.35 cm
initial inner grain diameter	2.10 cm	5.00 cm
nozzle throat diameter	2.03 cm	1.58 cm
propellant length to area-contraction length ratio	40	10
burning rate (r_0)	$0.5[p(kPa)]^{0.33}$ mm/s	$0.2[p(kPa)]^{0.36}$ mm/s
propellant density (ρ_s)	1740 kg/m^3	1730 kg/m^3
propellant specific heat (C_s)	1510 J/kg•K	1510 J/kg•K
flame temperature (T_f)	3060 K	3060 K
surface temperature of propellant (T_s)	1130 K	1130 K
initial temperature of propellant (T_{s_i})	294 K	294 K
surface roughness of propellant (ϵ)	400 μm	400 μm
gas specific heat (C_{p_g})	1845 J/kg•K	1845 J/kg•K
Prandtl number (Pr)	0.82	0.82
specific gas constant (R_g)	318 J/kg•K	318 J/kg•K
gas thermal conductivity (k_g)	0.184 W/m•K	0.184 W/m•K
gas dynamic viscosity (μ_g)	8.19×10^{-5} kg/m•s	8.19×10^{-5} kg/m•s
gas specific-heat ratio (γ_g)	1.21	1.21
particle mass fraction (α_p)	0 or 10 %	0%
mean particle diameter (d_p)	10 μm	
particle solid density (ρ_p)	2700 kg/m^3	
particle specific heat (C_p)	900 J/kg•K	

propellant burning). Hence, this model is essentially restricted to SRMs having a moderate to large propellant grain length to grain port diameter ratios (e.g., $L/D > 15$). Note that ΔH_s in Eq. (9) is a net surface heat of reaction that is included for completeness, because the summation of the endothermic surface pyrolysis reactions and exothermic propellant decomposition layer reactions are not necessarily equal. However, we have set $\Delta H_s = 0$ due to lack of information (Greatrix and Gottlieb, 1987).

This erosive burning model is used herein because it includes most of the factors that are known to affect erosive combustion (e.g., initial propellant temperature T_{s_i}, propellant surface roughness ϵ, and local grain port diameter D), and this model has been assessed against experimental results (Greatrix and Gottlieb, 1987). Transient burning rate effects on the flame zone due to rapidly changing core flow pressures and velocities, which are included in a few past erosive burning models (Baum and Levine, 1986; Von Elbe, 1966; Krier et al. 1968), are not incorporated in the present model, primarily because such transient phenomena are not well understood quantitatively (Kuo and Summerfield, 1984) and they still contain significant empiricism.

2.3 Numerical Solution Procedure and Accuracy. The equations of motion for the gas and particulate phases, equation of state, propellant burning expressions, and equations for viscous drag and heat transfer which couple the two-phase motion equations, are solved by using the random-choice method (RCM) of Glimm (1965) with improvements by Chorin (1976), Sod (1977), Colella (1982), Gottlieb (1988), and Gottlieb and Groth (1988), and with a recent addition to incorporate the second particulate phase by Miura and Glass (1982). The RCM is an explicit finite-volume method of integrating hyperbolic sets of partial differential equations, which solves Riemann problems separately for the gas and particulate phases between each pair of adjacent nodes, and then random samples these solutions in order to make an assignment to a node at the next time level. The time step is controlled by the Courant-Friedrichs-Lewy condition, that is $\Delta t = \frac{1}{2}\Delta x/(|u_{g_i}| + a_{g_i})_{\max}$ for the RCM. The Riemann problems in the RCM are based on the homogeneous equations of motion (left side of Eqs. (1) to (6), and the inhomogeneous terms on the right side are incorporated into the Riemann solutions as a correction by means of operator time-splitting technique (Sod, 1977).

An advantage of the RCM over finite-difference, finite-element and other numerical techniques is that the RCM does not introduce any numerical diffusion and dispersion—no smearing or phase distortion (Colella, 1978, 1982), and shocks and contact surfaces are thereby retained as discontinuities (although they have slightly random locations). This is not essential for numerical methods to obtain good results for rocket-motor flows, but it does eliminate errors from smearing. Most RCM details relevant to this study are available elsewhere (Greatrix, 1987).

The RCM has virtually a first-order convergence rate in both space and time (Colella, 1978, 1982), and Groth and Gottlieb (1990) have recently demonstrated this by solving a number of problems with known solutions on refined grids. The L_1-norm error defined as

$$E_{L_1} = \frac{1}{NI} \sum_{n}^{N} \sum_{i}^{I} |\rho_{g_i}^{n} - \rho_{g*}(x = x_i,\ t = t^n)|, \tag{13}$$

where I, N, $\rho_{g_i}^n$ and ρ_{g*} denote the number of spatial nodes, number of time steps, computed density at the i^{th} node and n^{th} time step, and exact density, can be expressed as $E_{L_1} \approx \kappa(\Delta x)^{-1}$. This linear dependence of the error E_{L_1} on the node spacing Δx means that the solution error using 200 nodes will be half the error associated with the solution obtained with 100 nodes. Numerical experiments were done with the same rocket-motor problem on refined grids in order to estimate κ and thereby determine the node spacing Δx required to make the L_1-norm error in the computed density and pressure less than 3 percent. This resulted in the requirement that more than 260 nodes would be needed for the combined motor chamber and nozzle length (about one meter long), and 300 nodes or a constant node spacing of $\Delta x \approx 3.33$ mm was used to obtain the numerical results presented in this paper.

3 Numerical Results and Discussion

3.1 Preliminary Comments. Numerical results will be given for a specific small-diameter cylindrical grain motor, sketched previously in Fig. 1. Essential motor characteristics are summarized in Table 1 for two different motors featuring some important differences. These data are characteristic of a nonaluminized ammonium perchlorate/hydroxyl-terminated polybutadiene propellant (AP/HTPD).

Pressure histories computed with a quasi-steady flow analysis for the head-end of motor 1 are illustrated first in Fig. 2,

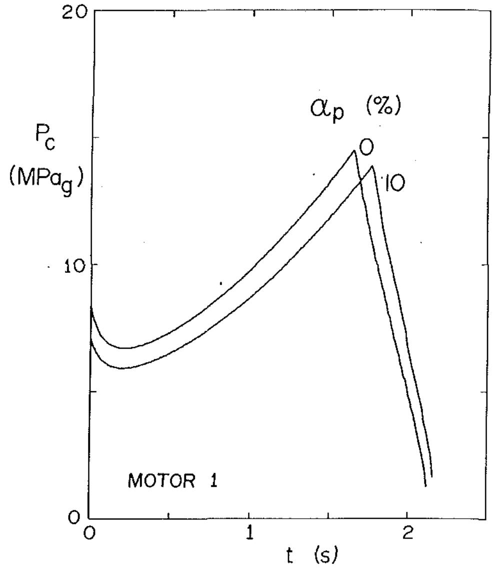

Fig. 2 Head-end pressure histories for two different particle loading percentages, from a quasi-steady flow analysis

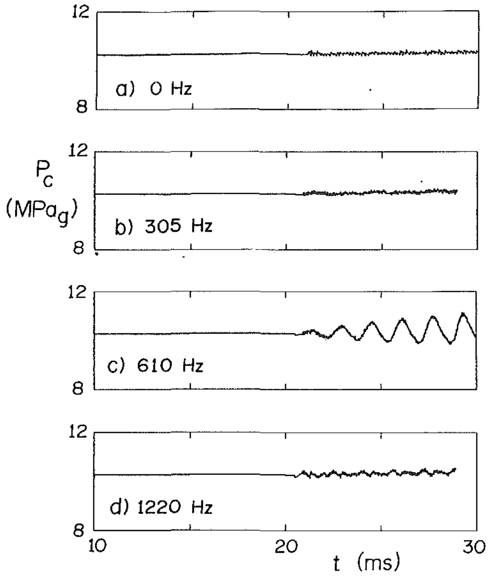

Fig. 3 Effects of motor oscillation frequency on the head-end pressure history for motor 2, for an oscillation amplitude Δx_m = 1 mm

for two different inert particulate loading percentages α_p of 0 and 10 percent, and without any acceleration effects. Both pressure histories depict progressive burning; the pressure rises through most of the firing, which is a standard feature of cylindrical grain motors in which the grain diameter expands radially with time and increases the burning surface until the burnout phase. The pressure curve for the case of a 10 percent particulate loading is somewhat lower than that for a 0 percent loading, primarily because the presence of inert particles in the propellant reduces the amount of mass and energy released during the propellant burning process (for the case of the same burning rate expression—Eq. (9)).

These quasi-steady flow results without acceleration effects are given here as a reference, because in some later results only a small part of the curve will appear prior to changes introduced when the longitudinal or oscillatory acceleration is initiated. Ideally one would like to compute the complete transient acceleration effects on an SRM's internal ballistics throughout the entire firing, from propellant burning initiation to burnout, but this is not readily feasible due to present computational limitations. Excessively long computer runs for long-duration unsteady flows of 1 to 2 s with acceleration effects were circumvented by starting the RCM unsteady flow runs from the quasi-steady flow results and then applying the acceleration field. This field was either a constant forward acceleration or an oscillatory acceleration in the form of an axial motor shaking or vibration.

3.2 Constant Motor Acceleration. The effects on internal ballistics of a solid-propellant rocket motor due to a constant acceleration applied suddenly during the quasi-steady burning process (e.g., 1 s into the firing for the case of motor 1) can be studied by means of a combined quasi-steady flow analysis and a fully unsteady flow analysis. In the first case of the quasi-steady flow analysis, it is fairly easy to show that the effects of even a very strong forward acceleration of 1000 m/s^2 are negligibly small (Langhenry, 1986; Greatrix, 1987). The primary result is a reduction in pressure by about 0.2 percent all along the propellant grain. If such results were plotted in Fig. 2, they would be indistinguishable from the previous quasi-steady flow calculations of the head-end pressure for the case of no acceleration. Although the quasi-steady flow analysis can predict the reduction in pressure along the propellant grain, it can neither predict the transient wave motion which produces this pressure reduction nor the time period for the readjustment to quasi-steady flow conditions.

In the other case of the fully unsteady flow analysis, the effects of a suddenly applied constant acceleration were also very small. Quasi-steady flow calculations were switched over to unsteady flow computations at times of 0.4, 0.8 and 1.2 s into the firing of motor 1 (to reduce CPU times and obtain results at different pressure levels and erosive burning rates in the motor chamber). A forward acceleration of 1000 m/s^2 was initiated shortly thereafter. The introduction of this sudden acceleration immediately produced very weak waves which were distributed along the grain. Although these waves were barely observable in the numerical results (which also contain some numerical noise from operator-splitting corrections), they appeared to criss-cross the motor chamber length wise and rapidly establish a slightly lower pressure all along the grain, in essential agreement with that calculated by the quasi-steady flow analysis. The readjustment time was difficult to quantify, because the wave motion was weak, but it appeared to be less than the time for a wave to propagate from the nozzle to the head-end.

3.3 Oscillatory Motor Acceleration. The oscillatory acceleration forced on the rocket motor is harmonic, given by the equation $x(t) = \Delta x_m \sin(2\pi f_f \Delta t)$, where Δt is the time measured from when the applied acceleration was initiated. This produces a motor acceleration given by $\beta(t) = -(2\pi f_f)^2 \Delta x_m \sin(2\pi f_f \Delta t)$. Note for interest that a maximum displacement of Δx_m = 1 mm and a forced frequency f_f = 610 Hz produces a maximum motor velocity of 3.83 m/s and maximum acceleration of 14,700 m/s^2.

The effects of different forced motor oscillation frequencies of 0, 305, 610, and 1220 Hz on motor 2 (with a maximum displacement Δx_m of 1 mm) are shown in Fig. 3. The first half of each curve for the head-end pressure history is calculated with the quasi-steady flow analysis (smooth part). Then, just as the motor oscillation is initiated, the fully unsteady flow analysis is used to continue the computations (portion with low level numerical noise). In the first case of no motor shaking (0 Hz), the unsteady flow computations simply continue the slowly rising pressure trend from the quasi-steady flow analysis, as expected for progressive propellant burning. In the second and last cases, the motor shaking at 305 and 1220 Hz produces low level fluctuations in the head-end pressure his-

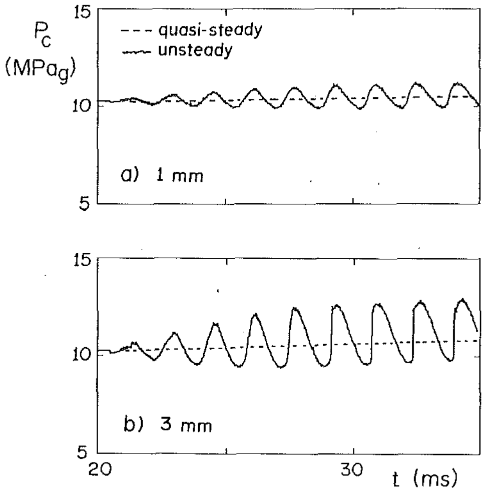

Fig. 4 Effects of motor oscillation amplitude on the head-end pressure history for motor 2, for an oscillation frequency of 610 Hz

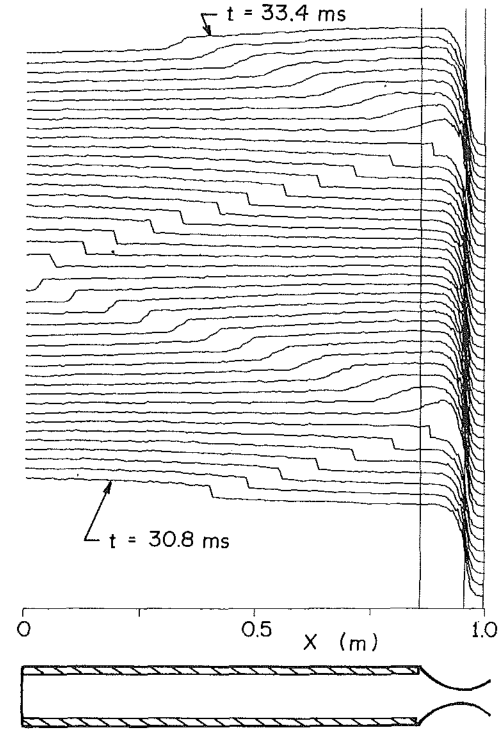

Fig. 5 Spatial distributions of pressure at time intervals from 30.8 to 33.4 ms for motor 2, showing a wave criss-crossing the chamber

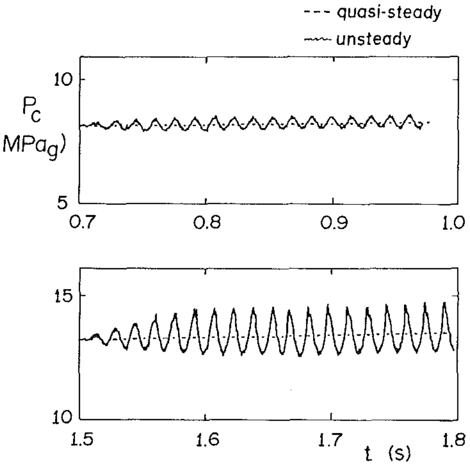

Fig. 6 Effects of later burning times on the amplitude of pressure fluctuations produced by motor shaking (motor 1, Δx_m = 1 mm, f_f = 650 Hz)

tory, which are the result of weak waves that build up and criss-cross the motor chamber length wise. For the third case with an oscillation frequency of 610 Hz, the pressure fluctuations grow to a much more significant amplitude, because the waves which criss-cross the chamber are much stronger. These fluctuations do not grow indefinitely, but rather become bounded in amplitude, as will be shown later. These four results for different motor oscillation frequencies aptly illustrate that the internal ballistics are sensitive to motor oscillations near the chamber natural frequency, which is about 610 Hz for motor 2. Note that this natural frequency is defined here as twice the length of the motor chamber (without the nozzle) divided by the time for a sound wave to propagate with the flow from the head-end to the start of the nozzle and against the flow back to the head-end.

The effects of different motor oscillation amplitudes for a motor shaking frequency which is constant at about the natural chamber frequency are illustrated in Fig. 4 for motor 2. In both cases (oscillation amplitudes Δx_m of 1 mm and 3 mm), the fluctuations in the head-end pressure build up and gradually reach a bounded amplitude. Furthermore, the base pressure or average of the pressure fluctuations are shifted upwards to a higher pressure (above the quasi-steady flow calculations shown by the dashed line), and these effects are stronger for a larger maximum vibration amplitude. Note that the larger fluctuations have steep fronts, because the compressive part of the wave that criss-crosses the motor chamber steepens into a shock.

The criss-crossing wave motion in the motor chamber and the manner in which the wave develops its shock front are illustrated clearly in Fig. 5, for the case of motor 2 with Δx_m = 3 mm and f_f = 610 Hz. Spatial distributions of pressure in the chamber at sequential times intervals from 30.8 to 33.4 ms are depicted. Each successive distribution is displaced slightly upwards from the previous one, both for clarity and to produce the effect of a time-distance diagram. Only one wave is criss-crossing the chamber. It develops a steepening front as it travels towards the head-end and also after reflecting from the head-end. This continued steepening produces a shock front as the wave moves towards the nozzle. The shock then leaves the chamber via the nozzle, but its interaction with the nozzle convergence produces a reflected compression wave which travels towards the head-end, initiating a new criss-crossing process.

The formation of a shock fronted wave depends on a number of factors. If the wave produced by the oscillatory motor acceleration is not very strong, because the shaking frequency is not near resonance, or the shaking amplitude is small, then this weak wave will not have a sufficient distance on travelling twice the motor length to develop a shock front. However, if the area convergence of the nozzle is more rapid, then the compression front of a reflected compression wave will be shorter and thereby lead to a more rapid steepening and subsequent shock front development.

The amplitude of the pressure fluctuations from the wave criss-crossing the motor chamber depends not only on the motor shaking frequency and maximum motor oscillation, but also on the initiation time in the firing. At later times in the firing, the motor chamber pressure is higher and the nozzle throat area divided by the grain port area is smaller. High chamber pressures and especially more severe area contractions result in a stronger reflected wave. This is illustrated in Fig. 6 for the case of motor 1, with a motor shaking frequency of 650 Hz and a maximum amplitude of 1 mm. When the motor

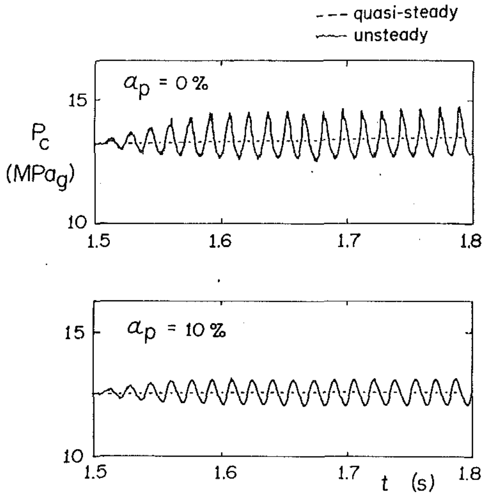

Fig. 7 Effects of particulate loading on the head-end pressure history (motor 1, Δx_m = 1 mm, f_f = 650 Hz)

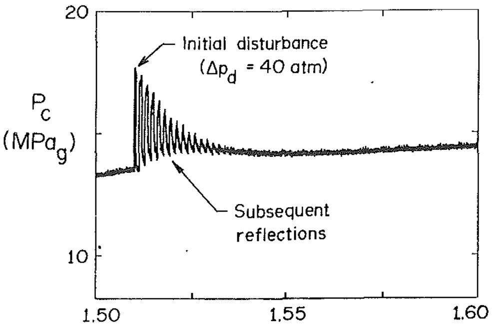

Fig. 8 Prediction of the head-end pressure history for an accelerating rocket with a pressure pulse disturbance initiated at 1.51 ms into the firing (motor 1, no inert particles)

shaking is initiated at a time of 0.7 s into the firing, the head-end pressure is about 8 MPa_g and the nozzle-throat to grain-port area ratio is about 4, whereas later in the progressive burn at 1.5 s the head-end pressure has risen to about 13 MPa_g and the throat-area to port-area ratio is approximately 9. The pressure fluctuations at the head-end for the first case (initiation time of 0.7 s) are fairly weak waves without steep fronts, whereas in the second case the wave reaches a fairly large bounded amplitude and it does develop a shock front. It is fairly obvious from these numerical results that head-end pressure fluctuations are more severe for cases with shaking initiation later in the firing when the chamber pressure is larger and the nozzle-throat to grain-port area ratio is smaller. A smaller area ratio or a larger area contraction at the nozzle is the dominant mechanism in producing larger pressure fluctuations.

The effect of varying the inert particulate loading for a constant motor shaking frequency of 650 Hz at a maximum amplitude of 1 mm is illustrated in Fig. 7 for motor 1. The head-end pressure history for the case of a particle loading of 10 percent has fairly significantly lower pressure oscillations than the original case with no particulates, and an upward shift in the base pressure is now completely depressed. Furthermore, the resulting weaker waves do not develop steep fronts. Therefore, the inert particulates tend to suppress the development of any strong wave motion from the forced motor oscillations. This might have been anticipated, because inert particles are often added to propellants to help suppress combustion instability.

3.4 Motor Acceleration With a Pulse Disturbance. During the acceleration phase of a rocket motor a small piece of propellant can sometimes break free from the grain, be entrained in the core flow, and finally be expelled from the motor through the nozzle. As this burning fragment is swept along the grain and through the nozzle throat by the core flow it will produce disturbances in the core flow, which are often greatest while it is in the nozzle (from additional flow choking). These disturbances affect the burning rate along the grain, and both of these in turn affect the motor thrust. If the motor thrust is rapidly decreased and then recovers from this effect, then the motor acceleration will likely follow this trend, and such a thrust fluctuation about a mean value might result in new or re-enforced wave motion in the chamber. Such coupling effects may be weak such that the disturbances decay with time, or they may be strong and cause the disturbances to grow into a combustion instability (Baum and Levine, 1986), or they might result in some sustained limit cycle. In this section the combined effects of a motor acceleration and pulse disturbance are investigated to see if any strong coupling effects might exist in our model.

For this case the SRM was released from a launch station at a time of 0.5 s into the firing, afterwhich it was considered in free flight. The pulse disturbance was initiated at a time of 1.51 s, while the rocket was accelerating forward. To obtain the SRM flight characteristics in a step-by-step manner along the rocket trajectory, while the propellant was being expended and the rocket accelerated, a simple nozzle design was considered so that the motor thrust could be computed easily at sequential times, and a simple drag coefficient varying with flight Mach number was used to incorporate this external aerodynamic retardation force. When the pulse disturbance was applied (at 1.51 s), the rocket velocity was 450 m/s and its acceleration was 320 m/s^2. The applied pulse was simple, consisting of suddenly increasing the pressure by 40 atm (4 MPa) over the front half of the motor chamber, next to the head-end, and then computing subsequent transient flow events.

The head-end pressure history from these computations are presented in Fig. 8 for motor 1. The head-end pressure increases suddenly when the pressure pulse is introduced, and this increase is magnified by increased propellant burning rate from the higher pressure. The resulting high-pressure region is released as expansion and shock waves accelerate these combustion products towards the nozzle exit, much like that which happens in a shock tube. However, the shock wave travelling towards and eventually through the nozzle eventually produces a reflected shock wave from its interaction with the area convergence preceeding the nozzle throat. This new shock wave travels the length of the chamber and then reflects from the head-end. After reflection it eventually passes out through the nozzle, but in the process it produces another reflected shock wave. In this example, each new reflected shock criss-crosses the motor chamber, becomes weaker, and thereby results in a decaying sequence of pressure oscillations of the head-end pressure history (Fig. 8). As these pressure oscillations decay, the propellant combustion in the motor chamber which is still accelerating returns to a process of essentially quasi-steady burning.

These results illustrate that coupling effects between the pulse disturbance, combustion process, and motor thrust and acceleration are fairly weak, because the pressure fluctuations from this rather severe disturbance decay fairly quickly. The fluctuating motor acceleration due to the fluctuating thrust, as shock waves criss-cross the chamber and leave through the nozzle, do not produce pressure-wave excursions (instability) in the motor chamber, or even sustained pressure oscillations which are bounded in amplitude.

4 Concluding Remarks

A fairly comprehensive numerical model has been presented to describe the effects of longitudinal acceleration on the behavior of internal ballistic flows in an SRM. Although approximations have been made concerning the nature of the unsteady two-phase core flow and the bounding flame zone, the overall effects of longitudinal accelerations under different motor firing conditions have been clarified. Strong forward accelerations during and after a rocket launch produce almost negligible effects, and strong disturbances in the core flow of an accelerating rocket decay with time (for the case of the present combustion model), rather than producing a sustained or an amplified feedback to cause sustained chamber pressure oscillations or a runaway excursion. On the other hand, motor shaking at frequencies near the natural frequency of waves criss-crossing the chamber can result in sustained chamber pressure oscillations of significant amplitude. Additionally, it has been shown that the effect of inert particles on an SRM's internal ballistics always suppresses pressure fluctuations in the motor chamber.

Excessive vibrations of a nonrigid test stand should likely be avoided during the static testing of rocket motors, since motor shaking near the natural chamber frequency can possibly cause sustained pressure oscillations in the combustion chamber. Although we have no direct experimental evidence of motor failure from this effect to support this recommendation, our study was initiated to determine numerically if test-stand vibrations could possibly explain some motor failures at the Defence Research Establishment Valcartier, Courcelette, Quebec.

The present combustion model does not contain the effects of transient propellant burning. Since transient burning effects often make the coupling between flow disturbances and the combustion response process more sensitive, the results of this study should be considered as providing a better understanding of rocket acceleration effects by illustrating the correct trends, but should not necessarily be considered as providing quantitative information.

Acknowledgment

This research was funded by the National Sciences and Engineering Council of Canada under grant no. A4539, and this support is much appreciated.

References

Baum, J. D., and Levine, J. N., 1986, "Modeling of Nonlinear Longitudinal Instability in Solid Rocket Motors," *Acta Astronautica*, Vol. 13, No. 6/7, pp. 339–348.

Chorin, A. J., 1976, "Random Choice Solution of Hyperbolic Systems," *Journal of Computational Physics*, Vol. 22, pp. 517–533.

Clift, R., Grace, J. R., and Weber, M. E., 1978, *Bubbles, Drops and Particles*, Academic Press, New York.

Colella, P., 1978, "An Analysis of the Effect of Operator Splitting and of the Sampling Procedure on the Accuracy of Glimm's Method," Ph.D. thesis, Department of Applied Mathematics, University of California, Berkeley, Calif.

Colella, P., March 1982, "Glimm's Method for Gas Dynamics," *SIAM Journal of Scientific and Statistical Computing*, Vol. 3, No. 1, pp. 76–110.

Glimm, J., 1965, "Solution in the Large for Nonlinear Hyperbolic Systems of Equations," *Communications in Pure and Applied Mathematics*, Vol. 18, pp. 697–715.

Gottlieb, J. J., 1988, "Staggered and Nonstaggered Grids with Variable Node Spacing and Local Time Stepping for the Random Choice Method," *Journal of Computational Physics*, Vol. 78, No. 1, pp. 160–177.

Gottlieb, J. J., and Coskunses, C. E., Feb. 1985, "Effects of Particle Volume on the Structure of a Partly Dispersed Normal Shock Wave in a Dusty Gas," UTIAS Report No. 295, Institute for Aerospace Studies, University of Toronto, Toronto, Ontario, Canada.

Gottlieb, J. J., and Groth, C. P. T., 1988, "Assessment of Riemann Solvers for Unsteady One-Dimensional Inviscid Flows of Perfect Gases," *Journal of Computational Physics*, Vol. 78, No. 2, pp. 437–458.

Greatrix, D. R., 1987, "Study of Combustion and Flow Behaviour in Solid-Propellant Rocket Motors," UTIAS Report No. 280, Institute for Aerospace Studies, University of Toronto, Toronto, Ontario, Canada.

Greatrix, D. R., and Gottlieb, J. J., Sept. 1987, "Erosive Burning Model for Composite-Propellant Rocket Motors with Large Length-to-Diameter Ratios," *Canadian Aeronautics and Space Journal*, Vol. 33, No. 3, pp. 133–142.

Greatrix, D. R., Gottlieb, J. J., and Constantinou, T., June 1987, "Quasi-Steady Analysis of the Internal Ballistics of Solid-Propellant Rocket Motors," *Canadian Aeronautics and Space Journal*, Vol. 33, No. 2, pp. 61–70.

Groth, C. P. T., and Gottlieb, J. J., 1988, "On the Actual Numerical Convergence Rate of the Random-Choice Method for Hyperbolic Conservation Laws," *SIAM Journal of Numerical Analysis*, submitted in Oct. 1990.

Kooker, D. E., and Zinn, B. T., Nov. 5–7, 1973, "Triggering Axial Instabilities in Solid Rockets: Numerical Predictions," AIAA/SAE 9th Propulsion Conference, AIAA Paper No. 73-1298, Las Vegas.

Krier, H., T'ien, J. S., Sirignano, W. A., and Summerfield, M., Feb. 1968, "Non-steady Burning Phenomena of Solid Propellants: Theory and Experiments," *AIAA Journal*, Vol. 6, No. 2, pp. 278–285.

Kuo, K. K., and Summerfield, M. (eds.), Oct. 1984, "Fundamentals of Solid-Propellant Combustion," *Progress in Astronautics and Aeronautics*, Vol. 90, p. 12, pp. 409–477, pp. 515–659.

Langhenry, M. T., June 16–18, 1986, "Acceleration Effects in Solid Propellant Rocket Motors," AIAA/ASME/SAE/ASEE 22nd Joint Propulsion Conference, AIAA Paper No. 86-1577, Huntsville, Ala.

Levine, J. N., and Baum, J. D., April 1983, "A Numerical Study of Nonlinear Instability Phenomena in Solid Rocket Motors," *AIAA Journal*, Vol. 21, No. 4, pp. 557–564.

Miura, H., and Glass, I. I., 1982, "On a Dusty-Gas Shock Tube," *Proceedings of the Royal Society of London*, Series A382, pp. 373–388.

Sod, G. A., 1977, "A Numerical Study of a Converging Cylindrical Shock," *Journal of Fluid Mechanics*, Vol. 83, pp. 785–794.

Von Elbe, G., 1966, "Solid Propellant Ignition and Response of Combustion to Pressure Transients," AIAA Paper No. 66-668.

Kenji Katoh
Lecturer,
Department of Mechanical Engineering,
Osaka City University,
Osaka 558, Japan

Hideomi Fujita
Professor,
Department of Mechanical Engineering,
Nagoya University,
Nagoya 464, Japan

Eiichiro Imazu
Engineer,
Toho Gas Co., Ltd.,
Atsutaku, Nagoya 456, Japan

Motion of a Particle Floating on a Liquid Meniscus Surface

A small particle floating on a liquid meniscus surface near a vessel wall tends to approach the wall spontaneously. This particle behavior was theoretically investigated. Because of the solid-liquid wettability, an unbalanced force is caused in the tangential direction to the liquid surface and the particle moves toward the wall. Since the particle is excessively drawn into the liquid due to the wettability, an excessive buoyant force acts on the particle in the vertical direction. The force caused by the wettability points in the normal downward direction to the liquid surface and is balanced with that component of the buoyant force. Then the tangential component of the buoyant force is not balanced and the particle moves upward along the meniscus surface. The particle trajectory calculation based on the above theoretical consideration agrees with the experimental one observed by a high-speed video camera system.

1 Introduction

A small particle floating on a liquid surface near a vessel wall tends to approach the wall spontaneously. For example, it is frequently observed in daily life that small tea leaves or bubbles on the tea gather near the cup wall. The liquid meniscus formed at the vessel wall is expected to play an important role in this particle behavior. When the liquid surface rises near the wall, as shown in Fig. 1(*a*), the particle moves toward the wall. On the other hand, when the liquid surface rises toward the center of the vessel, as shown in Fig. 1(*b*), it is observed that the particle moves toward the center away from the wall. In the problem of engineering, such behavior of a small particle on the liquid surface as stated above has close connection with that of flotation (Lucassen-Reynders and Lucassen, 1984).

The purpose of this study is to clarify the mechanism of the particle behavior observed on the liquid surface near the vessel wall. The equation governing the particle motion described above is derived theoretically by considering the effect of the solid-liquid wettability, in addition to the buoyant force acting on the particle. In order to confirm the validity of the theory, the particle behavior on the liquid surface is observed by a high-speed video camera system.

2 Particle Behavior on a Liquid Surface

2.1 Particle Behavior on a Horizontal Liquid Surface. Before considering the particle behavior on a meniscus, the mechanical equilibrium of a spherical particle floating on the horizontal liquid surface, as shown in Fig. 2, is investigated. When the solid-liquid affinity is strong and the liquid wets the particle well, as shown in Fig. 2(*b*), the particle is excessively drawn into the liquid and the displaced liquid volume V by the particle becomes greater than that shown in Fig. 2(*a*) in which the effect of the solid-liquid wettability is not taken into consideration. On the other hand, when the liquid does not wet the particle well as shown in Fig. 2(*c*), the particle is pushed up and the displaced liquid volume V decreases.

We consider the mechanical equilibrium condition on the particle as shown in Figs. 2(*a*), (*b*), and (*c*). First, for Fig. 2(*a*), in which the effect of the solid-liquid wettability is not considered, the gravitational force acting on the particle G is balanced with the buoyant force B which is proportional to the displaced volume of the liquid V and hence the following simple relation can be written.

$$B = \rho_L g V = G \tag{1}$$

where ρ_L is the liquid density and g is the gravitational acceleration.

When the solid-liquid wettability is taken into considerations, the mechanical equilibrium condition of the system should be different from that of Fig. 2(*a*) because of the existence of the liquid meniscus formed near the particle as shown in Fig. 2(*b*). The meniscus curve contacts the solid surface at the contact angle θ_Y (Katoh et al., 1990). We consider the force balance acting on the particle. The static pressure P (difference from the atmospheric pressure) acts on the part of the particle immersed in the liquid. If we assume an imaginary pressure P_{ab} (difference from the atmospheric pressure) acting on the outside of the *ab* surface shown in Fig. 2(*b*), which is the same magnitude as the liquid pressure acting on the inner side of the *ab* surface, the resultant of the liquid pressure $P - P_{ab}$ is equal to the gravitational force acting on the displaced volume V, namely, a relation $P - P_{ab} = \rho_L g V$ holds. Therefore, the actual pressure P can be written as $P = \rho_L g V + P_{ab}$. In the case of Fig. 2(*a*), in which the liquid surface is horizontal and the meniscus does not exist, P_{ab} is zero. In Fig. 2(*b*), since the meniscus surface is higher than the stationary liquid surface, P_{ab} is negative and is depicted as it directs upward. In addition to the liquid pressure, the resultant of liquid surface tension Σ acts downward on the particle.

Contributed by the Fluids Engineering Division for publication in the JOURNAL OF FLUIDS ENGINEERING. Manuscript received by the Fluids Engineering Division August 20, 1990. Associate Technical Editor: C. F. Freitas.

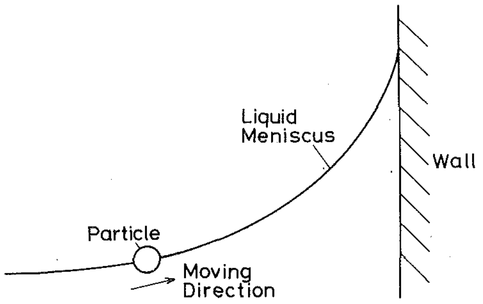

Fig. 1(*a*) Concave meniscus profile

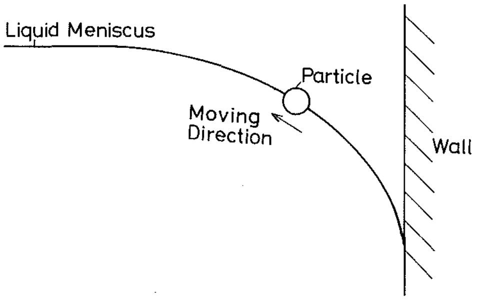

Fig. 1(*b*) Convex meniscus profile

Fig. 1 Small particle movement on liquid meniscus surface near vessel wall

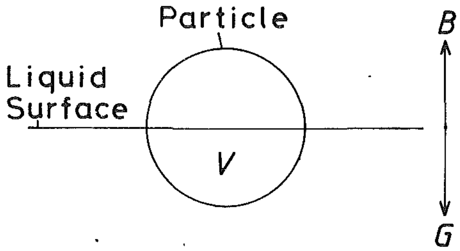

Fig. 2(*a*) Without solid-liquid affinity

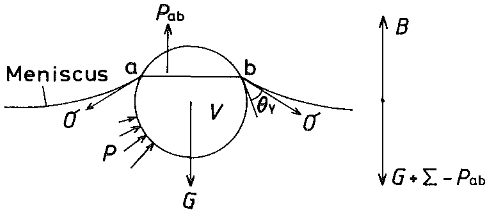

Fig. 2(*b*) With strong solid-liquid affinity

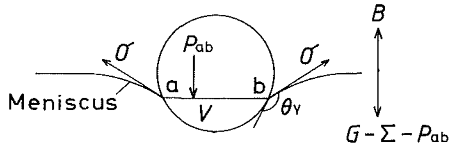

Fig. 2(*c*) With weak solid-liquid affinity

Fig. 2 Force acting on particle on horizontal liquid surface

$$\Sigma = \sigma l \sin \phi$$

where σ is the liquid surface tension, l is the length of the wetted perimeter, and ϕ is the angle between the meniscus curve at the attaching point to the particle and the vertical direction.

From the above discussion, the force balance on the particle can be written as

$$\rho_L g V + P_{ab} = \Sigma + G$$
$$\therefore B = \rho_L g V = \Sigma - P_{ab} + G \qquad (2)$$

As shown in Fig. 2(*b*), because the resultant of the surface tension Σ directs downward when the liquid wets the solid well and the contact angle θ_Y is small, the displaced volume of the liquid V and hence the buoyant force $B = \rho_L g V$ becomes greater than that in Fig. 2(*a*).

Figure 2(*c*) shows the case that the liquid does not wet the particle well and θ_Y is large. In this case, because Σ directs upward, V and hence the buoyant force becomes smaller on the contrary to the case of Fig. 2(*b*).

2.2 Particle Behavior on a Meniscus Surface. We consider the behavior of the particle on the liquid meniscus formed near the vessel wall. The density of the particle is smaller than that of the liquid. First, the case shown in Fig. 3(*a*) is discussed where the effect of the solid-liquid wettability is neglected. The Archimedes principle is valid also for the curved meniscus surface as well as for the horizontal liquid surface. This is obvious because the liquid forming the meniscus is at rest. Therefore, the particle of the same mass with the displaced liquid volume V is in mechanical equilibrium and it does not move spontaneously on the meniscus. The force balance on such a particle is illustrated in Fig. 3(*b*). If we assume the imaginary pressure P_{ab} on the *ab* surface in the same manner as the previous section, the resultant of the liquid pressure becomes $\rho_L g V$ in the upward vertical direction. The imaginary pressure P_{ab} is counterbalanced by considering negative P_{ab} in the inward normal direction to the meniscus surface *n*. The resultant of the surface tension Σ acts in the outward direction of *n*. As a result, in the vertical direction, the gravitational

Nomenclature

a = capillary constant = $\sqrt{\sigma/\rho_L g}$
B = buoyant force = $\rho_L g V$
D = viscous drag force
d = particle diameter
F = driving force for particle movement
G = gravitational force acting on a particle
g = gravitational acceleration
h_1 = height of a particle out of liquid
h_2 = meniscus height from stationary horizontal surface
l = length of wetted perimeter
m = mass of a particle
P = static liquid pressure
P_{ab} = imaginary liquid pressure
Re = Reynolds number
u = particle velocity
V = displaced liquid volume by a particle
x = coordinate in horizontal direction
z = coordinate in vertical direction
α = $\pi - \theta_Y$
θ_Y = contact angle
ν = kinematic viscosity
ρ = density
Σ = resultant of surface tension
σ = surface tension
τ = time
ψ = inclination angle of meniscus curve

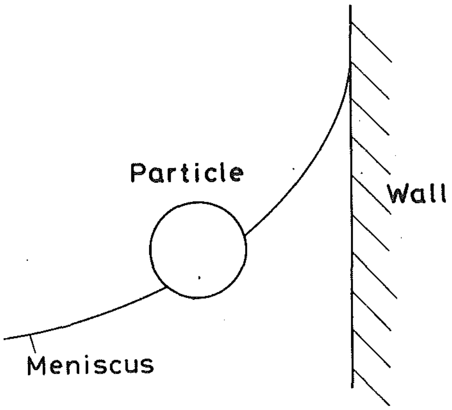

Fig. 3(*a*) Without solid-liquid affinity

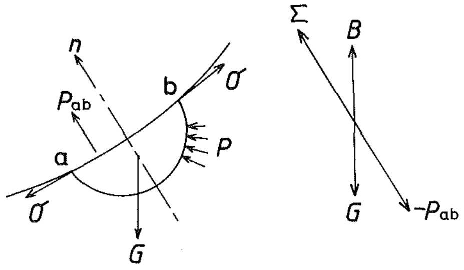

Fig. 3(*b*) Force acting on particle of (*a*)

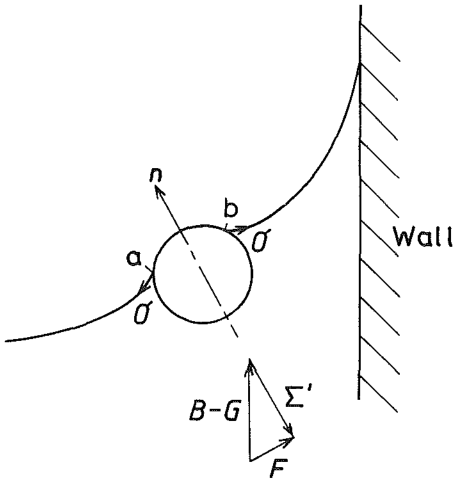

Fig. 3(*c*) With strong solid-liquid affinity

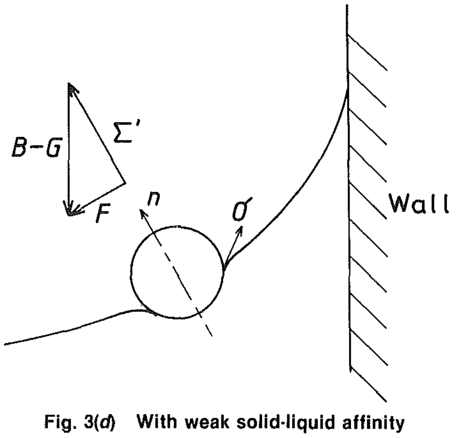

Fig. 3(*d*) With weak solid-liquid affinity

Fig. 3 Force acting on particle on meniscus surface

Table 1 Behavior of particle on meniscus surface for various conditions

Particle Density	Solid-liquid Affinity	Meniscus Shape	Particle Movement
$\rho < \rho_L$	Strong	Concave	Toward wall
		Convex	Apart from wall
	Weak	Concave	Apart from wall
		Convex	Toward wall
$\rho > \rho_L$	Strong	Concave	Sink into liquid
		Convex	Sink into liquid
	Weak	Concave	Apart from wall
		Convex	Toward wall

force acting on the particle G is balanced with the buoyant force $B = \rho_L g V$, and in the n direction Σ is balanced with $-P_{ab}$.

Next, we discuss the case that the effect of the solid-liquid wettability is taken into consideration, as shown in Fig. 3(*c*). Because the liquid wets the particle, an additional small meniscus is formed near the particle and the condition of mechanical equilibrium is different from that as described above for Fig. 3(*a*). When the solid-liquid affinity is strong and the particle is wetted by the liquid, as shown in Fig. 3(*c*), an excess force based on the surface tension Σ' acts inward to the meniscus surface. Since this excess force Σ' acts at the solid-liquid contacts such as *a* or *b* shown in Fig. 3(*c*) symmetrically around the circumference of the particle, Σ' points inward in the n direction. Therefore, the force balance in the n direction as shown in Fig. 3(*b*) is broken down and the particle is drawn excessively into the liquid. At that time, in the vertical direction, since the buoyant force $B = \rho_L g V$ becomes larger as the displaced liquid volume V increases, the difference $(B - G)$ becomes positive and acts upward. Because of the solid-liquid affinity, the particle is drawn into the liquid in the n direction and moves to the position at which the n-component of $(B - G)$ is balanced with Σ'. If the liquid surface inclines from the horizon, a force F appears in the tangential direction to the liquid surface, as shown in Fig. 3(*c*). It can be considered that this driving force F causes the particle movement and the particle rises along on the meniscus toward the wall. In other words, since the particle is drawn into the liquid excessively due to the solid-liquid affinity, an excess buoyant force acts on the particle and its tangential component to the liquid surface causes the particle movement. The driving force F increases as the solid-liquid affinity, the liquid surface tension or the inclination of the liquid surface increase. It is noted that F becomes zero for the particle on the horizontal liquid surface because the direction of Σ' and the buoyant force B coincides with each other.

When the solid-liquid affinity is weak and the liquid does not wet the particle well, as shown in Fig. 3(*d*), the particle is pushed up on the liquid surface and Σ' acts upward in the normal direction to the liquid surface. In this case, because the buoyant force B decreases and becomes smaller than G, $(B - G)$ acts downward in the vertical direction. Therefore, the driving force F acts downward in the tangential direction to the liquid surface, as shown in Fig. 3(*d*), and the particle moves apart from the wall along on the meniscus surface.

In the above discussion, although we considered the case that the density of the particle ρ is smaller than that of the liquid ρ_L, a similar consideration is also valid when the density of the particle is larger than that of the liquid. However, the discussion is limited to the case only when the solid-liquid affinity is weak, because if the liquid wets the solid well, the particle sinks into the liquid. According to the above discus-

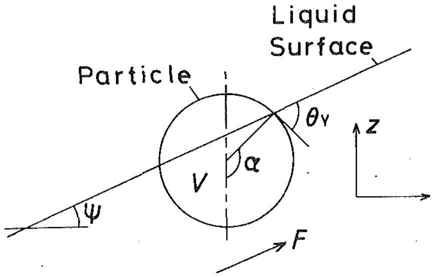

Fig. 4 Behavior of particle on inclined liquid surface

sion, since B becomes smaller than G, the particle moves downward along on the liquid surface and apart from the wall.

Moreover, we treated so far the meniscus curve with concave profile as shown in Fig. 1(*a*). A same consideration is also possible for the meniscus of convex shape, as shown in Fig. 1(*b*). In that case, the particle moves apart from or toward the wall whether the liquid wets or does not wet the particle well.

From the above consideration, it is possible to determine the particle behavior for various conditions such as the magnitude of the particle density ρ, the meniscus shape, or the degree of the solid-liquid wettability. The results are summarized in Table 1.

3 Equation for Particle Movement on Meniscus Surface

Based on the considerations in the foregoing chapter, the driving force F acting on the particle (refer to Figs. 3(*c*) and (*d*)) is calculated and the equation giving the trajectory of the particle movement is derived. The driving force F can be obtained as the tangential component to the liquid surface of ($B - G$), which is the difference between the buoyant force $B = \rho_L g V$ and the gravitational force acting on the particle G. First, in order to obtain B necessary for the calculation of F, the displaced liquid volume by the particle V is estimated.

As schematically shown in Fig. 3(*c*) or (*d*), an additional small meniscus may be formed around the particle. If its existence is taken into consideration, the calculation of V may be very difficult. The displaced liquid volume V by the spherical particle should be obtained by the equilibrium condition of the system, namely, that the meniscus contacts the solid surface at the contact angle θ_Y and that the forces acting on the particle balance with each other. If the particle diameter is much smaller than the curvature radius of the liquid surface profile and the liquid surface is not disturbed by the particle, it may be possible to neglect the existence of the small meniscus for the calculation of V. According to this assumption, the displaced volume V can be calculated by a simple geometrical condition that a inclined straight liquid surface contacts the particle at the angle θ_Y, as shown in Fig. 4. Hence the volume V can be obtained by the geometrical calculation as

$$V = \pi d^3 \left(\frac{1}{12} + \frac{1}{96} \cos 3\alpha - \frac{3}{32} \cos\alpha \right) \tag{3}$$

where d is the particle diameter and $\alpha = \pi - \theta_Y$ indicates the center angle from the attaching point of the meniscus at the spherical particle to the vertical line. The validity of the above assumption will be confirmed by the comparison with the experimental results in Section 4.2. From the above expression regarding to V, the driving force F acting on the particle in the tangential direction to the liquid surface can be obtained as

$$F = (\rho_L g V - G) \sin\psi \tag{4}$$

where ψ indicates the inclination angle of the liquid surface, as shown in Fig. 4. In addition to the above F, the viscous force cannot be neglected for the particle movement. For the Reynolds number range treated in the experiment stated in the following chapter, the drag force acting on the sphere was calculated by the following experimental expression (Bird et al., 1960):

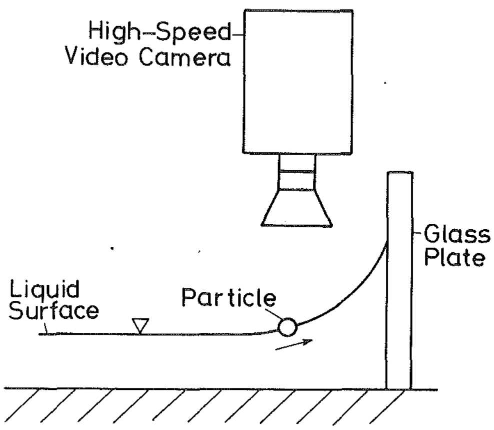

Fig. 5 Experimental apparatus for measuring particle movement

$$D = \frac{1}{2} \rho_L u^2 \cdot \frac{1}{4} \pi d'^2 \cdot \frac{18.5}{\mathrm{Re}^{3/5}} \quad (2 < \mathrm{Re} < 500) \tag{5}$$

where u is the velocity of the sphere and $\mathrm{Re} = ud'/\nu$ (ν: kinematic viscosity of liquid; d': diameter of an equivalent sphere). Since the particle is not entirely immersed in the liquid, we cannot consider d' as the particle diameter. In this study, we calculate d' as the sphere diameter of the same volume as V, the volume of the particle immersed in the liquid. For the coordinate system shown in Fig. 4, the differential equation for the particle movement in the x-direction can be written as

$$m \frac{d^2x}{d\tau^2} = (F - D) \cos\psi \tag{6}$$

where m is the particle mass and τ indicates the time. The functional relation of the inclination angle of the meniscus curve ψ to x and of x to z can be obtained by the solution of well-known Laplace equation and is described by the following expression (Chappius, 1982)

$$\begin{aligned} &\cos\psi = \sqrt{1 - z^2/2a^2} \\ &\quad x = \sqrt{4a^2 - z^2} - a \cdot \mathrm{arcosh}\left(\frac{2a}{z}\right) - a(\sqrt{2} - \mathrm{arcosh}\sqrt{2}) \end{aligned} \tag{7}$$

where a is the capillary constant defined by $a = \sqrt{\sigma/\rho_L g}$. In Eq. (7), the wall and the stationary liquid surface are described by $x = 0$ and $z = 0$, respectively, and the meniscus is assumed to be in contact with the vessel wall at 0 deg. In order to compare the theoretical results with experimental ones in Section 4, the boundary conditions of the differential Eq. (6) are chosen as follows:

$$\begin{aligned} &\tau = 0: \frac{dx}{d\tau} = 0, \\ &\tau = 1: x = 0 \end{aligned} \tag{8}$$

The particle trajectory $x(\tau)$ or velocity $u(\tau) = dx/d\tau$ can be obtained from the solution of Eq. (6). Equations (6) and (8) were solved numerically using Adam's method.

4 Trajectory of Particle Movement on Meniscus Surface

4.1 Experimental Apparatus. In order to confirm the validity of the theory as stated above, the particle behavior near the wall was observed by a high-speed video camera (NAC,

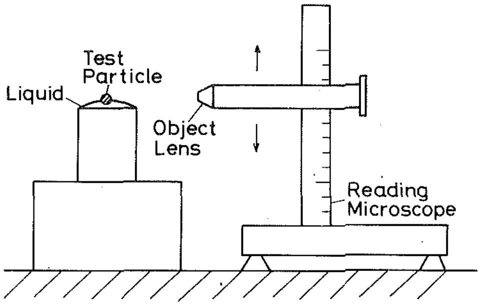

Fig. 6(*a*) Experimental apparatus

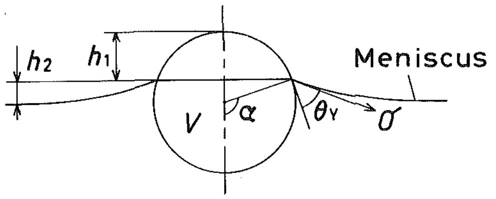

Fig. 6(*b*) Particle on liquid surface

Fig. 6 Measurement method of contact angle between particle and test liquid

Table 2 Contact angles between foaming phlystyrol and water

Particle Diameter (mm)	h_1 (mm)	h_2 (mm)	Contact Angle (°)
1.799	0.79	0.08	81.1
2.096	1.02	0.06	86.2
2.095	0.96	0.05	82.7
2.107	1.04	0.08	87.1
1.811	0.79	0.05	80.6
1.888	0.85	0.09	82.3
2.283	1.02	0.07	80.8
1.923	0.96	0.05	88.1
2.096	0.98	0.08	83.9
1.954	0.87	0.10	81.6
1.776	0.82	0.05	83.8
		Average	83.5

HSV-200) as shown in Fig. 5. The test liquids are water at 25°C (surface tension $\sigma = 7.28 \times 10^{-2}$ N/m, density $\rho_L = 998$ kg/m^3, kinematic viscosity $\nu = 0.8933 \times 10^{-6}$ m^2/s) and ethanol at 15°C ($\sigma = 2.37 \times 10^{-2}$ N/m, $\rho_L = 793$ kg/m^3, $\nu = 1.642 \times 10^{-6}$ m^2/s). A glass plate was used as the vessel wall to which the meniscus attached, and foaming phlystyrol (density $\rho = 69.7$ kg/m^3) was used as the particle.

4.2 Contact Angle Between Particle and Liquid. In order to calculate the driving force F based on the theoretical result stated in the previous section, the contact angle θ_Y between the particle and the liquid is needed. The particle used in this study is too small to measure the contact angle in the usual manner, so we measured θ_Y by the following method.

As described in Section 2, it is considered that the solid particle floating on the liquid contacts the liquid at the contact angle θ_Y (Katoh et al., 1990). θ_Y was measured based on this fact. Using the reading microscope as shown in Fig. 6(*a*), the height of the part of the particle out of the liquid surface h_1 and the meniscus height from the horizontal liquid surface h_2 as shown in Fig. 6(*b*) were measured. Regarding Eq. (2), which indicates the force balance on the particle, the following expression can be written

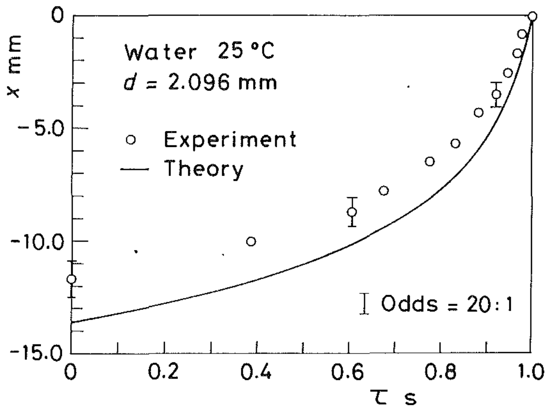

Fig. 7(*a*) For water

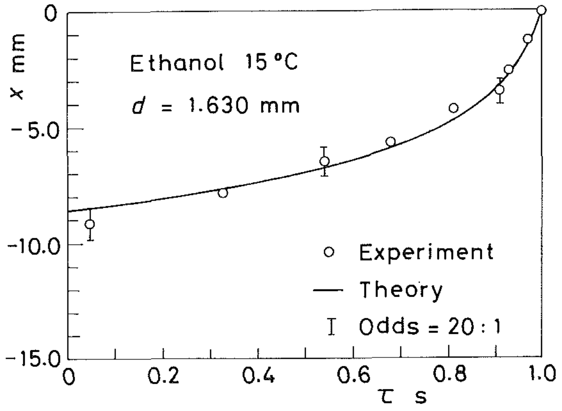

Fig. 7(*b*) For ethanol

Fig. 7 Comparison of calculated particle trajectory with experiment

$$\rho_L g\pi\left(\frac{1}{6}d^3-\frac{1}{2}dh_1^2+\frac{1}{3}h_1^3\right)-\rho_L g h_2\cdot\pi h_1(d-h_1)$$
$$=2\pi\sqrt{dh_1-h_1^2}\cos\left(\theta_Y+\alpha-\frac{1}{2}\pi\right)\cdot\sigma+\frac{1}{6}\rho g\pi d^3 \quad (9)$$

From Eq. (9), the contact angle θ_Y can be calculated as follows:

$$\theta_Y=\cos^{-1}\left(\frac{\rho_L g\{d^3/12-dh_1^2/4+h_1^3/6-h_1h_2(d-h_1)/2\}-\rho g d^3/12}{\sigma\sqrt{dh_1-h_1^2}}\right)-\sin^{-1}(1-2h_1/d) \quad (10)$$

The measured contact angles for water are shown in Table 2. The scatter of the results are within 5 deg and the uncertainty of each measured value (odds = 20:1) is ±1.9 deg. The average contact angle for ethanol is 24.1 deg and the uncertainty is ±2.8 deg. From these results, the validity of the method used in this study is verified.

The displaced liquid volume V, calculated by using measured h_1 of Fig. 6(*b*), agrees within 6 percent with that by Eq. (3), in which V is calculated based on the assumption that the additional small meniscus formed near the particle is neglectable. The validity of the assumption made in Section 3 is verified.

4.3 Results of Particle Trajectory. Figure 7 shows a comparison of the theoretical results of Section 3 with those measured by the high-speed video camera. The figure indicates the trajectory of the particle for 1 second before it reached the vessel wall. Figures 7(*a*) and (*b*) are the results for the water and the ethanol, respectively. Although for water the moving distance of the particle for 1 second is somewhat larger for the theoretical results than that for measurements, the theory represents well the particle movement observed experimentally. The mechanism of the particle behavior on the meniscus surface can be explained by the theoretical consideration in this report. The deviation between the theory and the measurements for water is caused from the estimation of the viscous drag calculated by Eq. (5). Because the contact angle θ_Y for water is large compared with that for ethanol, the volume of the part immersed in the liquid V calculated by Eq. (3) is nearly one half of the particle volume and hence the drag D calculated by Eq. (5), in which the equivalent diameter d' is used instead of the particle diameter d, includes some inaccuracy. For ethanol, however, the particle is almost immersed in the liquid and the viscous drag can be estimated accurately. So the theory agrees well with the experimental results for ethanol.

5 Conclusions

The particle behavior observed near the vessel wall was explained theoretically. Because the particle is excessively drawn into the liquid due to the solid-liquid wettability, an excessive buoyant force acts on the particle in the perpendicular direction. The tangential component to the liquid surface of the buoyant force causes the particle movement toward the wall. Based on the above consideration, the trajectory of the particle movement was theoretically calculated.

The particle behavior observed by the high-speed video camera agrees with that obtained theoretically.

References

Bird, R. B., Stewart, W. E., and Lightfoot, E. N., 1960, *Transport Phenomena*, Wiley, pp. 190-196.

Chappius, J. (Edited by Hewitt, G. F., Delhaye, J. M., and Zuber, N.), 1982, "Contact Angles," *Multiphase Science and Technology*, Vol. 1, pp. 407-409.

Katoh, K., Fujita, H., and Sasaki, H., 1990, "Macroscopic Wetting Behavior and a Method for Measuring Contact Angles," ASME JOURNAL OF FLUIDS ENGINEERING, Vol. 112, pp. 289-295.

Lucassen-Reynders, E. H., and Lucassen, J., 1984, "Thin Films, Contact Angles, Wetting," NATO Advanced Study Institute Series, Series E, No. 75, pp. 79-109.

The Magnitude of Basset Forces in Unsteady Multiphase Flow Computations

Li Liang

Efstathios E. Michaelides

Department of Mechanical Engineering,
Tulane University,
New Orleans, LA 70118

The equation of motion of a small spherical particle moving in a fluid is solved numerically with the radius of the sphere and the ratio of fluid to particle densities being parameters. The Basset force term is computed and compared to the total force on the particle for the case of turbulent flow in a duct. It is found that the Basset force may be neglected in the equation of motion of the particle only when the fluid to particle density ratio is very high and the particle diameter is greater than 1 μm. A dimensional analysis is also performed for the case when the particle size and the characteristic flow dimension are of the same order of magnitude. In the latter case, it is deduced that the Basset force is significant whenever the flow Reynolds number is greater than one.

Introduction

With the wide availability of computational power, the number of Lagrangian computations for flows involving dispersed particles or bubbles has increased dramatically in the last decade. Lagrangian dynamic simulation of ensembles of particles[1] and Monte-Carlo methods are frequently used tools in scientific and engineering applications (Berlemont et al., 1991; Brady, 1991; Michaelides et al., 1991). All of these computations typically start with the equation of motion of a particle in creeping flow (Maxey and Riley, 1983; Clift et al., 1978) and use closure equations or empirical coefficients (Clift et al., 1978; Brenner and Happel, 1964; Michaelides, 1988) to account for finite Reynolds numbers, acceleration effects or proximity to walls.

The vast majority of the Lagrangian computations have been made for situations where the history (or Basset) term in the equation of motion of the particle is very small in comparison to other terms. Therefore, this term is usually neglected in the equation of motion, a very convenient assumption, which not only reduces the order of the differential equation of the particle motion, but also diminishes the memory requirements of the computations by not retaining information on the history of the acceleration of the particles. This paper examines a few cases where this history term is comparable to the other terms in the equation of motion and its inclusion and computation may not be avoided. These cases are in general, particle flows where the ratio of the fluid to particle density, β, is of the order or less than one and cases where the characteristic dimension of the flow is comparable to that of the particle.

The Equation of Motion of a Particle

The dimensionless form of the equation of motion of a particle is as follows (Maxey and Riley, 1983):

$$\frac{dv_i}{dt}+\frac{1}{2}\beta\frac{d}{dt}\left(v_i-u_i-\frac{1}{10}\delta^2u_{i,jj}\right)+\left(v_i-u_i-\frac{1}{6}\delta^2u_{i,jj}\right)+\sqrt{\frac{9\beta}{2\pi}}\int_0^t\frac{\frac{d}{d\sigma}\left(v_i-u_i-\frac{1}{6}\delta^2u_{i,jj}\right)}{\sqrt{t-\sigma}}d\sigma=(1-\beta)\frac{2\rho_p\alpha^2}{9U_o\mu}g_i+\beta\frac{Du_i}{Dt}. \quad (1)$$

The operator d/dt denotes a derivative following the particle and D/Dt a derivative following the fluid. In creeping flow these two derivatives are approximately the same. The characteristic time of the particle ($\tau_p=2\rho_p\alpha^2/9\mu$) and the characteristic fluid velocity U_o have been used to make the foregoing equation dimensionless. The Laplacian operator (denoted by the repeated index jj) is made dimensionless by the characteristic distance L of the flow; α is the particle radius, β is the dimensionless density ρ_f/ρ_p, and δ is the ratio of the dimensions α/L. The subscripts f and p refer to the fluid and particles, respectively.

It must be pointed out that the third terms in the parentheses of the added mass, drag and Basset terms are the corrections due to the curvature of the undisturbed flow field. Since the equation is valid for $\delta \ll 1$ all three of these terms can be justifiably neglected; since for creeping flow $D/Dt \approx d/dt$ Eq. (1) is reduced to the one in Clift et al. (1978). It is obvious that the Basset force term can only be a priori neglected if $\beta^{1/2} \ll 1$. For the same reason the added mass term (which is proportional to β) should be also neglected. In this case the inertia term is balanced by the steady state drag and gravity.

Particle Flowing in a Turbulent Velocity Field ($L \gg \alpha$)

Calculations were made on the relative importance of Basset term for the case of an ensemble of particles flowing in a well defined turbulent velocity field. The flow field created in a

---

[1] The word "particle" is used in a generic context and includes droplets and bubbles, in addition to solid particles in the fluid.

Contributed by the Fluids Engineering Division for publication in the JOURNAL OF FLUIDS ENGINEERING. Manuscript received by the Fluids Engineering Division August 28, 1991. Associate Technical Editor: M. L. Billet.

horizontal pipe was chosen because the characteristics of turbulence are well known (Hinze, 1976). The diameter of the pipe was such as to always justify the inequality $\alpha \ll L$. Turbulence was simulated by a standard procedure known as Monte-Carlo simulation (Gossman and Ioannides, 1983). Turbulent eddies were simulated by Gaussian random numbers appropriately correlated (Hinze, 1976). The size of each eddy was related to the magnitude of its kinetic energy and, hence, to the magnitude of the random numbers (Hinze, 1976; Michaelides et al., 1992). The time scale of interaction of a particle with an eddy was taken as the smallest of two characteristic times: the life-time of the eddy and the time it would take the particle to traverse the eddy (Michaelides et al., 1992). For simplicity elastic collisions of particles with the walls were assumed. It was also assumed that all the particles were released from the centerline.

The history integral in the equation of motion of each particle was calculated as the sum of all the relative accelerations of the particle in the time interval from 0 to t. This procedure necessitated storage of all the particle accelerations from the commencement of motion. Since the equation of motion is implicit with respect to the particle acceleration, the latter was calculated by iteration: In the first trial the current particle acceleration was calculated by assuming its value in the Basset term to be zero. The value obtained in the first trial was inserted in the Basset term and a closer approximation was obtained, until the two values differed by less than 1 percent. This accuracy level was usually achieved in less than five iterations.

The ratio of the Basset force to the sum of all forces on the particle, F_B/F_T, was computed for four separate particles released at the centerline. Figure 1 depicts the average ratio F_B/F_T for the case of sand particle flow in water ($\rho_p/\rho_f=2.7$, $\alpha=10^{-4}$ m, Re = 30,000 for the pipe flow). It is observed that initially the Basset force terms accounts for approximately 30 percent of the total and that eventually (after a time interval of approximately $700\tau_p$) it levels off between 15 and 18 percent. Although the results of this figure were calculated for four individual particles, they are representative of the trends observed in all the particle trajectories.

Figure 2 shows the effect of particle radius on the Basset force term. The calculations were made for $\rho_p/\rho_f=0.0012$ (approximating the air to water density ratio) and for Reynolds number of 30,000. The calculations were accomplished for an ensemble of five hundred particles, which advance by a distance of fifty pipe diameters. The results depict the time and ensemble average of the history term after all particles have advanced by fifty pipe diameters. The logarithm of the particle diameter (measured in m) is of base 10. It is shown that the Basset force term accounts for approximately 24 percent of the total for $\alpha<10^{-4}$ m and that this term decreases rapidly for particles of greater size. It was observed that in the latter case the added mass and steady drag terms dominated the equation of motion.

Calculations were also performed for $\rho_p/\rho_f \gg 1$ (e.g., 1000), which are predominant in gas-solid flows. In all these cases it was found that the Basset terms were less than 5 percent of the total. This is of the same order as the accuracy of the particle equation of motion and of the computer program used for the present calculations. For this reason one may justifiably neglect the history term in the equation of motion of the particle.

Low Re Flow With $L \sim \alpha$

This case is met in many engineering applications such as particle flow through porous media, membranes with small cylindrical pores, filters and capillary tubes (for injection purposes). The implied proximity to the walls influences considerably the drag, added mass and Basset terms in the equation of motion of the particle. In general this influence can be modeled by the introduction of coefficients, which are derived analytically or empirically (Clift et al., 1978). Because of the geometry of the flow (very narrow passages) these coefficients differ in the three spatial directions (the fluid appears to be an anisotropic medium). Therefore, second order tensors are used as correction factors in the drag, added mass and history terms (Hinze, 1971; Dagan et al., 1982) which are largely unknown for most flow cases. These factors depend strongly on the relative distance of the particle from the wall and are in general of the order of one.

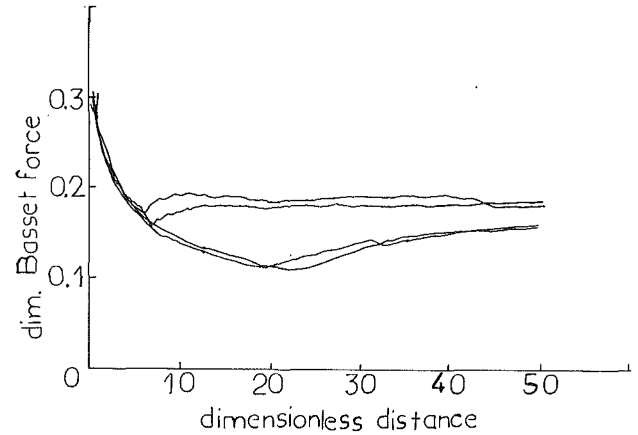

Fig. 1 Dimensionless Basset force for four particles of 100 μm radius in a random velocity field; ratio of densities 2.7

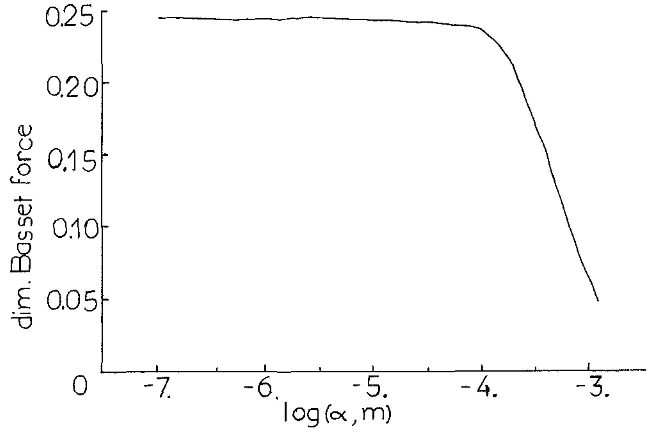

Fig. 2 The effect of particle diameter on the Basset force; ratio of densities 0.0012

Order of magnitude calculations prove that even when the fluid viscosity is very low (such as with air or water flow) the characteristic time of the particles τ_p is in general greater than the characteristic time of the flow L/U_o. Therefore, it is advantageous for the computations to use the latter in making the equation of motion of the particle dimensionless. In this case the equation of the motion of the particles with the anisotropic correction factors becomes:

$$\frac{dv_i}{dt}+\frac{1}{2}\beta\frac{d}{dt}\left(\eta^p_{ki}v_i-\eta^f_{ki}\left(u_i+\frac{1}{10}\delta^2u_{i,jj}\right)\right)$$
$$+\frac{9\beta}{2\mathrm{Re}\delta^2}\left(\theta^p_{ki}v_i-\theta^f_{ki}\left(u_i+\frac{1}{6}\delta^2u_{i,jj}\right)\right)$$
$$+\frac{9\beta}{2\delta\sqrt{\pi\mathrm{Re}}}\int_0^t\frac{\frac{d}{d\sigma}\left(\lambda^p_{ki}v_i-\lambda^f_{ki}\left(u_i+\frac{1}{6}\delta^2u_{i,jj}\right)\right)}{\sqrt{t-\sigma}}d\sigma$$
$$=(1-\beta)\mathrm{Fr}^{-2}x_i+\beta\frac{Du_i}{Dt}, \quad (2)$$

where Re is the Reynolds number of the flow $(U_o L/\nu)$, Fr the Froude number (U_o^2/Lg) and x_i a unit vector in the vertical direction. The tensors η_{ki}, θ_{ki}, and λ_{ki} are for the correction factors in the flow as explained above. The ratio of the Basset to the steady drag force coefficients is equal to $\delta\sqrt{\mathrm{Re}}/\sqrt{\pi}$. Given that δ is of the order of one this ratio is proportional to $\sqrt{\mathrm{Re}}$. Thus, for Reynolds numbers not much less than one, it is expected that the Basset term may be of higher significance than the steady drag force term. It must be pointed out that such flows are common in capillaries even with low viscosity fluids: e.g., water flow with velocity 0.1 m/s through a 10 μm capillary has a Reynolds number equal to 1.

It is also observed in the above equation that the ratio of the added mass to the steady drag term is equal to $4\mathrm{Re}\delta^2/9$, which is of the order of Re. Again as with the Basset force term, the added mass term becomes significant in the equation when the Reynolds number is not much less than one.

Conclusions

The conditions, under which the Basset term in the equation of motion of a particle becomes significant, have been investigated. It was found that the term should not be neglected when the fluid to particle density ratio is comparable to one and when the particle size is very small. Also dimensional analysis shows that both the added mass and the history terms should be accounted for whenever the characteristic dimension of the flow is comparable to the size of the particle and the Reynolds number of the flow is not much less than one.

Acknowledgments

One of the authors (L. L.) acknowledges the support of a study fellowship from the Ministry of Space and Aviation Industry of P. R. of China.

References

Berlemont, A., Desjonqueres, P., and Gouesbet, G., 1991, "Lagrangian Simulation of Dispersed Two-Phase Flows: Turbulent Modifications in Particle Laden Coaxial Confined Jets," *Turbulence Modification in Multiphase Flows*, eds., E. E. Michaelides, T. Fukano, and A. Serizawa, ASME, New York.

Brady, J. F., 1991, "Modeling Particulate Flows by Stokesian Dynamics Simulation," *Liquid-Solid Flows*, eds., M. C. Roco and T. Masuyama, ASME, New York.

Clift, R., Grace, J. R., and Weber, M. E., 1978, *Bubbles, Drops and Particles*, Academic Press, New York.

Dagan, Z., Weinbaum, S., and Pfeffer, R., 1982, "General Theory for the Creeping Motion of a Finite Sphere Along the Axis of a Circular Cylinder," *Journal of Fluid Mechanics*, Vol. 117, pp. 143-170.

Happel, J., and Brenner, H., 1986, *Low Reynolds Number Hydrodynamics*, Martinus Nijhoff Publ.

Hinze, J. O., 1987, *Turbulence*, McGraw-Hill, New York (reissue).

Hinze, J. O., 1971, "Turbulent Fluid and Particle Interaction," *Progr. in Heat and Mass Transfer*, Vol. 6, pp. 433-452.

Maxey, M. R., and Riley, J. J., 1983, "Equation of Motion of a Small Rigid Sphere in a Non-uniform Flow," *Phys. of Fluids*, Vol. 26, pp. 883-889.

Michaelides, E. E., Li, L., and Lasek, A., 1992, "The Effect of Turbulence on the Phase Change of Droplets and Particles Under Non-Equilibrium Conditions," in print, *Int. J. Heat and Mass Transfer*.

Michaelides, E. E., 1988, "On the Drag Coefficient and the Correct Integration of the Equation of Motion of Particles in Gases," ASME JOURNAL OF FLUIDS ENGINEERING, Vol. 110, pp. 339-342.

N. Hatta
Professor,
Department of Mineral Science
and Technology.

R. Ishii
Associate Professor,
Department of Aeronautics.

H. Fujimoto
Research Associate,
Department of Mineral Science
and Technology.

Kyoto University,
Kyoto 606, Japan

Numerical Analysis of Gas-Particle Two-Phase Subsonic Freejets

This paper describes a numerical analysis of gas-droplet two-phase subsonic free jets in the axisymmetric system. Thermal coupling through heat transfer to droplets, as well as momentum coupling through aerodynamic drag responsible for droplet motion, is taken into account in the present numerical model. The Navier-Stokes equations for a gas-phase interacting with particle phase are solved by a time-dependent difference technique and the particle-phase is solved by a discrete particle cloud model. The jet flow structures of mixture composed of air and water-droplets with 1 μm, 5 μm, and 30 μm, respectively, in diameter are calculated with a single particle size. Some of significant characteristics for the two-phase subsonic free jets are pointed out, in particular, focusing upon the effect of particle size on the flow structure.

1 Introduction

Gas-particle flows are used in a wide range of various industrial applications such as cyclone separators and classifiers, pneumatic conveying of powder, spray drying and cooling, as well as mist cooling, which is commonly applied to the secondary cooling zone in the continuous casting process of slabs. For analyzing gas-particle flow through a nozzle, a number of models have been developed. We also have extended the quasi-one-dimensional flow model which was described by Zucrow and Hoffman (1977) to the case where the continuous distribution of particle size is present, and we have nearly established the analytical procedure to evaluate all of the flow properties for both gas and particle phases in a nozzle (Hatta et al., 1988, 1989a, 1989b).

Gas-particle flows are characterized by coupling between phases. The thermal coupling through heat transfer from the gas-phase to the particle-phase and the momentum coupling through aerodynamic drag responsible for particle motion must be incorporated in the numerical flow model.

Next, as we discussed by Crowe (1982), the flow of a gas-particle mixture can be categorized according to the significance of particle-particle collisions on particle motion. A flow in which particle motion is controlled by collisions is a dense flow. A flow in which particle motion is controlled by the aerodynamic forces on the particle is regarded as a dilute flow. The delineation between dilute and dense flows is qualitatively established by the ratio of the aerodynamic response time $\bar{\tau}_A$ to the time between collisions $\bar{\tau}_c$. If $\bar{\tau}_A/\bar{\tau}_c < 1$, a particle has time to respond to the local gas velocity field before the next collision so its motion is dominated by aerodynamic forces. In such case, the flow can be regarded as a dilute one. Also, Ishii et al. (1989) have quantitatively given the criterion for the diluteness of gas-particle suspensions from a little different angle. They state that except some extreme situations particle-particle collisions can be neglected if the particle mass loading ratio ν is 0(1) and hence the particle volume fraction ϵ_p is $0(10^{-3})$. The effect of collisions is neglected in the present numerical model, because the mixture composed of air and water-droplet will be treated in an allowable range of ν.

This paper is concerned with a numerical analysis of subsonic gas-particle free jets exhausted from a round nozzle into a quiescent gas. Therefore, a system of equations governing the nonequilibrium, steady and quasi-one-dimensional nozzle flow of gas-particle mixture is numerically solved from a reservoir to a nozzle exit, and then all of the flow properties at the nozzle exit are applied to the boundary condition of two-phase free jets. The numerical model for gas-particle flows is constructed by incorporating the particle trajectory method (Crowe et al., 1977 and Dukowicz, 1978) into the system of gas-phase equations in the so-called two-fluid model (Harlow and Amsden, 1975). The particle clouds are divided into a large number of small subclouds according to the previous paper (Ishii et al., 1989). In each subcloud, the particles are approximated to have the same velocity and temperature. The particle flow field is solved by following the behavior of all the subclouds in the flow field. The axisymmetric Navier-Stokes equations for the gas-phase interacting with the particle-phase are solved using the Stokes hypothesis. In estimating the momentum and energy transfer rates between gas and particle phases, the contributions from the clouds to the gas-phase are averaged in a computational cell with an appropriate cross-sectional area. The present calculations are performed with a single particle size. Three cases are treated where $\bar{r}_p = 0.5$ μm, 2.5 μm and 15 μm, respectively, where $\bar{r}_p$ denotes the radius of droplet. Again, the mass loading ratio is taken to be $\nu_0 = 0.3$ in a reservoir for any case. The calculation has been made on Fujitsu VP-2600 super computer at the Data Processing Center of Kyoto University. The VP-rate in our computer program, which expresses a rough efficiency of the computation speed in vector computer, is approximately unity.

2 Governing Equations

The flow model for gas-particle mixtures is built up on

Contributed by the Fluids Engineering Division for publication in the JOURNAL OF FLUIDS ENGINEERING. Manuscript received by the Fluids Engineering Division July 23, 1990. Associate Technical Editor: E. E. Michaelides.

several usual assumptions as follows: (i) Particles are spherical water-droplets with a uniform diameter and a constant specific heat. (ii) Particles occupy negligible volume and are discrete, so that particle-particle collision, agglomeration and/or decomposition of the particles are neglected, as mentioned in the introduction. (iii) Gas-particle interaction occurs through aerodynamic drag responsible for particle motion. (iv) Energy exchange between particles and gas occurs only through convection. (v) Particles have a uniform internal temperature. (vi) No phase transformation takes place. (vii) Effects of gravity and fluid turbulence are neglected.

The equations governing the two-phase flow are described by introducing the following nondimensional quantities:

$$\left.\begin{aligned} &t=\frac{\bar{t}}{\bar{L}/\bar{c}_0},\ x=\frac{\bar{x}}{\bar{L}},\ y=\frac{\bar{y}}{\bar{L}},\ \rho=\frac{\bar{\rho}}{\bar{\rho}_0},\ p=\frac{\bar{p}}{\bar{p}_0},\\ &u=\frac{\bar{u}}{\bar{c}_0},\ v=\frac{\bar{v}}{\bar{c}_0},\ T=\frac{\bar{T}}{\bar{T}_0},\ c=\frac{\bar{c}}{\bar{c}_0},\\ &x_p=\frac{\bar{x}_p}{\bar{L}},\ y_p=\frac{\bar{y}_p}{\bar{L}},\ u_p=\frac{\bar{u}_p}{\bar{c}_0},\ v_p=\frac{\bar{v}_p}{\bar{c}_0},\ T_p=\frac{\bar{T}_p}{\bar{T}_0} \end{aligned}\right\} \tag{1}$$

where t, x, y are the time, axial distance and radial distance, respectively; ρ, p, u, v, T, and c are the density, pressure, axial velocity, radial velocity, temperature and speed of sound of the gas, respectively. $\bar{L}$ is a characteristic length of the flow field and the nozzle radius at the exit is taken as $\bar{L}$. The subscripts 0 and p denote the reservoir condition and particles, respectively, and overbars denote the dimensional quantities.

2.1 Particle-Phase. A discrete particle-cloud model (Ishii et al., 1989) is applied to solve the particle-phase. In this model, a whole particle cloud is divided into a large number of small subclouds. The particle flow field is obtained by following these individual subclouds separately in the whole flow domain.

By labelling the particle subclouds subscripts k ($k=1, 2, 3, \ldots$) and denoting the velocity components and temperature of a particle located at $(x_{pk}(t), y_{pk}(t))$ by $(u_{pk}(t), v_{pk}(t))$ and $T_{pk}(t)$, respectively, the momentum and energy equations of the kth particle subcloud are expressed by

$$\frac{d\mathbf{E}_{pk}}{dt}=\mathbf{I}_{pk} \tag{2}$$

in which

$$\mathbf{E}_p=\begin{bmatrix} x_p\\ y_p\\ u_p\\ v_p\\ T_p \end{bmatrix},\quad \mathbf{I}_p=\begin{bmatrix} u_p\\ v_p\\ A_p(u-u_p)\\ A_p(v-v_p)\\ B_p(T-T_p) \end{bmatrix} \tag{3}$$

The parameters A_p and B_p are defined by

$$A_p=\frac{f_p}{\Gamma_\tau},\quad B_p=\frac{2g_p}{3\Gamma_\tau \Pr\theta} \tag{4}$$

in which

$$f_p=\frac{C_D}{C_{D,\mathrm{Stokes}}},\quad g_p=\frac{\mathrm{Nu}}{\mathrm{Nu}_{\mathrm{Stokes}}} \tag{5}$$

$$\Gamma_\tau=\frac{\bar{\tau}_A}{\bar{\tau}_F},\quad \theta=\frac{\bar{C}_{pp}}{\bar{C}_{pg}},\quad \gamma=\frac{\bar{C}_{pg}}{\bar{C}_{vg}} \tag{6}$$

Again, $\bar{C}_{vg}$ and $\bar{C}_{pg}$ are the specific heats at constant volume and pressure of the gas, $\bar{C}_{pp}$ is the specific heat of the particle material. γ is the specific heat ratio of the gas. C_D is the particle drag coefficient and Nu is the Nusselt number. The subscript Stokes denotes the Stokes flow regime. Also, $\bar{\tau}_A$ and $\bar{\tau}_F$ are defined by

$$\bar{\tau}_A=\frac{\bar{\rho}_{mp}(2\bar{r}_p)^2}{18\bar{\mu}},\quad \bar{\tau}_F=\frac{\bar{L}}{\bar{c}_0} \tag{7}$$

Here, $\bar{\rho}_{mp}$ is the material density of the particles, and $\bar{\mu}$ is the gas viscosity given by

$$\bar{\mu}=\bar{\mu}_0 T^\delta \tag{8}$$

where δ is an appropriate constant. Again, the following nondimensional properties,

$$\mu=\frac{\bar{\mu}}{\bar{\mu}_0},\quad \lambda=\frac{\bar{\lambda}}{\bar{\lambda}_0}=1+\beta(\bar{T}-\bar{T}_0) \tag{9}$$

are introduced, where λ is the thermal conductivity of the gas.

C_D and Nu used in the present study are those given by Henderson (1976) and Carlson and Hoglund (1964), respectively. This sphere-drag coefficient accounts for rarefaction, inertial and compressibility effects and also that of a temperature difference between the particle and the gas. In addition,

Nomenclature

A_p = (see Eq. (4))
B_p = (see Eq. (4))
C_D = particle drag coefficient
$\bar{C}_{pp}$ = specific heat of particle material
$\bar{C}_{pg}$ = specific heat at constant pressure of gas
$\bar{C}_{vg}$ = specific heat at constant volume of gas
c = dimensionless speed of sound
$\bar{D}$ = nozzle diameter
e = dimensionless total energy per unit volume
f = CFL number
$\bar{L}$ = characteristic length of flow field
$\bar{m}_p$ = $(4/3)\pi\bar{r}_p^3\bar{\rho}_{mp}$
N_p = dimensionless number of particles of a ring subcloud per unit depth
Nu = Nusselt number
$\bar{n}_p$ = number density
Pr = Prandtl number
Re = Reynolds number
$\bar{r}_p$ = particle radius
p = dimensionless pressure
S_p = $\Delta x \cdot \Delta y$
T = dimensionless temperature
t = dimensionless time
u, v = dimensionless axial and radial velocities
x, y = dimensionless axial and radial coordinates
Γ_τ = $\bar{\tau}_A/\bar{\tau}_F$
γ = specific heat ratio
γ_τ = Stokes number
Δt = time interval
Δx, Δy = dimensionless cell size
ϵ_p = particle volume fraction
ζ = vorticity
θ = $\bar{C}_{pp}/\bar{C}_{pg}$
λ = dimensionless thermal conductivity
μ = dimensionless gas viscosity
ν = particle mass loading ratio
ρ = dimensionless density
$\bar{\rho}_{mp}$ = material density of particle
$\bar{\tau}_A$ = aerodynamic response time
$\bar{\tau}_F$ = $\bar{L}/\bar{c}_0$
τ_{pv} = A_p^{-1}
τ_{pT} = B_p^{-1}

Subscripts

E = nozzle exit condition
p = particle phase
0 = reservoir condition
∞ = ambient gas condition

Superscripts

$(\bar{\ })$ = dimensioned quantity
* = particle condition at nozzle exit

virtual mass force, pressure gradient force, and Basset force are all neglected. An order of magnitude study based upon the equation of motion given by Maxey and Reily (1983) reveals that virtual mass and pressure gradient are of the order of $\bar{\rho}/\bar{\rho}_{mp}$, and Basset force is of the order of $(\bar{\rho}/\bar{\rho}_{mp})^{1/2}$. Since $(\bar{\rho}/\bar{\rho}_{mp})$ is of the order of 10^{-3} for a typical gas-water droplet flow system in this study, the neglect of those forces may be justified.

For an axisymmetric flow system, the particle cloud in the physical space forms a ring cloud. Denoting the number of particles contained in the kth cloud per unit depth by $N_{pk}=(\bar{N}_{pk}/\bar{n}_{pE}/\bar{L}^2)$, where $\bar{n}_{pE}$ is the number density at the nozzle exit, the number of particles in the subcloud can be given by $2\pi y_{pk}N_{pk}$. Thus, we have

$$N_{pk}=(y_{pk}^{*}/y_{pk})N_{pk}^{*} \tag{10}$$

where the asterisk denotes the conditions of particles at the nozzle exit.

Table 1 Physical parameters for gas and droplets adopted

Gas (Air)	Particle (Water droplet)
$\gamma = 1.4$	$\bar{C}_{pp} = 4187$ J/kg·K
$\bar{C}_{pg} = 1009$ J/kg·K	$\bar{\rho}_{mp} = 1000$ kg/m^3
$\bar{\mu}_0 = 2.0 \times 10^{-5}$ Pa·s	
$\bar{\lambda}_0 = 0.028$ W/m·K	
$\delta = 0.76$ (see Eq. (8))	
$\beta = 2.68 \times 10^{-3}$ K^{-1} (see Eq. (9))	
Pr = 0.71	

Table 2 Numerical flow properties at nozzle exit for $\bar{r}_p = 0.5$ μm, 2.5 μm and 15 μm, respectively

$\bar{r}_p$(μm)	u_E	T_E	u_{pE}	T_{pE}
0.5	0.783	0.928	0.780	0.930
2.5	0.775	0.903	0.706	0.957
15.0	0.799	0.874	0.452	0.989

2.2 Gas-Phase. Introducing the Stokes hypothesis, the system of the axisymmetric Navier-Stokes equation for the gas-phase interacting with the particle-phase is given by

$$\frac{\partial \mathbf{Q}}{\partial t}+\frac{\partial \mathbf{F}_1}{\partial x}+\frac{\partial \mathbf{F}_2}{\partial y}+\frac{\partial \mathbf{G}_1}{\partial x}+\frac{\partial \mathbf{G}_2}{\partial y}+\frac{1}{y}\mathbf{H}+\mathbf{H}_p=0 \tag{11}$$

in which

$$\mathbf{Q}=\begin{bmatrix}\rho\\ \rho u\\ \rho v\\ e\end{bmatrix},\quad \mathbf{F}_1=\begin{bmatrix}\rho u\\ \rho u^2+p/\gamma\\ \rho uv\\ u(e+p/\gamma)\end{bmatrix},\quad \mathbf{F}_2=\begin{bmatrix}\rho v\\ \rho uv\\ \rho v^2+p/\gamma\\ v(e+p/\gamma)\end{bmatrix},$$

$$\mathbf{G}_1=\frac{1}{\mathrm{Re}_0}\begin{bmatrix}0\\ f_x\\ -\tau\\ uf_x-v\tau-\{1/(\gamma-1)/\mathrm{Pr}_0\}\lambda\partial T/\partial x\end{bmatrix},$$

$$\mathbf{G}_2=\frac{1}{\mathrm{Re}_0}\begin{bmatrix}0\\ -\tau\\ f_y\\ vf_y-u\tau-\{1/(\gamma-1)/\mathrm{Pr}_0\}\lambda\partial T/\partial y\end{bmatrix},$$

$$\mathbf{H}=\begin{bmatrix}\rho v\\ \rho uv-\tau/\mathrm{Re}_0\\ \rho v^2-\alpha/\mathrm{Re}_0\\ v(e+p/\gamma)+[vf_y-u\tau-\{1/(\gamma-1)/\mathrm{Pr}_0\}\lambda\partial T/\partial y]/\mathrm{Re}_0\end{bmatrix},$$

$$\mathbf{H}_p=\begin{bmatrix}0\\ F_{px}\\ F_{py}\\ \dot{Q}_p+\dot{W}_p\end{bmatrix} \tag{12}$$

with

$$\left.\begin{aligned}
&f_x=\frac{2}{3}\mu\left(\frac{\partial v}{\partial y}+\frac{v}{y}-2\frac{\partial u}{\partial x}\right),\quad f_y=\frac{2}{3}\mu\left(\frac{\partial u}{\partial x}+\frac{v}{y}-2\frac{\partial v}{\partial y}\right),\\
&\tau=\mu\left(\frac{\partial v}{\partial x}+\frac{\partial u}{\partial y}\right),\quad \alpha=2\mu\left(\frac{\partial v}{\partial y}-\frac{v}{y}\right),\\
&\mathrm{Pr}_0=\frac{\bar{C}_{pg}\bar{\mu}_0}{\bar{\lambda}_0},\quad \mathrm{Re}_0=\frac{\bar{L}\bar{c}_0\bar{\rho}_0}{\bar{\mu}_0}
\end{aligned}\right\} \tag{13}$$

Furthermore, F_{px}, F_{py}, $\dot{Q}_p$, and $\dot{W}_p$ are expressed by

$$\left.\begin{aligned}
&F_{px}=\frac{\nu_E}{S_p}\Sigma N_{pk}A_{pk}\Delta u_{pk}\\
&F_{py}=\frac{\nu_E}{S_p}\Sigma N_{pk}A_{pk}\Delta v_{pk}\\
&\dot{Q}_p=\frac{\nu_E}{S_p}\Sigma N_{pk}B_{pk}\Delta T_{pk}\\
&\dot{W}_p=F_{pk}u+F_{py}v-\frac{\nu_E}{S_p}\Sigma N_{pk}A_{pk}\{(\Delta u_{pk})^2+(\Delta v_{pk})^2\}
\end{aligned}\right\} \tag{14}$$

in which,

$$\left.\begin{aligned}
&\Delta u_{pk}=u-u_{pk},\ \Delta v_{pk}=v-v_{pk},\ \Delta T_{pk}=T-T_{pk},\\
&S_p=\frac{\bar{S}_p}{\bar{L}^2},\ N_p=\frac{\bar{N}_p}{\bar{n}_{pE}\bar{L}^2},\ \nu_E=\frac{\bar{n}_{pE}\bar{m}_p}{\bar{\rho}_E}
\end{aligned}\right\} \tag{15}$$

Here, the summation including in Eq. (14) is taken over the cloud whose centers (x_{pk}, y_{pk}) are in the computational cell with the sectional area $S_p(=\Delta x\bullet\Delta y)$. The subscript E denotes the nozzle exit condition. Also $\bar{n}_p$ is the number density and $\bar{m}_p=(4/3)\pi\bar{r}_p^3\,\bar{\rho}_{mp}$.

In addition, the total energy per unit volume of the gas e and the sound of speed c are given by

$$e=\frac{p}{\gamma(\gamma-1)}+\frac{1}{2}\rho(u^2+v^2)\quad (p=\rho T) \tag{16}$$

$$c=T^{1/2} \tag{17}$$

3 Numerical Procedure and Computational Conditions

Flow fields of gas-particle two-phase subsonic free jets are solved as a perturbation from the nozzle exit condition. Therefore, the system of equations governing the gas-particle mixture flow in a nozzle (Hatta et al., 1988) is numerically solved for determining the nozzle exit condition.

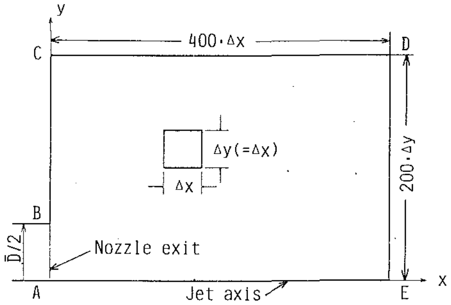

Fig. 1 Geometry of computational domain

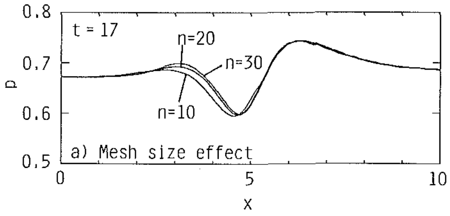

Fig. 2*(a)*

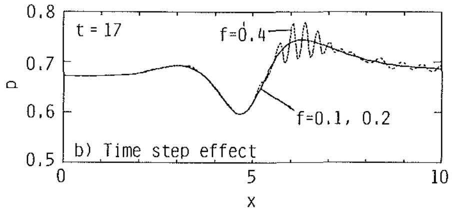

Fig. 2*(b)*

Figs. 2*(a)* and 2*(b)* Preliminary check on effects of mesh size (*a*) and computational time step (*b*) on numerical accuracy. Note that for the check of the numerical accuracy, the pressure distribution of gas-only jet flow in an axial direction is taken for example, and that computations shown in Fig. 2*(a)* are performed on the CFL number, $f = 0.2$. Also, $n = 30$, 20 and 10 correspond to $\Delta x = 1/30$, 1/20, and 1/10, respectively.

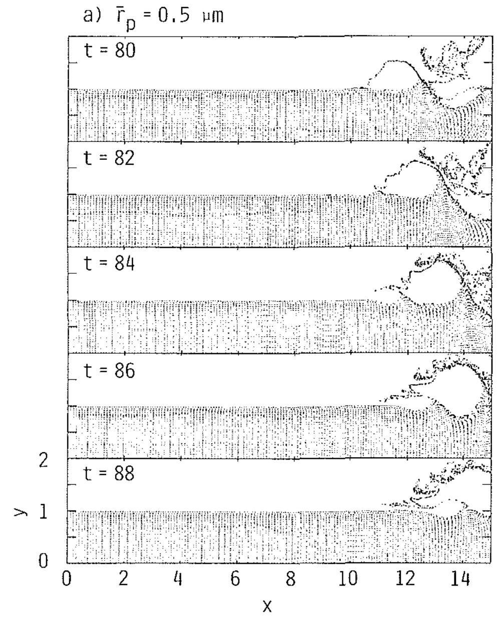

Fig. 3*(a)*

The gas-particle mixture composed of air and water-droplets of a single size is treated. Three cases are considered where $\bar{r}_p = 0.5$ μm, 2.5 μm and 15 μm, respectively. The mass loading ratio is assumed to be $\nu_0 = 0.3$ in a reservoir for any case.

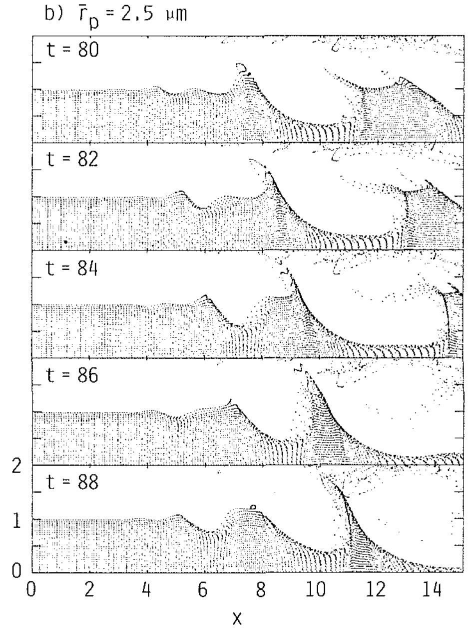

Fig. 3*(b)*

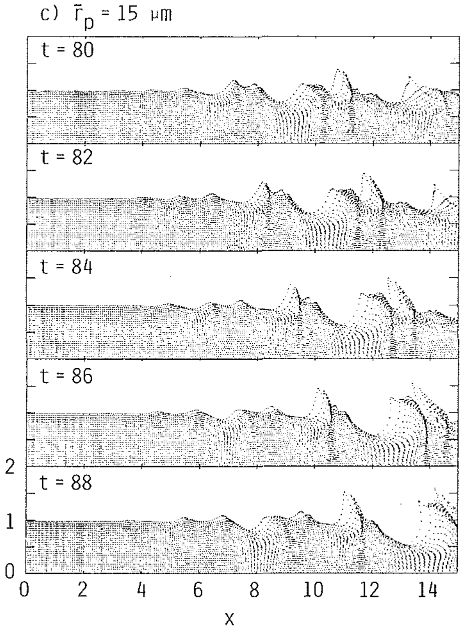

Fig. 3*(c)*

Figs. 3*(a)* to 3*(c)* Locations of centers of particle subclouds along streaklines for $\bar{r}_p = 0.5$ μm(*a*), 2.5 μm(*b*), and 15 μm(*c*)

The nozzle geometry is given by $A = (x+5)^2 + 1$ for $x \le -5$ and $A = 1$ for $-5 < x \le 0$, where A denotes the sectional area of the nozzle. It is noted that the nozzle exit at $x = 0$ corresponds to the origin of the jet axis. The nozzle radius in the constant area region is set to be $\bar{L} = \bar{D}/2 = 5 \times 10^{-3}$ m.

The reservoir condition is that $\bar{p}_0 = 1.8 \times 10^5$ Pa and $\bar{T}_0 = 323$ K. The ambient gas condition is that $\bar{p}_\infty = 1.0 \times 10^5$ Pa and $\bar{T}_\infty = 300$ K. Thus, the initial gas condition is that $p = 0.556$, $T = 0.929$ $(= 300/323)$ and $u = v = 0$ over the whole computational domain. Physical constants of the gas and particles used here are listed in Table 1.

The numerical flow properties at the nozzle exit are shown in Table 2. It is noted that $v_E = 0$ and $p_E = 0.556$ for all $\bar{r}_p$. The numerical results at $x = 0$ are applied to the jet boundary condition at the origin of the free jet region.

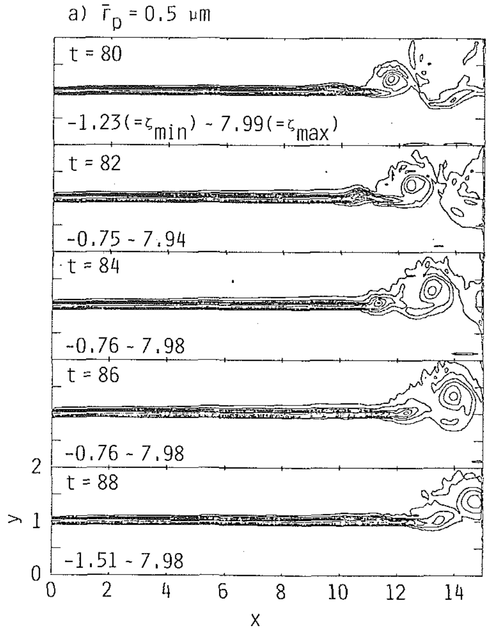

Fig. 4*(a)*

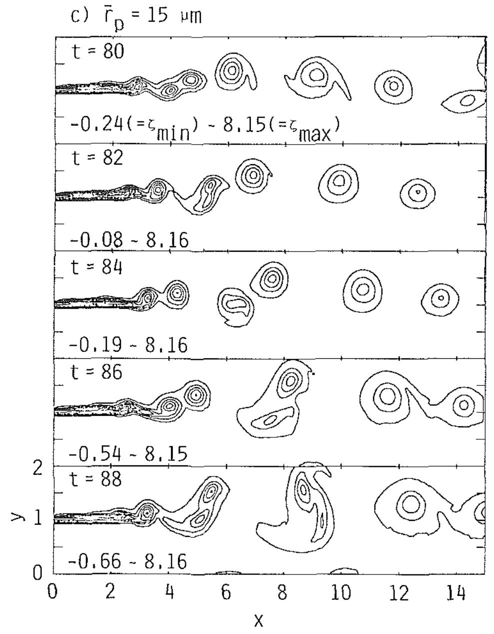

Fig. 4*(c)*

Figs. 4*(a)* to 4*(c)* Contours of equal vorticity ζ of gas flow. Note that these contours are drawn by dividing the difference between the maximum and minimum values (ζ_{max} and ζ_{min}) into 10 equal parts.

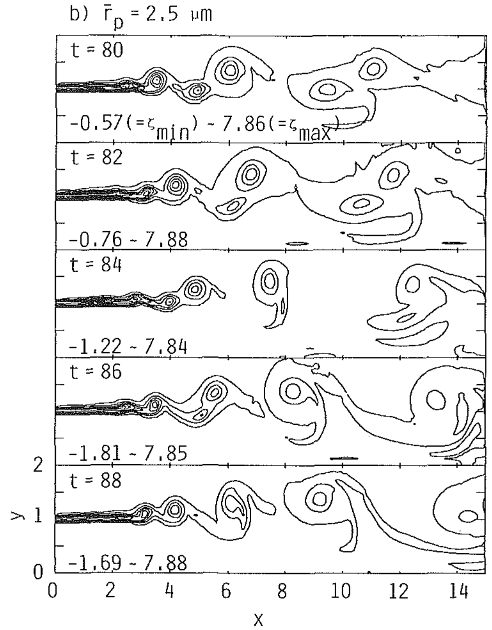

Fig. 4*(b)*

The equations for the gas-phase consist of the inviscid terms, the viscous terms, the axisymmetric term and the interaction term by the presence of particle-phase. The inviscid terms are solved by using a TVD (Total Variation Diminishing) scheme by Chakravarthy and Osher (1985) and the other terms are solved by using the central differencing scheme. Therefore, the computational domain is divided into a number of small cells and the physical variables are defined at the cell center. Also, the physical variables at interface between two neighboring cells are calculated by the Roe approach (1981).

Figure 1 indicates the geometry of the computational domain. The domain size corresponds to $10\bar{D}$ in the axial direction and $5\bar{D}$ in the radial direction in a half section. Here, the computational domain is divided into 400×200 cells in the x- and y-directions, respectively.

We wish to briefly mention the boundary condition of the computational domain. The ambient gas condition is imposed to the upstream boundary BC, the side one CD and the downstream boundary DE, the symmetric condition is done to the jet axis, AE, and the jet condition is applied to the jet exit plane AB (Matsuda et al., 1987).

Here, we consider the effect of selecting the cell size, $\Delta x(=\Delta y)$, on the numerical accuracy. Δx is determined by dividing the nozzle radius in n equal parts. For various n values, the numerical experiments have been performed for single-phase (gas-only) flows. The results have been compared with each other. Figure 2(a) indicates the calculated pressure distributions along $y=0.05$ at $t=17$ for $n=10$, 20, and 30, respectively. We wish to add that the value of $n=20$ is corrected by the Roe approach (1981). The numerical error is at most 3.8 percent between $n=10$ and $n=30$. Accordingly, $\Delta x=0.05$, corresponding to $n=20$, is selected in the present simulation.

Next we consider the effect of computational time interval, Δt, on the numerical accuracy. Δt is determined by the CFL (Courant-Friedriches-Lewy) condition for the gas-phase flow (Godunov, 1959). The numerical results obtained by various CFL numbers have been compared with each other. Figure 2(b) indicates the pressure distributions along the x-axis (precisely, $y=0.025$) at $t=17$ for $f=0.1$, 0.2 and 0.4, respectively, where f is the CFL number. The numerical result of $f=0.4$ is observed to be oscillatory downstream. No significant difference is recognized between $f=0.1$ and $f=0.2$. Therefore, we have selected $f=0.2$ throughout the present simulations. Also, we have found that Δt determined by this f is always much smaller than two kinds of characteristic non-dimensional times for the particle phase $\tau_{pv}(=A_p^{-1})$ and $\tau_{pT}(=B_p^{-1})$. Therefore, this Δt is also used for the particle-phase solution.

For the purpose of obtaining the time-converged two-phase flow structure, the numerical results at a sufficiently large number of time steps are required owing to using an explicit time-dependent difference scheme. In the present calculation, the gas-only flow field is solved for the first 10000 time steps, and then two-phase flow field is solved for the next 15000 time steps so that the time-converged solutions may be found in as a short computational time as possible.

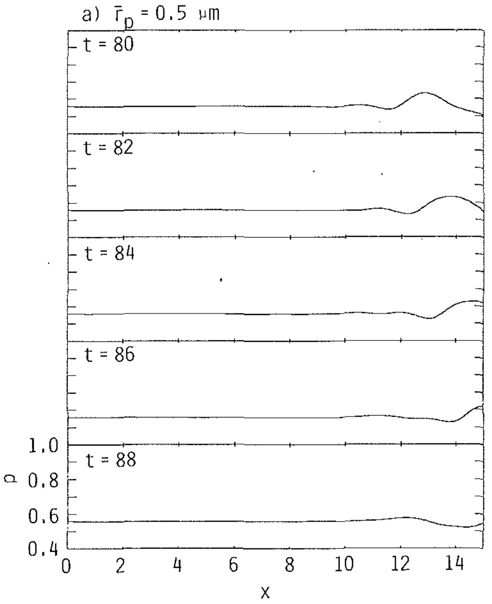

Fig. 5*(a)*

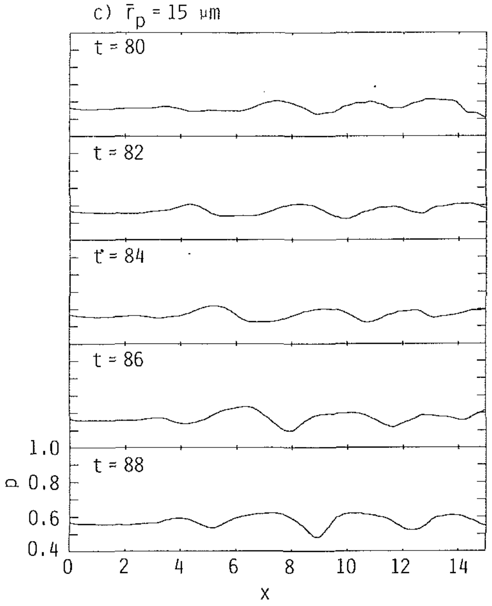

Fig. 5*(c)*

Figs. 5*(a)* to 5*(c)* Distributions of gas pressure along jet axis

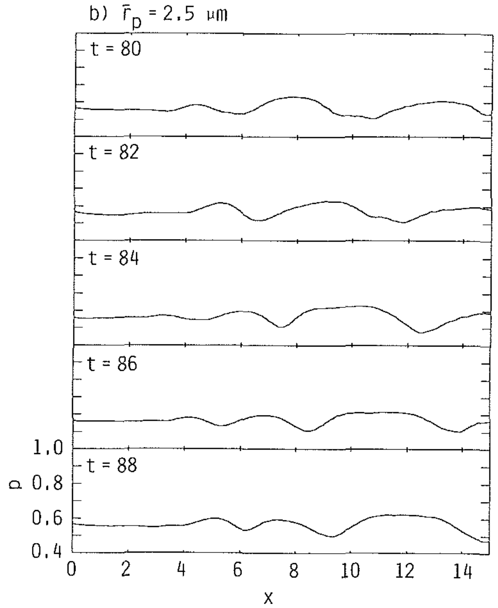

Fig. 5*(b)*

4 Numerical Results

In this section, the behavior of particles in the gas flow is demonstrated in detail. The particles are exhausted at $y^*_{pk} = (k-0.5)/30$ ($k = 1 \sim 30$) on the nozzle exit plane at every time interval Δt.

Figures 3(*a*) to 3(*c*) give the center locations of particle subclouds along streaklines in the mixture jet flow for $\bar{r}_p = 0.5$, 2.5 and 15 μm, respectively. It is noted that the particles in these figures are limited to only those exhausted at every 20 time steps. From these figures some significant and interesting features will be pointed out. The fluctuating scale in particle motion may be considered to depend upon the particle size. We notice, at a glance, from these figures that for smaller particles ($\bar{r}_p = 0.5$ μm), the fluctuation of the particle motion begins to occur in a relatively downstream region. This may be based upon the fact that the gas-phase continues to maintain more momentum to a relatively large distance in the axial direction, because the velocity and temperature of the particle-phase with $\bar{r}_p = 0.5$ μm at the nozzle exit are very similar to those of the gas-phase. On the other hand, for larger particles, the difference in velocity and temperature between the gas and particle phases becomes larger at the nozzle exit, and therefore the fluctuation of the particle motion begins to occur considerably upstream.

Figures 4(*a*) to 4(*c*) show the contours of equal vorticity $\zeta(=\partial v/\partial x - \partial u/\partial y)$ for $\bar{r}_p = 0.5$, 2.5, and 15 μm, respectively. We find that vortical structures occur due to the velocity difference between the main jet flow and the ambient gas at the jet boundary (Kelvin-Helmholtz instability). Comparing Figs. 3(*a*) to 3(*c*) with Figs. 4(*a*) to 4(*c*) for the corresponding particle radius at the same time, we can find that the region with a relatively large vorticity roughly corresponds to the particle-free region. Chung and Troutt (1988) state that particles tend to move away from the core of larger-vortex structures. The present numerical results are quite consistent with their results. One of the most important features to be noted in the present simulation is that a perfectly time-converged (steady) solution, in the conventional sense, can not be reached, even at $t \rightarrow \infty$. However, the global flow structure of the gas-particle mixture jet does not change with time. Rather, the vortical structures occur at the nozzle exit somewhat periodically. The vortices are convected downstream and agitate the jet boundary. That is, when a vortical structure is convected some distance downstream, another new vortex is produced at the nozzle exit. Thus process is repeatedly continued.

Figures 5(*a*) to 5(*c*) give the pressure distributions along the jet axis (strictly, $y = 0.025$) for $\bar{r}_p = 0.5$, 2.5 and 15 μm, respectively. It can be seen that pressure becomes almost constant upstream and fluctuates downstream, and that the position where pressure begins to change depends on the particle radius. The wavelength of pressure variation seems to be equal to $2\overline{D}$ or so. One of the most interesting features is that the low-pressure locations along the jet axis agree roughly with the x-coordinate of those with the larger vorticity (see Fig. 4), where the radial distance of outermost particle stream becomes smaller (see Fig. 3).

Figures 6(*a*) to 6(*c*) indicate the velocity distributions for the gas and particle phases along the jet axis. Here, the gas and particle phase velocities indicate $V = (u^2 + v^2)^{1/2}$ and $v_p = (u_p^2 + v_p^2)^{1/2}$, respectively. The behavior for both V and V_p

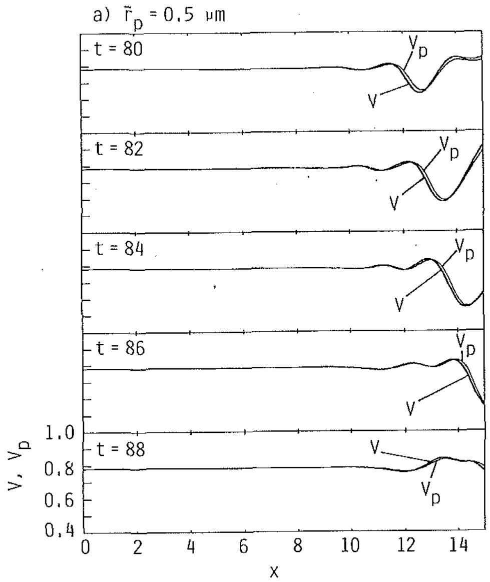

Fig. 6(*a*)

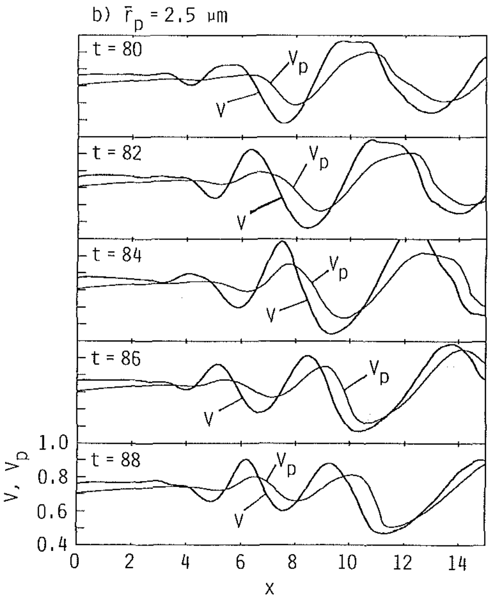

Fig. 6(*b*)

is seen to be widely different depending on the particle size. V_p for smaller particles ($\bar{r}_p=0.5$ μm) almost perfectly responds to the velocity fluctuation of the gas flow. However, for $\bar{r}_p=15$ μm, the particles do not have sufficient time to respond to the changing velocity field of the gas-phase. The particles of $\bar{r}_p=2.5$ μm reveal the intermediate velocity response between the cases of $\bar{r}_p=0.5$ μm and 15 μm.

Figures 7(*a*) to 7(*c*) show the temperature distributions for the gas and particle phases along the jet axis. The particle temperature T_p for a larger size ($\bar{r}_p>2.5$ μm) is almost constant regardless of a considerably large temperature fluctuation of gas-phase. This may be considered to be due to the effect of the thermal inertia. On the other hand, the behavior of T_p for smaller particles ($\bar{r}_p=0.5$ μm) is analogous to that of V_p and roughly responds even to the small temperature fluctuation of gas-phase. It may be concluded that the flow structure of two-phase mixtures containing particles smaller than $\bar{r}_p=0.5$ μm is approximately in velocity and thermal equilibrium between the two phases. That is, the transfer rate for both momentum

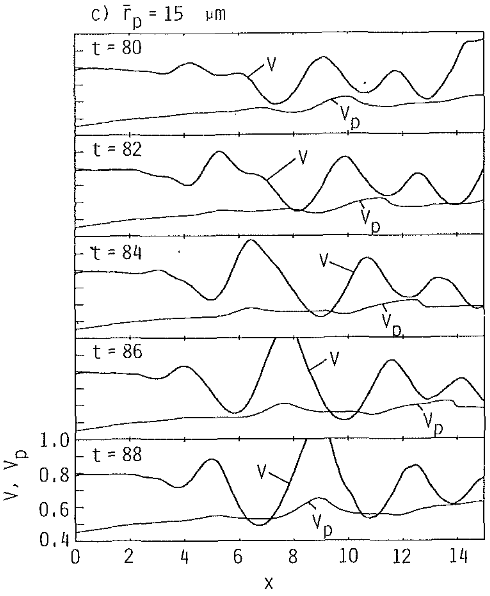

Fig. 6(*c*)

Figs. 6(*a*) to 6(*c*) Distributions of gas-phase velocity ($V=(u^2+v^2)^{1/2}$) and particle-phase velocity ($V_p=(u_p^2+v_p^2)^{1/2}$) along jet axis

and energy between the gas and particle phases is extremely sensitive for the case of smaller particles.

Figures 8(*a*) to 8(*c*) give variations in gas-phase pressure with time at five fixed positions ($\bar{x}=j\bar{D}$; $j=1\sim5$) along the jet axis from $t=50$ to 90. It can be seen from these figures *that the pressure variation with time occurs negligibly slightly* upstream and appreciably strongly downstream. Also, for the case of $\bar{r}_p=0.5$ μm, the amplitude of variation is very small even in the downstream region, while for larger particles the pressure fluctuates in a wide range. It is clearly understood that the pressure wave propagates from upstream to downstream with an almost constant velocity.

Figures 9(*a*) to 9(*c*) indicate the time-averaged pressure and temperature of the gas-phase over the time range from $t=60$ to $t=90$. Both the pressure and the temperature are kept almost constant everywhere along the jet axis for the three particle sizes, regardless of being an appreciable fluctuation of instantaneous pressure and temperature.

5 Experimental

Essentially it would be desirable to calculate mist flows for which experimental data are available so that a direct comparison could be made. Unfortunately, experiments which provide sufficient data to specify the mist flows do not appear to exist. Therefore, we have made a very simple experiment by using the experimental setup shown in Fig. 10. The air mist nozzle (Kyoritsu Gokin, KNT type) is attached on the top of the chamber. The straight nozzle of 2 mm in diameter and 3 mm in length is equipped on the bottom of the chamber. The gas-water droplets mixture is first injected from the upper nozzle into the chamber, and then exhausted from the straight nozzle to the atmospheric surrounding. The purpose of chamber would be that the two-phase jet flow from the upper nozzle is once stagnant so that the computational condition could be satisfied. However, in reality, an air/water separation appears to partly occur at the chamber bottom. This has been confirmed by the variation of droplet size along the jet axis. In the present experiment, the droplet size distribution, as well as the velocity distribution, has been measured by an LDA (Laser-Doppler anemometry) system.

Here, it should be noted that this LDA system, which is

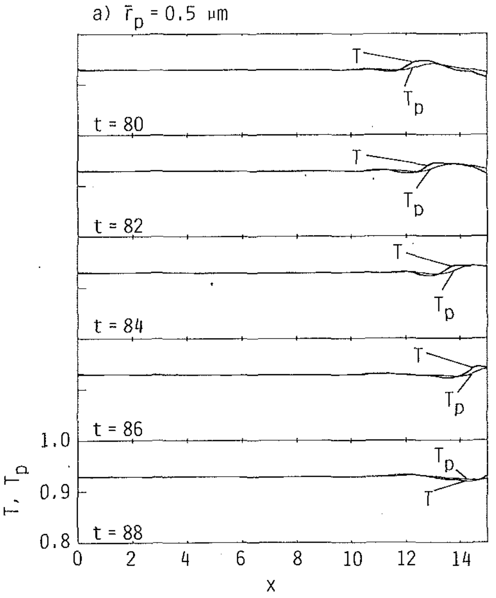

Fig. 7*(a)*

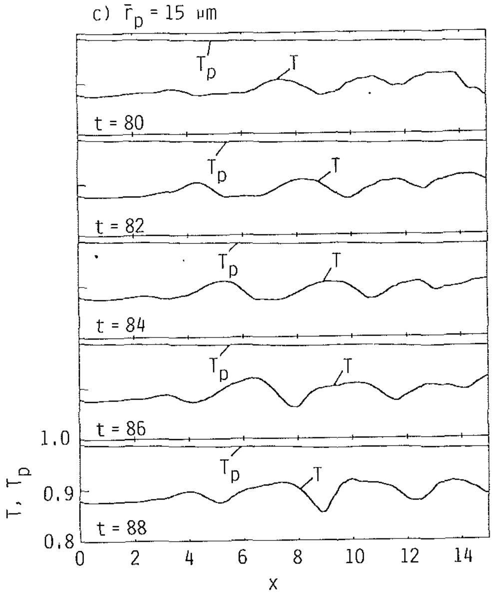

Fig. 7*(c)*

Figs. 7*(a)* to 7*(c)* Distributions of gas phase temperature (*T*) and particle-phase temperature (T_p) along jet axis

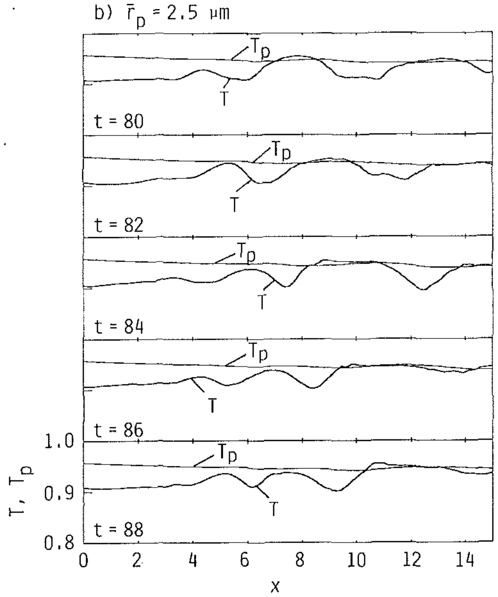

Fig. 7*(b)*

called the phase doppler particle analyzer, can measure not only the particle velocity, but also the particle size. Basically this belongs to the same optical system as the conventional LDA one, but three detectors are equipped at a constant space behind the receiver window. A particle passing through the crossing point of two beams scatters the light, and thereby the interference flinge pattern occurs. The flinge interval is proportional to the particle size and the particle size is determinable by measuring the spatial frequency of interference flinge pattern. Again, this system can be applied to a spherical particle of 0.5 μm to 3000 μm in diameter. But, the errors within plus or minus 1.0 percent or so for larger particles ($\gtrsim 100$ μm) and within 3.0 percent or so for smaller particles ($\lesssim 5$ μm) seem to be unavoidable.

The droplet size ranges from 7 μm to 75 μm downstream of 40 mm from the straight nozzle exit and the droplet velocity ranges from 15 m/s to 75 m/s in the region between 20 mm and 100 mm from the nozzle exit. Also, the mass loading ratio has been measured to be 1.2.

Figure 11 (*a*) indicates the measured mean droplet diameter distribution along the jet axis. It can be seen that the relatively large droplets at the location of 20 mm from the nozzle exit diminish in mean diameter downstream from there. Further, we note that the droplet size could not be measured in the region from the nozzle exit to the location 20 mm or so downstream from it. This may be due to the fact that a stable droplet size is not achieved near the nozzle exit.

Also, it must be noted that it was impossible to measure the gas-phase velocity owing to the presence of water-droplets. Even though the measurement is made by including small seed particles, the results so obtained must be unreliable due to the sticking effect of these particles and water-droplets.

It has been found that the mean droplet velocity distribution along the jet axis measured by the LDA system remains almost constant in the region between 20 mm and 50 mm from the nozzle exit. This implies that in such region the two-phase flow is kept approximately in velocity equilibrium. Therefore, for computational purpose, the gas and particle phases have been assumed to be in equilibrium with each other at the nozzle exit and the droplet velocity at the nozzle exit has been approximated to be the same as the measured mean droplet velocity.

The volume mean diameter, as well as the mean velocity has been obtained on the basis of the data processing. Such mean values have been introduced to computational data so that the calculation could be carried out.

Practically, the droplet velocity distribution has been calculated by using the present model on the conditions that $\bar{u}_E = \bar{u}_{pE} = 42$ m/s, $\bar{r}_p = 18.5$ μm and $\nu_E = 1.2$. Figure 11 (*b*) indicates the comparison of the calculated result with the measured one.

6 Discussion

To predict the particle motion in the jet flow, a Lagrangian approach is followed. The trajectory of each particle in the flow is numerically solved directly from the equations of motion. Some assumptions in the particle motion analysis have been introduced. We have already demonstrated that the neglect of virtual mass force, pressure gradient force and Basset force is justified on the basis of an order of magnitude study

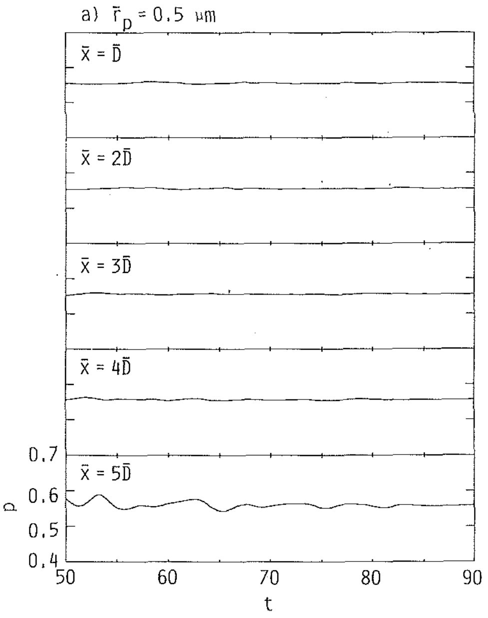

Fig. 8*(a)*

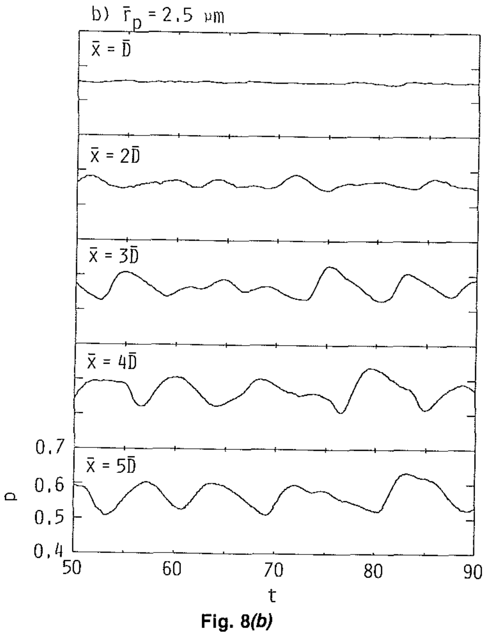

Fig. 8*(b)*

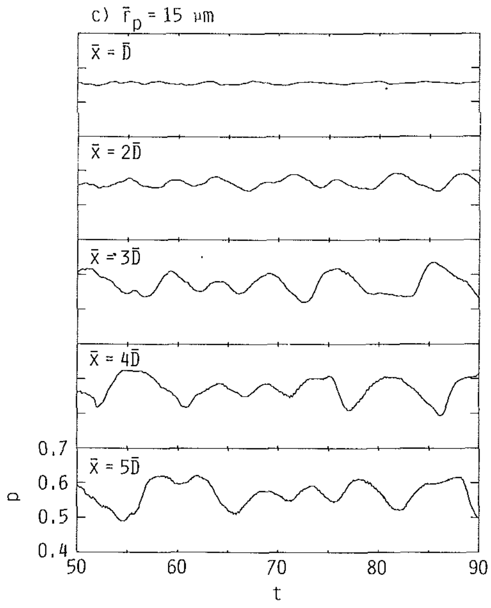

Fig. 8*(c)*

Figs. 8(*a*) to 8(*c*) Variations of pressure with time at five points ($\bar{x} = j\bar{D}$; $j = 1 \sim 5$) along jet axis from $t = 50$ to $t = 90$

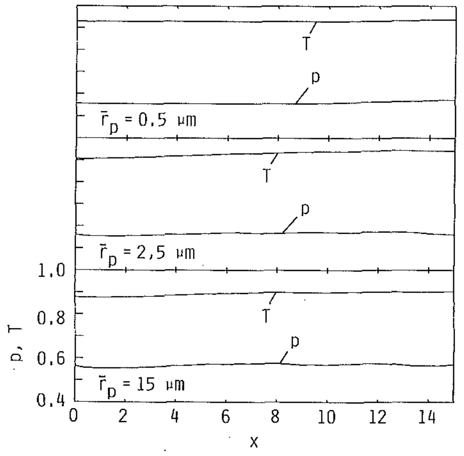

Figs. 9(*a*) to 9(*c*) Time-averaged pressure and temperature along jet axis. Note that time-averaged values are taken over a time period from $t = 60$ to $t = 90$

(Maxey and Riley, 1983). Also, the effect of fluids turbulence has been neglected in this analysis. The inclusion of this is inhivitively costly in terms of computer time and memory, in particular, for the two-phase flow problem. However, it may be valid from the numerical results presented here that no turbulence model is needed to establish the overall nature of the flow.

Next, in spite of drastic approximations, very good agreement between the calculated and the experimental results has been obtained. In this analysis, the assumption that the gas-phase is in velocity equilibrium with the particle-phase at the nozzle exit has been used. In reality, it may be reasonable to consider that at least in the vicinity of the nozzle exit the gas-phase is deviates from equilibrium with the droplet-phase, and that the former velocity at the nozzle exit is higher than the mean droplet ones measured in the range from 20 mm to 50 mm from the nozzle exit, while the latter velocity is lower than the measured values. However, a velocity equilibrium state may be reached immediately downstream from the nozzle exit (see Fig. 11(*b*)). We consider from such a point of view that the above assumption is not so far from the truth at least in the present situation, although it is very difficult to concretely discuss the validity.

Furthermore, we discuss the problem to characterize the particle behavior in a gas flow from a qualitative point of view. Chung and Troutt (1988) have numerically analyzed the particle dispersion in an axisymmetric jet by following particle trajectories in a jet flow simulated by discrete vortex rings. According to their analysis, the effectiveness of the large turbulent structures for moving particles in the mixing region can be characterized by the Stokes number, that is, the ratio of the aerodynamic response time $\bar{\tau}_A$ of a particle defined by Eq. (7) to the characteristic timescale $\bar{D}/\bar{u}_E$ of the flow field. For the ratio $\gamma_\tau(=\bar{\rho}_{mp}(2\bar{r}_p)^2\bar{u}_E/18\bar{\mu}\bar{D}) \gg 1$, the particles will not

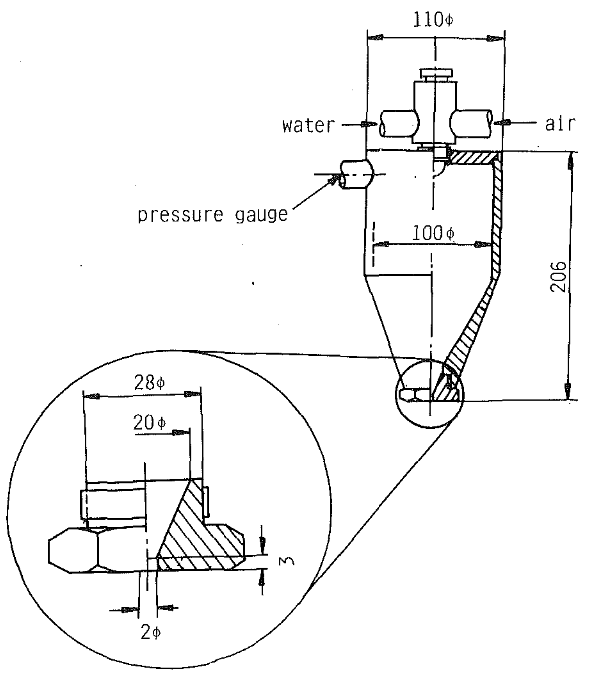

Fig. 10 Experimental apparatus

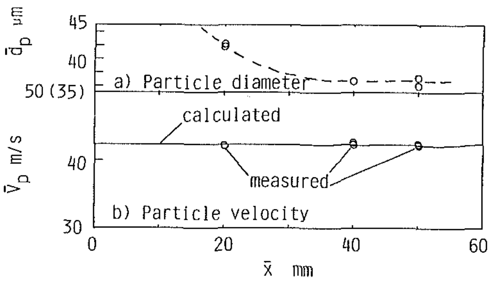

Figs. 11(*a*) and 11(*b*) Mean droplet diameter distribution along jet axis measured by LDA system (*a*) and comparison of mean droplet velocity distribution measured by LDA system with calculated one by using present numerical model. Note that 1000 samples are taken at measurement of one time as data for diameter as well as velocity, and that the time of measurement is all twice at the individual measuring point. (Experimental uncertainty in $\bar{d}_p$ (= 2$\bar{r}_p$) = ±0.5 μm, in $\bar{u}_p$ = ±0.7 m/s, in $\bar{x}$ = ±1 mm.)

have sufficient time to respond to the gas flow and will move in nearly rectilinear path. For $\gamma_\tau \ll 1$, the particles will have sufficient time to respond to the spreading velocity field of the gas jet. On the other hand, for the condition $\gamma_\tau \sim 0(1)$, the gas jet may be able to temporarily capture the particles and fling them beyond the fluid momentum mixing region.

The Stokes numbers for these individual mixtures are that $\gamma_\tau = 0.08$ for $\bar{r}_p = 0.5$ μm, $\gamma_\tau = 2.0$ for $\bar{r}_p = 2.5$ μm and $\gamma_\tau = 75$ for $\bar{r}_p = 15$ μm, respectively. The present results shown in Figs. 6(*a*) to 6(*c*) and Figs. 7(*a*) to 7(*c*) are clearly quite consistent with the previous discussion.

7 Conclusion

For understanding behavior characteristics of gas-particle two-phase free jets practically, a system of equations for the gas and particle phases has been numerically solved for the mixture composed of air and water-droplets. There are some variations in the instantaneous flow properties of the gas-phase depending upon the size of droplets contained in the mixture, but time-averaged values over a time period show a quasi-steady flow state. The vortical structure occurring at the jet boundary of the nozzle exit is convected along the boundary downstream and agitates the jet flow.

Again, the numerical water-droplet velocity distribution calculated by using the present flow model has been compared with the measured values. The overall agreement has been found to be remarkably good.

Additionally, it has been confirmed that the response of the particle motion to the gas flow can be specified by the Stokes number, and that the flow structure of mixture with very small particles is in the velocity and thermal equilibrium between the two-phases.

References

Carlson, D. J., and Hoglund, R. F., 1964, "Particle Drag and Heat Transfer in Rocket Nozzles," *AIAA Journal*, Vol. 2, pp. 1980–1984.

Chakravarthy, S. R., and Osher, S., 1985, "A New Class of High Accuracy TVD Schemes for Hyperbolic Conservation Laws," AIAA paper 85-0363, AIAA 23rd Aerospace Science Meeting, Reno, Nev.

Chung, J. N., and Troutt, T. R., 1988, "Simulation of Particle Dispersion in an Axisymmetric Jet," *Journal of Fluid Mechanics*, Vol. 186, pp. 199–222.

Crowe, C. T., 1982, "Review-Numerical Model for Dilute Gas-Particle Flows," ASME JOURNAL OF FLUIDS ENGINEERING, Vol. 104, pp. 297–303.

Crowe, C. T., Sharma, M. P., and Stock, D. E., 1977, "The Particle-Source-In Cell Method for Gas Droplet Flow," ASME JOURNAL OF FLUIDS ENGINEERING, Vol. 99, No. 2, pp. 325–332.

Dukowicz, J. K., 1978, "A Particle-Fluid Numerical Model for Liquid Sprays," *Journal of Computational Physics*, Vol. 35, pp. 229–253.

Godunov, S. K., 1959, "A Finite Difference Method for the Numerical Solutions of the Equations of the Fluid Dynamics," *Matemat. Sbornik*, Vol. 47, pp. 271–290, also Cornell Aeronautical Laboratory Translation.

Harlow, F., and Amsden, A., 1975, "Numerical Calculation of Multiphase Fluid Flow," *Journal of Computational Physics*, Vol. 17, pp. 19–52.

Hatta, N., Ishii, R., Takuda, H., Ueda, K., and Kokado, J., 1988, "Analytical Study on Subsonic Nozzle Flows of Gas-Particle Mixture," *Trans. Iron Steel Inst. Jpn.*, pp. 930–938.

Hatta, N., Takuda, H., Ishii, R., and Fujimoto, H., 1989, "A Theoretical Study on Nozzle Design for Gas-Particle Mixture Flow," *ISIJ International*, Vol. 29, pp. 605–613.

Hatta, N., Fujimoto, H., Ishii, R., Umeda, Y., and Kokado, J., 1989, "Numerical Study on Supersonic Flows of Gas-Liquid Particle Mixture in a De Laval Nozzle," *ISIJ International*, Vol. 29, pp. 911–918.

Henderson, C. B., 1976, "Drag Coefficients of Spheres in Continuum and Rarefied Flows," *AIAA Journal*, Vol. 14, pp. 707–708.

Ishii, R., Umeda, Y., and Yuhi, M., 1989, "Numerical Analysis of Gas-Particle Two-Phase Flows," *Journal of Fluid Mechanics*, Vol. 203, pp. 475–515.

Matsuda, T., Umeda, Y., Ishii, R., Yasuda, A., and Sawada, K., 1987, "Numerical and Experimental Studies on Chocked Underexpanded Jets," *Memoirs of the Faculty of Engg.*, Kyoto University, Vol. 49, Part 1, pp. 84–110.

Maxey, M. R., and Riley, J. J., 1983, "Equation of Motion for a Small Rigid Sphere in a Nonuniform Flow," *Phys. Fluids*, pp. 883–889.

Roe, P. L., 1981, "Approximate Riemann Solvers, Parameter Vectors, and Difference Schemes," *Journal of Computational Physics*, Vol. 43, pp. 357–372.

Zucrow, M. J., and Hoffman, J. D., 1977, *Gas Dynamics*, Vol. II, Wiley, New York, p. 53.

Water Quality Effects on Cavitation Inception in a Trailing Vortex

Roger E. A. Arndt
St. Anthony Falls Hydraulic Laboratory,
University of Minnesota,
Minneapolis, MN

Andreas P. Keller
Versuchsanstalt für Waserbau,
Obernach, Federal Republic of Germany

Tip vortex cavitation studies were made with a hydrofoil that was elliptical in planform, with an aspect ratio of 3, and having a modified NACA 66_2-415 profile. LDV measurements of the tangential velocity component in the vortex were used to determine that the minimum pressure in the vortex varies with lift coefficient squared, i.e., that the incipient cavitation number σ_i should follow a C_l^2 relation ($\sigma_i \approx C_l^2$). This is in contradiction to previous observations (Arndt et al. 1991) that the tip vortex cavitation index varied approximately with lift coefficient to the power 1.4. By carefully monitoring the tensile strength of the water, i.e., its susceptibility to cavitation, the discrepancy was traced to the capability of the test water to sustain a tensile stress. Cavitation in "weak" water (no tensile strength) does follow the C_l^2 relationship, whereas observations in "strong" water (rupture considerably below vapor pressure) more closely followed the previously observed variation, i.e., $\sigma_i \approx C_l^{1.4}$. Since the structure of the vortex cannot be affected by changes in the water quality, the discrepancy can be explained only by the amount of tension that can be sustained by the test water before inception occurs. Apparently a relatively larger value of tension can be sustained in the vortex as the strength of the vortex is increased (i.e., increasing C_l). This would explain the observed deviation from the expected C_l^2 law for water with measurable tensile strength.

I Introduction

Vortex problems are common in a variety of applications. In addition to tip vortices on propellers, vortex cavitation in the clearance passages of pumps and turbines, hub vortex cavitation, cavitation in secondary flows in corners, etc. are important related problems. Vortex cavitation is a major source of erosion in ducted propellers. In a recently conducted survey of water tunnel pumps, Abbot and Greeley (1984) identified vortex cavitation in clearance passages as the most significant noise source. This was an important consideration in the recently completed designs of two very large water tunnels in the United States and in Germany.

In spite of its practical importance, relatively little research has been directed toward the tip vortex cavitation problem, even though there is evidence that tip vortex cavitation can be a significant problem under certain circumstances. Platzer and Souders (1979) reviewed the available literature to that time and concluded that very little information was available on the phenomenon of tip vortex cavitation. A literature survey conducted during a recently completed tip vortex cavitation study by Higuchi et al. (1989) indicates that very little has been added to our body of knowledge since the review by Platzer and Souders. It should also be mentioned that Strasberg (1986) pointed out that vortex cavitation noise persists as an important problem that has not been explored.

Several significant issues warrant further study. For example, Arndt et al. (1991) found that nuclei size and number play a critical role in the inception process in the trailing vortex from an elliptically loaded hydrofoil. Tension has been observed and nuclei supplied from separated regions on the surface of a hydrofoil can play an important role when the separated flow is supersaturated. When cavitation is due entirely to the ingestion of free-stream nuclei, very small nuclei, approximately 2μm in diameter, are apparently active in the cavitation process, in spite of the availability of larger nuclei in the flow. In addition, it was found that the cavitation inception number scales with angle of attack to a power of about 1.4 rather than the power of 2.0, which would be expected if the strength of the vortex scaled with lift coefficient.

As a follow-up to the previous research at the St. Anthony Falls Hydraulic Laboratory, experiments were conducted in the water tunnel at the Versuchsanstalt für Wasserbau in Obernach, West Germany. A larger foil, identical in planform and blade section to that used in the Arndt et al. (1991) study, was tested over the same Reynolds number range studied in the previous work. The objectives of this study were to:

(*a*) determine whether the observed variation of cavitation number with velocity was due to Reynolds scaling effects, bubble dynamics effects, or a combination of both.

(*b*) correlate the cavitation inception index with the *measured* lift coefficient to determine the reason for the unexpected scaling of cavitation index with angle of attack.

(*c*) observe the cavitation inception process in detail to determine the effect of flow unsteadiness, and

(*d*) vary the nuclei content (tensile strength) of the water to determine whether vortex cavitation is as sensitive to nuclei content as alluded to in Arndt et al. (1991).

Contributed by the Fluids Engineering Division for publication in the JOURNAL OF FLUIDS ENGINEERING. Manuscript received by the Fluids Engineering Division April 6, 1991. Associate Technical Editor: M. L. Billet.

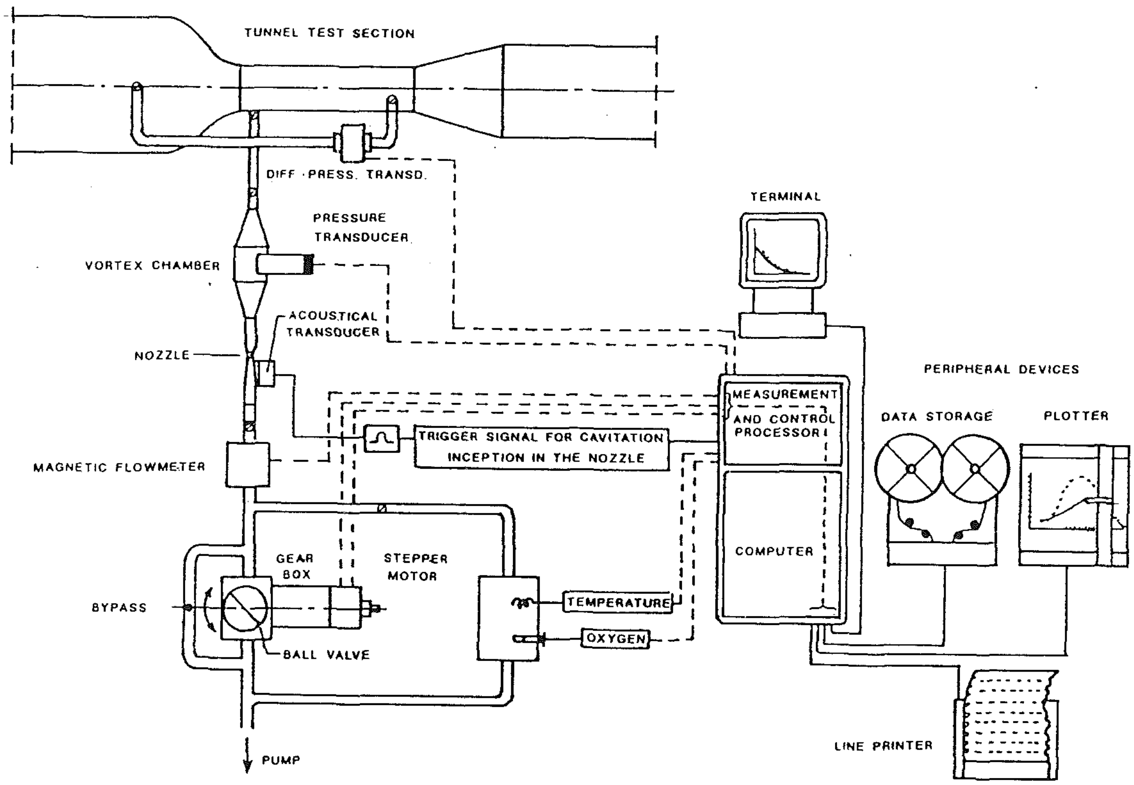

Fig. 1 Schematic of instrumentation used for cavitation studies

II Experimental Methods

The water tunnel used in this study is of standard Kempf-Remmers design, having a test section that is 30cm × 30cm in cross section and is 2.1m long. The maximum attainable water velocity is over 16 m/s. However, most of this study was carried out at flow velocities less than 12 m/s. The static pressure in the tunnel can be varied in the range 0.1 to 2.0 bar absolute, permitting studies over a wide range of cavitation number.

As shown in Fig. 1, a considerable degree of automation was used in the operation of the tunnel. The entire test procedure was under computer control. Water tensile strength and dissolved oxygen were measured at each data point. Cavitation inception was detected visually. At the instant of cavitation inception, the static pressure and flow velocity were recorded in computer memory and the value of cavitation index was calculated. Cavitation inception could be studied by either lowering pressure at constant velocity or by increasing the velocity at constant pressure in the stilling chamber. Visual observation of cavitation was supplemented with video and high speed cinematography at 5000 frames per second.

A venturi device (Keller, 1987) was used to measure the tensile strength of the water. It is well known that the tensile strength of the water is not a homogeneously distributed property of the water, but rather is a function of the spatial and temporal distribution of nuclei in the flow. Hence, each individual measurement of tensile strength has a degree of uncertainty associated with the instantaneous sample of water in the venturi nozzle at the instant of tensile strength measurement, which is made when the water sample cavitates in the test nozzle of the measuring device. For this reason, a high number of tests are necessary for each data point. Six or more tests were made to establish each value of cavitation index and tensile strength.

Nomenclature

a = core radius, or NACA meanline designation
A_R = aspect ratio = $8b/\pi c_0$
A_S = surface area = $\pi/2\ bc_0$
b = hydrofoil semi-span (Fig. 3)
c = chord length
c_0 = maximum chord length
C_p = pressure coefficient
C_D = drag coefficient $D/\frac{1}{2}\rho U_0^2 A_S$
C_{Df} = viscous drag coefficient defined in Eq. (10)
C_l = lift coefficient $L/\frac{1}{2}\rho U_0^2 A_S$
C_p = pressure coefficient
C_{p_c} = pressure coefficient in cavitating flow
$C_{p_{\min}}$ = pressure coefficient based on minimum mean static pressure
D = drag
k = unsteady pressure factor
L = lift
p = pressure
p' = rms pressure
p_{crit} = critical pressure
p_v = vapor pressure
r = radius
R_0 = nucleus radius
S = surface tension
T = tensile strength
u, v, w = velocity components
U_0 = free stream velocity
v_θ = peripheral velocity component
x, y, z = coordinates
α = angle of attack
α_0 = angle of zero lift
Γ = circulation
λ = dummy parameter
ν = kinematic viscosity
ρ = density
σ = cavitation index
Σ = total angular momentum per unit length

Subscripts

i = inception
iw = inception in weak water
is = inception in strong water
min = minimum

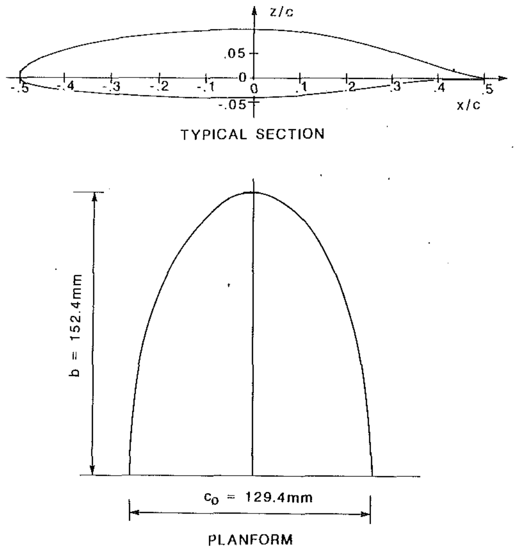

Fig. 2 Schematic of hydrofoil used in this study. An elliptic planform of aspect ratio 3 is used. The airfoil section is a modified NACA 66_2-415 (a = 0.8).

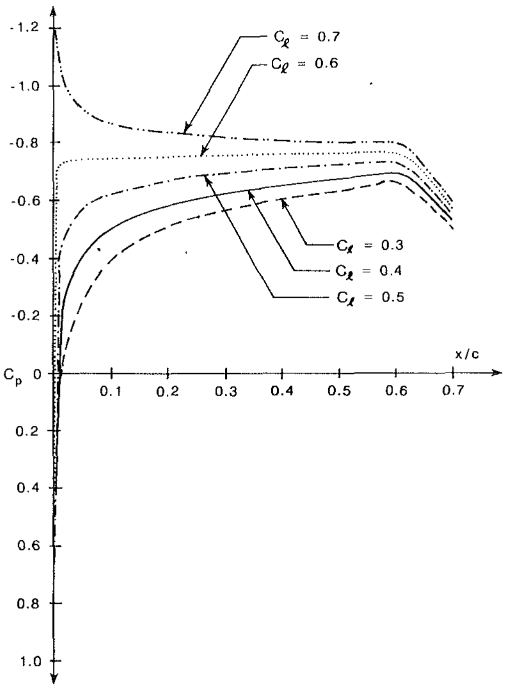

Fig. 3 Plot of pressure coefficient, $Cp = p - p_0/\frac{1}{2}\rho U_0^2$ for the suction side of the NACA 66_2-415 foil section. x is measured from the nose of the hydrofoil.

An important feature of this study was the variation of tensile strength, T defined as $T = p_v - p_{\text{crit}}$. This property can be varied over a wide range, and is a function of total gas content (determined from the measured dissolved oxygen reading), system pressure and prehistory of the water. It should be emphasized that the relationship between tensile strength and preconditioning of the water is facility dependent. The tensile strength obtained as a result of these procedures is specific to the water tunnel being used. Different water tunnels will require different procedures and a great deal of experience is necessary before water quality can be varied in a predictable manner. One of the authors (Dr. Keller) has had 25 years of experience with the facility used in this study. Care also has to be taken to insure that there is not an excess of bubbles in the flow which can result in pseudo cavitation at local pressures considerably in excess of the vapor pressure of the liquid. Prepressurization at 2 bars with very low flow rates for 15 minutes was the procedure used to pre-strengthen the water in this study. Tensile strengths as high as two bars could be achieved.

A series of measurements were made with water of "zero" tensile strength, which must be defined. This property was achieved by using water with a dissolved gas content adjusted to saturation at the static pressure in the test section at the inception point. The water was first cavitated in the test section before each test. Since the required pressure in the test section is not known before a given cavitation test, some "cut and try" procedures were necessary to establish the required conditions for "weak" water. In spite of these procedures, the water always had a slight, but measurable tensile strength. The measured tensile strength was used to correct the measurements in order to establish a trend of σ_{iw} versus lift coefficient in the absence of tensile strength.

In order to measure hydrodynamic forces on the hydrofoil, the roof of the water tunnel test section was replaced by a flush mounted force balance. This balance was designed to have minimum cross talk between the measurements of lift and drag. The hydrofoil used in this study is identical in cross section and planform to the one used in the SAFHL studies. It is elliptic in planform, with the same profile at each cross section, without geometric or aerodynamic twist. The profile used was a modified NACA 66_2-415 airfoil section with an $a = 0.8$ meanline (Fig. 2). The theoretical chordwise pressure distribution as a function of lift coefficient is shown in Fig. 3. As designed, the pressure distribution on the suction side of the foil is favorable until the 60 percent chord position in the range of lift coefficient 0.2 to 0.6 (±0.2 about the design value of 0.4). The foil was mounted on the force balance and held in place at the desired angle of attack with a dowel pin. The angle of attack could be varied in increments of two degrees. The actual position for zero lift was determined from the lift measurements. All angle of attack data were subsequently referenced to the measured zero lift angle.

Measurement of the axial and vertical velocities in the trailing vortex were made in a horizontal plane bisecting the center of the vortex using a TSI Laser Doppler Velocimeter, System 9100-3 with an IFA550 signal processor. With this orientation of the measurement system, the magnitude of the vertical velocity is equal to the tangential component of velocity in a cylindrical coordinate system whose axis is aligned with the center of the vortex. An automated, computer controlled, traversing mechanism was used to move the laser optics, and hence the optical measurement volume, across the test section of the tunnel. The backlash in this system was estimated to be less than 0.1 mm. Each measurement position in the tunnel test section was very repeatable. Repeatability was found to be ±1 step of the stepper motor which has a resolution of 100 steps per mm. The center of the vortex was determined by cavitation. The cavitation number was slightly less than the incipient value to insure proper visualization of the vortex trajectory. The degree of accuracy in positioning was estimated to be within 1 mm. The true center could be obtained from the plots of the vertical velocity versus position with the center being defined where the vertical velocity was just equal to zero. This center, as obtained graphically, was always within one mm of that obtained visually with cavitation. A minimum of 75 data points were used to establish the velocity profiles shown in Figs. 7 and 8.

The error in the velocity measurement is difficult to quantify since it is a function of turbulence intensity. According to material published by the manufacturer, the error should be less than 1 percent. The cross over volume of the LDV setup was 0.03 mm^3, and the shifting frequency was 2 MHz. The measurements are made in a very steep velocity gradient. For this reason, errors in positioning far outweigh any errors in the magnitude of the velocity.

There are two basic sources of error in the measured value of the cavitation index. The dynamic pressure, $\frac{1}{2}\rho U_0^2$, is measured by a differential pressure transducer with a maximum observed deviation of ±0.5 percent. Absolute pressure is also measured with a piezoresistive transducer with a maximum deviation from linearity of ±0.5 percent. This would infer an error in the recorded value of cavitation index of only 0.7 percent. However, the major uncertainty in the incipient cavitation number is the variation in size and number of nuclei in the minimum pressure region at the instant that cavitation is observed. This uncertainty is not truly a measurement error, but is rather an indication of the variability in the conditions at inception.

The force balance and recording system was calibrated as a system using weights. Repeatability was observed to be within 1 percent.

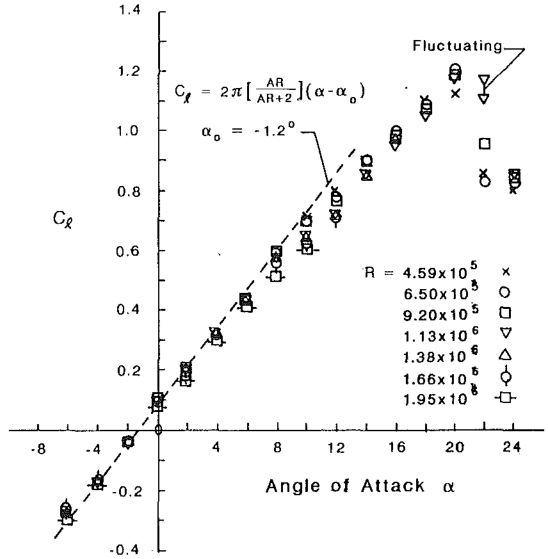

Fig. 4 Lift coefficient versus angle of attack in the Reynolds number range 4.6×10^5 to 2×10^6 (based on maximum chord length)

III Rationale for the Experiments

One of the purposes of these experiments is to determine the magnitude of the tension that can be sustained by a vortex at inception. Assuming vaporous cavitation, inception will occur when the minimum pressure in the flow falls below a critical value

$$p_{\min} = p_{\text{crit}} \tag{1}$$

The instantaneous value of minimum pressure can be less than the mean static pressure

$$p_{\min} = \bar{p}_{\min} - kp' \tag{2}$$

where $\bar{p}_{\min}$ is the minimum mean static pressure, p' is the root mean square of unsteady fluctuations in pressure about the mean, and k is a factor that is a complex function of the interaction of nuclei with the unsteady pressure field.

The critical pressure is less than the vapor pressure p_v:

$$p_{\text{crit}} = p_v - T \tag{3}$$

where the tension T can be estimated[1] from the equilibrium theory for a spherical bubble

$$T \cong \frac{4}{3}\frac{S}{R_0} \tag{4}$$

Equation (1)–(3) can be combined and rearranged to yield

$$\sigma_i = -C_{p_{\min}} + k\frac{p'}{\frac{1}{2}\rho U_0^2} - \frac{T}{\frac{1}{2}\rho U_0^2} \tag{5}$$

Unfortunately, the last two terms in Eq. (5) are of roughly the same order of magnitude. In order to separate these two effects, cavitation inception is measured in weak water (σ_{iw}) and the measured data is then compared with the results from measurements in "strong" water (σ_{is}). The σ_{iw} data are corrected to zero tensile strength, using the measured value of tension in the venturi device. Then

$$\frac{T}{\frac{1}{2}\rho U_0^2} = \sigma_{iw} - \sigma_{is} \tag{6}$$

$C_{p_{\min}}$ is extremely difficult to measure. However, its magnitude can be estimated from measurements of the tangential velocity distribution in the vortex. This is discussed in subsequent sections of this paper. Referring to Eq. (5), it can be seen that the effect of turbulence can be estimated by comparing the measurements of $C_{p_{\min}}$ and cavitation inception in weak water

$$k\frac{p'}{\frac{1}{2}\rho U_0^2} = \sigma_{iw} + C_{p_{\min}} \tag{7}$$

This procedure is qualitative at best since both the tension and the turbulence factor, k, are functionally dependent on the size and number of nuclei in the flow. Unfortunately, a better procedure for evaluating the complex interaction between turbulence and nuclei in the core of the vortex is unavailable at this time.

IV Discussion of Results

Lift and Drag. Lift data were collected over a range of Reynolds number from 4.6×10^5 to 2.0×10^6 (based on maximum chord length). Comparison is made with the expected result in Fig. 4. The expected trend for small angles of attack is given by

$$C_l = 2\pi\left(\frac{A_R}{A_R+2}\right)(\alpha - \alpha_0) \tag{8}$$

where

$$C_l = \frac{L}{\frac{1}{2}\rho U_0^2 A_S} \tag{9}$$

The measured value of the zero lift angle, α_0, was found to be −1.2 deg, which is close to the expected value (Abbott and von Doenhoff, 1958) and well within the expected tolerance of ±1 degree for the dowel pin system used to position the hydrofoil. There was a repeatable spread in the data at an angle of attack of about 10° ($\alpha - \alpha_0 = 11.2$ deg) with the value of C_l decreasing with increasing Reynolds number. There is no explanation for this, other than the observation in previous flow visualization studies that indicated that the boundary layer flow on the suction side is very sensitive to Reynolds number at this angle of attack. A sample comparison is shown in Fig. 5.

Because of the relatively small values involved, the measured drag values show more scatter as illustrated in Fig. 6. Comparison is made with the drag polar curve given by

$$C_D = C_{Df} + \frac{C_l^2}{\pi A_R} \tag{10}$$

where C_{Df} is approximated by the section drag coefficient for

---

[1] The actual shape of critical nuclei in a vortex is unknown at this time.

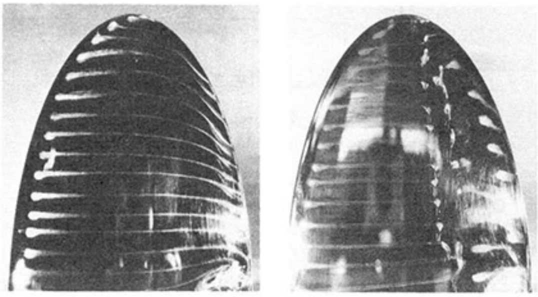

(*a*) (*b*)

Fig. 5 Comparison of boundary layer flow over the suction side of the foil at an effective angle of attack ($\alpha - \alpha_0$) of 12.5 deg. Comparison is made at a Reynolds number of 5.3 × 10^5 (Photo (*a*)) and 2.7 × 10^5 (Photo (*b*)) using an oil film visualization technique.

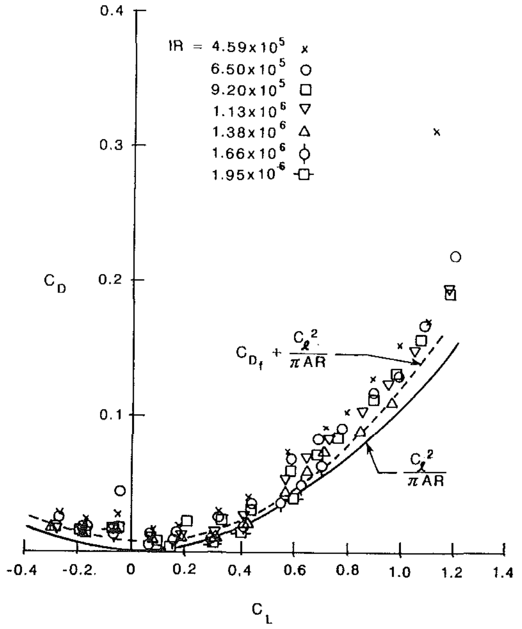

Fig. 6 Drag polar diagram. The measured drag is compared to an expected curve which is made up primarily of induced drag with a relatively small skin friction correction, based on airfoil data at a Reynolds number of 3 × 10^6.

the NACA 66_2-415 airfoil at a Reynolds number of 3 × 10^6 which is the lowest Reynolds number for which data are available. As expected, the major component of the total drag is induced drag. The majority of the data fall above the expected curve since the Reynolds numbers for these data are all less than 3 × 10^6. In summary, the measured lift and drag data follow expected trends even though the test Reynolds number range is less than for typical aerodynamics or hydrodynamic applications and there is a laminar separation bubble at about 60 percent of chord which does not exist at higher Reynolds numbers (Abbott and von Doenhoff, 1958).

Velocity Measurements. The measured vertical velocity (absolute value equal to v_θ) in the trailing vortex at one semi-span downstream is shown in Fig. 7. The data were obtained for five different values of lift coefficient. The data are depicted as seen by an observer looking downstream from the tip of the hydrofoil. The measurements were made along a horizontal line passing through the center of the vortex. From this perspective, the suction side of the hydrofoil mounted on the roof of the test section would be to the observer's left side. The horizontal distance from the center of the vortex, z, has been normalized with respect to the semi-span of the hydrofoil, b. All the data were collected at a constant Reynolds number of 9.7 × 10^5 based on maximum chord length. The data have been normalized with respect to lift coefficient, C_l, and free stream velocity, U_0, in order to clearly identify the effects of loading on the vortex structure. If there were no effects of loading on the structure of the vortex, the data would be self similar since Reynolds number was held constant.

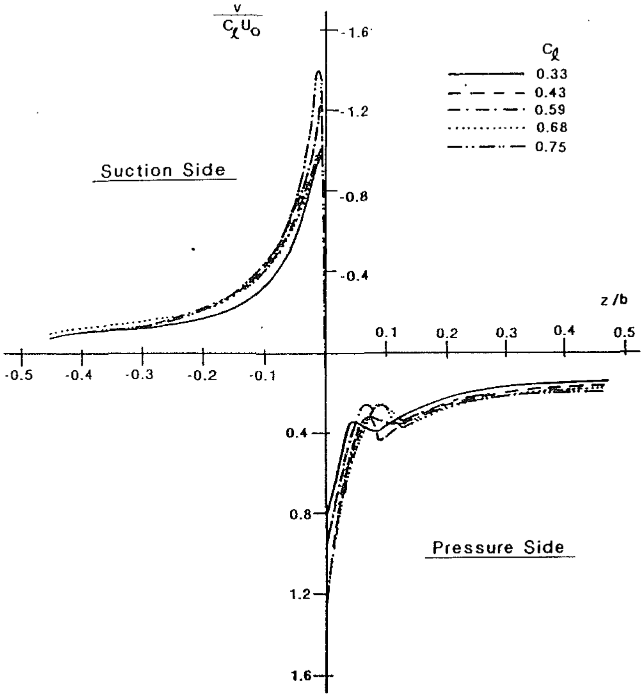

Fig. 7 Vertical velocity component in the trailing vortex one span length downstream. The data are normalized to free stream velocity, U_0, and lift coefficient, C_l.

Two points are immediately evident. The peak velocity is relatively higher at higher lift coefficient, and there is a secondary vortex positioned about 5 to 8 percent of the semi-span, b, from the center of the main vortex on the pressure side. There also appears to be a slight thickening of the vortex core with increasing loading. This can be due to relatively more boundary layer fluid on the hydrofoil being entrained in the core with increasing vortex strength (McCormick, 1962). The secondary vortex probably originates in the region close to the tip where there is a transition from a "short" to a "long" laminar separation bubble due to the reduction in chordwise Reynolds number (Higuchi et al., 1989; Arndt et al., 1991).

Also of interest is the fact that the axial velocity and turbulence intensity increase dramatically in the core region. This is shown in Fig. 8 where the same normalization is used as in Fig. 7. Unfortunately, there is not sufficient spatial resolution to determine precisely where the maximum intensity occurs. It would be expected that there should be significant fluctuations in pressure in the core region which could play a major role in the cavitation process (Green and Acosta, 1989).

Observations of Cavitation. As mentioned previously, observations of cavitation were made in "strong" and "weak" water. The onset of cavitation was quite different in the two cases. In strong water the inception point was very well defined. Inception was characterized by the sudden appearance of a well defined, fully cavitating vortex. The onset of cavitation in weak water was highly intermittent with a large reduction in the cavitation number being necessary before cavitation became more fully developed in the vortex core. The appearance of cavitation was always in the form of relatively long segments of cavitating core. No spherical bubbles or approximations thereof were ever observed in this study which is quite

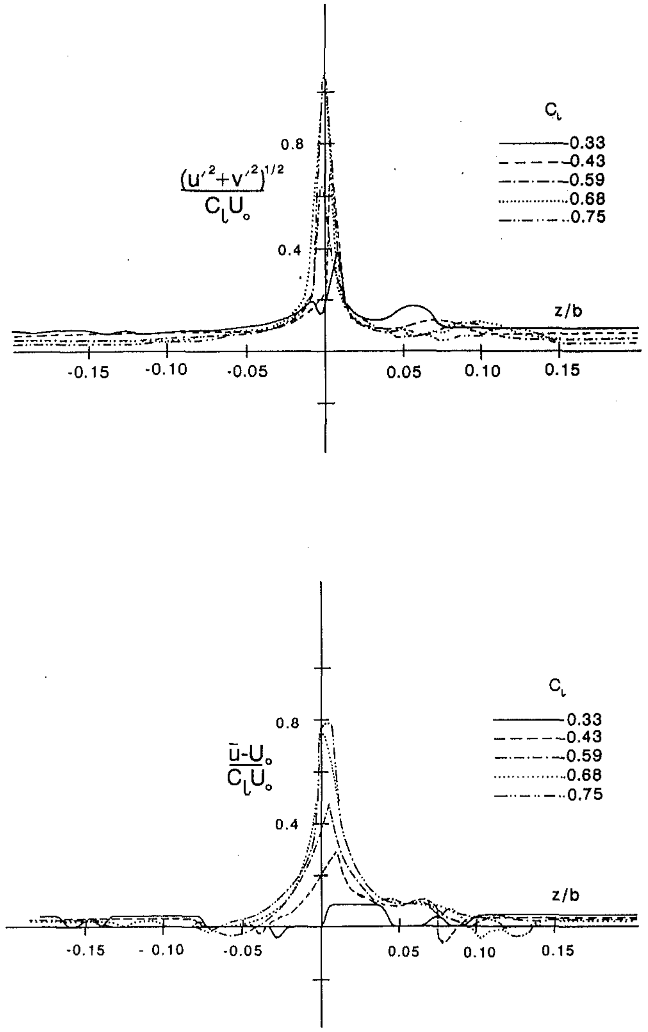

Fig. 8 *Axial velocity (left) and turbulent velocity (right) in the trailing vortex at one span length downstream*

different from the observations at SAFHL (Higuchi et al., 1989; Arndt et al., 1991). It should also be noted that although the cavitation number for inception in weak water could be considerably higher than in strong water, the degree of cavitation was identical to that observed at inception in strong water when the cavitation indices were identical. This was verified by repeatedly measuring the cavitation index at which cavitation in weak water was identical in appearance to inception in strong water.

The highly intermittent nature of inception in weak water may be explained by a simple two-dimensional Rankine vortex model. Analysis shows that when the cavitation number is identically equal to the minimum pressure coefficient, two different vortex structures are possible, having identical circulation and total angular momentum. The first is the classical single phase vortex, with maximum tangential velocity occurring at the edge of the viscous core, a. The second possibility is a vortex having a vapor filled core of radius equal to $a/\sqrt{2}$ and maximum velocity that is $\sqrt{2}$ higher than the maximum velocity in the noncavitating core. Details are given in the Appendix. Although the trailing vortex in this study is more complex than the simple Rankine model, it is possible that the observed intermittency at inception in weak water is due to a fluctuation between two possible flow modes, namely a single phase and a two-phase vortex system having identical values of circulation and total angular momentum.

Although cavitation inception in very weak water is very hard to define, the results are repeatable from day to day. On the other hand, cavitation inception in strong water is very easily observed because of the sudden onset of a fully developed cavitating vortex, but results from day to day vary considerably because of the difficulty in reproducing precisely the same water strength characteristics. In previous studies at SAFHL, the role of dissolved gas was found to be important when the flow in a laminar separation bubble on the surface of the foil is supersaturated. To determine the general validity of this hypothesis, studies were made in strong water at two angles

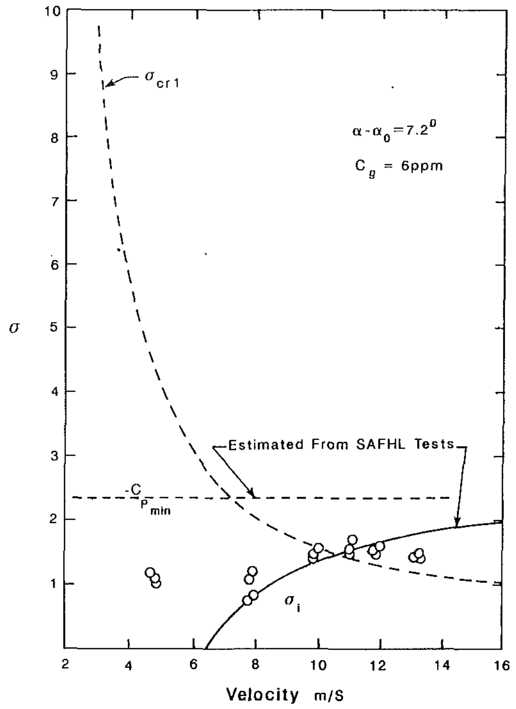

Fig. 9 **Cavitation in strong water compared with estimates derived from previous work at the St. Anthony Falls Hydraulic Laboratory—α − α_0 = 7.2 deg**

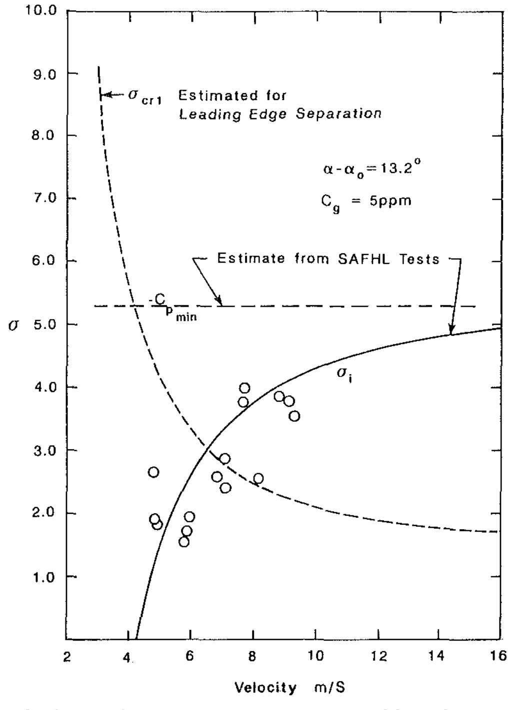

Fig. 10 *Cavitation in strong water compared with estimates derived from previous work at the St. Anthony Falls Hydraulic Laboratory—α − α_0 = 13.2 deg*

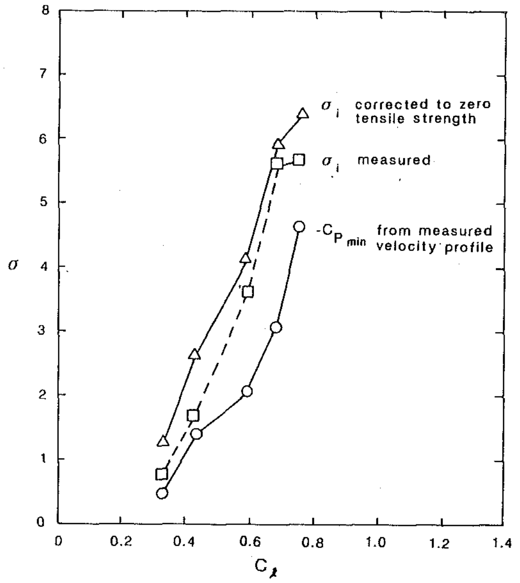

Fig. 11 Comparison of weak water results with $C_{p_{\min}}$ determined from the measured velocity profile. The "corrected" curve is obtained by adjusting the measured value of σ_i by the amount of measured tension.

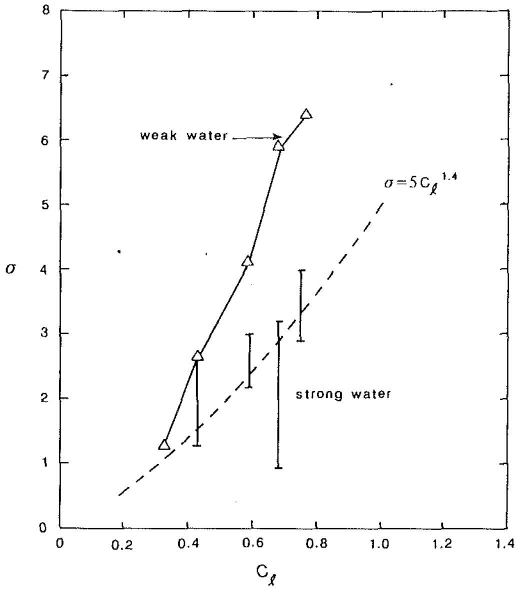

Fig. 12 Comparison of weak water and strong water results

of attack. The results are shown in Figs. 9 and 10. The expected curves in the diagrams are based on Arakeri et al. (1986). $-C_{p_{\min}}$ is assumed to be constant over the range of velocity shown. σ_{cr1} is the value of cavitation index at which the flow in the laminar separation bubble is just at the saturation level for the concentration of dissolved gas in the freestream. It is assumed that σ_i can be calculated for values greater than σ_{cr1}, when the vortex is under tension due to the size of free stream nuclei active in the cavitation process:

$$\sigma_i = -C_{p_{\min}} - \frac{8}{3}\frac{S}{R_0 \rho U_0^2} \tag{11}$$

R_0 was assumed equal to 2μm which produced the best fit to the data in the SAFHL studies. Further analysis of this point is given in subsequent sections of this paper. Only qualitative agreement with previous work was obtained. At the design angle of attack of $\alpha - \alpha_0 = 7.2°$, $C_l \cong 0.4$, the data show little variation with velocity. At a higher angle of attack, $\alpha - \alpha_0 = 13.2°$, $C_l \cong 0.75$, there is a larger predicted variation in cavitation index over the same range of velocity and the data qualitatively confirm this expectation.

Measurement of cavitation index at constant velocity was also made in weak and strong water over a range of lift coefficient C_l. In Fig. 11, the weak water results are compared with the estimate of pressure in the vortex core obtained by integrating the tangential velocity distribution from the suction side. This estimate was made at the axial position where inception was observed (x/b = 1.0). Measurements at x/b = 0.5 indicted that the vortex was already rolled-up at that axial position. For an axisymmetric vortex, the Navier Stokes equations reduce to

$$\frac{dp}{dr} = \rho \frac{v_\theta^2}{r} \tag{12}$$

or

$$C_{p_m} = -2\int_0^\infty \frac{1}{r}\left(\frac{v_\theta}{U_0}\right)^2 dr \tag{13}$$

Comparison is made with the "corrected" value of σ_i which is obtained by making an adjustment in the data for the measured value of tension (Keller, 1987). Each data point represents an average of at least six readings. The general trend of $C_{p_{\min}}$ and σ_{iw} with C_l appear similar. Both sets of data tend towards zero at a finite value of C_l which was also the case for the observations made at SAFHL. The value of σ_{iw} is consistently higher than $-C_{p_{\min}}$ implying that the effect of turbulence is significant. This is a highly complex issue (Arndt, 1981a, 1981b). Another important point is that both the σ_{iw} and $C_{p_{\min}}$ data vary approximately with C_l^2, in contradiction with the measured results for cavitation in strong water. This is shown in Fig. 12. For simplicity, strong water data are compared with the σ_{iw} curve corrected to zero tensile strength water. No cavitation data could be obtained in strong water at $\alpha - \alpha_0 = 5.2$ deg (C_l = 0.33), because surface cavitation would occur in the absence of vortex cavitation. Further lowering of the cavitation index resulted in more profuse surface cavitation, the foil then became unloaded and the strength of the vortex was weakened to the point that vortex cavitation could never be observed, even with further lowering of the cavitation index to the minimum value possible. The reason for this is illustrated in Fig. 13 which displays the variation of lift with cavitation index in weak water. The onset of vortex cavitation, patch cavitation, and then bubble cavitation as cavitation index is lowered is marked on the diagram. Note the sharp drop in lift with the onset of bubble cavitation. The sequence is reversed in strong water. Bubble cavitation occurs before vortex cavi-

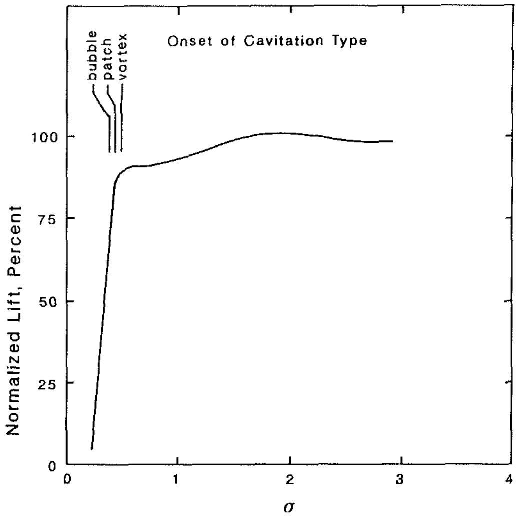

Fig. 13 Normalized lift vs. cavitation index for $\alpha - \alpha_0 = 5.2$ deg

Table 1 Apparent tension and calculated nucleus size

	Range of T in bars		Range of R_0 in microns	
C_l	Low	High	Low	High
0.43	0.3	0.8	1.21	3.23
0.59	0.4	1.6	0.61	2.43
0.68	0.8	1.8	0.54	1.21
0.75	0.6	1.2	0.81	1.62

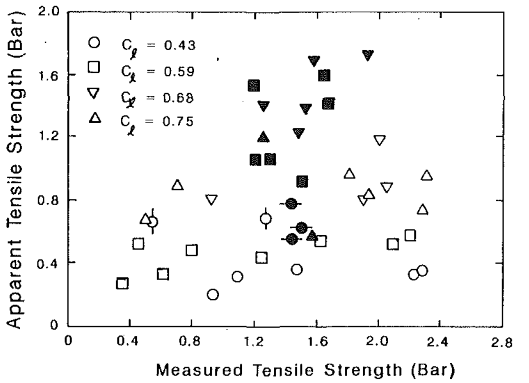

Fig. 14 Correlation of apparent tensile strength with measured values using the venturi technique. Solid symbols are for variable velocity tests.

tation. There is a sharp reduction in lift and the trailing vortex is weakened to the point that vortex cavitation does not occur. Unfortunately the measuring system response time was too slow to accurately portray the variation of lift versus cavitation number with the rapid lowering of pressure necessary for working with strong water. Pressure could be lowered as rapidly as one bar per second.

It is important to note the large scatter in the strong water results. Even lower values are obtainable by determining the inception point by increasing velocity with pressure held constant until cavitation occurs. With the tunnel used in this study, it was difficult to maintain the same water strength for long periods of time. This is quite different from the tests at SAFHL which were made in a tunnel with a special degassing system and a 100:1 contraction ratio nozzle. Very little scatter was encountered when a consistent method of pre-pressurization was used. In spite of the scatter in the current study, it is evident that the trend of σ_i with C_l is different with strong water than with weak water. For comparison, the trend observed in this SAFHL tests is sketched in as a dotted line in Fig. 12. Qualitatively, the same trend is observed in these tests. As already noted, the difference between the zero tension results, and the strong water results is the amount of tension sustained by the vortex (Eq. (6)). An estimate of effective nuclei size can be made using Eq. (4). The calculated values of tension and apparent nucleus size are given in Table 1.

There is an apparent trend of increasing tension and decreasing nuclei size with increasing lift coefficient.[2] The results for $C_l = 0.75$ are not quite comparable to the other sets of data since the details of the vortex formation are different due to a suction peak at the leading edge of the foil for lift coefficients greater than about 0.6 (Fig. 3). It should be noted that the apparent nucleus size is of the same order of magnitude noted in the SAFHL tests.

It should also be noted that attempts to correlate the apparent tensile strength with the measured value were unsuccessful. This is shown in Fig. 14. It is also important to point out that higher values of tension were always noted using the constant pressure/variable velocity technique rather than the constant velocity/variable pressure technique to determine cavitation inception.

V Conclusions

The experiments in the present program qualitatively confirm the findings in the SAFHL tests. Comparison between cavitation data for weak water and estimates of the mean static pressure in the core indicate the strong possibility that turbulence or flow unsteadiness is an important consideration in the cavitation process. Turbulence measurements show that the turbulence intensity is very high close to the edge of the vortex core. Unfortunately, further measurements are necessary to fully describe the vortex in enough detail to determine the effects of turbulence quantitatively.

Lift data, collected over a range of Reynolds number from 4.6×10^5 to 2×10^6, agreed well with the theoretical predictions. These data were used to correlate measurements of peripheral velocity in the form v_θ/C_lU_0 as a function of distance through the vortex. Surprisingly good correlation of the velocity data was in the range of lift coefficient from 0.33 to 0.75.

The observation that the strength of the vortex scales directly with lift coefficient is in contradiction to the previous observation that cavitation index scales with angle of attack to the power 1.4. However, the results of this study indicate that observations in weak water also closely follow a C_l^2 relationship whereas observations in strong water more closely follow the previously observed variation, i.e., $C_l^{1.4}$. This implies that the amount of sustainable tension, and the size of the nuclei active in the cavitation process, are a function of vortex strength.

The inception process in weak water was observed to be highly intermittent. Striated bubbles were observed to rapidly become the size of the core radius of the vortex. This observation is correlated with an ad hoc model of inception which indicates that angular momentum and circulation are conserved in two different vortex configurations. The first being a single phase vortex whose minimum pressure is just equal to vapor pressure and the second having a vapor filled core with a maximum tangential velocity that is 40 percent higher than in the single phase vortex.

Acknowledgment

Dr. Roger E. A. Arndt was supported by an Alexander von Humboldt Senior Scientist Award during the research. The assistance of many members of the staff of the Versuchsanstalt für Wasserbau is gratefully acknowledged. Preparation of this paper was supported by the Office of Naval Research under Contract No. N00014-91-J-1239.

References

Abbott, I. H., and von Doenhoff, A. E., 1958, *Theory of Wing Sections*, Dover, New York.

Abbot, P. A., and Greeley, D. S., 1989, "Cavitation Noise Investigations," *Proc. Symposium on Small Hydropower Fluid Machinery*, ASME, New York, NY, pp. 141-147.

Arakeri, V. H., Higuchi, H., and Arndt, R. E. A., 1986, "Analysis of Recent Tip Vortex Data," *Proc. 21st American Towing Tank Conference*, Washington, D.C.

Arndt, R. E. A., 1981a, "Cavitation in Fluid Machinery and Hydraulic Structures," *Annual Review of Fluid Mechanics*, Vol. 13.

Arndt, R. E. A., 1981b, "Recent Advances in Cavitation Research," *Advances in Hydroscience*, Academic Press, New York.

Arndt, R. E. A., Arakeri, V. H., and Higuchi, H., 1991, "Some Observations of Tip Vortex Cavitation," *Journal of Fluid Mechanics*, Vol. 229, Aug., pp. 269-289.

Green, S. I., and Acosta, A. J., 1989, "Relating Trailing Vortex Cavitation Inception to Single Phase Flow Measurements," *Proc. 22nd American Towing Tank Conference*, St. Johns, Newfoundland.

Higuchi, H., Arndt, R. E. A., Arakeri, V. H., and Killen, J. M., 1989, "The Structure of Tip Vortices Over a Wide Range of Cavitation Number," *Proc. 22nd American Towing Tank Conference*, St. Johns, Newfoundland.

---

[2] Unpublished calculations by Mr. Christian Dugue agree with this observation—maximum possible nucleus decreases as the centrifugal acceleration in the vortex core region increases. This warrants further study.

Keller, A., 1987, "A Vortex-Nozzle Cavitation Susceptibility Meter in Routine Application in Cavitation Inception Measurements," *Proc. Euromech. Colloquium 222—Unsteady Cavitation and its Effects*, Wageningen, The Netherlands.

McCormick, B. W., 1962, "On Cavitation Produced by a Tip Vortex Trailing from a Lifting Surface," ASME *Journal of Basic Engineering*, Vol. 84, pp. 369-379.

Platzer, G. P., and Souders, W. G., 1979, "Tip Vortex Cavitation Delay with Application to Marine Lifting Surfaces—Literature Survey," David Taylor Research Center Report, 79/051.

Strasberg, M., 1986, Keynote lecture to ASME Symposium on Cavitation and Multiphase Flow Noise.

APPENDIX

A Simple Model for Cavitation Inception in a Vortex

Consider a Rankine vortex having a core radius a and maximum circulation Γ. The velocity distribution is

$$v_\theta = \frac{\Gamma}{2\pi a^2} r \quad r \le a \tag{A-1}$$

$$v_\theta = \frac{\Gamma}{2\pi r} \quad r \ge a \tag{A-2}$$

The total angular momentum per unit length contained within a radius $r_0 \to \infty$ is

$$\Sigma = \frac{1}{2} \rho \Gamma \left\{ r_0^2 - \frac{1}{2} a^2 \right\} \tag{A-3}$$

Consider next a cavitating vortex such that

$$r \le r_1 \text{ (vapor)} \tag{A-4}$$

and

$$r \ge r_1 \text{ (water)} \tag{A-5}$$

with

$$v_\theta = \frac{\Gamma}{2\pi r_2^2} r \quad r_1 \le r \le r_2 \tag{A-6}$$

$$v_\theta = \frac{\Gamma}{2\pi r} \quad r \ge r_2 \tag{A-7}$$

The total angular momentum per unit length (neglecting the density of vapor in comparison to the density of water) is

$$\Sigma_c = \frac{1}{2} \rho \Gamma \left\{ r_0^2 - \frac{1}{2} r_2^2 - \frac{1}{2} \frac{r_1^4}{r_2^2} \right\} \tag{A-8}$$

For angular momentum held constant, Σ and Σ_c can be equated to yield

$$\left(\frac{r_2}{a}\right)^2 = \frac{1}{\left(1 + \left(\frac{r_1}{r_2}\right)^2\right)} \tag{A-9}$$

$$r_0 \to \infty$$

The pressure distribution in the single phase and cavitating vortices are, respectively,

$$C_p = \left(\frac{r}{a}\right)^2 - 2 \quad r \le a \tag{A-10}$$

$$C_p = -\left(\frac{a}{r}\right)^2 \quad r \ge a \tag{A-11}$$

for the noncavitating vortex and

$$C_{p_c} = \frac{r^2 a^2}{r_2^4} - 2\left(\frac{a}{r_2}\right)^2 \quad r_1 \le r \le r_2 \tag{A-12}$$

$$C_{p_c} = -\left(\frac{a}{r}\right)^2 \quad r \ge r_2 \tag{A-13}$$

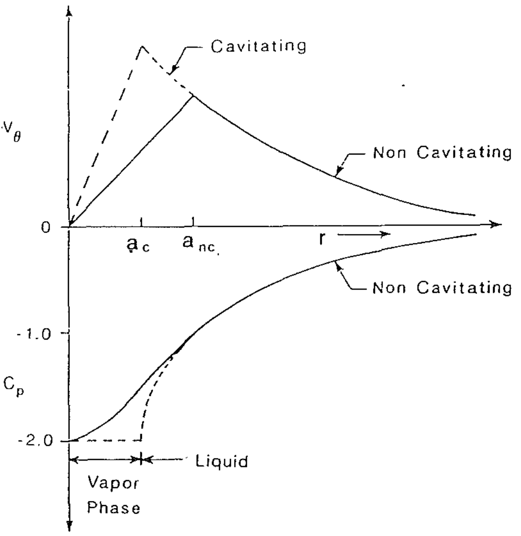

Fig. A-1 Schematic of single phase and equivalent cavitating vortex having equal maximum circulation and total angular momentum per unit length

where C_p is defined as

$$C_p = \frac{p - p_0}{\frac{1}{2}\rho\left(\frac{\Gamma}{2\pi a}\right)^2} \tag{A-14}$$

When σ is just equal to σ_i, the single phase vortex at incipient conditions is described by

$$C_{p_{\min}} = -2 = -\sigma_i \tag{A15}$$

Consider next the cavitating vortex. Let $C_p = -2$ at $r = r_1$. Then from Eq. (A-12)

$$\frac{r_1^2 a^2}{r_2^4} - 2\left(\frac{a}{r_2}\right)^2 = -2 \tag{A-16}$$

or

$$\left(\frac{a}{r_2}\right)^2 \left\{ \left(\frac{r_1}{r_2}\right)^2 - 2 \right\} = -2 \tag{A-17}$$

Noting Eq. (A-9)

$$\left(\frac{a}{r_2}\right)^2 = \left\{ 1 + \left(\frac{r_1}{r_2}\right)^2 \right\} \tag{A-18}$$

Equations (A-17) and (A-18) can be combined to yield an expression for $\lambda = r_1/r_2$:

$$(\lambda^2 - 2)(1 + \lambda^2) = -2 \tag{A-19}$$

The roots of Eq. (A-19) are $\lambda = 0, \lambda = \pm 1$. $\lambda = 0$ corresponds to inception. The other realistic solution is $\lambda = 1$ or

$$\frac{r_1}{r_2} = 1 \tag{A-20}$$

$$\frac{r_2}{a} = \frac{1}{\sqrt{2}} \tag{A-21}$$

Using Eqs. (A-6) and (A-7), it can be shown that the maximum velocity in the cavitating vortex is $\sqrt{2}$ higher than in the noncavitating vortex.

$$v_{\theta_{\max}}\big|_{\text{cav}} = \sqrt{2}\, v_{\theta_{\max}}\big|_{\text{noncav}} \tag{A-22}$$

This is illustrated in Fig. A-1.

A. S. Ramamurthy
Professor.

R. Balachandar
Research Associate.

Faculty of Engineering,
Concordia University,
Montréal, Canada, H3G 1M8

A Note on Choking Cavitation Flow Past Bluff Bodies

A model is developed to predict the choking cavitation number for sharp edged bluff bodies subject to wall interference effects. The fact that the forebody pressure distribution under cavitating conditions essentially resembles the values obtained in noncavitating flows is made use of in the development of the model. The model is verified using experimental results from present and previous studies for a specific case of choking flow past a two-dimensional prismatic body.

Introduction

The interference effects of the boundaries of a water tunnel on the cavity dimensions formed behind bluff bodies are significant (Waid, 1957). As the cavitation number of the flow is reduced, the cavity elongates. This elongation effect caused by the tunnel boundary may become so extreme that the cavity is expected to become infinitely long at a cavitation number σ greater than zero (Streeter, 1961; Cohen, 1958). Under these conditions, the water tunnel is said to be choked and further efforts to decrease σ by increasing the flow velocity are impossible. This choking effect is of considerable importance, since it limits the ability of a water tunnel to operate at small cavitation numbers. Consequently, not all cavitating flow conditions can be modeled in a water tunnel. It has been recently pointed out by Tullis (1989) that the worst condition at which to operate a pump, orifice or a valve is near the onset of choking, since erosion damage, noise, and vibration are maximum just before a hydraulic system chokes.

Several theoretical (Birkhoff, 1950; Cohen and Prima, 1958; Wu, 1971) and experimental (Palanichamy, 1976; Chandrashekara, 1973) studies have been carried out to analyze the wall interference effects on cavity flows. Both theory and experimental data indicate that a larger degree of blockage is associated with a higher value of choking cavitation number. Most of the earlier experimental results related to wall interference effects on cavitating sources were influenced by Reynolds number effects, since circular sources were used as the test bodies and the test Reynolds numbers spanned the critical regime of flow (Balachandar, 1988). In the present study, attention is focussed on sharp-edged bluff bodies with fixed separating edges to reduce or eliminate Reynolds number effects. Following Birkhoff (1950), a momentum balance approach is used to develop a model to predict choking cavitation numbers as a function of blockage. Here, blockage is defined as the ratio of the area of the model to the area of the test section. In two-dimensional flow, blockage $= b/B$, where b is the height of the body and B is the height of the test section (Fig. 1). The model developed is verified using experimental results from present and previous studies.

Theoretical Considerations

The following assumptions are made in the development of the model:

(*i*) At choking conditions, the density of the fluid in the cavity is negligible and the near wake pressure is constant. Hence, the pressure along the freestream line does not vary much and it is close to the vapor pressure P_v.

(*ii*) The maximum width W of the cavity behind a cavitating source (Fig. 1) approaches the value of the width of the wake predicted by potential flow solutions. The jet width B_j is given by

$$B_j=\frac{1}{2}(B-b)C_c \qquad (1)$$

where, C_c is the jet contraction coefficient obtained from potential flow studies (Shaw, 1969).

(*iii*) The boundary friction is negligible along the control surfaces (Fig. 1).

It will be shown in a subsequent section that the wake center line pressure distribution tends to be constant, as σ is reduced and choking conditions prevail. Consequently, for choking flows, the separating pressure P_s can be taken to be equal to the cavity pressure in the near wake. Considering unit width of flow for the control volume EFGHIJ (Fig. 1) and applying a momentum balance, one obtains,

$$P_{ch}B+\rho U_{ch}^2B=P_j(B-b)C_c+\rho U_j^2(B-b)C_c + P_s(B-(B-b)C_c)+\frac{1}{2}\rho U_{ch}^2 bC_D \qquad (2)$$

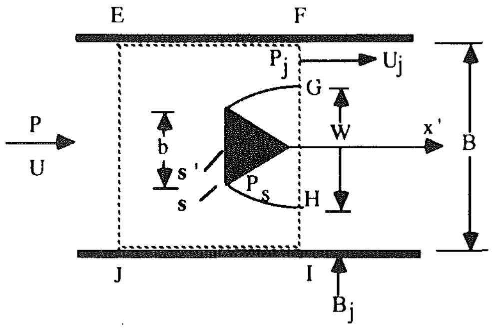

Fig. 1 Control volume

Contributed by the Fluids Engineering Division for publication in the JOURNAL OF FLUIDS ENGINEERING. Manuscript received by the Fluids Engineering Division January 15, 1991. Associate Technical Editor: A. Prosperetti.

where P_{ch} and U_{ch} refer to the freestream pressure and velocity in the approaching flow when choking conditions prevail, P_j = jet pressure in sections FG and HI, C_D = drag coefficient and ρ = density of fluid. Define the choking cavitation number σ_{ch} as,

$$\sigma_{ch}=\frac{P_{ch}-P_v}{\frac{1}{2}\rho U_{ch}^2} \tag{3}$$

Using the above assumptions and continuity relations, one can simplify Eq. (2) to obtain

$$\sigma_{ch}=\frac{2}{\left(1-\frac{b}{B}\right)C_c}+C_D\frac{b}{B}-2.0 \tag{4}$$

Equation (5) below defines C_D in terms of the fore and rear body pressure coefficients C_{pf} and C_{pr}

$$C_D=\int_{x=0}^{1} C_{pf}dx-\int_{x=0}^{1} C_{pr}dx \tag{5}$$

It should be noted that in Eq. (5), $x=0$ refers to the stagnation point s' and $x=1$ refers to the separation point s (Fig. 4). Using the data presented earlier (Ramamurthy, 1977), one can conclude that the forebody pressure distribution for cavitating flows, essentially resembles the forebody pressure distribution obtained in noncavitating flows. Using this argument, one can evaluate the value of the first term on the right-hand side of Eq. (5) from existing noncavitating test data at any given blockage. Consequently, at choking conditions,

$$C_D=C_D[\sigma_{ch},\, b/B]=\eta-\int_{x=0}^{1} C_{pr}dx\approx\eta+\sigma_{ch} \tag{6}$$

where,

$$\eta[b/B]=\int_{x=0}^{1} C_{pf}dx.$$

Using Eq. (6) in Eq. (3), one obtains

$$\sigma_{ch}=\frac{1}{\left(1-\frac{b}{B}\right)}\left[\frac{2}{\left(1-\frac{b}{B}\right)C_c}+\eta\frac{b}{B}-2.0\right] \tag{7}$$

In Eq. (7), C_c is a function of b/B. Further, based on existing noncavitating flow test data related to the dependence of η on b/B, σ_{ch} can be evaluated for two-dimensional sharp edged bluff bodies such as flat plates and wedges.

Experimental Setup and Procedure

The present experimental study was conducted in a water tunnel (Fig. 2) suitable for cavitation experiments (Tunnel A). Polished equilateral prisms made of brass formed the basic cavitating sources. The sources were always mounted such that the front face was normal to the flow. The blockages tested varied from 9.7 to 57.5 percent. Span-wise uniformity of the axial velocity distribution was checked at a location 50 mm downstream from the inlet to the test section, in a horizontal plane perpendicular to the flow (Fig. 3), using a 15mW He-Ne Laser Doppler velocimeter [TSI Inc.] in the forward scatter mode. In Fig. 3, the velocities are normalized by the center line velocity U_c. A pressure tap 0.5 mm in diameter was located at the center of the front face of the cavitating source to measure the stagnation pressure. The stagnation pressure was used to calculate the freestream pressure P (Fig. 1). The value of P was also independently obtained by direct measurement at undisturbed location upstream of the body. The pressures at the two separating points were measured by means of pressure taps located at the rear of the body very close to the separating edges. The maximum uncertainty in the reported values of the C_{ps} and σ is ±6 percent at 20 to 1 odds (Kline, 1953, 1985). A stroboscope (Bruel and Kjaer, Type 4912) and a battery of powerful lights aided visual observation. While conducting each test run, the water temperature and the air content were also noted. During almost all the tests, the air content ranged from 11 to 17 ppm at atmospheric conditions. During any given test, the change in air content was negligibly small. The discharge was measured with the help of a 60 degree V-notch and the maximum error in the discharge measurements was less than 3 percent. The wall-pressure fluctuations in the absence of the cavitating source was found to be of the order of 0.5 percent of the dynamic pressure. The frequency of pressure pulsations in the wake were obtained with the help

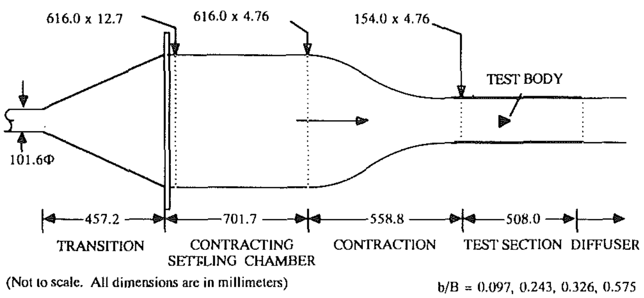

Fig. 2 Experimental setup

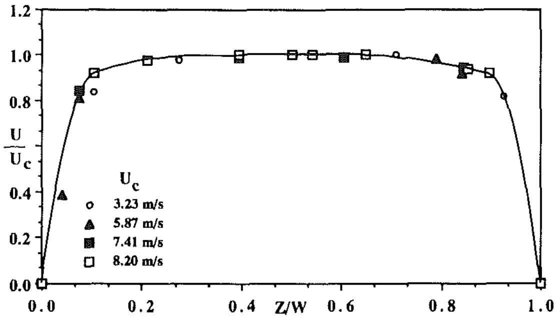

Fig. 3 Span-wise velocity distribution normalized by centerline velocity U_c

Nomenclature

b = width of bluff body
B = width of test section
b/B = blockage
C_c = contraction coefficient
C_D = drag coefficient
C_{pb} = base pressure coefficient
C_{pf} = forebody pressure coefficient
C_{pr} = rearbody pressure coefficient
C_{ps} = separating pressure coefficient
f = frequency of vortex shedding
P_{ch} = approaching freestream pressure under choking conditions
P_j = jet pressure
P_s = separating pressure
P_v = vapor pressure
S = fb/U, Strouhal number
U = free stream velocity
U_{ch} = free stream velocity under choking condition
U_j = jet velocity
W = span-wise of test section
σ = cavitation number (based on P_v)
σ_{ch} = choking cavitation number
η = variable, Eq. (6)

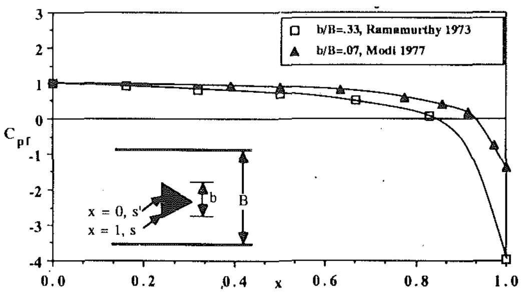

Fig. 4 Forebody pressure distribution for $b/B = 0.07$ and $b/B = 0.33$

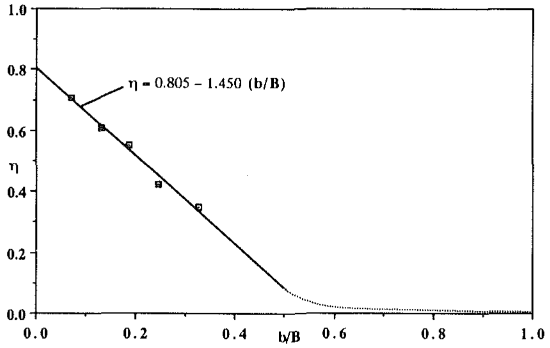

Fig. 5 Variation of η with b/B

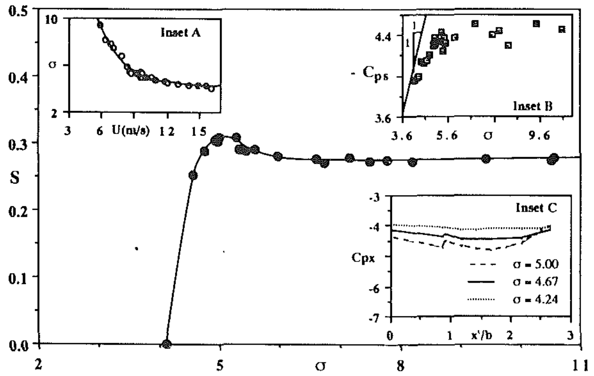

Fig. 6 Variation of S with σ
Inset A: Variation of σ with velocity
Inset B: Variation of C_{ps} with σ
Inset C: Pressure distribution along wake axis

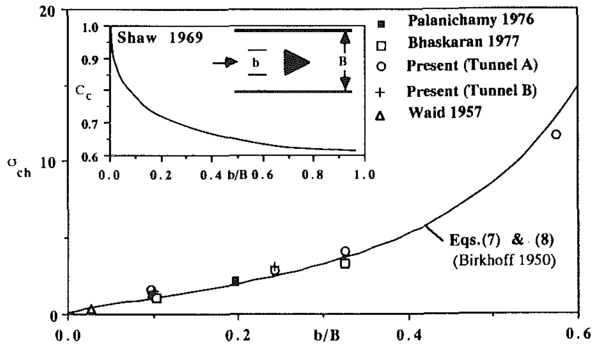

Fig. 7 Variation of σ_{ch} with b/B
Inset: Variation of C_c with b/B for sharp-edged bluff bodies (Shaw, 1969)

of pressure transducers located in the vicinity of the free shear layer. The output signal from the transducer demodulator was fed to a Fast Fourier transform analyzer (Wavetek, 5830-A) to carry out the spectral analysis. The accuracy of the frequency measurement was ±0.25 Hz. In the present series of tests, the Reynolds number varied from $1.0 < \mathrm{Re} \times 10^{-5} < 8.0$. Previous studies (Ramamurthy, 1973, 1977) have shown that in this range of Re, the hydrodynamic characteristics are independent of Reynolds number.

Additional tests were also conducted in an auxiliary water tunnel (Tunnel B). This water tunnel has a 10:1 contraction preceding the test section and yielded a nearly uniform velocity at the test section. The test section was 101.6 mm high, 50.8 mm wide and 508 mm long. Details of this tunnel are available elsewhere (Balanchandar, 1990). Since the cross sectional width of this test section is larger than the one described previously, higher aspect ratios (test body width/body height) can be obtained for the same blockage. For example, a blockage of 9.7 percent yields aspect ratios of 0.32 and 5.15 in tunnels A and B, respectively.

Analysis of Results

The forebody pressure distributions at various blockages are reported in one of our earlier studies (Ramamurthy, 1973) and also in the studies of Shaw (1971) and Modi et al. (1977). Figure 4 shows the pressure distribution for two typical blockages. Using data such as Fig. 4, the value of η at any particular blockage was evaluated by integrating the forebody pressure distribution. Figure 5 shows the variation of η with b/B. A straight line fit was obtained for η in the range $0 \leq b/B < 0.5$. The straight line fit is denoted as,

$$\eta = 0.805 - 1.450(b/B); \quad 0 \leq b/B \leq 0.5 \qquad (8)$$

It should be noted that as $b/B \rightarrow 1.0$, $\eta \rightarrow 0.0$ (Shaw, 1969). Using Eq. (8) in Eq. (7), σ_{ch} can be evaluated for a given blockage.

Figure 6 shows the variation of the Strouhal number S with σ for a typical blockage of 0.326. The value of S remains constant at the non-cavitating value over a range of σ. When one reduces σ further, the value of S increases, followed by a reduction in S. As σ is decreased even further, the value of S drops rapidly and a stage is reached when S approaches zero for $\sigma > 0$. Using these conditions, the time history of pressure fluctuation indicates that vortex shedding becomes highly intermittent and finally ceases. The corresponding spectra do not indicate a dominant frequency. The cavitation number of the flow at this stage is denoted as σ_{ch}. Inset A of Fig. 6 shows the variation of cavitation number σ with increasing velocities for a typical blockage of 0.326. With increasing velocities, a stage is reached when further increase in velocity does not result in a decrease in the value of σ. At choking conditions, insets B and C of Fig. 6 indicate that the pressures in the wake region are constant and are nearly equal to the vapor pressure. Figure 7 shows a fair agreement between the present experimental data and the variation of σ_{ch} with b/B obtained from Eqs. (7) and (8). Figure 7 also includes the experimental data of Waid (1957) and the theoretical results of Birkhoff (1950). The present method requires only the existing experimental data related to the distribution of pressure around the bluff body under noncavitating conditions and the theoretical contraction coefficient C_c obtained from potential flow studies (Inset, Fig. 7). Since, these data are generally available for sharp-edged bluff bodies, the suggested procedure can be used to determine σ_{ch} without recourse to experimentation under cavitating conditions.

Conclusions

A semi-empirical analysis is developed on the basis of a simple momentum balance approach to predict choking cavitation number σ_{ch} for sharp edged bluff bodies subject to wall interference effects. The procedure suggested enables one to determine σ_{ch} by using existing information related to noncavitating flow past two-dimensional, sharp edged bluff bodies. A fair agreement is seen to occur between the present experimental values of σ_{ch} and the proposed model.

References

Balachandar, R., Ranganathan, Y., and Ramamurthy, A. S., 1988, "Evaluation of Cavitation Damage Characteristics Using a Profilometer," *Proc. Inst. of Mech. Engrs.*, Vol. 202, No. C5, pp. 341-345.

Balachandar, R., 1990, "Characteristics of Separated Flows Including Cavitation Effects," Ph.D. thesis, Concordia University, Montreal, Canada.

Bhaskaran, P., 1977, "Characteristics of Cavitating Flow of Past Bluff Bodies," D. Engg. thesis, Concordia University, Montreal, Canada.

Birkhoff, G., Plesset, M., and Simmons, N., 1950, "Wall Effects in Cavity Flow, Part I," *Quarterly of Applied Mathematics*, Vol. 8, No. 2, pp. 151-168.

Chandrashekara, D. V., 1973, "Studies on Characteristics of Cavity and Cavitation Damage Behind Circular Cylinders in Water with a Venturi," Ph.D. thesis, I.I.Sc., Bangalore, India.

Cohen, H., and Di Prima, R. C., 1958, "Wall Effects in Cavitating Flows," *2nd Symposium on Naval Hydrodynamics*, pp. 367-390.

Kline, S. J., and McClintock, F. A., 1957, "Describing Uncertainties in Single-Sample Experiments," *Mechanical Engineering*, ASME, Jan.

Kline, S. J., 1985, "The Purpose of Uncertainty Analysis," ASME JOURNAL OF FLUIDS ENGINEERING, Vol. 107, June, pp. 153-160.

Modi, V. J., and El-Shirbiny, S., 1977, "A Free Strealine Model for Bluff Bodies in Confined Flows," ASME JOURNAL OF FLUIDS ENGINEERING, Sept., pp. 585-592.

Palanichamy, K., 1976, "Venturi Studies with Water on Cavitation Inception, Cavity Characteristics and Cavitation Erosion Behind Bluff Bodies," Ph.D. thesis, I.I.Sc., Bangalore.

Ramamurthy, A. S., and Balachandar, R., 1989, "Wake Characteristics of Constrained Cavitating Bluff Bodies," submitted for publication in the *J. of Engg. Mech.*, ASCE.

Ramamurthy, A. S., and Bhaskaran, P., 1977, "Constrained Flow Past Cavitating Bluff Bodies," ASME JOURNAL OF FLUIDS ENGINEERING, Dec., pp. 717-726.

Ramamurthy, A. S., and Lee, P. M., 1973, "Wall Effects on Flow Past Bluff Bodies," *Journal of Sound and Vibrations*, Vol. 31, No. 4, pp. 443-451.

Shaw, T. L., 1969, "Steady Flow Past Plate in Channel," *J. of Hydraulic Division, Proc. ASCE HY. 6*, Vol. 95, pp. 2013-2028.

Shaw, T. L., 1961, "Effect of Side Walls on Flow Past Bluff Bodies," *J. of Hydraulic Division, Proc. ASCE HY.1*, Vol. 97, pp. 65-79.

Streeter, V. L., editor, 1961, *Handbook of Fluid Dynamics*, McGraw-Hill, New York.

Tullis, J. P., 1989, *Hydraulics of Pipelines: Pumps, Valves, Cavitation and Transients*, John Wiley, New York.

Waid, R. L., 1957, "Water Tunnel Investigations of Two-Dimensional Cavities," Hydrodynamics Lab. Report No. E 73-6.

Wu, T. Y., Whitney, A. K., and Brennen, C., 1971, "Cavity Flow Wall Effects and Correction Rules," *Journal of Fluid Mechanics*, Vol. 49, pp. 223-256.

Applicability Tests for the Phase Doppler Anemometer for Cavitation Nuclei Measurements

H. Tanger

E.-A. Weitendorf

Hamburg Ship Model Basin (HSVA),
Hamburg, Federal Republic of Germany

A compromise between a reliable phase-diameter relationship and a good imaging of the control volume is necessary for the application of the PDA-instrument when measuring cavitation nuclei. The phase-diameter relationship for bubbles and particles were investigated theoretically, the imaging of the control volume experimentally. Further PDA-measurements were conducted for Latex spheres of different diameters as scattering objects in water and single air bubbles in transparent plastics. The concentrations and diameters measured by the PDA agreed very well with the results obtained by other methods. An investigation of the scattering from background particles in water was conducted with the PDA in the small HSVA cavitation tunnel. Also, nuclei measurements were performed with a gassing system in the tunnel. In 1972 the ITTC-Cavitation Committee defined specifications for the control of the free air content in routine and research cavitation tests. The tests completed so far show that the PDA-instrument fulfills these specifications for the major part.

1 Introduction

Cavitation research has shown that microbubbles are weak cavitation nuclei and dirt particles are strong ones, if one does not consider the complicated nature of pore nuclei. Since microbubbles always cavitate first compared to dirt, earlier nuclei determinations were focussed on the measurement of microbubbles as cavitation nuclei.

The Laser-scattered-light instrument according to Keller (1973) was originally applied for the above purpose at the cavitation tunnels of HSVA. However, this technique had physical difficulties, such as the inversion of the light intensity within the Laser beam (Weitendorf et al., 1981, 1982). This led to an inhomogeneous light intensity distribution in the measuring control volume. Therefore, it was found that either a correction method for the Laser-scattered-light instrument, as proposed by Billet (1984), or further instrument development would be necessary. Billet's endeavor led only to a partial success and Keller made the move to another method (Keller, 1986).

Due to these difficulties HSVA initiated a cooperation with DANTEC(DISA) Electronic A/S, Copenhagen, in 1980. The development of a new instrument was based on the specifications for an ideal nuclei measuring instrument defined by the International Towing Tank Conference (ITTC). A study by Knuhtsen and Jessen (1981) for a new instrument consisted of:

- Investigations of optical principles for the measurement of particle size and concentration
- Investigations of methods for signal processing and on-line data analysis and
- Recommendations for an optical principle and for the design of a practical instrument.

In the study the optical principles were divided into four groups:

- Holography
- Application of light scattering
- Optical processors and
- Some special alternatives, e.g., the combination of photomultipliers and microphones.

Holography as principle for a new instrument was not considered, since this method requires too much time for evaluating the measured data. Also, the principles of the latter two groups seemed to be unfavorable. Therefore, out of the group of light scattering methods, DANTEC(DISA) originally proposed the variable frequency grid method for further application. Yet, as the project developed, an even better principle came to the forefront and was proposed instead: the use of the phases from Laser Doppler bursts of two or more photomultipliers being proportional to the nuclei diameter (Saffman et al., 1984). Durst and Zare (1975) had originally used the same principle, but for much larger smooth bodies (or bubbles). Bachalo and Houser (1984) applied this phase-diameter relationship also, but for spray droplets. The instrument developed by DANTEC(DISA) was called Particle Dynamic Analyzer (PDA), the abbreviation stands also for Phase Doppler Analyzer.

2 Physical Principle, Investigations of Control Volume Image, and Phase-Diameter Relation

When a microbubble passes through the intersection of two laser beams as shown in the upper half of Fig. 1, the fringe pattern existing in the crossing point is projected into space mainly due to reflection from the bubble surface. This pro-

---

Contributed by the Fluids Engineering Division and presented at the Winter Annual Meeting, San Francisco, Calif., December 10-15, 1989 of THE AMERICAN SOCIETY OF MECHANICAL ENGINEERS. Manuscript received by the Fluids Engineering Division February 13, 1990. Associate Technical Editor: G. L. Chahine.

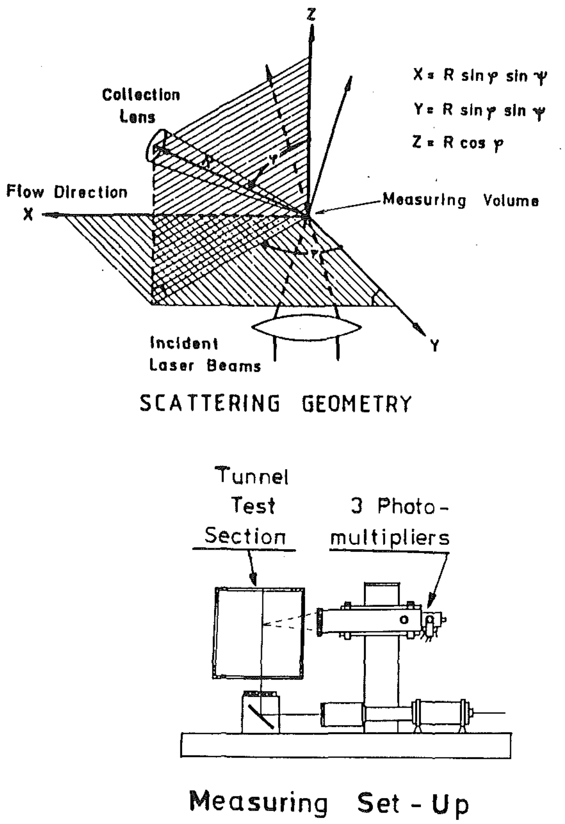

Fig. 1 The Phase Doppler Anemometer (PDA) method

jection is equivalent to the Doppler burst. Two or more photomultipliers at different points in space receive the same Doppler burst, but with a time lag that corresponds to the phase between the signals. This phase is linearly proportional to the diameter of the bubble. Three photomultipliers are necessary when the measuring range is large and when phase jumps occur. This offers the possibility for a spherical check of the signals to discriminate between bubbles and particles. For this purpose the electronic data acquisition of the PDA compares the two phase results obtained from the three photomultipliers. The lower half of Fig. 1 shows a sketch of the optical DANTEC system which has three multipliers. Further details of the physical principle and of the computations of the phase-diameter relationship which were performed during the development of the PDA by DANTEC(DISA) were given by Saffman et al. (1984).

All the relationships developed by Saffman et al. (1984) concerning the physical principle of the phase-diameter relationship and the control volume size are valid for air. Since the PDA-instrument is intended to be used for measuring bubbles in water it is crucial to account for the precise dimensions of the control volume in water. Also, it is important to know what the photomultipliers receive through the plexiglass windows of cavitation tunnels. These investigations were made in a small water basin using a luminescence diode. Figure 2 shows the results for receiving angles of 72 and 90 deg in air and in water for the three photomultipliers used. The dimensions of the control volume for a receiving angle of 72 deg in water are distorted and different for the three multipliers in the z-direction, i.e., perpendicular to the flow direction. On the other hand, at 90 deg there are no deficiencies for water and air. In this case the three photomultipliers have the same control volume dimensions for the observation of the Doppler bursts. Therefore, there was the hope that at receiving angles around 90 deg a good compromise for an acceptable imaging of the control volume and an acceptable phase-diameter relationship could be found.

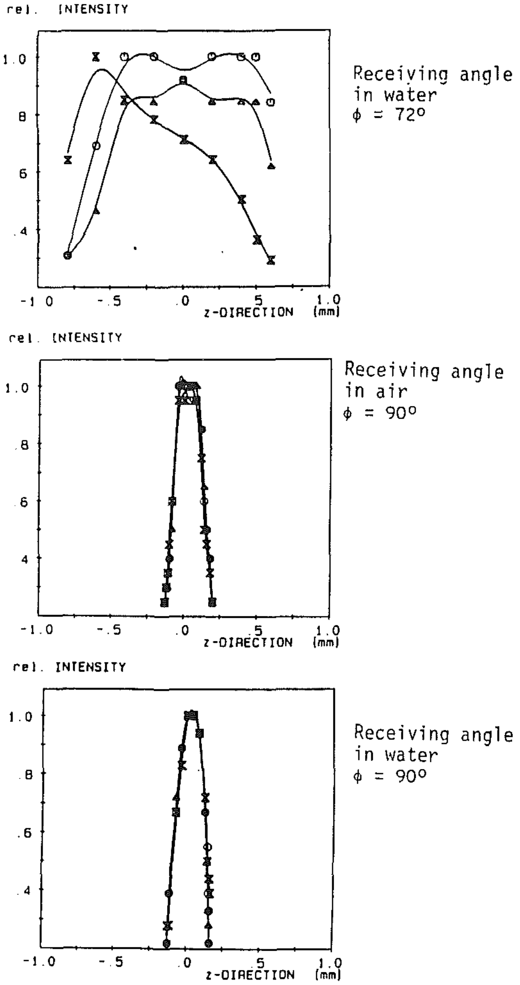

Fig. 2 Measured dimensions of control volume. Photomultiplier No. 1 ○; photomultiplier No. 2 △; photomultiplier no. 3 X.

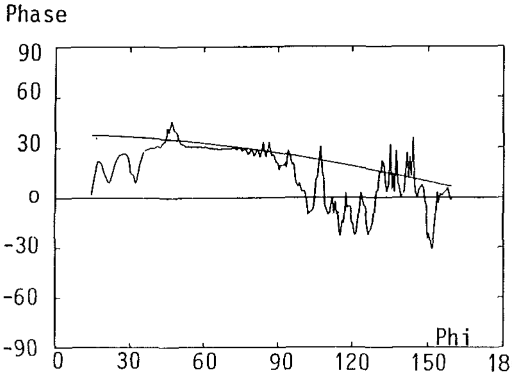

Fig. 3 Calculated phase-values for different receiving angles ϕ. Bubble diameter D = 10 μm

Calculations based on the Mie-theory were performed in order to find an acceptable phase-diameter relation around 90 deg. In Fig. 3 the results for the behavior of the phase as a function of the receiving angles are shown. Just below 90 deg there is almost no oscillation of the phase. Keeping this in mind further Mie-calculations for receiving angles of 72 deg as originally proposed by Saffman et al. (1984), 87 and 90 deg were carried out. It turned out that for 90 deg the phase-diameter relation is unacceptable. The results for the two other cases as shown in Fig. 4 reveal that at 72 deg the linear behavior of the phase-diameter relation is excellent and at 87 deg it can be taken as a reasonable compromise.

Equivalent Mie-calculations were also conducted for Latex-

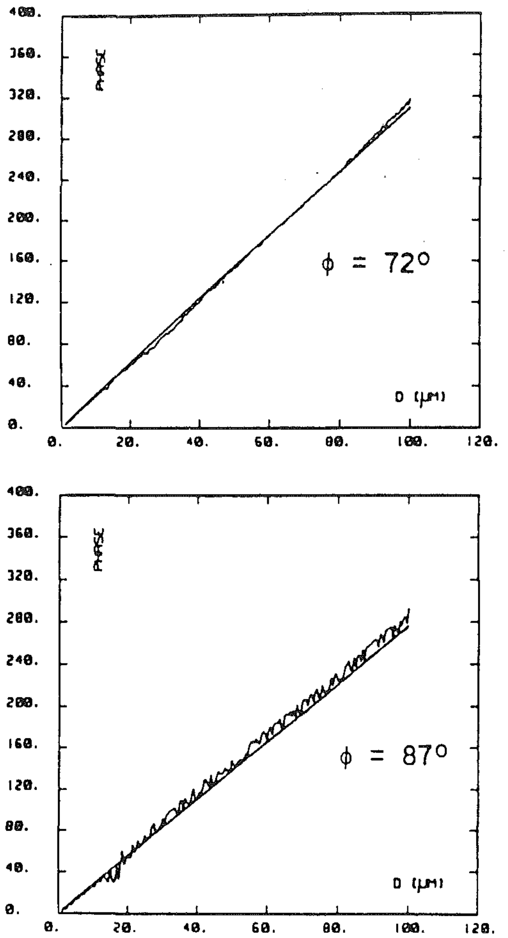

Fig. 4 Calculated phase-values for 3 receiving angles

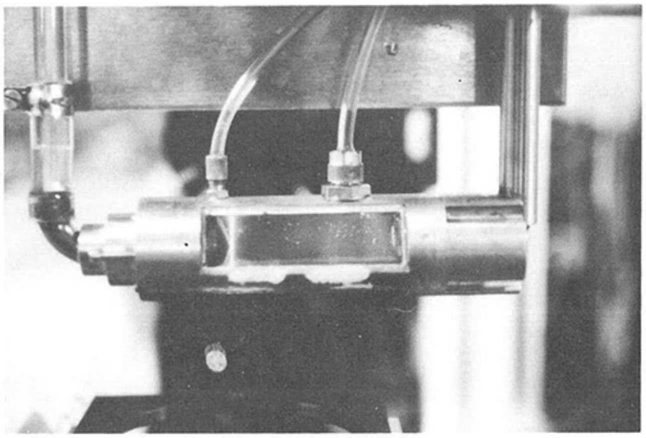

Fig. 5 Test loop

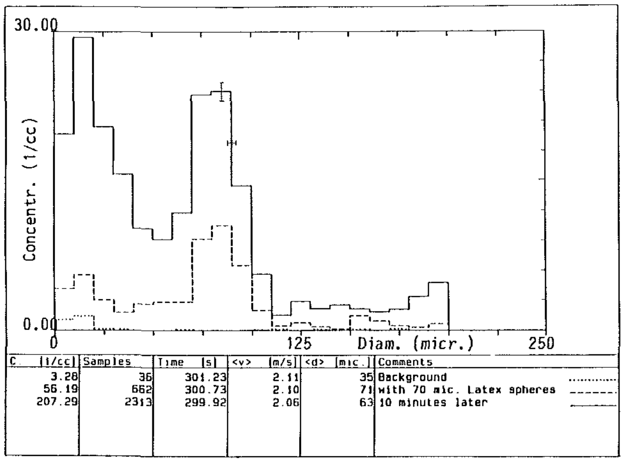

C [1/cc]	Samples	Time [s]	<v> [m/s]	<d> [mic.]	Comments
3.28	36	301.23	2.11	35	Background …………
56.19	662	300.73	2.10	71	with 70 mic. Latex spheres ------
207.29	2313	299.92	2.06	63	10 minutes later ———

Fig. 6 Latex spheres in filtered water

spheres and glass spheres in water. The results showed that Latex spheres in water have an acceptable behavior. On the other hand, glass spheres in water cause problems due to the small difference in the refraction indices between water and glass. Glass spheres were considered, since they were available with very small deviations from the mean values for different diameters. This was not the case for Latex-spheres. On the other hand, the application of Latex-spheres led to some experimental difficulties that will be described in the next section.

3 Special Tests With the PDA-Instrument

Concentration investigations with Latex-spheres were carried out in a special test loop shown in Fig. 5. Through a plastic tube above the window of the test loop Latex-spheres were added into the water. Air bubbles were extracted from the test water through a second tube, since they could possibly disturb the measuring results. The control volume with the two crossing laser beams was located just in front of the cone that can be seen within the left half of the test loop window in Fig. 5. The flow direction is from right to left and the water leaves the test loop chamber through a hole that is drilled in the cone. The flow quality immediately in front of the cone can be characterized by the PDA measurement itself. Since the PDA principally yields not only size measurements for particles or microbubbles but also velocity measurements, one can find from the narrow velocity histogram that there was no recirculating flow.

The results of concentration measurements obtained for 70 micron Latex-spheres and for filtered water are shown in Fig. 6. The result for the background measurement is represented by the dotted line. The dashed line in the middle shows the concentration immediately after the Latex-spheres were added to the filtered water. The maximum for this measurement lies at a diameter of 70 microns. The same water-Latex-sphere mixture was investigated again ten minutes later. The results are shown by the solid line. It is characterized by two maxima, one at about 20 microns and one at 70 microns. Both maxima are caused by dirt attached to the Latex-spheres. This is shown in the photograph in Fig. 7. After some time the dirt is washed off and is measured as small particles. The ratio between dirt and Latex-spheres was about 5:1. This disturbing dirt influence was discovered by observing the Latex-spheres with a microscope. Figure 7 shows a typical dirt photograph. Also, some of the smaller diameters shown in Fig. 6 are caused by small Latex parts that have been cut off from the original Latex-spheres by the pump working in the test loop.

The concentration investigations with Latex-spheres described up to now were performed for only one diameter. For newly developed nuclei measuring instruments it is always interesting whether or not it is possible to measure the correct diameters out of a mixture containing several diameters. Such a test was carried out for a mixture with 45 and 90 micron Latex-spheres. Two of the three maxima in the figure emerge at the correct diameters as is shown in Fig. 8. As explained previously, the third maximum at smaller diameters is caused by dirt. The dirt may be regarded as a third group of particles with diameters below 15 microns. The somewhat large scatter around the mean diameters 45 and 90 micron in Fig. 8 can be clearly explained by the strong variation of the diameters of the Latex-spheres. This fact was verified by microscopic inspection.

The basic examination of bubble diameters measured with the PDA was performed earlier by a comparison between photographically determined bubble diameters and those measured with the PDA. This result was shown by Tanger (1986).

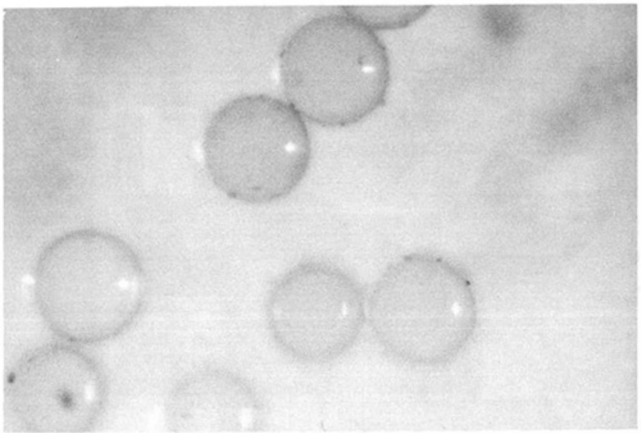

Fig. 7 Enlarged latex spheres with dirt

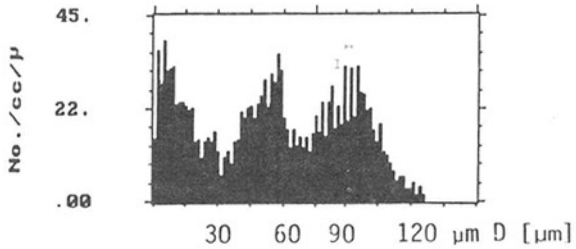

Fig. 8 Histogram for 45μm and 90μm latex spheres

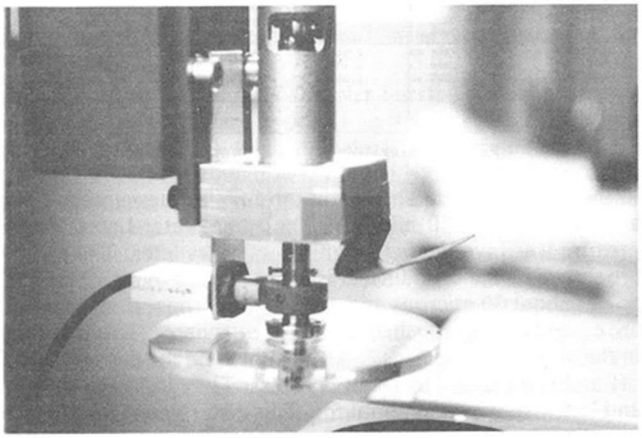

Fig. 9 Rotating disk with single bubbles

Many special investigations with the PDA were carried out with the Latex-spheres. However, the PDA is intended to be applied for bubble measurements. A possibility for the conservation of bubbles is offered by air bubbles cast in transparent plastic. In Fig. 9 a plastic disk is shown which contains single air bubbles that originated during the manufacturing process. The disk can be rotated to generate Laser Doppler bursts. This rotating disk was investigated with the PDA. Figure 10 displays a result showing that only one 87 micron bubble was measured by the PDA. The single bubbles in the disk have also been measured for control purposes using a microscope. In general the measurements from the PDA and the microscope agree well. It should be mentioned that the diagram in Fig. 10 represents a replotted histogram from the PDA and it is really striking that just one bubble diameter comes out so obviously in the histogram. This result illustrates the sound physical principle for measuring bubbles and the quality of the results for bubbles measured with the PDA.

The concentration for one bubble diameter in the rotating disk can be determined when the diameter of the single bubble, the measuring volume size, and the rotational velocity of the disk are known. Whereas the disk speed can be measured easily, the measuring volume size has to be determined by a special procedure. Using a displacement micrometer for this purpose the entire disk apparatus was shifted laterally to the laser beam; i.e., the individual bubble within the transparent plastic was moved through the control volume. Passing single bubbles through the center of the control volume, maximum signals could be measured. At the edge of the measuring volume the signals faded out. Using this procedure the measuring volume size was determined. The results of this concentration determination, which can be regarded as an experimentally determined direct method, were compared with the PDA-results. Figure 11 shows the comparisons between the PDA-measurements and the concentration determined by the direct method. It can be stated that the agreement between both methods is better for larger than for smaller bubbles. In general the result of the comparison is acceptable.

Additionally, the concentrations of Latex-sphere mixtures were measured not only using a microscope but also with the PDA. There was good agreement between the two methods.

4 Tunnel-Tests

Regardless of how many particles and/or pore nuclei contribute to the cavitation process, experience gained from routine cavitation tests and special research investigations (e.g., Weitendorf, 1979) have shown that the free air content as gas bubbles in water is an important influence on cavitation. Therefore, the PDA was used to measure the micro gas bubbles that are generated in cavitation tunnels at reduced pressures.

These investigations were carried out with the PDA in the small cavitation tunnel of HSVA. The tunnel without model was filled with water of normal quality. One result of the measurements showed that the dirt within the tunnel water reflects so intensively that it is measured as small bubbles. Therefore, before the next series of measurements was performed, the amplification of the PDA was decreased to such an extent that no bubbles and particles were measured at atmospheric pressure. In the following measurement series, the atmospheric pressure result was used as a reference and compared with those of gradually lowered tunnel pressures. The results showed that there is a sudden strong and surprising increase in the number of bubbles around a tunnel pressure of −74.1 kPa (25.9 kPa absolute). An additional significant increase in the number of bubbles did not occur when the tunnel pressure was reduced below −74.1 kPa. The question as to whether this behavior is typical for bubbles in cavitation tunnels or whether this is a typical tunnel characteristic was pursued in a second series of measurements. It was tested whether a similar behavior of bubbles can be observed when existing bubbles are exposed to a pressure change. This series of measurements started with the same background measurement as mentioned above; i.e., with normal tunnel water under atmospheric tunnel pressure the PDA amplification level was adjusted such that no bubble and particle detection occurred. Bubbles were then seeded into the small tunnel using the gassing system described by Hentschel et al. (1984). The upper diagram of Fig. 12 shows the results of this test with atmospheric tunnel pressures. The other two diagrams show the results for tunnel pressures of −24.7 and −49.4 kPa. Comparing the three histograms in Fig. 12 it can be stated that after a significant increase in the number of bubbles from atmospheric pressure to −24.7 kPa, a further essential increase cannot be observed. This result is consistent with the result of the first test series. Of course, this result does not answer the question as to whether this behavior is a typical bubble or tunnel characteristic.

Further problematic points concerning cavitation tests are:

- Degassing of the tunnel water, i.e., change of water quality during nuclei measurements,
- Necessary number of samples for results that are statistically sound.

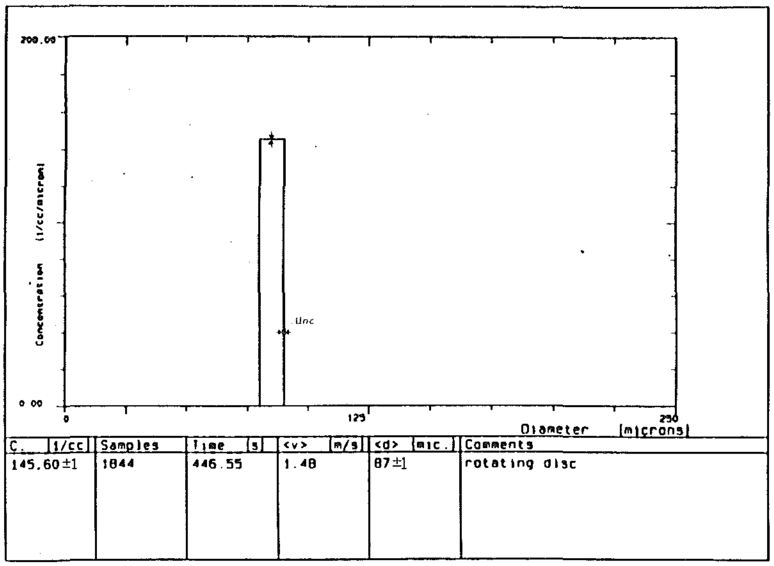

C. [1/cc]	Samples	Time [s]	<v> [m/s]	<d> [mic.]	Comments
145.60±1	1844	446.55	1.48	87±1	rotating disc

Fig. 10 Histogram of rotating single bubble

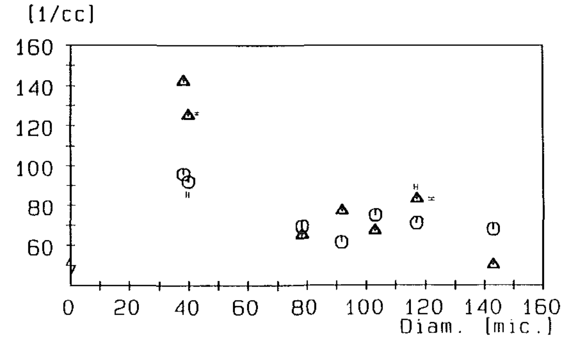

Fig. 11 Single bubbles in rotating disk. ⊙ PDA concentration; △ concentration by direct method

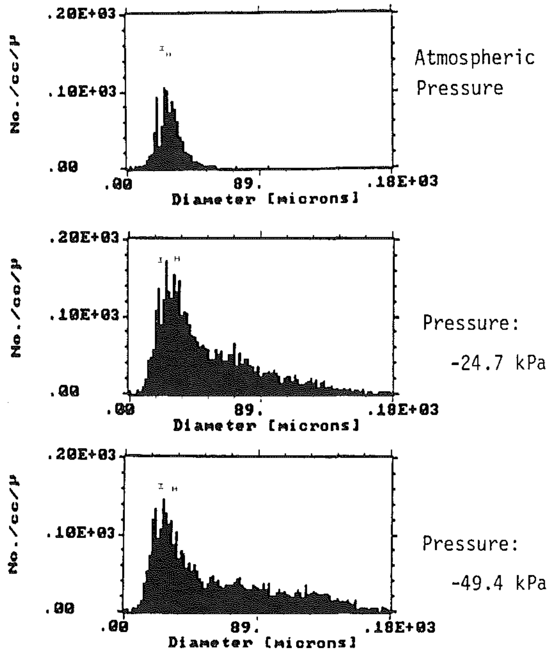

Fig. 12 Histograms from gassing-device in small HSVA cavitation tunnel

As published, Billet (1984) already treated the latter point for the scattered light technique according to Keller (1973). The inhomogeneous light distribution within the control volume of the scattered light instrument resulted in an unacceptable reproducibility of the measured results. For the PDA a test series was performed to check the reproducibility. This test series was carried out in the small HSVA cavitation tunnel with application of the gassing system published by Hentschel et al. (1984) that produces a large number of bubbles. The measuring procedure for different numbers of samples was carried out three times. The left diagram of Fig. 13 shows that a reproducibility of the concentration is obtained with 4000 samples. It is not clear why the concentration increases somewhat when the number of samples is increased to 8000. Apparently for a sample number below 1000 the scatter of the concentration is too large. The general validity of the left hand diagram in Fig. 13 still poses problems. The problem of measuring absolute nuclei distributions requires further investigation taking into account the influence of saturation, velocity, and varying bubble concentration in the tunnel water.

In the right-hand diagram of Fig. 13 the three size distribution histograms for the case with 4000 samples are reproduced. Here too, the scatter is acceptable. It should be mentioned that for this test series the amplification of the PDA-system was always set to the same level. This implies that the shape of the histograms depends on the amplification of the PDA.

Due to this amplification dependence of the PDA-histograms it must be kept in mind that only a relative, and not an absolute concentration can be obtained. Therefore, with each measurement it must be decided whether the nuclei belong to those participating in the cavitation process. These deliberations are of general significance for each nuclei histogram. On the other hand, Fig. 13 shows a reproducibility of +/− 3.6 percent for the PDA. This is a significant step forward regarding the evaluation of the water quality for cavitation tests.

Regarding the general uncertainty of PDA measurements one may state from the concept considerations for this instrument (Knuthsen and Jessen, 1981; Saffman et al., 1984) that in the measuring volume with a fringe spacing of about 6.5 microns bubbles from smaller 10 microns to 178 microns can be measured. For this case the control volume length is 5.8 mm and its diameter is 170 microns (at a distance of 500 mm for the receiving optics).

Due to its physical principle the PDA is especially suited for the detection of bubbles as mentioned in section 2. However, during the application of the PDA for bubble measurements it was discovered that it also detects many dirt particles. These particles have obviously reflecting surface qualities. To gain some experiences with the PDA in measuring pore nuclei or dirt particles the influence of filtering the tunnel water was

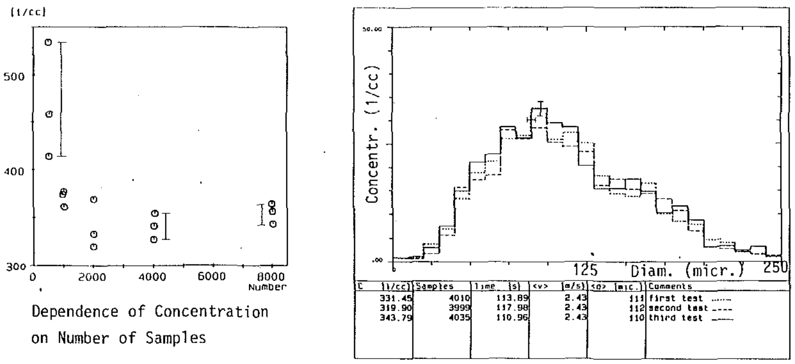

Dependence of Concentration on Number of Samples

C [1/cc]	Samples	Time [s]	<v> [m/s]	<d> [mic.]	Comments
331.45	4010	113.89	2.43	111	first test ......
319.90	3999	117.98	2.43	112	second test ----
343.79	4035	110.96	2.43	110	third test ——

Three Histograms for 4000 Samples

Fig. 13 Bubble concentrations and histograms from gassing-device in small HSVA cavitation tunnel

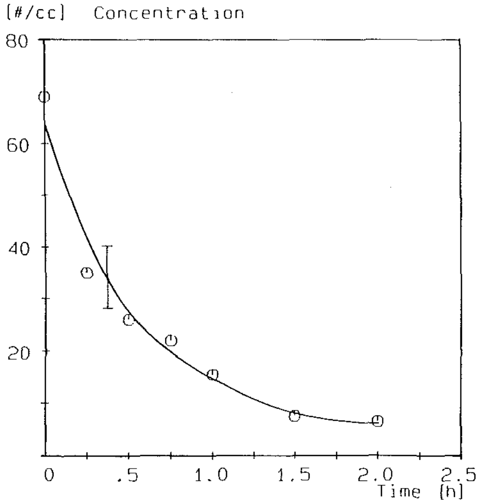

Filtration Influence on Solid Particles

Fig. 14 Influence of filtration on concentration and size distribution

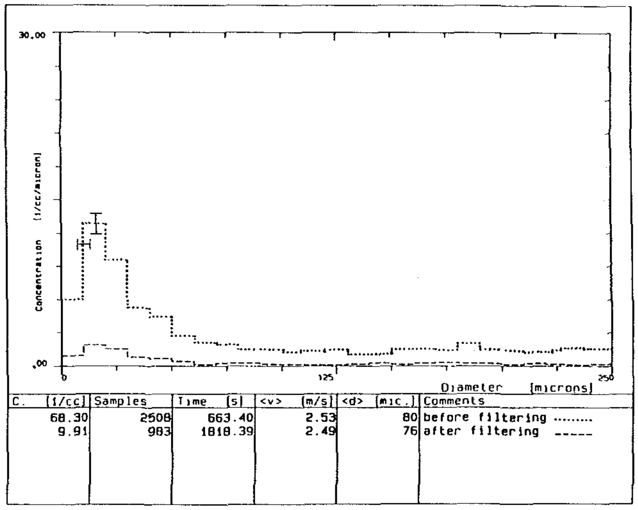

C. [1/cc]	Samples	Time [s]	<v> [m/s]	<d> [mic.]	Comments
68.30	2508	663.40	2.53	80	before filtering ....
9.91	983	1818.39	2.49	76	after filtering -----

Histograms of Unfiltered and Filtered Water

Fig. 14 (cont.)

investigated. For this series of measurements the small HSVA tunnel under atmospheric tunnel pressure was used with its filtering system (Hentschel et al., 1984). The tunnel water at the beginning of the test was of normal quality. For the previous background measurements for bubble investigations the amplification of the PDA was set to such a level that no particles and bubbles were detected. Here the measuring procedure for the dirt or pore nuclei investigations was different. In this case the PDA-amplification was set relatively high. The test series for filtering the tunnel water lasted two and a half hours. The first diagram of Fig. 14 shows the results of this series, continuing the histograms are shown for the beginning and end of the filtering. Regarding an evaluation of these histograms the aforementioned comments on absolute and relative measurements have to be considered again. On the other hand, the results in Fig. 14 reveal that with the PDA dirt particles or pore nuclei are also measurable. It is possible that those measurements could be not accurate enough and the nature of the dirt particles or pore nuclei cannot be determined clearly.

5 Summary and Conclusion

The detailed experimental investigations to determine the control volume and the theoretical analysis for the phase-diameter relationship in Figs. 2, 3, and 4 have shown that the PDA works for microbubble measurements. Further, the special investigations in a test loop (Fig. 5) revealed that with Latex-sphere mixtures (Figs. 6 and 8) diameter and concentration measurements can be carried out, although dirt particles clinging to the Latex-spheres (Fig. 7) cause complications. The tests with single bubbles cast in transparent plastic (Fig. 9) enable a reliable concentration determination (Figs. 10 and 11). Finally, the investigations in the small HSVA cavitation tunnel have shown that the PDA can be applied for bubble and, to a certain extent, for solid particle measurements (Figs. 12 and 14). Also, the reproducibility of the PDA-measurements has been verified (Fig. 13).

The latter fact is very important for the reliable application of this new instrument whose development lasted so long. Again, the proven reproducibility of the PDA does not solve the problem of an absolute nuclei measurement for all nuclei diameters. However, by adequate PDA-measurements a significant amount of the nuclei participating in the cavitation process should be measurable.

At present, when measuring cavitation nuclei in the form of microbubbles at HSVA, the PDA amplification is set to such a level that neither microbubbles nor particles are measured when performing background measurements. Since pressure changes and artificial bubble seeding in cavitation tunnels probably do not change the solid particle content, the recorded PDA signals should originate from microbubbles. The results of microbubble measurements using this procedure are shown in Figs. 12 and 13. The solid particle content in the tunnel should be determined by additional measurements, e.g., using a microscope.

The verified capabilities of the PDA have been compared with the specifications for an ideal instrument for performing nuclei measurements that were stipulated by the Cavitation

Table 1 ITTC specifications and PDA stage 1989

ITTC SPECIFICATIONS	PDA STAGE 1989
1. Measure nuclei size and distribution in flowing water.	Feasible
2. Operational in velocities from 0 to 25 m/s.	Feasible
3. Nuclei size from 10 to 250 micron in diameter.	Feasible
4. Measurement in number of nuclei/unit volume (spectrum).	Feasible
5. Volume measured compatible with volume based on frontal area of body being tested.	In principle feasible
6. The error in number and size of nuclei should probably be less than 25 percent in diameter and less than 10 percent in number so that the effect on cavitation inception can be studied accurately.	Size measurement is better feasible, number measurement does not yet reach 10 percent error
7. Measurement should be independent of the facility.	Feasible
8. Measurement should be direct, i.e., independent of theoretical calculations with numerous assumptions or extensive calibrations, or can easily calibrated.	Feasible
9. Must not disturb volume in which nuclei are being measured.	Feasible
10. Continuous and instantaneous operation, if not feasible, time lag not unduly large.	Feasible
11. Kind of nuclei (solid or air bubble) must be determined.	To certain extent feasible

Committee of the ITTC in 1972. Table 1 shows the result and it reveals that the PDA has the potential to fulfil these specifications.

Concerning the error of more than 10 percent in the concentration measurement it may be mentioned that tests are under way to improve the results for bubbles and pore nuclei. These tests are inception investigations for a hemispherical (Kokeshi) body. It should be mentioned that the capability of the PDA to determine the kind of nuclei, i.e., micro air bubbles or solid particles (pore nuclei) using the spherical check could be helpful in cavitation investigations. Detailed investigations of this capability are now under way.

In its recent report containing a comparison between the PDA and holography, the Cavitation Committee (1990) of the 19th International Towing Tank Conference stated that the latter remains the best method for discriminating between microbubbles and particles. However, holography also has resolution problems, it enables no on-line evaluation, and is not suited for sampling statistics. The PDA avoids these drawbacks. Also, the PDA has already yielded results for microbubbles below 10 microns in the absence of solid particles, as shown by Tanger (1986). On the other hand, the PDA records dirt particles (Fig. 14), but due to their varying surface contours and thus varying index of reflection, it does not size them accurately. An improvement of the PDA or a second measuring technique may be necessary. This latter could be a microscopic or an improved venturi type cavitation susceptibility method. However, these two methods have the drawback that they are not in-situ measurements, whereas the PDA is an in-situ and nonintrusive flow measurement.

Summarizing all results shown and discussed here it may be stated that the PDA is a promising tool for qualifying the water characteristics in routine and research cavitation tests. In spite of this, it is the opinion of the authors that more experience with the PDA is necessary, especially when measuring absolute nuclei distributions, and it would be appreciated if this could also be gained through international cooperation.

Acknowledgment

The authors thankfully mention the cooperation of their colleagues Dr. H. Streckwall and Dipl.-Phys. L. Mills of IfS (Institut für Schiffbau, Universität Hamburg) who carried out the Mie-calculations and performed and evaluated the measurements. Also, the patient supervision of the project through Dr. R. Dien of Germanischer Lloyd, Hamburg, contributed to the development of the PDA; this has to be acknowledged explicitly and gratefully. Also, for the financial support of all free air content projects with their pitfalls and achievements, the HSVA and the authors are indebted sincerely to the Federal Ministry of Research and Technology.

References

Bachalo, W. D., and Houser, M. J., 1984, "Phase/Doppler Spray Analyzer for Simultaneous Measurements of Drop Size and Velocity Distributions," *Optical Engineering*, Vol. 23, No. 15, p. 583.

Billet, M. L., 1984, "Cavitation Nuclei Measurements," *International Symposium on Cavitation Inception*, New Orleans, ASME FED-Vol. 16, pp. 33-47.

Cavitation Committee Report, 1990, *19th International Towing Tank Conference*, Madrid, Spain, Vol. 1.

Durst, F., and Zaré, M., 1975, "Laser-Doppler Measurements in Two-Phase Flows," *LDA-Symposium*, University of Denmark.

Hentschel, W., Lauterborn, W., Zarschizky, H., and Tanger, H., 1984, "Nuclei Seeding and Their Measurements by Means of Automatically Scanned Off-Axis Holograms," *International Symposium on Cavitation Inception*, New Orleans, ASME FED-Vol. 16, pp. 19-26.

Keller, A., 1973, "Experimentelle und theoretische Untersuchungen zum Problem der modellmäßigen Behandlung von Strömungskavitation," Bericht Nr. 26 der Versuchsanstalt für Wasserbau der Technischen Universität München.

Keller, A. P., and Matt, P. R., 1986, "New Experiments with the Further Developed Vortex-Nozzle Cavitation Susceptibility Instrument," *International Symposium on Propeller and Cavitation*, Wuxi, China, pp. 340-345.

Knuhtsen, J., and Jessen, J., 1981, "Development of an Instrument for the Measurement of Size and Concentration of Cavitation Nuclei," Report DISA Elektronik.

Saffman, M., Buchhave, P., and Tanger, H., 1984, "Simultaneous Measurement of Size, Concentration, and Velocity of Spherical Particles by a Laser Doppler Method," *Second International Symposium on Applications of Laser Anemometry to Fluid Mechanics*, Lisbon.

Tanger, H., 1986, "Fortführung der Untersuchungen des freien Gasgehaltes bei Kavitation und propellererregten Druckschwankunge," HSVA-Bericht 1546.

Weitendorf, E.-A., 1979, "Conclusions from Full-Scale and Model Investigations of the Free Air Content and of the Propeller-Excited Hull Pressure Amplitudes due to Cavitation," *International Symposium on Cavitation Inception*, New York, ASME, pp. 207-218.

Weitendorf, E.-A., Chao, K.-Y., Friesch, J., and Krohn, J., 1981, "Untersuchungen über den Einfluß des freien Gasgehates auf die Kavitation und von propellererregten Druckschwankungen," HSVA-Bericht 1520.

Weitendorf, E.-A., Friesch, J., Chao, K.-Y., 1982, "Kavitation und Druckschwankungen an Modell und Großausführung sowie deren Interpretation," *Jahrbuch der Schiffbautechnischen Gesellschaft*, Vol. 76, pp. 451-470.

R. Dowlati
Department of Chemical Engineering
and Applied Chemistry,
University of Toronto,
Toronto, Ontario, Canada M5S 1A4

A. M. C. Chan
Mechanical Research Department,
Research Division,
Ontario Hydro,
Toronto, Ontario, Canada M8Z 5S4

M. Kawaji
Department of Chemical Engineering
and Applied Chemistry,
University of Toronto,
Toronto, Ontario, Canada M5S 1A4

Hydrodynamics of Two-Phase Flow Across Horizontal In-line and Staggered Rod Bundles

The void fraction and friction pressure drop measurements have been made for vertical two-phase flow of air-water across staggered and in-line rod bundles with different pitch-to-diameter ratios. All void fraction data showed a strong mass velocity effect and were significantly less than the values predicted by a homogeneous flow model, but were well correlated using the dimensionless gas velocity, j_g^*. *The two-phase friction multiplier data could be well correlated with the Martinelli parameter for* $G > 200$ *kg/m*^{2}*s. The correlations developed for void fraction and two-phase friction multiplier were successfully tested in predicting the total pressure drop in boiling R-113 experiments.*

Introduction

Although shell-and-tube heat exchangers have been used in process industries to boil fluids for decades in the past, the hydrodynamics for flows across the shell-side of a tube bundle have only recently been studied in detail.

For in-line tube bundles, Schrage et al. (1988) and Dowlati et al. (1988) have presented results for two-phase air-water flow directly measured under known conditions of mass velocity and quality. They have both proposed void fraction and two-phase friction multiplier correlations for a bundle with pitch-to-diameter ratio (P/D) equal to 1.3.

Dowlati et al. (1990) have investigated the effect of P/D ratio on void fraction and two-phase friction multiplier for square in-line tube bundles with P/D equal to 1.3 and 1.75. In that study, the bundle average void fraction was found to be little affected by the P/D ratio, however, the two-phase friction multiplier was found to be significantly greater in the larger P/D bundle. The difference was physically attributed to the development of the two-phase wake behind each tube.

A recent review by Jensen (1988) revealed that there are no published data on void fraction and frictional pressure drop for staggered tube bundles under two-phase cross flow conditions.

Reinke and Jensen (1987) investigated and compared the two-phase total pressure drop and boiling heat transfer coefficients between an in-line and staggered tube bundle, having the same P/D ratio of 1.3. Based on the comparison of the total pressure drop data obtained in the two bundles, they speculated that at low mass velocities, the void fraction in the staggered tube bundle would be significantly greater than in an in-line tube bundle. They attributed the higher void fraction in a staggered tube bundle to greater turbulence level, which results in a more homogeneous two-phase mixture flow. At higher mass velocities ($G \geq 300$ kg/m^{2}s), they speculated that the two-phase friction multiplier would be greater for the staggered tube bundle than for the in-line tube bundle, again due to increased turbulence.

In the present work, void fraction and pressure drop characteristics have been experimentally investigated for vertical air-water two-phase flow across two horizontal staggered rod bundles with P/D = 1.3 and 1.75, respectively, at near atmospheric pressures. The data are compared with previous results from square in-line rod bundles with the same P/D ratios (Dowlati et al., 1990) and new correlations for bundle average void fraction and two-phase friction multiplier are proposed. They are then tested by predicting the total pressure drop in boiling two-phase flow experiments.

Experimental Apparatus and Procedure

The same air-water test loop (Fig. 1) used in our previous work (Dowlati et al., 1988, 1990) was used with the two staggered rod bundles, which consisted of 20 rows of five rods, with rod length of 80 mm. In the first bundle, 19.05 mm O.D. rods were arranged in a 60 degree (equilateral triangle) layout with P/D = 1.3. For the second bundle, 12.7 mm O.D. rods were arranged in a similar layout, but with P/D = 1.75. The two in-line rod bundles reported in our previous work (Dowlati et al., 1990) also consisted of 20 rows of rods with the same dimensions as above, arranged in a square array with P/D = 1.3 and 1.75, respectively. The circular rods used in all bundles were made of acrylic and had smooth surfaces. Half rods were used for the outside columns to minimize by-pass leakage. Thus, the minimum flow area, on which the mass velocity was based, was the same for both types of bundles with the same P/D ratio.

Void fraction measurements using γ-densitometry and pressure drop measurements using differential pressure transducers, were performed following the method outlined in Dowlati et al. (1990).

Contributed by the Fluids Engineering Division for publication in THE JOURNAL OF FLUIDS ENGINEERING. Manuscript received by the Fluids Engineering Division April 8, 1991. Associate Technical Editor: M. L. Billet.

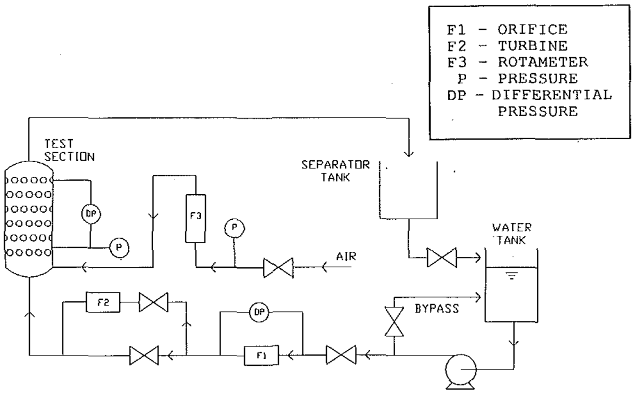

Fig. 1 Experimental flow loop

For a given two-phase flow run with the specified water and air flow rates, gravitational pressure drop was calculated using the bundle average void fraction and subtracted from the measured pressure drop to obtain the frictional two-phase pressure drop, $\Delta P_{2\phi}^{F}$. The accelerational pressure drop was neglected in the present analysis. The two-phase friction multiplier was then computed based on the pressure drop for the liquid phase flowing alone, ΔP_{1}^{F}, with the same liquid flow rate as in the two-phase flow run.

$$\phi_1^2 = \frac{\Delta P_{2\phi}^{F}}{\Delta P_1^{F}} \tag{1}$$

The experiments were conducted at near atmospheric pressures (101–180 kPa) under the following conditions:

P/D = 1.3	P/D = 1.75
$92 \le G \le 795$ kg/m^{2}s	$56 \le G \le 538$ kg/m^{2}s
$0 \le x \le 0.15$	$0 \le x \le 0.13$
$1770 \le \mathrm{Re}_1 \le 15{,}300$	$718 \le \mathrm{Re}_1 \le 7000$

The liquid Reynolds number above is defined in terms of the rod diameter and maximum velocity, $V_{\max}$, between the adjacent tubes. The experimental procedure followed in this work has been previously described in Dowlati et al. (1990). The estimated uncertainties in the data presented are given in Table 1.

Experimental Results and Analysis

Single-Phase Friction Factor. The pressure drop data for single-phase liquid runs were used to compute the bundle friction factor as follows,

Table 1 Estimated uncertainties in the data

Parameter	Uncertainty
f	±4%
Re	±2%
G	±2%
α	±0.05
x	±2%
χ_{tt}	±6%
j_g^*	±2%
ϕ_l^2	±3%

$$\Delta P_1^F = \frac{Nf[G(1-x)]^2}{2\rho_1} \tag{2}$$

The computed friction factors for both staggered rod bundles are shown in Fig. 2, along with a replot of the in-line rod bundle data for comparison. A Blasius type correlation was fitted to the data for the higher Reynolds number region. The present friction factor data for the staggered rod bundle with P/D = 1.3 are slightly higher than the correlation of Zukauskas (1972), however, they match the data from the in-line rod bundle for Re > 3000. The data for the P/D = 1.75 staggered rod bundle are in closer agreement with the correlation of Zukauskas, however, they are slightly higher in comparison to those of the in-line rod bundle of the same P/D. For greater accuracy, the measured single-phase pressure drop was directly used in the calculation of friction multipliers.

Void Fraction. The void fraction profiles measured across both staggered rod bundles showed a relatively uniform profile at different elevations in every run. These relatively uniform void profiles were also observed for the in-line rod bundles as reported in Dowlati et al. (1990). Consequently, the void fraction profiles could be readily averaged over the entire bundle to obtain reliable bundle-average void fraction data, which are analyzed below.

The bundle-average void fraction data are plotted against quality in Figs. 3(*a*) and 3(*b*) for both staggered rod bundles with P/D = 1.3 and 1.75, respectively. Comparison of the data reveals that the effect of P/D appears to be small for given values of mass velocity. This observation is consistent with that reported by Dowlati et al. (1990) for the in-line rod bundles with different P/D.

In comparison to the data from the in-line P/D = 1.3 rod bundle (Dowlati et al. 1990), the data of Fig. 3(*a*) show that the effect of tube layout also appears to be small. Increases in void fraction values of up to 10 percent are observed for the staggered rod bundle at intermediate qualities for all mass

Nomenclature

C = C factor, Eq. (7)
C_1, C_2 = coefficients, Eq. (5)
D = tube diameter, m
f = single-phase friction factor, Eq. (2)
G = mass velocity based on minimum flow area, kg/m^{2}s
g = gravitational constant, 9.806 m/s^2
j_g = Gx/ρ_g, superficial gas velocity, m/s
j_g^* = dimensionless gas velocity, Eq. (4)
m = exponent in Blasius-type equation
N = number of tube rows between pressure taps
ΔP = pressure drop, kPa
P = pitch, m
Re_1 = $(\rho_1 D V_{\max})/\mu$, liquid Reynolds number
$V_{\max}$ = maximum liquid velocity between adjacent tubes, m/s
x = quality
α = void fraction
μ = dynamic viscosity, kg/m-s
ρ = density, kg/m^3
ϕ^2 = two-phase friction multiplier
χ_{tt} = Martinelli parameter, Eq. (3)

Subscripts

g = gas phase only
1 = liquid phase only
2ϕ = two-phase flow

Superscripts

F = friction

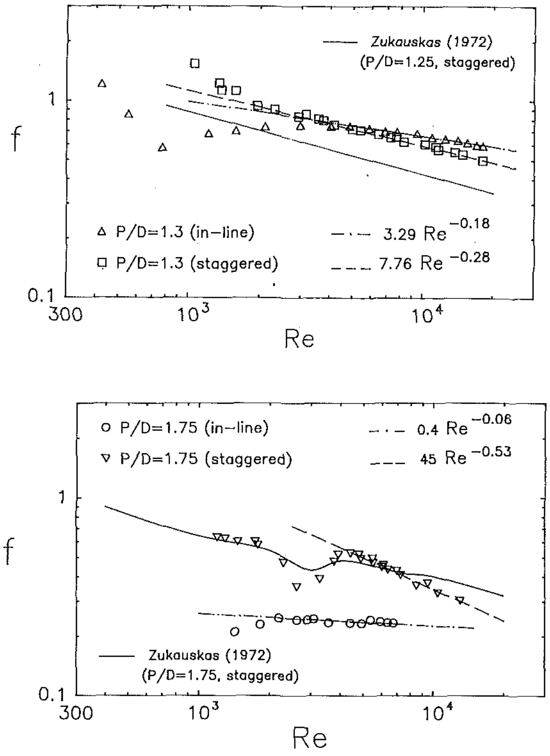

Fig. 2 Comparison of single-phase friction factor data

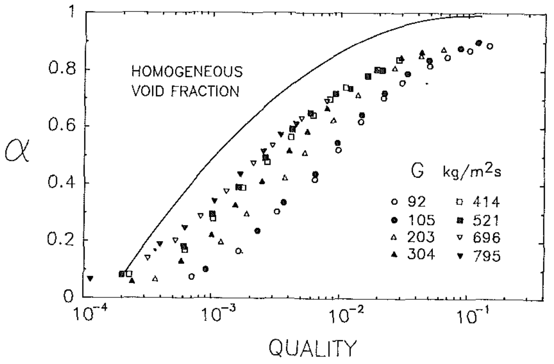

Fig. 3(*a*) Void fraction data and mass velocity effect for staggered rod bundle (P/D = 1.3)

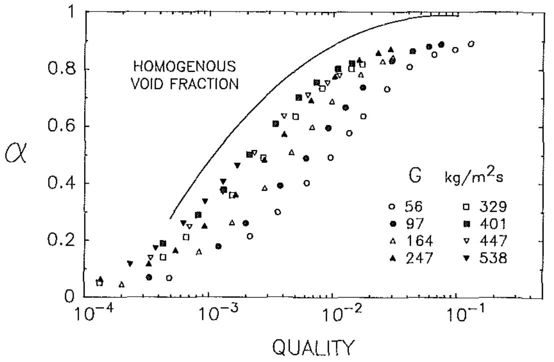

Fig. 3(*b*) Void fraction data and mass velocity effect for staggered rod bundle (P/D = 1.75)

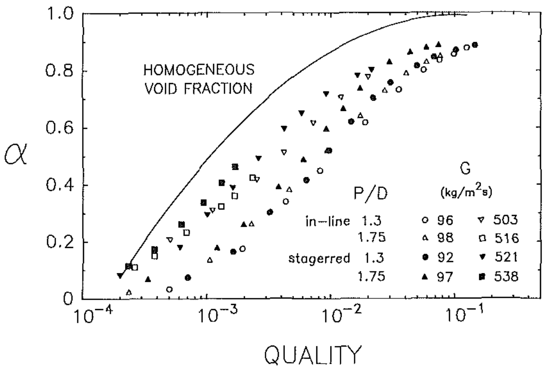

Fig. 3(*c*) Comparison of void fraction data for in-line and staggered rod bundles with different P/D

velocities. Similar results are obtained when comparing the data from the in-line P/D = 1.75 rod bundle (Dowlati et al., 1990) with those of Fig. 3(*b*). These results partially support Reinke and Jensen's (1987) speculation that void fraction in a staggered tube bundle would be higher than in an in-line tube bundle due to increased turbulence and mixing for low mass velocities.

In order to obtain a clearer picture of the bundle geometry effect on void fraction, data for all four staggered and in-line rod bundles are replotted in Fig. 3(*c*) for low and high mass velocities. For both P/D ratios, the void fractions in the staggered rod bundles are greater than those in the in-line rod bundles, and this difference appears to be slightly larger for P/D = 1.75.

The present data also show a strong mass velocity effect in each of the rod bundles tested. For a given quality, higher void fraction is generally obtained with increasing mass velocity (Figs. 3(*a*) and 3(*b*)) similar to the in-line rod bundle data.

The measured void fractions for the staggered rod bundles are significantly lower than the values predicted by the homogeneous flow model. Similar results were also obtained for the in-line rod bundles (Dowlati et al., 1990). The discrepancy is again attributed to the assumption of no slip between the phases in the homogeneous flow model, the validity of which depends on the degree of mixing achieved by the two phases. At low mass velocities, the effect of buoyancy is significant especially at low qualities, and there is a considerable difference in phase velocities. At high mass velocities and low values of quality the void fraction in the rod bundles tend to approach the values predicted by the homogeneous flow model. Here, the turbulence in the liquid phase helps in mixing the two phases and a more homogeneous mixture is obtained.

The mass velocity effect is still evident when the bundle average void fractions are plotted against the Martinelli parameter as shown in Fig. 4 for the staggered rod bundle with P/D = 1.3. Assuming turbulent regimes for both gas and liquid, the Martinelli parameter is given by,

$$\chi_{tt}^2 = \left(\frac{1-x}{x}\right)^{2-m} \left(\frac{\rho_g}{\rho_l}\right) \left(\frac{\mu_l}{\mu_g}\right)^m \qquad (3)$$

The value of m is derived from the Blasius type friction factor correlation as shown in Fig. 2. The presence of the strong mass velocity effect in Fig. 4 is not surprising, since the Martinelli parameter is a function of quality and this effect was also evident in the void fraction-quality plot (Fig. 3).

Because of the strong mass velocity effect, a Lockhart-Martinelli type correlation, used often for in-tube flows, is not applicable here. Similar results were also obtained for the in-line rod bundles (Dowlati et al., 1990) as well as for the staggered bundle with P/D = 1.75.

To eliminate the mass velocity effect, Dowlati et al. (1988, 1990) used the following dimensionless gas velocity given by Wallis (1969), to correlate fairly well the void fraction data obtained in in-line rod bundles with P/D = 1.26, 1.3 and 1.75.

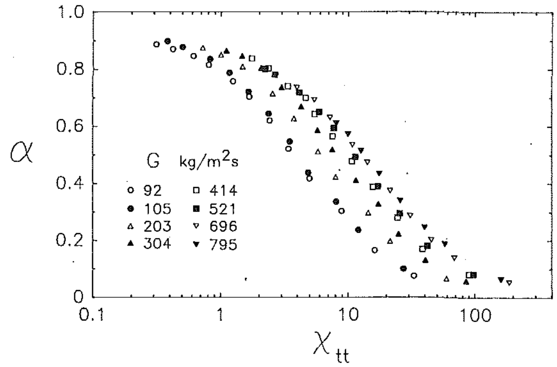

Fig. 4 Variation of void fraction with Martinelli parameter (staggered rod bundle, P/D = 1.3)

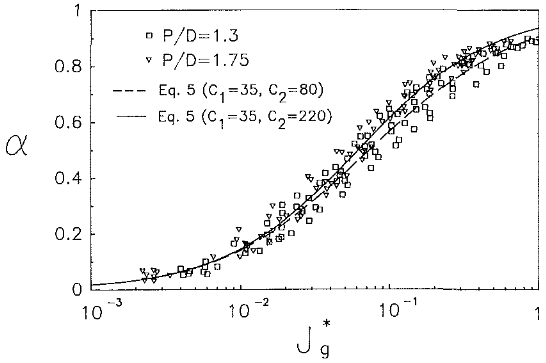

Fig. 5(*a*) Correlation of void fraction data with dimensionless gas velocity (staggered rod bundles)

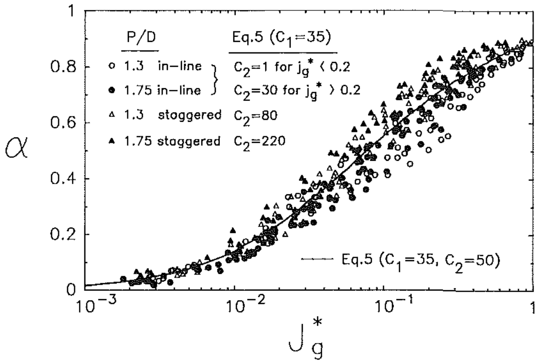

Fig. 5(*b*) Correlation of void fraction data with dimensionless gas velocity (all rod bundles)

$$j_g^* = \frac{\rho_g^{1/2} j_g}{\sqrt{gD(\rho_l - \rho_g)}} \tag{4}$$

Here, the superficial gas velocity, j_g, is defined in terms of the minimum flow area, the rod diameter is used for D, and the gas density is evaluated at the average test section pressure.

As shown in Fig. (5*a*), the void fraction data for both staggered rod bundles are also correlated quite well with the Wallis parameter above using the following correlation,

$$\alpha = 1 - \frac{1}{\sqrt{1 + C_1 j_g^* + C_2 j_g^{*2}}} \tag{5}$$

Equation (5) is similar in form to the correlation in terms of the Martinelli parameter suggested by Chisholm and Laird (1958) for two-phase flow in circular tubes. The values of constants, C_1 and C_2, selected as shown in Fig. 5(*a*) gave the best overall fit for void fraction data from each bundle, with an average deviation of 9 percent. It is noted that for $0.05 < j_g^* < 0.7$, the void fraction is about 10 percent greater in the staggered rod bundle with the higher P/D ratio. This increase in void fraction due to increase in pitch was not observed for the in-line bundle case (Dowlati et al., 1990), where no apparent P/D effect was revealed.

The present void fraction data, for $0.05 < j_g^* < 0.8$, are observed to be about 10–15 percent greater when compared to the in-line rod bundle data reported by Dowlati et al. (1990), for the same P/D ratio. For easier comparison, the values of constants in Eq. (5) which best fit the void fraction data for each of the staggered and in-line rod bundles are shown in Fig.5(*b*). For in-line bundles, changing the C_2 value from 1 (for $j_g^* < 0.2$) to 30 (for $j_g^* > 0.2$) yielded the best fit correlations. Also summarized in Fig. 5(*b*) are the void fraction data for all four bundles. A value of C_2 equal to 50 was obtained which best predicts the entire data set, resulting in an average deviation of about 12 percent.

As pointed out in Dowlati et al. (1990), the success of the use of j_g^* in eliminating the mass velocity effect may be explained by the fact that it contains both the total mass velocity and quality. This is clear when j_g^* is expressed in an alternate form,

$$j_g^* = \frac{Gx}{\sqrt{\rho_g g D(\rho_l - \rho_g)}} \tag{6}$$

Two-Phase Friction Multiplier. A model proposed by Lockhart and Martinelli (1949) to calculate the two-phase friction multiplier in horizontal tube flow and represented by a simple equation due to Chisholm and Laird (1958),

$$\phi_l^2 = 1 + \frac{C}{\chi_{tt}} + \frac{1}{\chi_{tt}^2} \tag{7}$$

has also been applied by various investigators for shell-side two-phase flow (Ishihara et al., 1979; Schrage et al., 1988; Dowlati et al., 1990). Thus, the two-phase friction multiplier data were plotted against the Martinelli parameter for each of the two staggered rod bundles as shown in Figs. 6(*a*) and 6(*b*), respectively. In calculating the Martinelli parameter, a value of 0.2 was used for m in Eq. (3) for all bundles, since this resulted in slightly less scatter than when m was allowed to vary according to the measured Reynolds number dependence. The reasons for less scatter in the correlation using $m = 0.2$ are not clear. Previous attempts at correlating data in terms of the Martinelli parameter also used this approach (Ishihara et al., 1979; Schrage et al., 1988; Dowlati et al., 1990).

For the staggered rod bundle with P/D = 1.3 (Fig. 6(*a*)), the data for $G \geq 200$ kg/m^{2}s follow the same trend suggested by Eq. (7) and the best fit curve is given by $C = 20$. For $G < 200$ kg/m^{2}s, a strong mass velocity effect is observed within a specific range of χ_{tt}, however, outside of this range, the data for $G < 200$ kg/m^{2}s appear to rejoin the remainder of the data. The reason for this behavior is presently not clear.

The data for the P/D = 1.3 in-line rod bundle, $G > 260$ kg/m^{2}s, were also reported to follow the same trend as Eq. (7), however, the best fit curve was given by $C = 8$ (Dowlati et al. 1990). For $G < 260$ kg/m^{2}s, a strong mass velocity effect was also observed. Ishihara et al. (1979) also found that a C-value of 8 best fit Eq. (7) to their data base, although large deviations were seen for $\chi_{tt} > 0.2$.

In Fig. 6(*b*), $C = 20$ also gave a fairly good correlation for $G > 200$ kg/m^{2}s in the staggered bundle with P/D = 1.75. Again, for $G < 200$ kg/m^{2}s, the data show a mass velocity effect within a specific range of χ_{tt}. In comparison, Dowlati et al. (1990) reported that $C \approx 50$ in Eq. (7) correlated in-line P/D = 1.75 rod bundle data fairly well for $G > 200$ kg/m^{2}s.

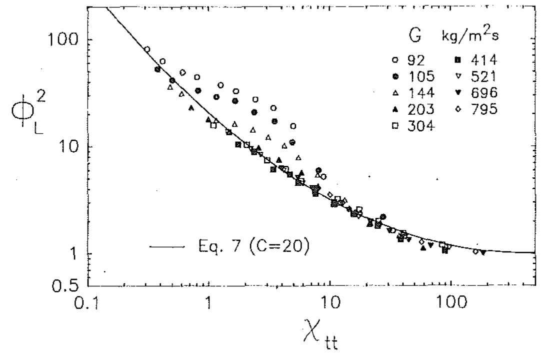

Fig. 6(*a*) Liquid-only two-phase friction multiplier data and Martinelli parameter (staggered rod bundle, P/D = 1.3)

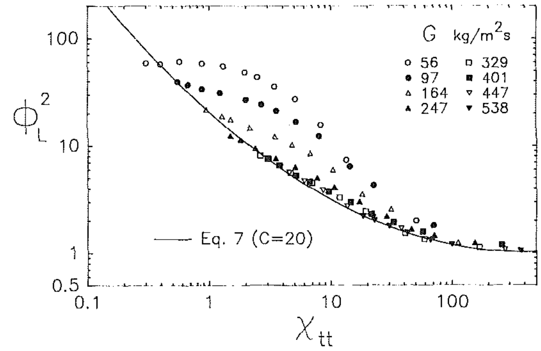

Fig. 6(*b*) Liquid-only two-phase friction multiplier data and Martinelli parameter (staggered rod bundle, P/D = 1.75)

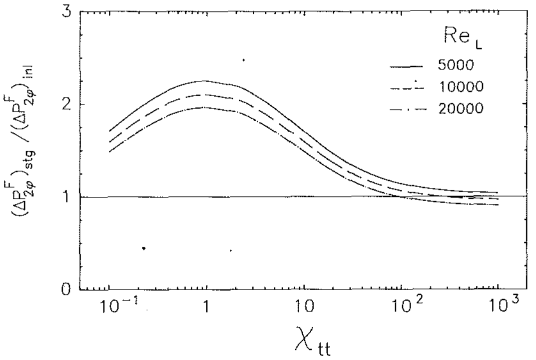

Fig. 7(*a*) Ratio of two-phase friction pressure drops for staggered to in-line rod bundles (P/D = 1.3)

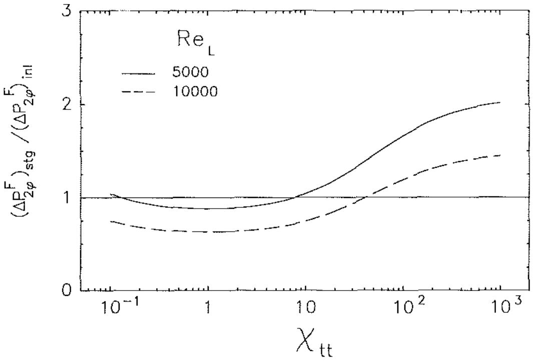

Fig. 7(*b*) Ratio of two-phase friction pressure drops for staggered to in-line rod bundles (P/D = 1.75)

In comparing Fig. 6(*a*) with the in-line rod bundle data with P/D = 1.3, it is clear that the two-phase friction multiplier, for a given value of χ_{tt}, is found to be greater for the staggered rod bundle as speculated by Reinke and Jensen (1987). In order to obtain a clearer picture of the tube layout effect, the two-phase friction pressure drops were calculated for both bundles using the two-phase friction multiplier given by Eq. (7) and the single-phase friction factor correlations shown in Fig. 2. The ratio of the friction pressure drops for the staggered to in-line rod bundles was then plotted, as shown in Fig. 7(*a*) against the Martinelli parameter for several values of Re_l, which correspond approximately to $G > 200$ kg/m^{2}s. A similar analysis was carried out previously by Dowlati et al. (1990) to determine the effect of P/D ratio on the friction pressure drop in in-line rod bundles.

For sufficiently large Martinelli parameters ($\chi_{tt} > 100$), the bundle average void fraction is still small ($\alpha < 0.2$), and the ratio of friction pressure drop for both bundles is seen to be nearly equal to unity (ie., friction pressure drop nearly equal). This is not surprising since at low void fractions, the flow behaves similar to a single-phase liquid flow, and as χ_{tt} increases above 100, the ratio of the two-phase friction pressure drops for a specified Reynolds number will asymptotically approach the ratio of the single-phase friction factors, which is close to unity for $5000 < \mathrm{Re}_l < 2 \times 10^4$ as seen from Fig. 2.

As the Martinelli parameter decreases to values below about 100 and the void fraction increases to above 0.2, the friction multiplier for the staggered rod bundle becomes larger and the ratio of pressure drops increases to values greater than unity. The ratio continues to increase until it reaches a peak at about $\chi_{tt} = 1$, where void fraction is about 0.8. For smaller χ_{tt} and void fractions greater than about 0.8, assuming that Eq. (7) is still applicable, the plot indicates a decreasing ratio of friction pressure drops.

At sufficiently low values of the Martinelli parameter (less than about 0.01), the friction pressure drop ratio is expected to again approach unity. At these small values of χ_{tt}, void fraction would be significantly greater than 0.8 and the flow is expected to be in dispersed droplet/liquid film flow regime and to behave similar to single-phase gas flow. The drop in the friction pressure drop ratio to values near unity would again be consistent with the similar friction factors for both bundles in single-phase gas flow. Thus, as χ_{tt} further decreases, the ratio of the two-phase friction pressure drops should asymptotically approach that of the single-phase friction factors.

In our previous study, (Dowlati et al., 1990), the two-phase friction pressure drop for in-line bundles was found to be greater for the bundle with a larger P/D ratio over a void fraction range from 0.2 to 0.8. It was speculated that this increase in two-phase friction pressure drop arises due to the development of a two-phase wake behind the tube and that the larger pitch offers less obstruction for its development. The same physical mechanism is considered to be responsible for the increase in two-phase pressure drop for the staggered rod bundle, as the distance between the tubes in the same column is twice the pitch for the staggered rod bundle in comparison with that for the in-line rod bundle.

Following the same procedure as above, the two-phase friction pressure drops were calculated for the staggered and in-line rod bundles with P/D = 1.75, and their ratio plotted in Fig. 7(*b*) against the Martinelli parameter for values of Re_l corresponding to approximately $G > 200$ kg/m^{2}s. The same argument used above to explain the behavior of the ratio at significantly high values of χ_{tt}, corresponding to low void fraction flow and approaching single-phase liquid flow, is also applicable here. The ratio of the two-phase friction pressure drops will asymptotically approach the ratio of the single-phase friction factors, which is greater than one for the P/D = 1.75 data for $5000 < \mathrm{Re}_l < 1 \times 10^4$ as seen from Fig. 2.

However, as χ_{tt} decreases, the two-phase friction pressure drop ratio also decreases. This decreasing trend is quite different from that shown in Fig. 7(*a*) and is attributed to the two-phase friction multiplier which, for a given value of χ_{tt}, was found to be lower for the staggered P/D = 1.75 rod bundle ($C = 20$ in Eq. (7)) compared to the in-line P/D = 1.75 rod bundle ($C \approx 50$ in Eq. (7)), for $G > 200$ kg/m^{2}s. The reason for this apparent reversal in trend is presently not clear, and perhaps additional factors aside from the two-phase wake development may be playing a significant role in the two-phase frictional pressure drop. Further tests, at different P/D ratios would help in identifying these mechanisms.

In comparing Figs. 6(*a*) and 6(*b*), the two-phase friction multiplier, for a given value of χ_{tt} and $G > 200$ kg/m^{2}s, is found to be nearly the same for the staggered rod bundles. This is consistent with our speculation regarding the two-phase wake development described above. Further increase in longitudinal pitch may not affect the two-phase friction multiplier in a staggered tube bundle if the two-phase wake downstream of a given rod is sufficiently developed in the present tests. Thus a plot of the ratio of two-phase friction pressure drops for the two staggered rod bundles, similar to that in Fig. 7(*a*) or 7(*b*) would only coincide with the ratio of their single-phase friction factors since their two-phase friction multipliers would be equivalent.

It is interesting to note that $C = 20$ in Eq. (7) is also reported to best fit the friction multiplier data for two-phase flow with both phases turbulent in horizontal tubes (Chisholm, 1967) and in other irregular flow channel geometries such as narrow rectangular channels (Ali and Kawaji, 1991).

Pressure Drop in Boiling Cross Flow. In order to test the applicability of the void fraction and friction multiplier correlations, Eqs. (5) and (7), respectively, to a boiling bundle, the total pressure drop data of Hsu (1987) and Reinke (1987) were analyzed. The prediction of Hsu's in-line, P/D = 1.3, tube bundle has been discussed in detail in Dowlati et al. (1990) and only Reinke's data are discussed here. Reinke used a staggered (60 degree layout), 5 × 27 tube bundle with 7.94 mm O.D. tubes and P/D = 1.3, to boil R-113 at pressures of 200–500 kPa, with a mass velocity range of 100–700 kg/m^{2}s. The static pressure profile in the bundle was obtained from several pressure drop measurements using inclined manometers connected to pressure taps located along the bundle height. To test the present correlations, the pressure drop between two elevations sufficiently far apart was computed from Reinke's data and compared with the predictions of the total pressure drop due to gravity, friction and acceleration.

The gravitational pressure drop between the two elevations was calculated by evaluating the local void fraction from quality using the void fraction correlation (Eq. (5)) and numerically integrating the results. Since Reinke did not measure the void fraction in his experiments, a direct comparison between the measured and predicted void fractions could not be made.

The two-phase friction pressure drop was calculated using Eq. (1), where Reinke's single-phase friction factor correlation (the same as that of Zukauskas, 1972) was used to determine the single-phase friction pressure drop, and the two-phase friction multiplier was computed using Eq. (7). The two-phase frictional pressure drop was then numerically integrated between the two quality values at the given elevations.

In applying Eq. (7) to predict the two-phase friction multiplier for $G \geq 200$ kg/m^{2}s, it was found that the value of $C = 15$ (instead of $C = 20$ as suggested in Fig. 6(*a*)) resulted in a better prediction of Reinke's data. The value of m in Eq. (3), used to calculate χ_{tt}, was derived from the single-phase friction factor correlation as given by Reinke, which agreed with that of Zukauskas (1972).

Due to the large variation in quality across the bundle, the accelerational pressure drop, ΔP_{acc}, was also taken into account. This was obtained from the separated flow model (Collier, 1981). More details of the calculation procedure are given in Dowlati et al. (1990).

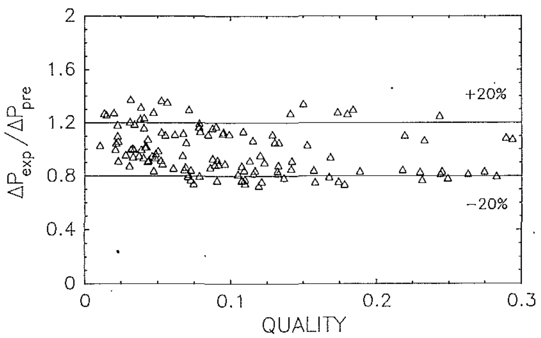

Fig. 8 Prediction of overall pressure drop data obtained by Reinke (1987) in R-113 boiling experiments

Figure 8 shows the ratio of the experimental overall pressure drop, as determined from Reinke's data, to the predicted pressure drop plotted against the average quality between the two elevations considered. Our correlations are successful in predicting 90 percent of the data points considered, within ±20 percent. Although the present correlations have been derived from experiments performed with air and water at near atmospheric pressures, it is clear from Fig. 8 that they also work well for predicting the total pressure drop for R-113 at the elevated pressures, with a slight modification in the *C*-value of Eq. (7).

Conclusions

New void fraction and friction pressure drop data have been obtained for vertical two-phase flow of air-water across two staggered rod bundles with different P/D ratios. The data were compared with those for in-line rod bundles reported earlier in Dowlati et al. (1990) and the general data trends were found to be similar, and therefore, similar conclusions are first summarized followed by new findings.

1) The bundle average void fractions were much smaller than the values predicted by a homogeneous flow model and showed a strong mass velocity effect. A void fraction correlation in terms of a dimensionless gas velocity was proposed.

2) The two-phase friction multiplier data could be correlated well in terms of a Martinelli parameter, however, strong mass velocity effects were observed for $G < 200$ kg/m^{2}s in both bundles.

New findings include,

3) For a given quality, higher void fraction (about 10–15 percent) was obtained in each of the staggered rod bundles in comparison with those of the in-line rod bundles for the same P/D ratio.

4) No P/D effect was observed on the two-phase friction multiplier for the staggered rod bundles. However, changing the in-line tube layout to a staggered layout for P/D = 1.3, lead to a higher two-phase pressure drop over a certain range of void fractions. The opposite effect was observed for P/D = 1.75.

5) The void fraction and two-phase friction multiplier correlations presented here were reasonably successful in predicting the total pressure drop across a staggered tube bundle with boiling R-113 at pressures up to 500 kPa.

References

Ali, M. I., and Kawaji, M., 1991, "The Effect of Flow Channel Orientation on Two-Phase Flow in a Narrow Passage Between Flat Plates," *Proceedings of the 3rd ASME/JSME Thermal Engineering Joint Conf.*, Reno, Nev., Mar. 17–22, Vol. 2, pp. 183–190.

Collier, J. G., 1981, *Convective Boiling and Condensation*, McGraw-Hill, 2nd ed., New York.

Chisholm, D., 1967, "A Theoretical Basis for the Lockhart-Martinelli Correlation for Two-Phase Flow," *Int. J. Heat Mass Transfer*, Vol. 10, pp. 1767-1778.

Chisholm, D., and Laird, A. D. K., 1958, "Two-Phase Flow in Rough Tubes," *Trans. ASME*, Vol. 80, pp. 276-286.

Dowlati, R., Kawaji, M., and Chan, A. M. C., 1988, "Void Fraction and Friction Pressure Drop in Two-Phase Flow Across a Horizontal Tube Bundle," *AIChE Symposium Series*, Vol. 84, No. 263, pp. 126-132.

Dowlati, R., Kawaji, M., and Chan, A. M. C., 1990, "Pitch-to-Diameter Effect on Two-Phase Flow Across an In-line Tube Bundle," *AIChE Journal*, Vol. 36, No. 5, pp. 765-772.

Hsu, J. T., 1987, "A Parametric Study of Boiling Heat Transfer in Horizontal Tube Bundles," Ph.D. thesis, University of Wisconsin, Milwaukee.

Ishihara, K., Palen, J. W., and Taborek, J., 1979, "Critical Review of Correlations for Predicting Two-Phase Pressure Drop Across Tube Banks," *Heat Transfer Engineering*, Vol. 1, No. 3, pp. 1-8.

Jensen, M. K., 1988, "A Model for the Recirculating Flow in a Kettle Reboiler," *AIChE Symposium Series*, Vol. 84, No. 263, pp. 114-119.

Lockhart, R. W., and Martinelli, R. C., 1949, "Proposed Correlation of Data for Isothermal Two-Phase, Two-Component Flow in Pipes," *Chemical Engineering Progress*, Vol. 45, No. 1, 1949, pp. 39-48.

Reinke, M. J., 1987, "A Comparison of the Boiling Heat Transfer and Two-Phase Pressure Drop Characteristics of an In-line and a Staggered Tube Bundle," M.Sc. thesis, University of Wisconsin, Milwaukee.

Reinke, M. J., and Jensen, M. K., 1987, "Comparison of Boiling Heat Transfer and Two-Phase Pressure Drop Between an In-line and Staggered Tube Bundle," *ASME HTD-Vol. 85*, pp. 41-50.

Schrage, D. S., Hsu, J. T., and Jensen, M. K., 1988, "Two-Phase Pressure Drop in Vertical Crossflow Across a Horizontal Tube Bundle," *AIChE Journal*, Vol. 34, pp. 107-115.

Wallis, G. B., 1969, "One-Dimensional Two-Phase Flow," McGraw-Hill, New York.

Zukauskas, A., 1972, "Heat Transfer from Tubes in Crossflow," *Advances in Heat Transfer*, Vol. 8, pp. 93-160.

Journal of Fluids Engineering

Technical Briefs

Experimental Investigation of Uniform-Shear Flow Past a Circular Cylinder

Tae Soon Kwon,[1] **Hyung Jin Sung,**[1] **and Jae Min Hyun**[1]

Extensive laboratory experiments were carried out to investigate the uniform-shear flow approaching a circular cylinder. The aim was to present the Strouhal number (St)- Reynolds number (Re) diagrams over a broad range of the shear parameter K ($0 \le K \le 0.25$) and at higher values of Re ($600 \le Re \le 1600$). An image processing technique, in conjunction with flow visualization studies, was used to secure more quantitative depictions of vortex shedding from the cylinder. The Strouhal number increases with increasing shear parameter. The drag coefficient decreases with increasing Re; also, C_d decreases as the shear parameter K increases.

1 Introduction

Flow past a circular cylinder constitutes a classical problem. The wake patterns, vortex shedding, boundary-layer separation, and drag, to name a few, are the prominent issues. The preceding studies, mostly experimental observations or numerical simulations, have mainly dealt with the cases of a uniform, constant oncoming flow about a cylinder (Roshko, 1954; Friehe, 1980; Williamson, 1989, etc.). However, there are a host of practical situations in which the oncoming flow is non-uniform. A canonical example of such a non-uniform oncoming stream about a body is uniform-shear flow, i.e., a flow with constant vorticity. The flow geometry is straightforward, and this flow poses an idealized model for more complex flow configurations. The research group of Kiya et al. (1980) presented a series of physically insightful and far-reaching publications on the subject of vortex shedding from a cylinder by uniform-shear flows. The Reynolds number range was extended to encompass $35 \le \text{Re} \le 1500$, and the shear parameter was varied up to 0.25. However, due to the difficulties in actual experimental measurements, the major results were concentrated to low and moderate Reynolds numbers. The data on the Strouhal number (St) were restricted to the range $50 < \text{Re} < 1000$.

In the present work, it is intended to undertake an expanded experimental program using a water tunnel to investigate the uniform-shear flow past a cylinder. One purpose is to incorporate a digital image processing technique (Nishno et al., 1989; Massons et al., 1989; Kobayashi and Yoshitake, 1989 etc.). This technique, interfaced with a computer, is capable of portraying and assessing the wake pattern and the Strouhal number in a specific and quantitative manner. The upper limit of the Reynolds number has been extended, i.e., $0 \le \text{Re} \le 1600$ and the shear parameter has been made to approach up to 0.25. These values are appreciably higher than those achieved by Kiya et al. (1980).

Another aim of the present study is to acquire detailed measurement data of drag coeffecient C_d. It is recalled that Tamura et al. (1980) calculated C_d in a similar situation, however, the data were given only for two specific, low values of the Reynolds number, i.e., Re = 40 and 80. In the present study, the variations of drag coefficient with the Reynolds number are plotted for varying strength of the shear in the oncoming stream.

2 Experimental Apparatus and Procedures

A recirculating water tunnel was built. The size of the rectangular-shaped test section was: width (W) 26 cm, depth (H) 30 cm, and the length in the stream direction (L) 3.7 m. The water in the test section had a free surface, open to the atmosphere. However, no appreciable waves were seen on the free surface during the entire course of the experiments (Kiya et al., 1980). The overall design and operation of this water tunnel are similar to those depicted in Rohr et al. (1988).

Twenty equally spaced channels were attached to the entrance of the shear generator. The channel walls were made of 19 stainless steel plates, each of which is 0.7 mm in thickness. The flow inside each channel was controlled individually by using twenty separate valves. In order to enhance the lateral uniformity, a cylindrical rod of 5 mm in diameter and a screen of 3 mm mesh size were installed at the entrance of each channel. The flow inside each channel, 70 cm long in the stream direction, was isolated from the adjacent layers.

The definition sketch of the circular cylinder and the approaching uniform-shear flow are illustrated in Fig. 1. The diameter of the cylinder is D. The magnitude of the oncoming velocity at the center of the cylinder is U_c. The Reynolds number is defined as $\text{Re} = U_c D/\nu$. The velocity gradient of the shear flow is denoted by G. The shear parameter K is defined as $K = GD/U_c$. In the present experiment, U_c was constant, and by varying the value of G, the value of K was adjusted.

A total of six circular cylinders, of diameters (D) ranging from 2 cm to 5 cm, and of axial length 26 cm to fit the width (W) of the water tunnel, were prepared and precision-machined. Consequently, the channel blockage ratio, D/H, ranged from 0.067 to 0.16. The aspect ratio of the cylinder was $5.2 \le W/D \le 13$. For over 84 percent of the data reported herein, the blockage ratio was less then $D/H \le 0.13$. In order to assess the effect of the blockage ratio, comparisons were made between the present data obtained for a uniform flow and the

---

[1] Department of Mechanical Engineering, Korea Advanced Institute of Science and Technology, Seoul, Korea. Dr. Hyun is a Mem. ASME.

Contributed by the Fluids Engineering Division of The American Society of Mechanical Engineers. Manuscript received by the Fluids Engineering Division July 7, 1991. Associate Technical Editor: J. A. C. Humphrey.

measurements of Roshko (1954). The deviations of the present results from those of Roshko were less than 4.7 percent. For the cases of relatively high D/H, the empirical formula of Roshko (1954) was consulted to quantify the effect of the blockage effect. By this procedure, for the highest value used in the present study, $D/H = 0.16$, the effect is seen to be smaller than approximately 6.1 percent. The aspect ratios lie within the range for which the three-dimensionality assumption could be made with reasonable accuracy (see Kiya et al., 1980; Richter and Naudascher, 1976). The lateral variations of velocities were carefully monitored for several sample cases. These efforts established that the three-dimensionalities were very weak for the parameter range of the present study.

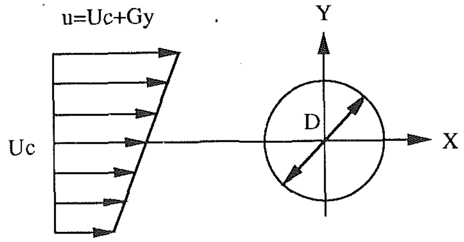

Fig. 1 ***Definition sketch of a uniform shear flow approaching a circular cylinder***

The principal components of the image processing system are a CCD-TV camera, a digital image processor (512 × 480 pixels, 256 gray levels), an image recorder, a 32-bit IBM/386 computer and a laser slit beam system. The fluid motion behind the cylinder was visualized by distributing fine tracer particles. A slit beam generator, 1 mm in depth, was equipped with a 35 mW He-Ne laser and a cylindrical lens. The tracer particles were made of polystyrene; the specific density was 1.04, and the average diameter of the tracer particles was less than 300 μm.

The uncertainties associated with the experimental measurements were appraised following mostly the procedures suggested by Moffat (1988). Possible elemental error sources of the present experiments may stem from the lens distortion effect, discrepancies in time intervals between the image frames, traceabilities of the particles to the fluid motions, and mistrackings of the tracer particles.

In order to perform more quantitative evaluations of the flow fields, the laser doppler velocimeter (TSI model 1990)

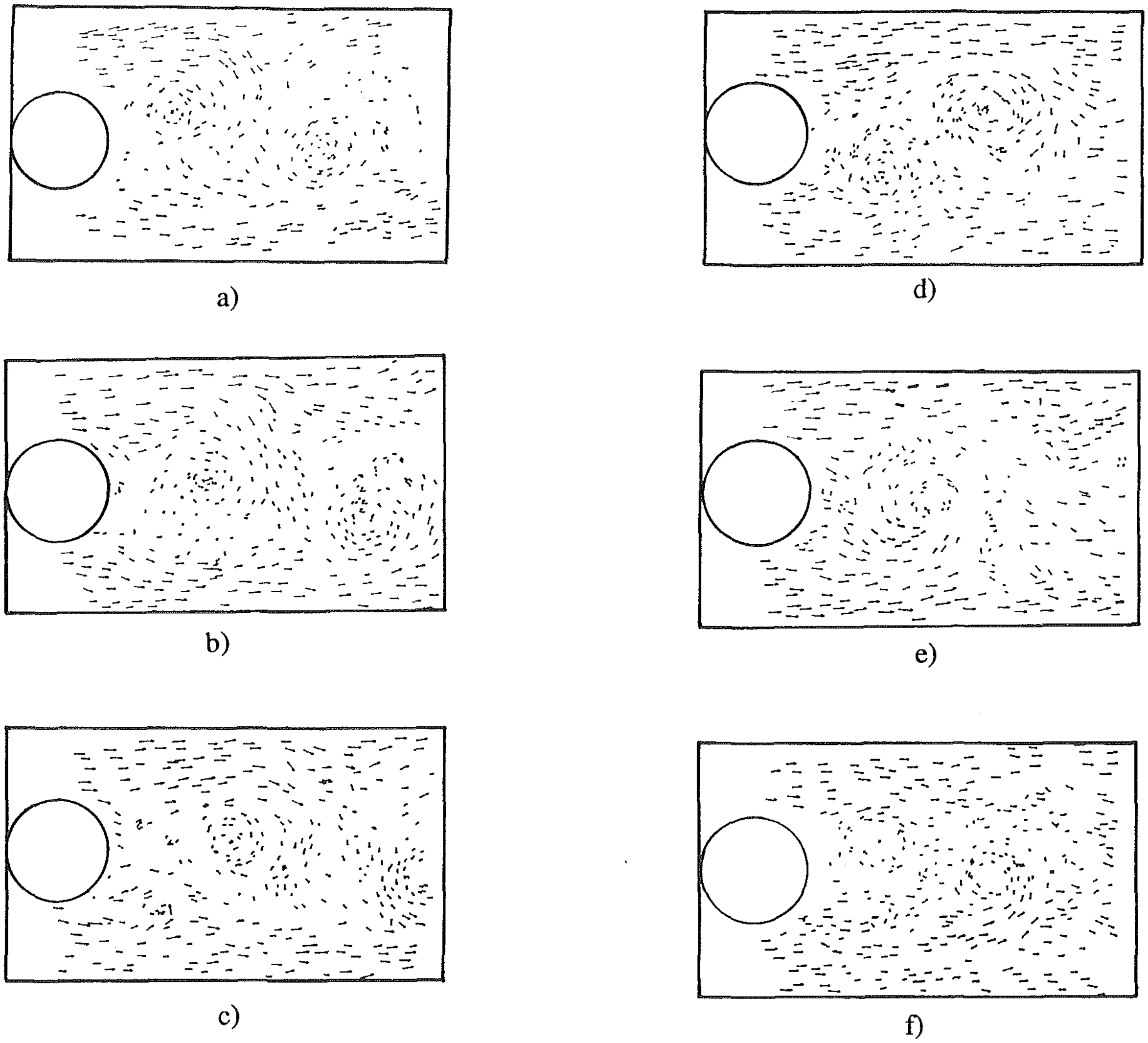
a)
d)
b)
e)
c)
f)

Fig. 2 **Exemplary pictures displaying the image enhanced flow field behind the cylinder. $K = 0.05$, Re = 900. Time instants are (*a*) t = To, (*b*) t = To + 1/5T, (*c*) t = To + 2/5T, (*d*) t = To + 3/5T, (*e*) t = To + /45T, (*f*) t = To + T, where To is the starting instant and T is the period.**

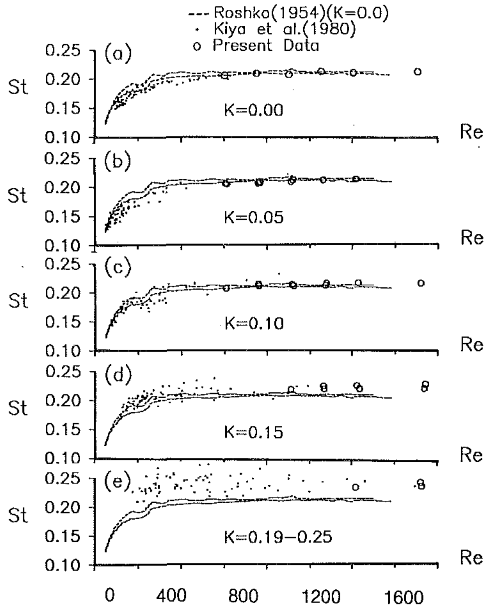

Fig. 3 Strouhal number (St) versus Reynolds number (Re) for uniform and shear flows (Uncertainty in St = ± 6.7 percent, in Re = ±1.5 percent, and K = +1.5 percent)

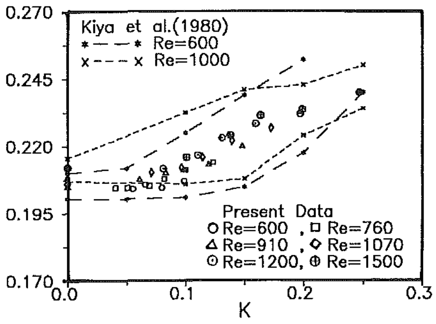

Fig. 4 Strouhal number (St) versus shear parameter (K) (Uncertainty in St = ±6.7 percent, in K = ±1.5 percent)

was utilized extensively. In the present studies, the data points were within ±1.5 percent deviation from the mean shear profile. The turbulence intensity distributions were below $u'/U \leq 0.015$.

A three-component force transducer, composed of 4-strain gages, was used to measure the drag force. The monotonical bias was compensated for in the analysis under typical operating conditions. When the drag was measured, a thin plate of thickness less than 0.6 mm was inserted at both ends of the cylinder. The cylinder was attached to the force transducer by using a rod of diameter 2 mm.

The drag coefficient C_d is defined by using the approach velocity at the center of cylinder, U_c:

$$C_d = \frac{F}{\frac{1}{2}\rho U_c^2 D L_a}$$

where F is the drag force, L_a the actual spanwise width of the cylinder.

3 Results and Discussion

Figure 2 exemplifies the instantaneous velocity vector distributions captured by image-processed flow visualizations. The frames in Fig. 2 are selected such that the flow behavior over one period (T) of vortex shedding is clearly illustrated. The outcome of these extensive flow analyses indicates that, in weak shear flows, the wake flows are substantially periodic in time in much of the wake region behind the cylinder.

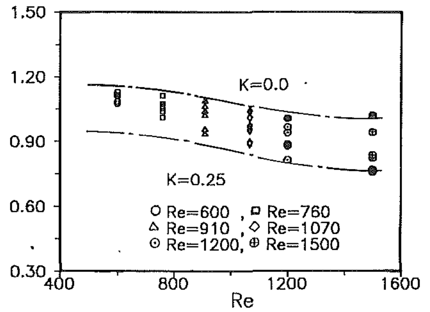

Fig. 5 Drag coefficient (C_d) versus Reynolds number (Re) (Uncertainty in C_d = ±4.3 percent, in Re = ±1.5 percent)

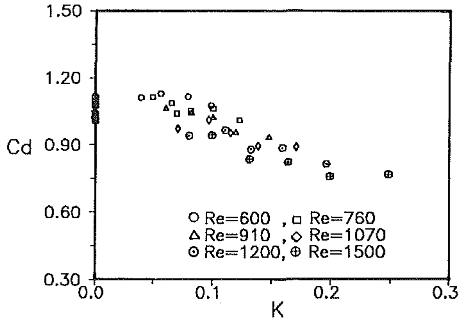

Fig. 6 Drag coefficient (C_d) versus shear parameter (K) (Uncertainty in C_d = ±4.3 percent, in Re = ±1.5 percent)

The results for a uniform flow (K = 0) are displayed in Fig. 3(a). These plots are for a standard benchmark test case, and the results here serve to validate the reliability and accuracy of the present experimental methodologies. Evidently, the present results are in good agreement with the well-documented data in the literature. The Strouhal number (St) increases rapidly with Re at low Reynolds numbers (Re ≤ 400). The rate of increase of St is reduced afterwards, and when Re ≥700, St reaches a plateau and the value of St is fairly constant around the well-known value St = 0.21 at large Reynolds numbers (700 ≤ Re ≤ 1400).

In Fig. 3(b)-(e), the St-Re diagrams are presented for uniform-shear flows. The range 600 ≤ Re ≤ 1500 is the parameter space which was left unexplored in the preceding investigations by Kiya et al. Inspection of Fig. 3(b)-(e) discloses a general trend that St increases with Re at low Reynolds numbers; however, the rate of increase of St falls off as Re increases, and when Re is large, say Re ≥ 400–800, St takes a fairly constant value. It is significant to note that St, in general, increases as K increases, at a fixed Reynolds number. At a high shear parameter (for K = 0.19–0.25), the value of St is appreciably higher than that of a uniform flow. Re-plotting the results, Fig. 4 exhibits the variation of St with K. This clearly demonstrates that the frequency of vortex shedding increases as the strength of the vorticity embedded in the oncoming stream increases.

Finally, the results of the drag measurements are presented in Fig. 5, which exhibits the time-averaged C_d versus Re. In Fig. 5, a total of six values of K, ranging from K = 0.0 to K = 0.25 with almost equal intervals, are shown by the data points. The behavior of C_d in a shear flow at high Reynolds numbers has not been dealt with explicitly in the prior literature. As stated earlier, the values of C_d were calculated numerically by Tamura et al. (1980) for two specific values of Re, i.e., Re = 40 and 80. The general trend is that C_d decreases with Re. However, the rate of decrease of C_d with Re becomes larger at high values of K. Re-plotting the data in the form of C_d-K is shown in Fig. 6. It is easily recognized that C_d decreases in a fairly monotonic fashion, as K increases. A physical explanation may be offered to delineate this qualitative behavior of C_d. If the circular cylinder is placed in a uniform stream, the approaching flow is equally divided at the forward stagnation point ($x = -D/2$, $y = 0$) into two parts. However, for a shear flow, the contribution of the upper (lower) part of the cylinder is to increase (decrease) the drag, as compared to the case of a uniform flow. On balance, however, the relative magnitude of the drag reduction stemming from the lower part of the cylinder outweighs the drag enhancement of the upper part of the cylinder. The overall effect, therefore, turns up as a drag reduction experienced by the cylinder, and this trend becomes more pronounced as the shear parameter increases. The experimental findings on the behavior of C_d, as portrayed in Figs. 5 and 7, are qualitatively consistent with this physical argument.

4 Conclusions

The Strouhal number St increases rapidly with the Reynolds number Re at small values of Re; however, when Re ≥ 400–700, St reaches a nearly-constant value in the neighborhood of St = 0.22. The Strouhal number, in general, increases as the shear parameter K increases. The scatter in data was appreciably smaller in the present experiments than for the case of the preceding experiments of Kiya et al. (1980). This may be attributed to the adoption of the nondisturbing image processing method in the present experiments. The measurements data on drag coefficient C_d are also provided. The C_d curves tend to decrease as Re increases; and C_d decreases with increasing parameter K.

Acknowledgments

Appreciation is extended to the referees whose constructive comments led to improvements in the paper.

References

Friehe, C. A., 1980, "Vortex Shedding from Cylinders at Low Reynolds Number," *Journal of Fluid Mechanics*, Vol. 100, pp. 237–241.

Kiya, M., Tamura, H., and Arie, M., 1980, "Vortex Shedding from a Circular Cylinder in Moderate-Reynolds Number Shear Flow," *Journal of Fluid Mechanics*, Vol. 101, pp. 721–735.

Kobayashi, T., and Yoshitake, Y., 1989, "Development of Digital Image Processing System for Pathline Picture," *JSME*, Part B, Vol. 466, pp. 1966–1970.

Massons, J., Gavalda, J., and Diaz, F., 1989, "Image Processing of Cylinder Wake Generation," *Phys. Fluids*, pp. 1415–1423.

Moffat, R. J., 1988, "Describing the Uncertainties in Experimental Results," *Experimental Thermal and Fluid Science*, Vol. 1, pp. 3–17.

Nishino, K., Kasagi, N., and Hirata, M., 1989, "Three-Dimensional Particle Tracking Velocitimetry Based on Automated Digital Image Processing," *Journal of Fluid Mechanics*, Vol. 111, pp. 391–394.

Richter, A., and Naudascher, E., 1976, "Fluctuating on a Rigid Circular Cylinder in Confined Flow," *Journal of Fluid Mechanics*, Vol. 78, Part 3, pp. 561–576.

Rohr, J. J., Itsweire, E. C., Helland, K. N., and Van Atta C. W., 1988, "An Investigation of the Growth of Turbulence in a Uniform-Mean-Shear Flow," *Journal of Fluid Mechanics*, Vol. 187, pp. 1–33.

Roshko, A., 1954, "On the Development of Turbulent Wakes from Vortex Streets," NACA-TN 1191.

Tamura, H., Kiya, M., and Arie, M., 1980, "Numerical Study on Viscous Shear Flow Past a Circular," *Bulletin of JSME*, Vol. 23, pp. 1952–1958.

Williamson, C. H. K., 1989, "Oblique and Parallel Modes of Vortex Shedding in the Wake of a Circular Cylinder at Low Reynolds Numbers," *Journal of Fluid Mechanics*, Vol. 26, pp. 576–626.

The Measurement of Solid-Liquid Contact Angles

Kenji Katoh,[1] Hideomi Fujita,[2] Hideharu Sasaki,[3] and Koichi Miyashita[4]

A new method is proposed for measuring solid-liquid contact angles. The well-known phenomenon where the liquid meniscus formed under a downward facing solid surface spontaneously breaks at a certain height is utilized in the contact angle measurements. The relation between the contact angle and the critical height of the solid surface where the instability occurs was derived theoretically from the solid-liquid wetting behavior using a thermodynamic approach. From the theoretical model the contact angles can be obtained by measuring the critical height of the solid. The validity of the analysis and the usefulness of the method were experimentally confirmed for various solid surfaces and test liquids.

1 Introduction

In an earlier communication (Katoh et al., 1990), we investigated theoretically the macroscopic wetting behavior from a thermodynamic viewpoint and clarified the mechanism by which a liquid meniscus formed under a solid cone surface becomes unstable and falls spontaneously from the surface at a certain cone height.

In this report, we propose a new method for measuring contact angles, which is a parameter describing solid-liquid wettability, based on the above unstable behavior of the meniscus. The usefulness of the proposed method was confirmed experimentally and the validity of the previous analysis of Katoh et al. (1990) is discussed using the experimental results.

2 Principle of the Present Method

2.1 Wetting Behavior of a Meniscus Existing Under a Solid Cone Surface. In our earlier investigation, a model of an axisymmetric liquid meniscus formed under a downward facing cone of half vertical angle ϕ, as shown in Fig. 1, was developed and the wetting behavior of the meniscus was examined by calculating the system free energy. In the figure r_0 is the meniscus radius at the point of attachment of the meniscus to the solid surface and H_B indicates the height of the cone vertex from the stationary liquid surface. Details concerning the system energy E comprise: (i) the energy change caused by the conversion of solid surface into solid-liquid interface $E_{SV\text{-}SL}$, (ii) the energy of meniscus formation E_M; namely, the change of the liquid surface energy and the meniscus potential energy.

In the above energies, E_M can be obtained by using the meniscus profile. For the calculation of $E_{SV\text{-}SL}$, we considered a hypothesis in the preceding report that the energy difference between the solid surface and the solid-liquid interface per unit area [i.e., ($\sigma_{SV} - \sigma_{SL}$) ($\sigma_{SU}$: solid surface tension; σ_{SL}: solid-liquid interfacial tension] could be calculated by modified Young's equation as

$$\sigma_{SV} - \sigma_{SL} = \sigma_{LV} \cos \theta_Y \qquad (1)$$

where σ_{LV} is liquid surface tension and θ_Y is the apparent contact angle observed macroscopically; $\theta_Y = \theta_{YR}$ (receding

---

[1] Lecturer, Department of Mechanical Engineering, Osaka City University, Osaka 558, Japan.

[2] Professor, Department of Mechanical Engineering, Nagoya University, Nagoya 464-01, Japan.

[3] Ishikawajima System Technology Co., Ltd., Tokyo 102, Japan.

[4] Nihongaishi Co., Ltd., Nagoya 467, Japan.

Contributed by the Fluids Engineering Division of THE AMERICAN SOCIETY OF MECHANICAL ENGINEERS. Manuscript received by the Fluids Engineering Division December 29, 1990. Associate Technical Editor: C. J. Freitas.

points. The behavior of C_d in a shear flow at high Reynolds numbers has not been dealt with explicitly in the prior literature. As stated earlier, the values of C_d were calculated numerically by Tamura et al. (1980) for two specific values of Re, i.e., Re = 40 and 80. The general trend is that C_d decreases with Re. However, the rate of decrease of C_d with Re becomes larger at high values of K. Re-plotting the data in the form of C_d-K is shown in Fig. 6. It is easily recognized that C_d decreases in a fairly monotonic fashion, as K increases. A physical explanation may be offered to delineate this qualitative behavior of C_d. If the circular cylinder is placed in a uniform stream, the approaching flow is equally divided at the forward stagnation point ($x = -D/2$, $y = 0$) into two parts. However, for a shear flow, the contribution of the upper (lower) part of the cylinder is to increase (decrease) the drag, as compared to the case of a uniform flow. On balance, however, the relative magnitude of the drag reduction stemming from the lower part of the cylinder outweighs the drag enhancement of the upper part of the cylinder. The overall effect, therefore, turns up as a drag reduction experienced by the cylinder, and this trend becomes more pronounced as the shear parameter increases. The experimental findings on the behavior of C_d, as portrayed in Figs. 5 and 7, are qualitatively consistent with this physical argument.

4 Conclusions

The Strouhal number St increases rapidly with the Reynolds number Re at small values of Re; however, when Re ≥ 400–700, St reaches a nearly-constant value in the neighborhood of St = 0.22. The Strouhal number, in general, increases as the shear parameter K increases. The scatter in data was appreciably smaller in the present experiments than for the case of the preceding experiments of Kiya et al. (1980). This may be attributed to the adoption of the nondisturbing image processing method in the present experiments. The measurements data on drag coefficient C_d are also provided. The C_d curves tend to decrease as Re increases; and C_d decreases with increasing parameter K.

Acknowledgments

Appreciation is extended to the referees whose constructive comments led to improvements in the paper.

References

Friehe, C. A., 1980, "Vortex Shedding from Cylinders at Low Reynolds Number," *Journal of Fluid Mechanics*, Vol. 100, pp. 237–241.

Kiya, M., Tamura, H., and Arie, M., 1980, "Vortex Shedding from a Circular Cylinder in Moderate-Reynolds Number Shear Flow," *Journal of Fluid Mechanics*, Vol. 101, pp. 721–735.

Kobayashi, T., and Yoshitake, Y., 1989, "Development of Digital Image Processing System for Pathline Picture," *JSME*, Part B, Vol. 466, pp. 1966–1970.

Massons, J., Gavalda, J., and Diaz, F., 1989, "Image Processing of Cylinder Wake Generation," *Phys. Fluids*, pp. 1415–1423.

Moffat, R. J., 1988, "Describing the Uncertainties in Experimental Results," *Experimental Thermal and Fluid Science*, Vol. 1, pp. 3–17.

Nishino, K., Kasagi, N., and Hirata, M., 1989, "Three-Dimensional Particle Tracking Velocitimetry Based on Automated Digital Image Processing," *Journal of Fluid Mechanics*, Vol. 111, pp. 391–394.

Richter, A., and Naudascher, E., 1976, "Fluctuating on a Rigid Circular Cylinder in Confined Flow," *Journal of Fluid Mechanics*, Vol. 78, Part 3, pp. 561–576.

Rohr, J. J., Itsweire, E. C., Helland, K. N., and Van Atta C. W., 1988, "An Investigation of the Growth of Turbulence in a Uniform-Mean-Shear Flow," *Journal of Fluid Mechanics*, Vol. 187, pp. 1–33.

Roshko, A., 1954, "On the Development of Turbulent Wakes from Vortex Streets," NACA-TN 1191.

Tamura, H., Kiya, M., and Arie, M., 1980, "Numerical Study on Viscous Shear Flow Past a Circular," *Bulletin of JSME*, Vol. 23, pp. 1952–1958.

Williamson, C. H. K., 1989, "Oblique and Parallel Modes of Vortex Shedding in the Wake of a Circular Cylinder at Low Reynolds Numbers," *Journal of Fluid Mechanics*, Vol. 26, pp. 576–626.

The Measurement of Solid-Liquid Contact Angles

Kenji Katoh,[1] Hideomi Fujita,[2] Hideharu Sasaki,[3] and Koichi Miyashita[4]

A new method is proposed for measuring solid-liquid contact angles. The well-known phenomenon where the liquid meniscus formed under a downward facing solid surface spontaneously breaks at a certain height is utilized in the contact angle measurements. The relation between the contact angle and the critical height of the solid surface where the instability occurs was derived theoretically from the solid-liquid wetting behavior using a thermodynamic approach. From the theoretical model the contact angles can be obtained by measuring the critical height of the solid. The validity of the analysis and the usefulness of the method were experimentally confirmed for various solid surfaces and test liquids.

1 Introduction

In an earlier communication (Katoh et al., 1990), we investigated theoretically the macroscopic wetting behavior from a thermodynamic viewpoint and clarified the mechanism by which a liquid meniscus formed under a solid cone surface becomes unstable and falls spontaneously from the surface at a certain cone height.

In this report, we propose a new method for measuring contact angles, which is a parameter describing solid-liquid wettability, based on the above unstable behavior of the meniscus. The usefulness of the proposed method was confirmed experimentally and the validity of the previous analysis of Katoh et al. (1990) is discussed using the experimental results.

2 Principle of the Present Method

2.1 Wetting Behavior of a Meniscus Existing Under a Solid Cone Surface. In our earlier investigation, a model of an axisymmetric liquid meniscus formed under a downward facing cone of half vertical angle ϕ, as shown in Fig. 1, was developed and the wetting behavior of the meniscus was examined by calculating the system free energy. In the figure r_0 is the meniscus radius at the point of attachment of the meniscus to the solid surface and H_B indicates the height of the cone vertex from the stationary liquid surface. Details concerning the system energy E comprise: (i) the energy change caused by the conversion of solid surface into solid-liquid interface $E_{SV\text{-}SL}$, (ii) the energy of meniscus formation E_M; namely, the change of the liquid surface energy and the meniscus potential energy.

In the above energies, E_M can be obtained by using the meniscus profile. For the calculation of $E_{SV\text{-}SL}$, we considered a hypothesis in the preceding report that the energy difference between the solid surface and the solid-liquid interface per unit area [i.e., ($\sigma_{SV} - \sigma_{SL}$) ($\sigma_{SU}$: solid surface tension; σ_{SL}: solid-liquid interfacial tension] could be calculated by modified Young's equation as

$$\sigma_{SV} - \sigma_{SL} = \sigma_{LV} \cos \theta_Y \qquad (1)$$

where σ_{LV} is liquid surface tension and θ_Y is the apparent contact angle observed macroscopically; $\theta_Y = \theta_{YR}$ (receding

---

[1] Lecturer, Department of Mechanical Engineering, Osaka City University, Osaka 558, Japan.

[2] Professor, Department of Mechanical Engineering, Nagoya University, Nagoya 464-01, Japan.

[3] Ishikawajima System Technology Co., Ltd., Tokyo 102, Japan.

[4] Nihongaishi Co., Ltd., Nagoya 467, Japan.

Contributed by the Fluids Engineering Division of THE AMERICAN SOCIETY OF MECHANICAL ENGINEERS. Manuscript received by the Fluids Engineering Division December 29, 1990. Associate Technical Editor: C. J. Freitas.

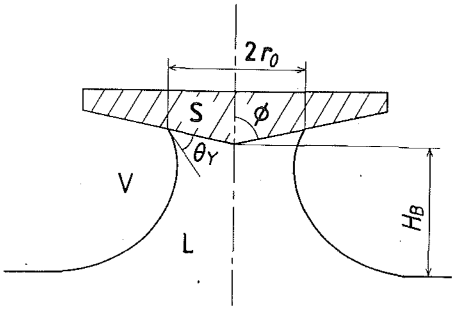

Fig. 1 Axisymmetric meniscus under a downward cone surface

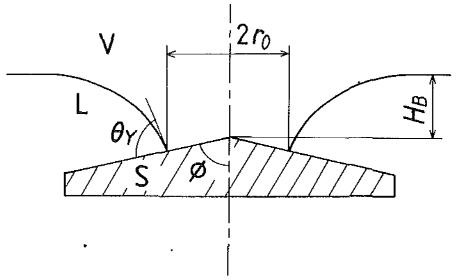

Fig. 3 Axisymmetric meniscus on an upward cone surface

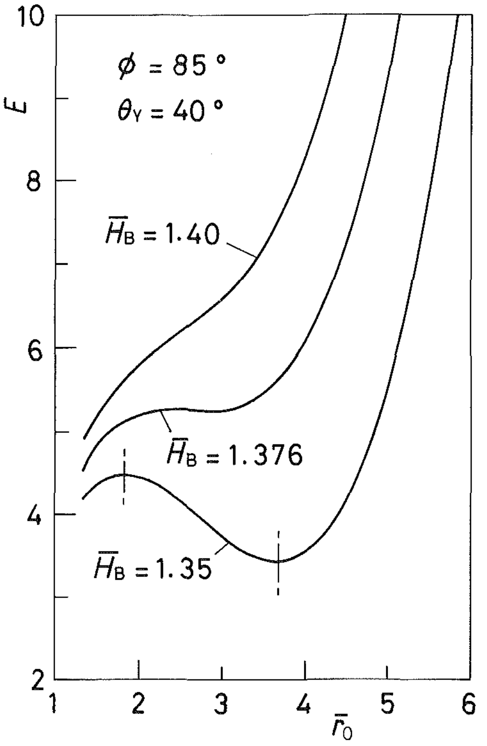

Fig. 2 Change of energy curve with $\overline{H}_B$ (downward cone)

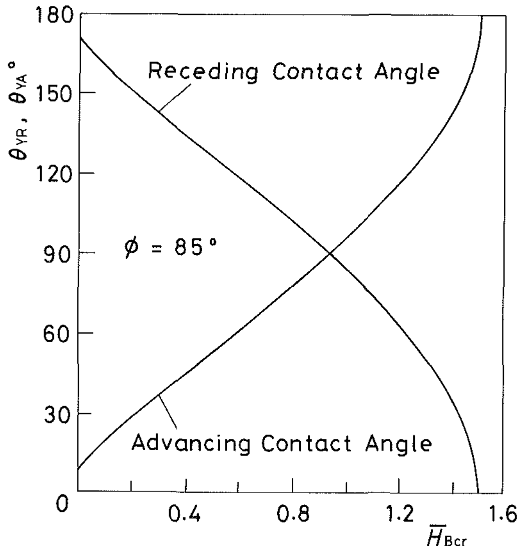

Fig. 4 Relation of apparent contact angle θ_Y to $\overline{H}_{Bcr}$

contact angle) when the liquid recedes on the solid surface and $\theta_Y = \theta_{YA}$ (advancing contact angle) when the liquid advances (Katoh et al., 1990). The application of the above modified Young's equation made the analysis of the macroscopic wetting behavior simple because the complicated effect of surface roughness or impurities on the wetting behavior can be incorporated in the value of θ_Y. The validity of this assumption will be confirmed in this study.

Details of the above analytical method are included in the preceding report.

Figure 2 shows the typical results of system energy calculated for apparent contact angle θ_Y = 40°. The symbols with an overbar, namely, $\overline{E}$, $\overline{r}_0$, *and* $\overline{H}_B$ in Fig. 2, are nondimensionalized values defined as

$$\overline{E}=E/\left(\frac{\sigma_{LV}^2}{\Delta\rho g}\right),\ \overline{r}_0=r_0/\sqrt{\sigma_{LV}/\Delta\rho g},\ \overline{H}_B=H_B/\sqrt{\sigma_{LV}/\Delta\rho g} \tag{2}$$

where $\Delta\rho$ is density difference between liquid and gas and g is gravitational acceleration. As shown in Fig. 2, when the cone height $\overline{H}_B$ is small, the meniscus is stable at the radius $\overline{r}_0$ corresponding to the minimum energy conditions. For larger $\overline{H}_B$ values such as $\overline{H}_B > 1.376$, since the system energy does not have minimum and decreases monotonously in the direction of decreasing r_0, the meniscus spontaneously shrinks and falls from the solid surface. In this case, the meniscus recedes on the surface and the occurrence of the instability relates to the receding contact angle θ_{YR}.

The wetting behavior of the meniscus formed on the upward facing cone as shown in Fig. 3 can be analysed in the same manner as above. Just as in Fig. 2, the meniscus becomes unstable for $\overline{H}_B$ larger than a critical value. When the instability occurs, the radius of the meniscus decreases spontaneously and the liquid wets the solid surface completely. Since the liquid advances on the solid surface, the critical $\overline{H}_B$ of the upward cone corresponds to the advancing contact angle θ_{YA}.

2.2 Proposed Method for Measuring Contact Angles. From the theoretical predictions for the axisymmetric meniscus on the cone surface, there is a functional relation between the apparent contact angle θ_Y and the critical height of the solid cone $\overline{H}_{Bcr}$ at which the meniscus becomes unstable. The calculated results for the relation between θ_Y and $\overline{H}_{Bcr}$ are shown in Fig. 4. As shown in the figure, θ_Y can be obtained from the measurements of $\overline{H}_{Bcr}$. The method proposed above can facilitate the measurement of contact angles because θ_Y is obtained simply from direct measurement of the cone height.

3 Experimental Methods and Results

3.1 Experimental Methods. Figure 5 shows the outline of the experimental apparatus for measuring contact angles by the proposed method. The solid cone sample 4 manufac-

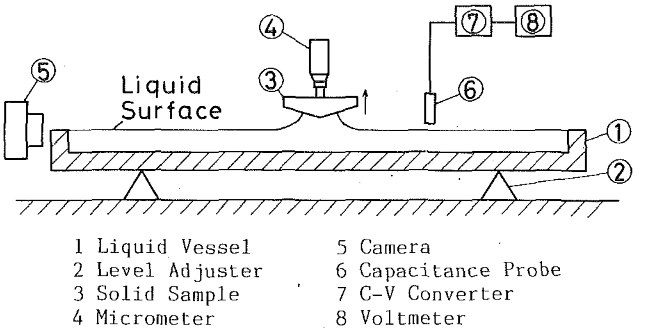

Fig. 5 Outline of experimental apparatus

Table 1 Properties of test liquids

Liquid	Temp. (°C)	Density (kg/m³)	Surface Tension (N/m)
Water	12 ~ 19	998 ~ 1000	0.0736 ~ 0.0743
Ethanol Solution	12 ~ 19	965 ~ 975	0.0368 ~ 0.0428

tured by a lathe is attached to the micrometer 5 and is adjusted vertical to the stationary liquid surface. The height of the cone vertex from the bottom of the liquid vessel 1 when the meniscus becomes unstable is measured by the micrometer. Then $\overline{H}_{Bcr}$ is obtained by subtracting the liquid depth measured by the capacitance probe 7 from the above cone height. In order to confirm the validity of the method using $\overline{H}_{Bcr}$, the contact angle was also measured from the meniscus profile photographed by the camera 6.

In the experiment, we used four kinds of solid samples (i.e., blass, duralmin, vinyl chloride, and teflon). Each surface of the above four kinds of solid samples except teflon was finished by two methods; namely, polishing and turning, in order to change surface characteristics and hence contact angle values. Therefore, seven kinds of solid samples with different surface characteristics were used. Teflon is too soft to produce a smooth finish by polishing and only the surface finished by turning was used.

Using water and ethanol-water solution, the contact angles were measured for various combinations of liquid and solid samples. The properties of the test liquids are summarized in Table 1.

Cone samples were washed sufficiently by water and neutral cleanser at every measurements in order not to change the surface characteristics. After drying up, $\overline{H}_{Bcr}$ was measured. The measurement of $\overline{H}_{Bcr}$ was repeated five or six times to confirm sufficient reproducibility. Then photographs of the meniscus were taken and the contact angles were measured. The scatter of measured $\overline{H}_{Bcr}$'s was less than 5/1000 mm for each measurement and hence good reproducibility was confirmed.

3.2 Experimental Results and Discussion. Figure 6 provides the plots of the receding and the advancing contact angles θ_{YR} and θ_{YA} measured by photograph versus measured $\overline{H}_{Bcr}$'s. The curve in the figure describes the theoretical results stated in Section 2, which indicates the theoretical contact angles calculated from $\overline{H}_{Bcr}$'s. As shown in the figure, both contact angles θ_{YR} and θ_{YA} measured by photograph agree well with theoretical values obtained by $\overline{H}_{Bcr}$, regardless of solid surfaces and liquids.

From the above experimental results, we can verify the validity of the analysis based on the assumption of modified Young's equation and of the proposed method for measuring contact angles. The method proposed in this study has some advantages compared with other methods proposed in the past (Bayramli and Mason, 1981; Chappius, 1982; Cain et al., 1983; and Huh and Reed, 1983), which are described as follows; (i) the advancing and receding contact angles can be obtained from relatively simple measurement, (ii) good reproducibility can be expected because the measurement applys clear phenomena of the meniscus fall down.

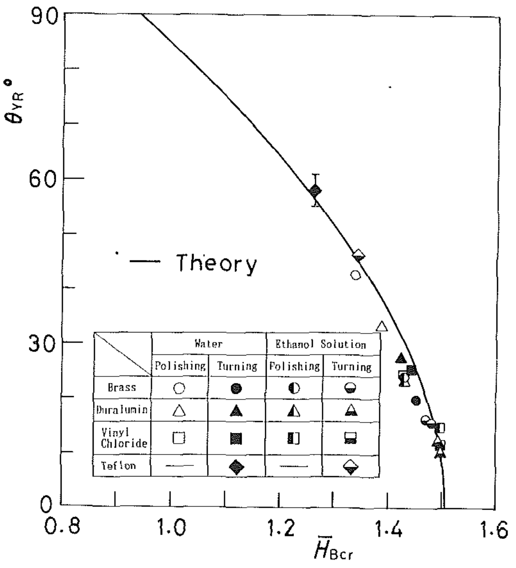

Fig. 6(a) Receding contact angles

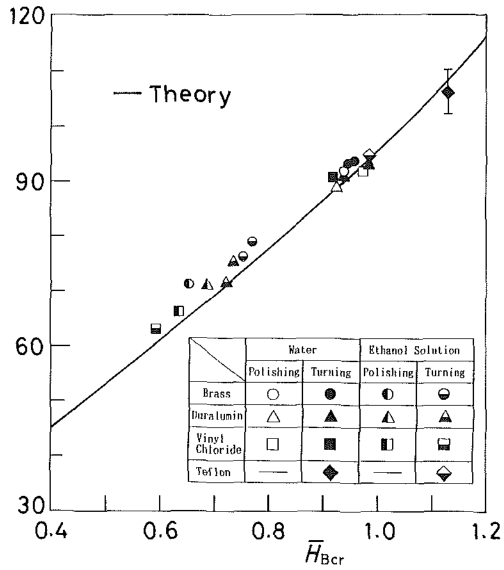

Fig. 6(b) Advancing contact angles

Fig. 6 Comparison of measured contact angles with theoretical ones (I: 95 percent confidence uncertainty of contact angles measured by photograph)

4 Conclusion

A new method for measuring contact angles based on the unstable behavior of meniscus on a solid cone surface was proposed and its validity and usefulness were confirmed by some experiments. The experimental results indicate also the validity of the hypothesis in the preceding report (Katoh et al. 1990) that Young's equation can be applied to a macroscopic system by use of apparent contact angles instead of Young's contact angle.

Acknowledgments

The authors thank Mr. Shiraki and Mr. Tachibana of Nagoya University for their effort of manufacture of experimental apparatus and solid cone examples. This research was supported by the Japanese Ministry of Education through a Grant-in-Aid for Scientific Research (grant No. 62750142).

References

Bayramli, E., and Mason, S. G., 1981, "Tensiometric Studies on Wetting II, Some Effects of Surface Roughness (Experimental)," *Can. J. Chem.*, Vol. 59, pp. 1962–1968.

Cain, J. B., Francis, D. W., Venter, R. D., and Neumann, A. W., 1983, "Dynamic Contact Angles on Smooth and Rough Surfaces," *J. Colloid Interf. Sci.*, Vol. 94, pp. 123–130.

Chappius, J., 1982, "Contact Angles," *Multiphase Science and Technology*, Vol. 1, Eds., Hewitt, G. F., Delhaye, J. M. and Zuber, N., pp. 387–505.

Huh, C., and Reed, R. L., 1983, "A Method for Estimating Interfacial Tensions and Contact Angles from Sessile and Pendant Drop Shapes," *J. Colloid Interf. Sci.*, Vol. 91, pp. 472–484.

Katoh, K., Fujita, H., and Sasaki, H., 1990, "Macroscopic Wetting Behavior and a Method for Measuring Contact Angles," ASME JOURNAL OF FLUIDS ENGINEERING, Vol. 112, pp. 289–295.

A Note on a Generalized Eddy-Viscosity Hypothesis

P. Andreasson[1] and U. Svensson[1]

The standard eddy-viscosity concept postulates that zero velocity gradient is accompanied by zero shear stress. This is not true for many boundary layer flows: wall jets, asymmetric channel flows, countercurrent flows, for example. The generalized eddy-viscosity hypothesis presented in this paper, relaxes this limitation by recognizing the influence of gradients in the turbulent length scale and the shear. With this new eddy-viscosity concept, implemented into the standard $k-\epsilon$ model, predictions of some boundary layer flows are made. The modelling results agree well with measurements, where predictions with the standard eddy-viscosity concept are known to fail.

1 Introduction

Boussinesq, in 1877, introduced the eddy-viscosity concept by suggesting an analogy of Newton's law of friction for turbulent flows. Prandtl (1925, 1945), influenced by the kinetic theory of gases, developed the eddy-viscosity idea by proposing that the eddy viscosity, ν_T, is proportional to the product of a fluctuating velocity u_T and a turbulent length scale l. For a shear flow with mean velocity gradients in only one direction, say y, we thus have:

$$-\rho\overline{uv} = \rho u_T l \frac{\partial U}{\partial y} = \rho \nu_T \frac{\partial U}{\partial y} \tag{1}$$

where $-\overline{uv}$ denotes the kinematic shear stress and ρ density. The basic idea of Eq. (1) can briefly be described as follows: Mass is exchanged across a plane perpendicular to y, at a rate of ρu_T (kg/s,m^2). Due to continuity across the plane, half of the exchanged mass is with upper layers and half with layers below the plane. The mass is considered to be exchanged in fluid lumps, having a "mean-free-path" of traveling, l, with the momentum unchanged. Hence:

$$-\rho\overline{uv} = \frac{1}{2} u_T \left[\left\{ \rho U + l \frac{\partial}{\partial y}(\rho U) \right\} - \rho U \right] + \frac{1}{2} u_T \left[\rho U - \left\{ \rho U - l \frac{\partial}{\partial y}(\rho U) \right\} \right] = \rho u_T l \frac{\partial U}{\partial y} \tag{2}$$

is the momentum exchange across the plane at y.

The eddy-viscosity concept has become extensively used. Most zero, one, and two-equation turbulence models apply ν_T for closure. However, the analogy to the kinetic theory of gases fails in many respects. The reason for this is not discussed here (see for example Reynolds, 1974 or Tennekes and Lumley, 1972). However, the resulting modeling limitations are mainly two:

1. Since the eddy-viscosity is defined as a scalar, the turbulent "momentum diffusivity" must be equal in all directions. Since isotropic diffusivity is unrealistic for complex flows, the ν_T concept may break down.
2. Equation (1) is a gradient transport law, where zero velocity gradient is accompanied by zero shear stress. This is true for Couette and Poiseuille flow, but not for wall jets, asymmetric channel flows, countercurrent flows, for instance. As will be shown later, Eq. (1) is only valid for flows where turbulent shear stresses ($-\overline{uv}$) are in local equilibrium, which limits the applicability of the equation.

The objective of the present paper is to derive and evaluate an eddy-viscosity hypothesis which relaxes limitation 2 above. The approach will be computational rather than physical, meaning that the recent evidence (see for example, Bernard and Handler, 1990) of pressure and viscous effects on the displacement of fluid lumps will not be considered. Instead the simplest possible generalization of Eq. (1) that relaxes limitation 2 and which can be used with a two-equation closure model is sought.

2 Reexamining Prandtl's Concept

In Eq. (2) it is assumed that l and $\partial U/\partial y$ is the same for fluid elements coming from above as for those coming from below the plane where the shear stress is evaluated. The basic idea in the eddy-viscosity hypothesis presented in this paper is to relax this assumption by introducing gradients in l and $\partial U/\partial y$. For a one-dimensionally sheared turbulent flow we can then, in analog with Eq. (2), write the shear stress as:

$$-\rho\overline{uv} = \frac{1}{2} u_T l_u \left[\frac{\partial}{\partial y}(\rho U) \right]_u + \frac{1}{2} u_T l_d \left[\frac{\partial}{\partial y}(\rho U) \right]_d \tag{3}$$

where "u" and "d" are indices for *up* and *down*, respectively. The length l_u may be expressed as the length l at y, plus the growth of l with y over l_u. Or, provided that $l \gg |l(\partial l/\partial y)|$

$$l_u \approx l + l\frac{\partial l}{\partial y} \text{ and } l_d \approx l - l\frac{\partial l}{\partial y}$$

Likewise, the velocity gradients may be approximated by

$$\left(\frac{\partial U}{\partial y}\right)_u \approx \frac{\partial U}{\partial y} + l\frac{\partial^2 U}{\partial y^2} \text{ and } \left(\frac{\partial U}{\partial y}\right)_d \approx \frac{\partial U}{\partial y} - l\frac{\partial^2 U}{\partial y^2}$$

Hence, Eq. (3) now becomes:

$$-\overline{uv} = \frac{1}{2} u_T \left[\left(l + l\frac{\partial l}{\partial y} \right) \left(\frac{\partial U}{\partial y} + l\frac{\partial^2 U}{\partial y^2} \right) + \left(l - l\frac{\partial l}{\partial y} \right) \left(\frac{\partial U}{\partial y} - l\frac{\partial^2 U}{\partial y^2} \right) \right]$$

or

$$-\overline{uv} = u_T l \frac{\partial U}{\partial y} + u_T l^2 \frac{\partial l}{\partial y} \frac{\partial^2 U}{\partial y^2} \tag{4}$$

The product $u_T l$ in Eq. (4), is "eddy diffusivity" for momentum corresponding to ν_T in Eq. (1). By introducing Γ_T as this eddy diffusivity, Eq. (4) may be expressed as

$$-\overline{uv} = \Gamma_T \frac{\partial U}{\partial y} + l\Gamma_T \frac{\partial l}{\partial y} \frac{\partial^2 U}{\partial y^2} \tag{5}$$

---

[1] Water Resources Engineering, Luleå University of Technology, Luleå, Sweden.

Contributed by the Fluids Engineering Division of THE AMERICAN SOCIETY OF MECHANICAL ENGINEERS. Manuscript received by the Fluids Engineering Division October 31, 1991. Associate Technical Editor: J. A. C. Humphrey.

apparatus and solid cone examples. This research was supported by the Japanese Ministry of Education through a Grant-in-Aid for Scientific Research (grant No. 62750142).

References

Bayramli, E., and Mason, S. G., 1981, "Tensiometric Studies on Wetting II, Some Effects of Surface Roughness (Experimental)," *Can. J. Chem.*, Vol. 59, pp. 1962–1968.

Cain, J. B., Francis, D. W., Venter, R. D., and Neumann, A. W., 1983, "Dynamic Contact Angles on Smooth and Rough Surfaces," *J. Colloid Interf. Sci.*, Vol. 94, pp. 123–130.

Chappius, J., 1982, "Contact Angles," *Multiphase Science and Technology*, Vol. 1, Eds., Hewitt, G. F., Delhaye, J. M. and Zuber, N., pp. 387–505.

Huh, C., and Reed, R. L., 1983, "A Method for Estimating Interfacial Tensions and Contact Angles from Sessile and Pendant Drop Shapes," *J. Colloid Interf. Sci.*, Vol. 91, pp. 472–484.

Katoh, K., Fujita, H., and Sasaki, H., 1990, "Macroscopic Wetting Behavior and a Method for Measuring Contact Angles," ASME Journal of Fluids Engineering, Vol. 112, pp. 289–295.

A Note on a Generalized Eddy-Viscosity Hypothesis

P. Andreasson[1] **and U. Svensson**[1]

The standard eddy-viscosity concept postulates that zero velocity gradient is accompanied by zero shear stress. This is not true for many boundary layer flows: wall jets, asymmetric channel flows, countercurrent flows, for example. The generalized eddy-viscosity hypothesis presented in this paper, relaxes this limitation by recognizing the influence of gradients in the turbulent length scale and the shear. With this new eddy-viscosity concept, implemented into the standard $k-\epsilon$ model, predictions of some boundary layer flows are made. The modelling results agree well with measurements, where predictions with the standard eddy-viscosity concept are known to fail.

1 Introduction

Boussinesq, in 1877, introduced the eddy-viscosity concept by suggesting an analogy of Newton's law of friction for turbulent flows. Prandtl (1925, 1945), influenced by the kinetic theory of gases, developed the eddy-viscosity idea by proposing that the eddy viscosity, ν_T, is proportional to the product of a fluctuating velocity u_T and a turbulent length scale l. For a shear flow with mean velocity gradients in only one direction, say y, we thus have:

$$-\rho\overline{uv} = \rho u_T l \frac{\partial U}{\partial y} = \rho \nu_T \frac{\partial U}{\partial y} \tag{1}$$

where $-\overline{uv}$ denotes the kinematic shear stress and ρ density. The basic idea of Eq. (1) can briefly be described as follows: Mass is exchanged across a plane perpendicular to y, at a rate of ρu_T (kg/s,m^2). Due to continuity across the plane, half of the exchanged mass is with upper layers and half with layers below the plane. The mass is considered to be exchanged in fluid lumps, having a "mean-free-path" of traveling, l, with the momentum unchanged. Hence:

$$-\rho\overline{uv} = \frac{1}{2} u_T \left[\left\{\rho U + l \frac{\partial}{\partial y}(\rho U)\right\} - \rho U\right] + \frac{1}{2} u_T \left[\rho U - \left\{\rho U - l \frac{\partial}{\partial y}(\rho U)\right\}\right] = \rho u_T l \frac{\partial U}{\partial y} \tag{2}$$

is the momentum exchange across the plane at y.

The eddy-viscosity concept has become extensively used. Most zero, one, and two-equation turbulence models apply ν_T for closure. However, the analogy to the kinetic theory of gases fails in many respects. The reason for this is not discussed here (see for example Reynolds, 1974 or Tennekes and Lumley, 1972). However, the resulting modeling limitations are mainly two:

1. Since the eddy-viscosity is defined as a scalar, the turbulent "momentum diffusivity" must be equal in all directions. Since isotropic diffusivity is unrealistic for complex flows, the ν_T concept may break down.
2. Equation (1) is a gradient transport law, where zero velocity gradient is accompanied by zero shear stress. This is true for Couette and Poiseuille flow, but not for wall jets, asymmetric channel flows, countercurrent flows, for instance. As will be shown later, Eq. (1) is only valid for flows where turbulent shear stresses ($-\overline{uv}$) are in local equilibrium, which limits the applicability of the equation.

The objective of the present paper is to derive and evaluate an eddy-viscosity hypothesis which relaxes limitation 2 above. The approach will be computational rather than physical, meaning that the recent evidence (see for example, Bernard and Handler, 1990) of pressure and viscous effects on the displacement of fluid lumps will not be considered. Instead the simplest possible generalization of Eq. (1) that relaxes limitation 2 and which can be used with a two-equation closure model is sought.

2 Reexamining Prandtl's Concept

In Eq. (2) it is assumed that l and $\partial U/\partial y$ is the same for fluid elements coming from above as for those coming from below the plane where the shear stress is evaluated. The basic idea in the eddy-viscosity hypothesis presented in this paper is to relax this assumption by introducing gradients in l and $\partial U/\partial y$. For a one-dimensionally sheared turbulent flow we can then, in analog with Eq. (2), write the shear stress as:

$$-\rho\overline{uv} = \frac{1}{2} u_T l_u \left[\frac{\partial}{\partial y}(\rho U)\right]_u + \frac{1}{2} u_T l_d \left[\frac{\partial}{\partial y}(\rho U)\right]_d \tag{3}$$

where "u" and "d" are indices for *up* and *down*, respectively. The length l_u may be expressed as the length l at y, plus the growth of l with y over l_u. Or, provided that $l >> |l(\partial l/\partial y)|$

$$l_u \approx l + l\frac{\partial l}{\partial y} \text{ and } l_d \approx l - l\frac{\partial l}{\partial y}$$

Likewise, the velocity gradients may be approximated by

$$\left(\frac{\partial U}{\partial y}\right)_u \approx \frac{\partial U}{\partial y} + l\frac{\partial^2 U}{\partial y^2} \text{ and } \left(\frac{\partial U}{\partial y}\right)_d \approx \frac{\partial U}{\partial y} - l\frac{\partial^2 U}{\partial y^2}$$

Hence, Eq. (3) now becomes:

$$-\overline{uv} = \frac{1}{2} u_T \left[\left(l + l\frac{\partial l}{\partial y}\right)\left(\frac{\partial U}{\partial y} + l\frac{\partial^2 U}{\partial y^2}\right) + \left(l - l\frac{\partial l}{\partial y}\right)\left(\frac{\partial U}{\partial y} - l\frac{\partial^2 U}{\partial y^2}\right)\right]$$

or

$$-\overline{uv} = u_T l \frac{\partial U}{\partial y} + u_T l^2 \frac{\partial l}{\partial y}\frac{\partial^2 U}{\partial y^2} \tag{4}$$

The product $u_T l$ in Eq. (4), is "eddy diffusivity" for momentum corresponding to ν_T in Eq. (1). By introducing Γ_T as this eddy diffusivity, Eq. (4) may be expressed as

$$-\overline{uv} = \Gamma_T \frac{\partial U}{\partial y} + l\Gamma_T \frac{\partial l}{\partial y}\frac{\partial^2 U}{\partial y^2} \tag{5}$$

---

[1] Water Resources Engineering, Luleå University of Technology, Luleå, Sweden.

Contributed by the Fluids Engineering Division of The American Society of Mechanical Engineers. Manuscript received by the Fluids Engineering Division October 31, 1991. Associate Technical Editor: J. A. C. Humphrey.

which is the generalized eddy-viscosity hypothesis sought.

If Eqs. (1) and (4) are compared, it is obvious that the difference (i.e., the additional term in Eq. 4) is due to the introduction of gradients in $\partial U/\partial y$ and l. One consideration behind expression (1) is that the same amount of momentum that is being transferred from upper layers is exchanged to lower layers. Evidently the net momentum gain is zero, with the standard eddy-viscosity expression (1). This is identical to a zero diffusive contribution (vertical net redistribution) to $-\overline{uv}$. This is not the case for expression (4), for which a net momentum gain (or loss) is possible. Evidently, the additional term $u_T l^2 (\partial l/\partial y)\,(\partial^2 U/\partial y^2)$ is due to a diffusive contribution to $-\overline{uv}$. Hence, the budget for $\overline{uv}$ needs no longer be in local equilibrium as was implicitly postulated by Eq. (1). This interpretation of the second term as a diffusive contribution will be discussed further, later in the paper.

The idea to introduce gradients of length scale and shear, it should be pointed out, is not new: see for example, Tennekes and Lumley (1972) and Doshi and Gill (1970). The expression derived above, Eq. (5), is however, to the authors' knowledge, novel.

3 A Comparison With the "Law of the Wall"

Prandtl (1925), assumed that the turbulent length scale is proportional to the distance from the wall, $l = \kappa y$, and that $u_T = l|\partial U/\partial y|$. For a constant-stress layer outside the buffer layer, where $-\overline{uv} = U_\tau^2$, these assumptions combined with the eddy-viscosity expression (1), yields the well known logarithmic velocity profile

$$\frac{U}{U_\tau} = \frac{1}{\kappa}\ln(y) + C \tag{6}$$

Analogous assumptions, except that $l = \alpha y$, give for Eq. (4) the differential equation

$$U_\tau^2 = \alpha^2 y^2 \left(\frac{\partial U}{\partial y}\right)^2 + \alpha^4 y^3 \frac{\partial U}{\partial y}\frac{\partial^2 U}{\partial y^2}$$

which satisfies

$$\frac{U}{U_\tau} = \frac{1}{\alpha\sqrt{1-\alpha^2}}\ln(y) + C \tag{7}$$

We see that Eqs. (6) and (7) are equal if $\alpha = 0.45$ $(\kappa = 0.4)$. Hence, the new expression does not contradict the (experimentally) well established log-law.

4 Integration With the k-ϵ Model

If Eq. (5) is to be used with the standard k-ϵ model, a relation between Γ_T and the eddy-viscosity in the k-ϵ model, ν_T, is needed. Also a relation between the length scale l in (5) and the integral length-scale, L, given by the k-ϵ model is required.

A relation between ν_T and Γ_T can be obtained from the logarithmic velocity profile (6). Using $l = \alpha y$, expression (5) becomes:

$$-\overline{uv} = \Gamma_T \frac{U_\tau}{\kappa y} - \Gamma_T \alpha^2 y \frac{U_\tau}{\kappa y^2} = \Gamma_T \frac{U_\tau}{\kappa y}(1-\alpha^2) \tag{8}$$

The standard eddy-viscosity concept, $-\overline{uv} = \nu_T(\partial U/\partial y)$, for the same profile, becomes

$$-\overline{uv} = \nu_T \frac{U_\tau}{\kappa y} \tag{9}$$

Apparently, if Eqs. (8) and (9) are compared, $\nu_T = \Gamma_T(1-\alpha^2)$, or $\Gamma_T = \nu_T/\sigma_m$ where $\sigma_m = (1-\alpha^2)$. Since $\alpha = 0.45$, $\sigma_m = 0.8$.

In the standard k-ϵ model an integral length scale can be determined from the Prandtl-Kolmogorov length scale, $L = C_D\,(k^{3/2}/\epsilon)$. Near the wall in a boundary layer, L satisfies κy. Since l in Eq. (5) should satisfy αy for such regions, it is implied that l may be expressed as $l = (\alpha/\kappa)\,L$ or $l = (\alpha/\kappa)\,C_D\,(k^{3/2}/\epsilon) = C'_D(k^{3/2}/\epsilon)$.

The standard (high Reynolds number) k-ϵ model (Rodi, 1980) reads

$$\frac{Dk}{Dt} = -\overline{uv}\frac{\partial U}{\partial y} - \epsilon + \frac{\partial}{\partial y}\left(\frac{\nu_T}{\sigma_k}\frac{\partial k}{\partial y}\right) \tag{10}$$

for turbulent kinetic energy k, and

$$\frac{D\epsilon}{Dt} = -C_{\epsilon 1}\frac{\epsilon}{k}\overline{uv}\frac{\partial U}{\partial y} - C_{\epsilon 2}\frac{\epsilon^2}{k} + \frac{\partial}{\partial y}\left(\frac{\nu_T}{\sigma_\epsilon}\frac{\partial \epsilon}{\partial y}\right) \tag{11}$$

for dissipation rate ϵ, $\{\sigma_k = 1.0,\ \sigma_\epsilon = 1.3,\ C_{\epsilon 1} = 1.92,\ C_{\epsilon 2} = 1.44\}$. These two transport equations are retained in their standard form. Also the standard eddy-viscosity expression is retained

$$\nu_T = C_\mu \frac{k^2}{\epsilon} \tag{12}$$

where $C_\mu = 0.09$. It is thus the standard form of the k-ϵ model which is to be used with the generalized eddy-viscosity concept. With $\Gamma_T = \nu_T/\sigma_m$ the final expression reads:

$$-\overline{uv} = \frac{\nu_T}{\sigma_m}\frac{\partial U}{\partial y} + \frac{\nu_T}{\sigma_m}\,l\,\frac{\partial l}{\partial y}\frac{\partial^2 U}{\partial y^2} \tag{13}$$

where

$$l = C'_D \frac{k^{3/2}}{\epsilon}$$

and $C'_D = (\alpha/\kappa)C_D$. With $C_D = 0.164$, $\alpha = 0.45$, and $\kappa = 0.4$ the coefficient C'_D becomes 0.185.

5 Numerical Calculations

A first evaluation of the eddy-viscosity hypothesis proposed will be carried out for the following wall-bounded shear flows: Poiseuille and Couette flows, the asymmetric channel flow and the wall jet. The first two of these are flows for which the standard k-ϵ model works fairly well and the main purpose of applying the new expression is to ensure that this agreement is not upset. The last two flows are classical examples on flows where the standard eddy-viscosity concept fails, as the shear stress and the velocity gradient do not change sign at the same position.

The new hypothesis was found to give almost identical predictions as the standard k-ϵ model, for the fully developed Poiseuille and Couette flows. This is encouraging as the standard k-ϵ model is in good agreement with, for example, the measurements by El Telbany and Reynolds (1980).

The asymmetric channel flow has previously been analyzed by Hanjali'c and Launder (1972), who used a Reynolds-stress closure to capture the difference in position between the change of sign of $\overline{uv}$ and $\partial U/\partial y$. Present predictions are summarized in Table 1, where also results from the standard eddy-viscosity expression and measurements are found. As expected, the standard eddy-viscosity expression does not capture the non-coincidence of the positions mentioned. However, with the new expression predictions are in perfect agreement with the measurements.

The turbulent wall jet is the final flow to be discussed. The measurements by Tailland and Mathieu (1967) are in Table 2 compared to present predictions. The predicted positions of zero shear-stress and zero velocity gradient, agree fairly well with measured positions. From the review by Launder and Rodi (1981) it is clear that measurements from different sources do deviate quite significantly, which means that the present predictions may be within the experimental uncertainty.

Table 1 Comparison of positions of maximum velocity and zero shear stress for the asymmetric channel flow (Reynolds number = 56 000). The positions are given as the nondimensional distance from the rough wall.

	Maximum velocity	Zero shear stress
Measured (from Hanjali'c and Launder, 1972)	0.76–0.77	0.82–0.83
Calculated, new expression	0.769	0.825
Calculated, standard expression	0.809	

Table 2 Comparison of positions of maximum velocity and zero shear stress for the wall jet (Reynolds number = 18 000). The positions are given as the distance from the wall normalized with $y_{1/2}$, the distance from the wall to where $U = 0.5\ U_{\max}$ and $\partial U/\partial y$ is negative.

	Maximum velocity	Zero shear stress
Measured (from Tailland and Mathieu, 1967)	0.14–0.15	0.07–0.08
Calculated, new expression	0.160	0.042
Calculated, standard expression	0.058	

The calculations presented, using the new eddy-viscosity hypothesis, should not be regarded as verification cases but do nevertheless indicate that the noncoincidence of zero shear stress and zero shear can be captured. It has also been demonstrated that the new expression can be used with the standard k-ϵ model, which is of interest from a practical point of view. Predictions presented were tested for grid-independence and can thus be considered as the true implication of the governing equations.

6 Discussion

The numerical calculations presented indicate that the generalized eddy-viscosity hypothesis can predict the noncoincidence of the zero shear stress and the maximum velocity in the asymmetric channel flow and the wall jet. This is the desired result and the suggested eddy-viscosity hypothesis thus deserves to be further tested and analyzed.

Support for the new hypothesis can be found from a high Reynolds number second-moment closure. Following, for example, Launder et al. (1975) the transport equation for $\overline{uv}$ may be written:

$$\frac{D\overline{uv}}{Dt}=P_{\overline{uv}}+\Phi_{\overline{uv}}+D_{\overline{uv}} \tag{14}$$

where the terms on the right-hand side represent production, pressure-strain (destruction), and diffusion of $\overline{uv}$. For stationary, one-dimensionally sheared flow, and with the model by Launder et al. (1975) applied (model 2), Eq. (14) becomes

$$0=-\overline{v^2}\,\frac{\partial U}{\partial y}-C_1\,\frac{\epsilon}{k}\,\overline{uv}+\gamma\overline{v^2}\,\frac{\partial U}{\partial y}+D_{\overline{uv}}$$

or rearranged

$$-\overline{uv}=\frac{(1-\gamma)}{C_1}\,\overline{v^2}\,\frac{k}{\epsilon}\,\frac{\partial U}{\partial y}-\frac{1}{C_1}\,\frac{k}{\epsilon}\,D_{\overline{uv}} \tag{15}$$

Now, let's consider the Algebraic Stress/Flux Model introduced by Rodi (1976), to determine $\overline{v}^2/k$. It has been used with success to determine the individual normal stress components of k.

$$\overline{u_iu_j}=k\left[\frac{2}{3}\,\delta_{ij}+\frac{(1-\gamma)\left(\frac{P_{ij}}{\epsilon}-\frac{2}{3}\,\delta_{ij}\,\frac{P}{\epsilon}\right)+(1-C_3)\left(\frac{G_{ij}}{\epsilon}-\frac{2}{3}\,\delta_{ij}\,\frac{G}{\epsilon}\right)}{C_1+\frac{P+G}{\epsilon}-1}\right]$$

which for the log-layer (local equilibrium, $P = \epsilon$, and no buoyancy effects, $G_{ij} = G = 0$) yields

$$\frac{\overline{v^2}}{k}=\frac{2}{3}\left(1-\frac{(1-\gamma)}{C_1}\right) \tag{16}$$

Equations (15) and (16) combined give (note that $k^2/\epsilon = \nu_T/C_\mu$)

$$-\overline{uv}=\frac{2}{3}\,\frac{(1-\gamma)}{C_1}\left(1-\frac{(1-\gamma)}{C_1}\right)\frac{1}{C_\mu}\,\nu_T\,\frac{\partial U}{\partial y}-\frac{1}{C_1}\,\frac{k}{\epsilon}\,D_{\overline{uv}} \tag{17}$$

A comparison between Eqs. (13) and (17) indicates two things

1. The Prandtl number for momentum apparently is

$$\sigma_m=\frac{3C_1C_\mu}{2(1-\gamma)}\left[1-\frac{(1-\gamma)}{C_1}\right]^{-1}$$

which with the model constants given by Gibson and Launder (1978) $\{C_1 = 1.8,\ \gamma = 0.6\}$, and $C_\mu = 0.09$ yield $\sigma_m = 0.8$. This is the same turbulent Prandtl number as was prescribed earlier from considerations of the log-law.

2. The second term on the right-hand side of Eq. (17), apparently corresponds to the additional term $(\nu_T/\sigma_m)\ (\partial l/\partial y)\ (\partial^2U/\partial y^2)$ in Eq. (13). Hence, this supports that the additional term is due to diffusive contribution to $-\overline{uv}$. $D_{\overline{uv}}$ in Eq. (17) is the net diffusive contribution to $-\overline{uv}$ per unit time, and k/ϵ is a turbulent time scale.

Even if Eqs. (13) and (17) have a similar structure one should note that the derivations are not related. The derivation by Hinze (1970) is however rather close to the present work. He expressed the shear stress as the sum of two terms, proportional to the first and second derivative of the mean velocity, respectively. The result of his derivation reads:

$$-\overline{u_2u_1}=u'^{\,2}_{2}t\,\frac{d\overline{U}_1}{dx_2}+\left[-\frac{1}{\sqrt{2\pi}}\,\frac{du'_2}{dx_2}\,u'^{\,3}_{2}t^3+\ldots\right]\frac{d^2\overline{U}_1}{dx_2^2} \tag{18}$$

in the notation from the original paper. Hinze states that the first term on the right-hand side of Eq. (18) "expresses the contribution of small scale turbulence, the second term the contribution of larger scale turbulence or of the transport of momentum over distances where the mean velocity gradient can no longer be considered as being constant." Hinze also noted that the eddy-viscosity, $u'^{\,2}_{2}t$ in (18), should be "slightly larger" than the corresponding viscosity in the standard eddy-viscosity hypothesis. This is in agreement with the introduction of $\sigma_m = 0.8$ in the present analysis.

7 Concluding Remarks

The objective of the paper is to derive, discuss and evaluate a generalized eddy-viscosity hypothesis. The theoretical aspects, i.e., relations to the log-law, the k-ϵ model, and the Reynolds stress closures, have been emphasized in this paper. It remains to evaluate the concept for scalar transport and carry out detailed verification studies before the applicability of the hypothesis can be established.

The main results can be summarized as:

- A generalized eddy-viscosity hypothesis can be derived by considering the gradients in the turbulent length scale and the shear.
- The resulting expression is found to be in agreement with the logarithmic law.
- The hypothesis is found to predict the noncoincidence

of the zero shear stress and maximum velocity in the asymmetric channel flow and the turbulent wall jet.

- Support for the new hypothesis can be found from a comparison with Reynolds stress closures and the theoretical investigation by Hinze (1970).

References

Bernard, P. S., and Handler, R. A., 1990, "Reynolds Stress and the Physics of Turbulent Momentum Transport," *Journal of Fluid Mechanics*, Vol. 220, pp. 99-124.

Doshi, M. R., and Gill, W. N., 1970, "A Note on the Mixing Length Theory of Turbulent Flow," *AIChE Journal*, Vol. 16, pp. 885-888.

El Telbany, M. M. M., and Reynolds, A. J., 1980, "Velocity Distributions in Plane Turbulent Channel Flows," *Journal of Fluid Mechanics*, Vol. 100, pp. 1-29.

Gibson, M. M., and Launder, B. E., 1978, "Ground Effects on Pressure Fluctuations in the Atmospheric Boundary Layer," *Journal of Fluid Mechanics*, Vol. 86, pp. 491-511.

Hanjali'c, K., and Launder, B. E., 1972, "A Reynolds Stress Model of Turbulence and Its Application to Thin Shear Flows," *Journal of Fluid Mechanics*, Vol. 52, pp. 609-638.

Hinze, J. O., 1970, "Turbulent Flow Regions With Shear Stress and Mean Velocity Gradient of Opposite Sign," *Appl. Sci. Res.*, Vol. 22, pp. 163-175.

Launder, B. E., Reece, G. J., and Rodi, W., 1975, "Progress in the Development of a Reynolds-Stress Turbulence Closure," *Journal of Fluid Mechanics*, Vol. 68, pp. 537-566.

Launder, B. E., and Rodi, W., 1981, "The Turbulent Wall Jet," *Prog. Aerospace Sci.*, Vol. 19, pp. 81-128.

Prandtl, L., 1925, "Bericht über Untersuchingen zur Ausgebildeten Turbulenz, *ZAMM*, Vol. 5, pp.136-139.

Prandtl, L., 1945, "Über ein Neues Formelsystem für die Ausgebildete Turbulenz," *Nachr. Akad. Wiss. Göttingen. Math.-Phys. Klasse.*, pp. 6-19.

Reynolds, A. J., 1974, *Turbulent Flows in Engineering*, Wiley, London.

Rodi, W., 1976, "A New Algebraic Relation for Calculating the Reynolds Stresses," *ZAMM*, Vol. 56, pp. T219-T221.

Rodi, W., 1980, "Turbulence Models and Their Application in Hydraulics," IAHR, Delft.

Tailland, A., and Mathieu, J., 1967, "Jet Pariétal," *Journal de Mécanique*, Vol. 6, pp. 103-131.

Tennekes, H., and Lumley, J. L., 1972, *A First Course in Turbulence*, MIT Press, Cambridge.